Transactions of the ASME®

Transactions of the ASME, Journal of Engineering for Gas Turbines and Power (ISSN 0742-4795) is published quarterly (Jan., Apr., July, Oct.,) for $130.00 per year by The American Society of Mechanical Engineers, 345 East 47th Street, New York, NY 10017. Second class postage paid at New York, NY and additional mailing offices. POSTMASTER: Send address changes to Transactions of the ASME, Journal of Engineering for Gas Turbines and Power, c/o THE AMERICAN SOCIETY OF MECHANICAL ENGINEERS, 22 Law Drive, Box 2300, Fairfield, NJ 07007-2300.
CHANGES OF ADDRESS must be received at Society headquarters seven weeks before they are to be effective. Please send old label and new address.
PRICES: To members, $40.00, annually: to nonmembers, $136.00.
Add $24.00 for postage to countries outside the United States and Canada.

INDEXED by Applied Mechanics Reviews and Engineering Information, Inc.
Canadian Goods & Services Tax Registration #126148048

Journal of Engineering for Gas Turbines and Power

Published Quarterly by The American Society of Mechanical Engineers
VOLUME 116 • NUMBER 2 • APRIL 1994

TECHNICAL PAPERS

(Contents Continued on page 284)

ANNOUNCEMENTS

Analysis of a Basic Chemically Recuperated Gas Turbine Power Plant

K. F. Kesser

M. A. Hoffman

J. W. Baughn

Department of Mechanical and Aeronautical Engineering, University of California, Davis, CA 95616

This paper investigates a "basic" Chemically Recuperated Gas Turbine (a "basic" CRGT is defined here to be one without intercooling or reheat). The CRGT is of interest due to its potential for ultralow NO_x emissions. A computer code has been developed to evaluate the performance characteristics (thermal efficiency and specific work) of the Basic CRGT, and to compare it to the steam-injected gas turbine (STIG), the combined cycle (CC) and the simple cycle gas turbine (SC) using consistent assumptions. The CRGT model includes a methane-steam reformer (MSR), which converts a methane-steam mixture into a hydrogen-rich fuel using the "waste" heat in the turbine exhaust. Models for the effects of turbine cooling air, variable specific heats, and the real gas effects of steam are included. The calculated results show that the Basic CRGT has a thermal efficiency higher than the STIG and simple cycles but not quite as high as the combined cycle.

Introduction

An analysis of the performance of the "basic" chemically recuperated gas turbine (CRGT) cycle shown in Fig. 1 is presented. The "basic" CRGT is defined in this paper to mean the cycle without intercooling or reheat. The results for the Basic CRGT will be compared to the steam-injected gas turbine cycle (STIG), the combined cycle (CC), and the simple cycle gas turbine (SC) shown in Fig. 2.

In the CRGT cycle, thermal power from the gas turbine exhaust is recovered in a heat-recovery methane-steam reformer (MSR). The MSR takes the place of the heat recovery steam generator (HRSG) used in the STIG and the combined cycle. The MSR contains an economizer section to heat the feedwater to the saturation temperature, an evaporator section to vaporize the water, and a reformer section. The main difference between the MSR and HRSG lies in the nature of the reformer section of the MSR. The tubes in the reformer (unlike the tubes in the HRSG superheater) are filled with a nickel-based catalyst that promotes a chemical reaction between steam (H_2O) and methane (CH_4). The primary products of this highly endothermic methane-steam chemical reaction are carbon dioxide (CO_2), carbon monoxide (CO), and hydrogen (H_2) plus excess methane and steam. The gaseous mixture exiting the reformer is known as a reformate and is the fuel fed into the gas turbine combustor.

One of the potential advantages of a CRGT cycle is that NO_x emissions are estimated to be lower than the NO_x emitted from the STIG cycle. In practice, NO_x concentrations as low as 25 ppm are possible with steam injection (International Power Technology, 1991), while the NO_x production in a CRGT has been estimated to be as low as 1 ppm (Janes, 1990).

To limit NO_x emissions in the STIG cycle, a portion of the steam produced in the HRSG is injected into the gas turbine combustor flame zone. Injecting steam in the flame zone lowers the flame temperature (and hence the NO_x production) by diluting the combustion reactants in the flame front. Flammability limitations and excess carbon monoxide formation limit the amount of steam that can be injected directly into the flame zone.

In the CRGT cycle the NO_x emissions are even lower, since hydrogen can extend the flammability limits of many different fuel-air-inert gas mixtures (Karim et al., 1985). Since the reformate contains hydrogen, higher steam injection levels into the flame zone should be possible with the CRGT, resulting in lower flame front temperatures in comparison to the STIG.

In order to study the effects of chemical recuperation on a gas turbine cycle, the *Basic* CRGT cycle without intercooling or reheat was chosen for this study. In addition to comparing the Basic CRGT to other cycles, we also wanted to see if the Basic CRGT would make a useful demonstration plant to test the chemical recuperation concept. When this project was started, commercial gas turbine codes (such as GATE, Erbes et al., 1989) did not include a methane-steam reformer. We had not yet become aware that the code developed by Consonni (1992) and used in the studies by Consonni (1992) and Lloyd (1991) was being adapted to study the Basic CRGT and the Advanced CRGT with intercooling and reheat. As a result, we developed our own computer code with simplified models for the components and turbine cooling to permit us to compare the different cycles using the same ground rules and assumptions. Independent studies by several groups are useful for a new concept such as the CRGT, particularly in the early stages.

Contributed by the Advanced Energy Systems Division for publication in the JOURNAL OF ENGINEERING FOR GAS TURBINES AND POWER. Manuscript received by the Advanced Energy Systems Division December 18, 1991; revision received October 12, 1993. Associate Technical Editor: M. J. Moran.

Overview of the UCDCRGT Computer Code

A computer program called UCDCRGT was developed to analyze the basic CRGT cycle, as well as the STIG, CC, and SC cycles. Figure 3 shows a simplified flowchart for the CRGT calculations. Input parameters required for all of the cycle components are listed in Tables 1(A) and 1(B) along with the values used for the reference cases (to be discussed later).

Total pressures are calculated at the beginning of the UCDCRGT code for each cycle state point based on the overall compressor pressure ratio (π_c) and the specified input pressure loss ratios for the combustor, turbine diffuser, and MSR. The air compressor, fuel compressor, and water pump outlet properties are calculated using isentropic efficiencies and the STANJAN chemical equilibrium subroutine (discussed in the next section). Next, the cold side economizer and evaporator outlet conditions are calculated using steam table equations inserted into the STANJAN subroutine. Then an iterative loop is entered where the reformer section, combustor, and turbine outlet properties are calculated until a self-consistent value of the turbine outlet temperature (T_4) is obtained. Each of the major models used in the UCDCRGT Code is discussed next.

Thermodynamic Properties

STANJAN, the chemical equilibrium code developed at Stanford University by Reynolds (1986), is used as a subroutine in UCDCRGT to calculate mixture compositions and thermodynamic properties at each cycle state point. Species thermodynamic properties utilized in STANJAN are derived from the JANAF thermochemical tables. Each of the species used in the cycle evaluations is considered to be a perfect gas with temperature-dependent specific heats with the exception of liquid and vapor water. The STANJAN FORTRAN source code has been modified for water using steam table equations developed by Irvine and Liley (1984).

Turbine Cooling Model

Figure 4 shows a diagram of the simplified turbine cooling model proposed by Oates (1988). We have adopted this approximate model and extended it to allow for cooling of the first three turbine stages. Inputs for the air-cooled turbine model include turbine stage efficiency (η_{ts}), number of turbine stages (N_{ts}), number of cooled turbine stages (N_{cts}, maximum of three), and the turbine stage *nozzle* cooling fraction (NF). The code permits the option of specifying either the cooling air fractions (CAF) or the rotor turbine inlet temperatures (total, absolute temperatures ahead of each rotor).

The NF is defined as:

$$NF = \dot{m}c_N / \dot{m}c_T \tag{1}$$

where $\dot{m}c_N$ is the stage nozzle cooling flow and $\dot{m}c_T$ is the total stage cooling flow. $\dot{m}c_T$ is defined as follows:

$$\dot{m}c_T = \dot{m}c_N + \dot{m}c_R \tag{2}$$

where $\dot{m}c_R$ is the stage rotor cooling flow. The CAF is defined as:

$$\mathrm{CAF} = \dot{m}c_T / \dot{m}_{\mathrm{air}} \tag{3}$$

where $\dot{m}_{\mathrm{air}}$ is the air compressor inlet flow. A description of the calculation procedure for each of the two options mentioned above is given in Appendix A.

Methane–Steam Reformer (MSR) Model

The MSR contains three separate sections: the economizer, the evaporator, and the reformer as mentioned earlier. Figure 5 shows a sketch of the temperature versus percentage thermal energy transferred for the MSR. (The linear segments are only approximations to the curves.) The primary design parameters for the MSR shown in Fig. 5 are the approach temperature difference (ΔT_{app}), the minimum pinch-point temperature difference (ΔT_{pp}), and the minimum stack temperature (T_{stack}). ΔT_{app} is always fixed at 20 K in the present work. Then either the ΔT_{pp} or the T_{stack} constraint determines the maximum steam flow ($\dot{m}_{st(\max)}$).

Another design parameter, the chemical equilibrium approach temperature difference (ΔT_{eq}), is used to model any chemical nonequilibrium at the exit of the reformer. ΔT_{eq} can either be specified or calculated from the following equation for a typical reformer using a nickel-based catalyst (Lloyd, 1991):

$$\Delta T_{eq} = 0, \quad T_{17} \geq 650^{\circ}\mathrm{C} \tag{4}$$

$$\Delta T_{eq} = 43.33 \times (1.0 - T_{17}/650), \quad T_{17} < 650^{\circ}\mathrm{C} \tag{5}$$

The actual size of the reformer required to give a selected ΔT_{eq} can be calculated using the reformer modeling computer code developed by Adelman (1992).

T_{17} is determined with the following equation:

$$T_{17} = T_4 - \Delta T_{\mathrm{app}} \tag{6}$$

Nomenclature

$\overline{\mathrm{CAF}}$ = cooling air fraction
CV = control volume
h = enthalpy, kJ/kg
HX_{loss} = fractional heat loss coefficient
$\dot{m}_{\mathrm{air}}$ = compressor inlet mass flow rate, kg/s
$\dot{m}_N$ = turbine flow rate across the nozzle, kg/s
$\dot{m}_{st(\max)}$ = maximum allowable steam flow rate, kg/s
$\dot{m}_R$ = turbine flow rate across the rotor, kg/s
$\dot{m}c_N$ = stage nozzle cooling flow rate, kg/s
$\dot{m}c_R$ = stage rotor cooling flow rate, kg/s
$\dot{m}c_T$ = total stage cooling flow rate, kg/s
M_k = cycle mass flow ratio
MW = molecular weight
N_{cts} = number of cooled turbine stages
N_{ts} = number of turbine stages
NF = nozzle cooling fraction
P = pressure, atm
PD = compressor bleed pressure drop factor
$\dot{Q}_{\mathrm{ECON(CS)}}$ = cold side economizer thermal power trans., kW
s = entropy, kJ/kg-K
SA = steam–air mass ratio
T = temperature, K
T_{eff} = reformate composition temperature, K
T_{stack} = minimum stack temperature, K
ΔT_{app} = approach temperature difference, K
ΔT_{eq} = chemical equil. app. temp. diff., K
ΔT_{pp} = pinch point temperature difference, K
v = specific volume, m^3/kg
$\dot{W}_{ts}$ = turbine stage power output, kW
$\dot{W}_{\mathrm{Net}}/\dot{m}_{\mathrm{air}}$ = specific work, kJ/kg
η_{th} = thermal efficiency (LHV)
η_{ts} = turbine stage efficiency
π_c = compressor pressure ratio
π_t = turbine pressure ratio

Subscripts

(number) = cycle state points (Fig. 1)
a = actual
cs = compressor stage
k = cycle state points (Fig. 1)
RI = rotor inlet
RO = rotor outlet
s = isentropic
ts = turbine stage

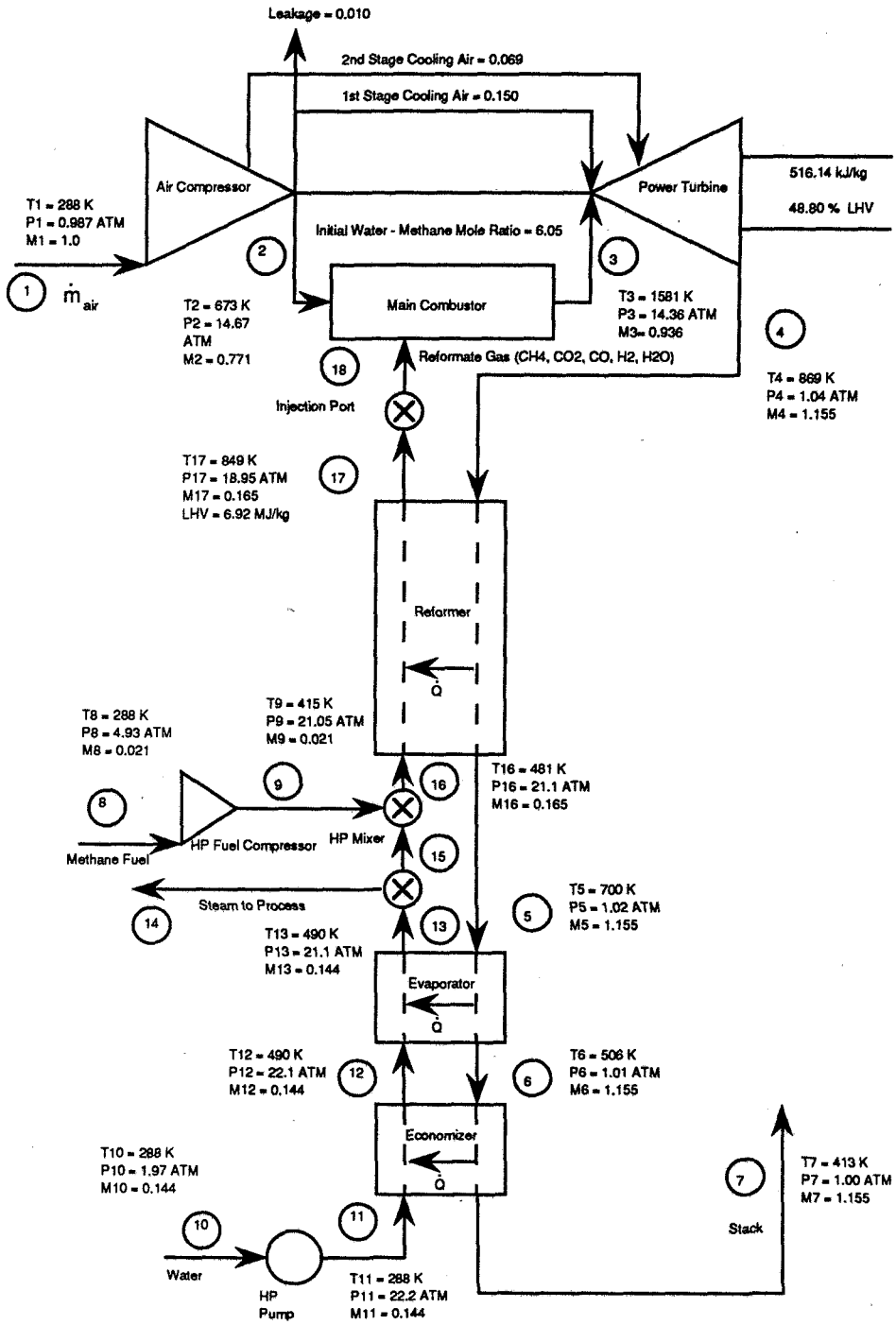

Fig. 1 The Basic Chemically Recuperated Gas Turbine Cycle (CRGT) showing the state numbering system and the values from the check case for the UCDCRGT Code (the steam to process at point 14 is always zero for the results presented in this paper)

where ΔT_{app} is one of the key fixed inputs to the model (defined in Fig. 5).

Next, ΔT_{eq} is subtracted from T_{17} and the STANJAN subroutine is utilized to calculate the *equilibrium* mixture composition at the resulting effective temperature ($T_{eff} = T_{17} - \Delta T_{eq}$). The main assumption in using this method is that the equilibrium composition calculated at T_{eff} is a good first approximation for the actual nonequilibrium composition at T_{17}. Finally, STANJAN calculates the mixture thermodynamic properties (h_{17}, s_{17}, v_{17}) at T_{17} for the composition found at T_{eff}. The details of the MSR calculation procedure are given in Appendix B.

An important parameter required to evaluate the performance of the CRGT, STIG, and combined cycles is the maximum steam flow, which can be produced in the steam generator (see Appendix B). This maximum value determines the maximum thermal efficiency of the cycle.

Comparison With Other Basic CRGT Computations

Lloyd (1991, Fig. 6.3) reports temperature, pressure, and cycle mass flow ratios (M_k) for a basic CRGT configuration. Cycle mass flow ratios are defined by:

$$M_k = \dot{m}_k / \dot{m}_{air}$$

where $\dot{m}_k$ is the mass flow rate at state k and $\dot{m}_{air}$ is the air compressor inlet flow rate. To compare results from the UCDCRGT code to Lloyd's results, the parameters from Lloyd's Fig. 6.3 (shown with the asterisks in Table 2) were entered into UCDCRGT as well as the fuel flow rate ($\dot{m}_8 = 1$ kg/s). Cooling flow to the first-stage nozzle was then varied to match Lloyd's turbine inlet temperature of 1523 K. Compressor and turbine stage efficiencies were adjusted to meet Lloyd's outlet temperatures for the compressor (673 K) and turbine (869 K).

Table 2 summarizes the key results of the comparison. (For a complete listing of the UCDCRGT code comparison outputs see Kesser, 1991, Appendix D.) Key state point properties from the UCDCRGT code results are shown in Fig. 1 for this check case. Overall, the results agree quite well. Table 2 shows the mass flow ratios of steam (0.165), methane (0.021), and air (1.0) from the UCDCRGT code are the same as Lloyd's as well as the water–methane mole ratio exiting the reformer. The most notable difference is in the specific work output, which is reflected in the cycle thermal efficiency (η_{th}) calculated by Lloyd

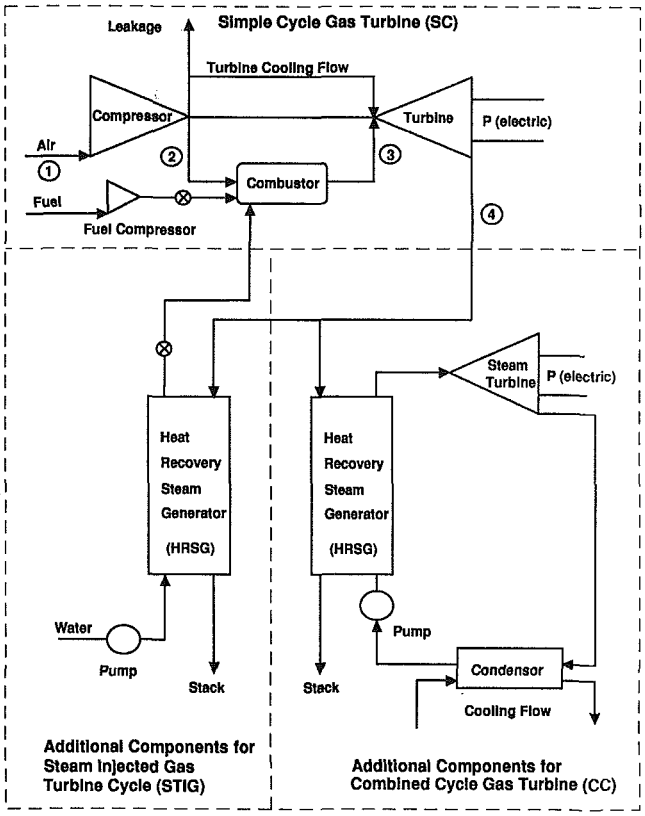

Fig. 2 Composite schematic showing the Simple Cycle (SC) gas turbine and the additional components for the Steam Injected Gas Turbine (STIG) cycle and for the Combined Cycle (CC) used in this study (HRSG stands for the Heat Recovery Steam Generator)

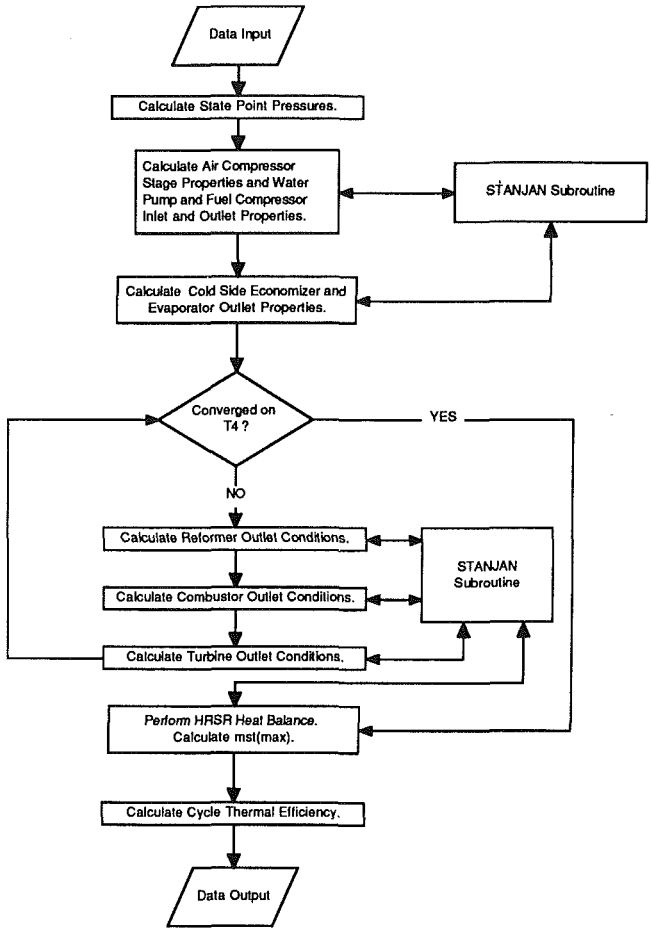

Fig. 3 Simplified flow chart for the UCDCRGT Code

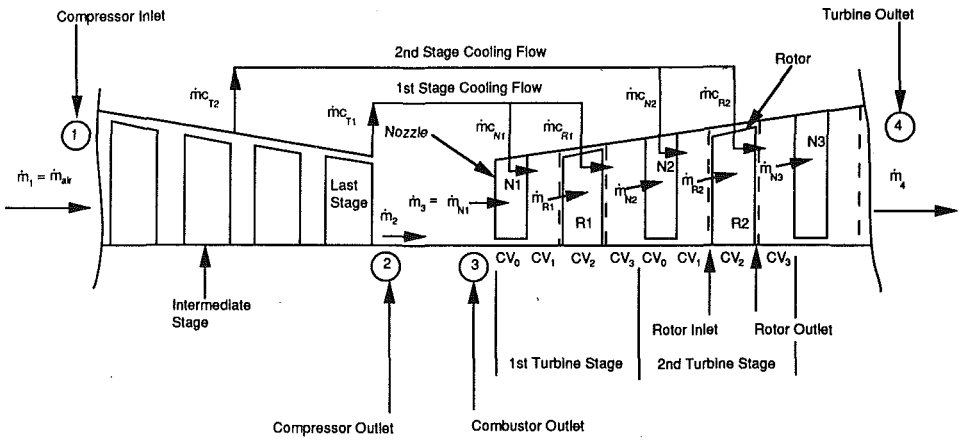

Fig. 4 Schematic showing the notation used for the air cooling model for the first two turbine stages. Control volumes 0 (CV_0) are around the nozzle blades. Control volumes 1 (CV_1) are just after the nozzle blades where the nozzle cooling air is assumed to mix with the main flow. Control volumes 2 (CV_2) are around the turbine rotors. Control volumes 3 (CV_3) are just after the rotor blades where the rotor cooling air is assumed to mix with the main flow.

Table 1(A) Gas turbine inputs for the CRGT, STIG, combined cycle, and simple cycle reference cases

Input Parameters		Reference Case 1	Reference Case 2	Source
COMPRESSOR				
Inlet Temperature, T_1	(K)	288	288	ISO Conditions
Inlet Pressure, P_1	(atm)	1.0	1.0	"
Relative Humidity, ϕ_1	(%)	60.0	60.0	"
Inlet Pressure Ratio, π_i		0.99	0.99	Oates, 1988
Number of Compressor Stages, N_{cs}		17	17	Brown, 1979
Compressor Stage Efficiency, η_{cs}		0.89	0.89	see text
Compressor Ratio, π_c		30.0	15.0	
COMBUSTOR				
Combustor Efficiency, η_{comb}		0.99	0.99	Oates, 1988
Combustor Pressure Ratio, π_{comb}		0.97	0.97	Oates, 1988
Combustor Outlet Temperature, T_3	(K)	1498	1498	Stai, 1985
TURBINE				
Number of Turbine Stages		6	4	Stai, 1985
Number of Cooled Turbine Stages		3	3	Stai, 1985
First Stage Rotor Inlet Temp., T_{R1}	(K)	1453	1453	Stai, 1985
First Stage Nozzle Cooling Fraction, NF_1		0.59	0.59	Stai, 1985
Second Stage Rotor Inlet Temp., T_{R2}	(K)	1270	1242	see text
Second Stage Nozzle Cooling Fract., NF_2		0.67	0.67	Stai, 1985
Third Stage Rotor Inlet Temp., T_{R3}	(K)	1125	1074	see text
Third Stage Nozzle Cooling Fract., NF_3		1.00	1.00	Stai, 1985
Compressor Bleed Fract. Pres. Drop, PD		0.30	0.30	El-Masri, 1987
Turbine Stage Efficiency, η_{ts}		0.88	0.88	see text
Turbine Diffuser Pressure Ratio, π_4		0.99	0.99	Lloyd, 1991
Gas Turbine Mechanical Efficiency, η_{GT}		0.996	0.996	Lloyd, 1991

Table 1(B) Inputs for the reference heat recovery steam reformer and the heat recovery steam generator (STIG and CC) models

Input Parameters		Reference Cases 1 & 2	Source
SR/HRSG (CRGT, STIG, CC)			
Fractional Heat Loss, HX_{loss}		0.02	Lloyd, 1991
Pinch Point Temp. Difference, ΔT_{pp}	(K)	10.0	Lloyd, 1991
REFORMER SECTION (CRGT)			
Approach Temp. Difference, ΔT_{app}	(K)	20.0	Lloyd, 1991
Hot-Side Reformer Pressure Ratio		0.98	Lloyd, 1991
Cold-Side Reformer Pressure Ratio		0.90	Lloyd, 1991
SUPERHEATER SECTION (STIG,CC)			
Approach Temp. Difference, ΔT_{app}	(K)	20.0	Lloyd, 1991
Hot-Side Superheater Pressure Ratio		0.97	Lloyd, 1991
Cold-Side Superheater Pressure Ratio		0.90	Lloyd, 1991
EVAPORATOR & ECONOMIZER SECTIONS			
Hot-Side Evaporator Pressure Ratio		0.99	Lloyd, 1991
Cold-Side Evaporator Pressure Ratio		0.98	Lloyd, 1991
Hot-Side Economizer Pressure Ratio		0.99	Lloyd, 1991
Cold-Side Economizer Pressure Ratio		0.98	Lloyd, 1991
STEAM CYCLE (CC)			
Steam Turbine Efficiency		0.85	Maghon, 1989
Steam Turbine Inlet Pressure	(atm)	47.0	Lloyd, 1991
Condensor Pressure	(atm)	0.08	Lloyd, 1991
FUEL COMPRESSOR			
Fuel Flow Rate, $\dot{m}_f$	(kg/s)	1.0	
Inlet Temperature	(K)	288	
Inlet Pressure	(atm)	4.9	Lloyd, 1991
Efficiency		0.85	
WATER PUMP			
Inlet Temperature	(K)	288	
Inlet Pressure	(atm)	2.0	Lloyd, 1991
Efficiency		0.90	
STACK			
Minimum Stack Temperature, T_{stack}	(K)	373	Lloyd, 1991
Outlet Pressure, P_7	(atm)	1.0	Lloyd, 1991

at 47.6 percent (LHV) and by UCDCRGT at 48.8 percent (LHV). Lloyd (1991) also included cycle calculations for the STIG and combined cycle. In a comparison of those cycles UCDCRGT's η_{th} was from 1.0 percentage point higher for the STIG cycle to 1.3 percentage points higher for the combined cycle.

We speculate that the larger losses in Lloyd's model may involve the turbine power output calculation, which is complicated by the strong effect of cooling air. Our turbine cooling model is different from the one in Consonni's code used by Lloyd, which may account for the fact that our efficiencies are all slightly higher than Lloyd's. While there are differences in the results using the two codes, these appear to be small, and the overall ordering of the technologies (CC, CRGT, STIG, etc.) by thermal efficiency is the same with the UCDCRGT code and Consonni's code.

Table 2 Data summary for the UCDCRGT code check case

CRGT Parameters	Lloyd	UCDCRGT
STATE POINT 1		
M_1 ($\dot{m}_1$ / $\dot{m}_{air}$)	1.0	1.0
T_1 (K) *	288	288
P_1 (atm) *	0.99	0.99
COMPRESSOR		
Number of Compressor Stages, N_{cs} *	NK	12
Compression Ratio, π_c *	15.0	15.0
Compressor Stage Efficiency, η_{cs} *	NK	0.89
Compressor Stage Pressure Ratio, π_{cs} *	NK	1.25
Compressor Air Leakage ($\dot{m}_{lk}$ / $\dot{m}_{air}$) *	0.01	0.01
STATE POINT 2		
M_2 ($\dot{m}_2$ / $\dot{m}_{air}$)	0.771	0.771
T_2 (K)	673	673
P_2 (atm) *	14.8	14.7
STATE POINT 17		
M_{17} ($\dot{m}_{17}$ / $\dot{m}_{air}$)	0.164	0.165
T_{17} (K)	849	849
P_{17} (atm)	19.0	19.0
CH_4 Mole Fraction	0.081	0.080
CO_2 Mole Fraction	0.045	0.044
CO Mole Fraction	0.004	0.004
H_2O Mole Fraction	0.680	0.682
H_2 Mole Fraction	0.190	0.190
Reformate LHV (MJ/kg)	7.02	6.92
COMBUSTOR		
Combustor Efficiency, η_{b} *	0.99	0.99
Combustor Pressure Ratio, π_{b} *	0.97	0.97
STATE POINT 3		
M_3 ($\dot{m}_3$ / $\dot{m}_{air}$)	0.936	0.936
T_3 (K) *	1581	1581
P_3 (atm)	14.36	14.36

* Input to UCDCRGT Computer Code NK - Not Known

CRGT Parameters	Lloyd	UCDCRGT
TURBINE		
Number of Turbine Stages, N_{ts} *	NK	4
1st Stage Rotor Temp., T_{R1} (K)	1523	1523
Turbine Stage Efficiency, η_{ts} *	NK	0.88
Turbine Stage Pressure Ratio, π_{ts}	NK	0.52
Total Turbine Cooling Fraction, CAF_T *	0.219	0.219
1st Stage Cooling Air Fraction, CAF_1 *	NK	0.150
1st Stage Nozzle Fraction, NF_1 *	NK	0.566
2nd Stage Cooling Air Fraction, CAF_2 *	NK	0.069
2nd Stage Nozzle Fraction, NF_2 *	NK	0.500
STATE POINT 4		
M_4 ($\dot{m}_4$ / $\dot{m}_{air}$)	1.154	1.155
T_4 (K)	869	869
P_4 (atm)	1.04	1.04
STATE POINT 7		
M_7 ($\dot{m}_7$ / $\dot{m}_{air}$)	1.154	1.155
T_7 (K) *	413	413
P_7 (atm) *	1.00	1.00
STATE POINT 10		
M_{10} ($\dot{m}_{10}$ / $\dot{m}_{air}$)	0.143	0.144
T_{10} (K)	NK	288
P_{10} (atm)	1.97	1.97
EVAPORATOR-ECONOMIZER		
Pinch Point Temp. Difference, ΔT_{pp} (K)	10.0	15.7
REFORMER		
Approach Temp. Difference, ΔT_{app} (K)	20.0	20.0
Chemical Equil. Approach Temp. Diff., ΔT_{eq} (K)	NK	3.6
OVERALL CYCLE PARAMETERS		
Water-Methane Mole Ratio, R_{SM}	6.0	6.1
Specific Work Output, $W_{Net}/\dot{m}_{air}$ (kJ/kg)	507	516
Thermal Efficiency, η_{th} (%)	47.6	48.8

* Input to UCDCRGT Computer Code NK - Not Known

Selection of Reference Cases 1 and 2

In order to compare the CRGT to the STIG, simple cycle and combined cycle, two gas turbine reference cases were developed for each of the four types of gas turbine power plants (Table 1A). Reference Case 1 ($\pi_c = 30.0$) is a best estimate of the GE LM5000 aeroderivative gas turbine, while Reference Case 2 ($\pi_c = 15.0$) is essentially a lower pressure ratio version of Reference Case 1 (representing a heavy-duty, industrial gas

Table 3 Summary of results for reference cases 1 and 2* (combustor outlet temperature $T_3 = 1498$ K)

Cycle	Compressor Ratio, π_c	Thermal Efficiency, η_{th} (%)	Specific Work, $\dot{W}_{Net}/\dot{m}_{air}$ (kJ/kg)	Total Cooling Air Fraction, CAF_T	Pinch Point Limited Steam-Air Ratio, SA
REFERENCE CASE 1					
CRGT	30.0	47.0	398	0.21	0.087
STIG	30.0	46.7	419	0.22	0.101
Combined Cycle	30.0	47.9	351	0.16	0.077
Simple Cycle	30.0	39.5	292	0.15	N/A
REFERENCE CASE 2					
CRGT	15.0	47.3	468	0.21	0.138
STIG	15.0	45.9	527	0.23	0.186
Combined Cycle	15.0	49.7	451	0.14	0.126
Simple Cycle	15.0	36.0	330	0.13	N/A

* Inputs for Reference Cases 1 and 2 are contained in Tables 1A and 1B.

turbine). Table 1(B) contains input data for the MSR for the CRGT and the HRSG for the STIG and combined cycle. Sources for the gas turbine, MSR, and HRSG inputs are listed in the last column of Tables 1(A) and 1(B).

Turbine manufacturers keep detailed design data for their turbines proprietary. However, in a report by Stai (1985) which analyzed the GE LM5000 aeroderivative gas turbine in a STIG cycle configuration for Southern California Edison, there is a detailed diagram of the STIG cycle, which includes the gas turbine cooling flows for the LM5000. This report was the best information we could find on the LM5000. Consequently, most of the key gas turbine input parameters listed in Table 1(A) come from this report. These input parameters include the combustor outlet temperature (T_3), the number of cooled turbine stages, the first-stage rotor inlet temperature (T_{R1}), and the first, second, and third-stage nozzle fractions (NF). (A description of how the second and third-stage turbine rotor inlet temperatures were determined is given in Kesser, 1991, Appendix B.)

The turbine and compressor stage efficiency values listed in Table 1(A) were back calculated as part of the code validation process described above. By this method, the calculated turbine stage efficiency of 88.0 percent includes the effect of cooling air; this is lower than the range (90.3 to 92.3 percent) given in current gas turbine technical literature (e.g., El-Masri, 1987). The reason for this difference is that turbine stage efficiencies (η_{ts}) reported in the literature are usually maximum values for uncooled turbine stages. Our use of the stage efficiency of 88.0 percent is only strictly correct for the cooled turbine stages, and results in a small penalty for the uncooled turbine stages.

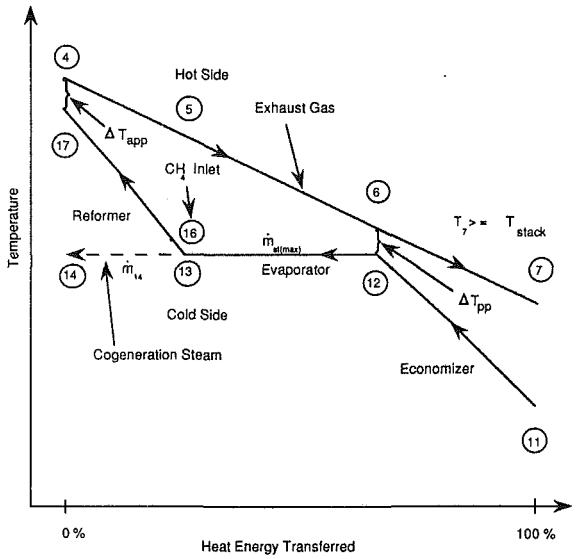

Fig. 5 *Idealized* temperature versus thermal energy diagram for the Heat Recovery Steam Generator (HRSG) (the horizontal dashed line represents the cases where there is excess steam generated ($\dot{m}_{14}$), which could be used for a cogeneration application)

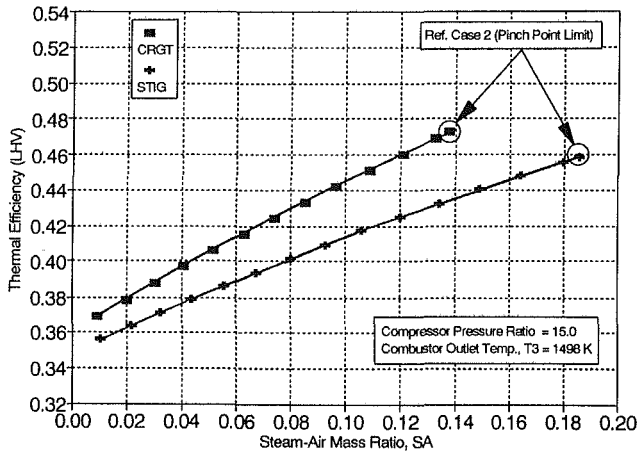

Fig. 6 Thermal efficiency calculations for the CRGT and the STIG for a fixed compressor pressure ratio of 15.0 and a fixed combustor outlet temperature of 1498 K. All the other inputs in Tables 1(A) and 1(B) are also fixed. The cooling air fraction, CAF, is varied as the steam-air mass ratio, *SA*, is varied to keep the three rotor inlet temperatures fixed.

Discussion of Results

Table 3 summarizes the key results for Reference Cases 1 and 2 for the CRGT, STIG, combined cycle, and simple cycle. A complete listing of the UCDCRGT output values for Reference Cases 1 and 2 for all four cycles is contained in Kesser (Appendix E, 1991). All reported thermal efficiency (η_{th}) values are lower heating value (LHV), first-law efficiencies and are calculated using the following equation:

$$\eta_{th} = \dot{W}_{\text{Net}}/(\dot{m}_{\text{CH4}} \times \text{LHV}) \tag{7}$$

In both Reference Cases 1 and 2, ΔT_{app} and ΔT_{pp} are the parameters that fix the maximum steam flow rate, $\dot{m}_{st(\max)}$, for the CRGT, STIG, and combined cycles.

As expected the simple cycle has the lowest η_{th} and specific work output ($\dot{W}_{\text{Net}}/\dot{m}_{\text{air}}$) because none of the thermal power in the turbine exhaust is recovered. Of the three cycles that do recover thermal power from the exhaust heat, the combined cycle has the highest η_{th} for both reference cases followed by the Basic CRGT and STIG.

The $\dot{W}_{\text{Net}}/\dot{m}_{\text{air}}$ is highest for the STIG cycle for both reference cases followed by the Basic CRGT and combined cycle. Furthermore, the $\dot{W}_{\text{Net}}/\dot{m}_{\text{air}}$ for the CRGT, STIG, and combined cycle are higher for Reference Case 2 ($\pi_c = 15.0$) when compared to Reference Case 1 ($\pi_c = 30.0$) because of the higher cycle steam mass flow rates associated with Reference Case 2. The steam flow rates are higher for Reference Case 2 because the lower cycle pressure ratio leads to higher turbine outlet temperature and hence more "waste" heat in the turbine exhaust.

Figure 6 represents a hypothetical family of gas turbine engines with a fixed compressor pressure ratio of 15 which can handle different steam/air ratios. (The steam/air mass flow ratio, *SA*, is limited by the size of the turbine flow passages.) The circled points are the Reference Case 2 points for the optimized engines, which can handle the maximum steam that can be produced within the limits of the constraint on the minimum pinch point temperature difference of 10°C.

It is interesting to compare the CRGT and the STIG cycles for an engine that can only handle a specific steam/air ratio, say 0.08. (For these cases, a higher pinch point temperature

difference than the minimum would result.) This gas turbine engine clearly has a better thermal efficiency in the CRGT cycle (about 43 percent) than in the STIG cycle (about 40 percent). Figure 6 shows that the CRGT has an efficiency advantage at all steam/air ratios (for the single-pressure heat recovery steam generator used in this study). Additional interesting results such as these can be found in Kesser (1991).

Summary

In comparing the four cycles, each using the maximum steam that could be produced, the combined cycle was shown to have the highest η_{th} followed by the Basic CRGT, STIG, and simple cycle. The STIG cycle was shown to have the highest $\dot{W}_{\text{Net}}/\dot{m}_{\text{air}}$ followed by the Basic CRGT, combined cycle, and simple cycle.

The Basic CRGT with a compressor pressure ratio of 30 has a thermal efficiency of about 47.0 percent (Reference Case 1), while for a pressure ratio of 15, the thermal efficiency is about 47.3 percent (Reference Case 2). Both these efficiencies are attractively high and indicate that a demonstration power plant using the Basic CRGT concept without intercooling or reheat might be a worthwhile undertaking. It would involve much less cost and development time than an Advanced CRGT with intercooling and reheat and would help identify any problems with the CRGT concept at an early stage.

In order to obtain a deeper insight into the origin of the losses in CRGT cycle (as well as the other cycles), it is strongly recommended that a second-law analysis be performed. In addition, it is recommended that a comparison study of the CRGT and STIG cycles operating in the cogeneration mode be undertaken. Finally, it is recommended that the use of multipressure heat recovery steam generators be incorporated in future comparison studies of the combined cycle, since this can enhance the thermal efficiency of the combined cycle.

Acknowledgments

We wish to thank the California Energy Commission for supporting Mr. Keith Kesser as a part time employee while he was doing this research at U.C.Davis. We also wish to thank Professor William Reynolds of Stanford University for providing us with the STANJAN source code.

References

Adelman, S., 1992, "Computer Code for Predicting the Size and Performance of a Steam-Methane Reformer for a Gas Turbine Power Plant," Master's Thesis, Department of Mechanical, Aeronautical, and Materials Engineering, University of California, Davis, CA.

Brown, D. H., 1979, "Steam Injected Gas Turbine Study: An Economic and Thermodynamic Appraisal," AF-1186 Technical Planning Study TPS 77-737, Electric Power Research Institute, Palo Alto, CA.

Consonni, S., 1992, "Performance Prediction of Gas–Steam Cycles for Power Generation," Ph.D. Thesis, Mechanical and Aerospace Engineering Department, Princeton University, Princeton, NJ.

El-Masri, M. A., 1987, "Exergy Balance Analysis of the Reheat Gas Turbine Combined Cycle," presented at the Joint ASME/JSME Conference, Honolulu, HI.

Erbes, M. R., Gay, R. R., and Cohn, A., 1989, "GATE: A Simulation Code for Analysis of Gas-Turbine Power Plants," ASME Paper No. 89-GT-39.

International Power Technology, 1991, "ETAP Responses to Interview Questions Regarding Proposed Project: Steam Use for Turbine Flow Path and Flame Cooling in Gas Turbines," California Energy Commission, Sacramento, CA.

Irvine, T. F., and Liley, P. E., 1984, *Steam and Gas Tables With Computer Equations*, Academic Press, Inc., Orlando, FL.

Janes, J., 1990, "Chemically Recuperated Gas Turbine," California Energy Commission Draft Staff Report P500-90-001.

Karim, G. A., Wierzba, I., and Boon, S., 1985, "Some Considerations of the Lean Flammability Limits of Mixtures Involving Hydrogen," *International Journal of Hydrogen Energy*, Vol. 10, No. 1, pp. 117–123.

Kesser, K. F., 1991, "Analysis of a Basic Chemically Recuperated Gas Turbine Power Plant," Master's Thesis, Department of Mechanical, Aeronautical, and Materials Engineering, University of California, Davis, CA.

Lloyd, A., 1991, "Thermodynamics of Chemically Recuperated Gas Turbines," MS Thesis, Mechanical and Aerospace Department, Princeton University, Princeton, NJ.

Maghon, H., Bergmann, D., Brueckner, H., Kriesten, W., and Termuehlen, H., 1989, "Combined Cycle Power Plants for Load Cycle Duties," submitted for presentation at the American Power Conference, Chicago, IL.

Oates, G. C., 1988, *Aerothermodynamics of Gas Turbine and Rocket Propulsion*, American Institute of Aeronautics and Astronautics, Inc., Washington, DC.

Reynolds, W. C., 1986, "The Element Potential Method for Chemical Equilibrium Analysis: Implementation in the Interactive Program STANJAN," Version 3, Department of Mechanical Engineering, Stanford University, CA.

Stai, D. F., 1985, "Steam Injected Gas Turbine (STIG) Application Study at the Redondo Beach Generating Station. Vol. 1. Final Report," Report No. 85-PDO-3, Southern California Edison, Rosemead, CA.

APPENDIX A

Turbine Cooling Calculation Procedure

There are two options in the UCDCRGT code for the calculation of the turbine cooling flows. For the first option where the cooling air fraction (CAF) is specified for each cooled stage, the code calculates the corresponding rotor inlet temperatures for the specified combustor outlet temperature, T_3. Although the CAF for each turbine stage is not readily available in the open literature, we felt that reasonable estimates could be made, and this option was used in some calculations.

For the second option where the combustor outlet temperature, T_3, and the turbine rotor inlet temperatures are specified, the code calculates the amount of cooling air necessary to achieve the specified rotor inlet temperatures using the energy equation across the nozzles. Since the rotor inlet temperatures (except for the first stage rotor) are proprietary information of the engine manufacturer, these inputs had to be estimated from the limited information available (e.g., Stai, 1985).

Another input parameter, the compressor-bleed fractional pressure drop (PD), is used to determine the appropriate compressor stage from which to bleed the turbine stage cooling air using the following criterion:

$$P_{cs} \geq P_{RI} * (1 + PD) \tag{A1}$$

where P_{cs} is the minimum compressor stage outlet pressure that meets the criterion above and P_{RI} is the turbine rotor inlet stagnation pressure. The only exception to this criterion is at the compressor outlet when $P_{RI} * (1 + PD)$ exceeds the compressor outlet pressure (P_2). In this case the compressor bleed air is taken from the compressor outlet with the bleed pressure drop set equal to $(P_2 - P_{RI})$. (In this approximate model, total pressures are used and no distinction is made between static and total pressures in the compressor bleed calculations; this introduces a small error.)

In our turbine model, the turbine stage pressure ratios are assumed equal for all N_{ts} stages (although equal enthalpy drops would be a more accurate approximation) and are calculated from the following equation:

$$\pi_{ts} = \pi_t^{(1.0/N_{ts})} \tag{A2}$$

where π_t is the overall turbine total pressure ratio, P_4/P_3.

Figure 4 shows that there are four control volumes (CV) associated with each cooled turbine stage. In CV_0 the turbine nozzle flow ($\dot{m}_N$) is assumed to pass through the nozzle blades with negligible pressure drop, which is clearly an optimistic assumption in Oates' (1988) model. The nozzle cooling flow ($\dot{m}c_N$) is then assumed to mix perfectly with the nozzle flow ($\dot{m}_N$) in CV_1. When the turbine stage cooling fraction (CAF) is specified (i.e., the first option in the UCDCRGT Code), the nozzle cooling flow $\dot{m}c_N$ is calculated using the following equation:

$$\dot{m}c_N = \text{CAF} \times NF \times \dot{m}_{\text{air}} \tag{A3}$$

The rotor flow is given by:

$$\dot{m}_R = \dot{m}c_N + \dot{m}_N \tag{A4}$$

The rotor inlet enthalpy (h_{RI}) is obtained from the energy balance for the mixing process in CV_1:

$$h_{RI} = \frac{\dot{m}c_N \times hc_N + \dot{m}_N \times h_N}{\dot{m}_R} \tag{A5}$$

where hc_N is the nozzle cooling flow enthalpy and h_N is the turbine nozzle flow enthalpy. The remaining stage thermodynamic properties (T_{RI}, s_{RI}, and v_{RI}) are calculated using STANJAN with P_{RI} and h_{RI} as the two input properties. The relative atomic molar concentrations for the rotor inlet gas flow have to be recalculated because cooling air has been added to the nozzle flow.

If the rotor inlet temperature (T_{RI}) is specified (i.e., the second option in the UCDCRGT Code), then the required nozzle cooling flow ($\dot{m}c_N$) is calculated using an iterative process. An initial guess is made for $\dot{m}c_N$ and then the following parameters are entered into STANJAN to calculate the rotor inlet temperature: the rotor inlet enthalpy (h_{RI}), the stage inlet pressure (P_{RI}), and the newly calculated atomic molar concentrations. The iterative process continues until convergence is reached for the specified rotor inlet temperature.

The rotor outlet properties are calculated in CV_2. The *actual* turbine stage outlet enthalpy (h_{ROa}) is given by:

$$h_{ROa} = h_{RI} - \eta_{ts} \times (h_{RI} - h_{ROs}) \tag{A6}$$

where the *isentropic* enthalpy (h_{ROs}) is calculated (using the STANJAN subroutine) from the two thermodynamic property inputs s_{RI} and the turbine stage outlet pressure (P_{RO}). The turbine-stage power output is then calculated from:

$$\dot{W}_{ts} = \dot{m}_R \times (h_{RI} - h_{ROa}) \tag{A7}$$

The rotor cooling flow ($\dot{m}c_R$) is mixed with the rotor gas flow in CV_3. The final enthalpy after the mixing process in CV_3 is given by an equation similar to Eq. (A5) for CV_1. (See Kesser, 1991, Appendix B, for further details.)

APPENDIX B

Calculation Procedure for the Methane–Steam Reformer

The maximum value of the steam produced, $\dot{m}_{st(\max)}$, is limited by two of the three key MSR design parameters: ΔT_{app}, and either ΔT_{pp}, or T_{stack}. First, the fixed ΔT_{app} is used to calculate $T_{17} = T_4 - \Delta T_{app}$ (Eq. (6)). Then the specified *minimum* ΔT_{pp} is used to calculate a first estimate of T_6 using the evaporator temperature, T_{12} (determined from the saturation pressure P_{12}):

$$T_6 = T_{12} + \Delta T_{pp} \tag{B1}$$

With the four key temperatures (T_{12}, T_6, T_{17}, and T_4) into and out of the evaporator plus reformer sections now known, it is a straightforward matter to use the mass and energy balance equations to calculate the heat transfer in each section and the maximum mass flow rate of steam.

The stack enthalpy is obtained from the energy balance across the economizer cold side:

$$h_7 = h_6 - \frac{\dot{Q}_{\mathrm{ECON}(cs)}}{(1.0 - HX_{\mathrm{loss}})\ \dot{m}_4} \tag{B2}$$

and T_7 is calculated by entering h_7 and P_7 into STANJAN. The calculated stack temperature (T_7) is compared to the specified *minimum* stack temperature (T_{stack}). If T_7 is greater than T_{stack}, the MSR heat balance is considered finished and ΔT_{app} and ΔT_{pp} are the only two constraints that fix $\dot{m}_{st(\max)}$. However, if T_7 is less than the minimum specified T_{stack}, the MSR heat balance is recalculated with T_7 set equal to T_{stack}. An economizer-evaporator energy balance (Kesser, 1991, Appendix C) gives a new h_6, and a new ΔT_{pp} (using Eq. (B1)). The resulting ΔT_{pp} will always be larger than the specified minimum ΔT_{pp}. Consequently, the two constraints that fix $\dot{m}_{st(\max)}$ in this case are ΔT_{app} and T_{stack}.

M. J. Moran
Department of Mechanical Engineering,
The Ohio State University,
Columbus, OH 43210

E. Sciubba
Dipartimento di Meccanica e Aeronautica,
Universitá di Roma "La Sapienza,"
00184 Roma, Italy

Exergy Analysis: Principles and Practice

The importance of the goal of developing systems that effectively use nonrenewable energy resources such as oil, natural gas, and coal is apparent. The method of exergy analysis is well suited for furthering this goal, for it enables the location, type and true magnitude of waste and loss to be determined. Such information can be used to design new systems and to reduce the inefficiency of existing systems. This paper provides a brief survey of both exergy principles and the current literature of exergy analysis with emphasis on areas of application.

1 Introduction

Contentious discussion and heated debate over exergy fundamentals at recent ASME-sanctioned symposia[1] suggest the need for surveys of both exergy principles and the current literature of exergy analysis. The present paper aims to provide these, beginning with a brief consideration of the literature.

Although numerous individuals have contributed to the principles and practice of exergy analysis over the past 100 years or more, the pace of development has quickened since the 1930s, and especially since the oil embargo of the early 1970s. F. Bosnjakovic, J. Keenan, Z. Rant, J. Szargut, and R. Gaggioli, to name only a few, have played pivotal roles in making the subject what it is today. Over the last dozen years, members of the ASME Advanced Energy Systems Division have been at the forefront of developments, sponsoring symposia both at WAM and in summer meetings at several sites around the globe. Summaries of the evolution of exergy analysis through the late 1980s are provided by Kotas (1985) and Szargut et al. (1988). A survey of key contributions up to 1990 is given by Moran (1990). For recent contributions, readers will want to refer to the symposium volumes, Boehm et al. (1992), Kouremenos et al. (1991), Reistad et al. (1991), Stecco and Moran (1990, 1992), Tsatsaronis et al. (1990), and Valero and Tsatsaronis (1992).

A review of the literature reveals that use of exergy principles enhances understanding of thermal/chemical processes and allows sources of inefficiency to be quantified. Such essentially thermodynamic considerations can be integrated with principles of engineering economics to determine the potential for cost-effective improvements of existing systems. Exergy and costing principles also can be used at the initial design stage to develop systems that are optimized in annualized cost, sparing in the use of coal, oil, and natural gas, and environmentally friendly. Indeed, the principal field of application of exergy analysis nowadays is to thermal/chemical system design and optimization, as discussed by Melli et al. (1990) and Sama (1992).

To avoid confusion with familiar energy-based methods for analysis and design of thermal systems, a careful distinction must be drawn between energy and exergy. Energy is conserved in every device or process. Energy entering with fuel, electricity, flowing streams of matter, and so on can be accounted for in the products and byproducts. Energy cannot be destroyed. The idea that something can be destroyed is useful. It should not be applied to energy, however, but to another variable: *exergy*. Moreover, it is *exergy* and not energy that properly gages the quality (utility) of, say, one kJ of electricity generated by a power plant versus one kJ in the plant cooling water stream. Electricity clearly has the greater quality *and* not incidentally, the greater economic value.

The simplified electrical generating power cycle shown schematically in Fig. 1 highlights the distinction between energy and exergy. Figure 1(*a*) is on an energy basis, and indicates that of 100 energy units entering with the fuel 30 energy units are obtained as electricity and the balance, 70 units, are discharged to the surroundings, to cooling water say. Invoking an oft-used approximation (see discussion following Eq. (17*b*)), we may consider that 100 units of exergy also enter with the fuel, as shown in Fig. 1(*b*). Since the generated electricity is *exergy in transit* (see comment following Eq. (25)), 30 units of exergy exit by this means. So, as for Fig. 1(*a*), there is a balance of 70 units to be accounted for; but when these 70 exergy units are considered, similarity with the previous case ends: We find that 67 to 68 units of this exergy are *destroyed* within the plant by various irreversibilities and just 2 to 3 units are *discharged* to the surroundings. Although considerable energy is discharged to the cooling water, its quality (utility) is low because the cooling water typically exits the plant at a temperature only a few degrees higher than that of the surroundings. Accordingly, to improve performance the energy analysis misleadingly points to reducing the energy discharged. The exergy analysis on the other hand not only shows that the discharge is a relatively minor area of concern but also that *significant* performance improvement can come only by identifying and remedying sources of inefficiency *within the system*.

[1]Flowers '92, Florence, Italy, June 8–12, 1992; Ecos '92, Zaragoza, Spain, June 15–18, 1992.

Contributed by the Advanced Energy Systems Division for publication in the JOURNAL OF ENGINEERING FOR GAS TURBINES AND POWER. Manuscript received by the Advanced Energy Systems Division June 25, 1992; revision received December 10, 1992. Associate Technical Editor: M. J. Moran.

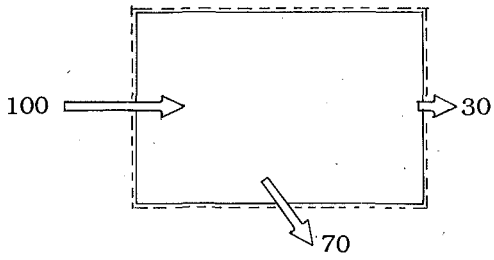

(a) Energy Basis

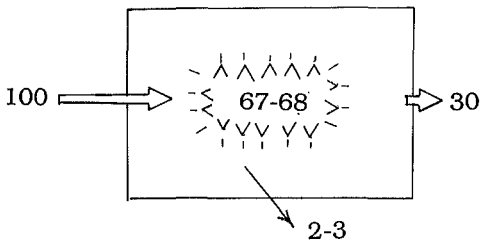

(b) Exergy Basis

Fig. 1 Power cycle

Moreover, as it is exergy that has economic value in the marketplace, serious misevaluations can result when systems are costed on an energy basis (Kenney, 1984).

We conclude this introduction by listing for ease of reference some important features of the exergy concept developed in subsequent sections of the paper:

- Exergy is the maximum theoretical work that can be extracted from a combined system of system and environment as the system passes from a given state to equilibrium with the environment—that is, passes to the dead state. At the dead state, the combined system possesses energy but no exergy.
- For all states of the system $E \geq 0$, where E denotes exergy.
- Exergy is an extensive property whose value is fixed by the state of the system once the environment has been specified. Exergy can be represented on an intensive basis: on a unit mass or a per mole basis.
- Exergy is a measure of the departure of the state of a system from that of the environment. The greater the difference, say, between the temperature T at a given state and the temperature T_o of the environment, the greater the value for exergy. This applies equally when $T > T_o$ and $T < T_o$.
- When measured relative to the environment, the kinetic and potential energies of the system contribute their full magnitudes to the exergy magnitude, for in principle each is fully convertible to work as the system passes to the dead state.
- Though not a requirement for its utilization, exergy can be expressed as the sum of the *chemical exergy* and the *thermomechanical exergy*. Thermomechanical exergy can be further classified as *physical, kinetic*, and *potential exergy*.
- Exergy can be *transferred* between systems and *destroyed* by irreversibilities within systems. Exergy is accounted for by an *exergy balance*.

2 Defining Exergy

An opportunity for doing work exists whenever two systems at different states are placed in communication, for in principle work can be developed as the two are allowed to come into equilibrium. When one of the two systems is a suitably idealized system called the *environment* and the other is some system of interest, *exergy* is the maximum theoretical shaft work or electrical work obtainable as the systems interact to equilibrium, heat transfer occurring with the environment only. Alternatively, exergy is the minimum theoretical shaft work or electrical work required to form a quantity of matter from substances present in the environment and bring the matter to a specified state.

Exergy is not generally conserved but is destroyed. A limiting case is when exergy would be complelety destroyed, as would occur if a system were to come into equilibrium with the environment *spontaneously* with no provision to obtain work. The opportunity to develop work that exists initially would be completely wasted in the spontaneous process. Moreover, since no work need be done to effect such a spontaneous change, we may conclude that the value of exergy (the maximum theoretical work obtainable) is *at least zero* and therefore *cannot be negative*.

Any system, whether a component in a larger system such as a steam turbine in a power plant or the larger system (power plant) itself, operates within surroundings of some kind. It is important to distinguish between the environment and the system's surroundings. As illustrated in Fig. 2, the term *surroundings* refers to *everything* not included in the system. The term *environment* applies to some *portion* of the surroundings, the intensive properties of each phase of which are uniform and do not change significantly as a result of any process under consideration. All significant irreversibilities are located within the system and its immediate surroundings. *Internal irreversibilities* are those located within the system. *External irre-*

Nomenclature

C_aH_b = hydrocarbon fuel
E, e = exergy, specific exergy
E_D = rate of exergy destruction
e_f = specific flow exergy
G, g = Gibbs function, specific Gibbs function
g = acceleration of gravity
h = specific enthalpy
KE = kinetic energy
$\dot{m}$ = mass flow rate
n_i = number of moles of substance i
PE = potential energy
p = pressure
Q_c = heat transfer to combined system
$\dot{Q}_j$ = heat transfer rate at temperature T_j
$\overline{R}$ = universal gas constant
S, s = entropy, specific entropy
S_{gen} = entropy generation
T = temperature
U, u = internal energy, specific internal energy
V, v = volume, specific volume
v = velocity
W_c = work of the combined system
$\dot{W}_{cv}$ = rate of work other than flow work
y_i = mole fraction of substance i
μ_i = chemical potential of substance i

Subscripts

e = control volume exit
F = fuel
i = substance i, control volume inlet
j = number of substances, location on control volume boundary
o = restricted dead state

Superscripts

CH = chemical exergy
e = environment
TH = thermomechanical exergy
$\overline{\ }$ = overbar denotes *per mole*

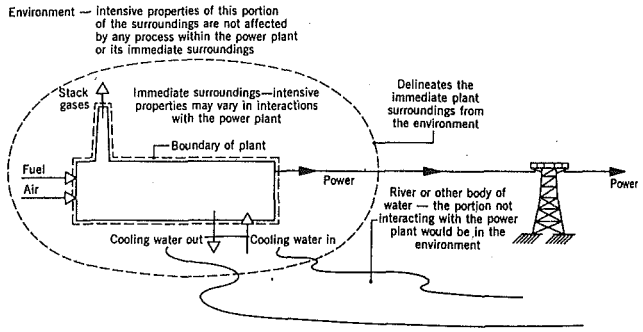

Fig. 2 System, immediate surroundings, and environment

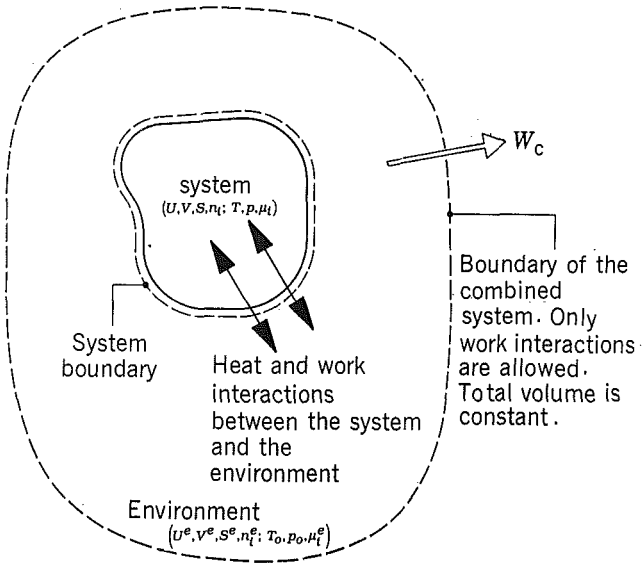

Fig. 3 Combined system and environment

versibilities reside in its immediate surroundings. The environment is regarded as free of *irreversibilities.*

The physical world is complicated, and to include every detail in an analysis is not practical. Accordingly, in describing the environment simplifications are made, and a model results. The validity and utility of an analysis using any model are, of course, restricted by the idealizations made in formulating the model. In this paper the environment is regarded as a *simple compressible system, large* in extent, and *uniform* in temperature, T_o, and pressure, p_o. In keeping with the idea that the environment has to do with the actual physical world, the values for p_o and T_o used throughout a particular analysis are normally taken as typical environmental conditions, such as 1 atm and 25°C (77°F). Although its intensive properties do not change, the environment can experience changes in its extensive properties as a result of interactions with other systems. All parts of the environment are considered to be at rest with respect to one another. Accordingly, a change in the energy of the environment can be a change in its internal energy only. The environment is composed of common substances that exist in abundance within the atmosphere, the oceans, and the crust of the earth. The substances are in their stable forms as they exist naturally and are in chemical equilibrium. There is no possibility of developing work from interactions—physical or chemical—between parts of the environment.

When one, or more, of pressure, temperature, composition, velocity, and elevation of a system is different from the environment, there is an opportunity to develop work. As the system changes state toward that of the environment, the opportunity diminishes, ceasing to exist when the two are in equilibrium. This state of the system is called the *dead state.* At the dead state, the conditions of mechanical, thermal, and chemical equilibrium between the system and the environment are satisfied. Thus, in addition to the pressures and temperatures, the chemical potentials of the substances of the system and environment must be equal. Under these conditions, there is no possibility of a spontaneous change within the system or the environment, nor can there be an interaction between them resulting in work.

Another type of equilibrium between the system and the environment can be identified. This is a *restricted* form of equilibrium where only the conditions of mechanical and thermal equilibrium must be satisfied. This state of the system is called the *restricted dead state.* At the restricted dead state, the fixed quantity of matter under consideration is imagined to be sealed in an envelope impervious to mass flow, at rest relative to the environment, and at the temperature T_o and pressure p_o.

3 Evaluating Exergy

Figure 3 shows a *combined system* consisting of a system and the environment. The system energy is the sum $U+KE+PE$, where U denotes the internal energy, KE the kinetic energy, and PE the gravitational potential energy. The kinetic and potential energies are evaluated relative to coordinates in the environment. The substances making up the system are either present within the environment or *formable* from environmental substances. For simplicity in the present derivation, however, all substances of the system are assumed to be actually present in the environment and do not react chemically as the system passes to the dead state. As the objective is to evaluate the maximum work that could be developed by the combined system, the boundary of the combined system allows only work transfers of energy across it, ensuring that the work developed is not affected by heat transfers to or from the combined system. Although the volumes of the system and environment may vary, the boundary of the combined system is located so that the total volume remains constant. This ensures that the work developed is fully available for lifting a mass, say, and is not expended in merely displacing the surroundings of the combined system.

Referring to Fig. 3, the *thermostatic* state of the system is described by the *extensive* properties internal energy U, volume V, entropy S, and the amounts of substances present n_i ($i=1, j$), and the *intensive* properties temperature T, pressure p, and chemical potentials μ_i. These quantities are related as follows (Moran and Shapiro, 1992):

$$U = TS - pV + \Sigma n_i \mu_i \tag{1}$$

The state of the environment is described by the extensive properties U^e, V^e, S^e, n_i^e, and the intensive properties T_o, p_o, μ_i^e. These quantities are related by

$$U^e = T_o S^e - p_o V^e + \Sigma n_i^e \mu_i^e \tag{2}$$

When system and environment have interacted to a final equilibrium state, the energy of the combined system is

$$U'^e = T_o S'^e - p_o V'^e + \Sigma n_i'^e \mu_i^e \tag{3}$$

Exergy can be evaluated by applying *energy*, *mass*, and *entropy* balances to the combined system as follows:

- An *energy balance* indicates that the change in energy equals the net energy transfer. That is

$$U'^e - [\underline{U^e + (U + KE + PE)}] = \mathcal{Q}_c - W_c \tag{4}$$

where W_c is the work developed by the combined system and the underlined term is the energy of the combined system initially. Solving for the work, and introducing Eqs. (2) and (3), we have

$$W_c = (U + KE + PE) + \underline{p_o(V'^e - V^e)} - T_o(S'^e - S^e) - \Sigma(n_i'^e - n_i^e)\mu_i^e \quad (5)$$

Because there is no change in the total volume of the combined system, the underlined term of Eq. (5) can be simplified using

$$V'^e = V^e + V \quad (6)$$

- Moreover, since we have assumed no change in the total amount of each substance present, we have

$$n'^e = n_i^e + n_i \quad (7)$$

- Finally, an *entropy balance* gives

$$S'^e = S^e + S + S_{\text{gen}} \quad (8)$$

where S_{gen} accounts for the generation of entropy within the combined system owing to irreversibilities as the system comes into equilibrium with the environment.

Collecting Eqs. (5)–(8),

$$W_c = (\underline{U + p_o V - T_o S - \Sigma n_i \mu_i^e} + KE + PE) - T_o S_{\text{gen}} \quad (9)$$

The underlined term of Eq. (9) is determined by two states of the system—the given state and the dead state—and is independent of the details of the process linking these two states. The value of the term S_{gen} depends on the nature of the process, however: S_{gen} is positive when irreversibilities are present and vanishes in the limiting case where there are no irreversibilities within the combined system. S_{gen} cannot be negative. Hence, the maximum theoretical value for the work of the combined system is obtained by setting S_{gen} to zero. By definition, exergy, E, is this maximum value:

$$E = U + p_o V - T_o S - \Sigma n_i \mu_i^e + KE + PE \quad (10)$$

As considered next, the exergy value can be expressed as the sum of two contributions: *chemical exergy* and *thermomechanical exergy*.

4 Chemical and Thermomechanical Exergy

The value of exergy at the restricted dead state is the maximum theoretical work obtainable as the system initially at T_o, p_o achieves chemical equilibrium with the environment. This exergy value is called the *chemical exergy*, E^{CH}. Applying Eq. (10) at the restricted dead state we have

$$E^{CH} = U_o + p_o V_o - T_o S_o - \Sigma n_i \mu_i^e \quad (11a)$$

where U_o, V_o, S_o denote the energy, volume, and entropy of the system at the restricted dead state. Applying Eq. (1) at the restricted dead state and using the result to reduce Eq. (11*a*) results in the following *alternative* expression for the chemical exergy:

$$E^{CH} = \Sigma n_i(\mu_{io} - \mu_i^e) \quad (11b)$$

where μ_{io} is the chemical potential of substance i at the restricted dead state. The chemical exergy also can be thought of as the minimum theoretical work input required to extract the system from substances present in the environment and bring the system to the restricted dead state.

The *thermomechanical exergy*, E^{TH}, is the maximum theoretical work obtainable as the system passes from some given state to the restricted dead state. The following alternative expressions are obtained, respectively, by subtracting Eqs. (11*a*) and (11*b*) from Eq. (10):

$$E^{TM} = (U - U_o) + p_o(V - V_o) - T_o(S - S_o) + KE + PE \quad (12a)$$

$$E^{TM} = U + p_o V - T_o S - \Sigma n_i \mu_{io} + KE + PE \quad (12b)$$

Expressions for the chemical exergy corresponding to various special cases of practical interest can be developed. The three cases to follow provide illustrations:

Case 1: When the system at the restricted dead state consists of an ideal gas mixture and each component also exists in the environment as a member of an ideal gas mixture, the chemical potentials of Eq. (11*b*) are expressible as follows (Moran and Shapiro, 1992):

$$\mu_{io} = \bar{g}_i(T_o, p_o) + \bar{R}T_o \ln y_i \quad (13a)$$

$$\mu_i^e = \bar{g}_i(T_o, p_o) + \bar{R}T_o \ln y_i^e \quad (13b)$$

where $\bar{g}_i$ is the molar Gibbs function of pure i and y_i, y_i^e denote the mole fraction of i within the mixture at the restricted dead state and environment, respectively. Inserting Eqs. (13) in Eq. (11*b*) gives an expression for the chemical exergy on a *per mole* of mixture basis in the form

$$\bar{e}^{CH} = \bar{R}T_o \sum_{i=1}^{j} y_i \ln \frac{y_i}{y_i^e} \quad (14)$$

Discussion of this expression is provided by Moran (1989).

Case 2: The chemical exergy concept is applicable when the system components are among the substances making up the environment, as in Case 1, and when one or more of the system components is absent from the environment but can be formed from environmental substances. In such an instance, the chemical potential *within the environment* of a substance not present in the environment is derived from the equilibrium condition applying to the reaction of formation of the substance from environmental substances (Ahrendts, 1982; Moran, 1989). As an illustration, consider a pure hydrocarbon C_aH_b at T_o, p_o and an environment containing O_2, CO_2, $H_2O(v)$ as members of an ideal gas mixture but from which C_aH_b is absent. The reaction of formation is

$$a\text{CO}_2 + \frac{b}{2}\text{H}_2\text{O} \Longleftrightarrow \text{C}_a\text{H}_b + \left(a + \frac{b}{4}\right)\text{O}_2 \quad (15)$$

The corresponding *equation of reaction equilibrium* (Moran and Shapiro, 1992) is

$$a\mu_{\text{CO}_2}^e + \frac{b}{2}\mu_{\text{H}_2\text{O}}^e = \mu_F^e + \left(a + \frac{b}{4}\right)\mu_{\text{O}_2}^e \quad (16)$$

where μ_F^e denotes the chemical potential *within the environment* of C_aH_b. Solving Eq. (16) for μ_F^e, and inserting the result into Eq. (11*b*) expressed on a molar basis gives

$$\bar{e}_F^{CH} = \mu_{F,o} - \mu_F^e = \mu_{F,o} - \left[a\mu_{\text{CO}_2}^e + \frac{b}{2}\mu_{H_2\text{O}}^e - \left(a + \frac{b}{4}\right)\mu_{\text{O}_2}^e\right] \quad (17a)$$

The chemical potential of the fuel equals its molar Gibbs function. Using Eq. (13*b*) to evaluate the chemical potentials for CO_2, H_2O, and O_2, Eq. (17*a*) can be written as

$$\bar{e}_F^{CH} = \underline{\left[\bar{g}_F + \left(a + \frac{b}{4}\right)\bar{g}_{\text{O}_2} - a\bar{g}_{\text{CO}_2} - \frac{b}{2}\bar{g}_{\text{H}_2\text{O}(v)}\right](T_o, p_o)} + \bar{R}T_o \ln \left[\frac{(y_{\text{O}_2}^e)^{a+b/4}}{(y_{\text{CO}_2}^e)^a (y_{\text{H}_2\text{O}}^e)^{b/2}}\right] \quad (17b)$$

The chemical exergy is determined mainly by the underlined term of Eq. (17*b*) involving Gibbs functions; the logarithmic term normally contributes only a few percent. Moreover, for hydrocarbons the underlined term is roughly approximated by the fuel *heating value*. So, for *back-of-the-envelope* calculations, the chemical exergy of a hydrocarbon is often taken as its heating value. Further discussion of Eq. (17*b*) is provided by Moran (1989).

Case 3: Because of the variation in conditions over the globe, the specification of an environment for the calculation of chemical exergies suitable for a particular application can involve extensive deliberation and study. Furthermore, once the environment is specified, a series of calculations is required to obtain chemical exergy values for all substances of interest

(Gaggioli and Petit, 1977). These complexities can be sidestepped by use of a *standard* environment (Ahrendts, 1982; Kotas, 1985; Moran, 1989; Szargut et al., 1988). Once a standard environment is defined, *standard* chemical exergies can be calculated and tabulated. Use of such a table greatly facilitates the application of exergy analysis since it eliminates the need for many intermediate calculations. When chemical exergy values are required, they may be selected directly from a table of standard values or calculated using table values. To illustrate, for a pure substance i at T_o, p_o, Eq. (11*b*) gives

$$\bar{e}_i^{CH} = \bar{\mu}_{io} - \mu_i^e$$

$$= \bar{g}_i(T_o, p_o) - \mu_i^e$$

On rearrangement

$$\mu_i^e = \bar{g}_i(T_o, p_o) - \bar{e}_i^{CH} \tag{18}$$

Applying Eq. (18) to O_2, CO_2, and $H_2O(v)$, and inserting the resulting expressions into Eq. (17*a*), the following expression for the standard chemical exergy of C_aH_b in terms of the standard chemical exergies and molar Gibbs function of O_2, CO_2, and $H_2O(v)$ is obtained:

$$\bar{e}_F^{CH} = \left[\bar{g}_F + \left(a + \frac{b}{4}\right)\bar{g}_{O_2} - a\bar{g}_{CO_2} - \frac{b}{2}\bar{g}_{H_2O(v)}\right](T_o, p_o) + a\bar{e}_{CO_2}^{CH} + \frac{b}{2}\bar{e}_{H_2O}^{CH} - \left(a + \frac{b}{4}\right)\bar{e}_{O_2}^{CH} \tag{19}$$

The term *standard* is a misnomer, however, for there is no one specification of the environment that suffices for all applications. Still, the use of a standard environment in preference to one that might be *tailored* to a particular application appears to introduce appreciable discrepancies only occasionally. Futhermore, chemical exergies calculated relative to alternative specifications of the environment are generally in good agreement. Accordingly, for a broad range of engineering applications the simplicity and ease of use of standard chemical exergies generally outweighs any lack of accuracy that might result.

5 Further Exergy Aspects

Exergy is a measure of the departure of the state of the system from that of the environment. It is therefore an attribute of the system and environment together. However, once the environment is specified, a value can be assigned to exergy in terms of property values for the system only, so exergy can be regarded as a property of the system.

Although exergy is an extensive property, it is often convenient to work with it on a unit mass or molar basis. The specific exergy on a mass basis, e, expressed as the sum of thermomechanical and chemical contributions is

$$e = \underline{(u - u_o) + p_o(v - v_o) - T_o(s - s_o)} + \frac{V^2}{2} + gz + e^{CH} \tag{20}$$

where u, v, and s are the specific internal energy, volume, and entropy, respectively, at a given state; u_o, v_o, and s_o are the same specific properties at the restricted dead state; $V^2/2$ is the specific kinetic energy and gz is the specific gravitational potential energy, each on a unit of mass basis. By inspection of Eq. (20), four components of exergy can be identified: the underlined term is known as the *physical* exergy, $V^2/2$ is the *kinetic* exergy, gz is the *potential* exergy, and e^{CH} is the *chemical* exergy.

Many practical applications require the proper evaluation of the exergy associated with a flowing stream entering or exiting a control volume. At such locations, there are exergy transfers accompanying mass flow *and* flow work. A single expression representing the sum of these contributions is convenient. The mass flow contribution is

$$\begin{bmatrix}\text{rate of exergy transfer}\\ \text{accompanying mass flow}\end{bmatrix} = \dot{m}e \tag{21}$$

On a time rate basis the flow work is $\dot{m}(pv)$, and the accompanying exergy transfer is given as follows (Moran, 1989; Moran and Shapiro, 1992):

$$\begin{bmatrix}\text{rate of exergy transfer}\\ \text{accompanying flow work}\end{bmatrix} = \dot{m}[pv - p_o v] \tag{22}$$

In writing these expressions, *one-dimensional flow* is assumed. A single expression consisting of the sum of these contributions is

$$\begin{bmatrix}\text{rate of exergy transfer}\\ \text{accompanying mass flow and flow work}\end{bmatrix} = \dot{m}[e + (pv - p_o v)] \tag{23}$$

The sum in square brackets is the *specific flow exergy*, e_f,

$$e_f = e + (pv - p_o v) \tag{24a}$$

Introducing Eq. (20), this can be expressed as

$$e_f = \underline{(h - h_o) - T_o(s - s_o)} + \frac{V^2}{2} + gz + e^{CH} \tag{24b}$$

where h_o and s_o denote the specific enthalpy and entropy, respectively, at the restricted dead state. The underlined term of Eq. (24*b*) is known as the *physical* component of the flow exergy.

The flow exergy appears explicitly in the control volume *exergy balance*[2], the steady-state form of which is:

$$0 = \sum_j \left(1 - \frac{T_o}{T_j}\right)\dot{Q}_j - \dot{W}_{cv} + \sum_j \dot{m}_i e_{fi} - \sum_e \dot{m}_e e_{fe} - \dot{E}_D \tag{25}$$

$\dot{Q}_j$ represents the time rate of heat transfer at the location on the boundary where the instantaneous temperature is T_j. The accompanying rate of exergy transfer is given by $(1 - T_o/T_j)\dot{Q}_j$. $\dot{W}_{cv}$ represents the time rate of work *other than flow work*. Note that shaft work and electrical work are *fully* transfers of exergy. The term $\dot{m}_i e_{fi}$ accounts for the time rate of exergy transfer accompanying mass flow *and* flow work at inlet i. Similarly, $\dot{m}_e e_{fe}$ accounts for the time rate of exergy transfer accompanying mass flow *and* flow work at exit e. The quantities e_{fi} and e_{fe} appearing in these expressions may be evaluated from Eq. (24*b*). Finally, the term $\dot{E}_D$ accounts for the time rate of exergy destruction due to irreversibilities *within* the control volume.

6 Applying Exergy

Thermal systems are supplied with exergy inputs derived directly or indirectly from the consumption of resources such as oil, natural gas, and coal. Accordingly, *avoidable* destructions and losses of exergy represent the waste of these resources. By devising ways to reduce such sources of inefficiency, better use can be made of fuels. The exergy balance can be used to determine the location, type, and true magnitude of the waste of energy resources, and thus can play an important part in developing strategies for more effective fuel use. For elementary illustrations of the use of the exergy rate balance for engineering analysis and design, refer to Kotas (1985), Moran (1989), Moran and Shapiro (1992), and Szargut et al. (1988). The symposium volumes referenced provide numerous additional illustrations involving more complex cases.

Readers are also directed to two companion articles in this issue of the JOURNAL OF ENGINEERING FOR GAS TURBINES AND POWER that utilize exergy for the analysis of an integrated

[2]As exergy can be destroyed, Spiegler (1983) prefers to use the term *exergy accounting* instead of *exergy balance*.

gasification-combined cycle power plant (Tsatsaronis et al., 1994). It is particularly noteworthy that exergy principles are used together with costing principles in the second of these articles. Since exergy properly gages the quality (utility) of different types of mass and energy flows, exergy can be used consistently for costing. Thus, while it does not make sense to compare the *energetic* cost of 1 kW·h of electricity with that of 1 kW·h of steam or cooling water, it does make sense to compare their *exergetic* costs.

Exergy analysis can help locate system nonidealities that either are not identified or misevaluated by energy analysis, as for example the combustion irreversibility. Accordingly, exergy analysis can be used as a tool to devise *better* processes or design *better* components, by testing whether their exergy destruction rates are lower than for the original process/component. Exergy analysis also can be used to assess the *real* effect of off-design conditions on individual components or overall plants.

Finally, exergy analysis can be applied *globally* to the industrial sector, the agricultural sector, or an entire nation to develop insights concerning the location and relative significance of key nonidealities. Such insights can be used to guide measures for improving the sector's overall conversion efficiency, reducing thereby resource waste attributable to that sector.

References

Ahrendts, J., 1982, "Reference States," *Energy*, Vol. 5, pp. 667–677.

Boehm, R. F., et al., 1992, *Thermodynamics and the Design, Analysis, and Improvement of Energy Systems—1992*, ASME AES-Vol. 27, New York.

Gaggioli, R. A., and Petit, P. J., 1977, "Use the Second Law, First," *Chemtech*, Vol. 7, pp. 496–506.

Kenney, W. F., 1984, *Energy Conservation in the Process Industries*, Academic Press, Orlando, FL.

Kotas, T. J., 1985, *The Exergy Method of Thermal Plant Analysis*, Butterworths, London, United Kingdom.

Kouremenos, D. A., Tsatsaronis, G., and Rakopoulos, C. D., 1991, *Analysis of Thermal and Energy Systems*, Proceedings of the International Conference, Athens, Greece, Greg. Foundas, Athens.

Melli, R., Paoletti, B., and Sciubba, E., 1990, "Design and Functional Optimization of Thermo-mechanical Plants via an Interactive Expert System," in: *Computer-Aided Energy-Systems Analysis*, G. Tsatsaronis et al., eds., ASME AES-Vol. 21, New York, pp. 39–48.

Moran, M. J., 1989, *Availability Analysis: A Guide to Efficient Energy Use*, ASME Press, New York.

Moran, M. J., 1990, "Second Law Analysis—What is the State of the Art?" in: *A Future for Energy*, proceedings of FLOWERS '90, The Florence World Energy Research Symposium, Florence, Italy, S. S. Stecco and M. J. Moran, eds., Pergamon Press, Oxford, pp. 249–260.

Moran, M. J., and Shapiro, H. N., 1992, *Fundamentals of Engineering Thermodynamics*, 2nd ed., Wiley, New York.

Reistad, G. M., et al., 1991, (*a*) *Thermodynamics and Energy Systems—Fundamentals, Education and Computer Aided Analysis*, ASME AES-Vol. 24, *and* (*b*) *Second Law Analysis—Industrial and Environmental Applications*, ASME AES-Vol. 25/HTD-Vol. 191, New York.

Sama, D. A., 1992, "A Common-Sense 2nd Law Approach to Heat Exchanger Network Design," in: *ECOS '92*, Proceedings of the International Symposium On Efficiency, Costs, Optimization and Simulation of Energy Systems, Zargoza, Spain, A. Valero and G. Tsatsaronis, eds., ASME, New York, pp. 329–338.

Spiegler, K. S., 1983, *Principles of Energetics*, Springer-Verlag, Berlin–Heidelberg.

Stecco, S. S., and Moran, M. J., 1990, *A Future for Energy*, Proceedings of FLOWERS '90, The Florence World Energy Research Symposium, Florence, Italy, Pergamon Press, Oxford, United Kingdom.

Stecco, S. S., and Moran, M. J., 1992, *Energy for the Transition Age*, Proceedings of FLOWERS '92, The Florence World Energy Research Symposium, Florence, Italy, Nova Science, New York.

Szargut, J., Morris, D. R., Steward, F. R., 1988, *Exergy Analysis of Thermal, Chemical, and Metallurgical Processes*, Hemisphere, New York.

Tsatsaronis, G., et al., 1990, (*a*) *Fundamentals of Thermodynamics and Exergy Analysis*, ASME AES-Vol. 19, (*b*) *Education in Thermodynamics and Energy Systems*, ASME AES-Vol. 20, (*c*) *Computer-Aided Energy-Systems Analysis*, ASME AES-Vol. 21, New York.

Tsatsaronis, G., et al., 1994, (*a*) "Exergetic Comparison of Two KRW-Based IGCC Power Plants," (*b*) "Exergoeconomic Evaluation of a KRW-Based IGCC Power Plant," ASME JOURNAL OF ENGINEERING FOR GAS TURBINES AND POWER, Vol. 116, this issue, pp. 291–306.

Valero, A., and Tsatsaronis, G., 1992, *ECOS '92*, Proceedings of the International Symposium on Efficiency, Costs, Optimization and Simulation of Energy Systems, Zaragoza, Spain, ASME, New York.

Exergetic Comparison of Two KRW-Based IGCC Power Plants

G. Tsatsaronis

T. Tawfik

L. Lin

Center for Electric Power,
Tennessee Technological University,
Cookeville, TN 38505

D. T. Gallaspy
Southern Electric International,
Atlanta, GA 30338

In studies supported by the U.S. Department of Energy and the Electric Power Research Institute, several design configurations of Kellogg-Rust-Westinghouse (KRW)-based Integrated Gasification-Combined-Cycle (IGCC) power plants were developed. Two of these configurations are compared here from the exergetic viewpoint. The first design configuration (case 1) uses an air-blown KRW gasifier and hot gas cleanup while the second configuration (reference case) uses an oxygen-blown KRW gasifier and cold gas cleanup. Each case uses two General Electric MS7001F advanced combustion turbines. The exergetic comparison identifies the causes of performance difference between the two cases: differences in the exergy destruction of the gasification system, the gas turbine system, and the gas cooling process, as well as differences in the exergy loss accompanying the solids to disposal stream. The potential for using (a) oxygen-blown versus air-blown-KRW gasifiers, and (b) hot gas versus cold gas cleanup processes was evaluated. The results indicate that, among the available options, an oxygen-blown KRW gasifier using in-bed desulfurization combined with an optimized hot gas cleanup process has the largest potential for providing performance improvements.

Introduction

Integrated gasification-combined-cycle (IGCC) power plants are currently under development to provide a clean, efficient, and cost-effective option for generating electric power from coal. The gasification island of an IGCC power plant converts coal to a clean combustible gas that fuels a combustion turbine. The combustion turbine exhaust heat is used to produce steam, which drives a turbine generator. The integration between the gasification island and the power island (combined cycle) mainly involves (*a*) generation of saturated steam in the gasification island and use of this steam in the power island, and (*b*) supply of steam at various temperature and pressure levels by the power island to cover the steam demands of the gasification island.

Southern Company Services, Inc. (SCS), under cooperative agreements with the U.S. Department of Energy (DOE), Morgantown Energy Technology Center (METC), and the Electric Power Research Institute (EPRI), has developed and studied various design configurations of IGCC power plants that use a Kellogg-Rust-Westinghouse (KRW) gasifier (Gallaspy et al., 1990; Tsatsaronis et al., 1991). The objectives of these studies include evaluation and comparison of various IGCC power plant configurations from the cost, performance, and reliability viewpoints. Of particular interest was the comparison between (*a*) an air-blown gasification-based power plant with hot gas cleanup (case 1) and (*b*) an oxygen-blown gasification-based power plant with cold gas cleanup (reference case). The studies should also determine whether these plants can compete against pulverized-coal plants with flue-gas desulfurization. For purposes of the studies, the power plants were assumed to be located at the Plant Wansley site of Georgia Power Company, an operating subsidiary of the Southern Company.

To facilitate the comparison between case 1 and the reference case, to understand the underlying performance differences, and to identify design improvements, detailed exergy analyses were conducted for each case. The complexity, the variety of equipment options, and the integrated nature of gasification-combined-cycle power plants make optimization of these plants considerably more difficult than that of conventional power plants. An exergy analysis and, particularly, an exergoeconomic analysis (appropriate combination of exergetic and economic analysis) are very useful tools for the performance and cost optimization of IGCC power plants (Tsatsaronis, 1993). Exergy principles are reviewed in the companion paper (Moran and Sciubba, 1994).

This paper discusses the performance comparison between case 1 and the reference case. The design of case 1 was developed in a DOE supported study (Southern Company Services, 1990), whereas the final design of the reference case was developed in two stages. The first version of the reference case is reported by Gallaspy et al. (1990). This version was modified by Tsatsaronis and Tawfik (1990) to consider performance updates of the General Electric MS7001F gas turbine and to make the design configuration of the reference case comparable with the case 1 design. This paper discusses the comparison of case 1 with the updated version of the reference case.

The team, which developed the design configurations discussed in this paper, was led by Southern Company Services, which was responsible for the project management, the environmental assessment, the overall cost estimates, the design integration, the design and costs of the steam cycle, the ma-

Contributed by the Advanced Energy Systems Division for publication in the JOURNAL OF ENGINEERING FOR GAS TURBINES AND POWER. Manuscript received by the Advanced Energy Systems Division February 24, 1992; revision received December 4, 1992. Associate Technical Editor: M. J. Moran.

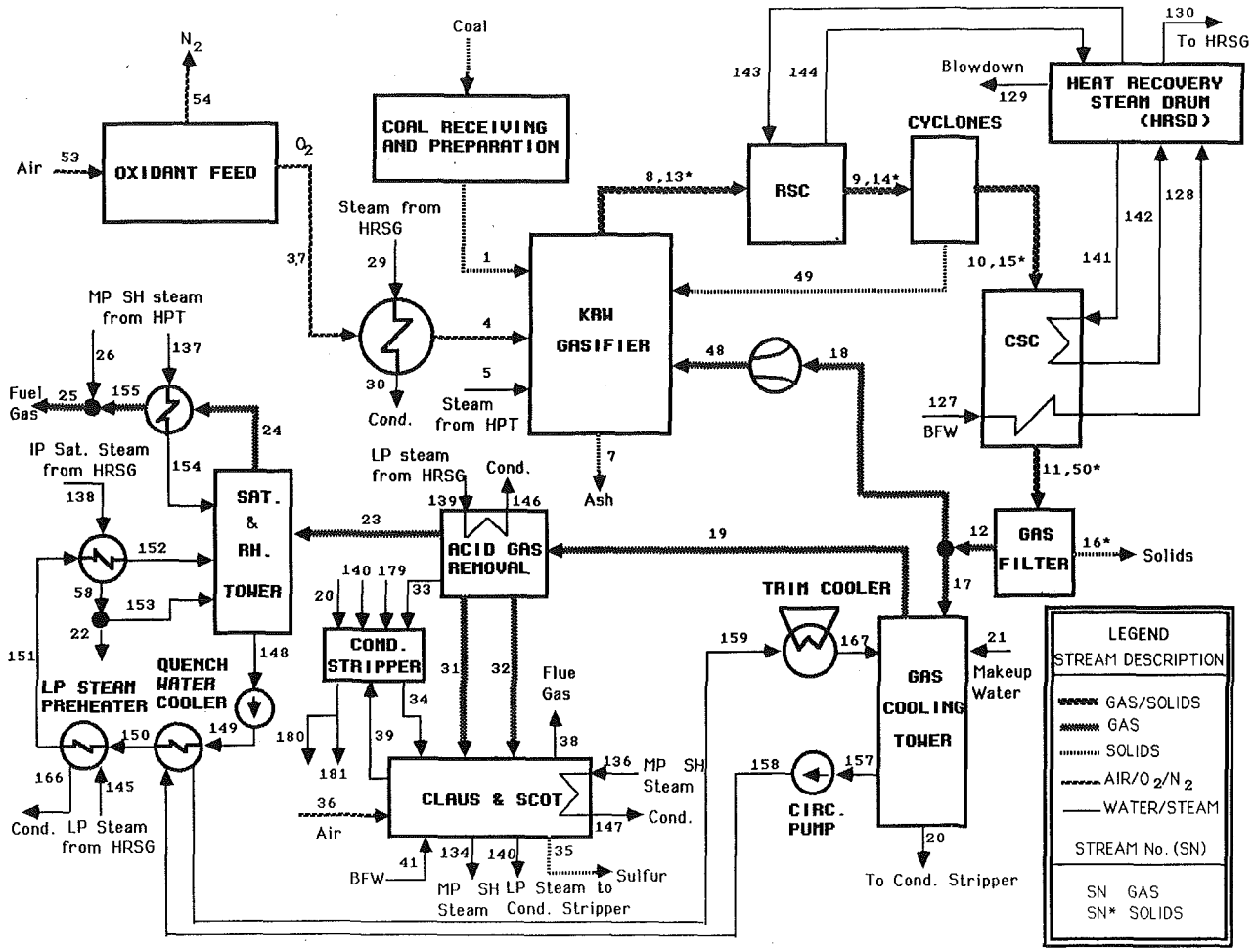

Fig. 1 Simplified flow diagram of the gasification island in the reference case

terials handling processes, and the reliability analysis. Other participants were the M. W. Kellogg Company (design and costs of the gasification island), General Electric Company (performance and costs of the gas turbine system), and the Center for Electric Power at Tennessee Technological University (exergy analysis, pinch analysis, and exergoeconomic evaluation and optimization). This paper deals with the exergetic evaluation and performance comparison of the reference case and case 1.

Description of the Reference Case Design

Figures 1, 2, and 3 show simplified flow diagrams of the gasification island, the gas turbine system, the Heat-Recovery Steam Generator (HRSG), and the steam cycle in the reference case. The main plant consists of the following component groups: coal receiving and preparation (not shown in the figures); oxidant feed system including an air separation unit (ASU) and oxygen compression; gasification system including an oxygen heater, a KRW gasifier, a radiant syngas cooler (RSC), a cyclone, and an ash handling unit; gas cooling and fines removal including a convective syngas cooler (CSC), a gas filter, a fines handling unit, and a gas cooling tower; acid gas removal (Selexol®); sulfur recovery (CLAUS) and tail gas treating (SCOT); fuel gas saturator and reheater; gas turbine system; heat recovery steam generator; and steam turbine system. The numbers given in parentheses in the following refer to the material streams shown in Figs. 1-3.

The coal gasifier (three trains) uses a feed stream of 95 percent pure oxygen (4) provided by the oxidant feed system (single train). All of the air and oxygen compressors in the oxidant feed system are electric motor driven. The total power requirement of the air separation unit is about 29 MW for a mass flow rate for stream 37 of 24.64 kg/s. Illinois No. 6 coal was assumed to be the fuel. The ambient temperature was assumed to be 32.2°C (90°F).

Coal (1) from the coal preparation area is sent to the gasification system after size reduction and preparation. The gasifier including coal pressurization was designed to process approximately 3720 metric tons per day of as-received Illinois coal in three gasification trains. The Kellogg-Rust-Westinghouse (KRW) coal-gasification process used here is an oxygen-blown, dry ash agglomerating fluidized-bed process. In the Illinois coal case, the gasifier operates at approximately 3.21 MPa (465 psia) and 1010°C (1850°F).

Recycle gas (48) in the gasification system assists in conveying coal to the feed tube, recycling fines back to the gasifier, cooling and separating the ash in the gasifier bottom, and achieving gasifier fluidization. High-pressure superheated steam (5) and oxygen (4) are introduced as reactants. The oxygen is heated to 232.2°C (450°F) through an oxygen heater using medium-pressure steam (29) to improve the efficiency of the gasifier and to avoid condensation of steam in the oxidant tube.

The normal coal feed rate into the three KRW gasifiers is 145.34 metric tons/h (320,423 lb/hr). The carbon conversion loss to the ash agglomerates is minimal. The fines leaving with the gas stream are recovered and recycled back to the gasifier (49). The gasifier has a cold gas efficiency of about 85.3 percent. The chemical products of the gasification reactions are

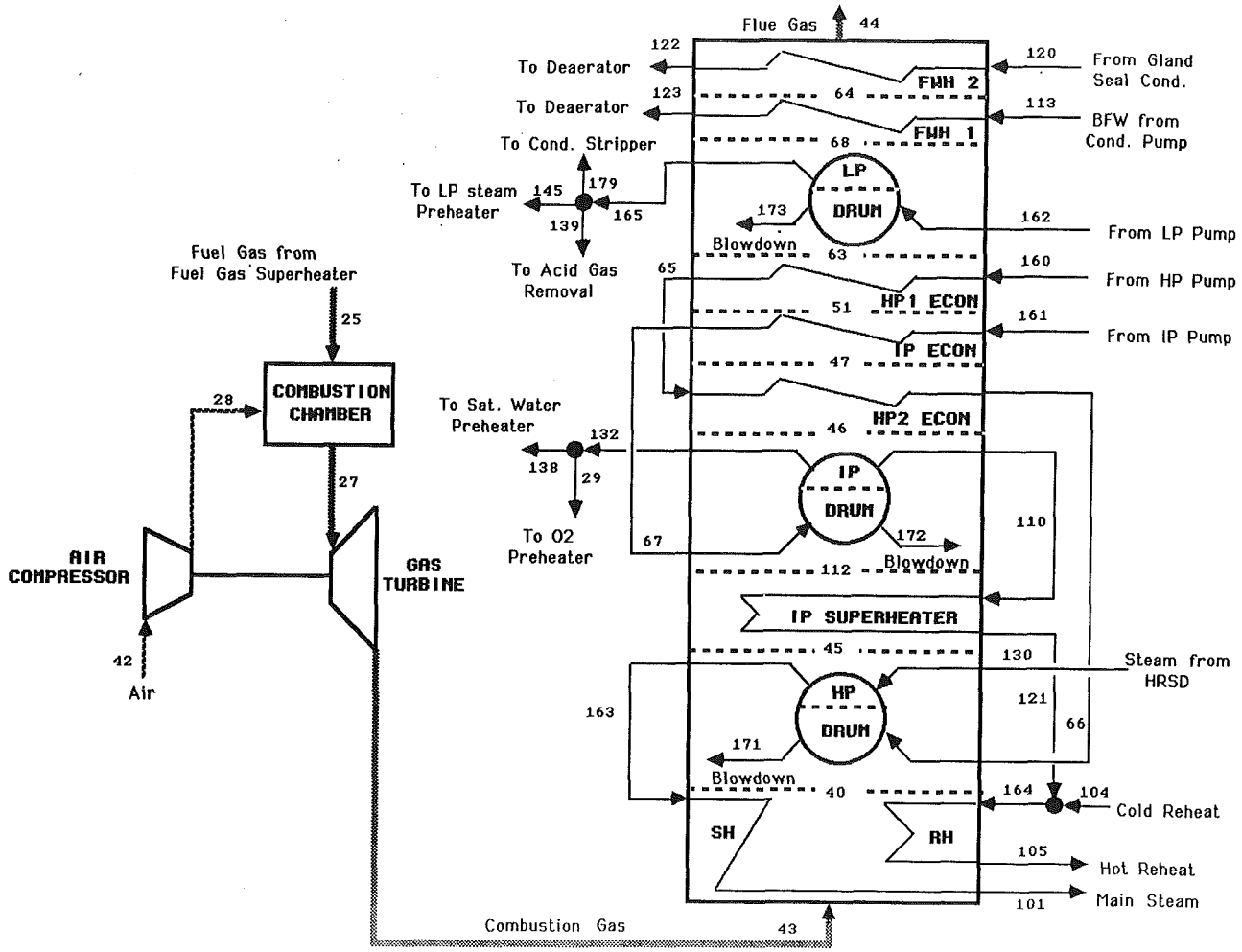

Fig. 2 Simplified flow diagram of the gas turbine system and the HRSG in the reference case

CO, H_2, CH_4, CO_2, H_2O, N_2, and small amounts of H_2S, NH_3, and COS. The crude gas is free of tars and oils because of the high reactor temperatures.

The high-temperature (radiant) syngas cooler is designed to cool the gas leaving the gasifier (8) at 1010°C (1850°F) to approximately 704°C (1300°F), while generating high-pressure (10.5 MPa = 1525 psia) saturated steam (144). The cyclones, located downstream of the high-temperature syngas cooler, and designed to recover 95 percent of the fines entering with the gas stream (9) and to recycle these fines back to the gasifier (49). Recycle gas (part of stream No. 48) is used to assist in this operation. The raw gas leaving the cyclone (10) is sent to the low-temperature (convective) syngas cooler.

The convective syngas cooler was designed to cool the gas leaving the cyclone (10) from about 705°C (1300°F) to 238°C (450°F), while generating high-pressure steam (142) and preheating boiler feedwater (127). The partially cooled gas from the convective syngas cooler (11) enters the fines removal section (two operating trains and one spare train) where the remaining solids are removed. The fines removal system consists of a sintered metal gas filter, a fines let-down hopper, an accompanying vent filter, and a fines discharge hopper.

The filtered particulate-free gas (17) enters the gas cooling tower where the gas is cooled by direct contact with circulating water. Gas cooling, acid gas removal, gas saturation, and reheating are accomplished in a single train. The cooled gas (19) leaves at the top of the tower and is sent to the acid gas removal system. Most of the water in the feed gas is condensed and accumulated in the bottom of the tower from which a purge stream (20) is taken and sent to the sour water stripping section. The circulating water is cooled by two heat exchangers, which indirectly remove the heat taken from the gas by circulating water. A portion of this waste heat is used to heat up the saturator/reheat tower condensate (149). Fresh make-up water (21) is added to the top tray of the tower to ensure proper cooling as well as to maintain an acceptable level of chlorides in the circulating water.

Raw gas from the gas cooling tower (19) enters the Selexol® acid gas removal unit. This unit consists of a feed/overhead exchanger, an H_2S absorber, a hydraulic turbine, a flash drum, a lean solvent cooler, a rich/lean solvent exchanger, a refrigeration package, an H_2S stripper, lean solvent pumps, a stripper reboiler, an H_2S stripper condenser, a stripper reflux drum, and stripper reflux pumps. The Claus process is used for recovering elemental sulfur from acid gases. The overall sulfur removal for the entire plant is 95 percent. Sulfur recovery in the Claus unit is 92 percent with the unrecovered sulfur being sent to the SCOT tail gas treatment unit and subsequently recycled back to the Claus unit. This unit consists of two catalytic reactors, three condensers, a reaction furnace, an air blower, an acid water pump, and a reheat exchanger. The Shell Claus off-gas treating (SCOT) process is used for recovering H_2S from the Claus unit tail gas.

The clean fuel gas (23) from the acid gas removal section enters the fuel gas saturator/reheat tower. It leaves the tower at 152°C (450°F) with a moisture content of approximately 20 percent by weight. The circulating water is preheated using waste heat from the gas cooling tower and low-pressure (145)

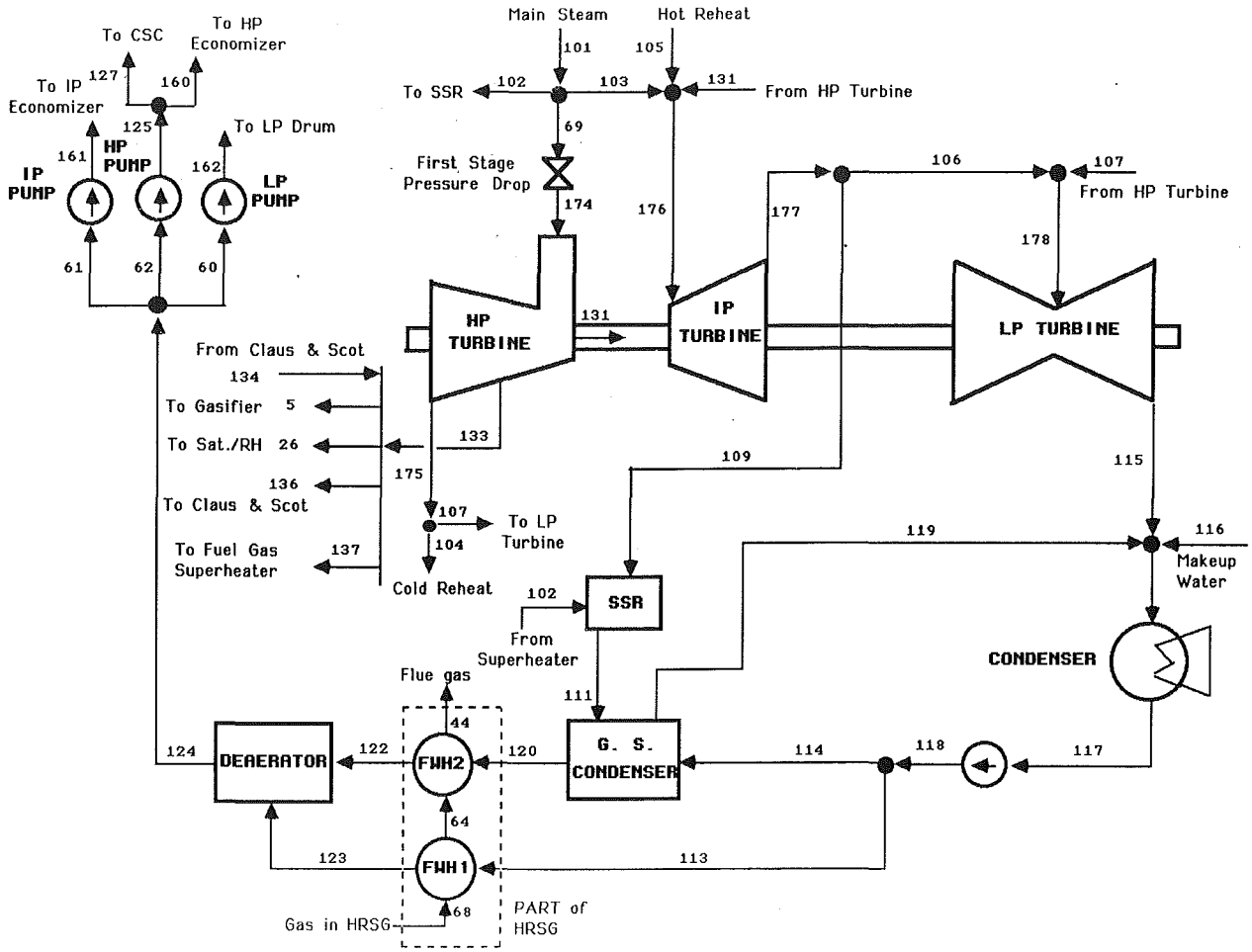

Fig. 3 Simplified flow diagram of the steam cycle in the reference case

and medium-pressure (138) steam. The gas leaving the saturation tower (24) is further heated by medium-pressure superheated steam (137); a small amount of superheated steam (26) is added to the fuel gas to match the gas turbine requirements. The superheated fuel gas (25) then flows to the gas turbines.

Two General Electric MS7001F combustion gas turbines were assumed in the combined cycle. These advanced combustion turbines will have a firing temperature of about 1260°C (2300°F). Fuel gas (25) is introduced to the gas turbine combustor along with air (28) supplied by the compressor driven by the gas turbine expander, Fig. 2. The hot gas exiting the combustor (27) is supplied to the hot gas expander, which in turn drives the gas turbine generator. The electric power output at the gas turbine is about 298 MW.

The exhaust gas from each combustion turbine (43) enters a heat-recovery steam generator that provides superheating of high-pressure (HP) steam, reheating of intermediate-pressure (IP) steam, and supplements intermediate-pressure and low-pressure (LP) steam generation.

The combined-cycle steam turbine consists of a high-pressure, intermediate-pressure, and low-pressure section, Fig. 3. The HP section accepts the 10.3 MPa/538°C (1500 psia/1000°F) steam (101) from the two HRSGs. The exhaust steam (104) from the HP turbine is reheated to 538°C (1000°F) by the HRSGs and returns to the IP turbine (105). The IP exhaust steam (106) is then routed to the LP turbine from which it is condensed at a design back pressure of 11.85 kPa (3.5 in. Hg). The steam turbine generates about 159 MW.

Condensate from the condenser (117) enters two vertical motor-driven condensate pumps and subsequently passes through the gland seal condenser where it experiences a 1°C (1.8°F) temperature rise. Steam for this heating is provided by the steam seal regulator (SSR).

Subsequently, the condensate (120) is heated to 77°C (170°F) in the low-pressure feedwater heater before it enters (122) the two deaerators, which operate at 172 kPa (25 psia), heat the feedwater to 110°C (230°F), nd are an integral part of each HRSG. Finally, the electric motor driven HRSG feed pumps pump the feedwater (124) to its HRSG feedwater inlets (160, 161, 162) and to the gasification process (127).

Description of the Case 1 Design

In the design of the reference case, the hot gas from the coal gasifier must be cooled to near-ambient temperatures to facilitate cleanup of sulfur, particulates, and other contaminants. The gas must then be reheated before being burned in a combustion turbine system. In the same case, the volume of gas that must be cleaned is reduced by using oxygen from an air separation plant as the primary fuel oxidant in the gasifier. The requirements of gas cooling/reheating and air separation result in capital cost and thermal efficiency penalties, which adversely affect the economics of such IGCC power plant designs.

Hot stream cleanup, in which sulfur and particulates are removed from gas streams at high temperatures, has the potential to increase greatly the cost competitiveness of IGCC plants. Using air as the coal oxidant rather than oxygen could yield further performance and cost advantages. One of the

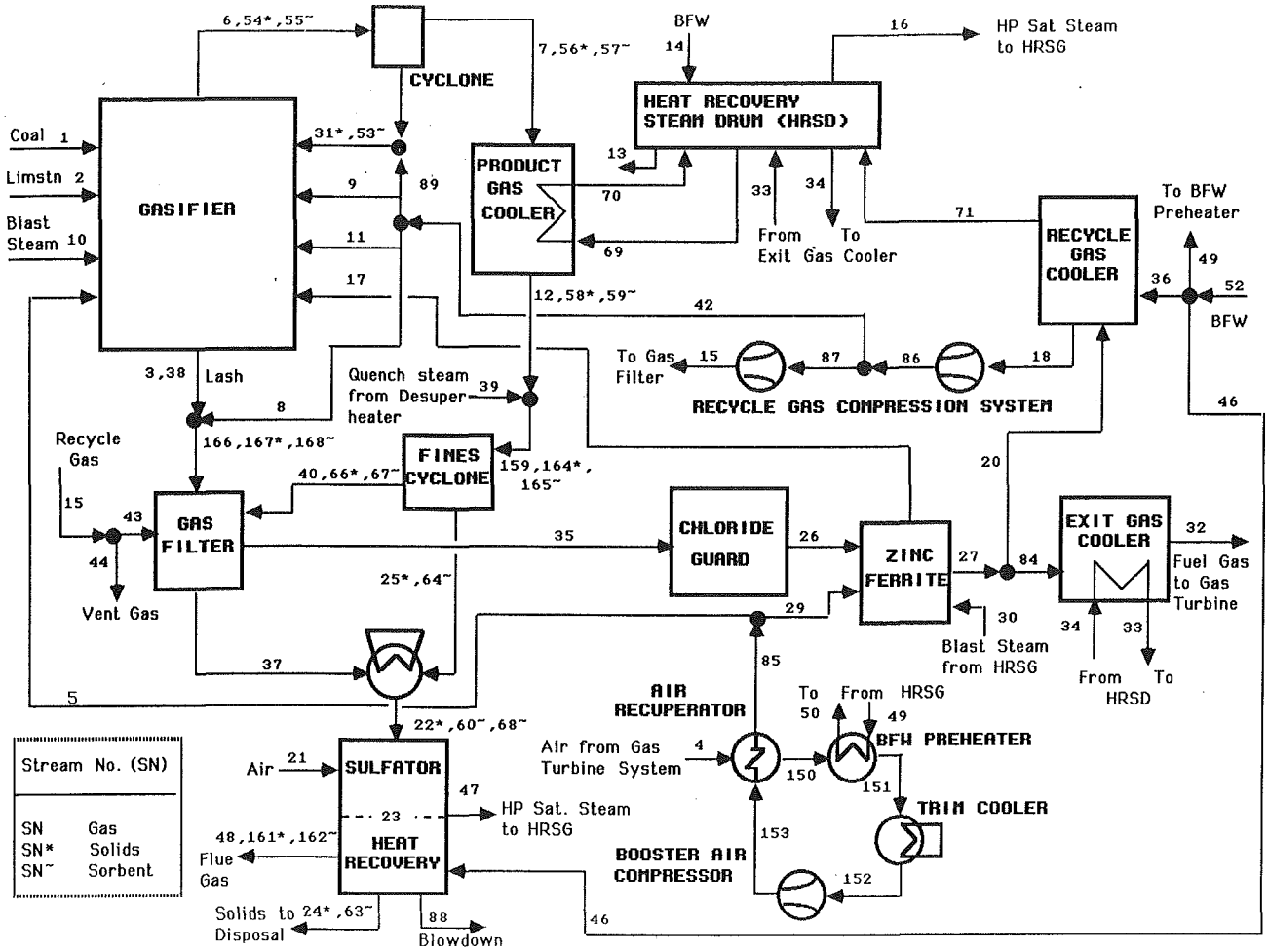

Fig. 4 Simplified flow diagram of the gasification island in case 1

objectives of the U.S. DOE-supported study, in which the case 1 design was developed, was to quantify the magnitude of these improvements.

Figures 4–6 present simplified flow diagrams of the gasification island, the gas turbine system, the HRSG, and the steam cycle of case 1. Only a brief description of case 1 is given here. A more detailed description is given by Tsatsaronis et al. (1991a). The main plant consists of the following component groups: coal and limestone receiving, handling, and preparation (not shown in the figures); boost air compression system; coal gasification; recycle gas compression; gas conditioning; external gas desulfurization; gasifier solids sulfation; gas turbine system; heat recovery steam generator; and steam turbine system. The numbers given in parentheses in the following refer to the material streams shown in Figs. 4–6.

Case 1 uses bulk sulfur removal with limestone in the KRW gasifier with a zinc ferrite polishing step for additional sulfur removal. This case has four separate processing trains for the gasification island with two combustion turbines, two heat recovery steam generators, and one steam turbine.

Flue gas from the sulfator (48) is used to dry the feed coal (1) whereas an oil-fired heater is used to dry the limestone (2). The product gas from the gasifier (6) is cooled (in the product gas cooler and through mixing with quench steam) to nominally 538°C (1000°F) prior to entering a fines cyclone, which removes the coarse particulates from the product gas, and a high-temperature ceramic filter, which removes fine particulates. Both the coarse and fine particulates are fed to the sulfator together with the limestone and ash (LASH) from the gasifier. The particulates provide a carbon fuel source used in the sulfator for the conversion of calcium sulfide to calcium sulfate in the LASH. The heat generated in the sulfator is used to produce HP saturated steam (47) and to dry the feed coal.

After the hot-gas filtration of particulates, the product gas (35) passes through a chloride guard bed and enters the zinc ferrite polishing system where the remaining sulfur from the product gas is removed. Since chlorides can severely affect the structural integrity of the zinc ferrite sorbent, the chlorine guard is used to remove chloride from the fuel gas. The regeneration gas (17) from the zinc ferrite system, mainly consisting of sulfur dioxide, nitrogen, and water vapor, is recycled back to the gasifier. The chemical reactions in the zinc ferrite unit are exothermic. A part of the clean product gas (20) is cooled in the recycle gas cooler and, after compression, is recycled back to the gasifier (42) and the gas filter (15). The major part of the clean product gas (84) is cooled to about 538°C (1000°F) in the exit gas cooler where HP saturated steam (33) is produced.

The cleaned product gas (32) from the gasification island is combusted in two GE MS7001F gas turbines to generate approximately 312 MW of electric power. Air for the gasifier (5) is initially compressed to 1.38 MPa (200 psia) in the gas turbine compressor (4) followed by additional pressurization in a booster compressor to deliver air at the proper pressure for the gasifier.

The 592°C (1098°F) flue gas from the gas turbine (75) is sent to an HRSG to generate steam that is used in the steam turbine and in the gasification island. The design of the steam

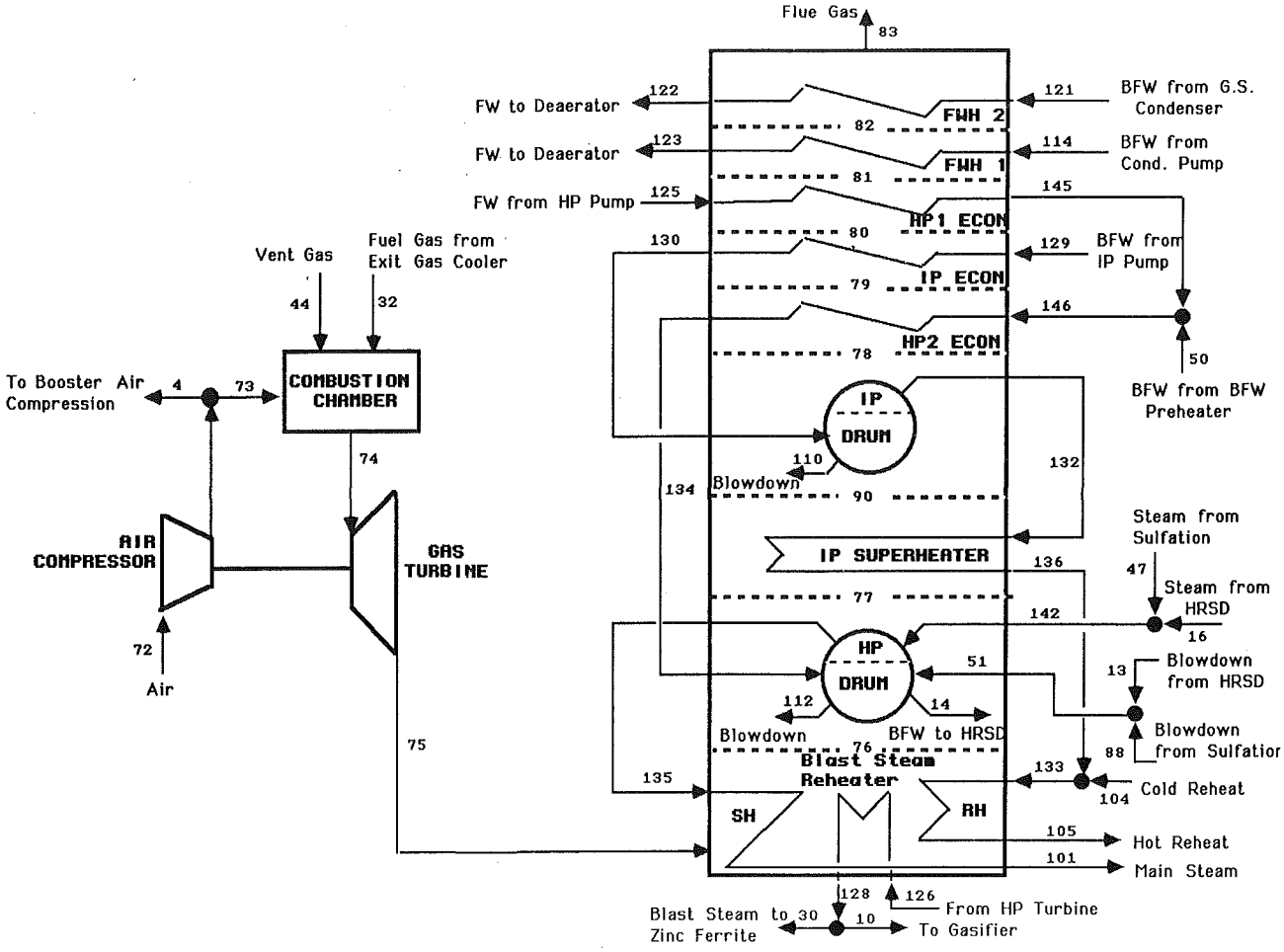

Fig. 5 Simplified flow diagram of the gas turbine system and the HRSG in case 1

cycle in case 1 is similar to the corresponding design of the reference case.

Results and Discussions

Table 1 shows a comparison of selected variables of case 1 and the reference case. The major differences between these cases lie in the following:

- Oxidant feed: the air feed to the oxidant feed system was taken from the gas turbine system in case 1.
- Coal gasifier: An oxygen-blown gasifier is used in the reference case as opposed to an air-blown gasifier in case 1. The coal moisture at the gasifier inlet is 11.12 percent by weight in the reference case versus 4.98 percent by weight in case 1. The gasification temperature is 1038°C (1900°F) in case 1 versus 1010°C (1850°F) in the reference case.
- Solids to be disposed: Stream No. 16 (from gas filter to fines handling) in the reference case contains 4.11 percent of the carbon supplied to the gasifier with the coal whereas stream No. 24 (solids to disposal) in case 1 contains less than 0.07 percent of the carbon fed with the coal into the gasifier.
- Gas cleaning process: Case 1 uses an advanced hot gas cleanup process whereas the reference case uses commercially available cold gas cleanup processes. The temperature of the fuel gas at the inlet to the combustion chamber is, therefore, approximately 300°C higher in case 1 than in the reference case.
- Byproducts: Case 1 has no useful byproducts as opposed to the reference case where almost pure nitrogen and elementary sulfur are generated.

The comparison between the reference case and case 1 is conducted with the aid of (*a*) the dimensionless ratio y_D, which is the ratio between the exergy destruction rate in a plant component and the coal exergy rate supplied to the corresponding power plant and (*b*) the dimensionless ratio y_L, which is the ratio between the exergy loss (the exergy rate of a stream leaving the total plant) and the exergy rate of the coal stream supplied to the corresponding power plant. These dimensionless variables represent objective measures of the component performance and the thermodynamic value of a stream, respectively. These variables allow for the comparison of power plants with different capacities, different design configurations, and different types of coal. A comparison of the values of these dimensionless variables is shown in Tables 2 and 3 and in Fig. 7.

The oxygen-blown KRW gasifier has a considerably higher thermodynamic efficiency than the air-blown KRW gasifier. This difference is mainly caused by the additional combustion required to heat the nitrogen up to the gasifier operating temperature. The product gas from the gasifier contains relatively more carbon monoxide and hydrogen and considerably more methane in the reference case than in case 1.

From the thermodynamic viewpoint, the lower gasifier operating temperature and the higher coal moisture in the reference case represent an advantage and disadvantage, respectively, compared with case 1. The thermodynamic advantage of the oxygen-blown KRW gasifier is, however, partially offset in the gas turbine system. In the reference case, a larger air flow rate than in case 1 must be compressed in the

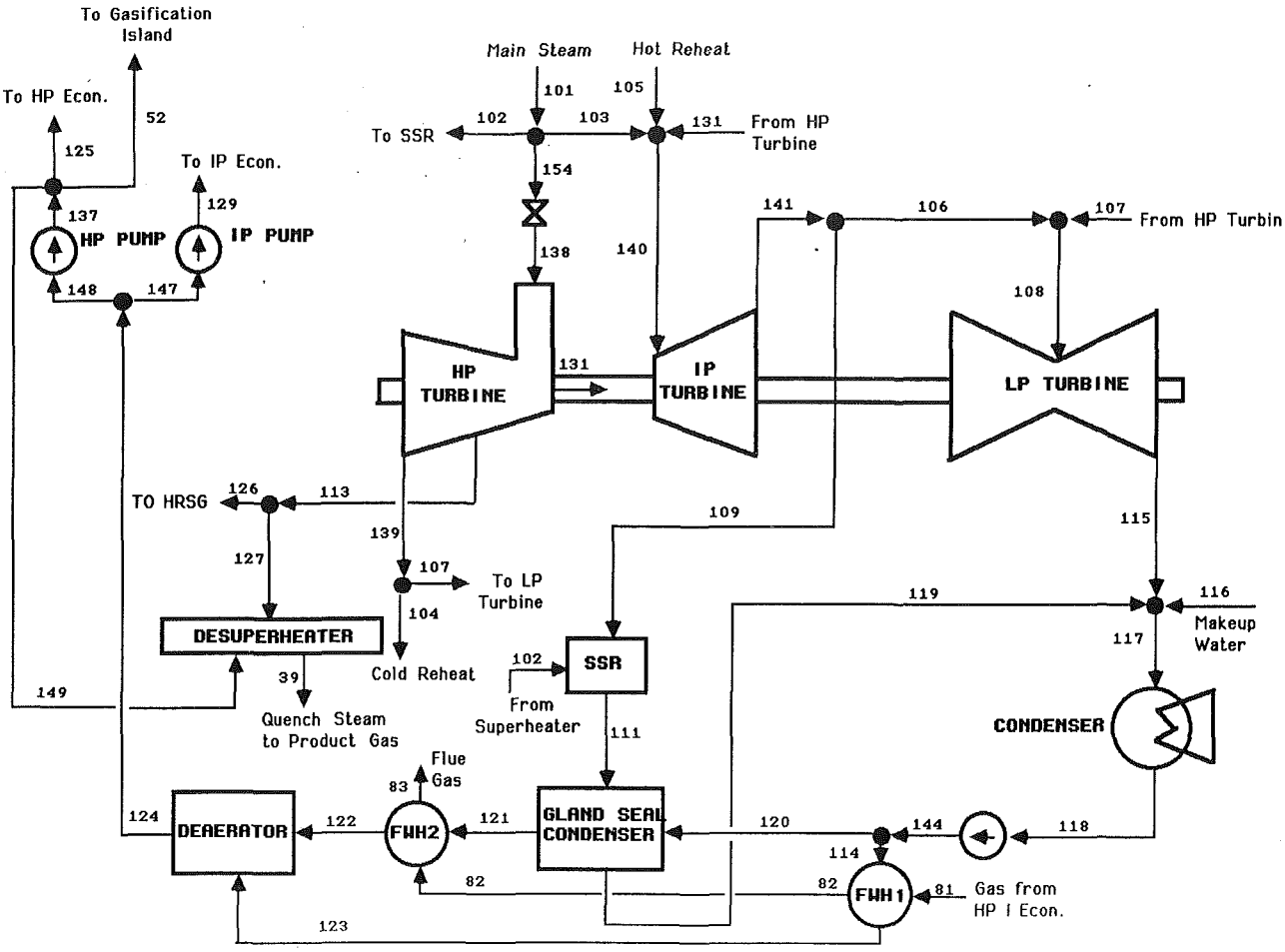

Fig. 6 Simplified flow diagram of the steam cycle in case 1

air compressor and, more importantly, heated in the combustion chamber. The values shown in Table 3 and Figure 7 and the exergetic efficiencies calculated for various groups of plant components allow for the overall effect of the primary oxidizer in KRW gasifiers to be estimated. In these calculations, we assume that the exergetic efficiency of the components or groups of components not immediately affected by the changes being considered remain constant. Our calculations indicate that the difference in the overall efficiency between two IGCC power plants, which have been designed under identical technical approaches and assumptions with the only exception that the first plant uses an oxygen-blown KRW gasifier and the second plant an air-blown KRW gasifier, should be of the order of 0.2 to 0.8 percentage points with the first plant having a higher overall thermodynamic efficiency.

In order to determine if IGCC plants based on an oxygen-blown KRW gasifier are more cost effective than plants based on an air-blown KRW gasifier, the relative fuel savings resulting from the efficiency difference must be compared with the relative increase in the overall investment costs for the former plants compared with the latter ones.

The figures shown in Table 3 and additional estimates used to compare the two cases indicate that the overall plant efficiency improvement that can be attributed only to the high-temperature gas cleanup process used in case 1 compared with the low-temperature gas cleanup process of the reference case is of the order of 0.4–0.8 percentage points depending on the design of the remaining plant components. This relatively small value of the total efficiency improvement is due to the relatively high exergy destruction in the areas of gas conditioning and external desulfurization for case 1, particularly to the mixing

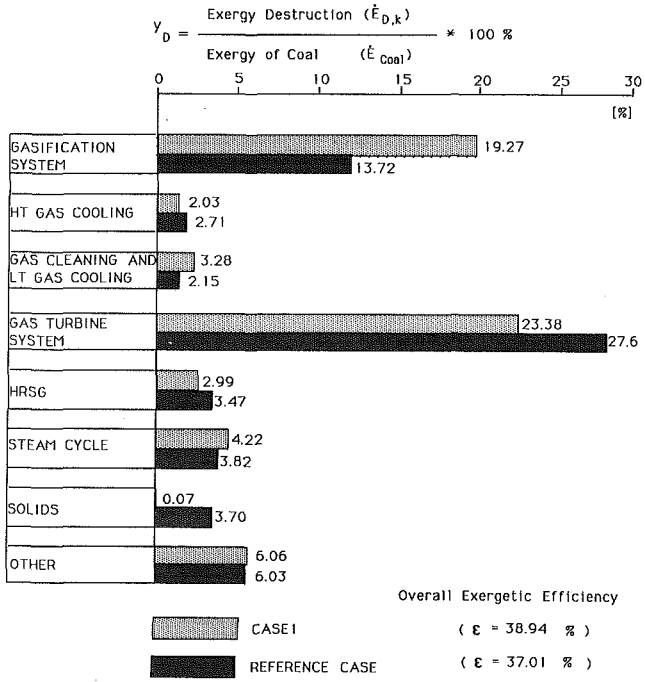

Fig. 7 Comparison of the relative exergy destruction and exergy losses in various areas of the IGCC plant in case 1 and in the reference case

Table 1 Comparison of selected variables of case 1 and the reference case

VARIABLE	CASE 1	REFERENCE CASE
Gasifier operating temperature [°C]	1,038	1,010
Coal flow rate [kg/s]	39.81	40.37
Coal exergy flow rate [MW]	1,177.1	1,116.6
Gasification pressure [bar]	27.6	32.1
Temperature at the outlet of the product gas cooler [K]	946.5	510.9
Air flow rate to gas turbine system [kg/s]	753.32	760.00
Gas turbine firing temperature [K]	1,497	1,497
Gas temperature at the HRSG inlet [K]	865.4	873.7
Ambient temperature [K]	305.4	305.4
Main steam temperature [K]	810.9	794.3
Main steam pressure [bar]	100.0	93.1
Reheat steam pressure [bar]	24.1	24.1
Condenser pressure [bar]	0.1186	0.1186
Steam turbine gross power [MW]	182.2	159.1
Gas turbine gross power [MW]	311.6	298.8
Total net power [MW]	458.4	413.2
Ratio of electric power generated in the gas turbines and steam turbines	1.71	1.87
Total thermal (energetic) efficiency [%]	39.70	37.72
Total exergetic efficiency [%]	38.94	37.01
Gasification island exergetic efficiency [%]	76.91	81.73
Heat rate [Btu/kWh]	8,594	9,045

of streams 12 and 39 in Fig. 4. As shown in Table 3, if only gas cleaning and low-temperature gas cooling are compared, the exergy destruction in case 1 is considerably higher than in the reference case.

The exergy losses associated with material streams exiting the boundaries of the total plants considered here are mainly responsible for the difference in the overall efficiency between the reference case and case 1. In the reference case, approximately 3.7 percent of the total exergy supplied to the plant by the coal is rejected to the environment with the solids-to-disposal stream as opposed to 0.07 percent in case 1. This loss should be reduced in future design options based on the oxygen-blown KRW gasifier.

The comparison of the values given for the HRSG in Table 3 shows that the HRSG design in case 1 is thermodynamically more efficient than in the reference case. This is due in part to the fact that the temperature profiles in the HRSG can be better matched in case 1 than in the reference case.

The analysis of the heat exchanger network of the total plant according to the pinch method (Linnhoff et al., 1983) shows that in both cases heat is transferred across the pinch (Tsatsaronis and Tawfik, 1990; Tsatsaronis et al., 1990). This ineffectiveness, which increases both the energy and the capital costs, is an example of the fact that both cases can be improved from the thermodynamic and cost viewpoints. The potential for improvement is considerably higher for the reference case than for case 1.

In the optimization of the overall heat exchanger network, the following variables should be simultaneously considered: all heat-recovery devices in the gasification island; the entire HRSG; and the values of temperature, pressure, and mass

Table 2 Exergy destruction, dimensionless ratio between exergy destruction and exergy of coal (y_D) or between exergy loss and exergy of coal (y_L), and exergetic efficiency

	CASE 1			REFERENCE CASE		
COMPONENT	EXERGY DESTRUCTION [MW]	RATIO y_D or y_L [%]	EXERGETIC EFFICIENCY [%]	EXERGY DESTRUCTION [MW]	RATIO y_D or y_L [%]	EXERGETIC EFFICIENCY [%]
Oxidant Feed System	8.07	0.69	87.9	17.49	1.57	39.8
Oxygen Preheater	--	--	--	0.22	0.02	70.9
Gasifier	216.96	18.43	82.4	135.42	12.13	89.3
Cyclones	1.74	0.15	99.2	0.33	0.00	99.9
Radiant Cooler	--	--	--	15.79	1.41	66.5
Convective Cooler	--	--	--	9.80	0.88	73.3
Product Gas Cooler (Including Drum)	23.92	2.03	67.0	--	--	--
Gas Conditioning	20.83	1.77	89.3	--	--	--
Sulfator	15.10	1.28	55.5	--	--	--
Zinc Ferrite System	8.66	0.74	99.1	--	--	--
Exit Gas Cooler	6.96	0.59	73.9	--	--	--
Recycle Gas Cooler	1.55	0.13	70.0	--	--	--
Recycle Gas Compressor 1	0.42	0.04	70.0	0.02	0.00	83.7
Recycle Gas Compressor 2	0.12	0.01	58.8	--	--	--
Gas Turbine and Air Compressor	82.65	7.02	79.0	82.88	7.42	78.3
Combustion Chamber	192.57	16.35	82.6	225.17	20.17	80.2
HRSG	35.24	2.99	84.6	38.79	3.47	82.9
Steam Turbines	30.10	2.55	85.8	27.97	2.51	85.0
Remaining Steam Cycle	19.68	1.67	--	14.72	1.31	--
Other Components	0.59	0.05	--	45.28	4.06	--
Sum	665.16	56.5	--	613.88	54.98	--
Exergy Losses	55.46	4.71	--	91.70	8.21	--
Exergy Other Than Coal Exergy to Total Plant	(1.90)	(0.16)	--	(2.20)	(0.20)	--
Total Plant	718.72	61.06	38.9	703.38	63.00	37.0

Table 3 Comparison of the values of exergy destruction in selected groups of plant components and of the exergy loss associated with streams leaving the plant in the reference case and case 1. The values in the first two columns are given as a percentage of the coal exergy supplied to the corresponding IGCC power plant.

VARIABLE	REFERENCE CASE	CASE 1	DIFFERENCE
I. Exergy Destruction			
Gasification System (including Oxidant Feed System)	13.72	19.27	-5.55
Gas Turbine System	27.59	23.38	+4.21
High-Temperature Gas Cooling	2.71	2.03	+0.68
Gas Cleaning and Low-Temperature Gas Cooling	2.15	3.28	-1.13
Heat Recovery Steam Generator	3.47	2.99	+0.48
Steam Turbine	2.51	2.55	-0.04
Remaining Steam Cycle	1.31	1.67	-0.36
Other Components	1.52	1.33	+0.19
Sum I	54.98	56.50	-1.52
II. Exergy Loss			
Solids to Disposal	3.70	0.07	3.63
Flue Gas	2.36	2.83	-0.47
Sulfur	1.39	---	1.39
Other Exergy Losses	0.76	1.90	-1.14
Sum II	8.21	4.80	3.41
Sum of Total Exergy Destruction and Exergy Loss	63.19	61.30	1.89

flow rate of the main steam and reheat steam. The simultaneous optimization of these parameters has the potential to increase the overall plant efficiency significantly.

Conclusions

Exergy analysis techniques were used to compare an IGCC power plant design, which uses an oxygen-blown KRW gasifier and commercially available cold gas cleanup processes, with the design of an IGCC plant, which employs an air-blown KRW gasifier and advanced hot gas cleanup processes. These techniques are very useful tools in evaluating the potential for improving the plant efficiency and in drawing conclusions without redesigning the total plant.

The design configurations discussed here are neither at thermodynamically nor at economically optimal conditions. The analysis of the heat exchanger network based on the pinch method shows that in each configuration heat exchangers exist where some heat transfer through the pinch occurs. These heat exchangers are the IP economizer, the IP drum, the recycle gas cooler in case 1, the convective syngas cooler, the fuel gas reheater, and the HP drum in the reference case.

The comparison of the thermodynamic performance between case 1 and the reference case shows that the oxygen-blown KRW gasifier has a higher overall efficiency than the air-blown KRW gasifier. Part of these thermodynamic gains in the gasifier is offset in the gas turbine system. In addition, an IGCC plant based on hot gas cleanup is thermodynamically more efficient than a similar plant that uses cold gas cleanup even when the irreversibilities associated with the hot gas cleanup are significant as happens in case 1.

The exergy losses in the reference case have a considerable impact on the overall efficiency. The efficiency of this case can be significantly improved by reducing the losses associated with the solids-to-disposal stream and optimizing the heat exchanger network.

From the above discussion and the numbers shown in Fig. 7 it is apparent that an IGCC power plant that uses (*a*) an oxygen-blown, KRW fluidized-bed gasifier employing in-bed desulfurization, (*b*) an optimized hot gas cleanup process, (*c*) a device to burn any residual carbon remaining in the char fines and use the generated heat to raise HP steam, and (*d*) an optimized heat exchanger network integrated with the steam cycle should demonstrate significant performance improvements compared with the two design options discussed in this study.

Efficiency is only one aspect to be considered in the comparison of the two IGCC power plants. Other aspects include reliability, operability, environmental effects, and economics. A detailed comparison of the two cases in the above areas is given by Gallaspy et al. (1991). Here, only the final results of the economic analysis are mentioned. The estimated ten-year levelized cost of electricity for case 1 is 6.7¢/kWh (4.9¢/kWh in constant 1990 dollars) versus 7.4¢/kWh (5.3¢/kWh in constant 1990 dollars) for the reference case. Case 1 has significantly lower capital costs (13 percent) and a better heat rate (5 percent) than the reference case. A fair cost and performance comparison of the two cases, however, should be based on an optimized version of each configuration because the potential for improving each case from the cost and performance viewpoints is different. The exergoeconomic optimization of case 1 is discussed by Tsatsaronis et al. (1991b).

Acknowledgments

This work was prepared with the support of the U.S. Department of Energy (Cooperative Agreement No. DE-FC21-89MC26019) and the Electric Power Research Institute (Research Project No. 2773-5). However, any opinions, findings, conclusions, or recommendations expressed herein are those of the authors and do not necessarily reflect the views of the DOE or EPRI.

References

Gallaspy, D. T., Johnson, T. W., and Sears, R. E., 1990, "Southern Company Services' Study of a KRW-Based GCC Power Plant," EPRI Final Report GS-6876, RP 2773-S, Electric Power Research Institute, Palo Alto, CA, July.

Linnhoff, B., et al., 1983, *A User Guide on Process Integration for the Efficient Use of Energy*, The Institution of Chemical Engineers, United Kingdom.

Moran, M. J., and Sciubba, E., 1994, "Exergy Analysis: Principles and Practice," ASME JOURNAL OF ENGINEERING FOR GAS TURBINES AND POWER, Vol. 116, this issue, pp. 285–290.

Southern Company Services, 1990, "Assessment of Coal Gasification/Hot Gas Cleanup Based Advanced Gas Turbine Systems," Final Report submitted to the U.S. Department of Energy, Morgantown Energy Technology Center, Cooperative Agreement No. DE-FC21-89MC26019, Southern Company Services, Inc., Birmingham, AL, Dec.

Tsatsaronis, G., and Tawfik, T., 1990, "Study of a Revised KRW-Based GCC Power Plant for Plant Wansley," Final Report prepared for Southern Company Services (SCS) and Electric Power Research Institute, EPRI RP-2773-5, SCS Contract No. SS90-1384, Center for Electric Power, Tennessee Technological University, Cookeville, TN, Dec.

Tsatsaronis, G., Tawfik, T., and Lin, L., 1990, "Assessment of Coal Gasification/Hot Gas Cleanup Based Advanced Gas Turbine Systems—Exergetic and Thermoeconomic Evaluation," Final Report prepared for Southern Company Services (SCS) and the U.S. Department of Energy, DOE Contract No. DE-FC21-89MC26019, SCS Contract No. 196-89-004, Center for Electric Power, Tennessee Technological University, Cookeville, TN, Oct.

Tsatsaronis, G., Lin., L., Tawfik, T., and Gallaspy, D. T., 1991a, "Exergoeconomic Evaluation of a KRW-Based IGCC Power Plant," in: *Second Law Analysis—Industrial and Environmental Applications*, G. M. Reistad, M. J. Moran, W. J. Wepfer, and N. Lior, eds., ASME AES-Vol. 25/HTD-Vol. 191, pp. 19–32.

Tsatsaronis, G., Lin, L., Pisa, J., and Tawfik, T., 1991b, "Thermoeconomic Design Optimization of a KRW-Based IGCC Power Plant," Final Report prepared for the U.S. Department of Energy, DOE Contract No. DE-FC21-89MC26019, Tennessee Technological University, Cookeville, TN, Nov.

Tsatsaronis, G., 1993, "Thermoeconomic Analysis and Optimization of Energy Systems," *Progress in Energy and Combustion Systems*, Vol. 19, pp. 227–257.

G. Tsatsaronis

L. Lin

T. Tawfik

Center for Electric Power,
Tennessee Technological University,
Cookeville, TN 38505

D. T. Gallaspy
Southern Electric International,
Atlanta, GA 30338

Exergoeconomic Evaluation of a KRW-Based IGCC Power Plant

In a study supported by the U.S. Department of Energy, several design configurations of Kellogg-Rust-Westinghouse (KRW)-based Integrated Gasification-Combined-Cycle (IGCC) power plants were developed. One of these configurations was analyzed from the exergoeconomic (thermoeconomic) viewpoint. This design configuration uses an air-blown KRW gasifier, hot gas cleanup, and two General Electric MS7001F advanced combustion turbines. Operation at three different gasification temperatures was considered. The detailed exergoeconomic evaluation identified several changes for improving the cost effectiveness of this IGCC design configuration. These changes include the following: decreasing the gasifier operating temperature, enhancing the high-pressure steam generation in the gasification island, improving the efficiency of the steam cycle, and redesigning the entire heat exchanger network. Based on the cost information supplied by the M. W. Kellogg Company, an attempt was made to calculate the economically optimal exergetic efficiency for some of the most important plant components.

Introduction

Several studies of Integrated Gasification-Combined-Cycle (IGCC) power plants have shown that these plants offer a very attractive option for generating electricity from coal. Compared with conventional pulverized-coal steam power plants with flue gas desulfurization, IGCC plants have a higher efficiency, are expected to generate electricity at a lower cost, and have a smaller impact on the environment by reducing airborne emissions, solid wastes, and water requirements.

Southern Company Services, Inc. (1990), under a cooperative agreement with the U.S. Department of Energy (DOE), Morgantown Energy Technology Center, has developed and studied various design configurations of IGCC power plants using Kellogg-Rust-Westinghouse (KRW) gasifiers. The objectives of this work included evaluating and comparing these configurations from the cost, performance, and reliability viewpoints. One of the most promising IGCC plant design configurations (case 1) was evaluated from the exergoeconomic viewpoint. This paper presents the most important results of this evaluation. A comparison of the detailed exergy analysis results between case 1 and another IGCC design configuration (reference case) is reported in this issue by Tsatsaronis et al. (1994). The exergetic comparison identified the causes of performance differences between the two cases and helped evaluate the potential for using different gasification processes and different gas cleanup processes.

The team, which developed the design configuration discussed in this paper, was led by Southern Company Services, which was responsible for the project management, the environmental assessment, the overall cost estimates, the design integration, the reliability analysis as well as the design and costs of the steam cycle, and the materials handling processes. Other participants were the M. W. Kellogg Company (design and costs of the gasification island), General Electric Company (performance and costs of the gas turbine system) and the Center for Electric Power at Tennessee Technological University (exergy analysis, pinch analysis as well as exergoeconomic evaluation and optimization).

The greater complexity, the variety of options for equipment and operating parameters, and the integrated nature of IGCC power plants make determining the optimum plant arrangement much more difficult compared with Rankine-cycle steam-generating plants. An exergoeconomic analysis (e.g., Tsatsaronis, 1984, 1993; Tsatsaronis and Winhold, 1984, 1985) considerably facilitates plant optimization by calculating the real energy waste and the associated cost and by comparing the actual with the economically optimal exergetic (second-law) efficiency of plant components.

Figure 1 shows a block flow diagram of the IGCC power plant. More detailed flow diagrams and the plant description are presented in a companion paper (Tsatsaronis et al., 1994). The exergoeconomic evaluation was conducted for three different cases of the described IGCC power plant design. In the following, cases 1A, 1, and 1B refer to gasification temperatures of 982°C (1800°F), 1038°C (1900°F), and 1093°C (2000°F), respectively. In all these cases, the energy flow rate to the combustion system based on the higher heating value of the gas was the same. This was achieved by increasing the coal flow rate to the gasifier with increasing gasification temperature, as shown in Table 1.

Exergoeconomic Analysis

A complete exergoeconomic analysis consists of (*a*) an exergy analysis, (*b*) an economic analysis, (*c*) exergy costing, and (*d*)

Contributed by the Advanced Energy Systems Division for publication in the JOURNAL OF ENGINEERING FOR GAS TURBINES AND POWER. Manuscript received by the Advanced Energy Systems Division February 24, 1992; revision received December 4, 1992. Associate Technical Editor: M. J. Moran.

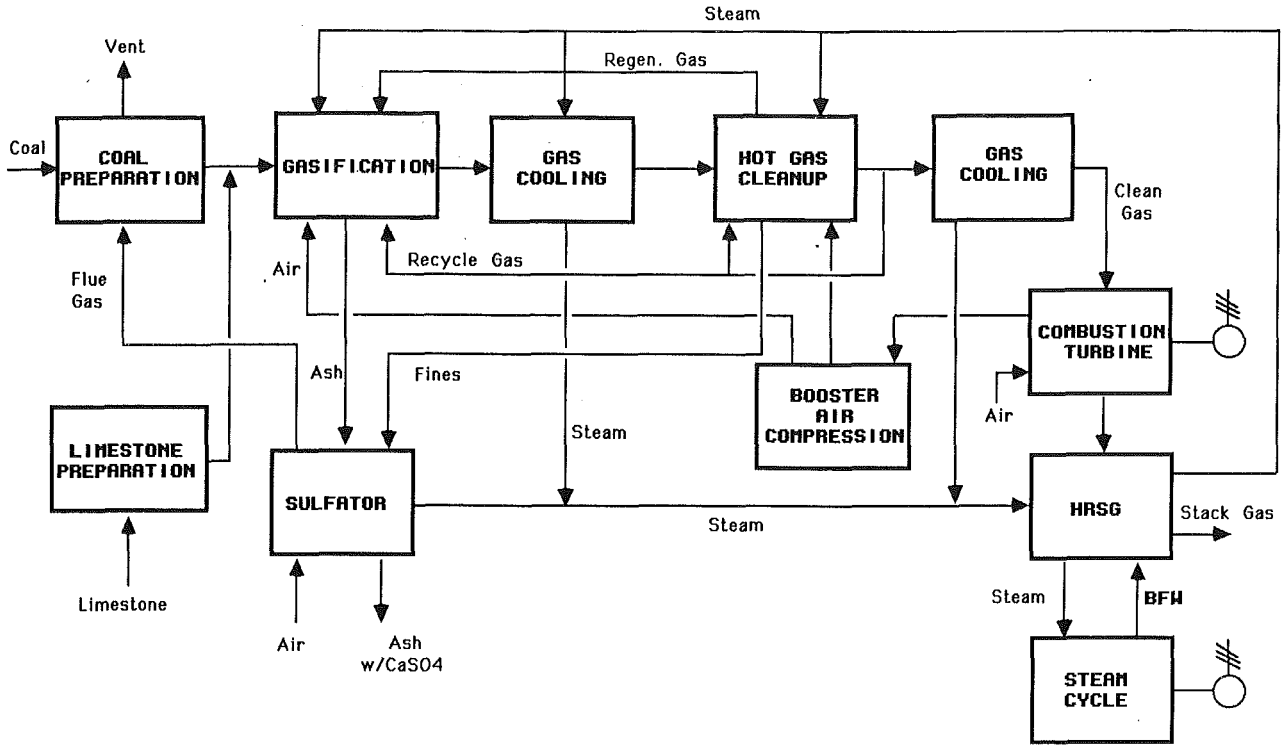

Fig. 1 Simplified schematic of the system configuration in case 1

an exergoeconomic evaluation of each plant component. In the exergy analysis, we calculate, among others, the exergy of all streams in the plant as well as the rate of exergy destruction, $\dot{E}_D$, and the exergetic (second-law) efficiency, ϵ, for each plant component.

For the entire exergoeconomic analysis, it is helpful to define a fuel and a product for each component (Tsatsaronis, 1984; Tsatsaronis and Winhold, 1984, 1985; Tsatsaronis et al., 1986). The exergetic efficiency of the kth plant component is then defined as the ratio between the exergy value of the product, $\dot{E}_{P,k}$, and the exergy value of the fuel, $\dot{E}_{F,k}$,

$$\epsilon_k = \frac{\dot{E}_{P,k}}{\dot{E}_{F,k}}. \tag{1}$$

The rate of exergy destruction in the kth component is then calculated from the following equation:

$$\dot{E}_{D,k} = \dot{E}_{F,k} - \dot{E}_{P,k} - \dot{E}_{L,k}. \tag{2}$$

Here $\dot{E}_{L,k}$ represents the exergy loss in the kth component, which includes the exergy flow rate of all streams leaving this component and not further used in the total plant.

Exergy costing is based on the finding that exergy is the only rational basis for assigning costs to streams and to energy waste. In exergy costing, we calculate (*a*) the cost of each stream in the plant, (*b*) the cost of providing the fuel and generating the product, and (*c*) the cost of exergy destruction in each plant component.

The exergoeconomic evaluation of the kth plant component is based on the following variables:

1 The rate of exergy destruction, $\dot{E}_{D,k}$, in this component, Eq. (2)

2 The dimensionless ratios

$$y_{D,k} = \frac{\dot{E}_{D,k}}{\dot{E}_{\text{coal}}}, \tag{3a}$$

which indicates what percentage of the coal exergy was destroyed in the component being considered, and

$$y_{L,i} = \frac{\dot{E}_{L,i}}{\dot{E}_{\text{coal}}}, \tag{3b}$$

which represents the exergy loss associated with the ith stream as a percentage of the coal exergy supplied to the total plant.

3 The exergetic efficiency, ϵ_k, Eq. (1), which shows what

Nomenclature

$\dot{c}$ = cost per exergy unit
$\dot{D}$ = cost flow rate
$\dot{E}$ = exergy flow rate
f = thermoeconomic factor denoting the contribution of the capital costs, Z, to the relative cost difference, r, between fuel and product in a plant component
g = constant in Eq. (7) expressing the dependence of total net investment for a plant component on the efficiency and capacity of the component
I = investment cost
m = exponent in cost Eq. (7)
n = exponent in cost Eq. (7)
r = relative cost difference between average cost per exergy unit of product and average cost per exergy unit of fuel
y = dimensionless ratio of the flow rates of exergy destruction (or exergy loss) and coal exergy
Z = capital cost associated with a plant component and considered in cost equations
ϵ = exergetic efficiency

Subscripts

D = exergy destruction
F = fuel (according to the definition of exergetic efficiency)
G = gasification
i = material flow stream
k = plant component
L = exergy loss
P = product (according to the definition of exergetic efficiency)

Table 1 Comparison of selected variables for three IGCC design configurations

VARIABLE	CASE 1A	CASE 1	CASE 1B
Gasifier operating temperature [°C]	982	1,038	1,093
Coal flow rate [kg/s]	38.89	39.81	41.06
Coal exergy flow rate [MW]	1150	1177	1214
Gasification pressure [bar]	27.6	27.6	27.6
Temperature at the outlet of the product gas cooler [°C]	1225	1244	1213
Air to gas turbine system [kg/s]	755.25	753.32	750.72
Gas turbine firing temperature [°C]	1,225	1,225	1,225
Gas temperature at the HRSG inlet [°C]	592	592	592
Ambient temperature [°C]	32.2	32.2	32.2
Main steam temperature [°C]	538	538	538
Main steam pressure [bar]	100	100	100
Reheat steam pressure [bar]	24	24	24
Condenser pressure [bar]	0.118	0.118	0.118
Steam turbine gross power [MW]	175.02	182.20	191.65
Gas turbine gross power [MW]	311.64	311.64	311.64
Total net power [MW]	451.75	458.41	467.19
Ratio of electric power generated in the gas turbines and steam turbines	1.78	1.71	1.63
Total thermal (energetic) efficiency [%]	40.05	39.70	39.24
Total exergetic efficiency [%]	39.28	38.94	38.49
Gasification island exergetic efficiency [%]	77.68	76.91	76.09
Heat rate [Btu/kWh]	8,520	8,594	8,696

Table 2 Exergy destruction rate, dimensionless ratios between (*a*) exergy destruction and exergy of coal (y_D) or (*b*) exergy loss and exergy of coal (y_L), and exergetic efficiency for cases 1A, 1, and 1B

COMPONENT	CASE 1A			CASE 1			CASE 1B		
	$\dot{E}_D$ [MW]	y_D or y_L [%]	ϵ [%]	$\dot{E}_D$ [MW]	y_D or y_L [%]	ϵ [%]	$\dot{E}_D$ [MW]	y_D or y_L [%]	ϵ [%]
Oxidant feed system	7.59	0.66	87.9	8.07	0.69	87.9	8.71	0.72	87.9
Oxygen preheater	--	--	--	--	--	--	--	--	--
Gasifier	208.13	18.10	82.7	216.96	18.43	82.4	231.33	19.06	81.8
Cyclones and mixing	1.67	0.15	99.2	1.74	0.15	99.2	1.84	0.15	99.3
Radiant cooler	--	--	--	--	--	--	--	--	--
Convective cooler	--	--	--	--	--	--	--	--	--
Product gas cooler (including drum)	19.68	1.71	67.3	23.92	2.03	67.0	31.67	2.61	65.8
Gas conditioning	20.39	1.77	89.1	20.83	1.77	89.3	21.00	1.73	89.5
Sulfator	14.33	1.23	56.8	15.10	1.28	55.5	16.17	1.33	53.6
Zinc ferrite system	6.81	0.59	99.3	8.66	0.74	99.1	5.86	0.48	99.4
Exit gas cooler	6.81	0.59	73.5	6.96	0.59	73.9	7.38	0.61	73.6
Recycle gas cooler	1.57	0.14	70.0	1.55	0.13	70.0	1.58	0.13	70.0
Recycle gas compressor 1	0.43	0.04	70.0	0.42	0.04	70.0	0.43	0.04	70.0
Recycle gas compressor 2	0.12	0.01	58.6	0.12	0.01	58.8	0.13	0.01	58.8
Gas turbine and air compressor	80.52	7.00	79.5	82.65	7.02	79.0	85.37	7.03	78.5
Combustion chamber	192.77	16.76	82.5	192.57	16.36	82.6	192.29	15.84	82.6
Heat recovery steam generator	35.82	3.12	84.2	35.24	2.99	84.6	35.60	2.93	84.4
Steam turbines	28.97	2.52	85.8	30.10	2.55	85.8	31.56	2.60	85.9
Remaining steam cycle	19.05	1.66	--	19.68	1.67	--	20.72	1.71	--
Other components	0.29	0.02	--	0.59	0.05	--	0.59	0.05	--
SUM	644.95	55.98	--	665.16	56.50	--	692.23	57.02	--
Exergy losses	55.13	4.79	--	55.46	4.71	--	56.39	4.65	--
Exergy other than coal exergy to total plant	(1.88)	(0.16)	--	(1.90)	(0.16)	--	(1.89)	(0.16)	--
Total plant	698.20	60.72	39.3	718.72	61.06	38.9	746.73	61.51	38.5

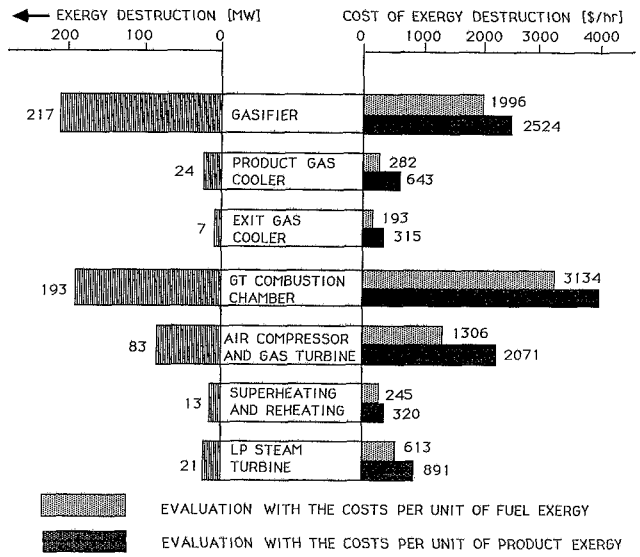

Fig. 2 Exergy destruction and associated costs for selected plant components in case 1

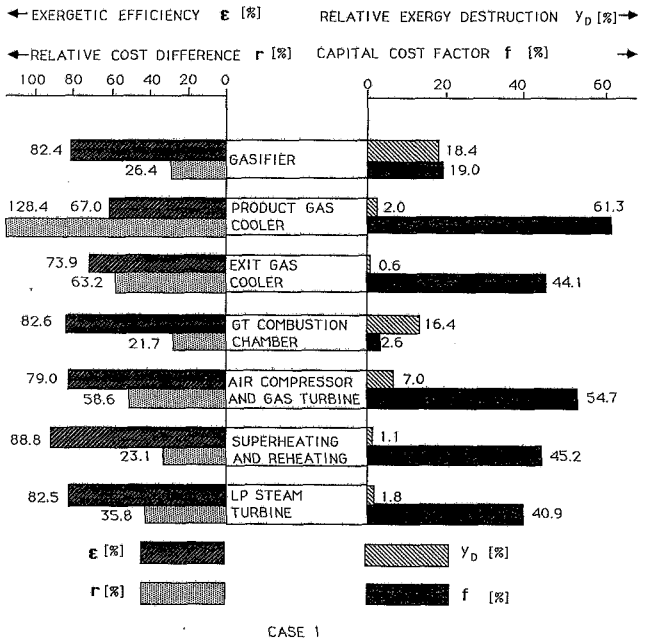

Fig. 3 Exergetic efficiency (ϵ), relative cost difference (r), relative exergy destruction ratio (y_D), and exergoeconomic factor (f) for selected plant components

percentage of the fuel exergy of the kth component can be found in the exergy of the product.

4 The relative cost difference, r_k, between cost per unit of product exergy ($c_{P,k}$) and cost per unit of fuel exergy ($c_{F,k}$), which is defined by

$$r_k \equiv \frac{c_{P,k}-c_{F,k}}{c_{F,k}} = \frac{1-\epsilon_k}{\epsilon_k} + \frac{\dot{Z}_k}{c_{F,k}\dot{E}_{P,k}}. \quad (4)$$

Here, $\dot{Z}_k$ expresses the contribution of the investment costs and the operating (excluding fuel) and maintenance (O&M) costs associated with the kth plant component. Equation (4) reveals the real cost sources in the kth component, which are the irreversibilities and exergy losses (expressed by the first term on the right side) and the capital and O&M expenditures. In general, the higher the relative cost difference, r_K, the more attention should be paid to the kth component.

5 The cost rate of exergy destruction in the component being considered, $\dot{D}_{D,k}$, which is calculated here from the following relationships:

$$\dot{D}_{D,k} = c_{F,k}\dot{E}_{D,k} \quad (5a)$$

or

$$\dot{D}_{D,k} = c_{P,k}\dot{E}_{D,k}. \quad (5b)$$

Unless indicated otherwise, the cost per unit of fuel exergy ($c_{F,k}$) is used to evaluate the cost rate of exergy destruction, Eq. (5a).

6 The exergoeconomic factor f_k

$$f_k = \frac{\dot{Z}_k}{\dot{Z}_k + \dot{D}_{D,k}}, \quad (6)$$

which expresses the contribution of the capital and O&M costs to the relative cost increase r_k.

7 The optimal exergetic efficiency from the economic viewpoint, ϵ_k^{opt}. This efficiency is calculated when the investment costs associated with the kth component (I_k) can be approximated by the following equation:

$$I_k = I_{o,k} + g_k\left(\frac{\epsilon_k}{1-\epsilon_k}\right)^{n_k}\dot{E}_{P,k}^{m_k}. \quad (7)$$

$I_{o,k}$, g_k, n_k, and m_k are constants depending only on the plant component being considered. They are determined using data from the literature and curve fitting techniques. A comparison of the optimal efficiency with the actual one for a plant component indicates whether it is more cost effective for the electricity generated by the total plant to increase the capital expenditures associated with the component and reduce the cost of exergy destruction in the component or vice versa.

More details about an exergoeconomic evaluation are discussed by Tsatsaronis (1993). In the following, we present the results obtained from a detailed exergoeconomic evaluation of cases 1A, 1, and 1B.

Results and Discussion

Table 1 shows a comparison of selected design variables for cases 1A, 1, and 1B. Table 2 shows the exergy destruction, the dimensionless ratios r_k, $y_{D,k}$, and $y_{L,i}$ given in Eqs. (3) and (4), and the exergetic efficiency of selected plant components. Some of the most important results are graphically presented in Figs. 2 and 3. More detailed results are shown in the report by Tsatsaronis, et al. (1990). The investment cost values used for equipment items include only direct material and subcontract costs. Thermoeconomic analyses were conducted for plant capacity factor values of 65 percent and 85 percent. If the capacity factor is not given, a value of 65 percent is implied.

Gasifier. As the gasifier operating temperature increases from 982°C (1800°F; case 1A) to 1038°C (1900°F; case 1) and then to 1093°C (2000°F; case 1B), the exergoeconomic variables vary as indicated in Table 3. In the three cases being considered here, the gasifier has the highest exergy destruction among all plant components. Approximately 18 to 19 percent (y_D value) of the coal exergy is destroyed in the gasifier alone. Out of the 217.0 MW of exergy destruction in case 1, 28.3 MW and 8.0 MW are due to the preheating (from the inlet temperature to the gasifier operating temperature) of nitrogen and oxygen in the air, respectively, and 5.1 MW of exergy destruction are caused by the vaporization and superheating of the water contained in the coal (4.98 percent by weight). The pressure drop in the gasifier causes approximately 2 MW of exergy destruction. The remaining 173.6 MW of exergy destruction are mainly due to the irreversibilities of the chemical reactions in the gasifier.

The gasifier operating temperature, T_G, is one of the most important design parameters in this power plant. With increasing gasifier operating temperature, both the exergetic ef-

Table 3 Variation of exergoeconomic variables for the gasifier in cases 1A, 1, and 1B; the values given in parentheses for cases 1A and 1B refer to the percentage change compared with case 1

VARIABLE	CASE				
	1A		1	1B	
Exergy Destruction, $\dot{E}_D$ [MW]	208.1	(-4.10%)	217.0	231.3	(+6.59%)
Dimensionless Ratio y_D	0.181	(-1.63%)	0.184	0.191	(+3.80%)
Exergetic Efficiency, ϵ [%]	82.70	(+0.36%)	82.40	81.80	(-0.73%)
Fuel Exergy, $\dot{E}_F$ [MW]	1204	(-2.19%)	1231	1270	(+3.20%)
Product Exergy, $\dot{E}_P$ [MW]	996	(-1.80%)	1014	1039	(+2.49%)
Investment Cost Contribution, I [K$]	20,801	(+19.53%)	17,402	16,178	(-7.04%)
Cost per Unit of Fuel Exergy, c_F [$/GJ]	2.549	(-0.27%)	2.556	2.571	(+0.59%)
Cost per Unit of Product Exergy, c_P [$/GJ]	3.238	(+0.02%)	3.231	3.260	(+0.90%)
Relative Cost Difference, r [%]	27.0	(+2.3%)	26.4	26.8	(+1.5%)
Cost Rate of Exergy Destruction, $\dot{D}_D$ [$/hr]	1,910	(-4.31%)	1,996	2,141	(+7.26%)
Exergoeconomic Factor, f [%]	22.64	(+19.28)	18.98	16.88	(-11.06%)

Table 4 Variation of thermoeconomic variables for the product gas cooler and steam drum in cases 1A, 1, and 1B

VARIABLE	CASE		
	1A	1	1B
Exergy Destruction, $\dot{E}_D$ [MW]	19.67	23.92	31.67
Dimensionless Ratio, y_D [%]	1.71	2.03	2.61
Exergetic Efficiency, ϵ [%]	67.3	67.0	65.8
Fuel Exergy, $\dot{E}_F$ [MW]	59.79	72.12	91.10
Product Exergy, $\dot{E}_P$ [MW]	40.10	48.19	60.41
Investment Costs, I [K$]	15103	16625	19538
Cost per Unit of Fuel Exergy, c_F [$/GJ]	3.273	3.270	3.303
Cost per Unit of Product Exergy, c_P [$/GJ]	7.691	7.468	7.448
Relative Cost Difference, r [%]	135.0	128.4	125.5
Cost Rate of Exergy Destruction, $\dot{D}_D$ [$/hr]	232	282	316
Exergoeconomic Factor, f [%]	63.63	61.34	58.24

ficiency, ϵ, and the investment costs, I, decrease whereas the coal throughput and, consequently, the exergy flow rates of fuel, $\dot{E}_F$, and product, $\dot{E}_P$, increase. The cost data provided for the gasifier in this study were insufficient to calculate all constants in Eq. (7) and, consequently, the cost optimal exergetic efficiency. Exergoeconomics, however, still permits calculation of the cost optimal gasification temperature for the given design configuration. The cost per unit of product exergy, c_P, for the gasifier is used for this purpose.

If we use the gasifier operating temperature as the only decision variable, the values of cost per unit of product exergy, c_P (Table 3 and Fig. 4), indicate that the cost minimum for the gasifier is obtained in the T_G range between 1010°C (1850°F) and 1021°C (1870°F). This optimum value is obtained by considering the gasifier only and does not necessarily need to be the optimum gasifier operating temperature when the total plant is considered. However, because of the position of the gasifier (near the total plant inlet) and its importance to the IGCC plant, the optimal T_G value for the total plant should not be far from the above-mentioned T_G range. In fact, detailed simulations and economic analyses conducted for several total plant configurations (similar to those of cases 1A, 1, and 1B) in T_G steps of 5.6°C (10°F) in the range of T_G = 982°C–1093°C confirm this claim. For a total plant capacity factor

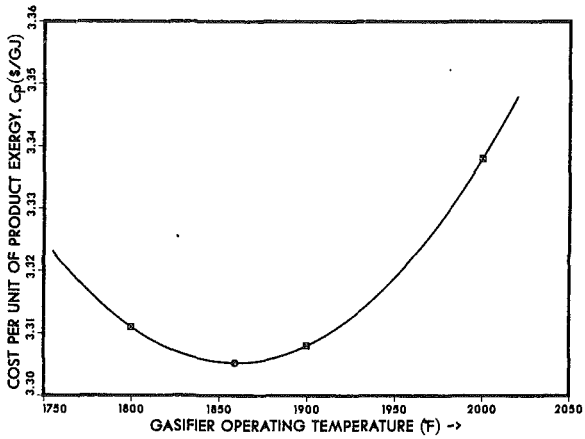

Fig. 4 Cost per unit of product exergy in the gasifier as a function of operating temperature

of 65 percent, the minimum cost of electricity is obtained at T_G^{opt} = 1021°C (1870°F) while at a capacity factor of 85 percent the optimal gasifier operating temperature is 1013°C (1855°F). The design changes discussed in the following might slightly affect these optimal values.

These results do not contradict the findings in the study by Tsatsaronis et al. (1991) where a global cost optimal gasification temperature of about 1050°C (1920°F) is reported. The latter refers to the cost optimal design configuration for the entire IGCC plant whereas the results of this study refer to the given design configuration (original case 1).

Product Gas Cooler and Heat Recovery Steam Drum. Depending on the case being considered, the exergy destruction in the product gas cooler and the heat-recovery steam drum (HRSD) varies from 19.67 MW (case 1A) to 31.67 MW (case 1B). This represents 1.71 percent and 2.61 percent of the coal exergy, respectively. The exergy destruction is mainly caused by the heat transfer from gas to steam.

With increasing gasifier operating temperature, both the investment costs, I, and the amount of steam raised in the components being considered (and, consequently, the exergy flow rate of product, E_P) increase whereas the exergetic efficiency, ϵ, decreases, Table 4. The cost data provided for the product gas cooler in this study were insufficient to calculate the cost optimal exergetic efficiency of this component. The values of cost per unit of product exergy suggest that if (*a*) the product gas cooler and the HRSD are considered isolated, and (*b*) the gasifier operating temperature is the only decision variable then the cost performance of these components is best around T_G = 1038°C (1900°F).

The relative cost difference r (Table 4) between cost of product and cost of fuel is relatively high. As the exergoeconomic factor f indicates, approximately 58 percent to 64 percent of this difference is caused by investment costs. This is a relatively high number for a heat exchanger. At plant capacity factors below 65 percent, elimination of these two components might be cost effective.

Mixing of Steam and Gas From the Product-Gas Cooler. The exergy destruction in the mixing process of steam (stream 39) with the gas exiting the product gas cooler (stream 12) is considerable, 17.0 MW for all cases. In a new design developed for case 1, every effort should be made to reduce the irreversibilities at this point by reducing the mass flow rate of steam to the absolute minimum required for the operation of the zinc ferrite unit.

Sulfation. The exergy destruction in the group of plant components associated with sulfation is 14.3 MW, 15.1 MW, and 16.2 MW for cases 1A, 1, and 1B, respectively. The ex-

ergetic efficiency for each of the three cases is approximately 55 percent. The calculated economically optimal efficiency for this group of components is above 80 percent. Thus, it might be cost effective to increase the capital expenditures for this area if this would lead to an increase in the efficiency of this area. One option to accomplish this more efficient operation is to reduce the temperature at which the sulfator flue gas leaves this area by generating more steam in the sulfator and then mixing this flue gas with the gas entering the HRSG. In addition, it does not seem cost effective first to dry the coal in coal preparation and then to add high-pressure steam to the gas exiting the product gas cooler.

Booster Air Compression. The exergy destruction rate in the air recuperator, the BFW preheater, the trim cooler, and the booster air compressor is approximately 1.7 MW, 0.6 MW, 1.9 MW, and 3.9 MW, respectively, and the cost associated with the exergy destruction is about \$55/h, \$17/h, \$63/h, and \$139/h, respectively. All components in this area operate near their cost optimal exergetic efficiency values. It should be emphasized again, that Eq. (7) calculates the cost optimal exergetic efficiency for a component considered in isolation. The overall plant optimum might require operation of a plant component at conditions far from the conditions corresponding to its cost optimal exergetic efficiency.

Zinc Ferrite Reactors and Chloride Guard Reactors. These reactors are responsible for 8.7 MW and 1.5 MW of exergy destruction and for an associated cost rate of \$119/h and \$29/h, respectively. The capital expenditures cause approximately 65 percent (f value) of the relative cost difference r = 2.5 percent for the zinc ferrite reactors. No specific recommendations based on the exergoeconomic analysis can be made for the zinc ferrite and the chloride guard reactors.

Exit-Gas Cooler. The exergy destruction in the exit-gas cooler is about 7 MW and the associated cost \$193/h. The actual exergetic efficiency of 73.9 percent is only slightly higher than the economically optimal efficiency of 70–71 percent at a plant capacity factor of 65 percent.

Recycle-Gas Cooler. The recycle-gas cooler operates at an exergetic efficiency of about 70 percent in all cases. The exergy rate of the product is 3.7 MW, 3.6 MW, and 3.9 MW for cases 1A, 1, and 1B, respectively, whereas the corresponding investment costs are 3.23, 3.19, and 3.23 million dollars. The high values of the relative cost difference r (126.7 percent) and the thermoeconomic factor f (66.2 percent) lead to the conclusion that higher temperature differences than the actual ones might be economically preferable since they will lead to a reduction in the investment costs of the recycle-gas cooler. This conclusion, however, is drawn when the cooler is considered separately from the other heat exchangers in the total plant.

The analysis of the heat exchanger network of the total plant based on the "pinch method" (Linnhoff et al., 1983) and the composite curves show that in the recycle-gas cooler some heat transfer occurs across the pinch, which is at T_{hot} = 520 K and T_{cold} = 495 K. This ineffectiveness needs to be studied further before conclusions are drawn.

Recycle-Gas Compressor. The exergy destruction in the recycle-gas compressor is 0.5 MW and the associated cost \$16.80/h. The large values of the relative cost difference r and the exergoeconomic factor f are caused by the investment costs. These high values are typical for compressors and pumps.

Gas Turbine System. This area is responsible for the highest exergy destruction rate among all IGCC plant areas. A total of 275.2 MW of exergy (i.e., 23.4 percent of the coal exergy) are destroyed in this system. The estimated exergy destruction in the combustion chamber of 192.6 MW (16.4 percent of the coal exergy) represents the second highest value of exergy destruction in a single plant component. The cost rate associated with the exergy destruction is \$3134/h (the highest among all plant components) for the combustion chamber and \$1306/h for the system air compressor/gas turbine. These numbers, combined with the extremely low contribution of the investment costs to the r value of the combustion chamber, indicate that the cost effectiveness of the total plant might be improved significantly if a gas turbine process with a reheat stage is used. There is an urgent need to study the economic feasibility of mature reheat gas turbine systems.

Heat-Recovery Steam Generator (HRSG). The exergy destruction rate in the total HRSG varies from 35.8 MW in case 1A to 35.6 MW in case 1B. The corresponding exergetic efficiency is of the order of 84.6 percent. Significant exergy destruction occurs in the superheater/reheater/blast steam reheater (12.9 MW with an associated cost rate of \$245/h), feedwater heater 1 (4.2 MW with an associated cost rate of \$80/h), HP1 economizer (4.0 MW with an associated cost rate of \$76/h), feedwater heater 2 (3.5 MW and \$64/h), HP drum (3.4 MW and \$65/h) and IP drum (2.9 MW and \$72/h).

In the IP drum, 1.3 MW of heat is transferred across the heat exchanger network pinch (at 495 K/520 K). This inefficiency must be reduced in future design configurations of the HRSG.

Estimates based on the values of the HRSG exergoeconomic variables indicate that it might be cost effective to increase the temperature differences in the HP2 economizer and IP superheater and to decrease the minimum temperature difference in the HP drum. At this point, it must be emphasized that the HRSG should not be optimized by itself. An optimization study must simultaneously consider the HRSG, all heat recovery devices in the gasification island, and the steam turbine performance. The temperature, pressure, and mass flow rate values of the main steam and the reheat steam must be kept variable in such an optimization study. Our studies indicate that a good match of temperature profiles in the HRSG has the potential to increase the overall plant efficiency significantly.

Steam Cycle. The total exergy destruction in the steam cycle (including the exergy losses in the condenser) is 48.0 MW, 49.8 MW, and 52.3 MW for cases 1A, 1, and 1B, respectively. The actual steam cycle design considered by itself is cost efficient. The cost optimal design for this area, however, can be obtained through an integrated optimization of the overall heat exchanger network and the steam turbines. It is apparent that the exergy destruction in the desuperheater can and must be eliminated, i.e., no desuperheating should occur under design conditions.

Conclusions

The exergoeconomic analysis applied here identifies and evaluates the real energy waste and the real cost sources in an IGCC design option. This analysis is a very useful tool in evaluating the potential for improving the plant efficiency and cost effectiveness. With the aid of this analysis, conclusions can be drawn without redesigning the total plant.

This study shows that the cost effectiveness of case 1 might be improved if the following design changes were made:

1 Operate the gasifier at a temperature ranging from 1010°C to 1021°C.

2 Cool the gas at the outlet of the product-gas cooler to a lower temperature before steam is added to the gas. Keep the steam amount to the absolute minimum required by the zinc ferrite unit. Before adding the steam to the gas, do not desuperheat the steam under design conditions.

3 Redesign the recycle-gas cooler, IP economizer, and IP drum to reduce heat transfer across the pinch. Optimize the

heat exchanger network in the total plant in conjunction with the steam turbines. This optimization might result in a reduction of both capital expenditures and energy costs. In addition, a reduction in the overall pinch temperature from about 34°C (61°F) in the current design to about 25–30°C (45–54°F) might prove to be cost effective, particularly at a plant capacity factor of 85 percent.

4 Study the economic feasibility of a gas turbine system with a reheat stage. The thermoeconomic analysis indicates that this change should result in considerable cost savings.

5 Enhance the heat-recovery operations in the sulfation area at the expense of coal drying. Compare the cost effectiveness of coal drying versus steam raising.

Subsequent work in this project focused on the exergoeconomic optimization of the IGCC power plant design discussed here (Tsatsaronis et al., 1991).

Acknowledgments

This work was prepared with the support of the U.S. Department of Energy, Cooperative Agreement No. DE-FC21-89MC26019. However, any opinions, findings, conclusions, or recommendations expressed herein are those of the authors and do not necessarily reflect the views of the DOE.

References

Gallaspy, D. T., Johnson, T. W., and Sears, R. E., 1990, "Southern Company Services' Study of a KRW-Based GCC Power Plant," EPRI Final Report GS-6876, Project 2773-5, Electric Power Research Institute, Palo Alto, CA, July.

Linnhoff, B., et al., 1983, *A User Guide on Process Integration for the Efficient Use of Energy*, The Institution of Chemical Engineers, United Kingdom.

Southern Company Services, 1990, "Assessment of Coal Gasification/Hot Gas Cleanup Based Advanced Gas Turbine Systems," Final Report submitted to the U.S. Department of Energy, Morgantown Energy Technology Center, Cooperative Agreement No. DE-FC21-89MC26019, Southern Company Services, Inc., Birmingham, AL, Dec.

Tsatsaronis, G., 1984, "Combination of Exergetic and Economic Analysis in Energy-Conversion Processes," *Energy Economics and Management in Industry*, Proceedings of the European Congress, Algarve, Portugal, Apr. 2–5, Pergamon Press, Oxford, United Kingdom, Vol. 1, pp. 151–157.

Tsatsaronis, G., and Winhold, M., 1984, "Thermoeconomic Analysis of Power Plants," EPRI AP-3651, RP 2029-8, Final Report, Electric Power Research Institute, Palo Alto, CA, Aug.

Tsatsaronis, G., and Winhold, M., 1985, "Exergoeconomic Analysis and Evaluation of Energy Conversion Plants. Part I—A New General Methodology," *Energy—The International Journal*, Vol. 10, No. 1, pp. 69–80.

Tsatsaronis, G., Winhold, M., and Stojanoff, C., 1986, "Thermoeconomic Analysis of a Texaco-Based Integrated Gasification-Combined-Cycle Power Plant," EPRI Report, RP 2029-8, Final Report, Electric Power Research Institute, Palo Alto, CA, Aug.

Tsatsaronis, G., Tawfik, T., and Lin, L., 1990, "Assessment of Coal Gasification/Hot Gas Cleanup Based Advanced Gas Turbine Systems—Exergetic and Thermoeconomic Evaluation," Final Report prepared for Southern Company Services (SCS) and the U.S. Department of Energy, DOE Contract No. DE-FC21-89MC26019, SCS Contract No. 196-89-004, Center for Electric Power, Tennessee Technological University, Cookeville, TN, Oct.

Tsatsaronis, G., Lin, L., Pisa, J., and Tawfik, T., 1991, "Thermoeconomic Design Optimization of a KRW-Based IGCC Power Plant," Final Report prepared for the U.S. Department of Energy, Contract No. DE-FC21-89MC26019, Tennessee Technological University, Cookeville, TN, Nov.

Tsatsaronis, G., 1993, "Thermoeconomic Analysis and Optimization of Energy Systems," *Progress in Energy and Combustion Science*, Vol. 19, pp. 227–257.

Tsatsaronis, G., Tawfik, T., Lin, L., and Gallaspy, D. T., 1994, "Exergetic Comparison of Two KRW-Based IGCC Power Plants," ASME JOURNAL OF ENGINEERING FOR GAS TURBINES AND POWER, Vol. 116, this issue, pp. 291–299.

Working Group Activities of AGARD Propulsion and Energetics Panel

A. S. Ucer
Chairman of AGARD Propulsion and Energetics Panel,
Department of Mechanical Engineering,
METU,
Ankara, Turkey

One of the major activities of AGARD panels is to form working groups, which assemble experts who work on the particular subject for two or three years. As a result of the work, an advisory report is published, which compiles the state-of-the-art knowledge on the chosen specific topic. This paper explains the philosophy and procedures adopted during the formation of working groups of the Propulsion and Energetics Panel. Working groups concerning gas turbine technologies are presented. The selected working groups aim to improve the computational and experimental knowledge that would lead to the design of advanced aero gas turbine engines. Objective, scope, procedure, and important results of each working group will be explained. Working groups that were active during the 1980s and which were presently active are covered.

Introduction

The Advisory Group for Aerospace Research and Development, AGARD, was initiated in 1951 by the late Theodore von Karman in order to mobilize, for the mutual advantage of NATO nations, their scientific and technical skills, manpower, and facilities.

The mission of AGARD in short is to provide scientific and technical advice to NATO bodies, the Military Committee, and all the NATO community. AGARD strives to stimulate advances in the aerospace sciences and improve the communication between the member nations in aerospace research and development. AGARD promotes the exchange and dissemination of scientific and technical information in order to fulfill this mission. AGARD works under the military committee and consists of nine panels covering all aspects of Aerospace Science. These panels are: Aerospace Medical Panel (AMP), Avionics Panel (AVP), Electromagnatic Wave Propagation Panel (EPP), Flight Mechanics Panel (FMP), Fluid Dynamics Panel (FDP), Guidance and Control Panel (GCP), Propulsion and Energetics Panel (PEP), Structures and Materials Panel (SMP), and Technical Information Panel (TIP).

For exchanging scientific and technical information AGARD organizes symposia, specialist meetings, lecture series, and short courses. It publishes proceedings, advisory reports, and AGARDographs. Panel have working groups, which work on a chosen subject and produce advisory reports.

The Propulsion and Energetics Panel (PEP) was one of the original panels established in 1952 as the Combustion Panel. In 1962 the present name was adopted and its terms of reference were extended. PEP is now concerned with all aspects of aerospace propulsion systems like air-breathing engines, including auxiliary on-board power generation units, solid and liquid rockets, guns, and munitions. The concern includes necessary energy release and conversion processes.

This paper describes the working group activities on gas turbine technologies that have taken place since 1980. Seven working groups covering a wide variety of important topics that need clarification are addressed.

Topic Selection and Initiation of Working Groups

Several ways are used to identify the need for a working group. A request of the Military Committee, which is transferred to the panel by the National Delegates Board, is one of the possibilities. Working group subjects are also selected among the proposals of the panel members, which directly reflect the needs of the propulsion community. The need for a working group is sometimes identified as a conclusion of a symposium or a specialist meeting. The discussions of the assembled specialists and rigorous technical evaluation by the technical evaluator may identify areas that may need further investigation. The Propulsion and Energetics Panel is a collection of experts in the propulsion field from NATO nations selected by the national authorities. However, it is not always possible to find the correct expertise on a specific topic in the panel. When a project is to be undertaken in which outside expertise is needed, working groups are formed.

The main task of the working group is to prepare a technical/scientific document that would serve the defence research community on the particular subject. Working groups also compile expert knowledge on the selected subject.

Working groups in fulfilling the tasks related to their terms of reference sometimes are forced to undertake testing, computing, and software modification or development. Working

Contributed by the International Gas Turbine Institute and presented at the 38th International Gas Turbine and Aeroengine Congress and Exposition, Cincinnati, Ohio, May 24-27, 1993. Manuscript received at ASME Headquarters March 17, 1993. Paper No. 93-GT-343. Associate Technical Editor: H. Lukas.

groups sometimes use questionnaires in order to compile the opinions of all the experts of the subject. All this work relies on national voluntary contributions. The AGARD contribution is minimal and it only covers the publication costs of the final advisory report.

The procedure of establishing a working group takes about two years and starts usually with an ad-hoc committee consisting of interested panel members. The ad-hoc committee investigates the interest in different nations and identifies nonpanel member experts who would be willing to take part in the working group. The committee also finalizes the terms of reference of the working group. Working groups start their activities after approval by the panel and the National Delegates Board. Usually a working group is expected to terminate in two or three years and in four to six meetings; however, working groups of longer periods are common.

(WG 12) Throughflow Calculations in Axial Turbomachines

This working group was initiated as a result of the conclusions of the specialist meeting held in 1977 on throughflow calculations. One of the conclusions of this meeting was that although the basic calculation methods could be considered satisfactory, large differences appeared in the performance predicted for same test cases by different authors. This was mainly due to the loss and deviation correlations used in the throughflow calculations.

This working group started in 1978 and published Advisory Report 175 in 1981. From the start of the working group, two separate subgroups were formed to analyze the turbine and compressor fields with their own specific problems. The objectives of both subgroups were to make a critical review of the blade element and end wall correlations available in the open literature. Emphasis was put on design performance prediction and transonic range of operation. It was decided to back up this critical review by performance prediction comparisons of single and multistage machines with experimental results. The second objective was to investigate the effect of variables such as streamtube thickness, chordwise losses, and turning variation through advanced blade-to-blade calculations in the performance prediction efforts. It was also hoped to obtain new correlations in this second phase.

The first task of the working group was to collect representative and reliable test cases of single and multistage machines. This appeared as a difficult task, due to the lack of publicly available and well documented multistage data. This finding later on led to a new working group on the test cases, WG 18. Nevertheless, each subgroup succeeded in collecting and presenting several test cases: three single-stage machines (two turbines and one compressor), 2 two-stage machines (one turbine and one compressor), a four-stage compressor, and a six-stage low-pressure steam turbine.

The second task was to review and attempt to summarize the existing correlations. Five main turbine correlations for turning and loss predictions based on loss component analysis, including secondary and clearance losses, were discussed. None of the correlations appeared to have a sufficiently strong and adequate physical bases.

Regarding the compressor correlations, it appeared clearly that many correlations had common points, such as the concept of diffusion factor to characterize the loading level of a compressor blading. Important differences exist when more detailed effects have to be estimated. A comprehensive literature search by experts was done on diffusion factor predictions and profile losses, shock and shock-boundary layer interaction loss prediction; end wall boundary layer calculation methods, correlations for secondary flows and clearance effects, Reynolds number effects and influence of blade surface roughness, part-span damper losses, and deviation angle correlations. A note was also prepared on stall and surge. A questionnaire was distributed to various industries and organizations involved in design work in order to gain some information on how some of the questions raised in the working group are answered by the people designing the actual compressors.

Both subgroups attempted a series of throughflow calculations with different correlations on the various test cases. As a general conclusion it can be said that the detailed flow predictions are generally poor mainly due to the lack of prediction methods for secondary flow deviations, although overall performance is fairly well predicted.

It is the working group's opinion that from a coherent use of fundamental experiments with the systematic use and the analysis of viscous flow calculations a more rigorous basis would be given to the necessary correlations.

Observations and Conclusions of Working Group 12. There is a lack of reliable and publicly available data especially for multistage compressors. Moreover, it was also observed that great care should be given to the accuracy of the data recording and more particularly to the data reduction programs. It was established that generally the experimentalists deduce detailed flow data from a reduced set of measurements taken behind the stators. The determination of the losses and the deviations behind the rotors for instance are obtained from the data reduction codes based on some assumptions with regard to the streamline shape.

The interaction between the throughflow program and loss and turning correlations also affect the results due to the strong nonlinearity of the equations: The particular procedure could affect the overall result.

With the addition of internal stations in throughflow calculations, assumptions have to be made with regard to the law of variation, with chordwise distance, of losses and deviations.

Both subgroups, turbine and compressor, came to the conclusion that with the present level of experimental accuracy, the existing methods of throughflow were compatible with the level of accuracy of the correlations, especially with regard to the overall performance prediction.

The level of accuracy needed for performance prediction is not equivalent for the losses and the deviations. It appeared clearly that, in the turbine field as well as in the compressor field, the required accuracy for deviations is appreciably higher than for losses. The predicted radial distribution of properties is influenced considerably with one or two degrees of deviation angle.

The predicted flow behavior is less sensitive to small variations in the loss coefficient.

WG 12 Recommendations. The following recommendations came forward in addition to the observations and conclusions depicted above:

- An important effort should be made to obtain good and reliable multistage compressor and turbine data.
- A deep physical understanding is needed with regard to the various loss sources and their particular generation mechanism. Basic experiments allowing one to separate and understand the various contributions should be considered.
- Care should be taken to define a consistent set of relations within the correlations in order to avoid the duplication of effects and influence of parameters.
- A particular effort is required with regard to secondary flow deviations and end wall boundary layer effects.
- Even with the development of three-dimensional viscous flow calculations and the increase of the computing power of digital computers, it is not likely that throughflow calculations in a multistage environment will be replaced by full viscous calculations in the near future. Therefore the need for good correlations will continue to be of great importance.

Table 1 Analytical test cases

SANZ supercritical compressor cascade
Supersonic staggered wedge cascade
SANZ subcritical turbine cascade
SANZ supercritical turbine cascade
HOBSON transonic symmetric turbine choked cascade
HOBSON transonic symmetric turbine non choked cascade

Table 2 Experimental test cases

Description	Code types to be used
Low subsonic compressor cascade NACA 65	3D
High subsonic compressor cascade DCA	Q3D
High subsonic compressor cascade 115	2D
Low supersonic compressor cascade MCA	Q3D
Transonic compressor cascade ARL SL 19	Q3D
Subsonic turbine cascade T 106	2D
Subsonic turbine cascade LA	Q3D,3D
Transonic turbine cascade	2D
Single low speed compressor rotor	TF, Q3D,3D
Single transonic fan rotor	TF, Q3D,3D
Single subsonic compressor stage	TF, Q3D,3D
Single transonic compressor stage	TF, Q3D,3D
Low speed two-stage compressor	TF, Q3D,3D
Low speed S-shape duct	3D
Annular diffuser	TF
Low speed annular turbine blade row	3D
Transonic annular turbine blade row	3D
Single stage subsonic blade turbine	TF
4-stage low speed turbine	TF

2D 2-dimensional flow calculation, Q3D quasi-3-dimensional flow calculation,3D 3-dimensional flow calculation, TF through-flow calculation

(WG 18) Test Cases for Computation of Internal Flows in Aero-engine Components

This working group started its activities in 1984, and advisory report 275 was published in 1990. It was initiated following the conclusions of WG 12. It was formed in order to compile an analytical and experimental data base intended to support the development of new codes and the refinement of the existing codes for computing internal flows in aero engine components, specifically in cascades, compressors, turbines, and ducts ahead and between them. The data presented in the working group's advisory report AR 275 are believed to represent the highest quality analytical and experimental test cases available until the beginning of the 1990s. More information can be found from Fottner (1989).

The scope of the working group was also extended to assess what measurements are required for each type of test case and with what accuracy.

The working group was divided into six subgroups, including analytical, cascades, compressors, ducts, turbines, and a subgroup concerned with the validity of test cases.

The analytical test cases presented in the report are relevant to two-dimensional inviscid flow calculations for cascades. Six test cases were identified as shown in Table 1.

The working group initially considered 27 potential experimental test cases. This number was reduced to 19 test cases after decisive criteria were applied to each test case by a questionnaire that facilitated an objective evaluation of the data. The selected experimental test cases are outlined in Table 2. Eight cascade test cases were identified. Each test case is documented in a similar format with the following headings:

1 Description of the test case, facility, and instrumentation
2 Information on geometric details
3 Experimental conditions and results
4 Evaluation method and data uncertainty
5 Recommendations for comparison with calculation methods
6 Nomenclature

Working Group Advisory Report 275 addresses measurement problems and gives recommendations for more reliable measurements.

Some Observations of Working Group 18. It was established that most of the analytical test cases are rather academic and do not include some of the important features of real turbomachine blades.

In a comparison of results from the experiments with the results from the fluid dynamic calculation procedures, no differences should occur. If there are differences this is due to measurement inaccuracies, to different boundary conditions, or to imperfections of the theoretical solution. Only in an iterative procedure between theory and experiment can the actual reason be detected. Thus a close collaboration between theoreticians and experimentalists is necessary. A meaningful validation of computational results requires knowledge of the experimental procedures and measuring problems.

In order to validate a calculation method by an experimental test case, it is necessary to model the experimental boundary conditions in the best possible way. Therefore the experiments should be designed to reproduce the necessary numerical boundary conditions accurately.

Compressor cascades should often be regarded as three-dimensional test cases, but they are not usually documented for this.

WG 18 Recommendations. Regarding the recommendations concerning analytical test cases, a blunt leading edge with a detached shock would be a desirable test case. Recommended experimental test cases and required measurements are outlined below.

All transonic cascade configurations and choked cascades with strong, normal shocks exhibit strong three-dimensional flow features and require full three-dimensional measurements for three-dimensional code validation. Future tests should provide: (1) clearly defined upstream flow conditions including turbulence flow properties, (2) detailed boundary layer measurements including heat transfer and turbulence data, and (3) information on trailing edge vortex formation to allow better modelling of the wake mixing process.

The major omission from the range of compressor test cases is a good multistage machine. One can argue the need for three test cases: (1) a repeating stage low-speed tests case with highly detailed internal measurements; (2) a high subsonic test case of four or more stages with interrow aerodynamic traversing measurements backed up with some laser aneomometry; (3) fan test case of two or more transonic stages with laser measurements. There is also a future need to include more advanced configurations, which could test the computational methods more severely.

Concerning the range of operating conditions, modeling of off-design operation will become more tractable as computational methods improve; the operating conditions of interest include part speed as well as "near-surge" cases, especially for transonic rotor stages and multistage machines.

For ducts the major omissions from the test cases are: (1) annular diffuser with and without upstream moving blade rows; (2) annular S-shaped duct with and without upstream blade rows, both moving and stationary.

For turbine throughflow calculations, a test case with more details of the blade row loss distributions including tip leakage and with radial and circumferential traverses after the stators is needed.

(WG 14) Suitable Averaging Techniques in Nonuniform Internal Flows

This working group started in 1979 and published its advisory report in 1983. It was established as a consequence of two primary issues in the field of gas turbine technology. The first is the trend toward lower aspect ratio, more heavily loaded blading. The second is the increasing need to understand the effects of flow nonuniformities on engine performance and on its stability.

The objective of the working group was to review known averaging methods and to present their differences, to quantify inaccuracies or uncertainties inherently associated with different averaging procedures, and to arrive at recommendations for practical applications. The scope of work was restricted to consider only the following propulsion systems: turbojet (with and without reheat); turboshaft engines (without heat exchange and propellers); and turbofan engines (with and without mixing and reheat). Furthermore, the averaging methods considered by WG 14 are applicable only to steady-state component and system performance analysis.

Initially, existing models of component and system performance analysis were reviewed. It was seen that flowpath-averaging practices vary depending on the engine component, the user's design philosophies, the user's test facilities and equipment, accuracy requirements, and available resources. A systematic theoretical analysis was undertaken that covers component and system performance, based upon integral relations for stationary finite control volumes with fixed boundaries. The general compressible fluid relations are then written for steady time-averaged flows. The representations of parameters as uniformly distributed averaged quantities are then derived. On the basis of this work, known averaging methods are discussed, classified, and their limitations are defined.

Two groups of averaging methods were identified:

- averaging methods based on "integral system effects"
- averaging methods based on "complete equilibrium"

In addition, Dzung's "Consistent Averaging Method" was treated. An extensive discussion and evaluation was performed on the existing averaging methods. This work was concluded by proposing a new method. This method leads to averaged quantities, which represent the usefulness to the function of the engine component located downstream, of the considered nonuniform flow. This method takes into account the specific character of each component of a turbojet/fan and ensures coherence between various components of the engine.

The averaging procedures are tested by computing a selected group of typical samples. Comparisons between the results of different averaging methods in calculating the average values of total pressure showed little difference; at most ± 0.1 percent. Although the differences were very small, they lead to significant differences in component efficiency figures calculated from them. In one example a difference of 1.5 percent in compressor efficiency was found. If errors of this order are acceptable, the simplest method, area weighting, may be used. If, as in many test rigs, steps have been taken to ensure an almost uniform inflow, area weighting is also acceptable.

Recommendations of Working Group 14. Stagnation temperature should be averaged using mass-weighted stagnation enthalpy. In many practical cases mass-weighted stagnation temperature is adequate.

Except in the case of propelling nozzles, stagnation pressure should be averaged by either the Dzung or Pianko method.

In engine thermodynamic calculations, the same pressure averaging method should be used for all components used to construct the cycle.

(WG 19) Recommended Practices for Measurement of Gas Path Pressures and Temperatures for Performance Assessment of Aircraft Turbine Engines and Components

This working group started to work in 1988 and published Advisory Report 245 in 1990.

The objective of Working Group 19 was to establish recommended practices for the instrumentation for performance evaluation of aviation gas turbine components undergoing development in rigs and engines. The intent was to provide a common understanding between manufacturers, research organizations, and procurement agencies of the factors affecting performance test data.

It is hoped that the application of these recommended practices will ensure confidence in the mutual understanding of the quality and consistency of data obtained in test programs. This should therefore be of particular value in multicompany or multinational engine programs.

The scope of the working group was limited to the measurement of the key gas path parameters of pressure and temperature as they relate to component performance. Only steady-state measurements were considered, with the component or engine operating in an equilibrium condition. Steady-state conditions are defined as those where the machine is running at a nominally fixed operating point and the measurements are essentially constant with time. The work concerns instrumentation required during the development phase, where the development team is largely concerned with isolating and correcting deficiencies in engine performance.

In WG 19's advisory report, the measurement requirements for each aerodynamic component of an aviation gas turbine are reviewed and suitable configurations for the distribution of pressure and temperature measurements at the inlet and discharge planes of engines, compressors, combustors, turbines, afterburners, and propelling nozzles are detailed. Consideration is given to averaged and mean flows, uniform and distorted flow conditions, size effects and their impact on the use of fixed rakes and traversing probes.

General requirements for engine and component testing are discussed in detail. The document is restricted to measurement of pressure and temperature. The forms of measurement will include total pressure, static pressure (including those on surfaces), differential pressures, and total temperature. Furthermore measurements that can be adequately quantified by a single average or mean value are considered only.

The state of the art for steady-state gas temperature and pressure measurement as applied to gas turbine component development is described in the advisory report. These measurements have a wide variety of applications, including:

1. Assessment of component performance; especially efficiency, mass flow, and surge margin
2. Study of blockage and aerodynamic losses
3. Determination of nozzle coefficients
4. Determination of gas velocity and Mach number
5. Measurement of the spatial distribution of flow, boundary layer thickness, and flow separation

The working group confined itself to the pressure and temperature measurements over approximately the following ranges:

Pressure	10 to 4000 kPa
Temperature	200 to 2200 K
Mach No.	0.05 to 1.2

In general it recommended practices that are appropriate for most of the above ranges. It does not cover the temperature range above the limits of readily available sensors, nor does

it cover any of the unique problems of designing probes for transonic and supersonic flow regimes.

The advisory report explains standard measurement identification codes, and requirements for testing intakes, compressor fans and associated ducts, combustion chambers, turbines and associated ducting, afterburners, and propelling nozzles. Test cell environment and component testing in engines are also addressed. Uncertainty analysis including estimation of uncertainty prior to testing, post-test evaluation of uncertainty, and methods for combining pretest and post-test results are explained. A part of the advisory report is devoted to special factors that must be taken into account when dealing with the testing of small engines.

(WG 23) Transient Measurement in Gas Turbines

This working group started its activities in 1989. Its advisory report is to be published in 1993.

As it is explained in the previous working group activity (WG 19) transient measurements were not considered. Working group 23 is on transient measurement techniques. "Transient conditions" are those in which a relatively slow variation of machine operation is deliberately induced (e.g., engine acceleration), and for which a single spatially averaged value is an adequate description of the flow at the time of measurement. Dynamic measurements are those in which the conditions are varying in high frequency and for which an instantaneous point measurement or spectral behavior characteristics are required to adequately define the flow. The accurate quantification of the steady-state operating conditions of engines and components is a very necessary part of gas turbine research and development. However, it has for many years been recognized that the operating conditions within each component also need to be understood when moving between steady-state operating points. Control systems may then be turned to enable a safe and swift response to changes when demanded.

The objective of this working group is to produce a document that provides the user with a guide for the measurement of transient aerothermodynamic performance parameters of aircraft gas turbine engine components. Topics covered include typical types of transients, sensed parameters, frequently used sensors and transducers, and the desired level of accuracy. Data acquisition and reduction procedures, measurement uncertainty, and worked-out examples will be described. The working group will try to develop a document that will serve engine developer/designers, test agency/test subcontractors, certifier/licensing authorities or aircraft customers, and operator/aircraft users.

The scope of the work is limited to transient tests of operational engines that would be carried out in ground-based test facilities. These could be ground-level test beds (commonly referred to sea-level cells) or altitude chambers. Although rig tests are not specifically addressed, in general many of the techniques described are applicable.

The working group report is going to address typical types of transients, the requirements of engine test facilities, examples of test methods, and general parameters to be recorded during the transient. Also introduced is the concept of defined measurement process, which, if followed in the planning stages, will greatly enhance the probability of success.

The measurement uncertainty methodology for transient measurements, the essential step in the planning process, is explained thoroughly. A clear understanding of bias and precision errors, combined with the stated experimental objectives, should determine the relative or absolute accuracy of the parameters. A method is proposed that depends on separating the error sources into steady-state and transient components, which, when combined, will yield the total uncertainty.

A part of the advisory report will be devoted to transient measurement systems, including the integration of data in space and time together with detailed information on pressure, temperature, fuel and air flow, geometry, force and torque, and control system parameters. In dealing with each sensor, type, basic theory, advantages and disadvantages, signal conditioning, calibration procedures, and specific design examples will be explained.

Two design examples of instrumentation systems, required for two different types of tests, will then be given. The first example, applicable to both engine developers and overhaul agencies who have a requirement to determine compressor pressure ratio in surge, is a complex one requiring specialized instrumentation. The second example, directed at an engine overhaul agency or operator, is a common test procedure employing conventional instrumentation, who as a part of the acceptance test must record the acceleration time to 100 percent of rated engine thrust. The reader will also be guided in implementing the complete process, from the statement of need, through sensor selection, test techniques, measurement uncertainty, up to data display.

(WG 15) The Uniform Engine Test Program

Performance of the propulsion system must be known to a high degree of accuracy throughout the entire flight envelope to achieve the level of operational capability demanded from today's high performance aircraft. During the late 1970s joint engine development and licensed production programs among companies from different countries were becoming common. Further, engines developed in one country were often used in airframes developed in another. Both situations require engine performance information, which can be interpreted internationally and provide a valid basis for performance comparisons.

The Uniform Engine Test Program (UETP) is one of the most extensive experimental and analytical programs ever sponsored by AGARD. The objectives of the program were:

> "To provide a basis of upgrading the standards of turbine engine testing within NATO countries by comparing test procedures, instrumentation techniques, and data reduction methods, thereby increasing confidence in performance data obtained from engine test facilities.
> To compare the performance of an engine measured in ground-level test facilities and in altitude facilities at the same nondimensional conditions and establish the reason for any observed differences."

The UETP involved testing two turbojet engines in five countries (US, Canada, France, Turkey, and UK) using four altitude test facilities and four ground-level test beds. The testing program began in 1981 and extended over a period of approximately seven years, with the supporting data analysis program progressing concurrently on a cooperative multinational basis. The working group's Advisory Report was published in 1990. In connection with the work of WG 15, an AGARDograph entitled "Measurement Uncertainty Within the UETP" was published in 1989.

The test vehicle selected for the program was the Pratt & Whitney J57-P-19W twin spool turbojet. This engine was chosen because of its rugged, mature configuration with minimum mechanical variable geometry features, which could introduce small performance variations from test to test. It was also of a size that made it acceptable for testing in the facilities under consideration. The fact that, by modern standards, it is of modest aerothermodynamic design was of no consequence. Two engines were loaned to the program by the US Air Force. Due to higher priority test workload at some of the participating facilities, it was not possible to test both engines in all facilities as was the original intention. Table 3 gives the list of facilities at which the engines were tested.

At the commencement of the program a General Test Plan

Table 3 Test facilities and test program

National Aeronoutics and Space Administration (NASA)	2 engines at altitude
Arnold Engineering Development Center (AEDC)	2 engines at altitude
National Research Council of Canada (NRCC)	2 engines at ground-level
Center d'Essais des Propulseurs (CEPr)	1 engine at altitude 2 engines at ground-level
Turkish Air Force Overhaul Base (TUAF)	1 engine at ground-level
Royal Aircraft Establishment Pyestock (RAE(P))	1 engine at altitude
Naval Air Propulsion Center (NAPC)	1 engine at ground-level (open air facility)

Table 4 Altitute interfacility differences

Engine Parameter	Independent Variable	Inter-facility Spread (max-min)/median (percent)
Net Thrust	Engine Pres. Ratio	3.4 - 5.4
Specific Fuel Cons.	Net Thrust	0.9 - 2.4
Airflow	Low Rotor Speed	1.3 - 3.6

Table 5 Ground level interfacility differences

Engine Parameter	Independent Variable	Inter-facility spread (percent)
Thrust	Engine Press. ratio	0.7
Secific Fuel Cons.	Net Thrust	1.8
Airflow	Low Rotor Speed	1.9

was prepared that defined the location and extent of the engine instrumentation, the test conditions, the test procedure, and the equations to be used for calculating the engine performance parameters. Test results were only interchanged between facilities after each completed their test program so that each facility went into its testing "blind" and with no bases for comparison. As the program progressed, interfacility comparisons became possible and extensive investigations were undertaken to discover the cause of the observed differences.

The measure of agreement between the four altitude facilities was assessed using engine performance curves based on six sets of fundamentally related parameters. The agreement was generally good with four of the six parameter sets having virtually 90 percent of all their data points within 1 percent (plus or minus) of the mean curves over the entire engine thrust range tested. The exceptions were fuel flow (63 percent) and net thrust (69 percent) where the data from one facility were significantly different at some test conditions than those from the other three facilities. Omitting the data from the one facility increased the proportion of data points within the 1 percent band to 85 percent for fuel flow and 92 percent for net thrust. Generally, the experimental results validated the facility uncertainty estimates. This is considered a good result and gives confidence in the engine performance measurements obtained in different altitude facilities.

An alternative measure of the altitude interfacility differences is given by the spread in the engine performance parameters. The magnitudes of these spreads depend on the choice of independent variable held fixed as the basis of comparison as well as on the engine power setting. Table 4 shows the spread in results taken over all ten conditions tested, which were evaluated at approximately the midthrust level of the engine power range for the fixed parameters indicated.

Three of the ground-level test beds were compared along with the only altitude facility capable of reproducing the sea-level static test conditions (AEDC). One might expect the spreads in data from the ground-level test beds to be less than those from the altitude facilities since only one test condition is possible in the ground-level beds and it is at relatively high pressure conditions. However, the variation in ambient temperature at the various test sites adds considerable variability. Even with this additional variability, the experimental results generally validated the facility uncertainty estimates. Maximum spreads for ground-level conditions are noted in Table 5.

Altitude and ground test facility data were compared by adjusting the data to a common environment through use of specified UETP referred equations. The adjustment technique was shown to be adequate for small inlet temperature differences. Engine performance results derived from ground-level beds and from altitude test cells generally agree when test environmental factors are properly introduced through the use of the engine mathematical model.

Results of UETP. Key contributions of the UETP to the participating countries are:

- A standard methodology for objective assessment of the quality of measured engine performance in the various test facilities was derived and implemented.
- A data base of standard engine performance parameters was created for each test facility. This information permits future evaluation of current capabilities of engine test facilities and provides the basis and impetus for facility improvements.
- Each participant in the UETP found anomalies in his facility test and evaluation techniques that have caused an internal reevaluation. Problems varied in degree, but in some cases the problem would not have been discovered without the ability to compare with the other facilities. This has emphasized the importance of providing redundant instrumentation and analyses in solo testing programs so the performance cross-checks can be applied.
- Experienced turbine engine testing experts from each country participated in the UETP. Their analysis of the UETP test data and facility differences have explained the sensitivities of many test parameters that have not previously been explored for lack of a unique set of comparative test data.
- Well-established national test centers have been provided with an incentive to improve their turbine engine test data by adopting better methodology, procedures, or equipment.
- Test facilities that were previously used primarily for logistic overhaul evaluations have been placed well up the learning curve as they seek research and development test status.
- Those AGARD countries that did not test the engines but provided active experts for the analysis have gained unique experience. Such experience can prove invaluable as those countries build or modify their own test facilities or as turbine engine test data are interpreted across international borders.

(WG 20) Engine Life Assessment Test Cases

This working group is a typical example of collaborative work between two panels, the Propulsion and Energetics Panel and the Structures and Materials Panel. It addresses an interface technology area between the two technologies. This working group started in 1988 and produced its report in 1992.

The worldwide trend toward producing lighter, more efficient aircraft propulsion systems presents a special challenge to the engine component designer. Higher cycle temperatures, increased aerodynamic loads, and higher rotating speeds coupled with reduced component weights all work in opposition to component life and durability. Over the past decade there has been considerable progress in the development of advanced

structural analysis and life prediction codes for gas turbine engine components. Validation of these codes on the component level is a real challenge because of the scarcity of well-documented data packages on actual engine components tested to failure. Hence, the Engine Life Assessment Working Group was formed. The objective of the group was to assemble a comprehensive number of well-documented test cases that would enable advanced code validation on the component level.

The scope of the working group's efforts was limited to the development of test cases involving crack initiation and crack propagation under elastic and elasto-plastic loading conditions.

Table 6 Test case data categories

Catagory	Definition
Component Geometry	Sufficient Dimensional and Shape Data to Permit Structional Analysis. Precise Dimensions and Tolerances Generally not Required.
Part Pocessing Information	Pertinent Heat Treatments, Surface Hardening, Residual stresses and and Surface Finishes as Appropriate.
Operating Conditions	Full Description of Actual Test Conditions to which Test Article (Component) Was Subjected.
Boundary Conditions for Stress Analysis	Complete Description of Mechanical and Thermal Interface Between Test Article and Test Vehicle.
Heat Transfer Information	Thermal Environment in Which Test Was Conducted.
Materials Data	Physical Property Data, Monotonic and Cyclic Mechanical Property Data, and Crack Growth Data Applicable to Material Heat from which Test Article was Drawn.
Field Data, Service History	Location on Test Article of Crack Initiation or Other faliure Sites; Crack Growth Measurements.

Two questions had to be answered for each test case:

What constitutes a complete, usable test case?

How can assurance be provided that a test case is not only complete, but is self-consistent?

Seven categories were identified that if fully addressed, would ensure completeness of the data package. These categories and their definitions are given in Table 6. The second question of self-consistency and detailed sufficiency of test case data bases was addressed through independent validity analyses that were conducted on each test case. The analyses were conducted to verify that enough information in each data category was provided and that there was reasonable agreement between the analytically and the actually observed failure mode and lifetime.

Six text cases were identified, which included a collection of problems that consider crack propagation in hot and cold section engine components. A broad range of component configurations and loading conditions is included. A detailed listing of test cases is included in Table 7.

Concluding Remarks

This paper describes the activities of seven AGARD working groups on gas turbine technologies from the late 1970s to the present. The working groups covered a broad range of topics.

Two of the working groups were involved in the collection of test cases for the gas turbine community to use in code validation. Each working group dealt with different computational technologies. One compiled test cases for internal aerodynamics codes, the other for structural analysis and life prediction codes.

Two of the working groups described in this paper were concerned with theoretical work. Working Group 12 reviewed the state-of-the-art knowledge on the performance prediction of turbomachinery and recommended areas that should be further investigated. The working group on averaging techniques addresses an area at the interface of theoretical and experimental work. Recommendations are made for averaging multidimensional flows.

The measurement techniques used for component and gas turbine testing involve many challenging problems. Standardization of measurement methodology and the need for more accurate measurements is becoming more and more important due to multinational programs and due to the ongoing work

Table 7 Test case summary

TEST CASE DESCRIPTION					ENVIRONMENTAL FEATURES					LIFE ELEMENTS			OTHER CONSIDERATIONS			
CASE NO.	SOURCE	ENGINE	COMPONENT	LOCATION	PLASTIC	STRESS CONC.	MULTI-AXIAL	MISSION	TEMP.	INITIATION SITE	FATIGUE	CRACK GROWTH	RESIDUAL STRESS	MAT'L	TEST METHOD	COMMENTS
1	SNECMA	LARZAC	TURBINE	AFT ARM FILLET	YES	NO	YES	NO	ELEV	DEFORMATION	YES	YES	NO	IN718	SPIN PIT	INITIATION AND PROPAGATION IN BIAXIAL STRESS FIELD
2	MTU	RB199	3RD STAGE	BOLT HOLE & RIM SLOT	YES	YES	NO	NO	RT & ELEV	DEFORMATION	YES	NO	NO	CORROSION RESIST. STEEL	SPIN PIT	HOLE AND SLOT SURFACE RESIDUAL MACHINING STRESSES MAY BE INFLUENTIAL
3	GEAE	CF6-6	COMPRESSOR	BLADE LOCK SLOT	YES	YES	NO	NO	150F 66C	ARTIFICIAL	NO	YES	YES (SHOT PEEN)	TI 6-4	SPIN PIT	MEASURED CRACK GROWTH FROM STRESS CONCENTRATION IN 200 CYCLE INCREMENTS
4	RR	RB211 -524	HP TURBINE DISK	DISK BORE REGION (SUB-SURFACE)	NO	NO	NO	NO	932F 500C	INCLUSION	NO	YES	YES (QUENCH STRESSES AT BOXE)	WASPALOY	SPIN PIT	SUBSURFACE CRACK GROWTH FROM INCLUSION
5	ALLISON	T41-A-1 T41-A-2	LOW PRESSURE COMPRESSOR DRIVE SHAFT	OIL HOLES	YES	YES	NO - TORQUE	YES MAJOR/ MINOR	ELEV	CORROSION PITS IMPERFECTIONS IN HOLES	YES (FROM FLAWS)	YES (UNDER TORSIONAL LOADING)	NO	EMS 64600 STEEL	TORQUE TEST RIG	INITIATION AND PROPAGATION FROM FLAWS IN HOLES UNDER MULTILEVEL TORQUE LOADING
6	P&WA	F100	FAN DISK (STAGE 2)	BOLTHOLE	YES	YES	NO	YES	70F 21C	ARTIFICIAL	NO	YES	YES (HOT PRESPIN)	TI 6-4	FERRIS WHEEL	CRACK GROWTH TRACKED FROM STRESS CONCENTRATIONS IN TWO TESTS

PLASTIC-Local stresses exceed yield strength, STRESS CONC.-Stress concentration, MISSION-Complex test stress cycle, TEMP.-All cases were stady state, FATIGUE-Case involves fatigue crack initiation, CRACK GROWTH-Case involves fatigue crack growth, RESIDUAL STRESS-Residual stress information provided in test case for, INITIATION SITE-DEFORMATION-Crack initiation not associated with initial flaw, INITIATION SITE-ARTIFICIAL-Crack growth from artificial crack starter notch, INITIATION SITE-INCLUSIONS-Crack initiation from inclusion.

of continuous marginal performance improvements. Therefore, one working group was concerned with steady-state and another with transient measurement techniques.

The Uniform Engine Testing Program is unique. This program gave the opportunity to the participating testing sites to critically assess their testing methodologies. This work is a valuable contribution to the multinational engine development programs.

The Propulsion and Energetics Panel has recently launched a new working group on "Humidity Effects in Gas Turbines." The group will examine the data available for humidity corrections to the performance of gas turbines, and assess its suitability to current "in service" and "scheduled for service" engines. One other working group related to gas turbine technologies is at its preliminary stages. This working group entitled "CFD Validation for Propulsion System Components" will establish the criteria to be used in the process of validating CFD codes. Issues related to numerical accuracy, grid sensitivity, turbulence, and transition modeling will be addressed. The group will evaluate the state of the art in conventional turbulence and transition modeling for internal flows, and assess the potential of more advanced developments, such as LES and DNS. The group will also identify and select test cases, based on the most recent experiments, to be used for comparative validation.

Acknowledgments

The bulk of this paper contains short summaries from the advisory reports of the respective working groups. My sincere thanks go to the editors and/or working group chairmen: Ch. Hirsch, J. D. Denton (WG 12); M. Pianko, F. Wazelt (WG 14); J. J. Mitchell, P. F. Ashwood (WG 15); L. Fottner (WG 18); H. I. H. Saravanamuttoo (WG 19); R. C. Bill (WG 20); D. M. Rudnitski (WG 24).

I would also like to thank all members of the working groups who contributed to the success of each working group and for their efforts in producing the valuable literature.

References

AGARDograph, 1989, "Measurement Uncertainty Within the Uniform Engine Test Program," AGARD AG 307.

Fottner, L., 1989, "Overview on Test Cases for Computation of Internal Flows in Turbomachines," ASME Paper No. 89-GT-46.

WG 12, AGARD Propulsion and Energetics Panel, 1981, "Throughflow Calculations Calculations in Axial Turbomachines," AGARD-AR-175.

WG 18, AGARD Propulsion and Energetics Panel, 1990, "Test Cases for Computation of Internal Flows in Aero Engine Components," AGARD-AR-275.

WG 14, AGARD Propulsion and Energetics Panel, 1983, "Suitable Averaging Techniques in Non-uniform Internal Flows," AGARD-AR-182.

WG 19, AGARD Propulsion and Energetics Panel, 1990, "Recommended Practices for Measurement of Gas Path Pressures and Temperature for Performance Assessment of Aircraft Turbine Engines and Components," AGARD-AR-245.

WG 15, AGARD Propulsion and Energetics Panel, 1990, "The Uniform Engine Test Programme," AGARD-AR-248.

WG 20, AGARD Propulsion and Energetics Panel, 1992, "Test Cases for Engine Life Assessment Technology," AGARD AR 308.

Comments on the Development of the Early Westinghouse Turbojets, 1941–1946

S. Way
Whitehall, MT 59759

The early thinking leading to the American Turbojet engine is reviewed. This included ideas pertaining to ramjets and rockets, and culminated in the axial flow turbojet engine concept. The role of the NACA Subcommittee on Jet Propulsion under the leadership of Dr. W. F. Durand is stressed. Early problems with the new engine are mentioned, including flame tube light-off, interconnecting tubes, and fuel injection problems. An early major design innovation was the change to a single annular combustion chamber, replacing the 24 cans. This change culminated in the 19XB engine. The purposes of this paper are to show the magnitude of the problems encountered, and to give credit to the many dedicated persons who made the American Axial Flow Turbojet Engine a success.

The development of American aircraft jet propulsion was given its initial stimulus through the efforts of the NACA[1] special Subcommittee on Jet Propulsion. This group had been assembled in early 1941 under the leadership of Dr. William F. Durand, Professor Emeritus of Mechanical Engineering at Stanford University. Dr. Durand was a remarkable gentleman of some 82 years of age, who had already had a distinguished career with the United States Navy, where he contributed to the design of the first steel ships. He also edited a well-known series of volumes on aerodynamic theory [1].

The membership of the NACA Subcommittee included the following:

Dr. William F. Durand, Chairman
Professor C. Richard Soderberg, Vice Chairman, MIT
Mr. R. C. Allen, Allis Chalmers Co.
Professor A. G. Christie, Johns Hopkins University
Dr. Hugh L. Dryden, U.S. Bureau of Standards
Dr. J. C. Hunsaker, MIT
Dr. George W. Lewis, NACA
Dr. A. R. Stevenson, Jr., General Electric Co.
Professor E. S. Taylor, MIT
Dr. L. W. Chubb, Westinghouse Research Laboratories
Capt. S. B. Spangler, USN
Col. Donald J. Keirn, USA
Mr. R. E. Littell, Secretary, NACA

The subcommittee was assigned the tasks of examining the potential advantages of various fuels, reviewing jet-assisted take-off possibilities, and considering speed-boost systems for military aircraft.

Some work on jet-assisted take-off was already in progress at the California Institute of Technology in Pasadena, under the leadership of Professor Theodore von Kármán [2], Frank Malina, and H.S. Tsien. A JATO equipped airplane had demonstrated outstanding performance in take-off tests.

It should be mentioned here that by 1941 jet engine technology was well advanced in England, under the leadership of turbojet inventor Frank Whittle and the Power Jets Co., and also in Germany, chiefly at Junkers, A. G. However, these activities were only slightly known to American engineers. In 1941, a Whittle engine had been brought to the General Electric Co. in the United States, to be used for further study and development. Similar engines were subsequently built and flown on the Bell P-59 airplane. These matters were classified "Secret" at the time.

The writer had been asked by Dr. Chubb, Director of the Westinghouse Research Laboratories, to give some attention to matters under consideration by the Jet Propulsion Subcommittee. The rocket engine had demonstrated its capabilities in the assisted take-off tests; now there was interest in sustained high-speed flight at high altitudes. It was obvious that the rocket engine was greatly handicapped by the necessity for transporting oxidizer material to high altitudes. Why should this be necessary when the aircraft is surrounded by a vast ocean of air?

It appeared that it should be possible to admit air near the front end of the jet motor, burn it with the fuel, and eject the products as a propulsion jet. Thus was born the idea of the ramjet engine. We should say the ramjet was "reinvented," as some earlier work had been done by Lorin [3] in 1908 and by Fono [4] in 1928. The writer prepared some design studies [5] of the ramjet (called "open duct propulsion" at the time) for Dr. Chubb, to bring to the attention of the subcommittee; a simple sketch of a ramjet device is shown in Fig. 1. Electrically heated ramjet models were built and tested [6] by the writer in 1941–42; see also Fig. 2. It had been independently conceived and tested by NACA engineers earlier in 1941.

The ramjet concept met with favorable response. However, it had two serious shortcomings: It could not produce any thrust for take-off, and extraordinarily high flight speed would

[1]NACA: National Advisory Committee for Aeronautics, predecessor of NASA.

Contributed by the International Gas Turbine Institute and presented at the 38th International Gas Turbine and Aeroengine Congress and Exposition, Cincinnati, Ohio, May 24–27, 1993. Manuscript received by the International Gas Turbine Institute June 1, 1993. Associate Technical Editor: H. L. Julien.

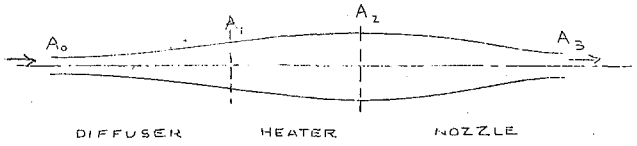

Fig. 1 Ramjet engine concept

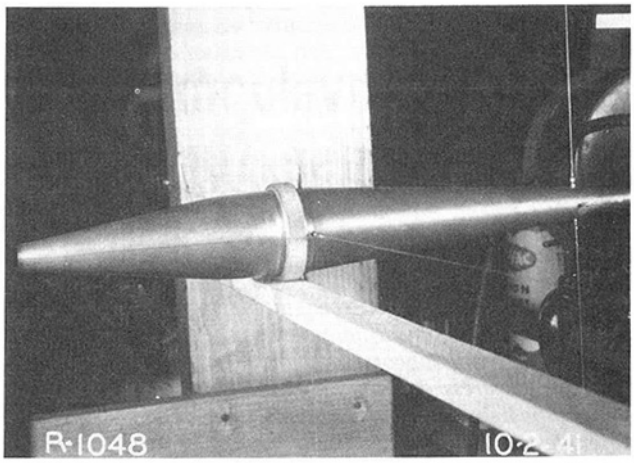

Fig. 2 Ramjet model on test

be necessary to attain good efficiency. It appeared that these deficiencies could be removed if an internal turbo-compressor were combined with the ramjet.

We now turn attention to another matter that was being considered by the subcommittee. Mr. R. C. Allen of the Allis Chalmers Co., in the spring of 1941, had made a presentation of a combination turbocompressor and ducted fan. These components comprised a double-duct jet engine. Although the device was large and heavy, the design showed attractive performance features. However, it appeared to some of us that a single duct system was superior. It would consist of an axial flow compressor, a combustion chamber, a turbine, and a jet-exhaust nozzle. The device resembled the Whittle engine (unknown to us at the time) but there were major differences, in that an axial flow compressor was used, along with a submerged combustion chamber. Further studies were made of this Single Duct Jet Engine, sketches were made, and preliminary performance calculations were carried out [7]; see Fig. 3.

The U. S. Navy (Bureau of Aeronautics) had been watching closely the theoretical studies of jet propulsion put together by Westinghouse. The idea of a simple, single-duct axial flow engine had much appeal from the standpoint of low frontal area, low drag, low weight, and high thrust. A meeting between Westinghouse and the Bureau of Aeronautics on December 8, 1941, resulted in a request from the Navy for specific gas turbine performance. On January 7, 1942, a letter of intent

SM-106
Restricted

S. Way
August 14, 1941

The Single Duct Hot Air Jet Motor

This memorandum aims to review the possibilities of a jet motor consisting of a straight duct, in which is mounted an axial flow compressor, a heating device and a turbine which drives the compressor, and which terminates with a nozzle from which streams the propulsion jet. The turbine output is equal to the compressor input (except for bearing and windage losses).

A schematic diagram is shown in Figure 1:

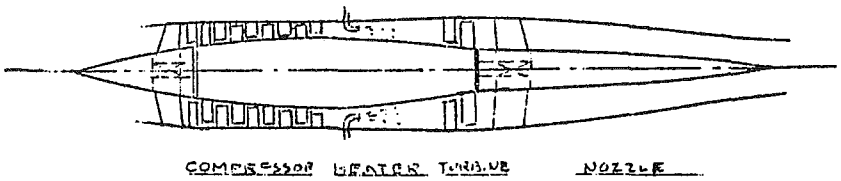

This report consists of the following sections:

(1) Overall efficiencies at 25000 and 40000 ft.

(2) Comparison of weight per horsepower with that of a double duct machine of the type proposed by R. C. Allen, for 4:1 compression ratio.

(3) Effect on the weight per horsepower of varying the pressure ratio.

(4) Effect of using a built-in diffuser to secure part of compression.

I. Over-all Efficiencies at 25,000 and 40,000 ft. Elevation.

In calculating the over-all efficiencies, the efficiencies of turbine and compressor were both taken at 85%.

Fig. 3 Page 1 of early turbojet engine memorandum

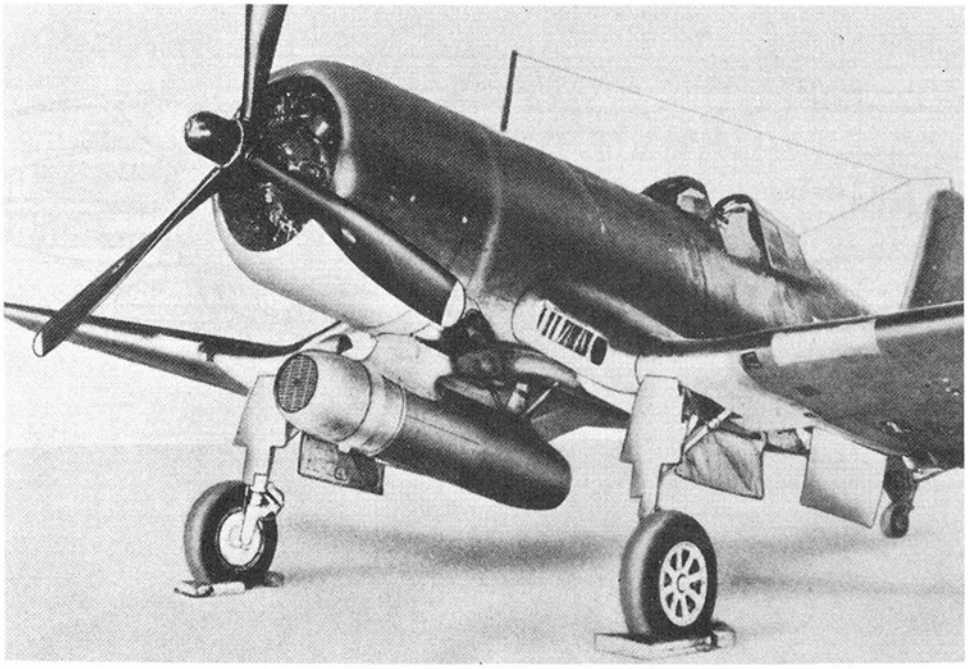

Fig. 4 Westinghouse 19-A engine mounted on Chance-Vought F4-U airplane for first flight test, January 1944

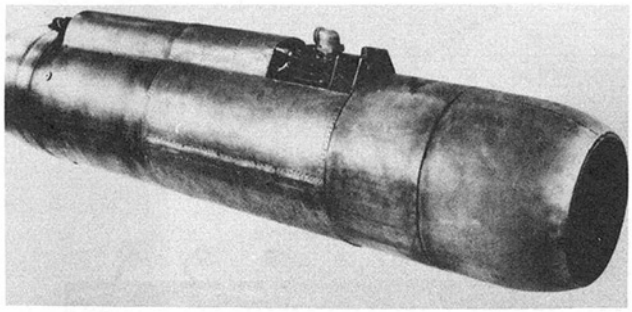

Fig. 5 Completed Westinghouse 19-A turbojet engine in late 1943

was sent to Westinghouse for a study and design contract. Westinghouse received a contract on October 22, 1942, to construct two X19 engines (axial flow, single duct, 600 hp thrust at 25,000 ft).

A design team was quickly organized at the Development Engineering Department of the Westinghouse Steam Turbine Division in South Philadelphia. This team, under the leadership of Mr. R. P. Kroon, was assigned the task of carrying out the necessary design studies.

The prodigious task confronting this group included:

- Further preliminary overall engine design.
- Aerodynamic design of the compressor and turbine.
- Detailed mechanical design and stress analysis.
- Testing and identification of appropriate materials.
- Complete studies of bearings and lubrication.
- Instrumentation and control systems.
- Development of the combustion system.
- Construction and testing of prototype engines.

The engineering group included R. P. Kroon of the Steam Turbine Division Development Engineering Section, O. E. Rodgers, Mark Benedict, Charles A. Meyer, W. R. New, P. G. deHuff, H. J. Clyman, A. H. Redding, Joe Chalupa, and John Rivell, Test Engineer. These were all quite young men, mostly in their twenties and thirties.

The mechanical design details were entrusted to O. E. Rodgers; turbine and engine thermodynamics were under C. A. Meyer; A. H. Redding took over the compressor problem; P. G. deHuff the metallurgical and material studies; Joe Chalupa followed manufacturing and production; and Mark Benedict the engine installation. W. R. New had earlier made contributions in gas turbine engineering with the invention of a closed-cycle system.

The team went to work under the direction of Rein Kroon and progress on the various tasks was soon realized. Between the compressor and turbine stood a large question mark. Little was known about combustion at the rates needed and in the small available space. Burning rates had to exceed those of conventional equipment by a factor of ten or more. The combustion problem was assigned to the Research Laboratories for study, design, and development under the direction of the writer.

The only device that came close to matching the combustion requirements was the internal combustion engine. But here, very high turbulence and mixing are present. We should mention here, with great respect, a man who contributed very greatly to the jet engine combustion studies, Dr. A. E. Hershey, who came to us from the University of Illinois. Dr. Hershey not only brought his knowledge and keen insight gained from automotive engine studies, but was also a great friend and inspiration to all of us on the project.

Good progress was made. The first experimental combustion chamber consisted of an array of tubes, each with an inlet diffuser, a flameholder, and a gas torch igniter. It showed little promise. It was followed by the burner of "perforated can" type. This arrangement showed good performance and was subsequently pursued intensively. One reason for selection of a burner "can" configuration was that it lent itself to development studies of one small can alone.

The engine design and assembly proceeded rapidly. In just over 15 months after that first meeting, and 5 months after the contract to build the engine, the first engine was ready to test. Two engine units, designated 19A type, were prepared; they were the 9100 and the 9101. The combustion system consisted of 24 chambers or "cans" arranged in eight groups of three, each group occupying a 45 deg sector of the space between compressor and turbine. Outlets were blended together to form the turbine inlet annulus. Each of the 24 burner cans had its own spark plug. The plugs were fired sequentially by an "in-house" built distributor.

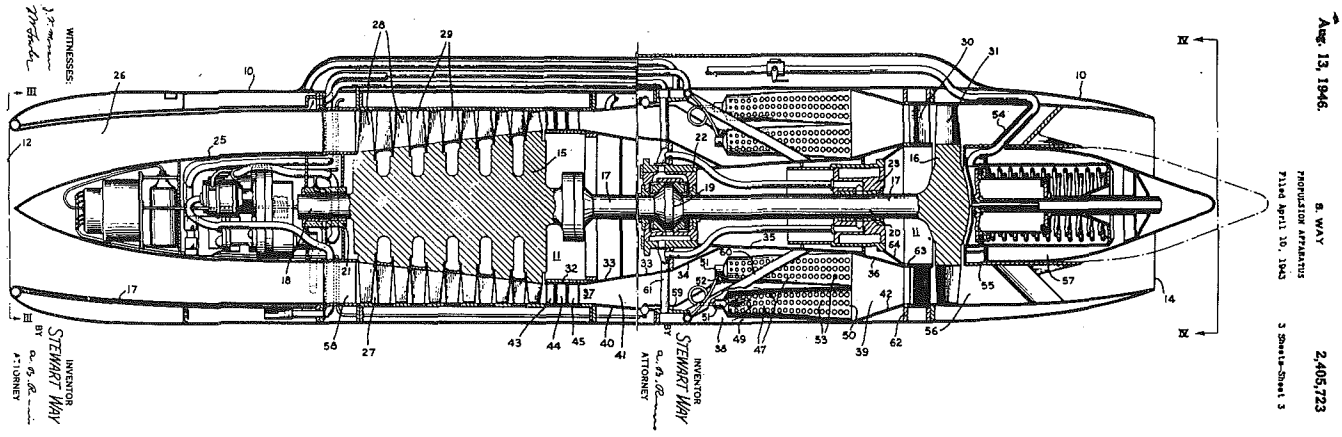

Fig. 6 Propulsion apparatus

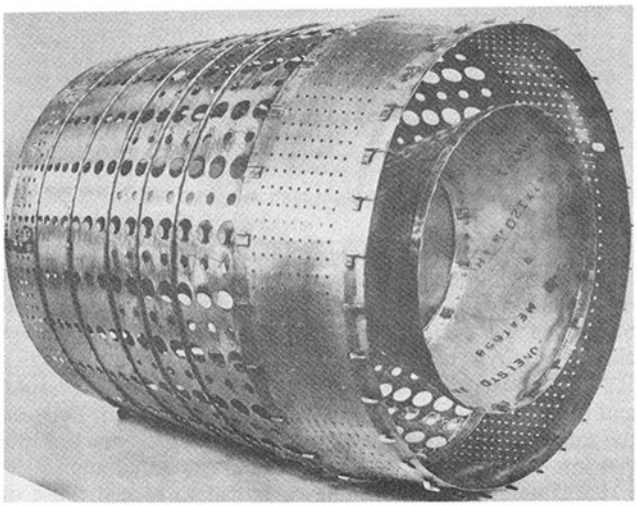

Fig. 7 19-XB annular burner shell, or flame tube

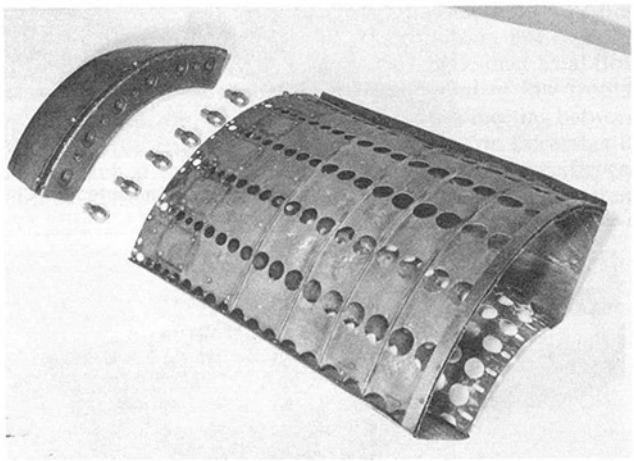

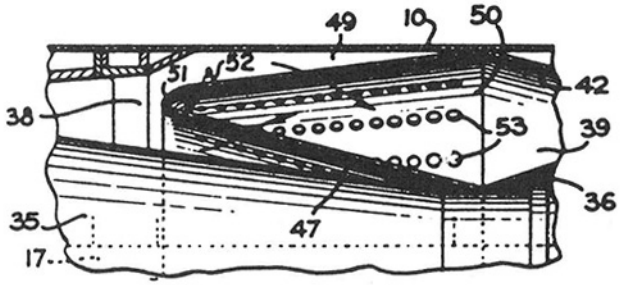

Fig. 8 19-XB burner sector model for test

A set of three cans was tested in the Research labs, with fair success. But when the attempt was made to light up 24 burners, it was found that only about half would light. Not enough heating was produced to run the turbine at design speed, and the engine could not be run up to full speed without the starting air blast. This was the first major problem of the new engine. The problem was partially solved by ingenious starting techniques, including attempts to light across the outlet ends from one burner to its neighbors.

The multiburner ignition problem was not solved until the introduction of interconnecting tubes. For two adjacent burners, one burning and one not burning, pressure in the lit-burner will be higher than the unlit burner (because of momentum change) and consequently an interconnecting tube would carry a crossflow of burning gases from the lit to the unlit burner. This arrangement also resulted in a great simplification since the number of spark plugs could be reduced from 24 to 3 or 4. However, some problems still remained. The interconnecting tubes had to be tightly connected to the burners, or air would leak in, causing the burner to blow out. Other problems cropped up with fuel injection nozzles. In attempts to break up the low-pressure fuel bubble that forms due to surface tension, wire "whiskers" were attached to the fuel injector face. (The "wire whisker" idea persisted for about six months.) All these endeavors required time and much patience, with many assemblies and disassemblies of the engine and train trips between Pittsburgh and Philadelphia.

At one point all problems were blamed on combustion. Even when a ring of straightening vanes at the compressor outlet was once installed backward, disrupting the air flow completely, the word went out: "combustion problems again"! The mistake was quickly rectified and the engine ran satisfactorily.

By July 1943 matters were pretty well in hand and the engine had completed a 100 hour test, as planned, with very satisfactory thrust. Representatives from the NACA subcommittee witnessed some of the tests.

An engine of the 19A type was mounted in an airplane and flight tested in January 1944. The plane was the Chance-Vought F4U Corsair (Fig. 4). Figure 5 shows the engine alone and Fig. 6 shows a schematic drawing.

A major design change was made in the winter of 1943–44. An annular combustion chamber had been designed and was installed in the Westinghouse 19B engine.

The annular combustor eliminated multiple spark plugs and interconnecting tubes since there were no separate burner cans. One smooth, continuous annular combustor replaced the 24 cans. Except for some undesired peaks and dips in the turbine

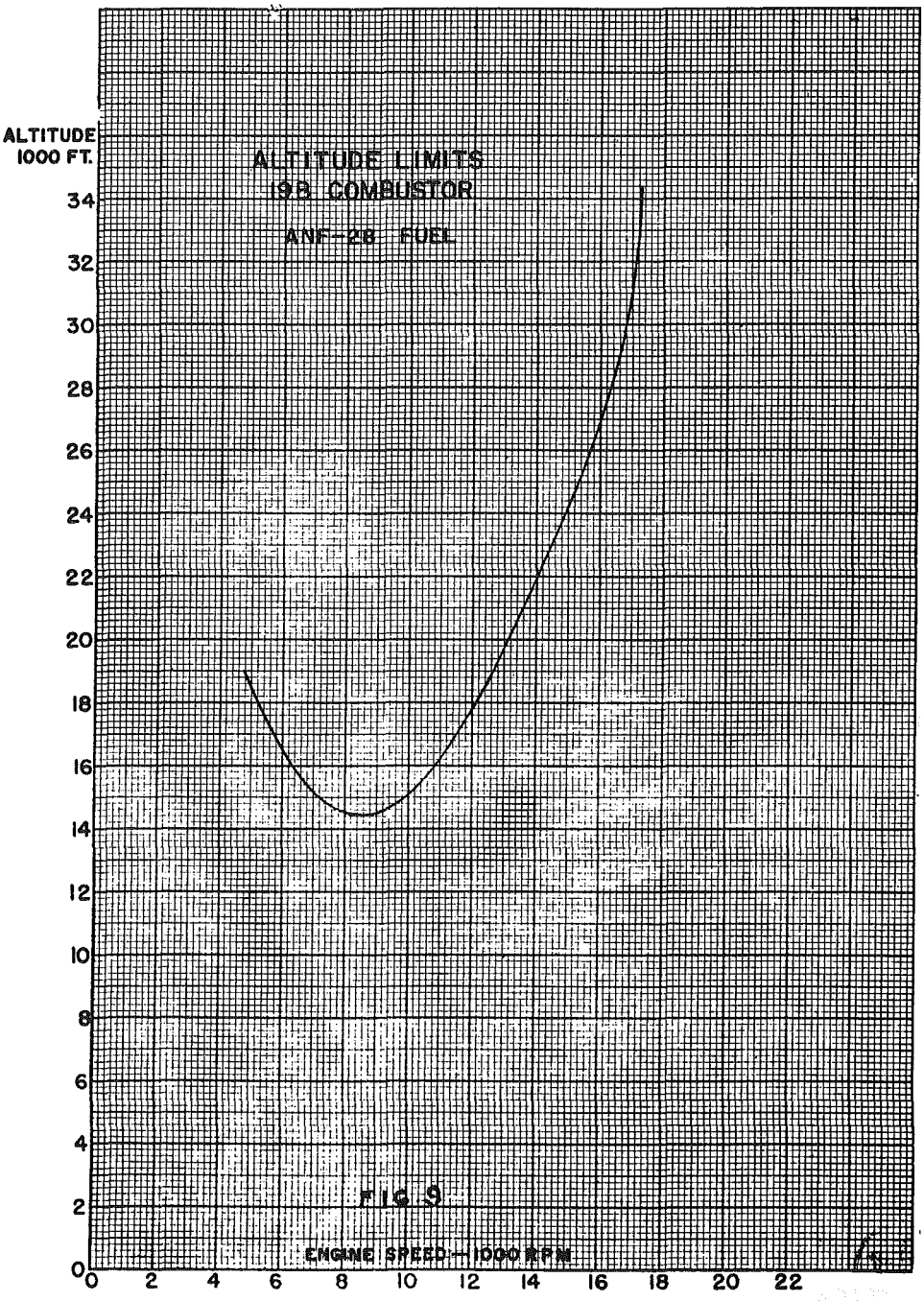

Fig. 9 Altitude limits of 19B combustor

inlet temperature pattern, the combustion operation and engine performance generally appeared to be satisfactory. Thrust was admirable, exceeding design expectations. The annular burner, Fig. 7, could be laboratory tested by use of a sector shaped unit as in Fig. 8.

Westinghouse engine testing was initiated in 1944 at the high-altitude wind tunnel in the Lewis Flight Propulsion Laboratory of the NACA in Cleveland, Ohio. Here the engine could be started, accelerated, and operated at various engine speeds and simulated flight speeds and altitudes up to 36,000 ft. This broad range of conditions brought to light new problems.

It was found that above a certain altitude, the engine could not be accelerated to full speed. The engine could be operated at full rpm if it was first brought up to speed at lower altitude. At a given (high) altitude there was a certain nonoperabe engine speed range. This gave rise to what was termed the "dead-band."

A typical dead-band curve for a 19B engine is shown in Fig. 9, based on tests at the Lewis High-Altitude Tunnel. This phenomenon creates a very hazardous situation for the flight personnel. If the engine were throttled back at high altitude it would die. It could be restarted once it slowed down sufficiently, but would still be unable to accelerate up to full speed and power. To regain full control the pilot would have to descend to a lower altitude. The situation would be unthinkable for military operation, and fraught with grave dangers, from mountains and other hazards, in civilian flight circumstances.

The problem had to be resolved. Extensive work was done in combustion chamber testing in conjunction with the wind tunnel tests. It was shown that the cause of the dead-band was that the combustion chamber capability under certain conditions of pressure and velocity was inadequate for the engine requirements for steady continuous operation.

This left unanswered the question of what should be done.

Extensive combustion chamber tests were run. Work in other laboratories in the U.S. and abroad was reviewed. Fundamental laboratory tests were made of the detailed behavior of the combustor. The combustion chamber had to be redesigned. The most notable change was enlargement of cross-sectional dimensions at the flame tube upstream end. The 19B upstream end was widened from about 1 in. to 2 in. to reduce velocities inside the chamber. Some changes were also made in the wall hole patterns. The revised design was designated as the 19XB configuration. In this way the dead-band problem was greatly alleviated, or removed from the critical range.

In subsequent years, further combustion research [8] showed that a critical parameter was the ratio of fuel loading in energy units per unit volume per unit time to reaction (chemical transformation) rate in similar units. Since reaction rate for second-order reactions depends on the square of the pressure, it is evident that reduced pressure (high altitude) will materially reduce reaction rate and impair combustor performance. At higher engine speeds the effect of higher compression ratio finally predominates and burning stability is restored.

The 19XB engine was used successfully in the McDonnell Phantom airplanes during the late 1940s. In recounting the Westinghouse experience we should mention the "baby engines," the 9.5A and B. Maximum diameter (at the combustor) was 9.5 in. (later 10.5 in.). A single annular combustor was used. A photo of a 19B engine and its "little brother" the 9.5B is shown in Fig. 10.[2] This little engine developed 300 lb of thrust and ran at 34,000 rpm. It was used for guided missiles and target drones.

Another important engine development was the 24C, otherwise known as the J-34. This engine was of about 32 in. diameter and put out 3000 lb of thrust. It was used extensively by the US Navy in the McDonnell Banshee. The combustion chamber for the J-34 was of double annulus type, designed by Dr. Egon deZubay of Westinghouse Research Laboratories. Still another Westinghouse development was the J-40 jet engine of 40 in. diameter, and 7500 lb thrust, built in the Kansas City plant. The engine performed as expected, but its reputation was damaged by unanticipated increases in air frame weight and drag.

This writer has given particular attention to Westinghouse contributions to jet engine development. It is important to call attention to other important activities. The General Electric Co. had become interested in the turboprop type of engine in 1941, and about the same time Westinghouse came out with its turbojet, designed and built the axial flow turboprop known as the TG-100. The group leader was Mr. Alan Howard. The TG-100 was quickly followed, also under Howard's direction, by the TG-180. This was a pure turbojet of axial flow config-

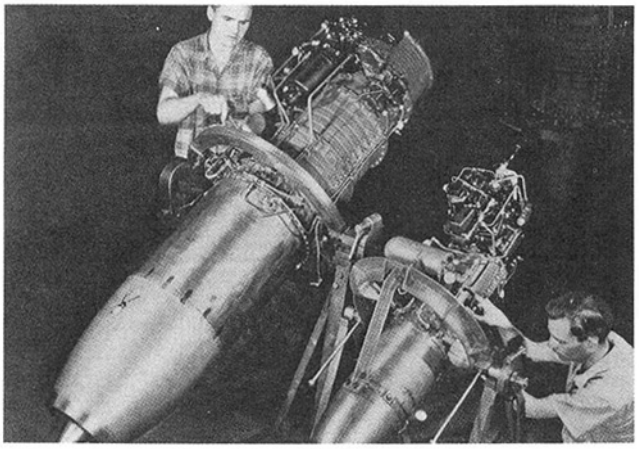

Fig. 10 19-B and 9.5-B jet engines, 1944

[2]This figure is from the book *Battlefronts of Industry* [9] by David O. Woodbury, Wiley, New York, 1948, p. 277.

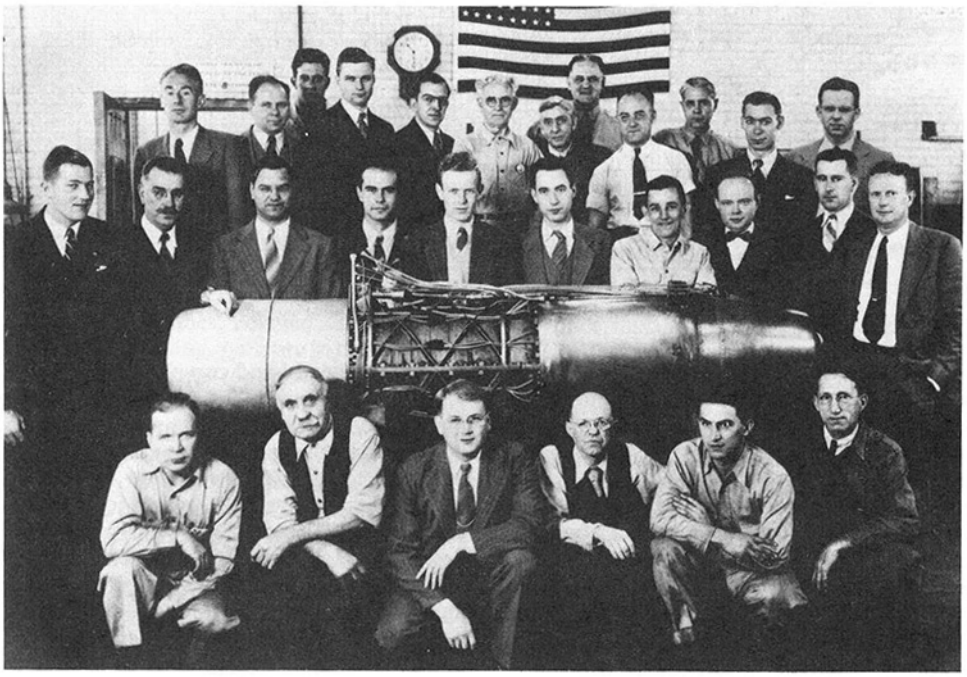

Fig. 11 Pioneers: Gathered around the first American turbojet engine is the pioneering group of engineers and mechanics who designed and built this successful engine in but 16 months. Back row: R. P. Kroon, C. C. Davenport, R. Gantz, A. S. Thompson, J. H. Borton, W. D. Kane, R. L. Macartney, W. M. Keenan, J. S. Fieldhouse, J. L. Hall, G. W. Briebel, O. E. Rodgers. Middle row: A. H. Redding, B. V. Anoschenko, J. F. Chalupa, C. A. Knapp, D. P. Darwin, C. D. Flagle, H. A. Jackson, W. R. Nes, C. A. Meyer, W. H. Dickinson. Front row: J. W. Rivell, C. Deiner, H. B. Saldin, K. B. Coster, V. Proscino, W. D. Eckard.

uration. The TG-180 was a well-designed engine that became very successful in service and was very widely used on various aircraft. A man at General Electric who made great contributions in the study of combustion was Mr. Tony Nerad. A good report of jet engine development at both G.E. and Westinghouse has been given by Mack Taylor [10].

In connection with the combustion problems relating to the jet engines, it is important to give special credit to people associated with the NACA Subcommittee on Combustion. We mention in particular Mr. Ted Olson of NACA and Professors Glen Williams, Hoyt Hottel and Jack Longwell of MIT; also Dr. Bernard Lewis, who was at that time with the U.S. Bureau of Mines. All these gentlemen helped by guiding their own fundamental researches, and guiding the thinking of others along sound and fruitful lines.

We mention here that others involved in the combustion phase of the jet engine development at Westinghouse in the 1940s were Mr. R. L. Hundstad, Mr. Harold Hildestad, Dr. Ray Friedman, Dr. W. C. Johnston, Dr. Egon deZubay, Mr. J. R. Hamm, Mr. E. P. Walsh, Mr. K. V. Smith, Mr. Willard Christiansen, and Dr. W. E. Young.

In closing the writer would like to mention again the gratitude everyone connected with the Westinghouse jet engine project feels toward Rein P. Kroon. He was a man of many talents and humanistic interests who provided reliable technical leadership and knowledge. He is sorely missed by all his friends and associates.

References

1 Durand, W. F., ed. in chief, *Aerodynamic Theory*, Springer, Berlin, 1935.

2 Gorn, M. H., *The Universal Man: Theodore von Kármán's Life in Aeronautics*, Smithsonian Institute Press, Washington, DC, 1992, p. 89 and illus.

3 Lorin, R., "Système de Propulsion," Brevet d'Invention, French Patent No. 390256, May 14, 1908.

4 Fono, A., "Luftstrahl Motor für Hochflug," German Patent No. 554906, May 26, 1928.

5 Way, S., "Open Duct Jet Propulsion," Westinghouse Research Laboratories Report No. SM101, Pittsburgh, PA, July 14, 1941.

6 Way, S., "Open Duct Jet Propulsion Model Test," Westinghouse Research Laboratories Report No. SM111, Oct. 1, 1941; "Preliminary Experimental Study of Open Duct Propulsion Models," Report No. SR114, Jan. 30, 1942; Pittsburgh, PA.

7 Way, S., "The Single Duct Hot Air Jet Motor," Westinghouse Research Laboratories Report No. SM106, Pittsburgh, PA, Aug. 14, 1941.

8 Way, S., "Combustion in the Turbojet Engine," presented at the Second AGARD Combustion Colloquium, Liege, Belgium, Dec. 1955; see also Way, S., "Problems in the Development of Turbojet Combustion Chambers," Westinghouse Scientific Paper No. 1421, Mar. 8, 1949.

9 Woodbury, D. O., *Battlefronts of Industry: Westinghouse in World War II*, Wiley, New York, 1948.

10 Taylor, M., "Uncle Sam's Young Jet Power," *PIC*, July 1948.

M. Badger

A. Julien

A. D. LeBlanc

S. H. Moustapha

A. Prabhu

A. A. Smailys

Pratt & Whitney Canada, Inc.,
Montreal, Quebec, Canada

The PT6 Engine: 30 Years of Gas Turbine Technology Evolution

The PT6 engine entered service in the mid-1960s. Since then, application of new technology has enabled low-cost development of engines approaching 1500 kW, the introduction of electronic controls, improved power-to-weight ratio, higher cycle temperature, and reduced specific fuel consumption. At the same time, PT6 field experience in business, commuter, helicopter, and trainer applications has resulted in engines with low Direct Operating Cost and a reputation for rugged design and a high standard of engine reliability. This paper will highlight some interesting examples of this technical evolution, including the development of electronic controls and the application of the latest three-dimensional aerodynamic and stress analysis to both compressor and turbine components.

Introduction

The first PT6 entered service in 1963. Since then, it has spawned a wide family of turboprop and turboshaft engines, which have become renowned for their rugged design, durability, and reliability. The original configuration has been maintained throughout the engine family (Fig. 1) and this has allowed rapid development of new engine models with low risk and at low development cost. A few statistics on the PT6 engine family are shown in Fig. 2. Typical PT6 installations include the Beech King Air family of aircraft (C-90 to KA-350); commuter airliners, for example the Beech B-1900D model and Shorts SD-360; the Pilatus PC-7 and PC-12 and Beech Mark PC9 II trainer aircraft; and a new generation of executive pusher turboprop aircraft, for example the Beech Starship and Piaggio Avanti. Helicopter applications cover the Bell Models 212 and 412 and the Sikorsky S-76B.

Growth through evolution and continuous application of new technology has enabled a tripling of output power within the same engine diameter while adding only 26 cm to the basic engine length. A unique feature of the PT6 is the so-called "free" power turbine, which allows great flexibility and diversity of application, as well as ease of hot end inspection and maintenance. The gas generator is comprised of a compressor with three or four axial stages and a single centrifugal stage, coupled to a single-stage high pressure turbine. The reverse flow folded annular combustor is of sheet metal construction with splash louvre cooling for low weight and cost. For propeller applications, a two-stage epicyclic gearbox provides a speed reduction by a factor of 15:1, to around 2000 rpm and for helicopter applications a higher output shaft speed (6600 rpm) is obtained by removing one of these stages.

Contributed by the International Gas Turbine Institute and presented at the 38th International Gas Turbine and Aeroengine Congress and Exposition, Cincinnati, Ohio, May 24-27, 1993. Manuscript received at ASME Headquarters February 12, 1993. Paper No. 93-GT-6. Associate Technical Editor: H. Lukas.

Power Growth

In order to achieve power growth within the same engine size as the original PT6A-6 (Fig. 3), advancements have been made in all relevant engineering specialist technologies, including compressor and turbine aerodynamics, materials and structural analysis of rotating components and of the static structure of the whole engine. Increased cycle temperature has been made possible, in particular, by better nickel-based alloys. This, combined with a doubling of engine massflow has enabled power growth (Fig. 4), while specific fuel consumption has resulted from increased cycle pressure ratio and improved component efficiencies.

Increasing mass flow and pressure ratio within the 48 cm diameter has imposed a continuing challenge on compressor designers to improve efficiencies while relative Mach numbers and blade loadings have all significantly increased. Similarly, stress engineers have had to continually improve power-to-weight ratios while maintaining high durability with increased operating temperatures (Fig. 5).

Accurate cycle synthesis of steady-state and transient engine performance throughout the whole engine operating range and flight envelope has been used to select optimum growth paths for the PT6. Every new model has been extensively tested in rigs, spin pits, sea level and altitude test facilities as well as in a flying test bed, for an accumulated development running time in excess of 300,000 hours. As well, improved understanding of engine operability has contributed to achieving the fast acceleration times required by helicopter applications, and high cruise altitudes achieved by new turboprop applications as well as the very stringent requirements of trainer aircraft. This has in turn required the introduction of sophisticated engine controls. One example is the fully integrated engine/propeller control system that has been developed for the PT6A-68 Joint Primary Aircraft Training System (JPATS).

Compressor Technology

The evolution of the PT6 compressor has proceeded through

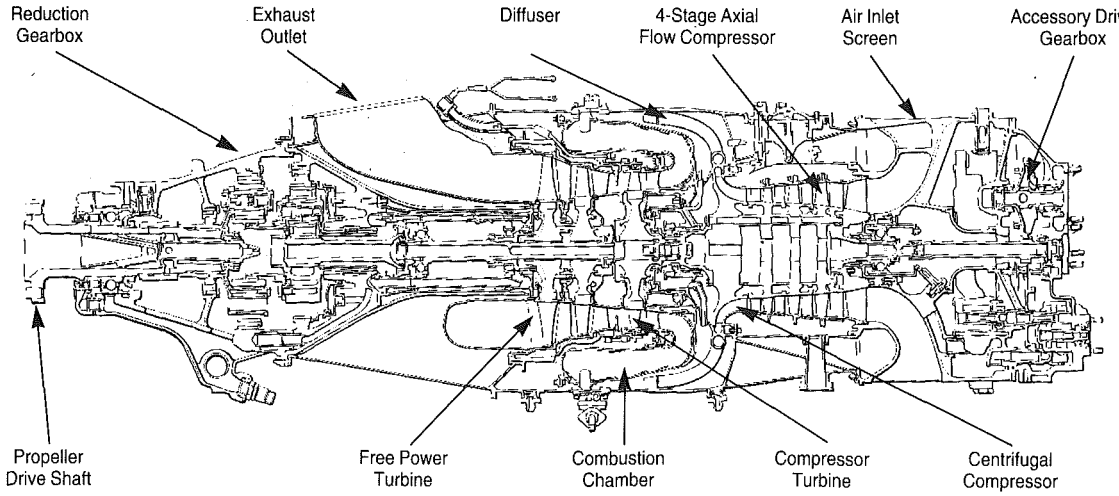

Fig. 1 PT6 gas turbine

	PT6 Turboprops	PT6 Turboshafts
Engines delivered	23,599	6323
Certified aircraft applications	83	13
Applications	95	15
Different operators	4955	359
Regional operators/aircraft	458/1771	3/10
Aircraft in operation	11,287	2244
Different countries	151	85
Highest total time - hours	39,583	21,471
Operating time - hours	179,477,766	24,044,560

Fig. 2 PT6 engine statistics

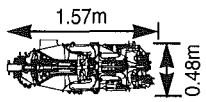

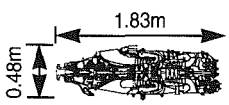

PT6A-6	Engine Model	PT6A-68
1963	Year	1992
123	Weight (Kg)	251
455	Thermal power (Kw)	1365
3.70	Power/weight (Kw/Kg)	5.44
410	Max. gearbox power (Kw)	930 (1200 in dev.)
0.39	ESFC (Kg/Kw–hr)	0.3
X	Turbine inlet temperature	X+200°C
2.6	Compressor flow (kg/sec)	5.3
6.2	Pressure ratio	11.0
Pneumatic	Control	Full Authority Digital Electronic Channel (single channel with hydro mechanical backup)
	Special features	Aerobatic capability
Beech 18 & 90 Series	Installation	Beech Mark II (JPATS)

Fig. 3 Evolution of PT6 engines

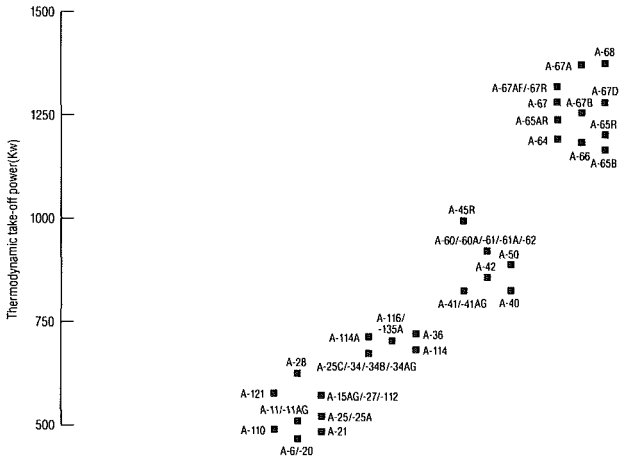

Compressor		Axial	3 stage	3 stage	3 stage	4 stage
		Centrifugal	1 stage	1 stage	1 stage	1 stage
Hot end	First stage	Vane	Uncooled	Cooled	Cooled	Cooled
		Turbine	1 stage	1 stage	1 stage	1 stage
	Second stage	Vane	Uncooled	Uncooled	Uncooled	Uncooled
		Turbine	1 stage	1 stage	2 stage	2 stage

Fig. 4 PT6 growth by design

extensive research and concept development, as well as by greatly improved aerodynamic design and analysis capability. The initial configuration of three axial stages closely coupled to a centrifugal stage has been optimized and grown to four axial stages over the years. The six tie-bolt rotor attachment, load bearing diffuser, and cantilevered stators are structural concepts that have been refined and retained on all models.

The improvement achieved in compressor performance is illustrated in Fig. 6. Both massflow and pressure ratio, as well as efficiency and surge margin (Yoshinaka, 1977), have been significantly increased. This has been achieved through extensive testing in a gas generator test facility shown in Fig. 7. Full compressor maps (Fig. 8), as well as individual stage characteristics (Yoshinaka and LeBlanc, 1980) can be obtained by testing only the gas generator portion of the engine, which allows for extensive instrumentation, including traverse and Laser 2F measurements.

An early innovation was the introduction of flankmilling of impeller blades. The manufacturing and aerodynamic design of impeller aerofoils have been integrated since the 1960s to allow the flank of a conical cutter to produce the blade surface in one cutting pass. More recently, the flankmilling process has been extended to axial compressors so that newer PT6 engines will incorporate flank milled Integrally Bladed Rotors (IBR) as shown in Fig. 9. IBRs offer improved performance, greater low cycle fatigue life, reduced part count, and a stiffer rotor construction. Recent improvements in cutting tool design and in machine capability appear to offer the opportunity for

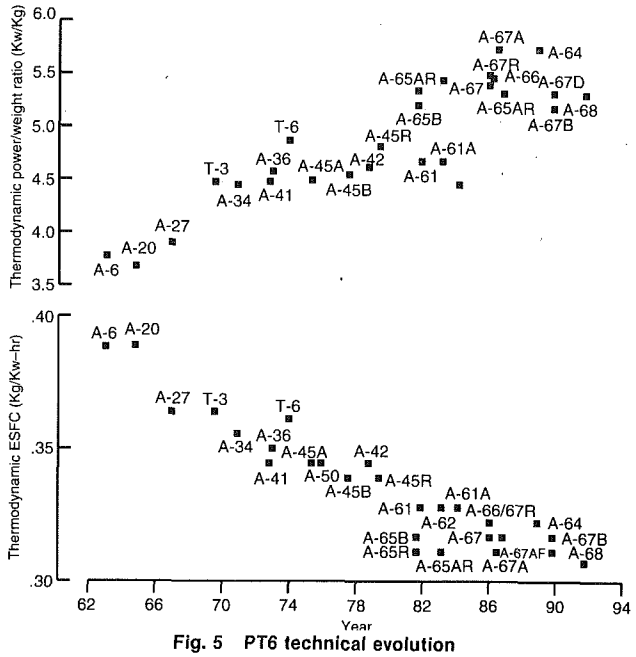

Fig. 5 PT6 technical evolution

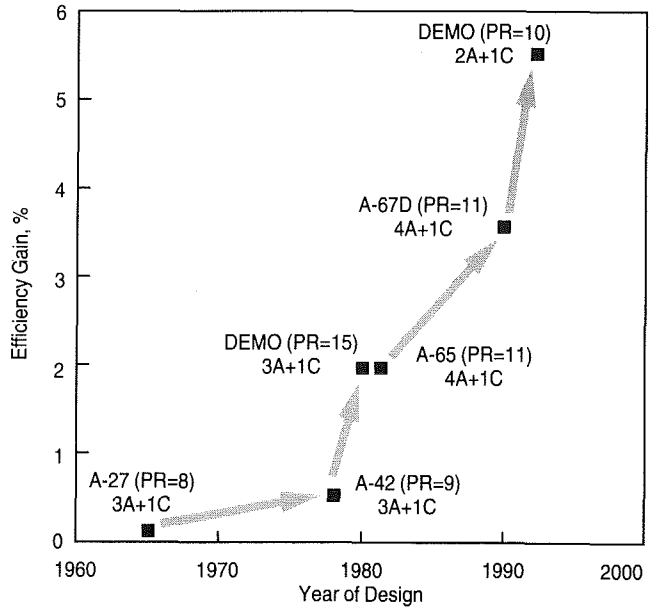

Fig. 6 Continuous improvement in compressor performance

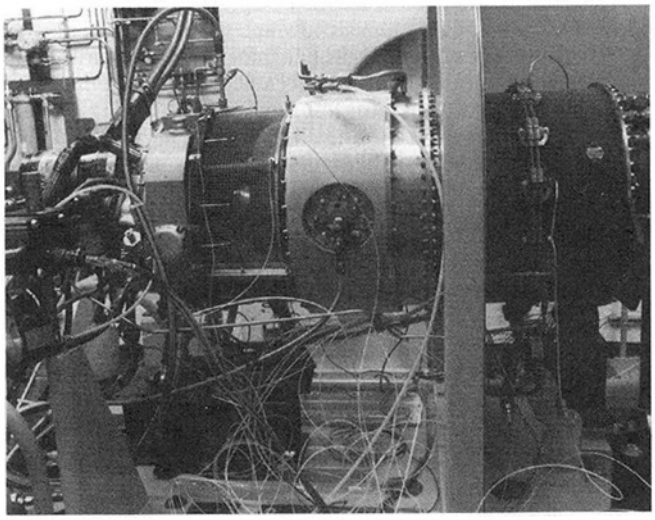

Fig. 7 Gas generator test facility

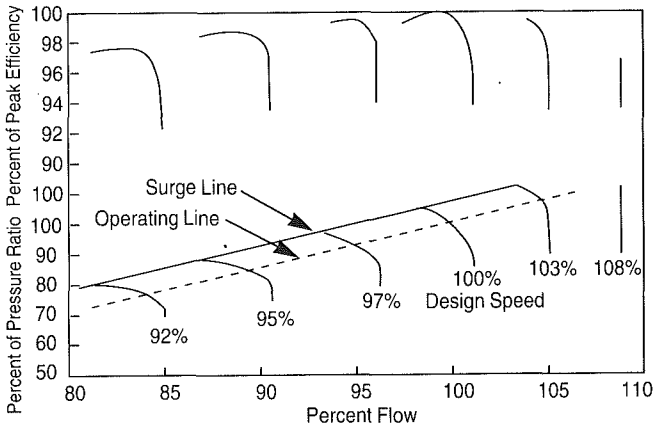

Fig. 8 PT6A-67 compressor map

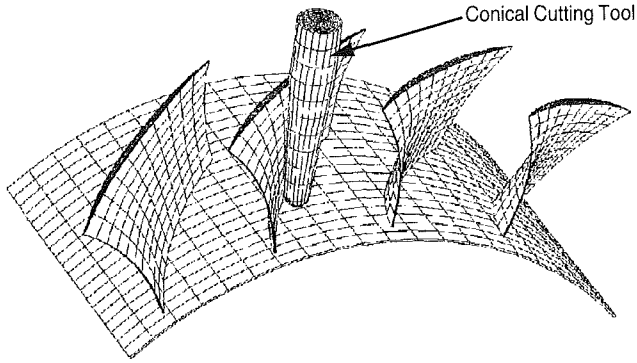

Fig. 9 Integrally bladed rotor (flank milling)

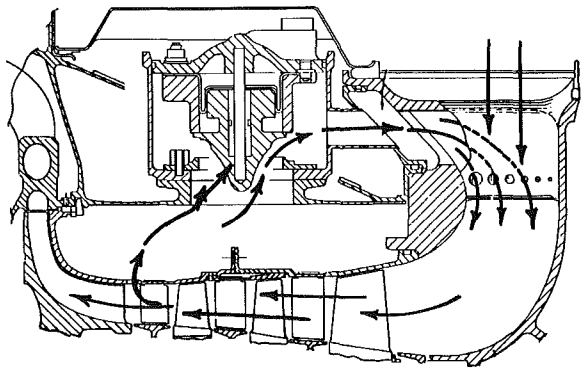

Fig. 10 Compressor jet flap

another step reduction in manufacturing cost at the same time with improved machining quality.

The novel pipe diffuser was first introduced on the PT6 engine and is now standard company design practice because of its demonstrated superior performance and compactness (Kenny, 1973). Manufacturing technology has developed to meet stringent diffuser aerodynamic design requirements, while new designs are done using three-dimensional viscous codes to enhance compressor surge margin.

Another innovative concept introduced into the PT6 is the so-called "Jet Flap," as illustrated in Fig. 10. It provides better handling, lower turbine inlet temperatures at off-design conditions, and a simpler installation without the need for overboard bleed. The Jet-Flap system is fed by a pneumatically operated valve, which bleeds air at the interface between the axial and centrifugal compressors. Bleed air is directed tangentially into the inlet through the intake struts so that in effect the Jet-Flap operates as a "passive" variable stage.

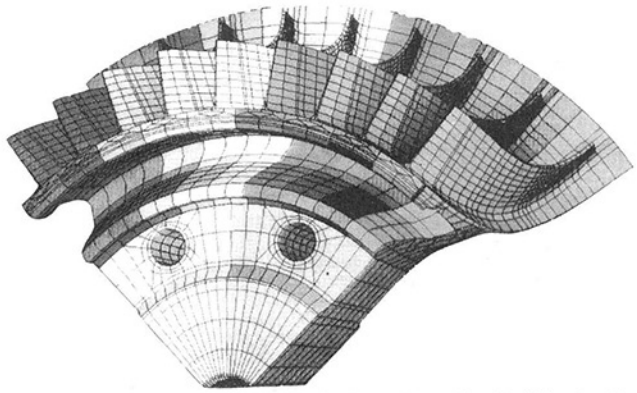

Fig. 11 Impeller structural analysis three-dimensional grid network

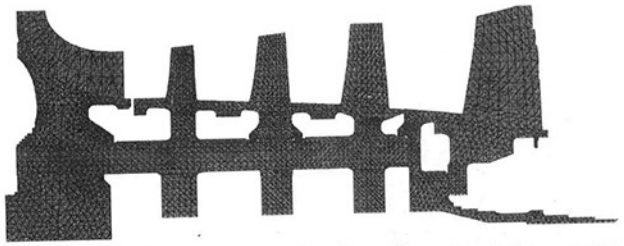

Fig. 12 Complete compressor rotor: three-dimensional stress model

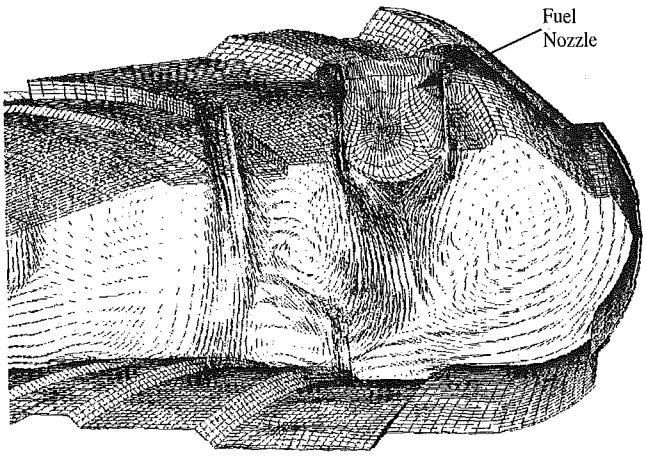

Fig. 13 Three-dimensional velocity vectors in plane of fuel nozzle

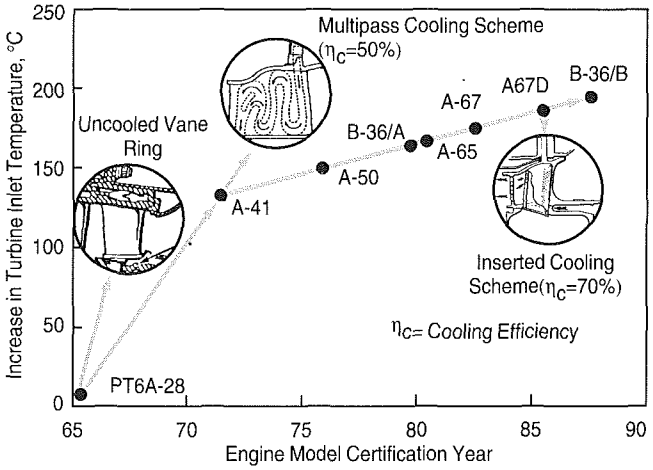

Fig. 14 Evolution of PT6 integral vane cooling concepts

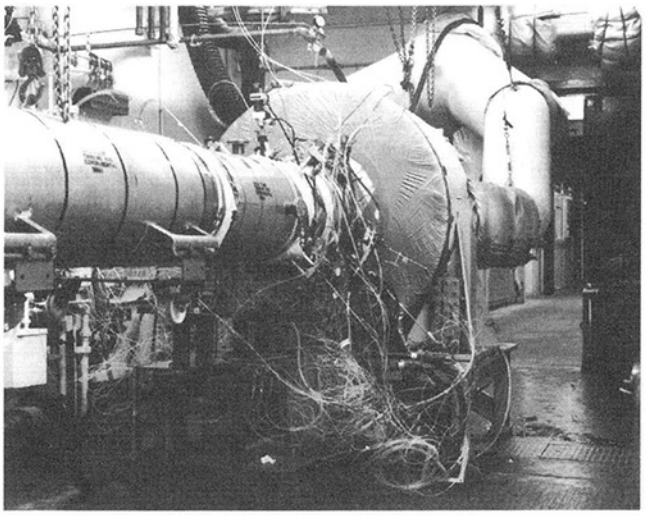

Fig. 15 Cold flow turbine test facility

Aerodynamic design capability has improved dramatically since the 1960s. Early designs were done using empirical rules and employed standard airfoil shapes. Blade-to-blade analysis was introduced in the late 1970s, three-dimensional and quasi-three-dimensional Euler codes in the 1980s and today fully viscous three-dimensional codes are in routine use (Bansod and Rhie, 1990; Habashi et al., 1992). In addition, a flexible and highly robust finite element throughflow analysis code is used to optimize the spanwise work distribution. In this way, highly loaded transonic rotors with good efficiency and range can be reliably designed, which, as well as ensuring good engine performance, also reduce development risk and therefore cost.

Structural analysis is done using three-dimensional finite element codes as shown in Fig. 11. Steady stress and thermal analysis as well as dynamic blade response are all included in the analytical design of components and verified with selected strain gage and thermocouple tests, typically in a gas generator. Low cycle fatigue life is closely substantiated by extensive spin pit testing (Shohet and Tadros, 1989). In this way, published lives are highly reliable. The whole rotor assembly is analyzed (Fig. 12) to study the change in tip clearance with thermal and steady loads, and in the extreme case due to unbalance following a possible turbine blade release.

Hot End Technology

Despite the higher operating conditions, the annular, reverse flow combustor has become progressively more compact (Critchley et al., 1984), which in turn has allowed for turbine growth within the same engine envelope. Machined construction has been introduced in critical areas to achieve good air flow control and hence improve consistency of turbine inlet temperature to maximize turbine life. The advantages of a split construction have been retained by using a bolted flange joint, which gives positive sealing yet good access for inspection and repair. The application of thermal barrier coating to the combustor hot side surfaces provided for an extra 200°C increase in exit temperature. The fuel injection system has also been developed (Critchley and Sampath, 1991) and now includes full dual orifice nozzles in order to optimize cold lighting and circumferential temperature distributions. Figure 13 shows the velocity vectors in the fuel nozzle plane, as obtained from a typical three-dimensional viscous analysis.

The compressor turbine evolved from a single-stage, subsonic uncooled turbine with a pressure ratio of 2.5, to a transonic turbine with a pressure ratio of 3.6, and incorporating vane cooling. Cooling technology (Arora and Abdel Messeh, 1985, 1990) has been directed at maximizing cooling effectiveness to cater for increased turbine inlet temperatures (Fig.

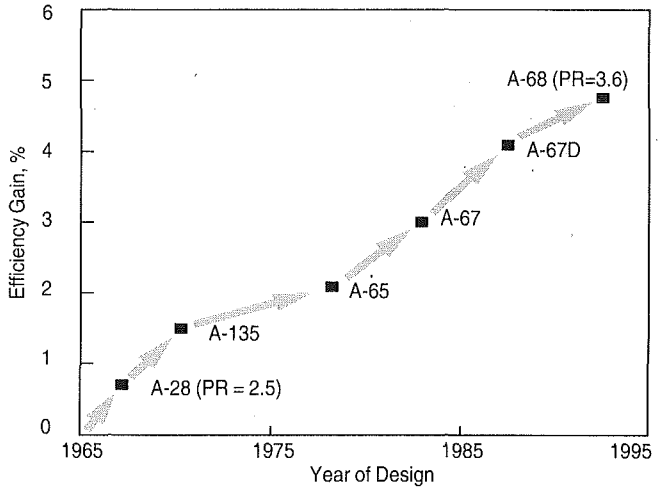

Fig. 16 Continuous improvement in turbine performance

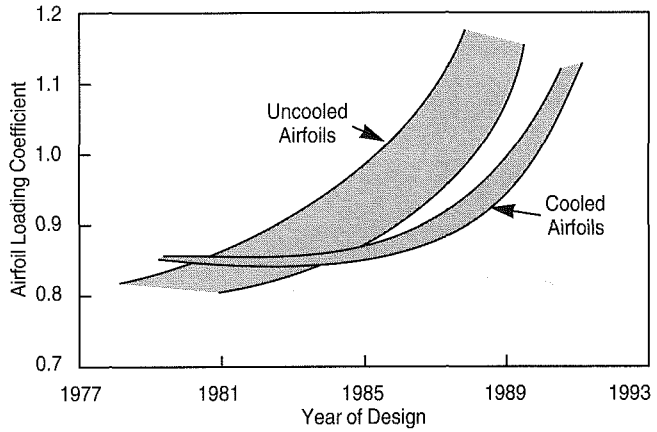

Fig. 17 Increased turbine airfoil loading

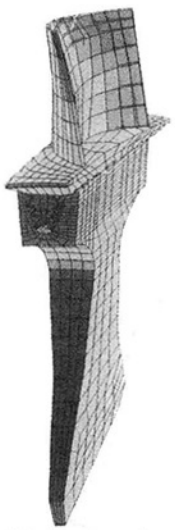

Fig. 18 Three-dimensional finite element network used for the stress analysis of the compressor turbine blade and disk fixing

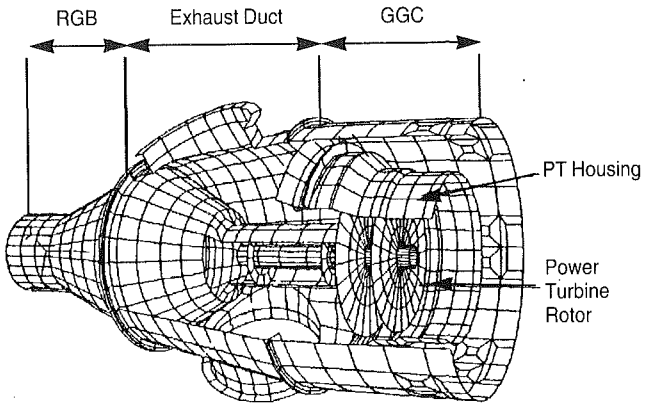

Fig. 19 Complete hot end three-dimensional stress model

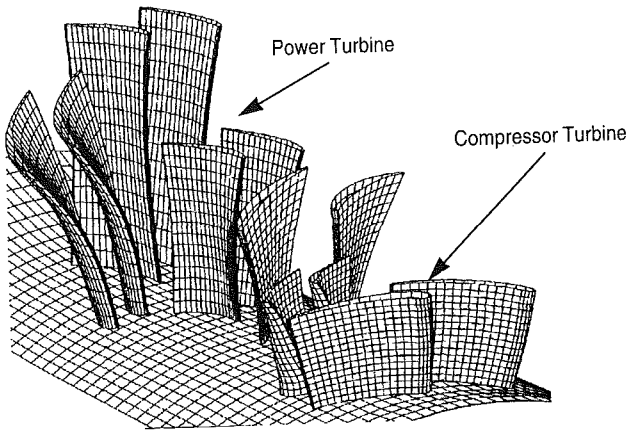

Fig. 20 Three-dimensional multistage flow analysis

14). A multipass cooling scheme without trailing edge ejection was first used on early models. In order to reduce the cooling air consumption and also mixing losses at the supersonic exit Mach numbers, recent models use an inserted cooling scheme with pressure surface ejection and state-of-the-art heat transfer augmentation devices.

Continuous research (Moustapha, 1990; Okapuu, 1974) in a Cold Flow Turbine Rig (Fig. 15) has resulted in an improvement of about 0.2 efficiency points per year on PT6 gas generator turbines (Fig. 16). Outer wall contouring and circumferential lean were introduced into the nozzle design to control secondary flow vortices and radial pressure gradients. Blade tip geometry and loading have been optimized using three-dimensional analysis to reduce tip leakage losses and turbine stage reaction has dropped over the years to reduce the blade metal temperature and provide for growth potential, while still maintaining good efficiency. As well, the number of vanes and blades has been reduced (Moustapha et al., 1987) with only a small efficiency penalty in order to reduce weight and cost (Fig. 17).

Detailed three-dimensional finite element stress analysis has been used to optimize the life of turbine disks (Fig. 18) using experimental data obtained from heat transfer rig testing and material characterization (Nguyen and Saad, 1989; Gautron and Saad, 1990). The disk attachment profile has been optimized to double the service life and the blade fixing low cycle fatigue life has been enhanced by high-intensity shot peening the firtree necks. Improved sealing in the hot end has been achieved by introducing metal seals in the critical joints. The material of the shroud housing has been modified on recent models for improved thermal response, optimum startup characteristics (higher pinch margin) and hence better tip clearance control. A complete hot end, three-dimensional finite element stress/deflection analysis has been used to isolate the effect of carcass bending, due to aircraft maneuvers and propeller loading, on the running tip clearance of the turbine rotors (Fig. 19).

The counterrotating shrouded power turbine, originally a single stage, has two stages in the higher power models. The PTA-67 and A68 last turbine rotor is transonic with low hub-

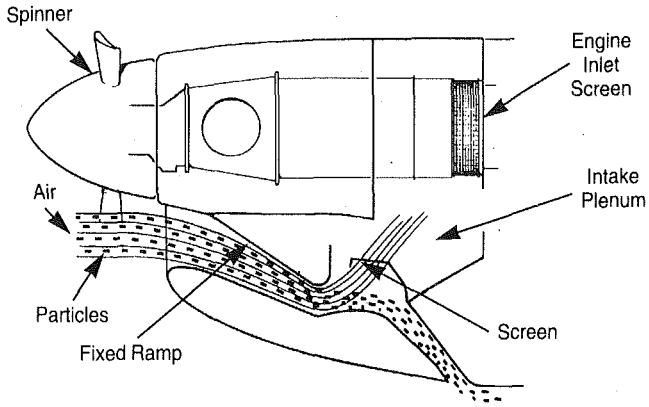

Fig. 21 Constant geometry inertial particle separator (schematic)

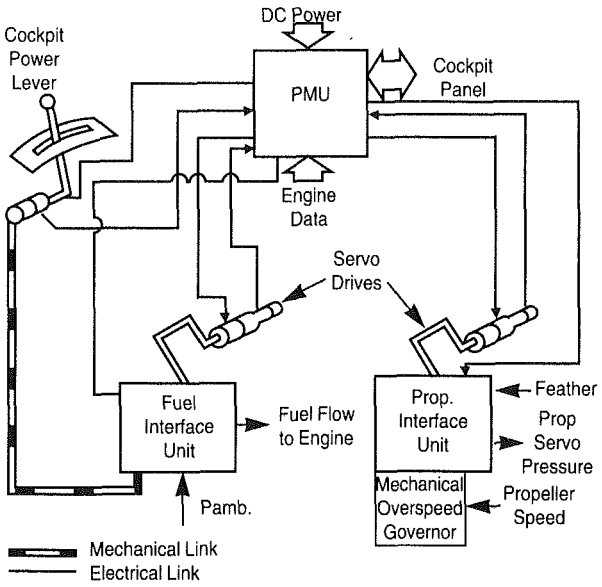

Fig. 22 Electronic power management system

to-tip radius ratio and has a high tip speed and "flow area speed square function." This poses some exceptional design challenges to satisfy both aerodynamic performance and stringent durability requirements. The turbine gas path, flare angle, and radial work distribution have been optimized using the finite element throughflow analysis. The airfoils have been designed for tolerance to off-design operation and to provide a good lapse rate with altitude. Multistage three-dimensional flow analysis has been used to optimize the stacking of the airfoils and to account for interaction effects between airfoils and stages (Fig. 20).

Finally, it is worth mentioning that over the last decade the required time to design PT6 turbines has been reduced by almost 50 percent. This is mainly due to the previously mentioned three-dimensional aerodynamic and structural design tools. Other contributing factors include three-dimensional airfoil surface visualization, concurrent design, and early interaction with the manufacturing process.

Installation

The reverse flow configuration makes the PT6 singularly well suited for efficient installations in both tractor and pusher applications. To date, the tractor propeller configuration has been dominant; however, PT6-powered aircraft with pusher propellers have recently been introduced in the marketplace. The more typical PT6 installation is therefore the tractor nacelle, and several important features are related to the peculiarities of the engine layout.

The aft-location of the engine air intake offers about 80 percent of the engine length for the design of an efficient inlet duct. A significant degree of diffusion may be obtained inside the duct, which makes it possible to lower velocities and hence losses in the inlet system. The space inside the nacelle at the height of the engine intake is wide enough to fit a plenum, which distributes the air flow uniformly all around the circumference of the engine. As a result of this, in conjunction with the inherently stabilizing characteristic of a radial inlet, the PT6 is practically insensitive to inlet flow distortion.

The axial length of the inlet system also affords space for an Inertial Particle Separator (IPS), which deflects dust, supercooled water droplets, and snow from the engine inlet into a bypass stream, which is ducted overboard. While the IPS was principally designed for protection in icing, the concept of a constant geometry separator shown on Fig. 21 has added a basic protection when operating in a polluted environment. Although typical separation efficiencies for AC-COARSE sand mixtures range only from 70 to 80 percent, these numbers are significantly higher for the larger, potentially more damaging components of the particle spectrum. This is considered to be one of the major factors that has helped to establish the reputation of high reliability for the PT6.

While the forward position of the engine exhaust represents a challenge in terms of nacelle drag and exhaust plume separation, if mastered it offers the possibility of designing a very efficient exhaust system. Its radially expanding passages attain pressure loss levels equivalent to, or better than straight-out exhausts.

Engine Control

Pneumatic control systems were ideal candidates for early PT6 engines and the basic pneumatic architecture and hardware design were retained until the late seventies on all engine models. By the mid-1970s, however, large PT6 engines had been introduced into commercial and commuter, as well as corporate markets. Specific fuel consumption became a competitive focus. Also, engine operability requirements became more stringent. In addition, control systems were required to provide additional functions such as temperature and torque limiting.

In helicopter applications, agility during specific maneuvers such as recovering from auto-rotation puts additional demands on the engine response capability. In addition, system anticipation in order to manage highest acceleration/deceleration rates without rotor overspeeds or droops and without engine overspeed, flameout, or surge is required.

By the 1970s, the maturity of the digital electronics industry made possible the design and manufacture of gas turbine engine control systems that would meet all flightworthy requirements. In particular, hardware packaging immune to EMI and lightning strike and capable of sustaining high temperature and vibration environments with adequate service life became possible.

With expertise gained in commercial aviation and a program of systematic research, a diversified product line of control systems for turbofan, turboprop, and turboshaft engines and auxiliary power units has been developed. A modern system development facility has evolved, capable of control logic design, picture to code generation, software verification, and system validation. The results of such continued efforts are seen in the latest control system developed for the proposed JPATS single engine trainer application using the PT6A-68 engine.

The PT6A-68 power management system makes possible the provision of turbofan-like operation at turboprop operating cost. The control both modulates the propeller blade angle

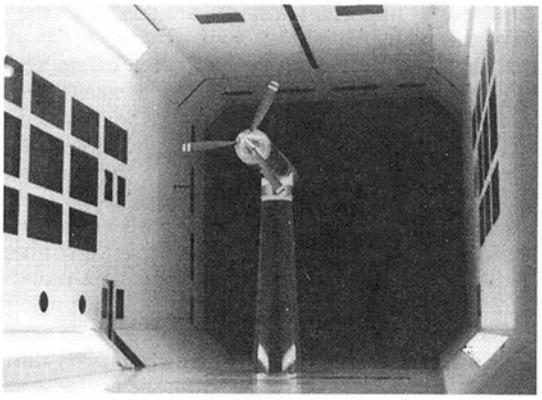

Fig. 23 10 × 10 m wind tunnel facility

and schedules fuel flow. This allows the scheduling of power and propeller speed so that a turboprop aircraft may closely simulate the thrust characteristics of a turbofan aircraft. A single cockpit lever schedules the engine power as a function of ambient conditions. There are two operating modes: the normal (electronic) mode and the manual (mechanical) mode as a fail-safe backup.

The major components of the power management system are the power management unit (PMU), the fuel metering unit (FMU), and the propeller interface unit (PIU). The PMU is a full authority digital electronic control (FADEC) with separate control and protection channels to provide full redundancy for safety. Figure 22 shows the power management system and interfaces. The complete system includes engine sensors and harness, plus interface to the airframe data buses and discrete inputs. The following is a summary of the features and benefits of the power management system:

- Integrated engine and propeller control, using multivariable control loop logic, for ground and flight mode operation including automatic engine starting.
- Fail fixed and automatic transfer to fully capable hydromechanical system.
- Monitoring and exceedance limiting of engine parameters torque, temperature, and speed.
- Fault accommodation for safe continued operation.
- Serial data bus (ARINC429) to the cockpit for engine parameters and status indicators.
- Minimum blade angle protection.
- Auto rigging of the airframe power level.
- Engine data acquisition and fault data for maintenance action.
- Utilization of picture to code software development tools to generate software from logic diagrams (meeting DOD-STD-2167A and RTCA/DO-178 requirements).
- Software coded in Ada high-level language.
- Utilization of real time simulation/integration testing for system verification and validation.
- Provision of service proven reliable electronic hardware with EMI and lightning protection.

Reduction Gearbox

The PT6 reduction gearbox is a two-stage planetary epicyclic design for turboprop applications and a single-stage design for helicopters. The reduction ratios achieved have varied from approximately 15:1 to 23:1 for the turboprop application. This basic gearbox configuration has been maintained throughout the evolution of the PT6, except for the use of a star system in some models to reverse the rotational direction of the propeller. The development and application of technology to this gearbox configuration has enabled it to grow from 400 kW to 1200 kW without a commensurate growth in size or weight while maintaining reliability.

A three-dimensional finite element (FE) gear tooth contact analysis has been developed, which includes the effects of tooth profile modifications, crowning, and lead errors. The detailed analysis of the gear tooth allows the effects of misalignments and gear train deflection to be studied in order to minimize gear tooth contact and bending stresses. The analytical results are compared to gear design allowable obtained through gear fatigue rig testing and field experience.

Finite element contact analysis has also been extended to the planet gear, ring gear, and casing (Sundararajan and Amin, 1991) to predict the ring gear spline contact stresses and slip as a function of time. This analysis, combined with extensive fretting wear testing conducted on various gear and casing material combinations, has provided a reliable method to minimize wear. By tuning the ring gear and casing stiffness and by optimizing the spline pressure angle, the loads and relative displacements between the ring gear and the casing are minimized, thus enabling higher powers to be transmitted for a given ring gear size.

Journal bearing reliability has been enhanced by minimizing the possibility of touchdown or bush spinning. To ensure that touchdown or metal-to-metal contact does not occur, the journal bearing fluid film is analyzed using F.E. methods to account for the various loads on the bearing as well as the effects of structural deflection and misalignment in the carrier, planet gear rim, and journal bearing pin (Das and Gupta, 1980). The analysis assures that under the most adverse conditions the fluid film thickness and peak pressures are within acceptable limits. These pressures are also applied to a mode of the journal bearing bushing and plane gear to ensure that the bushing does not creep or spin within the planet gear (Rodriguez et al., 1990). In addition, new materials have been developed for the bushes, which allow much tighter fits between the bushing and the gear. This allows higher loads to be transferred through the bearing while increasing the bearing reliability and assuring a good bond between the bushing and the lining material for fatigue resistance.

Since PT6 engines are extensively used in heavy-duty cycle commuter applications as well as for military trainers, high bending moments are imposed on the reduction gearbox by once-per-revolution ($1P$) aerodynamic loads, which result from inclined or nonaxisymmetric air flow into the propeller. To address this, aircraft and propeller aerodynamic modeling techniques have been developed and calibrated to predict the flow field into the propeller for various maneuvers and also the resulting propeller loads on the engine and propshaft (Gates and Smailys, 1989). The $1P$ load prediction method has been calibrated using full-scale propeller testing in a large windtunnel (Fig. 23) as well as extensive flight test data.

A methodology and criteria has been developed for the design of fretting fatigue free joints such as propshaft flanges and press fits (Smailys and Brownridge, 1987). In addition, more precise shaft lifing techniques, accounting for HCF/LFC interaction, and the thorough characterization of the material has resulted in reliable yet lightweight propshafts. Optimized elliptical fillets have also been used to reduce stresses and increase reliability further.

Aerobatic Capability

Certain PT6A models are certified for aerobatic operation. The modifications to the lubrication system that provide this capability are confined to the internal oil tank. These include a two-way gravity valve at the pressure pump inlet, and at the oil tank breather inlet. Substantiation of aerobatic capability is initially performed on a variable attitude test rig, which can be rotated 360 deg in two planes and accommodate any combination of pitch and roll (Fig. 24). Although the rig cannot

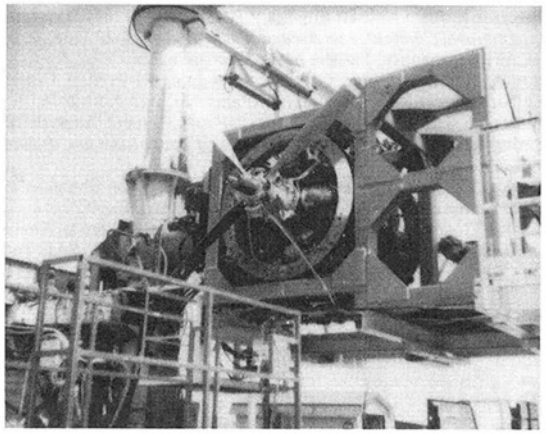

Fig. 24 Attitude test facility

Fig. 25 PT6 service history

reproduce in-flight maneuver loads, it can be used to demonstrate that the lubrication systems will operate satisfactorily in all attitudes.

Operating Cost

Figure 25 shows the basic in-flight shutdown (IFSD) rate achieved over the life of the PT6, together with the accrued running hours. This figure illustrates the manner in which technology evolution has built upon proven experience, resulting in relatively low risk for subsequent model derivatives.

Efforts in recent years have particularly focused on understanding and controlling operating costs. In conjunction with the operator community, costs have been broken down into categories for which influencing factors have been identified. One such area is overhaul. Figure 26 shows the variation in hourly cost with time between overhaul (TBO). Engine sampling has been developed to allow the TBO to be increased from the introductory certified interval, thereby reducing operating cost.

Due to its small size, the PT6 has a greater sensitivity to clearance control, dirt, and FOD than that of larger engines. A two-stage program to improve the understanding of these influences has been undertaken, with the objective of further reducing operating costs.

The first phase has been directed at identifying component sensitivity to typical wear and erosion experienced throughout the engine overhaul life. This has been carried out by comparison of two engines; one having "as new" performance, the other having been removed from service for overhaul. Based on these findings, significant changes to part replacement requirements have been defined.

A second phase has the objective of establishing repair limits for aerodynamic components, and is being carried out in conjunction with the National Research Council (NRC) of Canada. This program will investigate the sensitivity of performance deterioration to component damage, thereby establishing a basis for part repair or replacement in conjunction with the findings from phase one.

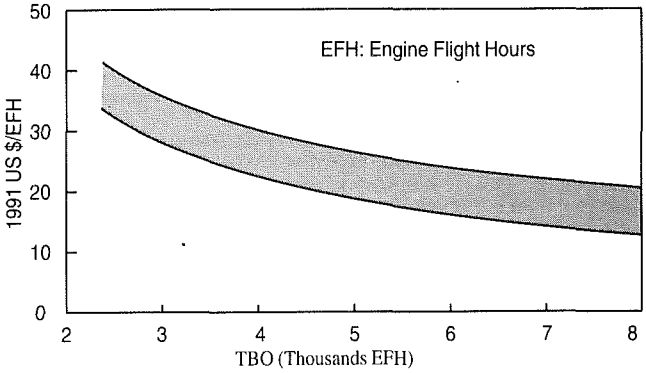

Fig. 26 PT6A-65 series overhaul cost

Conclusion

The PT6 has an extremely long history for an engine still in production. During this time, it has grown from approximately 375 kW to approaching 1500 kW. Much of this growth has been achieved through technology evolution with a number of significant technology steps, while maintaining the same basic layout and size. Use has been made of many avenues of evolution ranging from new materials to advanced aerodynamic design.

Acknowledgments

Industry, Science and Technology Canada has participated in the support of the different phases of the PT6 engine development programs. The authors also wish to extend their sincere appreciation to all personnel at Pratt & Whitney Canada who have contributed to this paper. In particular, we gratefully acknowledge the valuable input provided by A. E. McBurney, Director Engine Development.

References

Arora, S. C., and Abdel Messeh, W., 1985, "Pressure Drop and Heat Transfer Characteristics of Circular and Oblong Low Aspect Ratio Pin Fins," AGARD Conference Proceedings 390, PEP Symposium, Bergen, Norway.

Arora, S. C., and Abdel Messeh, W., 1990, "Characteristics of Partial Length Circular Pin Fins as Heat Transfer Augmentors for Airfoil Internal Cooling Passages," ASME *Journal of Turbomachinery*, Vol. 112, No. 3.

Bansod, P., and Rhie, M. C., 1990, "Computation of Flow Through a Centrifugal Impeller With Tip Leakage," AIAA Paper No. 90-2021.

Critchley, I. L., Sampath, P., and Gratton, M., 1984, "Alternate Fuels Combustion Research," AFWAL-TR-84-2042, July.

Critchley, I. L., and Sampath, P., 1990, "Cold Weather Ignition Characteristics of Advanced Small Gas Turbine Combustion Systems," AGARD-CP-480.

Das, P. K., and Gupta, S. S., 1980, "An Analytical Method to Calculate Misalignment in the Journal Bearing of a Planetary Gear," *Wear Journal*, Vol. 61, pp. 143–156.

Gates, F., and Smailys, A., 1989, "Prediction of 1-P Aerodynamic Loads on Tractor Aircraft Engine Installations," presented at the AIAA/ASME/SAE/ASEE 25th Joint Propulsion Conference, July.

Gautron, C. S., and Saad, N. R., 1990, "High Strength Nickel-Base Superalloy Evaluation for Turbine Discs," *CASI Proceedings*, Oct.

Habashi, W. G., Peeters, M. P., Robichaud, M. P., Nguyen, V.-N., and Bhat, M. V., 1992, "Finite Element Solution of Viscous Compressible Flows in Gas Turbine Ducts and Diffusers," AGARD Proceedings 510, CRD Techniques for Propulsion Applications, Feb.

Kenny, D. P., 1973, "A Comparison of the Predicted and Measured Performance of High Pressure Ratio Centrifugal Compressor Diffuser," ASME Paper No. 72-GT-54.

Moustapha, S. H., Okapuu, U., and Williamson, R. G., 1987, "Influence of

Rotor Blade Aerodynamic Loading on the Performance of a Highly Loaded Turbine Stage," ASME *Journal of Turbomachinery*, Vol. 109, No. 2, pp. 155–162.

Moustapha, S. H., 1990, "Turbine Aerodynamics Research at Pratt and Whitney Canada," 8th Canadian Symposium on Advanced Technology in General Aviation Aircraft, Montreal, May.

Nguyen, M. H., and Saad, N. R., 1989, "Heat Transfer Measurements for Rotating Turbine Discs," ASME Paper No. 89-GT-236.

Okapuu, U., 1974, "Some Results From Tests on a High Work Axial Gas Generator Turbine," ASME Paper No. 74-GT-81.

Rodriguez, E. S., III, Duong, L., and Arvanitis, S., 1990, "Planet Gear Sleeve Spinning Analysis," Paper No. AIAA-90-2154.

Shohet, K. N., and Tadros, R. N., 1989, "The Survivability of Centrifugal Compressors in Modern Aircraft Engines," *Proceedings of the 15th Symposium of the International Committee on Aeronautical Fatigue*, 21–29 June, Jerusalem, Israel; ICAF, Aeronautical Fatigue in the Electronic Era.

Smailys, A., and Brownridge, C., 1987, "Designing for Fretting Fatigue Free Joints in Turboprop Engine Gearboxes," Paper No. AIAA-87-2046.

Sundararajan, S., and Amin, S., 1991, "Finite Element Analysis of Ring Gear/Casing Spline Contact," *AIAA Journal of Propulsion and Power*, Vol. 7, pp. 602–606.

Yoshinaka, T., 1977, "Surge Responsibility and Range Characteristics of Centrifugal Compressors," ASME/GTSJ/JSME Paper No. 46.

Yoshinaka, T., and LeBlanc, A. D., 1980, "Test Results From an Analytically Designed Axial Compressor Stage of 1.65:1 Pressure Ratio," SAE Technical Paper No. 800629.

Materials Performance in Advanced Combustion Systems

K. Natesan
Materials and Components Technology Division,
Argonne National Laboratory,
Argonne, IL 60439

A number of advanced technologies are being developed to convert coal into clean fuels for use as feedstock in chemical plants and for power generation. From the standpoint of component materials, the environments created by coal conversion and combustion in these technologies and their interactions with materials are of interest. The trend in the new or advanced systems is to improve thermal efficiency and reduce the environmental impact of the process effluents. This paper discusses several systems that are under development and identifies requirements for materials application in those systems. Available data on the performance of materials in several of the environments are used to examine the performance envelopes for materials for several of the systems and to identify needs for additional work in different areas.

Background

The production of clean liquid and gaseous fuels from coal offers a means of reducing U.S. dependence on imported oil while using our vast coal reserves in an environmentally acceptable fashion. A significant reserve of high-sulfur coal is available for energy use, provided it can be cleaned before or during conversion to meet federal emission standards for effluents. Coal is a complex and relatively dirty fuel that contains varying amounts of sulfur and a substantial fraction of noncombustible ash constituents. Over the last 20 years, significant progress has been made toward the conversion of coal into synthetic fuels and toward the generation of electric power through coal combustion.

An examination of the use of fossil fuels in U.S. electric power generation (see Fig. 1) shows that coal use in this sector grew dramatically from 1978 to 1986, after which it stabilized at about 80 percent (DOE, 1990). Consumption of natural gas and crude oil in the power sector declined during the same period, to about 14 and 6 percent, respectively. Further gains for coal in this sector are considered unlikely in view of the more stringent environmental regulations for power plants and the logistics of those plants that must use gas or oil as fuel. Even though the relative percentage of coal consumption may not change significantly, the tonnage use of coal is expected to increase as demand for electricity increases.

In recent years, extensive discussions have been held in public forums and policy meetings on global warming, CO_2 generation, acid rain, more stringent New Source Performance Standards, and environmental compliance, as well as on the role of fossil-fired power plant effluents in all of the above. It is evident that electric utilities are concerned with these deliberations and their effects on utility use of different coal feedstocks. Especially vulnerable are utilities that use eastern high-sulfur coal. Because of current and future legislation and anticipated stricter emission standards, it is obvious that systems with higher thermal efficiency and lower impact on the environment be the norm of the future.

The advanced systems of interest are:

(*a*) Pulverized-coal-fired boilers with advanced steam cycles (PC)
(*b*) Integrated gasification combined cycle (IGCC)
(*c*) Fluidized-bed-combustion cogeneration (FBC)
(*d*) Magnetohydrodynamic topping cycles (MHD)
(*e*) High-performance power system (HIPPS)
(*f*) Low-emission boiler system (LEBS)

Pulverized-Coal-Fired Boilers

Over the past few years, extensive studies have been conducted to develop PC boilers with advanced steam-cycle conditions to improve the thermal efficiency of these systems (Culler, 1985). The staged development of these systems has

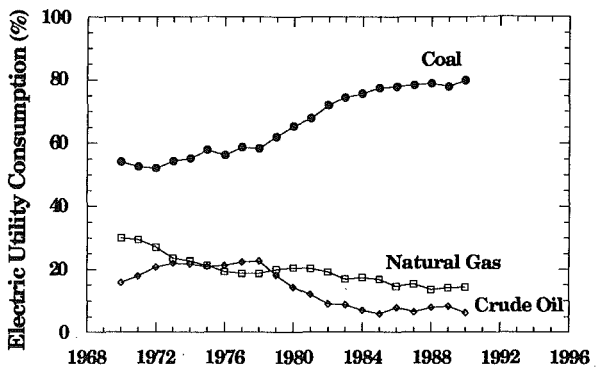

Fig. 1 Fossil fuel consumption in electric power production, 1970–1990

Contributed by the International Gas Turbine Institute and presented at the 38th International Gas Turbine and Aeroengine Congress and Exposition, Cincinnati, Ohio, May 24–27, 1993. Manuscript received at ASME Headquarters March 3, 1993. Paper No. 93-GT-201. Associate Technical Editor: H. Lukas.

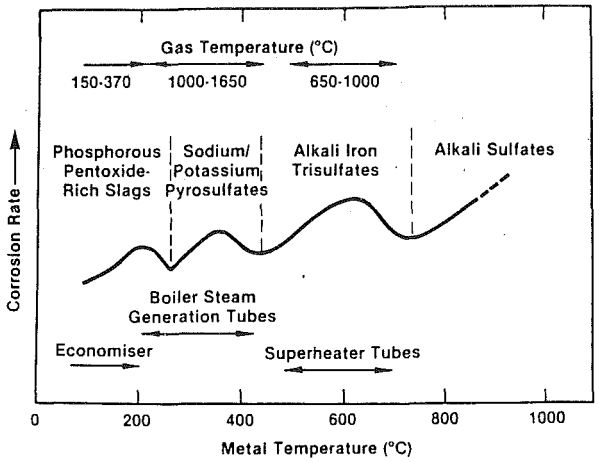

Fig. 2 Regimes of fireside corrosion in coal-fired boilers

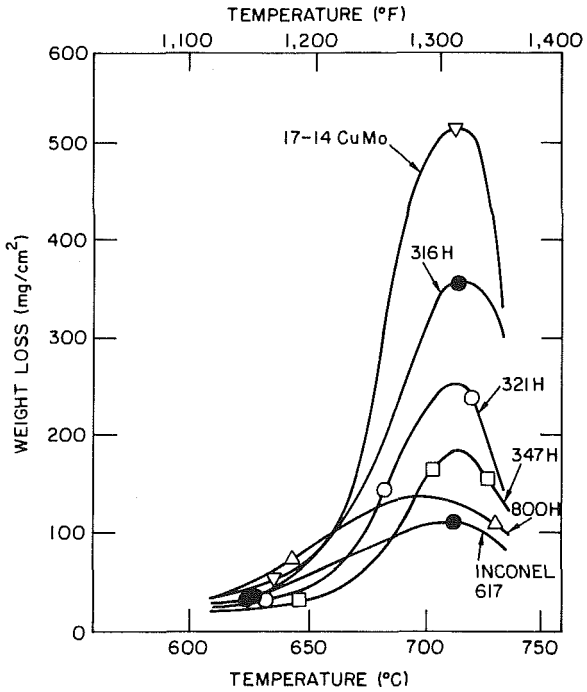

Fig. 3 Corrosion test data for several alloys exposed to coal-fired boiler environments

the ultimate goal of achieving steam pressure and temperature of 34.5 MPa (5000 psig) and 650°C (1200°F), respectively, from the current values of 540°C (1000°F) and 16.5–24 MPa (2400–3500 psig). Fireside metal wastage in coal-fired boilers can occur via gas-phase oxidation or deposit-induced liquid-phase corrosion. The former can be minimized by using materials that are oxidation resistant at service temperatures of interest. On the other hand, deposit-induced corrosion of materials is an accelerated type of attack influenced by the vaporization and condensation of small amounts of impurities such as sodium, potassium, sulfur, chlorine, and vanadium, or their compounds, which are present in the coal feedstock. The effect of boiler deposits on the corrosion of structural materials has been fairly well established by Reid (1971) and Wright et al. (1978), and the temperature regimes in which this corrosion occurs are summarized in Fig. 2.

A number of factors, including sulfur, alkali, chlorine in coal feedstock, excess air level used in the combustion process, and metal temperature, determine the extent of corrosion of superheater materials in coal-fired boilers. Typical corrosion

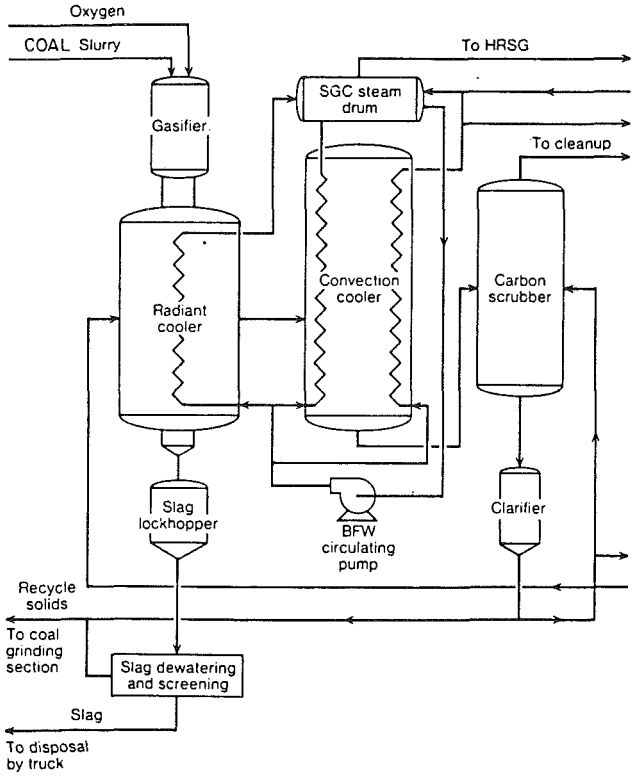

Fig. 4 A schematic diagram of the slagging gasifier and syngas cooler

data, developed by Kihara et al. (1983), for several candidate alloys are shown in Fig. 3. It is evident that at steam temperatures of 540–565°C (1000–1050°F), the metal temperature will be in the range of 600–630°C (1112–1165°F) and the corrosion rates will be acceptable for long-term service. In advanced steam cycles with anticipated steam temperatures and pressures of 650°C (1200°F) and 34.5 MPa, metal temperature can attain 700°C or higher, resulting in increased corrosion rates. It is obvious that new materials or corrosion protection of existing materials are needed for reliable service of superheaters in advanced steam-cycle plants.

Several materials have been evaluated by Gold and Jaffee (1984) for advanced steam turbine applications from the standpoint of rotor size, rotor material strength, embrittlement characteristics, thermal cracking, bolting and transition joints. It has been concluded that available materials (developed over the last 10 years with "clean steel" technology) will be adequate for turbine applications in advanced steam-cycle systems.

Gasification Combined Cycle

The coal gasification technologies emphasize production of intermediate-energy syngas by using oxygen and steam to gasify the coal. Both dryash and slagging gasifiers are being developed. Slagging gasifiers, into which finely ground coal is injected through a burner, have the advantages of rapid gasification rate and lower consumption rate of steam and water. Further, the process lends itself to lower emission of toxic materials because all potentially harmful organics are destroyed at the elevated temperature of the process. Figure 4 shows a schematic diagram of an entrained slagging gasifier with syngas coolers. From the materials standpoint, the components of interest in these systems are:

(*a*) Syngas coolers
(*b*) Refractory lined vessels
(*c*) Hot gas cleanup system
(*d*) Gas turbines

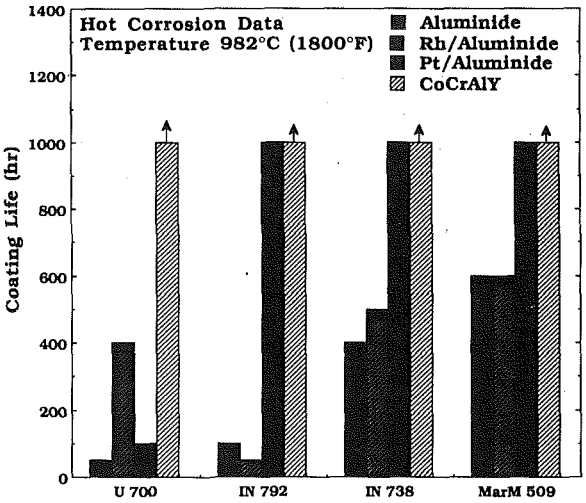

Fig. 5 Life for several coatings in hot-corrosion environments

Syngas coolers are generally used to recover the sensible heat from the raw gas; these components are very large (especially compared to the gasifier) and are fabricated with metallic materials. Syngas coolers are rare generally used as evaporators but generation of superheated steam is also a possibility. The metal temperature of the syngas system is at 300–500°C and the metal will be exposed to a highly reducing atmosphere in the presence of hydrogen sulfide, the concentration of which will be determined by the sulfur content of the coal feedstock. In addition, the environment will contain hydrogen chloride. The gas temperature in the cooler will be 1100–1300°C (2000–2350°F) and the cooler will experience on/off service, resulting in corrosion contribution during downtime. Sulfidation is the major mode of material degradation and is accompanied by pitting/crevice corrosion of materials that are susceptible to aqueous corrosion during downtime. Extensive test programs have been conducted to evaluate the corrosion performance of several materials in simulated syngas environments and in syngas coolers of large gasifier systems. These materials include low-alloy steels, aluminized and chromized steels, and several types of austenitic stainless steels. Corrosion rates have been established, but there is concern about extrapolating the relatively short time data to long-term predictions on life of the component, because the materials are susceptible to breakaway or accelerated corrosion when exposed to mixed-gas environments (Natesan, 1987; Perkins and Bakker, 1987).

Corrosion and wear performance of refractory materials largely determine the overall availability of plants in coal gasification schemes. Chemical compatibility of refractories with coal slags has been the subject of intense study for the past 10 years or so. It has been shown that refractories containing mainly chromia–alumina solid solutions formed thick scales of an $(Mg,Fe)(Cr,Al)_2O_4$ spinel that seemed to be the most stable phase in contact with coal slags (Kennedy, 1981). Correlations of refractory wear data with operating conditions have shown wear rates of <0.01 mm/h during periods of steady-state operation. Even though a two-year life for the refractory lining is currently possible and the gasifier can be relined on an established maintenance schedule, development of long-life refractory bricks with adequate corrosion resistance in molten coal-slag environments while maintaining adequate mechanical integrity, e.g., resistance to creep and thermal shock, is still needed.

The hot gas clean-up system involves passing the raw gas from the gasifier into a porous ceramic filter, which lets the gases pass through while the particulates are trapped in the filter. The filters are periodically pulsed with a gas flow in the reverse direction to clean the filters of particulate material.

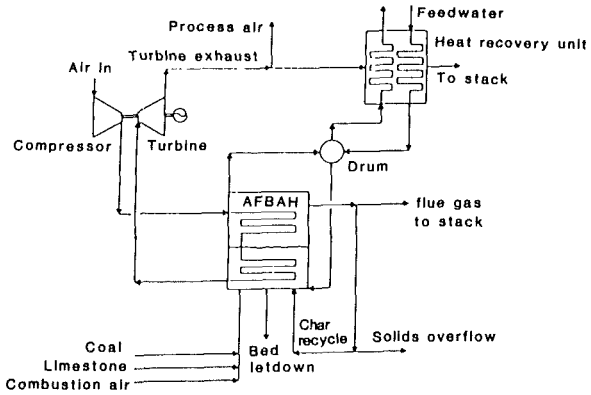

Bubbling Fluidized Bed System

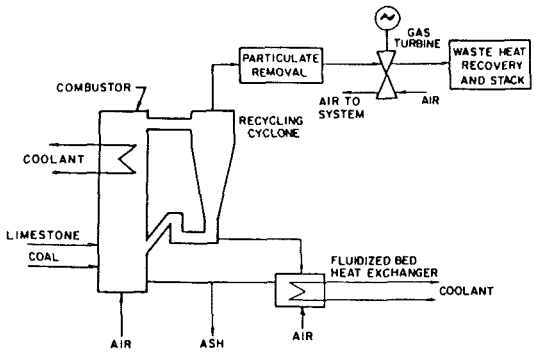

Circulating Fluidized Bed System

Fig. 6 Schematic diagrams of bubbling- and circulating-fluid bed systems

The filter designs considered include fabrics made from ceramic fibers, candles made of ceramic fibers or powders, and monolithic crossflow type. The materials considered are cordierite, silicon carbide, quartz, zirconia, alumina, and mullite, and a combination of them.

Corrosion of gas turbine materials in the presence of liquid sodium sulfate, either by itself or in combination with sodium chloride, has been a problem in gas turbines; this corrosion process has been termed "hot corrosion" to differentiate it from gas-phase sulfidation attack. In addition, the gas velocity in the turbine can range from 200–500 m/s, which causes erosion degradation of blade material. The combination of hot corrosion/erosion is of serious concern in obtaining adequate life for land-based turbines, especially those that utilize coal-derived products. Discussions on corrosion evaluation of gas turbine materials and coatings is beyond the scope of this paper. Comparative data for corrosion of simple aluminides, aluminides with rhodium and platinum bond coats, and CoCrAlY overly coating after exposure to a hot corrosion environment at 982°C (1800°F) are shown in Fig. 5 (Kemp, 1980). The results show that the performance of a given coating is strongly influenced by the substrate alloy and a bond coat of precious metal platinum (rather than rhodium) is beneficial in reducing corrosion in nickel-base superalloys. The overlay CoCrAlY coating on a cobalt-base MarM-509 alloy exhibited the best performance among all the coatings examined in this study.

Fluidized-Bed Cogeneration

This approach employs the technology of coal-fired cogeneration in the form of a combined-cycle atmospheric or moderately pressurized fluidized bed in which an air heater

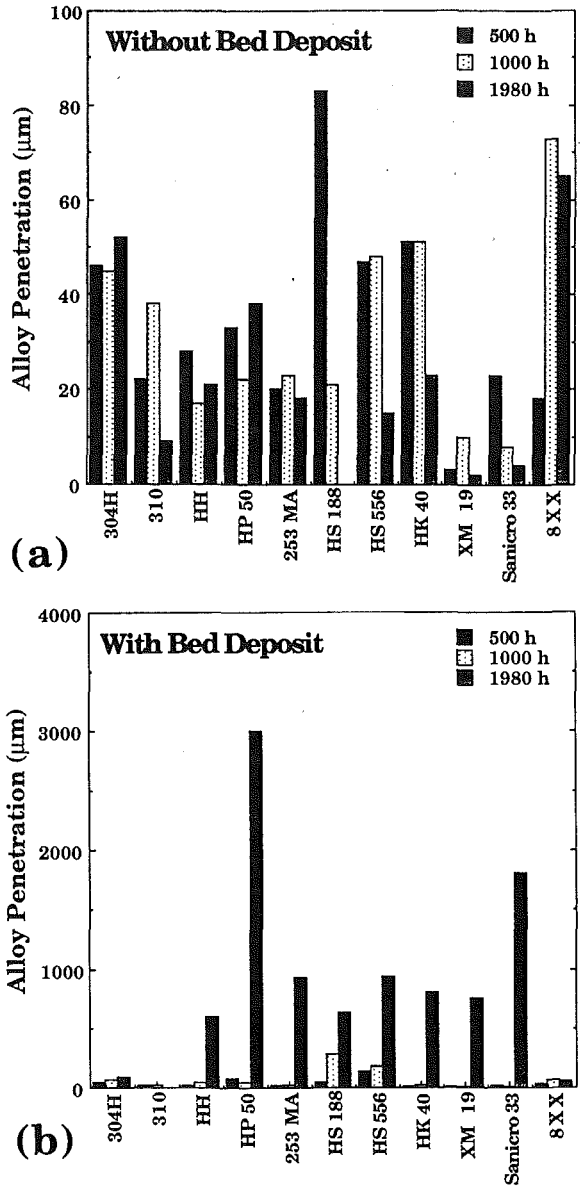

Fig. 7 Corrosion penetration in alloys exposed in (*a*) absence and (*b*) presence of sulfated sorbent deposits in FBC environments

heats the air in a gas turbine cycle for the cogeneration of electricity and useful thermal energy. Figure 6 shows schematic diagrams of typical bubbling- and circulating fluid-bed systems. The key components of relevance in these systems are

(*a*) In-bed air-tube heat exchanger
(*b*) Steam-tube heat exchanger
(*c*) Gas turbines

The fluidized-bed combustion of coal produces gas that principally contains O_2, CO_2, H_2O, SO_2, and N_2, together with minor amounts of SO_3, nitrogen oxides, chlorides, and other volatilized salts. The gas composition depends importantly on the air/coal stoichiometric ratio. In addition, SO_2 concentration in the gas phase will be determined by the type and amount of sulfur sorbent and the sulfur content of the coal used in the combustion process. However, the local chemistry beneath the deposit could be quite reducing relative to the bulk gas composition. This can have important implications for the initiation/propagation of sulfidation penetration of alloys and can lead to substantial reduction in component life.

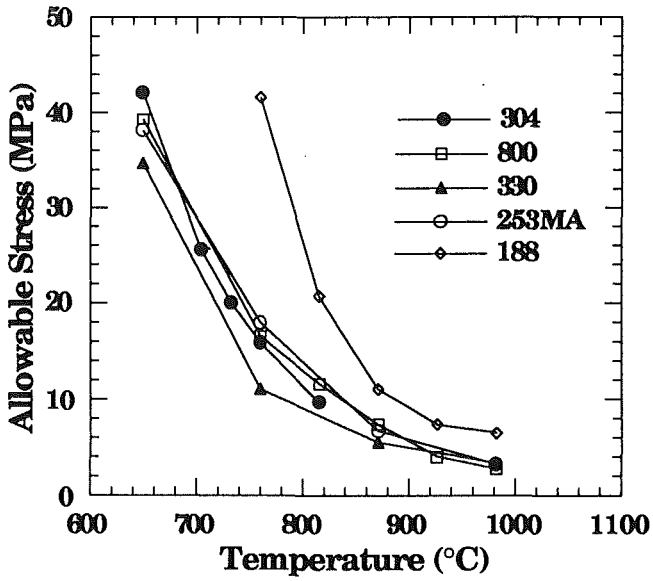

Fig. 8 Estimated allowable stress values as a function of temperature for several candidate alloys

Materials/environment interactions in FBC systems indicate that structural alloys develop predominantly oxide scales when exposed to O_2–SO_2 gas mixtures of combustion atmospheres at elevated temperatures (Natesan, 1990). Natesan et al. (1987) made a detailed evaluation of materials information developed from exposures of cooled and uncooled corrosion/erosion probes in 13 FBC facilities. In addition, materials tests were conducted for 3000 h in simulated combustion atmospheres at Argonne National Laboratory and for 2000 h in the DOE atmospheric fluidized-bed combustion facility in California (Natesan and Podolski, 1988; Natesan et al., 1991). Corrosion information developed from these studies has been used to assess performance of several candidate materials as a function of specimen orientation, exposure location in the combustor, and time of exposure. Some of the conclusions drawn from these studies are discussed in the following paragraphs.

For air-tube heat exchanger applications at temperatures near that of the bed, corrosion is the dominant degrading mechanism for the materials; erosion is generally not of concern. Under these conditions, performance of austenitic stainless steels, e.g., Types 304, 310, and 330, and alloys such as HR 3C, FW 4C, and 8XX is adequate and these materials have exhibited low depths of penetration after exposure in (*a*) an AFBC facility, (*b*) a laboratory test under gas cycling conditions, and (*c*) a more severe laboratory test under low oxygen partial pressure (pO_2).

Alloys such as HS 188, HS 556, HK 40, and 800H exhibited catastrophic corrosion in the presence of deposit material and sustained low-pO_2, based on a 3000 h laboratory test. Although these test conditions are more severe than those the materials will be subjected to in a typically well-run FBC system, the data nevertheless suggest the susceptibility of these materials to accelerated corrosion. Alloys such as HH, HP 50, 253 MA, XM 19, Sanicro 33, HS 556, and HS 188 exhibited unacceptable corrosion behavior when the alloys were in contact with bed material. Figure 7 shows a comparison of corrosion penetration in alloys exposed to FBC environments with and without sulfated sorbent deposits.

Another aspect to materials selection for the air heater tubes in cogeneration systems is the mechanical properties of the materials at elevated temperatures. At the high temperatures of interest, time-dependent properties such as creep rate and creep rupture life will determine the adequacy of the material. Although the ASME code does not specify information for

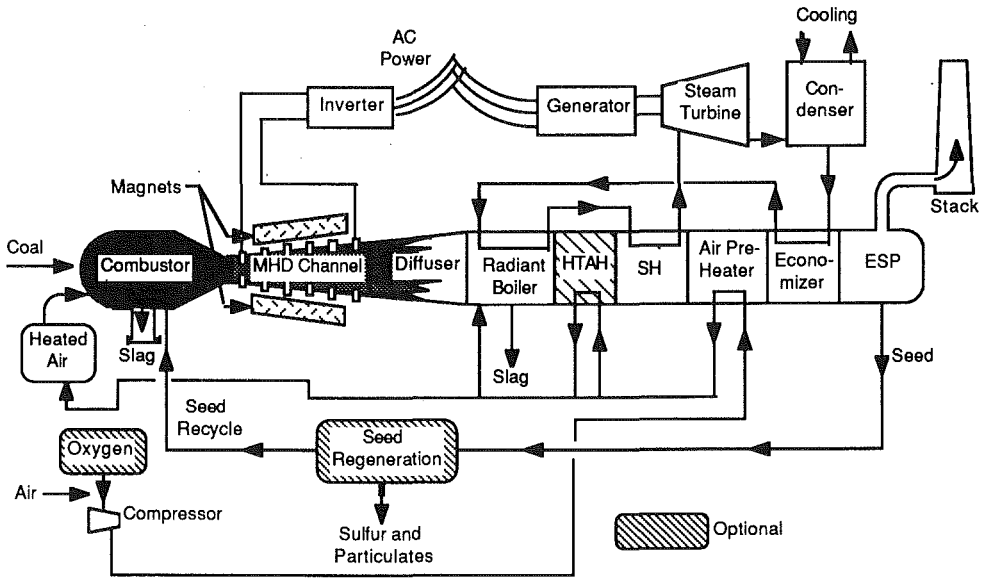

Fig. 9 A schematic diagram of a coal-fired MHD system

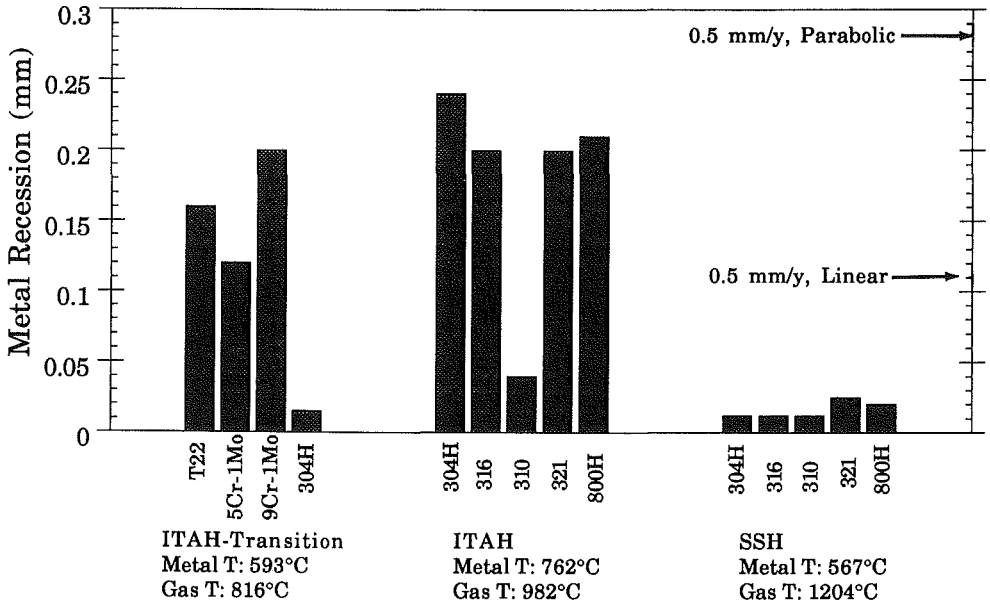

Fig. 10 Metal recession data for several alloys coated with MHD deposit and exposed to different conditions for up to 2000 h

temperatures beyond 816°C, the criteria on maximum allowable stress can probably be extrapolated to higher temperatures. These criteria specify that the maximum allowable stress for the material shall not exceed the lowest of the following: 100 percent of the average stress for a creep rate of 0.01 percent in 1000 h, 67 percent of the average stress for rupture at the end of 100,000 h, or 80 percent of the minimum stress for rupture at the end of 100,000 h. A compilation has been made of the available data on the creep properties of candidate alloys to examine the effect of metal temperature on the creep strengths and creep rates (Natesan, 1992). Based on the criteria of 67 percent of the average stress for rupture at the end of 100,000 h, allowable stress values were computed (many of the alloys are not coded under ASME rules, but it is assumed that the criteria used for the coded materials will be applicable to noncoded alloys). The computed values are shown in Fig. 8. The allowable stress values are ≈6.9 MPa (1000 psi) at 871°C (1600°F), based on air test data without allowance for fireside corrosion effects.

For steam-tube heat exchanger applications at temperatures in the range of 500–650°C, both corrosion and erosion processes need to be considered in the assessment of materials performance. Further, tube bank geometry, tube band distance from the air distributor, coal and limestone feedstock chemistries, and bed operating conditions all influence material performance. A number of materials have performed well as evidenced by the data developed over the years by exposure of corrosion/erosion probes in TVA-20MW and TVA-160MW atmospheric FBC facilities.

The gas turbine materials in cogeneration systems that use air as the working fluid will be exposed predominantly to heated air, with supplemental heat from the burning of clean fuel such as natural gas. In the FBC effluent, corrosion of materials has been observed over a much wider temperature range (600–950°C) in contrast with that (800–950°C) in conventional gas turbines. Corrosion test data obtained in the effluent of a pressurized FBC system showed that both nickel- and cobalt-base alloys were equally susceptible to accelerated

corrosion. This susceptibility to accelerated corrosion at lower temperatures was attributed to the presence of potassium in the FBC effluent (Haskell et al., 1987). Information on the performance of coating/substrate combinations under low-temperature hot-corrosion conditions is particularly lacking at present.

Magnetohydrodynamic Topping Cycle

Magnetohydrodynamic (MHD) generation of power is based on the direct conversion of fuel energy into electrical energy by flowing a heated, electrically conducting fluid through a magnetic field. In a coal-fired open-cycle MHD system, the working fluid is utilized on a once-through basis and consists of multiphase fossil fuel combustion products. Figure 9 shows a schematic of the open-cycle MHD system. The overall plant consists of a topping cycle, where the electrical energy is directly produced by the MHD generator, and a steam-bottoming plant, where additional heat energy and the seed material are recovered. Key components of interest in this system are

(*a*) Slagging combustor
(*b*) Channel electrodes and insulators
(*c*) Radiant boiler
(*d*) Downstream superheaters and evaporators

The MHD combustor system consists of an oil-fired heater, a precombustor, slagging first stage, and a second stage. The oil-fired unit produces an oxidant at ≈650°C (1200°F) for use by the precombustor. The precombustor further heats the oxidant to about ≈1600°C (2900°F), using a fraction of the total coal flow to the combustor. Within the first stage, the remainder of the coal is burned under fuel-rich conditions, and potassium compounds are injected near the exit of the first stage to increase the electrical conductivity of the gas. Oxygen is injected into the second stage to complete the combustion process. A test program was conducted at Argonne to evaluate candidate materials in slag-side and water-side environments that simulate those anticipated in a prototype MHD combustor (Natesan et al., 1989). Based on corrosion information from this study and code-allowable stress values for different materials, maximum permissible operating temperatures were estimated for candidate materials at various locations in an MHD combustor. The results are shown in Table 1.

The life of an MHD channel is determined chiefly by the design and material selection of the internal wall elements—electrodes, sidebars, and insulators—which are collectively called the gas-side design. Adequate performance of materials selected for the MHD channel construction is mandatory for successful application of this technology in retrofit and commercial coal-fired energy systems. In the high-temperature environment of the MHD channel, vaporization of several coal/seed components and subsequent deposition of these materials on the walls of the channel can occur. This hostile environment generally contains potassium compounds, sulfur compounds, and ash/slag constituents. In the proof-of-concept design, the channel is made of oxygen-free high-conductivity copper (OFHC); the caps are W, Pt, and stainless steel at different locations, and BN is used as the insulating material.

The major functions of the radiant boiler are to produce steam, remove the slag from the high-temperature combustion gases leaving the combustor, and cool the gases in a controlled manner to minimize NO_x concentration in the gas phase. At present, combustion in the primary combustor is optimized to achieve the maximum power from the MHD channel, which implies an air/coal stoichiometric ratio of 0.50–0.60. These reducing conditions also result in low nitric oxide concentration. When the combustion ratios are substoichiometric, the gases entering the radiant boiler will be predominantly reducing (having a low pO_2), and the sulfur levels in the gas can be high because of the use medium- to high-sulfur coal. Studies conducted at Argonne have shown that carbon steel and low-alloy steels will perform adequately up to 400°C and that these materials, if protected with a stainless steel cladding or a ramming refractory coating, will be suitable for application in radiant boilers up to 550°C.

Table 1 Maximum permissible operating temperatures (°C) for several candidate alloys for application in an MHD slagging combustor

Component	Low-alloy steel	Low-carbon stainless steel	Glidcop	OFHC
Pre-combustor	355[a]	465[b]	315[d]	–
Slagging stage	345[c]	370[c]	315[e]	–
Second stage	–	–	315[e]	205

[a]Oxidation limit based on data from Natesan, (1986).
[b]ASME code allowable stress limit.
[c]Sulfur corrosion limit.
[d]Waterside corrosion at 12 m/s; 230°C and fouling on fireside may lower this value.
[e]Waterside corrosion at 7 m/s; 230°C and fouling on fireside may lower this value.

The gases that enter the secondary superheater (SSH), reheater, intermediate temperature air heater (ITAH), and economizers will have pO_2 values that correspond to an air/coal stoichiometric ratio of 0.95–1.05, the actual value dictated by the nitric oxide concentration in the exit gas. Extensive testing of materials, conducted by Natesan and Swift (1989) at Argonne, showed that austenitic alloys will be adequate for SSH application at a metal temperature of 593°C. However, the same alloys under ITAH conditions (at 762°C) exhibit substantial corrosion. Figure 10 is a plot of metal recession data developed for several alloys under the ITAH, SSH, and ITAH transition conditions. Also indicated in the figure are the corrosion limits of 0.5 mm/yr calculated by either linear or parabolic kinetics for the corrosion process. When linear kinetics are used, the low- to medium-chromium steels under ITAH transition conditions and most of the austenitic alloys (except 310 steel) under ITAH conditions exhibit corrosion rates much higher than the limit. On the other hand, when parabolic kinetics were used, all the austenitic alloys exhibited metal recession rates of <0.5 mm/yr under ITAH conditions; however, once the scale cracks/spalls or erodes away in the exposure environment, the chromium-depleted zone underneath the original scale will result in fast-growing iron oxide, and accelerated/breakaway corrosion would occur.

High-Performance Power System

The high-performance power system has the ultimate goal of producing electricity from coal with an overall thermal efficiency of 47 percent or higher (compared with ≈35 percent for current systems) and to reduce CO_2 emissions by 25–30 percent (Ruth, 1991). The pulverized-coal high-temperature advanced furnace (HITAF) in the HIPPS concept will heat air to an intermediate temperature of ≈980°C (1800°F), and will burn supplemental clean fuel to boost the temperature of air to the turbine inlet to 1260°C (2300°F) or higher. Use of

supplemental fuel can be reduced as HITAF technology evolves to permit air to be heated to higher temperatures in the furnace.

HITAF represents a major departure from conventional pulverized-coal-fired boilers in which steam is raised to a maximum of 538–600°C (1000–1110°F). Important differences are seen in the chemical/physical characteristics of the ash deposit layers, which are likely to be dominated by alkali sulfates rather than pyrosulfates or alkali-iron-trisulfates; and in the increased mobility of corrosion-accelerating agents in the deposit layers due to the much higher temperature of the heat transfer surfaces. A major challenge is to develop methods to combat severe deposition, erosion, and corrosion (DEC) of heat transfer surfaces exposed to higher than normal temperatures. These methods could include fuel selection; cleaning of aggressive contaminants from coal; fine grinding of coal; use of sorbents/additives; mitigation of deposit accumulation; and selection of advanced corrosion-resistant alloys, coatings, and ceramic materials for vulnerable heat transfer sections. A substantial body of information on a wide range of materials (many of them new and some yet to be developed) will be required in order to achieve adequate performance of components and enhanced reliability.

Low-Emission Boiler System

This system would utilize staged combustion to develop a power plant that will drastically reduce SO_2, NO_x, and particulate emissions from current levels. Even though LEBS is an extension of current boiler technology, the first stage of combustion will have fuel-rich or air-lean conditions with a resultant gas chemistry that will be reducing for the internal structural components, and the deposit characteristics will be sulfides of different elements rather than the sulfates/oxides that are prevalent in conventional coal-fired boilers. In this case, a better evaluation of currently used structural alloys in the LEBS environment will be needed to establish performance envelopes/limitations for the materials.

Acknowledgments

This work was supported by the U.S. Department of Energy, Office of Fossil Energy, Advanced Research and Technology Development Materials Program, under Contract No. W-31-109-Eng-38.

References

Culler, F. L., 1985, "Advanced Fossil Fuel Based Power Plants," *Proc. Materials for Future Energy Systems Conf.*, American Society for Metals, Metals Park, OH, pp. 101–111.

DOE, Annual Energy Review 1990, DOE/EIA-0834, Energy Information Administration, U.S. Department of Energy.

Gold, M., and Jaffee, R. I., 1984, "Materials for Advanced Steam Cycles," *Proc., Materials for Future Energy Systems*, American Society for Metals, Metals Park, OH, pp. 113–122.

Haskell, R. W., Doering, von E., Le Blanc, O. H., and Luthra, K. L., 1987, "A Mechanistic Study of Low-Temperature Corrosion on Materials in the Coal Combustion Environment," Final Report ORNL/Sub/84-00224/01.

Kemp, F. S., 1980, "Parameter Monitoring for Corrosion Control of Utility Gas Turbines," Electric Power Research Institute Report EPRI AP-1369.

Kennedy, C. R., 1981, "Compatibility of Water-Cooled Refractories With a Basic Coal Ash Slag at 1500°C," *J. Mat. Energy Sys.*, Vol. 2, pp. 11–20.

Kihara, S., Isozaki, T., and Ohtomo, A., 1983, "Laboratory Evaluation for Fireside Corrosion of Superheater Tube in Coal-Fired Boiler," *Proc. JIMIS-3 High Temperature Corrosion*, Tokyo, Japan, p. 655.

Natesan, K., 1986, "Role of FBC Deposits in the Corrosion of Heat Exchanger Materials," *High Temperature Technology*, Vol. 4(4), p. 193.

Natesan, K., 1987, "Alloy Performance in Coal Gasification Environments," *Proc. Materials for Coal Gasification*, American Society for Materials, Metals Park, OH, pp. 51–60.

Natesan, K., Miller, S. A., and Podolski, W. F., 1987, "An Assessment of the Performance of Heat Exchanger Materials in Fluidized-Bed Combustors," Argonne National Laboratory Report ANL-86-42.

Natesan, K., and Podolski, W. F., 1988, "Laboratory Tests in Support of Atmospheric Fluidized-Bed Cogeneration Air Heater Experiment: Summary Report," Argonne National Laboratory Report ANL-88-36.

Natesan, K., and Swift, W. M., 1989, "Corrosion Behavior of Materials for MHD Steam Bottoming Plant," *Proc. 27th Symp. on Engineering Aspects of Magnetohydrodynamics*, Reno, NV, pp. 3.2-1 to 3.2-10.

Natesan, K., Wang, D. Y., and Soppet, W. K., 1989, "Materials Tests in Support of an MHD Coal Combustor," Argonne National Laboratory Report ANL/MHD-89/2.

Natesan, K., 1990, "Laboratory Studies on Corrosion of Materials for Fluidized Bed Combustion Applications," Argonne National Laboratory Report ANL/FE-90/1.

Natesan, K., Podolski, W. F., Wang, D. Y., Teats, F., Gerritsen, W., Stewart, A., and Robinson, K., 1991, "The Atmospheric Fluidized-Bed Cogeneration Air Heater Experiment Materials Performance: Summary Report," Argonne National Laboratory Report ANL-91/4.

Natesan, K., 1992, "Materials Performance in Fluidized-Bed Air Heaters," Paper No. 125, CORROSION 92, National Assn. for Corrosion Engineers, Houston, TX.

Perkins, R. A., and Bakker, W. T., 1987, "Laboratory Corrosion Studies in Simulated Syngas Cooler Environments," *Proc. Materials for Coal Gasification*, American Society for Materials, Metals Park, OH, pp. 85–96.

Reid, W. T., 1971, *External Corrosion and Deposits in Boilers and Gas Turbines*, American Elsevier, New York, p. 150.

Ruth, L. A., 1991, "Combustion 2000," PETC Review, Issue 4, Office of Fossil Energy, U.S. Department of Energy.

Wright, I. G., Price, C. W., and Herchenroeder, R. B., 1978, "State of the Art and Science Report on Design of Alloys Resistant to High Temperature Corrosion-Erosion in Coal Conversion Environments," Electric Power Research Institute Report EPRI-FP-557.

Advanced Hot Gas Cleaning System for Coal Gasification Processes

R. A. Newby
Westinghouse Science and Technology Center, Pittsburgh, PA 15235

R. L. Bannister
Westinghouse Electric Corporation, Orlando, FL 32826

The United States electric industry is entering a period where growth and the aging of existing plants will mandate a decision on whether to repower, add capacity, or do both. The power generation cycle of choice, today, is the combined cycle that utilizes the Brayton and Rankine cycles. The combustion turbine in a combined cycle can be used in a repowering mode or in a greenfield plant installation. Today's fuel of choice for new combined cycle power generation is natural gas. However, due to a 300-year supply of coal within the United States, the fuel of the future will include coal. Westinghouse has supported the development of coal-fueled gas turbine technology over the past thirty years. Working with the U.S. Department of Energy and other organizations, Westinghouse is actively pursuing the development and commercialization of several coal-fueled processes. To protect the combustion turbine and environment from emissions generated during coal conversion (gasification/combustion) a gas cleanup system must be used. This paper reports on the status of fuel gas cleaning technology and describes the Westinghouse approach to developing an advanced hot gas cleaning system that contains component systems that remove particulate, sulfur, and alkali vapors. The basic process uses ceramic barrier filters for multiple cleaning functions.

Introduction

Coal-fueled combustion turbine system concepts are in various stages of development (Scalzo et al., 1992). Westinghouse's first commitment in gasification processes on a commercial level was first demonstrated in 1987 when two 501D5 units were converted to burn a synthetic coal gas (Hendry and Pillsbury, 1987). These two 104 MW units, shown in Fig. 1 with other plant components, are operating in an oxygen-blown integrated gasification combined cycle (IGCC) that includes a cold gas cleanup system. To date the Westinghouse combustion turbines have operated with average availabilities in excess of 95 percent (Geoffroy and Amos, 1991).

At the Dow Chemical installation a 50–50 water slurry of subbituminous coal is introduced into a pressurized gasifier along with oxygen. Ash is removed as molten slag, which is water-quenched, ground, and ejected through a pressure letdown valve. Altogether, the gasification process and the combustion turbine exhausts can produce up to 2500 tons per day of steam for use in various plant processes and in a steam turbine drive.

Other concepts being developed at Westinghouse include incorporating combustion turbines in a coal-fueled combined cycle for Advanced Pressurized Fluidized Bed (APFB) and Direct Coal-Fired (DCF) technologies. These concepts, discussed in recent references (Garland and Pillsbury, 1992; Bannister et al., 1992), require a hot gas cleanup system to protect the turbine and reduce environmental emissions.

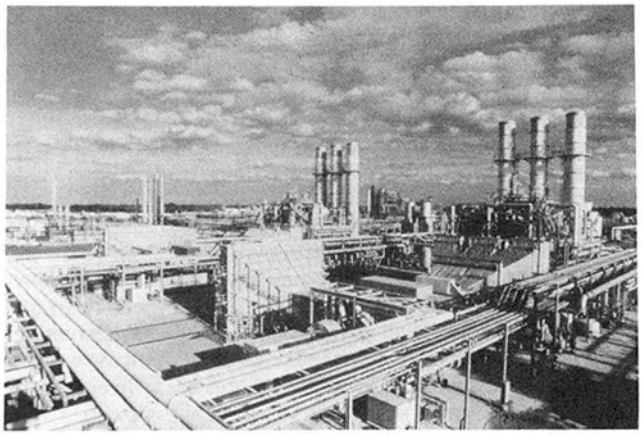

Fig. 1 IGCC with Westinghouse Gas Turbines at Dow Chemical Plant in Plaquemine, LA

The objectives of clean coal technologies are to provide high-efficiency, high-reliability, cost-competitive, and environmentally superior power generation compared to conventional coal-fueled power generation technology. There are two major aspects of such plants that may limit their success. First, in advanced power generating plants, the combustion turbine may be subjected to contaminant levels exceeding current expansion gas contaminant specifications. As a result, the combustion

Contributed by the International Gas Turbine Institute and presented at the 38th International Gas Turbine and Aeroengine Congress and Exposition, Cincinnati, Ohio, May 24–27, 1993. Manuscript received at ASME Headquarters March 17, 1993. Paper No. 93-GT-338. Associate Technical Editor: H. Lukas.

turbine may have corrosion and deposition problems that would increase maintenance and degrade performance. Secondly, the fuel sources and the high-temperature nature of the plant may result in excessive emissions of regulated pollutants such as SO_2 and particulates.

There are two approaches that can be applied, either independently or in concert, to ensure high-efficiency, high-reliability turbine performance. Utilizing integrated equipment for hot gas cleaning to provide turbine protection is one approach. Hot gas cleaning functions include particulate removal as well as alkali removal, and both can be integrated into a single system. The system can also incorporate emissions control functions, such as sulfur control, unrelated to turbine protection.

Increasing the tolerance of the combustion turbine to the primary contaminants that cause erosion, deposition, and corrosion is a second approach. The subject of this paper is hot combustion cleaning for the current generation of high-performance utility gas turbines in IGCC plants. The principles discussed are also applicable to other coal-fueled concepts.

It should be noted that hot gas piping and control valve technical feasibility are also issues that have been under consideration for decades during the development of first-generation PFBC, second-generation PFBC, and IGCC. Piping systems for temperatures in excess of 1700°F (926°C) are feasible, though close integration of the plant components is required to minimize cost. Hot valving for temperatures up to 1300°F (704°C) is currently available, and higher temperature valves are under development. Conventional gas turbine combustors and gas inlet configurations cannot be used with these systems, and again are the subjects of various ongoing development efforts.

Coal Gasification Processes

At least 20 coal gasification technologies are currently available, or are being demonstrated at commercial capacity, that are appropriate for electric utility IGCC application, and several are being demonstrated in U.S. Clean Coal Technology programs (Epstein, 1992). They fall primarily into the generic classes of moving bed gasifiers, fluidized bed gasifiers, and entrained bed gasifiers. Even within each class they vary significantly in equipment and process details. The generic gasifier types generally produce raw fuel gases having significantly different temperatures: moving bed gasifiers range around 1000°F (538°C), fluidized bed gasifiers about 1500° to 2000°F (815° to 1092°C), and entrained gasifiers about 1900° to 2800°F (1037° to 1536°C). The raw fuel gases are subject to additional cooling, either by direct quenching or indirect cooling, to adjust the fuel gas to the temperature selected for the cleaning functions. Two-stage gasifiers, in effect, inject coal into the primary high-temperature fuel gas to reduce its temperature while generating a richer fuel gas. Moving bed gasifiers may require fuel gas quenching to a temperature of less than 400°F (204°C) to remove tars, and may not be suitable for hot gas cleaning applications because of this. There is concern that such tars will condense on ceramic barrier filter elements, blinding the filter elements and making filter cake remove difficult.

Only fluidized bed and entrained bed technologies are considered further in this evaluation. Other key parameters that define the gasifier characteristics are choice of oxidant (air or oxygen), and use of dry coal feed or coal-water slurry.

The characteristics of the fuel gases produced of importance to the hot gas cleaning system design are listed in Table 1. The natures of the fly ash particles produced in each gasifier class also differ due to the different particle histories in the gasifiers. The plant basis for the estimates is summarized in the table, the IGCC power plant being a relatively small-capacity plant. All the gasifiers considered are single-stage gasifiers. Both air- and oxygen-blown cases are included in the table as appropriate to the gasifier technologies. The values presented in Table 1 are representative estimates based on reports in the open literature and Westinghouse process models, and are not intended to resemble closely any specific gasification system.

Table 1 Fuel gas characteristics

Plant Basis
Coal: Bituminous, Illinois No. 6
sulfur content 3.7 wt% (as received)
ash content 9.6 wt% (as received)
Nominal plant generating capacity: 75 MW_e (net)
Turbine inlet temperature: 2100°F

Gasifier Type:	Moving Bed	Fluidized Bed	Fluidized Bed	Entrained Bed
Oxidant:	air	air	oxygen	oxygen
Coal form:	dry	dry	dry	slurry
Raw Fuel Gas Characteristics				
Fuel gas pressure (psia):	300	385	385	500
Fuel gas temperature (°F)[a]:	1000	1700	1700	1700
Fuel gas flow (acfm)[b]:	13,000	12,650	8,000	5,800
Fly ash loading (ppmw)[c]:	2300	8500	10,000	9900
Fuel gas H_2S+COS (ppmv):	5700	6400	10,100	10,800
Fuel gas alkali (ppmv)[d]:	negligible	1 to 2	1 to 2	1 to 2

a: Maximum gas cleaning temperature that can be considered
b: Volumetric flow at specified temperature and pressure
c: Loading in fuel gas without injected sorbents
d: Alkali estimate (total Na + K) based on limited measurements

Hot Gas Cleaning Requirements

The requirements placed on a gas cleaning system primarily relate to meeting environmental emissions regulations for the power plant and satisfying turbine protection standards. Many other factors are also important and may constrain the gas cleaning system design with respect to space and layout, performance, operation, modularity of design, and cost.

Turbine protection standards have been developed by vendors from related field experience and from engineering models of performance (erosion, corrosion, and deposition) where no experience exists. The turbine protection standards relating to erosion damage and deposition damage are usually expressed in terms of allowable particle loading and size distribution carried in the turbine expansion gas. Dependent on the turbine design, the acceptable on-line and off-line cleaning intervals, and the acceptable blade replacement interval, the allowable expansion gas particulate content can vary significantly. For example, specifying a 100-hour on-line cleaning interval, a 2500-hour off-line cleaning interval, and a 20,000-hour blade inspection interval, the criteria are expressed as the particle loading in key particle size ranges that relate to both erosion and deposition damage occurring. Essentially no particles greater than 20 μm in diameter are permitted. For two other characteristic size ranges (0–2 μm and 1–20 μm) the following limits on the particle concentrations in the expansion gas are estimated for the specified cleaning and inspection periods: particles 0–2 μm in diameter, no more than 2.2 to 3.0 ppmw; particles 1–20 μm in diameter, no more than 4.4 to 5.8 ppmw.

The ranges of particle concentrations given above represent estimates for the various Westinghouse turbine expanders available, and do not relate to other manufacturers' turbines. They are presented only to provide perspective on the gas cleaning requirements and are sensitive to many parameters. Larger machines, Fig. 2, are more tolerant to erosion, and higher inlet temperature machines are more sensitive to deposition. The erosion and deposition behavior of the fly ash particles also depends upon the fly ash particle erosivity and sticking coefficient, and these will differ between gasifier types and feedstocks. The particle limits corresponding to the fuel gas are less stringent by a factor that accounts for the dilution of the fuel gas by secondary combustion air.

Corrosion protection regulates the allowable concentrations

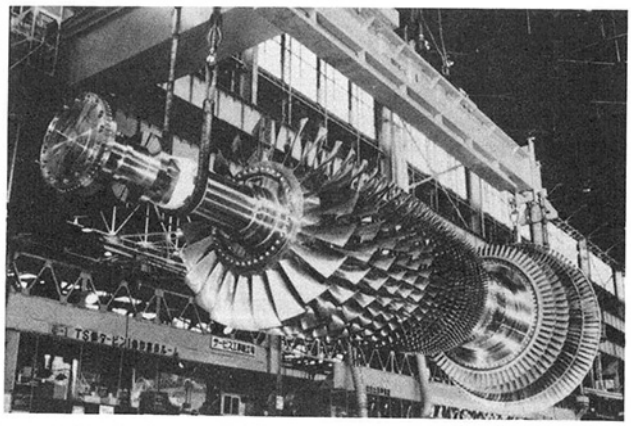

Fig. 2 Westinghouse 501D5 rotor; 19-stage compressor and 4-stage expander

of several contaminants in the turbine expansion gas (vanadium, lead, calcium, and primarily sodium and potassium vapor content in coal-based systems). In the turbine expansion gas, the current Westinghouse standards call for total sodium (Na) plus potassium (K) vapor less than 50 ppbv, although these limits are not founded on coal-based fuel experience. In the fuel gas, the alkali content is equivalent to higher maximum alkali content (Na plus K) that again accounts for the dilution of the fuel gas by secondary combustion air. The sulfur content of the fuel gas has little impact on turbine corrosion and is not limited by turbine protection standards, although downstream, heat recovery components will be influenced.

In an economic evaluation of process alternatives for a direct coal-fueled gas turbine combined cycle (Horazak et al., 1990), it was determined that the turbine reblading interval had little effect on cost of electricity (COE) margin as long as the shortest time between rebladings is at least 5000 hours. At shorter reblading intervals, turbine down-time begins to reduce the capacity factor of the power plant. Blade lives of 2000 and 1000 hours reduced the nominal 70 percent availability to 58 percent and 46 percent, respectively. This severely reduced the COE margin.

Large, coal-fired power plant emissions are regulated by New Source Performance Standards (NSPS) for sulfur oxides, nitrogen oxides, and particulate, and other pollutants, such as carbon monoxide, may also be regulated. The current NSPS call for 70 to 90 percent sulfur removal, depending on the coal sulfur content, for an emission ranging from about 0.6 to 1.2 lb SO_2/MMBtu. The recent amendments to the Clean Air Act set a cap on total sulfur emissions in the U.S., and this implies much more stringent sulfur emission control will be desirable for electric utilities. A sulfur removal level of 97 percent is expected to be representative of the performance that will be acceptable in the near future, and is applied as the basis for a coal gasification plant.

For NO_x, the current NSPS for large, coal-fired power plants is 0.6 lb NO_2/MMBtu for bituminous coals, and 0.5 lb/MMBtu for subbituminous coals. The U.S. Environmental Protection Agency (EPA) is currently developing new standards for NO_x. The NO_x emissions are controlled primarily by combustor design and operation, and for most IGCC fuel gases, less than 0.1 lb NO_2/MMBtu should be achievable. It is possible that gas cleaning functions such as ammonia removal or destruction could be included in the hot gas cleaning system, but this is not considered in this paper. Likewise, carbon monoxide emissions are primarily a function of combustor performance.

Particulate emissions based on the NSPS of 0.03 lb/MMBtu for large coal-fired power plants result in particulate limits for emissions from IGCC power plants of about 15 to 20 ppmw in the stack gas. These limits are generally less stringent than the particle limits required for turbine protection.

Table 2 Requirements for hot gas cleaning

Plant Basis
Coal: Bituminous, Illinois No. 6
sulfur content 3.7 wt% (as received)
ash content 9.6 wt% (as received)
Nominal plant generating capacity: 75 MWe (net)
Turbine inlet temperature: 2100°F

Gasifier Type:	Fluidized Bed	Fluidized Bed	Entrained Bed
Oxidant:	air	oxygen	oxygen
Coal form:	dry	dry	slurry
Particulate Removal			
Expander requirement (ppmw):	6	6	6
Clean fuel gas loading (ppmw):	49	90	95
Particle removal (%):	99.4	99.1	99.0
Plant emission (lb/MMBtu):	0.018	0.017	0.018
Sulfur Removal			
Sulfur removal required (%):	97	97	97
SO_2 emission (lb/MMBtu):	0.18	0.18	0.18
Clean fuel gas H_2S (ppmv):	192	303	297
Alkali Removal			
Expander requirement (ppbv):	50	50	50
Clean fuel alkali (ppbv):	410	750	790
Alkali removal (%):	80	60	60

The plant solid waste must comply with National Resource Conservation and Recovery Act (RCRA) standards, as well as state and local regulations. This may mean that active sulfides and oxides in the solid waste streams need to be processed to render them inert and to provide a nonhazardous classification for the waste. Some entrained gasifier systems use fly ash recycle to the gasifier to promote complete solid waste in the form of slag, considered to be relatively inert based on prior characterization studies.

Based on these considerations, and the characteristics of the fuel gases listed in Table 1 for the generic gasifiers, the cleaning requirements for the hot gas cleanup system are listed in Table 2. This table shows estimates for the hot gas cleanup system's performance requirements for removal of particulate, sulfur, and alkali. The first item under each of these headings corresponds to the primary cleaning requirement, and the other items listed result from that primary requirement.

Status of Fuel Gas Cleaning Technology

Commercial cleanup systems for today's coal-based fuel gases operate at temperatures near ambient and require large heat exchange equipment to precede the cleanup functions. Even though the commercial, low-temperature fuel gas cleaning system can achieve very high levels of cleaning, the low-temperature cleaning results in power plant costs and efficiencies that are only marginally better than conventional PC-boiler plants. In an effort to improve IGCC power plant efficiency and economics, the U.S. Department of Energy (DOE), the Electric Power Research Institute (EPRI), and others, have been sponsoring the development of hot gas cleaning technologies that will efficiently remove sulfur species and particulate materials from fuel gases at higher temperatures.

Hot gas cleaning systems currently under development contain components for high-temperature particle removal and sulfur removal. Particle removal technology capable of operating reliably at temperatures up to about 1700°F (926°C) is nearing commercial demonstration. The leading technology for particle removal is the ceramic barrier filter, with a variety of ceramic filter element forms being developed for this application (ceramic candle, crossflow, tube, or bag filter elements) (Lippert et al., 1992a). There are some issues in the long-term durability of ceramic filter elements due to interactions with alkali vapors, and other species, that are currently being studied to see if they have any influence on performance feasibility. These studies have shown that the use of oxide-

based ceramics, such as mullite, increases the filter element durability (Alvin et al., 1992). The application of alkali sorbents within the filter vessel will minimize alkali-ceramic interaction possibilities.

High-temperature sulfur sorbent systems that can remove H_2S and COS efficiently at temperatures up to about 1200°F (649°C) are currently planned for demonstration in several Clean Coal Technology programs (DOE/METC, 1992). Fixed bed, moving bed, and fluidized bed versions are under development (Cook et al., 1992; Robin et al., 1992). These use zinc-based sorbents (zinc ferrite and zinc titanate) in the form of fabricated pellets that are expensive and must be regenerated, having a cost of about $2000 to $8000/ton. Even with a sorbent regeneration step, the losses of the expensive sorbent resulting from physical and chemical attrition can lead to a significant increase in the cost of electricity produced by the power plant. Efforts to improve the durability of polishing sorbents are being sponsored by DOE (Ayala et al., 1992; Gangwal et al., 1992). The temperature of operation of the zinc-based sorbents is limited to less than about 1300°F (704°C) requiring significant cooling of the fuel gas prior to cleaning. Also, some of the zinc-based sorbents require the injection of steam into the fuel gas to maintain sorbent performance, a further system energy penalty. The sorbent regenerator produces a gaseous sulfur stream that is converted to elemental sulfur or sulfuric acid for final disposition. Effective generation of elemental sulfur requires processing the regenerator SO_2 concentration from the regenerator decreases. Sulfuric acid production from the regenerator SO_2 stream may be simpler and cheaper than elemental sulfur recovery, but the storage of the product is more difficult (Newby et al., 1978). In any case, the difficulty of marketing such byproducts, especially by small power plants, may not make this a generally acceptable option.

Fuel gas alkali removal to protect the turbine from corrosion has been given limited attention in prior hot gas cleaning system development. The fuel gas alkali content at zinc-based cleanup temperatures of 1000° to 1200°F (538° to 649°C) is probably not a concern, with the vapor phase alkali condensing out on the fuel gas cooler heat transfer surfaces. Such condensation is reported to occur extensively in the fuel gas cooler of entrained coal gasifiers, and can result in plugging of flow channels.

Advanced Hot Gas Cleaning System Description

An advanced hot gas cleanup system is shown schematically in the general plant diagram of Fig. 3. Coal, oxidant (oxygen or air), and steam are combined in the gasifier to produce a high-temperature, high-pressure fuel gas. In some gasifiers, in-situ sulfur sorbents may be used to remove a portion of the sulfur. Some particle removal functions, such as slag impact targets and cyclones, may be used to remove a portion of the entrained particles from the fuel gas. A fuel gas cooler is used to reduce the fuel gas to the temperature required for the hot gas cleaning functions, raising steam or preheating air. The fuel gas may be directly cooled by the injection of water, steam, or recycled fuel gas.

The hot gas cleaning system contains component systems that remove particulate, sulfur, and alkali vapors from the fuel gas to meet both the gas turbine tolerance requirements and the plant environmental emission requirements. The basic process principles applied are to utilize ceramic barrier filters for multiple cleaning functions, particle removal as well as sorbent-contaminant reactions, and to use relatively fine sorbent particle sizes for improved reaction performance.

The primary filter is a ceramic barrier filter that removes fly ash from the fuel gas. The primary filter is very similar to other ceramic barrier filter systems being developed for coal-fired power generation systems. However, calcium-based sorbent particles (e.g., pulverized calcitic limestone, dolomitic limestone, or hydrated lime) are also injected into the fuel gas upstream of the primary filter to remove a bulk portion of the sulfur species (mainly H_2S and COS) from the fuel gas:

$$CaCO_3 + H_2S = CaS + H_2O + CO_2 \quad (1)$$

for calcitic or dolomitic limestones, and for hydrated limes

$$Ca(OH)_2 = CaO + H_2O \quad (2)$$

$$CaO + H_2S/CO_2 = CaS/CaCO_3 \quad (3)$$

The entrained removal of H_2S and COS occurs within the fuel gas piping, within the large, well-mixed volume of the primary filter vessel, and within the filter cake layer. The primary filter vessel provides a well-mixing, gas-particle contactor for the sulfur removal reactions, as well as a combined particle removal device. The primary sulfur removal technology is an extrapolation of extensive fluid bed limestone H_2S removal experience, and small-scale entrained H_2S removal experience. It is being tested at subscale in an ongoing Westinghouse program under DOE/METC sponsorship (Lippert et al., 1992b). The calcium-based sorbent is sized to be fine enough to be highly reactive, but coarse enough to be fluidizable for

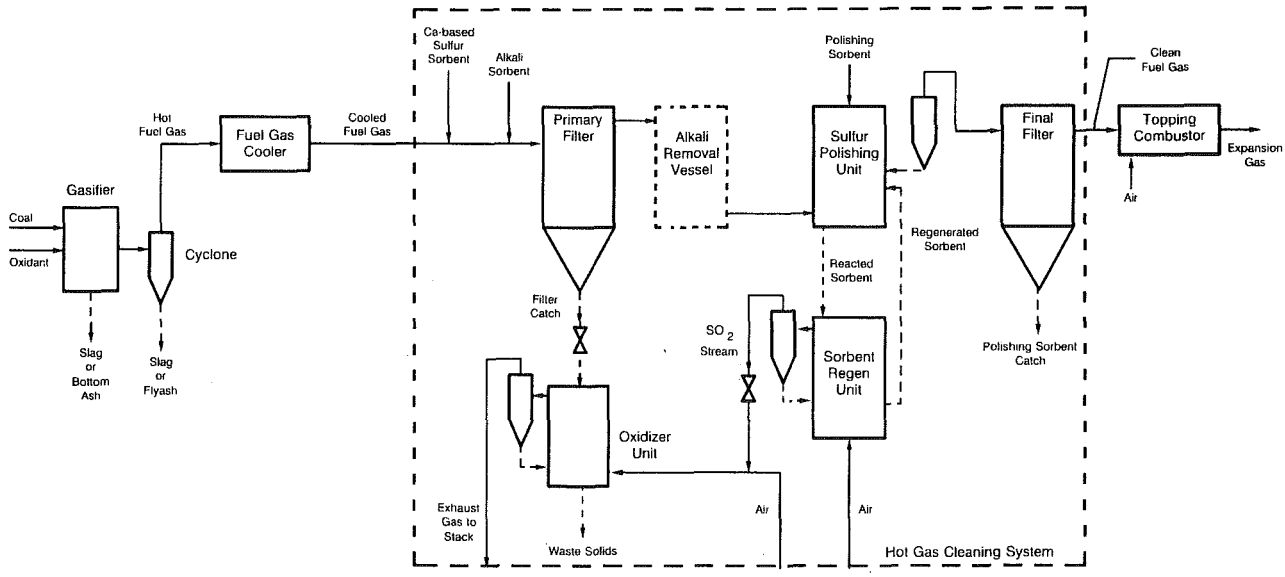

Fig. 3 Gasification/combustion process and hot gas cleaning system definition

later treatment, a size of about −70 mesh being appropriate. The sulfur removal target for the primary sulfur removal stage is about 90 percent, depending on the gasification process and the coal properties, with a calcium-to-sulfur feed ratio of less than 2.0. Depending on the gasifier equivalence ratio and the coal sulfur content, higher levels of removal, or lower Ca/S ratios are possible. Fly ash filter cakes produced by gasifiers are known to be potentially difficult materials for filters, having low permeability and being difficult to pulse clean. The injected calcium sorbent also functions to promote an easily cleaned filter cake in the primary filter.

Similarly, pulverized alkali sorbent particles (e.g., emathlite, bauxite, and others micronized to −325 mesh) may be injected into the fuel gas to remove alkali vapors from the fuel gas within the filter vessel. Optionally, a packed bed of alkali sorbent pellets is placed after the primary filter to remove alkali vapor as a batch process. Both alkali removal technologies follow from past, small-scale kinetics tests and simulations conducted in continuing U.S. DOE development programs (Lippert et al., 1992b; Robertson et al., 1992).

In some cases only the primary sulfur removal step will be required, the calcium-based sorbent removing sufficient sulfur to meet the power plant emission goals. In this case, the hot gas cleaning system functions would be completed after the primary sulfur removal step. The fuel gas would pass on to a topping combustor where combustion is completed to generate an expansion gas having the prescribed turbine inlet conditions. If additional sulfur removal is required, the sulfur polishing step would be applied. The sulfur polishing stage is a fluidized bed desulfurizer of advanced, regenerative sorbent particles, which remove sufficient additional sulfur to meet the plant sulfur emission goal. Advanced, regenerative polishing sorbents, such as zinc-based, copper-based, iron-based, and manganese-based sorbents, would be selected for a specific application based on their thermodynamic potential to achieve the desired sulfur emission, and their compatibility with the fuel gas environment. These advanced sorbents are being developed in many forms, such as mixed oxides, that may contain combinations of the sorbent components supported on high-surface structures, such as porous alumina, silica or zeolites (Atimtay et al., 1990; Tamhankar et al., 1986). The polishing sorbent particle size is selected to be both reactive and effectively fluidized, at about −35 mesh, with a mass-mean particle size of about 200 μm.

The major reactions in the system may involve both the reduction of the metal oxide to lower oxide states, and the sulfidation of the metal oxide(s). For example, for copper-based sorbents:

$$CuO + H_2/CO = Cu + H_2O/CO_2 \quad (4)$$

$$2Cu + H_2S = Cu_2S + H_2 \quad (5)$$

This unit is designed to remove at least 70 percent of the remaining fuel gas sulfur at nominal operating conditions. The use of cheap, calcium-based sorbent to do bulk sulfur removal permits the consumption of the move expensive polishing sorbent to be minimized and the operating cost of the plant to be maintained at an acceptable level. The use of a ceramic barrier filter as the final filter allows the entrained polished sorbent particles to be effectively collected as uncontaminated material for reprocessing as sulfur sorbent, minimizing total sorbent loss. This also allows small polishing sorbent particles to be used.

Our review of the performance data reported in the literature over the past 20 years on regenerative sorbents for H_2S has shown a clear trend: The physical/chemical/thermal degradation of sorbent particles occurring on repeated regeneration-sulfidation cycles, and leading to particle attrition and loss of reactivity, is significantly reduced as particle size is decreased from the large pellet size typical of moving bed desulfurizers to relatively small (about 200 μm), fluidizable particle sizes.

The polishing sorbent regenerator is also a fluidized bed that reacts air with the sulfided sorbent to produce an active sorbent and an SO_2-rich gas stream. The fluidized bed reactor and solids handling aspect of the technology is well developed.

The polishing sorbent is regenerative and the system functions to minimize costs associated with sorbent consumption. The regenerator is a fluid bed reactor that regenerates the polishing sorbent, and generates an SO_2-rich gas stream. The major reactions in the regenerator are, for a copper-based sorbent:

$$Cu + 1/2\ O_2 = CuO \quad (6)$$

$$Cu_2S + O_2 = 2Cu + SO_2 \quad (7)$$

The sulfur polishing system and the primary filter are integrated with the oxidizer. The SO_2-rich gas stream from the polishing regenerator is contacted with the excess calcium-sorbent in the oxidizer vessel, a circulating, fluidized bed operating at atmospheric pressure. In the oxidizer, three functions are performed: (1) The SO_2 from the regenerator is efficiently removed (about 98 percent capture) and the exhaust gas is cooled, filtered and released to the plant stack; (2) the sulfided calcium-sorbent particles from the primary filter are oxidized to a stable sulfate form for disposal; and (3) unburned carbon in the gasifier fly ash is combusted. The solids stream from the primary filter is depressurized through a conventional lock hopper system, and is fed to the atmospheric-pressure oxidizer using a high-temperature, rotary feeder. Alternatively, the oxidizer vessel may be operated at elevated pressures, and the off-gas may be either recycled to the gasifier or to the topping combustor as preheated oxidant. The major reactions in the oxidizer are:

$$CaCO_3 = CaO + CO_2 \quad (8)$$

$$CaO + SO_2 + 1/2\ SO_2 = CaSO_4 \quad (9)$$

$$CaS + 2O_2 = CaSO_4 \quad (10)$$

$$C + O_2 = CO_2 \quad (11)$$

The use of the relatively fine calcium-sorbent permits very effective conversion of CaS to $CaSO_4$. The oxidizer produces waste solids containing waste calcium-based sorbent (CaO, $CaSO_4$, traces of CaS and $CaCO_3$, and inerts), waste alkali sorbent (emathlite clay reacted to inert, glass-phase surface layer particles), and coal ash.

Again, the fluidized bed reactor design principles and solids handling principles for the oxidizer are well known, but the integrated, multifunctions of the reactor have only been established independently, and at small scale.

Performance Estimates

The selection of the sulfur removal sorbents and the operating conditions is based, in part, on the thermodynamic potential of alternative sulfur sorbents, illustrated in Fig. 4, specifically for the case of the air-blown, fluidized bed gasifier. The figure shows that calcium-based sorbents have an optimum thermodynamic performance in the expected fuel gas at a temperature ranging from 1600° to 1800°F (870° to 981°C), having high thermodynamic potential to achieve at least 90 percent sulfur removal, and emission of about 0.6 lb SO_2/MMBtu. The kinetics of calcium-based sulfidation suggests good kinetic performance for fine particles at these conditions, although the calcium-based sorbent, if injected in the fuel gas at a slightly higher temperature, will calcine and potentially result in better sulfidation kinetics. The zinc-based sorbents have the highest sulfur removal performance, but are limited to about a maximum of about 1300°F (704°C) due to the formation of zinc metal and its subsequent loss due to vaporization. The copper-

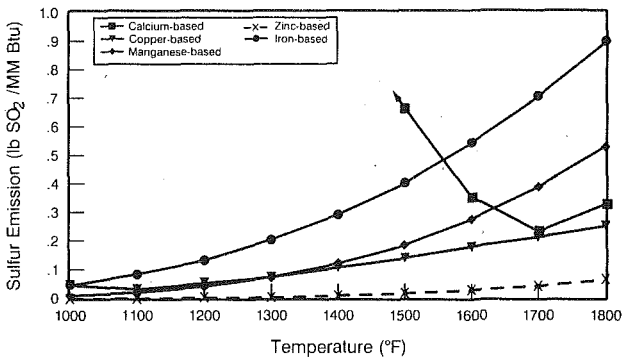

Fig. 4 Equilibrium sulfur removal potential, Illinois No. 6 coal

based sorbents are the only alternative sorbents that can meet the power plant goal of 0.18 to 0.2 lb SO_2/MMBtu at a temperature near that of the primary sulfur removal stage, 1600° to 1700°F (870° to 926°C). The other sorbents would need to be applied at significantly lower temperatures, requiring an intermediate stage of fuel gas cooling. If the fuel gas were cooled to about 1200°F (649°C), then relatively cheap iron-based sorbents could be used for sulfur polishing. The thermodynamic performances of the sulfur sorbents for the oxygen-blown gasifiers are somewhat poorer because of the less favorable gas composition generated. Table 3 lists the operable temperature ranges of the sulfur sorbents for the fluidized bed and entrained bed gasifiers.

Westinghouse has developed preliminary designs of the hot gas cleaning system to estimate the overall performance of the system. The hot gas cleaning system consists of an integrated, single train of shop fabricated vessels. In Table 4, the hot gas cleaning component system conditions and performance estimates are summarized, the system meeting the requirements outlined in Table 2. The primary stage sulfur removal sorbent is calcitic limestone, although others (dolomitic limestone and lime hydrate) will function equally well. The polishing sorbent is a copper-based sorbent capable of meeting the sulfur emission goal at the specified conditions. The estimates in Table 4 are conservative, based on the available kinetic evidence, related pilot plant data, and reactor modeling results. Note that significant fuel gas temperature reduction occurs across the primary filter vessel due to the endothermic nature of the desulfurization reactions. The sulfur sorbent is injected at a temperature about 50°F (28°C) hotter than the filter inlet. The overall hot gas cleaning system pressure drop is acceptable for IGCC applications.

Table 3 Thermodynamic temperature ranges for sulfur removal

	Potential Temperature Range (°F)		
Gasifier Type:	Fluidized Bed	Fluidized Bed	Entrained Bed
Oxidant:	air	oxygen	oxygen
Primary-Stage removal (Ca-based):	1600-1800[a]	1600-1750[a]	1600-1800[b]
Polishing-Stage removal[c]			
Zinc-based sorbents:	< 1300	< 1300	< 1300
Copper-based sorbents:	< 1700	< 1600	< 1700
Manganese-based sorbents:	< 1500	< 1500	< 1400
Iron-based sorbents:	< 1300	< 1300	< 1150

a: 90% sulfur removal potential
b: 50 to 80% sulfur removal potential
c: emission of 0.18 to 0.2 lb SO_2/MMBtu

Table 4 Hot gas cleaning system conditions and performance estimates

Gasifier Type:	Fluidized Bed	Fluidized Bed	Entrained Bed
Oxidant	air	oxygen	oxygen
Primary Filter			
Inlet temperature (°F):	1650	1650	1650
Inlet loading (ppmw):	48,000	86,000	90,000
Outlet loading (ppmw):	<10	<10	<10
Primary Sulfur Removal			
Sorbent:	limestone	limestone	limestone
Injection temperature (°F):	1700	1700	1700
Ca/S:	1.5	1.5	1.5
Sulfur removal (%):	90	90	60
Alkali Removal			
Sorbent:	emathlite	emathlite	emathlite
Feed rate (lb/1000 lb gas):	0.5	0.3	0.3
Inlet alkali (ppmv):	2	2	2
Outlet alkali (ppbv):	<400	<750	<300
Polishing Sulfur Removal			
Temperature (°F):	1620	1520	1570
Sorbent:	Cu-based	Cu-based	Cu-based
Cu/S makeup:	0.05	0.05	0.05
Cu/S total:	3.0	3.0	4.0
Sulfur removal (%):	71	71	94
Oxidizer			
Temperature (°F):	1600	1600	1600
Ca/S (based on unused Ca):	8.4	8.4	2.4
Sulfur removal (%):	98	98	98
Final Filter			
Temperature (°F):	1630	1530	1580
Inlet loading (ppmw):	300	180	180
Outlet loading (ppmw):	<20	<20	<20
Overall System Performance			
Sulfur removal (%):	97	97	97
Sulfur emission (lb SO_2/MMBtu):	0.18	0.18	0.18
Expander inlet loading (ppmw):	<6	<6	<6
Particle emission (lb/MMBtu):	<0.001	<0.001	<0.001
Solid waste (lb/lb coal):	0.19	0.19	0.21
Total pressure drop (psi):	25	25	25
Total temperature drop (°F):	70	170	120

Hot Gas Cleanup System Cost

Installed equipment costs have been estimated, based on the preliminary designs, for the major equipment components in the hot gas cleaning system using recent cost quotes, and from general equipment cost correlations for similar pressure vessels and process equipment. General correlation factors have been used to estimate engineering and installation costs for the equipment. The installed equipment costs have been applied to a cost format developed by EPRI and adapted by DOE for program cost evaluations. The results, for the Total Capital Requirement, and the COE associated with the hot gas cleaning system are shown in Table 5. Small process and project contingencies were applied that assume a mature technology.

If only 90 percent sulfur removal were required, then only first-stage, calcium-based sulfur removal would be required. This would, for example, reduce the Total Capital Requirement for the air-blown, fluidized bed gasifier case to about 100 $/kW and the COE adder to about 7 mills/kWh.

Table 5 Hot gas cleaning system estimated costs

Gasifier Type:	Fluidized Bed	Fluidized Bed	Entrained Bed
Oxidant:	air	oxygen	oxygen
Total Capital Requirement ($/kW)[a]:	297	255	233
Cost of Electricity (mills/kWh)[b]:	19.0	17.4	17.6

a: 1992 dollars; 10% contingency
b: Levelized, constant $, based on: limestone $15/ton; emathlite $55/ton; copper sorbent $3000/ton; waste disposal $9/ton; plant capacity factor 50%

Conclusions

The technical requirements placed on a gas cleaning system used in a coal-fueled combined cycle power plant primarily relate to meeting environmental emissions regulations and sat-

isfying turbine protection standards. Other important factors to be considered include: system performance, operation, equipment footprint, modularity of design, and cost.

An advanced hot gas cleaning system that contains component systems that remove particulate, sulfur, and alkali vapors from the fuel gas to meet both the gas turbine requirements and the plant environmental emission requirements has been presented in this paper. The basic process principles applied are to utilize ceramic barrier filters for multiple cleaning functions, particulate removal as well as sorbent-contaminant reactions, and to use relatively fine sorbent particle sizes for improved reaction performance.

Hot gas cleaning requirements and performance estimates have been presented in this paper for IGCC plants whose gasification process is either an air- or oxygen-blown fluidized bed or an oxygen-blown entrained bed. Performance results show that the advanced hot gas cleaning system is a viable concept that can be utilized to support the commercialization of IGCC plants and other coal-fueled power generation concepts that require gas cleaning.

References

Alvin, M. A., et al., 1992, "Thermal/Chemical Stability of Ceramic Cross Flow Filter Materials," *Proceedings DOE/METC Twelfth Annual Gasification and Gas Stream Cleanup Systems Contractors Review Meeting*, Morgantown, WV.

Atimtay, A. T., et al., 1990, "A Novel Supported Sorbent for Hot Gas Desulfurization," presented at the 199th ACS National Meeting.

Ayala, R. E., et al., 1992, "Enhanced Durability of High-Temperature Desulfurization Sorbents for Moving-Bed Applications," *Proceedings DOE/METC Twelfth Annual Gasification and Gas Stream Cleanup Systems Contractors Review Meeting*, Morgantown, WV.

Bannister, R. L., Newby, R. A., and Diehl, R. C., 1992, "Developing a Direct Coal-Fired Combined Cycle," *Mechanical Engineering*, Vol. 114, No. 12, pp. 64–70.

Cook, C. S., et al., 1992, "Integrated Operation of a Pressurized Fixed Bed Gasifier and Hot Gas Desulfurization System," *Proceedings DOE/METC Twelfth Annual Gasification and Gas Stream Cleanup Systems Contractors Review Meeting*, Morgantown, WV.

DOE/METC, 1992, "Reviews of IGCC Demonstration Projects," *Proceedings DOE/METC Twelfth Annual Gasification and Gas Stream Cleanup Systems Contractors Review Meeting*, Morgantown, WV.

Epstein, M., 1992, "Commercial Size Gasification Projects, Domestic and Foreign," *Proceedings DOE/METC Twelfth Annual Gasification and Gas Stream Cleanup Systems Contractors Review Meeting*, Morgantown, WV.

Gangwal, S. K., et al., 1992, "Enhanced Durability of Desulfurization Sorbents for Fluidized-Bed Applications," *Proceedings DOE/METC Twelfth Annual Gasification and Gas Stream Cleanup Systems Contractors Review Meeting*, Morgantown, WV.

Garland, R. V., and Pillsbury, P. W., 1992, "Status of Topping Combustor Development for Second-Generation Fluidized Bed Combined Cycles," ASME JOURNAL OF ENGINEERING FOR GAS TURBINES AND POWER, Vol. 114, pp. 126–131.

Geoffroy, G. A., and Amos, D. J., 1991, "Four Years Operating Experience Update on a Coal Gasification Combined Cycle Plant With Two 100 MW Class Gas Turbines," presented at the Second Annual Combined Heat and Power and Independent Power Procedures Conference, Birmingham, United Kingdom.

Hendry, R. L., and Pillsbury, P. W., 1987, "Commercial Demonstration of the Dow Gasification Process in an Integrated Combined Cycle," *Proceedings American Power Conference*, Vol. 49, pp. 149–153.

Horazak, D. A., Buchanan, T. L., Bannister, R. L., and Pillsury, P. W., 1990, "Economic Evaluation of Process Alternatives for Direct Coal-Fueled Combustion Turbine Combined Cycle," *Advances in Solid Fuels Technologies*, ASME FACT-Vol. 9, pp. 39–46.

Lippert, T. E., Newby, R. A., Alvin, M. A., Bachovchin, D. W., Bruch, G. J., and Smeltzer, E. E., 1992a, "Development of Hot Gas Cleaning Systems for Advanced, Coal Based Gas Turbine Cycles," ASME Paper No. 92-GT-431.

Lippert, T. E., et al., 1992b, "Integrated Low Emission Cleanup System for Direct Coal-Fueled Turbines," *Proceedings DOE/METC Ninth Annual Coal-Fueled Heat Engines, Advanced Pressurized Fluidized Bed Combustion and Gas Stream Cleanup Systems Contractors Review Meeting*, Morgantown, WV.

Newby, R. A., et al., 1978, "Regeneration of Calcium-Based SO_2 Sorbents for Fluidized-Bed Combustion: Engineering Evaluation," EPA-600/7-78-039, Mar.

O'Hara, J. B., et al., 1987, "Sulfur Recovery From Hot Coal Gas Desulfurization Processes," DOE/MC/21097—2338, Apr.

Robertson, A., 1992, "Hot Gas Cleanup and Gas Turbine Aspects of an Advanced PFBC Power Plant," *Proceedings DOE/METC Ninth Annual Coal-Fueled Heat Engines, Advanced Pressurized Fluidized Bed Combustion and Gas Stream Cleanup Systems Contractors Review Meeting*, Morgantown, WV.

Robin, A. M., et al., 1992, "Integration and Testing of Hot Gas Desulfurization and Entrained Flow Gasification for Power Generation Systems," *Proceedings DOE/METC Twelfth Annual Gasification and Gas Stream Cleanup Systems Contractors Review Meeting*, Morgantown, WV.

Scalzo, A. J., Amos, D. J., Bannister, R. L., and Garland, R. V., 1992, "Status of Westinghouse Coal-Fueled Combustion Turbine Programs," *American Power Conference Proceedings*, Vol. 54, pp. 1193–1204.

Tamhankar, S. S., et al., 1986, "Mixed-Oxide Sorbents for High-Temperature Removal of Hydrogen Sulfide," *Ind. Eng. Chem. Process Des. Dev.*, Vol. 25, p. 429.

Effect of Pressure on Second-Generation Pressurized Fluidized Bed Combustion Plants

A. Robertson
Foster Wheeler Development Corporation,
Livingston, NJ 07039

D. Bonk
U.S. Department of Energy,
Morgantown, WV 26507

In the search for a more efficient, less costly, and more environmentally responsible method for generating electrical power from coal, research and development has turned to advanced pressurized fluidized bed combustion (PFBC) and coal gasification technologies. A logical extension of this work is the second-generation PFBC plant, which incorporates key components of each of these technologies. In this new type of plant, coal is devolatilized/carbonized before it is injected into the PFB combustor bed, and the low-Btu fuel gas produced by this process is burned in a gas turbine topping combustor. By integrating coal carbonization with PFB coal/char combustion, gas turbine inlet temperatures higher than 1149°C (2100°F) can be achieved. The carbonizer, PFB combustor, and particulate-capturing hot gas cleanup systems operate at 871°C (1600°F), permitting sulfur capture by lime-based sorbents and minimizing the release of coal contaminants to the gases. This paper presents the performance and economics of this new type of plant and provides a brief overview of the pilot plant test programs being conducted to support its development.

Introduction

A new generation of coal-fired electricity generating plants is on the horizon—second-generation pressurized fluidized bed combustion (PFBC) plants. They offer the prospect of a 45-percent cycle efficiency and can meet present and future New Source Performance Standards (NSPS). Additional advantages of these plants are:

- Lower capital costs
- High reliability and availability
- Shorter design and construction lead times
- Modularity

These are all aimed at lowering the cost of electricity (COE) and minimizing the risk of surplus capacity. Foster Wheeler Development Corporation (FWDC) is leading a multicompany team working to make this new type of plant a commercial reality.

The team is currently in the second phase of a three-phase DOE-funded program to develop the technology for this new type of plant—a plant with a COE at least 20 percent lower than the COE of a conventional pulverized-coal-fired plant with a stack gas scrubber and with 45-percent efficiency (based on the higher heating value of the coal). A conceptual design and an assessment of the R&D needs of a nominal 500-MWe plant were the products of Phase 1. Pilot plant construction has been completed in Phase 2, and FWDC is currently conducting tests at the John Blizard Research Center—Foster Wheeler's research location in Livingston, NJ—to determine how individual components perform when burning different coals in concert with varied sorbents.

Once Phase 2 has been completed, the plant will be operated in an integrated mode to determine how well the units "cooperate" and the overall effects of integration.

Plant Concept

The second-generation PFBC combined-cycle plant being developed by the FWDC team is shown in a simple process block diagram in Fig. 1.

In operation, coal is fed to a pressurized carbonizer, where it is pyrolyzed/devolatilized at a low temperature, producing a low-Btu fuel gas and char. After the fuel gas passes through a cyclone and a ceramic barrier filter to remove gas-entrained particles, it is burned in a topping combustor to produce the energy to drive a gas turbine.

This gas turbine drives a generator and a compressor that feeds air to the carbonizer, to a circulating pressurized fluidized bed combustor (CPFBC), and to an external fluidized bed heat exchanger (FBHE). Char from the carbonizer is burned in the CPFBC with high excess air, heating the flue gas to 871°C (1600°F); vitiated air from the CPFBC supports combustion of the fuel gas in the topping combustor.

Surplus heat from the CPFBC is transferred to the FBHE by the recirculation of sorbent between the two units, which is controlled by cyclone separators and nonmechanical valves.

If the fuel gas produced in the carbonizer were not treated, it would contain hydrogen sulfide and sulfur-containing tar/light oil vapors. But lime-based sorbents injected into the carbonizer catalytically enhance tar cracking and capture sulfur

Contributed by the International Gas Turbine Institute and presented at the 38th International Gas Turbine and Aeroengine Congress and Exposition, Cincinnati, Ohio, May 24-27, 1993. Manuscript received at ASME Headquarters March 17, 1993. Paper No. 93-GT-357. Associate Technical Editor: H. Lukas.

in situ as calcium sulfide. The raw fuel gas is fired hot, eliminating fuel gas heat exchangers and chemical or sulfur-capturing bed cleanup systems. Such expensive, complex systems are an intrinsic part of the coal gasification combined-cycle plants now being developed. High-temperature filters capture the elutriated particles of char and calcium sulfide. The result is an almost particle-free fuel gas, one that meets NSPS. Along with the carbonizer bed drains, the captured material is collected in a central hopper and is injected into the CPFBC through a nitrogen-aerated nonmechanical valve. Once in the CPFBC, the calcium sulfide is transformed into sulfate by the excess air; it can then be safely disposed of with the normal CPFBC spent sorbent.

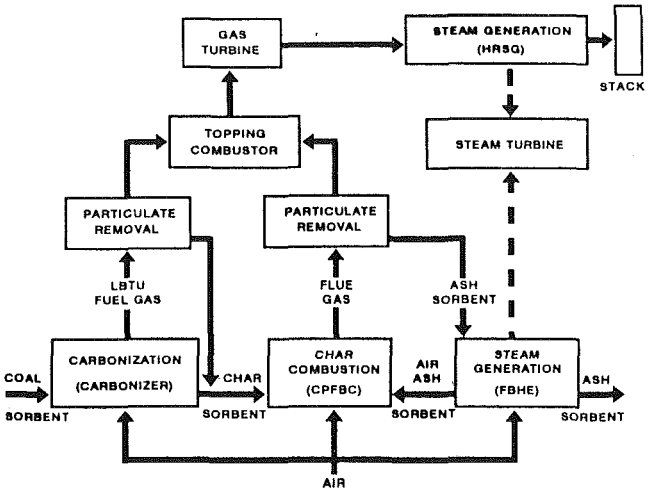

Fig. 1 Simplified process block diagram—second-generation PFB combustion plant

All cooling tube surface is in the FBHE, a move that virtually eliminates tube erosion because of the low FBHE fluidizing velocity [≤ 0.15 m/s ($\leq 1/2$ ft/s)]. Erosion and fouling of downstream equipment can be caused by the exhaust gases leaving the carbonizer and the CPFBC. These gases contain particles of char, sorbent, and fly ash. To prevent erosion and fouling, the gases are cleaned to <20 ppm solids loading by a hot gas cleanup (HGCU) system before they enter the topping combustor and the gas turbine. Although the leading candidates for the final filtration stage are the ceramic crossflow and ceramic candle filters, other devices such as ceramic bag filters and screenless granular-bed filters are possible alternatives.

The topping combustor consists of metallic-wall multiannular swirl burners (MASBs), which are already being developed (Garland et al., 1986) and will be provided in two external combustion assemblies (topping combustors) on opposite sides of the gas turbine. Each MASB contains a series of swirlers that aerodynamically create fuel-rich, quick-quench, and fuel-lean zones to minimize NO_x formation during the topping combustion process. The swirlers also provide a thick layer of air at the wall boundary to control the temperature of the metallic walls.

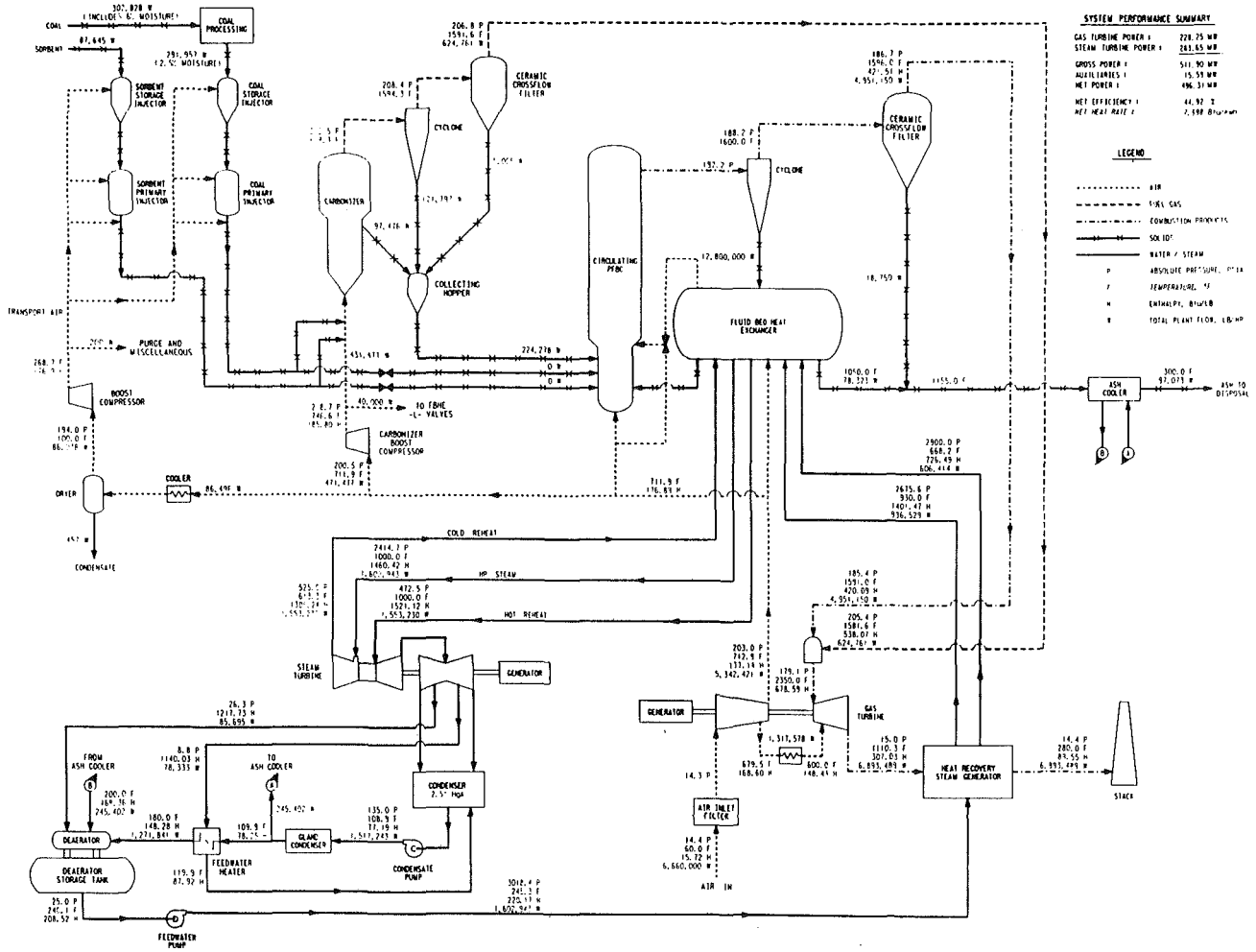

Fig. 2 Heat and material balances for a 14 atm/496-MWe second-generation PFBC plant

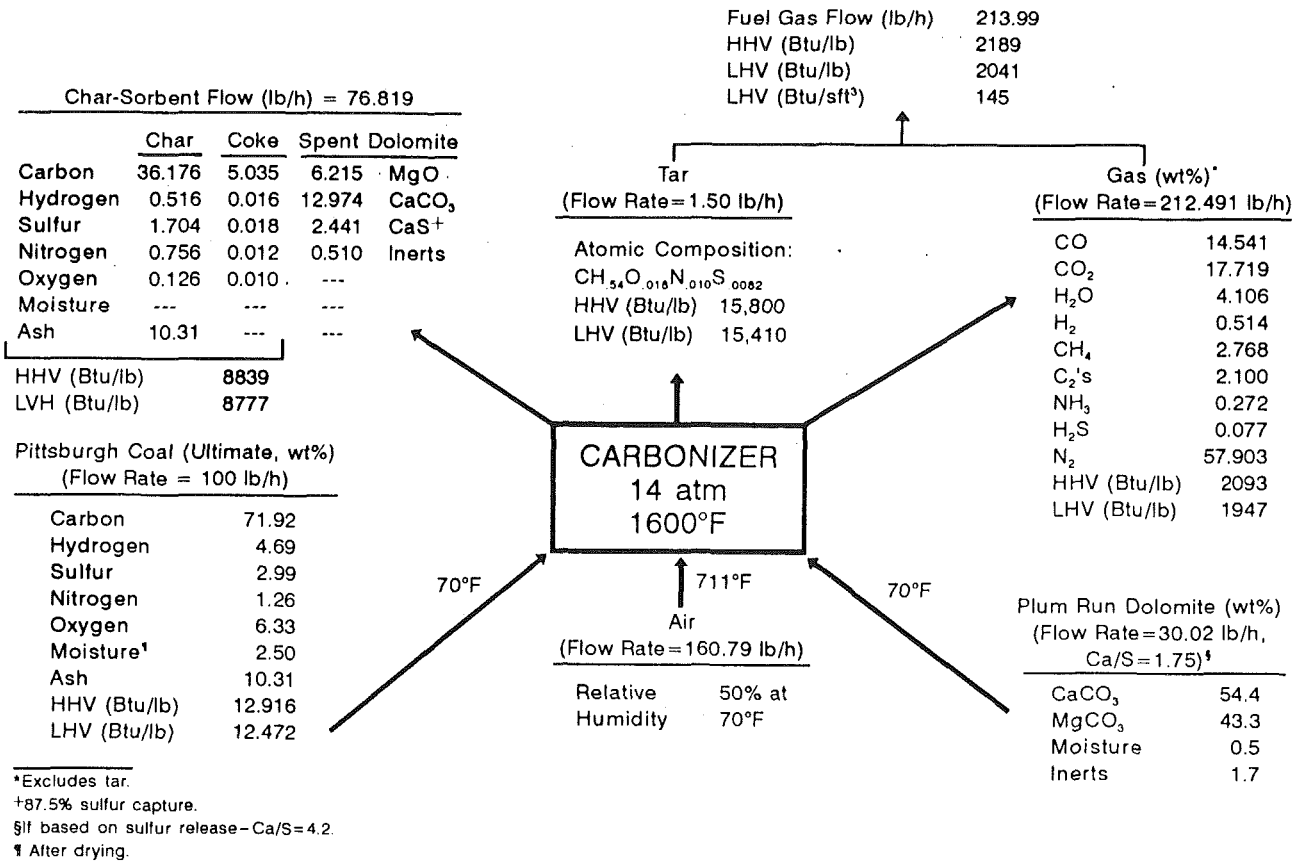

*Excludes tar.
+87.5% sulfur capture.
§If based on sulfur release–Ca/S=4.2.
¶ After drying.

Fig. 3 1.42 MPa (14 atm)/871°C (1600°F) carbonizer performance

Plant Design, Performance, and Economics

Plant efficiency rises when the amount of coal energy transferred to the fuel gas in the carbonizer increases, without creating the need for a fuel-gas chemical cleanup system. Carbonizer performance characteristics are thus important to second-generation PFBC plants. Based on the limited carbonizer data available in the literature when FWDC began the project, 816°C (1500°F) appeared to be the low-temperature limit from the standpoint of sulfur-capture efficiency and potential fuel gas tar/oil vapor levels for bituminous coals.

To avoid substantial extrapolation of very limited data on carbonizer operation, the team chose that temperature for a baseline plant configuration, but they also investigated carbonizer operation at 871°C (1600°F) during a sensitivity study. Based on first-generation PFBC plant experience, 871°C (1600°F) was chosen for the CPFBC to eliminate the need for alkali getters while precluding gas turbine hot corrosion.

Operating as an integrated subsystem, the carbonizer, CPFBC, FBHE, and gas turbine form a modular building block to achieve plants with varied electrical outputs. Figure 2, a heat and material balance of a second-generation PFB combustion plant operating with an 871°C (1600°F) carbonizer, shows one module of a plant that utilizes two of each of these building blocks. The flow rates given are representative of the two-module plant, which produces 496 MWe of net power at 44.9 percent efficiency. The feedstocks for this plant (2.9 percent sulfur Pittsburgh No. 8 coal and Ohio Plum Run dolomite) are crushed to 12.7 mm (1/2 in.)×0, dried to less than 1 percent surface moisture, and injected into each carbonizer—coal at 66,215 kg/h (145, 979 lb/h) and dolomite at 19,878 kg/h (43, 823 lb/h)—by separate lock-hopper/pneumatic transport feed systems. Each carbonizer produces 141,694 kg/h (312,381 lb/h) low-Btu fuel gas with a 5.40 MJ (145 Btu/sft^3) heating value and 50,865 kg (112,139 lb) of a char/coke/sorbent mixture. The mixture is burned in an 871°C (1600°F) CPFBC operating at approximately 200 percent excess air to produce 1,122,903 kg (2.476×10^6 lb) high-excess-air flue gas and an FBHE steam duty of 0.44 MJ (420×10^6 Btu/h).

The carbonizer fuel gas passes through cyclone separators and ceramic cross-flow filters and is burned in the topping combustor, heating the CPFBC flue gas to 1288°C (2350°F), the ideal firing temperature for the carbonizer performance level shown in Fig. 3.

Each gas turbine produces 114.1 MWe. The turbine exhaust gas is cooled by an HRSG from 599 to 138°C (1110 to 280°F) before it enters the stack. With the HRSG and FBHE of each module operating together, 16.5-MPa gage/538°C/538°C/8.5 kPa Hg (2400 psig/1000°F/1000°F/2.5 in. Hg) steam is produced. The total plant flow rate [727,084 kg/h (1.602×10^6 lb/h)] results in steam turbine electrical power generation at 283.7 MWe.

Coal ash and spent sorbent are removed at the FBHE and the CPFBC ceramic cross-flow filter vessels, depressured by restricted-pipe discharge systems (Knowlton et al., 1986), and cooled by screw coolers to 149°C (300°F). The plant spent-bed material/bottom ash poses no toxicological or waste-disposal problems. After the char/coke/sorbent residue has been burned in the CPFBC at 871°C (1600°F), its composition is very much the same as the material leaving a first-generation PFBC system and less damaging to the environment than the residue from conventional pulverized-coal-fired plants.

Operating with a calcium-to-sulfur molar feed ratio of 1.75, the plant achieves 90-percent coal sulfur capture. Despite an overall plant excess-air level of 124 percent, the plant operates with an NO_x release that is less than half that allowed by NSPS because of staged combustion in both the CPFBC and topping combustor combined with the relatively low heating value of the carbonizer fuel gas. Particulate release, also well below the

Table 1 Performance: PFBC plant versus conventional PC-fired plant

Description	Second-Generation PFBC Plant		Conventional PC-Fired Plant With Scrubber
	816°C (1500°F) Carbonizer	871°C (1600°F) Carbonizer	
Power Summary			
Net Capacity, MWe	452.8	496.3	500.9
Net Plant Efficiency, % (HHV)	43.6	44.9	35.9
Gross Power			
Gas Turbine, MWe	195.2	228.2	—
Steam Turbine, MWe	272.3	283.7	540.4
Turbine Parameters			
Gas Turbine Topping Combustor, °C (°F)	1149 (2100)	1288 (2350)	—
Main Steam Flow, kg/s (10^3 lb/h)	193.9 (1538.6)	200.3 (1602.9)	499.9 (3967.9)
Consumables and Wastes			
Pittsburgh No. 8 Coal, kg/s (lb/h)*	35.8 (284,410)	38.2 (302,828)	53.8 (382,928)
HHV, MJ/kg (Btu/lb)*	30.02 (12,450)	30.02 (12,450)	30.02 (12,450)
Sulfur, wt%	2.89	2.89	2.89
Ash, wt%	9.94	9.94	9.94
Sorbent Flow, kg/s (lb/h)			
Dolomite	10.4 (82,315)	11.0 (87,645)	—
Limestone	—	—	5.5 (43,606)
Lime	—	—	0.3 (2,019)
Ash Production, kg/s (lb/h)			
Ash/Spent Sorbent	11.5 (91,144)	12.2 (97,073)	1.0 (7,612)
Fixed Sludge	—	—	8.9 (70,740)

*As received/before drying.

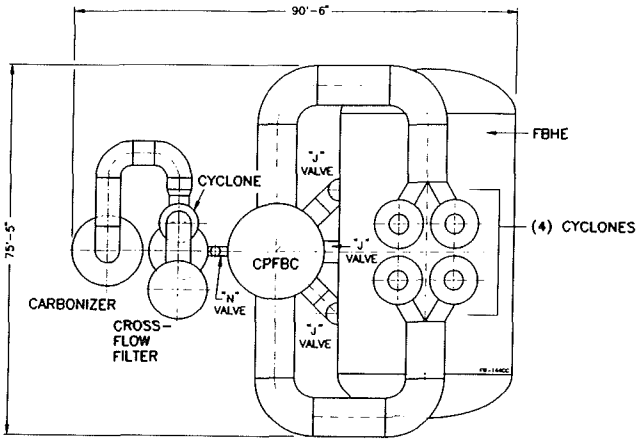

Fig. 4 Plan view—carbonizer/CPFBC/FBHE module

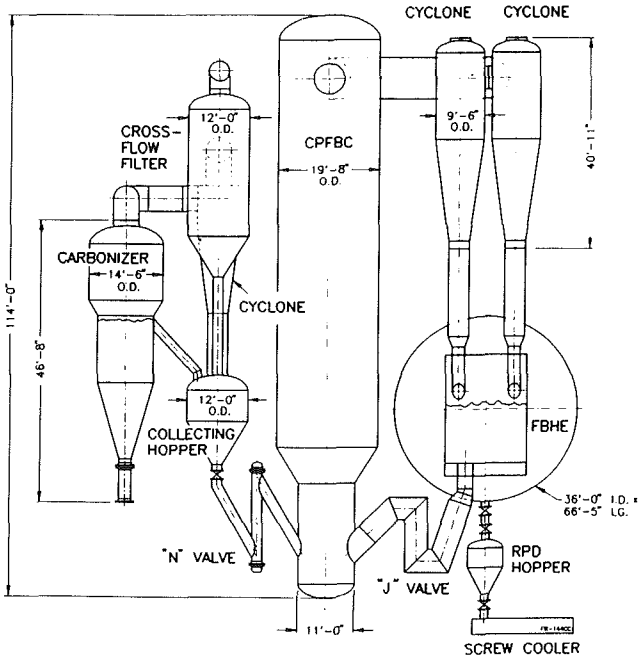

Fig. 5 Elevation view—carbonizer/CPFBC/FBHE module

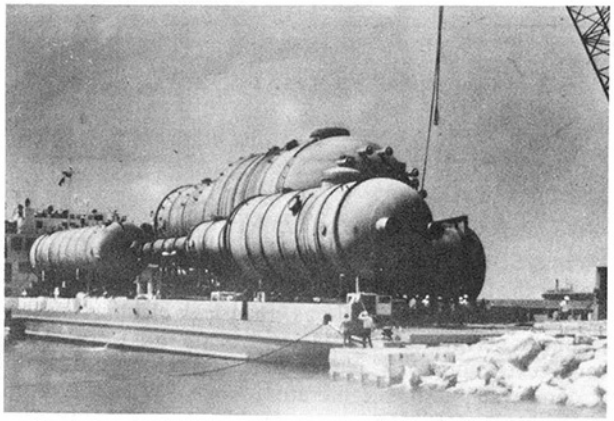

Fig. 6 Vessels arriving by ship

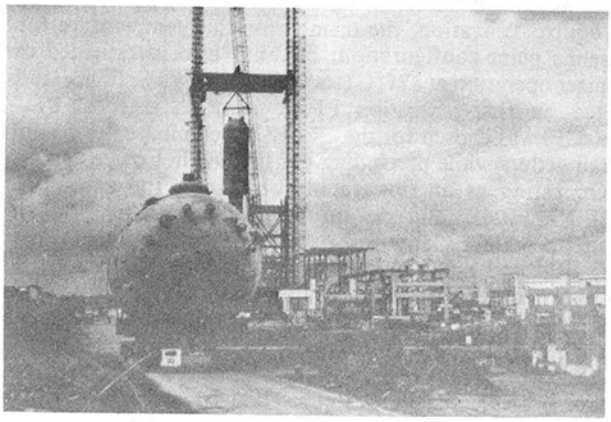

Fig. 7 Crawler transporting vessel to site

NSPS-mandated level, is the result of the high collection efficiency of the ceramic crossflow filters. Their success eliminates the need for any particulate collection at the stack.

Overall plant performance is presented in Table 1, where both the 816 and 871°C (1500 and 1600°F) carbonizers are compared with a conventional pulverized-coal-fired plant with a scrubber.

Shown in plan and elevation views in Figs. 4 and 5, second-generation plant components are small enough to be assembled in a shop and shipped by barge to many plant sites throughout the United States. Once the vessels reach the docking area, they begin their overland trip to the plant site by crawler transporters. Figures 6 and 7 show units, designed by Foster Wheeler for a refinery in Venezuela, making such an overland trip.

The same plants compared for performance in Table 1 are compared for their economics in Table 2, which clearly shows the benefits of the second-generation plants. EPRI's *Technical Assessment Guide* (Electric Power Research Institute, 1986) was used to determine the economics of the three 30-year life plants in 1987 dollars, with first-year delivered coal and do-

lomite costs of $1.70/GJ ($1.79/10^6 Btu) and $0.0197/kg ($17.9/ton), respectively. The values presented in the table are based on shipping the modular units by barge.

Effect of Reduced Pressure Ratio

Having determined the effect of carbonizer temperature on plant performance, an analysis was conducted to identify baseline plant sensitivity to gas turbine pressure level. A 1.0-MPa (10-atm) pressure was selected. The lower pressure has only a slight effect on the carbonizer performance level. Figure 8 is a heat and material balance for the new plant. The lower-pressure plant continues to operate with an 1149°C (2100°F) topping combustor temperature (the optimum firing temperature is relatively insensitive to pressure in this range). The resultant efficiency is 0.12 percentage points higher than the baseline plant efficiency.

Table 2 Economics: PFBC plant versus conventional PC-fired plant

Description	Second-Generation PFBC Plant		Conventional PC-Fired Plant With Scrubber
	816°C (1500°F) Carbonizer	871°C (1600°F) Carbonizer	
Unit Size, MWe net	452.8	496.3	500.0
Net Plant Efficiency, % (HHV)	43.6	44.9	35.9
Total Plant Cost, $/kW	906.1	875.8	1192.6
Total Plant Investment, $/kW	980.6	947.8	1307.7
Total Capital Requirement, $/kW	1037.0	1002.1	1375.3
First Year Costs:			
Total O&M, $/kW • yr	38.0	35.6	45.6
Fixed O&M, $/kW • yr	24.7	23.2	29.5
Variable O&M, mills/kWh	2.34	2.19	2.79
Consumables, mills/kWh	3.37	3.24	2.85
Fuel Cost, mills/kWh	14.0	13.6	16.8
Levelized O&M:			
Fixed, $/kW • yr	43.2	40.4	51.8
Variable O&M, $/kW • yr	4.1	3.8	4.9
Consumables, mills/kWh	5.9	5.7	5.0
Fuel, mills/kWh	26.6	25.9	32.4
Levelized Carryover Charge, $/kW • yr	179.6	173.4	237.9
Levelized Busbar Cost, mills/kWh (at 65% capacity factor)	75.7	72.9	93.2

The PFBC island component arrangements are identical to those of the baseline plant, but physical dimensions differ because of differences in flow rate and operating pressure. For instance, the carbonizer fuel gas volumetric flow rate is roughly 45 percent higher than the baseline plant, necessitating about a 20-percent increase in carbonizer IDs. The CPFBC flue gas volumetric flow rate is roughly 52 percent higher, necessitating about a 23-percent increase in IDs. The carbonizer and CPFBC vessel heights remain similar to baseline plant values. Compared with the baseline plant, the FBHE duty is roughly 31 percent lower, requiring an 18-percent decrease in its heat transfer surface area. Although the gas turbine output is 2.7 percent lower than in the baseline plant, the hot valving, piping, and blade path of the gas turbine are 25 to 30 percent larger because of the lower pressure. The gas turbine compressor contains fewer high-pressure stages because of the lower operating pressure of the cycle, and its discharge temperature is reduced to 311°C (591°F) [baseline plant value is 377°C (711°F)].

Because of the lower temperature involved, the heat exchanger incorporated in the baseline plant to cool a portion of the compressor air for gas turbine blade cooling is eliminated. Since this heat exchanger was a source of hot air for coal drying in the baseline plant, the 1.0-MPa (10-atm) plant uses an oil-fired burner to reheat a portion of the HRSG exhaust gas. The steam turbine is essentially identical to the baseline unit, although the output is 3.9 percent lower.

The economics and performance of the 1.4- and 1.0-MPa (14- and 10-atm) plants are presented in Tables 3 and 4. Although the lower pressure raised the plant efficiency by 0.5 percentage points, the plant COE is 5 percent higher because

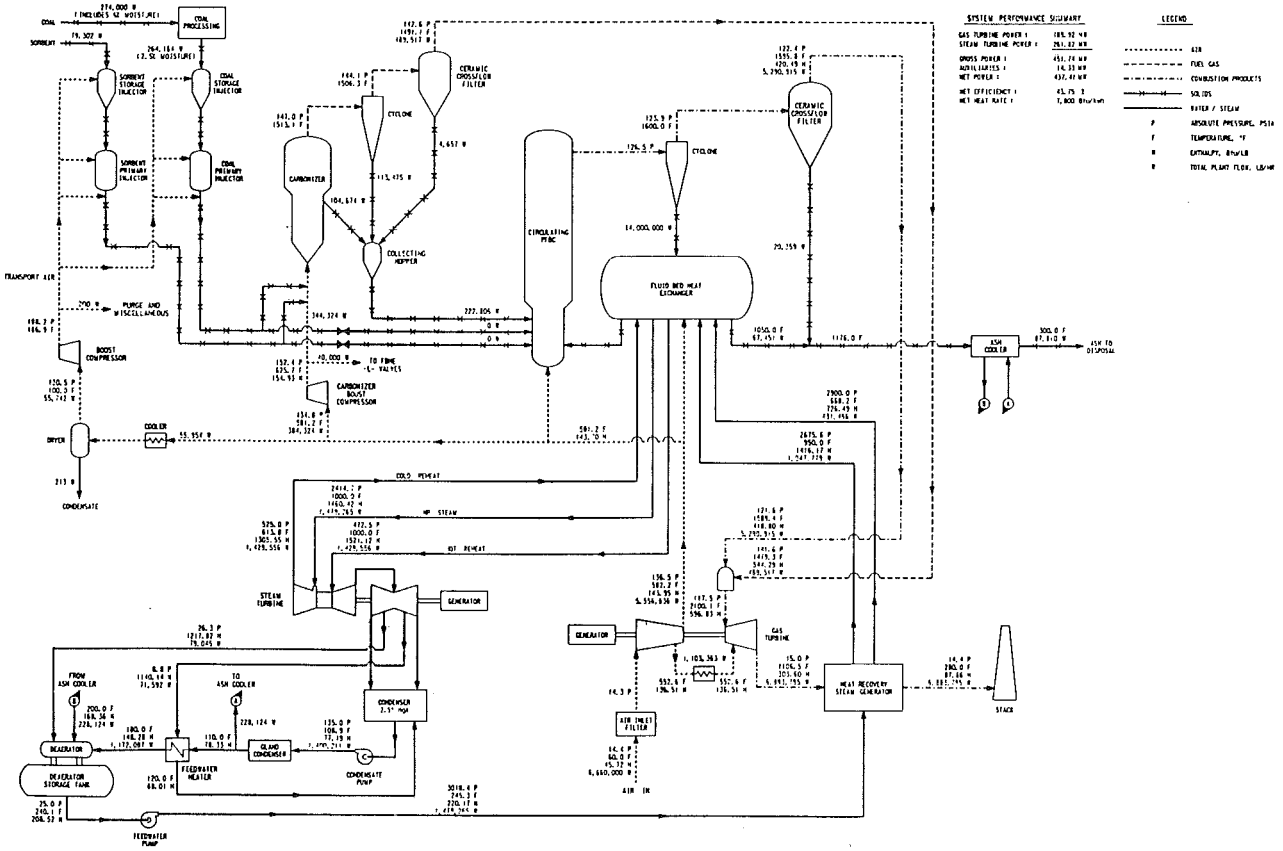

Fig. 8 Heat and material balances for a 1.0-MPa (10-atm) 437-MWe second-generation PFBC plant

Table 3 1.4-MPa (14-atm) versus 1.0-MPa (10-atm) PFBC plant performance

Description	Second-Generation PFBC Plant	
	1.4 MPa (14 atm)/ 816°C (1500°F) Carbonizer	1.0 MPa (10 atm)/ 816°C (1500°F) Carbonizer
Power Summary		
Net Capacity, MWe	452.8	437.4
Net Plant Efficiency, % (HHV)	43.6	43.8
Gross Power		
Gas Turbine, MWe	195.2	189.9
Steam Turbine, MWe	272.3	261.8
Turbine Parameters		
Gas Turbine Topping Combustor, °C (°F)	1149 (2100)	1149 (2100)
Main Steam Flow, kg/s (10^3 lb/h)	193.9 (1538.6)	186.4 (1479.2)
Consumables and Wastes		
Pittsburgh No. 8 Coal, kg/s (lb/h)*	35.8 (284,410)	34.5 (274,000)
HHV, MJ/kg (Btu/lb)*	30.02 (12,450)	30.02 (12,450)
Sulfur, wt%	2.89	2.89
Ash, wt%	9.94	9.94
Sorbent Flow, kg/s (lb/h)		
Dolomite	10.4 (82,315)	10.0 (79,302)
Limestone	—	—
Lime	—	—
Ash Production, kg/s (lb/h)		
Ash/Spent Sorbent	11.5 (91,144)	11.1 (87,810)
Fixed Sludge	—	—
Coal and Dolomite Drying—No. 2 Fuel Oil, m^3/h (gal/h)	0.36 (94)	0.83 (216)
Water Consumption, 10^3 m^3/d (10^3 gal/d)	21.1 (5575)	20.19 (5334)
*As received/before drying.		

Table 4 1.4-MPa (14-atm) versus 1.0-MPa (10-atm) PFBC plant economics

Description	Second-Generation PFBC Plant	
	1.4 MPa (14 atm)/ 816°C (1500°F) Carbonizer	1.0 MPa (10 atm)/ 816°C (1500°F) Carbonizer
Unit Size, MWe net	452.8	437.4
Net Plant Efficiency, % (HHV)	43.6	43.8
Total Plant Cost, $/kW	906.1	977.9
Total Plant Investment, $/kW	980.6	1058.2
Total Capital Requirement, $/kW	1037.0	1117.2
First Year Costs:		
Total O&M, $/kW • yr	38.0	41.4
Fixed O&M, $/kW • yr	24.7	26.9
Variable O&M, mills/kWh	2.34	2.54
Consumables, mills/kWh	3.37	3.62
Fuel Cost, mills/kWh	14.0	14.0
Levelized O&M:		
Fixed, $/kW • yr	43.2	46.4
Variable O&M, $/kW • yr	4.1	4.4
Consumables, mills/kWh	5.9	6.3
Fuel, mills/kWh	26.6	26.6
Levelized Carryover Charge, $/kW • yr	179.6	193.3
Levelized Busbar Cost, mills/kWh	75.7	79.5

of higher plant equipment costs. This is not surprising, since the lower pressure increases the gas volumetric flow rates; thus the diameters of the gas-carrying components increase accordingly, along with refractory requirements, structures, piping length, and other supporting services to the components.

Conclusions

The proposed second-generation PFBC plant concept appears ideal for meeting the future power needs of the electric utility industry. When fired with high-sulfur bituminous coal, it can provide a COE at least 20 percent lower than that of conventional PC-fired plants with wet limestone flue gas desulfurization and an operating efficiency of 45 percent based on the lower heating value of the coal. Higher efficiencies and lower COEs may also be possible. Emissions per megawatt of net power produced are considerably lower than those of PC-fired units, and components are amenable to shop assembly and barge shipment. In addition, it is modular; electric utilities can add power in smaller increments without sacrificing efficiency or economics.

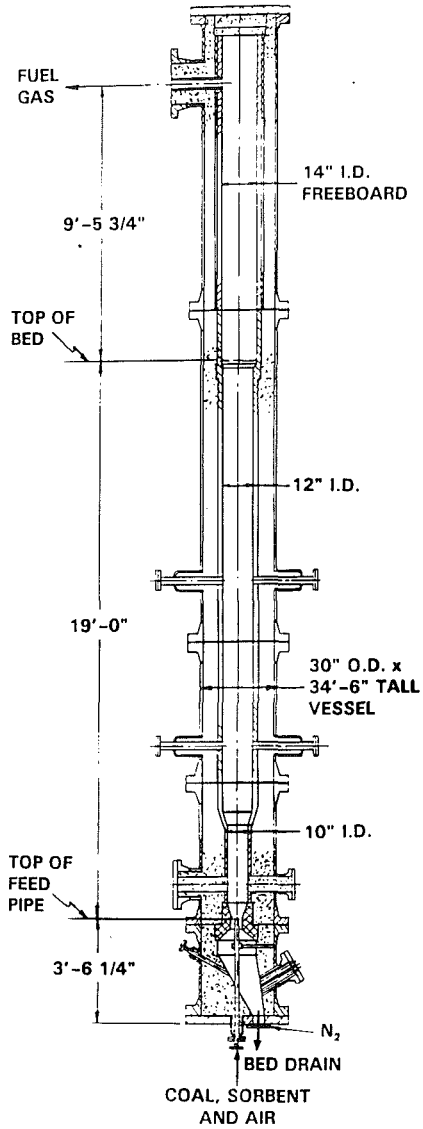

Fig. 9 254-mm (10-in.) carbonizer test unit

Phase 2 Testing Program

The proposed plant is attractive from many standpoints—COE, efficiency, etc., but it is not without risks. Pressurized carbonizer tests with in-situ tar cracking and sulfur capture must be performed. The gas streams and solid effluents from both the carbonizer and CPFBC must be characterized, their compatibility with HGCU equipment currently under development must be demonstrated, and topping combustion tests must be run. In Phase 2 of our DOE program, the needs and uncertainties regarding this plant are being addressed via a series of laboratory-scale tests on these separate components.

The first part of the planned Phase 2 test program—carbonizer testing—began in November 1991 at FWDC's Research Center in Livingston, New Jersey. Eight test series were completed in the carbonizer test unit shown in Fig. 9. Pittsburgh No. 8 and Illinois No. 6 bituminous coals and Eagle Butte

subbituminous coal have been successfully tested along with dolomite and limestone sorbents. Results from these tests have been most encouraging, bettering our commercial plant predictions. Preliminary information from these tests revealed greater than 90-percent sulfur capture, only half the coal nitrogen released in the carbonizer converted to ammonia, no tars in the carbonizer gas, and heating values of the gas close to those predicted. The unit has been modified for CPFBC testing, which should be completed by the third quarter of 1993. Integrated carbonizer/CPFBC testing will be conducted by FWDC in 1994.

Acknowledgments

FWDC is grateful to its team members—Gilbert/Commonwealth, Inc.; the Institute of Gas Technology; Westinghouse Electric Corporation (Power Generation Business Unit and Science and Technology Center); and Foster Wheeler Energy Corporation—for their contributions to the program and to the information presented in this paper.

References

Electric Power Research Institute, 1986, *TAG™—Technical Assessment Guide*, Vol. 1, EPRI P-4463-SR, Palo Alto, CA.

Garland, R. V., Pillsbury, P. W., and Vermes, G., 1986, "Generic Studies of Advanced Fluidized Bed Air Heater Technology," DOE/DE/40543-5, Westinghouse Electric Corporation, Orlando, FL.

Knowlton, T., et al., 1986, "Solids Pressure Reduction Without Lockhoppers: The Restricted Pipe Discharge System," presented at the Annual AIChE Meeting, Miami Beach, FL.

Criteria for Design With Structural Materials in Combined-Cycle Applications Above 815°F

R. W. Swindeman
Oak Ridge National Laboratory,
Oak Ridge, TN 37831

D. L. Marriott
Stress Engineering Services,
Cincinnati, OH 45246

A number of materials issues related to the design of piping and support components in high-temperature fluidized bed combustor systems were examined. These issues included the availability of long-time design data on structural materials, the general character of the creep and stress rupture behavior, the performance of weldments, and the assessment of damage accumulation. Emphasis was placed on alloy 800H, but several other alloys were briefly examined for use at temperatures above 816°C (1500°F). It was concluded that the character of the creep curve ranged significantly with chemistry, processing variables, and environment, and that the specification of design allowable stresses and life estimation techniques must be approached with caution for service above 816°C (1500°F).

Introduction

The development of combined-cycle power technology is being aggressively pursued throughout the world, and in the U.S. several systems of interest have been described by Bajura and Webb (1991). A schematic diagram of a second-generation pressurized fluidized bed combustor (PFBC) is shown in Fig. 1. Here, coal is fed to a carbonizer, which produces fuel gas, and char from the carbonizer is fed to a PFBC where complete combustion occurs. A calcium-based sorbent is used in both the carbonizer and PFBC to reduce sulfur dioxide emissions by 90 to 95 percent. Both gas streams are filtered to remove ash particles and fed to a topping combustor that delivers gas to the turbine at temperatures exceeding 1150°C (2100°F) (*Heat Engineering*, 1986). A heat recovery system on the turbine exhaust raises steam for additional power.

Gasifiers, carbonizers, and fluidized bed combustors are being designed for combined-cycle applications, and decisions are being made regarding the materials of construction for vessels, piping, and hardware for hot-gas cleanup systems. Issues that are being addressed also include design configurations of pressure vessels and piping to accommodate thermal stresses that result from cyclic operation to very high temperatures. This paper considers some of the materials issues that must be resolved for safe and reliable long-time operation of combined-cycle plants. The focus is on the PFBCs, but many of the issues are important to combined-cycle systems that incorporate gasifiers and carbonizers. The design and construction methods used in second-generation combined-cycle systems are similar to those incorporated into current PFBC, and many of these are outlined in a recent publication (ASME, 1991). Current designs for combined-cycle plants call for refractory-insulated vessels and piping to permit the use of structural steel operating at near ambient temperature, and provisions are made to accommodate the differential thermal expansion between the structural steel, the insulation, and the liner. When it is practical, components are water cooled to reduce temperatures and thereby eliminate hot corrosion and severe thermal stresses. Often, it is difficult to avoid the use of high-strength, corrosion-resistant alloys in critical structural components. This paper reviews the available pressure vessel materials, reviews alternate structural materials that may be candidates for pressure boundary and structural applications, and summarizes some material performance considerations that bear on the issue of reliability.

Alloys for High-Temperature Pressure Boundary Application

Pressure-bearing components are required to meet construction codes such as the American Society of Mechanical Engineers (ASME) B31.1 piping code or the ASME Boiler and Pressure Vessel (BPV) Code. If the piping is not insulated from the process stream temperature, then the materials selection is limited for service above 816°C (1500°F). In Fig. 2, a comparison is made of the allowable stresses for alloys currently approved for construction under the rules of Sect. VIII, Div. 1 of the ASME BPV Code. The stress tables are provided in various Code Cases or in Sect. II, Part D. Alloys include two cobalt-bearing alloys (alloy 617 and alloy 556), two high-strength nickel base alloys (alloy 230 and alloy 625), and two grades of alloy 810 and alloy 811). Also, in the ASME BPV Code Sect. I, one stainless steel (253MA®) is approved for use to 900°C (1650°F). Only two materials (alloy 617 and alloy 810) have allowable stresses to 982°C (1800°F). The cobalt-bearing alloys and the nickel-base alloys have the highest strengths, alloy 810 and alloy 811 are intermediate in strength, and 253MA stainless steel is the weakest.

Contributed by the International Gas Turbine Institute and presented at the 38th International Gas Turbine and Aeroengine Congress and Exposition, Cincinnati, Ohio, May 24-27, 1993. Manuscript received at ASME Headquarters March 3, 1993. Paper No. 93-GT-203. Associate Technical Editor: H. Lukas.

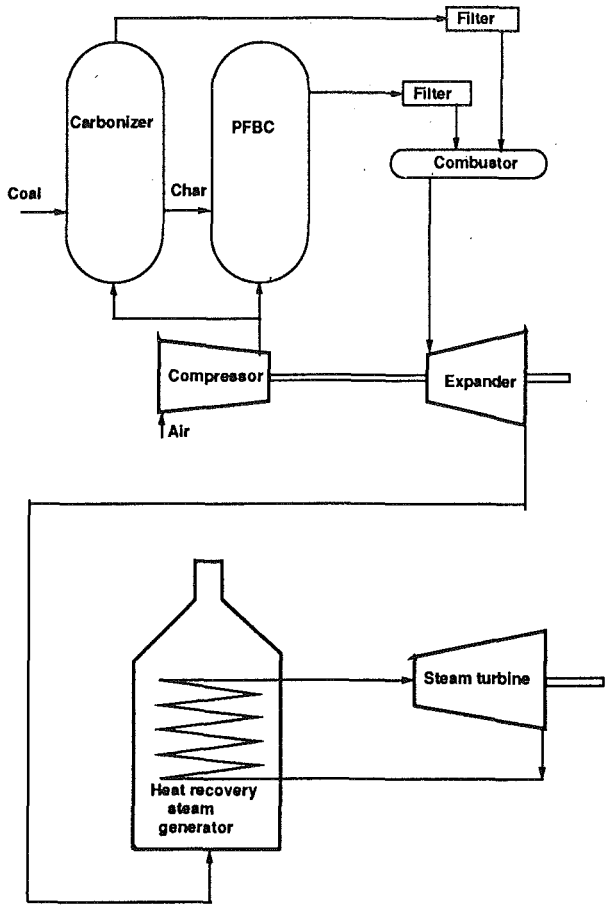

Fig. 1 Schematic drawing of a second-generation combined-cycle power plant

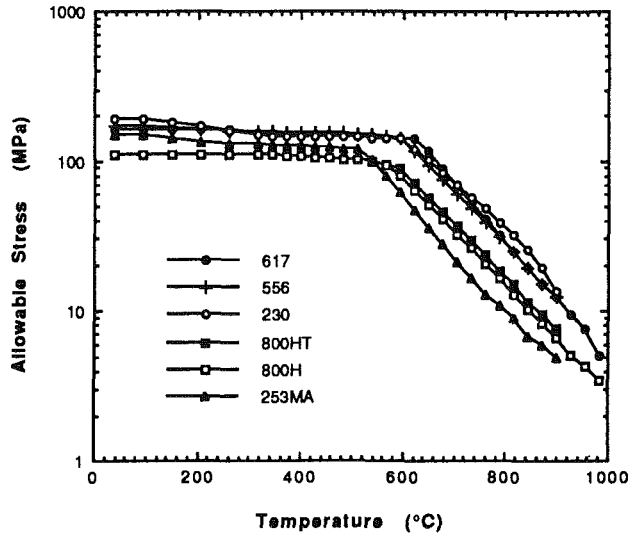

Fig. 2 Stress versus temperature for several alloys; Code approved for service above 816°C

The allowable stresses plotted in Fig. 2 are derived from one of the strength criteria identified in appropriate construction code, and in most cases the stresses at 816°C (1500°F) and above are based on 67 percent of the average stress to produce rupture in 100,000 h at the design temperature. Concerns exist regarding the adequacy of this criterion for very long time service, and these concerns are described later in the paper. The selection of an alloy from an available group, of course, depends on such issues as cost, fabricability, corrosion resistance, and strength requirements. A number of reviews to guide in the materials selection are available, and a recent paper by Natesan and Podolski (1991) provides information on corrosion behavior of 29 alloys in FBC cogeneration environments. The Code-approved alloys included in their evaluations are alloy 800H, alloy 556, and 253MA stainless steel. These and other alloys were exposed in laboratory tests and in a variety of locations in FBC systems. Natesan and Podolski (1991) showed that the relative ranking of the materials was highly variable and changed greatly with temperature and gas composition.

Alternate High-Temperature Structural Alloys

The alloys that are available for structural applications, apart from pressure boundary applications, that are included in the corrosion evaluations of Natesan and Podolski (1991) range from cobalt-based alloys to nickel-based alloys and to cast and wrought stainless steels. The selection is too great to be covered here in any detail, so only representative alloys are discussed. For oxidizing environments containing sulfur, cobalt-based alloys are found to perform relatively well. For the oxidizing environments expected for the PFBC, the high nickel-chromium-iron alloys serve well. If strength is not of great concern, less expensive materials such as types 304 and 310 stainless steels are adequate. Although the extension of type 304 stainless steel for pressure containment above 816°C (1500°F) was judged to be impractical by Bynum et al. (1992) because of poor strength, interest remains in extending the use of type 310 stainless steel to 871°C (1600°F) (Prager, 1992). Type 310 stainless steel, for example, is used as liner piping in the Tidd plant PFBC. Newer alloys with improved corrosion resistance have also been proposed for service above 816°C (1500°F) and could serve a similar function. These include a silicon-aluminum modified 18-8 stainless steel identified as RA85® (Kelly, 1989), a high-strength Fe-Ni-Cr-Nb-N alloy identified as HR-120® (Myers, 1991; Ernst and Lai, 1992) and a high-strength cobalt-bearing alloy identified as HR-160® (Haynes International, 1990). Experience is being gained in the use of these materials, and the data needed to produce allowable design stresses are being accumulated. Figures 3(*a*) and 3(*b*) compare typical alloys on the basis of creep strength at 10,000 h reported by alloys vendors. Figure 3(*a*) includes the alloys approved for pressure boundary applications in the BPV Code, while Fig. 3(*b*) compares the alternate structural alloys. It may be seen that a wide range of strength levels exists, and at 982°C (1800°F) the difference in strength between the weakest material (253MA stainless steel) and the strongest (alloy 617) is a factor of two. The developmental alloys HR-120 (essentially a nickel-based alloy) and HR-160 (containing cobalt) have excellent strengths at 982°C (1800°F), while both RA333® and RA85H have much improved strength relative to type 310 stainless steel. RA333 and type 310 stainless steel have been used for components in the PFBC hot-gas cleanup vessel at Grimethrope pilot plant (Stringer et al., 1991) and are used in the hot-gas cleanup vessel at the Tidd plant, where strength, fabricability, and corrosion resistance are needed (Manjoine and Filstrup, 1992). Much remains to be learned about fabrication technology before the full potential of the newer alloys can be exploited, and issues related to fabrication technology are discussed later.

Design Criteria Issues

Most of the experience in the design and operation of components for long-time service above 816°C (1500°F) has been gained in the petroleum and petrochemical industries. Frequent inspection, repair, and replacement of components are common, and special procedures are used to estimate remaining life. The American Petroleum Institute (API) Recommended

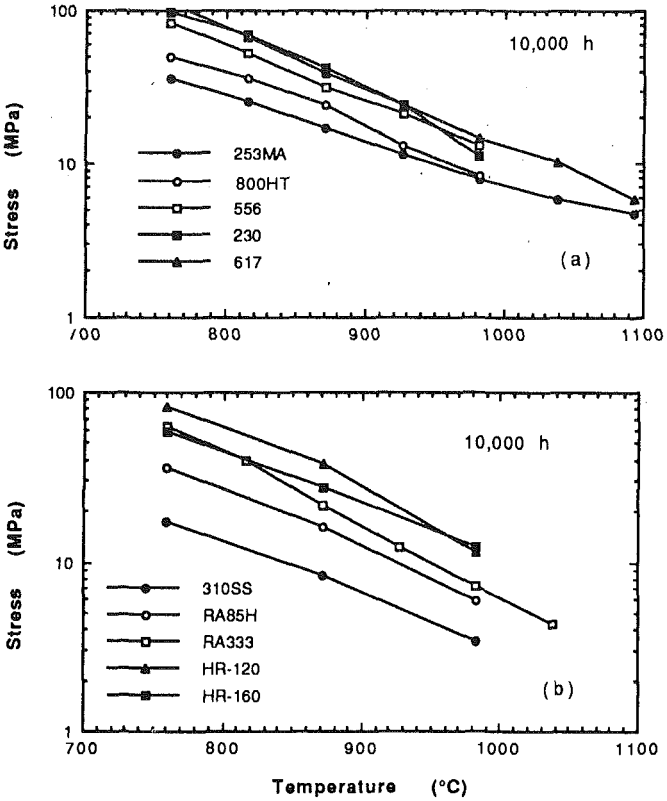

Fig. 3 Stress to produce rupture in 10,000 h versus temperature: (*a*) Code alloys and (*b*) alternate alloys

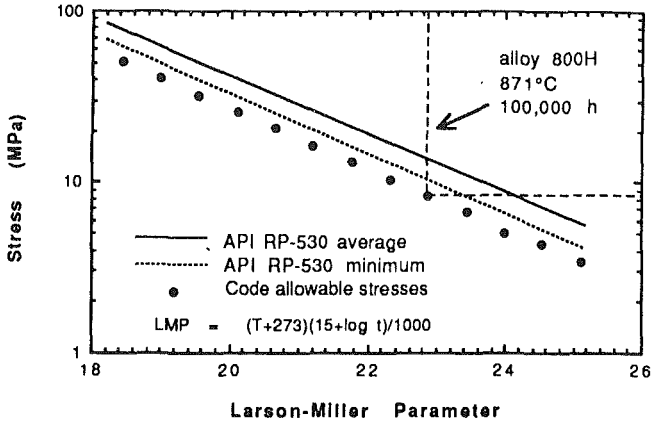

Fig. 4 Log stress versus the Larson-Miller parameter for API RP-530 average and minimum strength curves and ASME Code allowables for alloy 800H

Practice (RP) 530 is an example of the design philosophy for heater tubes. Similar to the ASME piping codes B31.1 and B31.3 and BPV Code, specific alloys are approved, and temperature limits are set for each. In contrast to the ASME piping codes and the BPV Sect. I and VIII, however, data are provided in RP-530 that identify the stresses corresponding to design lives of 20, 40, 60, and 100 thousand hours. Damage and residual life assessments are commonly performed on serviced components using RP-530. ASME Sect. I and Sect VIII only address new construction, one allowable stress is provided for each material as a function of temperature, and there is no time limit. Also, RP-530 provides information on corrosion allowances and guidelines for accommodating creep-fatigue, whereas the ASME Sect. I and Sect. VIII codes provide no information on fatigue and creep-fatigue for service above 427°C (800°F), and rules for expansion joints, needed in PFBC piping, have only recently been introduced into the ASME BPV code (Becht, 1989).

The complexity of establishing rules for construction at very high temperatures is discussed in connection with the ASME Sect. III Code Case N-47 by Corum and Blass (1991). Here, alloy 617 is being considered for use to 982°C (1800°F) in modular high-temperature gas-cooled reactors. Lacking long-time experience, the draft code case for alloy 617 requires design for finite life, consideration of strain limits, consideration of creep-fatigue damage interaction, and the construction of isochronous stress versus strain curves for use in analysis for times extending to 100,000 h. Data for most structural materials of interest to second-generation combined-cycle systems are inadequate to develop a code case comparable to N-47, and, even if a comparable design methodology could be developed, the expense of using such a procedure is prohibitive for many applications. Nevertheless, awareness of the design margin that comes from a design-by-analysis code case is needed for reliable design of second-generation combined-cycle structural components.

The design margin provided by the existing ASME criteria is estimated to be at least a factor of 20 in life at temperatures to 816°C (1500°F). The question that must be addressed in the use of existing alloys or the approval of new alloys concerns the adequacy of the current ASME code criteria to assure safety margins of at least 20 for temperatures above 816°C (1500°F). The criteria for setting allowable stresses are identified in Appendix 1 and Appendix 2 of ASME Sect. VIII, and Sect. II, Part D. In the creep range, the allowable stresses are based on the lowest of the following: 100 percent of the average stress to produce a creep rate of 0.01 percent/1000 h; 67 percent of the average stress to cause rupture at the end of 100,000 h; and 80 percent of the minimum stress to cause rupture at the end of 100,000 h. Usually, the average rupture strength controls the allowable stress at high temperature, and the breaks in the curves plotted in Fig. 2 correspond to the change in the controlling criterion from tensile (time-independent) to stress rupture (time-dependent). In some materials, creep or creep rate is the time-dependent criterion, but such information is not easily obtained. Generally, fewer creep data and creep rate data are available than rupture data. Also, creep data tend to show much more variability than rupture data, hence the analysis of creep data is generally more difficult than analysis of rupture data. For these reasons, it is easier to examine design margins that are based on rupture life.

If one assumes that a simple power law relates life, t_r, to stress, σ, at any given temperature, T, then:

$$t_r = A\sigma^{-n} \tag{1}$$

where A and n are temperature-dependent constants. Generally, n tends to decrease with temperature, being greater than 10 at very low temperature and less than 2 at very high temperature. Typically, n is in the range 4 to 8. Assuming that the governing stress criterion is 67 percent of the average strength at 100,000 h (t_o) and calling this stress σ_o, one can substitute into Eq. (1) and obtain:

$$t_r/t_o = (\sigma_o/\sigma)^n = (1.5)^n \tag{2}$$

Thus, the design margin given by the ratio t/t_o will vary from more than 25 when n is 8 to 5 when n is 4. The actual scatter in the rupture life becomes a very important consideration at temperatures where n is small because of the reduced design margin, yet design codes do not provide much information regarding the scatter in the data code. Some information may be gleaned from the RP-530 document, which supplies values of n over a useful temperature range as well as a Larson–Miller parametric curve for average rupture strength and minimum rupture strength. This information is provided in Fig. 4 for alloy 800H. Here, the Larson–Miller Parameter (LMP) is given by:

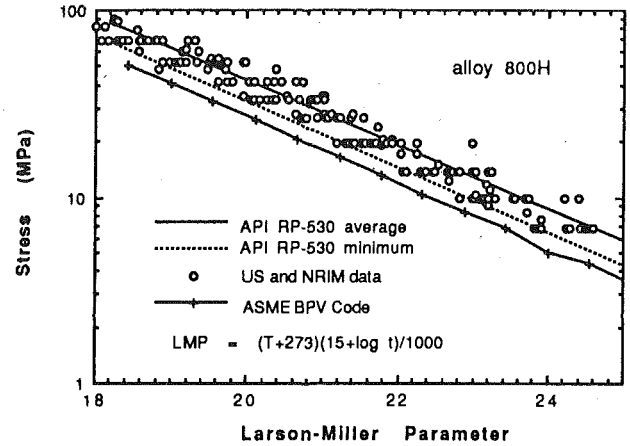

Fig. 5 Comparison of log stress versus Larson-Miller parameter for alloy 800H data with the API RP-530 curves and the ASME Code allowables

$$\text{LMP} = (T+273)(C+\log_{10} t_r)10^{-3} \quad (3)$$

where T is temperature in Celsius and t_r is time in h, and the Larson-Miller constant, C, is 15. Included in the figure are allowable stresses for alloy 800H from ASME Sect. VIII. The allowable stresses for this material appear to be less than 67 percent of the average strength, and the margin on life based on the design stress and the average life at the design stress is approximately a factor of 12. The margin based on minimum life is approximately a factor of 2.5. These margins are smaller than observed at temperatures below 816°C (1500°F). Trends are shown more clearly by an examination of some of the stress-rupture data for alloy 800H relative to the design curves. In Fig. 5 the RP-530 curves and ASME allowable stress trend curves have been redrawn, and data from U.S. and Japanese (NRIM, 1978a) sources have been plotted. Examination of the data relative to the curves reveals that the RP-530 curve represents a reasonable minimum, but the data tend to fall below the average curve as the stress decreases and the LMP increases. The smaller margins on life that appear to exist at higher temperatures must cover the effects of many uncertainties that relate to both design and materials related factors. The margins are adequate for alloy 800H, but experience is lacking in the application of new materials in new technology areas. Concerns regarding the effect of materials behavior on design margins for new alloys include the influence of composition, grain size, cold work, environment, and weldments. Examples of these effects are provided in the next section, using alloy 800H as a reference.

Factors Influencing Creep, Stress Rupture, and Fatigue

Alloy 800H often exhibits a creep curve with a large tertiary component at temperatures below 816°C (1500°F) (Booker, 1983). Because of concerns regarding the geometric stability of components fabricated from materials with low tertiary strain thresholds, the ASME CC N-47 includes the time to teritary creep and strain limits into the criteria for setting allowable stresses in the creep regime. A similar concern exists above 816°C (1500°F), but it must be recognized that materials with low tertiary strain limits have been successfully used for many years at these temperatures. Depending on the composition, processing variables, degree of cold work, grain size, and environment, the tertiary creep characteristics of alloy 800H vary significantly at temperatures above 816°C (1500°F). Nickel et al. (1986) find that tube products at 950°C (1740°F) and 30 MPa exhibit tertiary creep starting at strains in the range of 1 to 10 percent, while bar products exhibit tertiary creep from the start of the test. Typical trends that they report

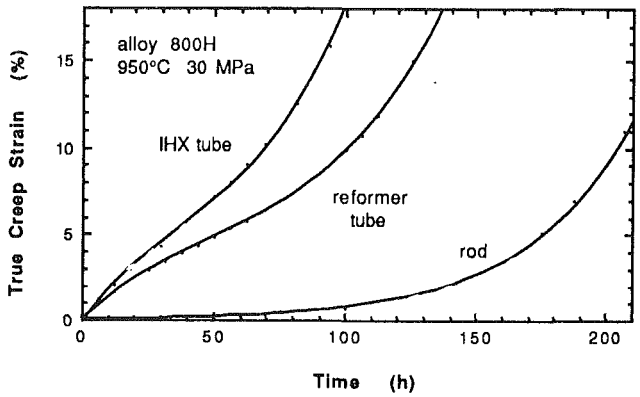

Fig. 6 Shape of the creep curve for alloy 800H reported by Nickel et al. (1986) at 950°C and 30 MPa

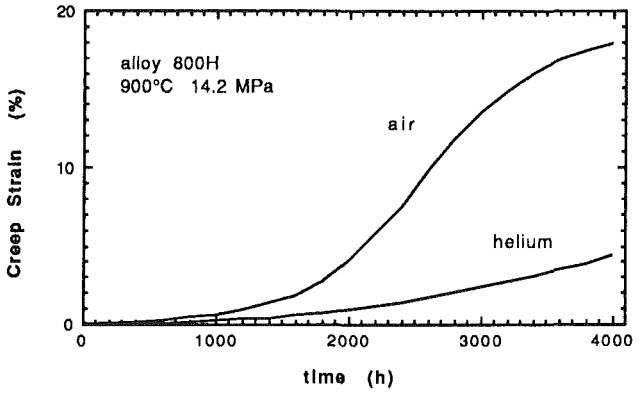

Fig. 7 Shape of creep curves for alloy 800H in helium and air reported by Cook and Sutton for 900°C and 14.2 MPa

are illustrated by the creep curves in Fig. 6. The kinds of differences shown in Fig. 6 are accommodated within the scatter of the stress rupture scatterband but could give rise to difficulties in defining design criteria based on creep rate or creep strain. Cook and Sutton (1978) observe a sigmoidal shaped creep curve for alloy 800H tested in air at 900 and 950°C (1650 and 1742°F). Tertiary creep appears very early in the air test but the creep rate then decelerates to a near constant rate and eventually decreases again when strains exceeded 10 percent. The trend for one test at 900°C (1650°F) is sketched in Fig. 7. Tests in helium reveal only tertiary character, as shown in Fig. 7, but the creep rate is lower in helium than in air. Cook and Sutton attribute the sigmoidal creep behavior in air to a strengthening effect by internal oxidation. Since the design curves for high temperature are based on air testing, some of the design margin may be lost in reducing and inert environments. Environments within the bed of PFBCs are highly variable and difficult to predict. However, compositions are generally defined for the gas stream passing through the piping and gas cleanup vessels. Page et al. (1984) describe the creep of alloy 800H in air and a sulfur-bearing "complex mulitoxidant gas" (CMG) at 815°C. The equilibrium partial pressures of sulfur and oxygen contents at 815°C and 6.9 MPa are reported to be 1.29×10^{-8} and 3.32×10^{-19}, respectively. Page et al. (1984) find the creep curve to be relatively stable in air but to have a tertiary character in the CMG, as indicated by the sketch in Fig. 8. Creep in CMG is more rapid than creep in air, and the rupture strength is less in CMG than in air, apparently eroding away most of the design margin. However, as stresses are lowered, the rupture lives in CMG tend toward lives observed in air at comparable stresses. Studies by Smolik and Flinn (1985) on alloy 800H indicate that the rupture lives of pressurized tubes in sulfur-containing atmos-

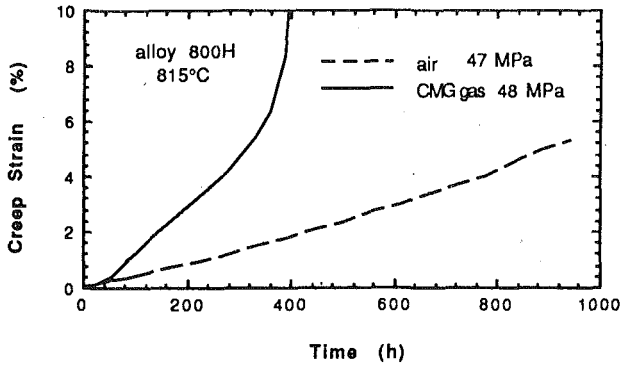

Fig. 8 Shape of creep curves for alloy 800H in CMG gas and air reported by Page et al. (1984) at 815°C

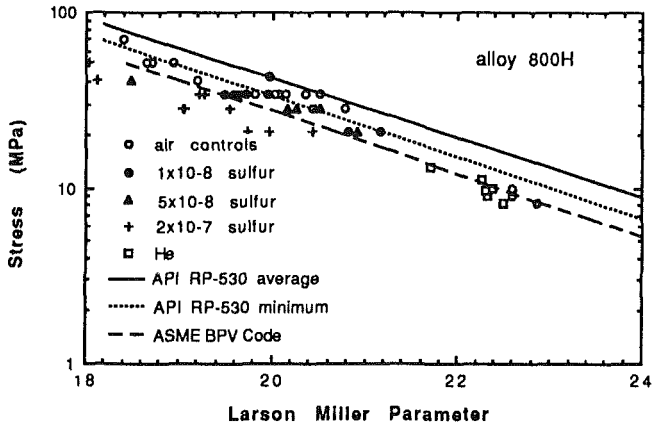

Fig. 9 Comparison of log stress versus the Larson-Miller parameter for alloy 800H data obtained in various environments with the API RP-530 and ASME curves

pheres are less than those in air, and the loss of life increases with increasing sulfur partial pressures. Creep ductilities are lower in the sulfur-containing gas. Consistent with the findings of Cook and Sutton (1978), the stress rupture lives of tubes tested in low sulfur-containing gas ($<10^{-7}$ atm) tend toward the life of tubes tested in air as stresses decrease.

It is clear that the changing and inconsistent relationships between time to 1 percent creep, minimum creep rate, and rupture life are issues that are important in the design of components fabricated from alloy 800H, as well as the possible loss in design margins due to reducing, inert, or very aggressive (sulfidizing) environments. Stress-rupture data obtained in "other environments," as well as results from "control tests" in air, are plotted as log stress versus the LMP in Fig. 9 for alloy 800H. The RP-530 and ASME curves are included in the figure for comparison. It may be seen that several data fall short of performance expectations. Highly sulfidizing atmospheres produce data that fall short of the ASME design curve, and one needs to employ large corrosion factors when using the material in an aggressive atmosphere. Even data from some of the tests in helium and control tests in air fall near the ASME design curve, albeit data come from short-time testing programs.

Materials other than alloy 617 and 800H exhibit essentially tertiary creep behavior at temperatures above 816°C (1500°F), but little or no information is available in the open literature for a systematic study. Vendors often report design curves such as the stress versus the average time to produce a specific strain level or the stress to produce an average creep rate. Such information is available for alloy 556 (Haynes International, 1988), alloy 230 (Haynes International, 1987), and 253MA stainless steel (Kelly, 1983). The design curves represent "disassociated" or "processed" data. Data sets are needed where temperature, stress, time to specific strains, and rupture data are reported for each test. Such full data sets are rarely available in the literature, even for the alloys approved for pressure vessel service, and without such information it is difficult to establish design margins that are based on strains or strain rates. In a few cases, the shape of the creep curves are provided. Page et al. (1984) show creep curves for type 310 stainless steel in air and CMG at 815°C. The curves have a tertiary character and indicate no environmental effect. They also show the heat-to-heat variation in the minimum creep rate for both type 310 stainless steel and RA333 tested in CMG. The variation in creep rate is more than an order of magnitude. Kelly (1984) provides data for RA333 tested in air that include several heats and product forms. Sufficient information is available to conclude that RA333 is stable in creep at high stresses and tends toward a tertiary creep character at low stresses. Heat-to-heat variation in minimum creep rate is approximately an order of magnitude for the same stress and temperature. Prager (1992) reports results from a recent testing program designed to expand the data base for types 309 and 310 stainless steels. Testing temperatures are limited to 871°C (1600°F) and below, but results for several heats are provided. Negative creep is reported at the start of some tests, and tertiary creep often begin at strains below 1 percent. By prior aging, Prager was able to eliminate the negative creep at the start of testing. Grain size is found to be influential, with coarser grain size producing lower creep rates and longer lives at 816 and 871°C.

The issue of cold work in solid solution nickel- and cobalt-based alloys at temperatures above 815°C is addressed by Klarstrom (1991), and the evaluation includes both alloy 230 and alloy 625. Generally, small levels of cold work, say 5 percent, affect the kinetics of carbide precipitation and produce small improvements in life. Large levels of cold work promote recrystallization, and conditions that cause very fine grain size produce a loss in rupture life. Similar effects are observed by Persson (1978) in alloy 800. He reports stress rupture data after solution treating and cold working 10, 20, and 30 percent. At 800°F (1472°F), 10 percent cold work produces approximately 20 percent strengthening that endures for at least 20,000 h, while 30 percent cold work produces approximately 20 percent loss in strength. At 900°C (1650°F), all three levels of cold work produce at least 20 percent loss in strength at 10,000 h.

The high-temperature fatigue and creep-fatigue behavior of alloy 617 has been examined extensively for the development of ASME Sect. III draft Code Case, and design fatigue curves to 982°C (1800°F) are described by Corum and Blass (1992). Low-cycle fatigue curves at temperatures above 816°C (1500°F) have been produced on other alloys of interest for second-generation combined-cycle applications. These include RA333 (Kelly, 1984; Manjoine, 1991), alloy 556 (Krukemyer, 1991), and alloy 230 (Rothman, 1991). Generally, the high-temperature alloys exhibit similar fatigue curves. Stronger alloys tend to have better fatigue resistance as the cycles increase. Differences may be seen in Fig. 10, which compares the design fatigue curve for alloy 617 at 871°C (1600°F) to fatigue curves for several alloys. All data fall above the design curve for alloy 617. Direct comparisons of one alloy to another, however, are not meaningful since testing frequencies vary from one group of data to another.

Weldments

Some hardware and components in the PFBC piping and gas cleanup systems contain structural weldments, and the available rods, electrodes, and filler metals for BPV Code applications are chosen from ASME, Sect. II, Part C. Even when constructed to Code requirements, the integrity of weld-

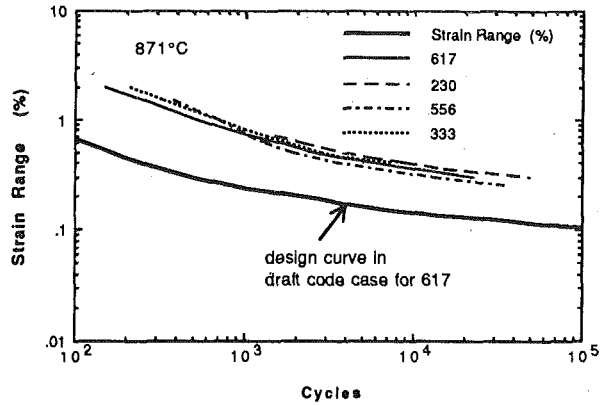

Fig. 10 Fatigue curves for several high-temperature alloys at 871°C compared to the design curve for alloy 617 from Corum and Blass (1991)

ments under creep and creep-fatigue loadings conditions remains an issue for high-temperature service. Weldment strength reduction factors linked to design life have been developed for CC-47, but the estimation of reduction factors remains as a major issue to be resolved in the development of rules for high-temperature construction codes (Corum and Blass, 1991). For construction with alloy 800H at temperatures above 816°C (1500°F), dissimilar metal welds are recommended when strength is required (INCO, 1986). Materials include welding electrode 117 and filler metal 617. Both of these alloys exhibit strengths well in excess of alloy 800H, since they are matching weld metals for alloy 617 (INCO, 1979). An overmatch in strength causes an uncertainty weldment performance, since weldment reduction factors are based on the relative creep strength of deposited weld metal to base metal and do not incorporate restraint effects produced by different creep strengths in the dissimilar metals. Filler metals for alloy 556, RA333, and 253MA stainless steel have essentially the same compositions as the base metals, and meager data indicate that the weld metals have similar strengths to base metal (McCoy and King, 1985; Swindeman et al., 1990). Alloy 556 has been used to join HR-160 and HR-120 but stress rupture data have not been available for these joints. An important issue in the use of weldments at temperatures above 815°C is whether or not to perform solution treatment after welding. It seems likely that residual stresses will be relieved during service, and often cast structures in welds will have better strength than wrought structures. Exploratory studies in RA333 indicate that solution treated weldments have better life and ductility (Swindeman et al., 1990). Little is known about the performance of weldments under stress and PFBC environments, although Natesan and Wang (1991) report data on the corrosion of weld metals in AFBC environments.

Damage Estimation

Capability is needed to estimate remaining life in PFBC components after large operational temperature or pressure changes in the duty cycle and thermal transients caused by turbine trips or PFBC instabilities. Excessive creep distortion, thermal fatigue, creep-fatigue interactions, creep-ratcheting, corrosion-fatigue, and erosion-corrosion are damage mechanisms that lead to loss of function. Often, a judgment is made in regard to the predominant failure mode, and an analysis is made on that basis. For example, McFarlane (1991) chose not to consider cycling in evaluating the life of components fabricated from alloy 617 and alloy 800H and operating in oil refinery and similar process applications. The number of cycles was judged to be too low to accumulate much fatigue damage, so only linear damage based on time fractions was used. However, he found it necessary to take into consideration the thermal stresses and their redistribution in order to arrive at a reasonable estimation of life. Gommans et al. (1992) examined several approaches to estimate damage in alloy 800H components at 800°C (1472°F) and chose a creep strain limit of 7 percent. This approach eliminated the need to consider tertiary creep in damage summation and permitted an estimate of remaining life based on strain rate rather than life fractions. Manjoine and Filstrup (1992), on the other hand, had an application for alloy RA333 in a PFBC vessel. The primary stresses were very low but the thermal stresses were very high. They chose to use a fatigue analysis in which the low-cycle fatigue curve was assumed to be strain rate dependent and damage was summed on a cyclic life-fraction basis. They were able to qualify their design for the intended life by this procedure.

Often, the designer uses linear damage accumulation methods that incorporate time fractions for creep damage and cycle fractions for fatigue damage. When significant creep and fatigue damage is expected, the procedure outlined by Campbell (1975) is followed. Here, both time fractions for creep damage and life fractions for fatigue damage are summed.

One of the limitations in the use of linear damage based on life and cycle fractions is the lack of understanding concerning continuum damage relationships. A promising alternate approach is Kachanov damage concept. Here, the creep rate, $d\epsilon/dt$, in a component under constant stress, σ, and temperature is given by:

$$d\epsilon/dt = K\sigma^{n'}/(1-\omega)^m \tag{4}$$

$$d\omega/dt = B\sigma^p/(1-\omega)^q \tag{5}$$

where ω is known as damage and B, K, n', m, p, and q are material constants. Solving the differential equations gives an equation for the creep curve of the form:

$$\epsilon_c = \lambda\epsilon_0 t_r[1-(t/t_r)^{1/\lambda}] \tag{6}$$

$$t_r = 1/[(1+q)\sigma^p] \tag{7}$$

$$\lambda = (1+p)/(1+p-q), \tag{8}$$

where ϵ_0 is an integration constant, m, p, and q are constants of the same order of magnitude as n' and the stress exponent in the Norton law for the minimum creep rate, mcr:

$$\text{mcr} = K\sigma^{n'}. \tag{9}$$

Typically, n' is in the range 4 to 8 and is often close to the stress exponent, n, observed in the stress versus rupture life correlation given by Eq. (1). Assuming that ω is zero at the time zero, then inspection of Eqs. (4) and (9) reveals that minimum creep rate will occur at time zero, and the creep rate will increase throughout the life. Rupture occurs at t_r, and the creep strain at rupture, ϵ_r, is obtained from Eq. (6) as:

$$\epsilon\rho = \lambda\epsilon_0 t_r \tag{10}$$

The continuous increase in creep rate is consistent with the tertiary character of the creep curve for many of the materials tested at temperature above 816°C (1500°F), especially some of the testing that was performed in inert atmospheres. Hence, the use of the Kachanov approach is attractive for application to very high temperatures. Experimental data are required to quantify the constants given above, and these constants may vary with temperature, stress, environment, and metallurgical factors such as grain size and heat treatment. When n is close to n', the constant ϵ_0 may be obtained from the Monkman–Grant (M–G) plot of log rupture life versus log mcr, and this is a measure of the material's tolerance to creep strain. The constant λ is a measure of the material's tolerance to local strain concentration. A high value for λ, say 5 or more, may be observed in a creep ductile material and low value, say 1 or 2, would correspond to a creep brittle material.

The M–G plot requires paired values for minimum creep rate and rupture life. Such data are available for alloy 800HT and RA333, and trends are shown in Figs. 11 and 12, respec-

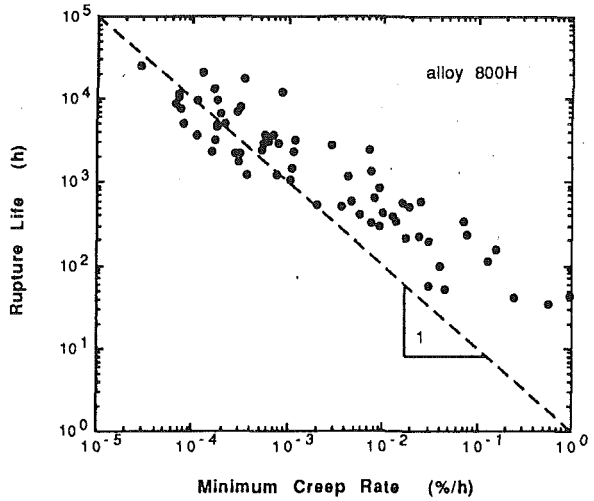

Fig. 11 Monkman-Grant plot of log rupture life versus log minimum creep rate for alloy 800H

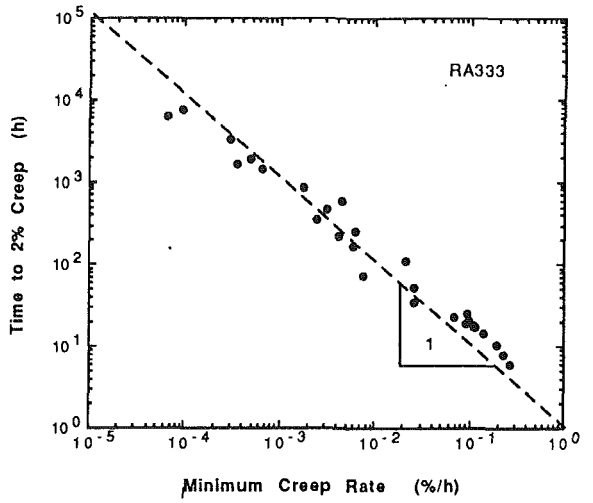

Fig. 13 Plot of log time to 2 percent creep strain versus log minimum creep rate for RA333

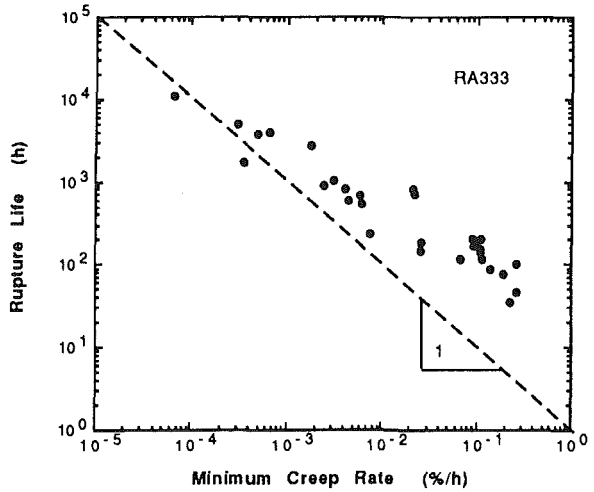

Fig. 12 Monkman-Grant plot of log rupture life versus log minimum creep rate for RA333 (Kelly, 1984)

tively. In both figures, it is apparent the scatter of data is large and that rupture life is not inversely proportional to the mcr for alloy 800H and RA333. It follows that Eq. (10) is not always applicable for the alloys under the assumption of constant λ and ϵ_0. The slope of the curves suggests a decreasing rupture ductility with increasing test time. The problem may be resolved by introducing an exponent in the M-G correlation to account for a decreasing strain tolerance with decreasing mcr. Another approach is to base the M-G correlation on a strain limit such as 5 percent. A strain limit presents no problem in the use of the Kachanov damage summation approach and reduces the influence that recrystallization, internal oxidation, and necking have on the correlating of mcr with the failure criterion. Data that couple temperature, stress, and the time to a specific strain are not readily available in the open literature, but enough information was found to construct M-G plots for a few alloys. Figure 13 shows the log time to 2 percent strain versus log mcr for RA333, and data were taken from Kelly (1984). Trends indicate that, to a first approximation, there exists linear relationship between mcr and the time to 2 percent creep strain.

Summary and Conclusions

Much work is needed to develop a consensus for design methodologies and material performance criteria for pressure vessels and piping in second-generation combined-cycle applications. The various aspects covered in this paper only provide a limited view of the issues and problems that must be addressed, and it is only through shared experiences that meaningful solutions to potential problems will be developed.

Because of the large base of experience and data, alloy 800H is used to identify some of the concerns regarding material behavior. It is shown that the design margins built into construction codes are less than a factor of 20 in life for temperature above 816°C (1500°F), and that environmental effects may consume a significant portion of the margin. It is shown that the creep curves for alloy 800H are highly variable and the correlation between the minimum creep rate and rupture life (Monkman-Grant plot) exhibits wide scatter. It is suggested that the use of a strain limit, say 2 or 5 percent, as a substitute for rupture life may be a useful criterion on which to set design stresses.

Acknowledgments

This work was supported in part by the U.S. Department of Energy, Fossil Energy Advanced Research and Technology Development (AR&TD) Materials Program, [DOE/FE AA 15 10 10 0, Work Breakdown Structure Element ORNL-2(B)] under contract DE-AC05-84OR21400 with Martin Marietta Energy Systems, Inc. and the Welding Research Council through PVRC Grant 92-05. Reviewers of the paper at ORNL were H. E. McCoy and R. R. Judkins.

References

ASME, 1991, *Proceedings of the 1991 International Conference on Fluidized Bed Combustion*, American Society of Mechanical Engineers, New York.

Bajura, R. A., and Webb, H. A., 1991, "The Marriage of Gas Turbines and Coal," *Mechanical Engineering*, Sept., pp. 58-63.

Becht, C., IV, 1989, "Fatigue and Elevated Temperature Design of Bellows," *Metallic Bellows and Expansion Joints-1989*, ASME PVP-Vol. 168, pp. 27-36.

Booker, M. K., 1983, "Analysis of the Creep Strain-Time Behavior of Alloy 800," ORNL/TM-8449, Oak Ridge National Laboratory, Oak Ridge, TN, May.

Bynum, J. E., Ellis, F. V., Roberts, B. W., and Canonico, D. A., 1992, "High Temperature Creep of Type 304 Stainless Steel," *Stress Classification, Robust Methods, and Elevated Temperature Design*, ASME PVP-Vol. 230, New York, pp. 67-83.

Campbell, R. D., 1975, "Creep-Fatigue Calculation Procedure for Code Case 1592," *Advances in Design for Elevated Temperature Environment*, ASME, New York, pp. 45-56.

Cook, R. H., and Sutton, J. C., 1978, "Creep Cracking of Alloy 800H in Air and Helium at 850-950°C," HTMP Report No. 34, Flight Refuelling, Ltd., Wimborne, Dorset, United Kingdom, Dec.

Corum, J. M., and Blass, J. J., 1991, "Rules for the Design of Alloy 617 Nuclear Components to Very High Temperatures," *Fatigue, Fracture, and Risk 1991*, ASME PVP-Vol. 215, pp. 147-153.

Ernst, S. C., and Lai, G. Y., 1991, "A New High Strength Fe-Ni-Cr-Nb-N Alloy for Elevated Temperature Applications," *Heat Resistant Materials*, ASM International, Materials Park, OH, pp. 115–121.

Gommans, R. J., Verheesen, K. F., and Heerings, J. H., 1992, "Oxidation Cracking and Residual Creep Life of an Incoloy 800H Bottom Manifold in a Steam Reformer at 800°C," *Creep: Characterization, Damage, and Life Assessment*, ASM International, Materials Park, OH, pp. 257–263.

Grabke, H. J., and Schnaas, A., 1978, "Review on High-Temperature Gaseous Corrosion and Mechanical Performance in Carburizing and Oxidizing Environments," *Alloy 800*, North-Holland Publishing Co., Amsterdam, pp. 195–211.

Haynes International, 1987, "Haynes Alloy No. 230," Haynes International, Inc., Kokomo, IN.

Haynes International, Inc., 1988, "Haynes Alloy No. 556," Haynes International Inc.,Kokomo, IN.

Haynes International, 1990, "Haynes Alloy HR-160," Haynes International, Inc., Kokomo, IN.

Heat Engineering, 1986, Vol. LII No. 6, Foster Wheeler Corporation, Livingston, NJ, Sept.

INCO, 1979, "INCONEL Alloy 617," Inco Alloys International, Inc., Huntington, Huntington, WV.

INCO, 1986, "INCOLOY Alloys 800 and 800HT," Inco Alloys International, Inc., Huntington, WV.

Kelly, J., 1983, "Physical Metallurgy and Mechanical Properties of Rolled Alloys 253MA," Rolled Alloys, Temperance, MI.

Kelly, J., 1984, "Metallurgy and Mechanical Properties of Alloy RA 333," Rolled Alloys, Inc., Temperance, MI, Sept.

Kelly, J., 1989, "RA85H Data Sheet," Rolled Alloys, Inc., Temperence, MI, June.

Klarstrom, D., 1991, "Heat Treatment/Property Relationships for Solid-Solution Strengthened Heat Resistant Alloys," *Heat Resistant Materials*, ASM International, Materials Park, OH, pp. 243–249.

Krukemyer, T., 1991, "Creep-Fatigue of a 22Cr-20Ni-18Co-Fe Alloy at Elevated Temperatures," Master's Thesis, University of Toledo, Toledo, OH, Aug.

McCoy, H. E., and King, J. F., 1985, "Evaluation of HD 556 and Incoloy 802 for High-Temperature Gas-Cooled Reactor Applications," ORNL/TM-9382, Oak Ridge National Laboratory, Oak Ridge, TN, Jan.

McFarlane, R. A., 1991, "A Comparative Creep Damage Model," *Fatigue, Fracture, and Risk 1991*, ASME PVP-Vol. 216, pp. 155–165.

Mallett, R. H., Thompson, J. M., and Swindeman, R. W., 1991, "Experience With Conventional Inelastic Analysis Procedures in Very High Temperature Applications," *Fatigue, Fracture, and Risk 1991*, ASME PVP-Vol. 216, pp. 167–174.

Manjoine, M. J., 1991, "Creep Fatigue Damage at Ultra-high Temperatures," *Fatigue, Fracture, and Risk 1991*, ASME PVP-Vol. 216, pp. 195–200.

Manjoine, M. J., and Filstrup, A. W., 1992, "Damage Evaluations of Filter Support System," *Pressure Vessel Technology*, Verband der Technischen Überwachung-Vereine e.V. (VdTÜV), Esse, Germany, pp. 18–36.

Myers, R. J., 1991, "New Nitrogen Strengthened Fe-Ni-Cr Alloy Exhibits Favorable Properties for Use up to 2000°F," *Industrial Heating*, Feb., pp. 42–44.

Natesan, K., and Podolski, W. F., 1991, "Materials for FBC Cogeneration Systems," *Heat Resistant Materials*, ASM International, Materials Park, OH, pp. 549–558.

Natesan, K., and Wang, D. Y., 1991, "Development of Weldments for Sulfur-Containing Combustion Environments," *Heat Resistant Materials*, ASM International, Materials Park, OH, pp. 395–408.

Nickel, H., Schubert, F., Rödig, M., and Penkalla, H.-J., 1986, "Multiaxial Creep of Tubes at Temperatures Above 800°C," *Proceedings of the International Conference on Creep*, Japan Society of Mechanical Engineers, Tokyo, Japan, pp. 509–513.

NRIM, 1978a, "Data Sheets on the Elevated Temperature Properties of Iron Base 21Cr-32Ni-Ti-Al Alloy for Heat Exchanger Seamless Tubes (NCF 2 TB)," National Research Institute for Metals, Tokyo, Japan.

NRIM, 1978b, "Data Sheets on the Elevated Temperature Properties of Iron Base 21Cr-32Ni-Ti-Al Alloy for Heat Exchanger Seamless Plates for Corrosion and Heat Resistant Applications (NCF 2 P)," National Research Institute for Metals, Tokyo, Japan.

Page, R. A., Hack, J. E., and Brown, R. D., 1984, "Behavior of Fe-Ni-Cr Alloys in a Complex Multioxidant Environment Under Conditions of Dynamic Straining," *Metallurgical Transactions*, Vol. 15A, Jan., pp. 11–22.

Persson, N. C., 1978, "Mechanical Properties of Alloy 800 Above 600°C," *Alloy 800*, North-Holland Publishing Co., Amsterdam, pp. 135–149.

Prager, M., 1992, "Deformation Considerations in the Elevated Temperature Stress Rupture Behavior of 309 and 310 Stainless Steel," *Stress Classification, Robust Methods, and Elevated Temperature Design*, ASME PVP-Vol. 230, pp. 85–100.

Rothman, M. F., 1991, "Pressure Vessel Code Construction Capabilities for a Nickel-Chromium-Tungsten-Molybdenum Alloy," *New Alloys for Pressure Vessels and Piping*, ASME MPC-Vol. 31, pp. 170–187.

Schubert, F., et al., 1984, "Creep Rupture Behavior of Candidate Materials for Nuclear Process Heat Applications," *Nuclear Technology*, Vol. 66, Aug., pp. 230–236.

Smolik, G. R., and Flinn, J. E., 1985, "Behavior of Pressurized Incoloy 800H Tubes in Environments Pertaining to Coal Gasification," EGG-MS-6852, EG&G Idaho, May.

Stringer, J., Leitche, A., and Clark, R. K., 1991, "The EPRI Hot Gas Filter Pilot Plant at Grimethrope: What Worked, What Broke and Where Do We Go Now?" *Proceedings of the 1991 International Conference on Fluidized Bed Combustion*, ASME, New York, NY, pp. 971–984.

Swindeman, R. W., Bolling, E., and Mallett, R. H., 1990, "Materials Data for the Design and Analysis of a Hot-Gas Filter Tubesheet," Draft Report, Oak Ridge National Laboratory, Sept.

Performance and Economic Enhancement of Cogeneration Gas Turbines Through Compressor Inlet Air Cooling

M. De Lucia

R. Bronconi

E. Carnevale

Dipartimento di Energetica,
Università di Firenze,
Firenze, Italy

Gas turbine air cooling systems serve to raise performance to peak power levels during the hot months when high atmospheric temperatures cause reductions in net power output. This work describes the technical and economic advantages of providing a compressor inlet air cooling system to increase the gas turbine's power rating and reduce its heat rate. The pros and cons of state-of-the-art cooling technologies, i.e., absorption and compression refrigeration, with and without thermal energy storage, were examined in order to select the most suitable cooling solution. Heavy-duty gas turbine cogeneration systems with and without absorption units were modeled, as well as various industrial sectors, i.e., paper and pulp, pharmaceuticals, food processing, textiles, tanning, and building materials. The ambient temperature variations were modeled so the effects of climate could be accounted for in the simulation. The results validated the advantages of gas turbine cogeneration with absorption air cooling as compared to other systems without air cooling.

Introduction

Gas turbines are increasingly being used to generate steam in cogeneration and repowering plants. Since the air they consume is taken from the environment, their performance is strongly affected by weather conditions—for example, power ratings can drop by as much as 20 percent with respect to ISO conditions when ambient temperatures exceed certain limits. One way of restoring, or even bettering, operating conditions is to add an air cooler at the compressor inlet. The air cooling system serves to raise turbine performance to peak power levels during the warmer months when the high atmospheric temperatures cause the turbines to work at off-design conditions, with reduced power output.

According to Ebeling et al. (1992), adding an air cooling system to peaking gas turbines, i.e., those designed to generate peak power, provides a 21–25 percent increase in power output. In the case of cogeneration plants, however, generalizations cannot easily be made, due to extensive differences in plant types and applications, as well as to operating conditions that involve large numbers of variables. For this reason, only the industrial sectors for which cogeneration is a viable solution have been considered.

This work examines the operation of cogeneration gas turbines with and without an air cooling system. The two solutions were simulated and the results were compared. The technical evaluation was accompanied by an economic evaluation, since power plant energetic and economic optimizations do not necessarily coincide—mainly as a result of the complexity of the utility's tariff system (De Lucia et al., 1992; Hill, 1992).

Modeling Inputs

All the assumptions and simplifications in the climate modeling regarding turbine performance and air cooling systems are based on the most conservative values.

Climate Data. In order to evaluate gas turbine performance in relation to atmospheric conditions so that cooling plant solutions can be compared, it is necessary to know temperatures and relative humidities on a yearly basis. Since the minimum and maximum temperatures were easily obtained for several sites, these values were used to build a model that could provide a curve to indicate daily temperature variations. (The temperatures, furnished by the UCEA, the Italian government agricultural and ecological support agency, consisted of statistical averages referring to the last 20 years.) Since the incident solar radiation follows a sinusoidal curve (France and Thornley, 1984; Kreith and Kreider, 1980; Marsili-Libelli, 1989) and assuming that the temperature depends upon the incident solar radiation, we can impose maximum temperature when the solar radiation is maximum and vice versa so that

Contributed by the International Gas Turbine Institute and presented at the 38th International Gas Turbine and Aeroengine Congress and Exposition, Cincinnati, Ohio, May 24–27, 1993. Manuscript received at ASME Headquarters February 18, 1993. Paper No. 93-GT-71. Associate Technical Editor: H. Lukas.

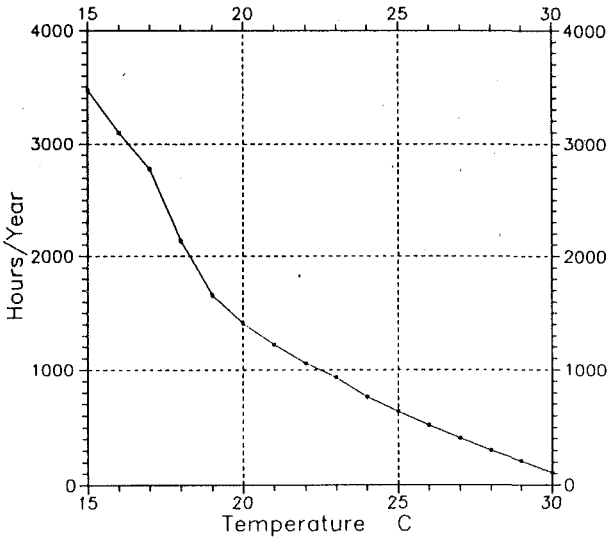

Fig. 1 Cumulative annual hours

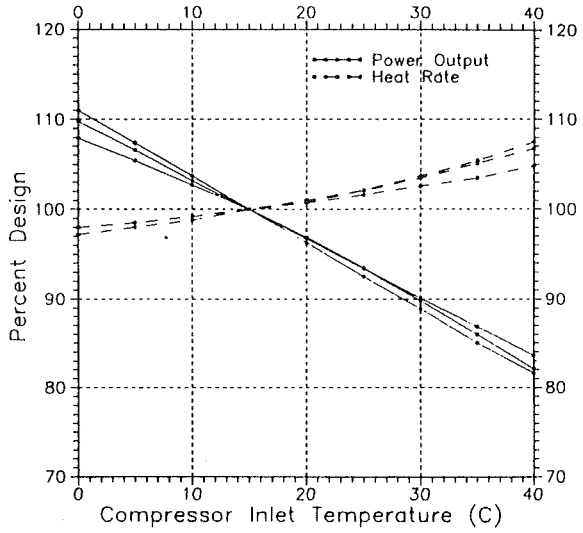

Fig. 2 Gas turbine performance

$$\begin{cases} T(t,N) = \dfrac{T_{\max}(N) - T_{\min}(N)}{2} \cdot \dfrac{1+\cos\left(\dfrac{2\pi(t-0.5)}{d(N)}\right)}{d(N)} \\ \text{for } 0.5 - \dfrac{d(N)}{2} < t < 0.5 + \dfrac{d(N)}{2} \\ T(t,N) = T_{\min}(N) \\ \text{for } 0 < t \le 0.5 - \dfrac{d(N)}{2} \text{ and } 0.5 + \dfrac{d(N)}{2} \le t \le 1 \end{cases} \quad (1)$$

where $d(N)$ is the length of the natural-light period in relation to the latitude δ, and ϕ is the solar declination, i.e., the angle between the straight line from the earth to the sun and the equatorial plane in relation to the meteorological day according to

$$d(N) = \frac{\cos^{-1}(-\tan(\varphi)\cdot\tan(\delta))}{\pi} \quad (2)$$

The night-time temperature was assumed to be the constant, minimum day temperature in the second term of Eq. (1).

This model is necessarily a compromise between the extremely complex meteorological models and the simple measurement of the maximum and minimum temperatures over a single year: It supplies an approximation of the real temperature variations occurring throughout the day, but fails to account for cloudiness and other microclimatic factors whose appreciable transient effects have been partly mitigated by the 20-year length of the statistical record.

The simulation results are significant for evaluation on a yearly basis. Figure 1 shows the cumulative curve representing the number of hours over a year-long period in which the ambient temperature equaled or exceeded the temperature in the x axis. At the site investigated (Central Italy, latitude 43°47′ N), the ambient temperature was 15°C for approximately 3500 hours per year, for a total of 40 percent. In the warmest period (April–September), a cooling system, activated only when 15°C is exceeded, would be almost constantly operating. The number of hours of temperatures exceeding 15°C would increase appreciably for sites with warmer climates than Italy and for lower latitudes. Since relative humidity does not affect gas turbine performance to any great extent, a mean value was assumed that was not correlated to the temperature variation.

Gas Turbines. Gas turbine inputs were obtained from three General Electric heavy-duty gas turbines, between 26 MW and 150 MW. Actual performance curves were utilized in the climate simulation and to evaluate the feasibility and cost effectiveness of the cooling system. Figure 2 shows the variations in the turbines' heat rates and power outputs in relation to ambient temperature—evidently their ratings hardly affected relative performance. At temperatures of 35°C, the output decreased by approximately 15 percent, while there was an increase of approximately 5 percent in the heat rate corresponding to the same decrease in efficiency.

Two other factors contribute to reducing the net power output: the exhaust gas back pressure resulting from the flow to the heat recovery steam generator (HRSG) and the inlet depression resulting from the flow exiting the air cooling coil directed toward the compressor. However, these effects can be appreciably reduced by careful system design.

Nomenclature

C = cost
d = natural-light period
F = electricity billing period
I = uniformity index
K = power output weighted average
N = meteorological day
P = power output
R = weighted cost average
T = temperature
t = time
TER = thermal-to-electric ratio
UC = cost per $kWh_{electric}$ per period
Z = percentage of energy consumed
δ = latitude
η = efficiency
ϕ = solar declination

Subscripts

e = electric
i = electricity billing period
m = mean
max = maximum
min = minimum
T = total hours per day considered

Table 1 Characteristic indexes according to industrial sector

Industry	Power Output Weighted Average (K)			Percentage of Energy Consumed (Z)			Weighted Cost Average (R)			Uniformity Index (I)
	Electricity Billing Period			Electricity Billing Period			Electricity Billing Period			
	F2	F3	F4	F2	F3	F4	F2	F3	F4	
Food Processing	109	107	87.6	15.9	51.3	32.8	25.0	53.9	23.4	102.3
Textiles	145.2	129	45.2	21.2	61.8	17.0	33.3	65.0	12.1	110.4
Paper and Pulp	100	100	100	14.6	47.9	37.5	22.9	50.4	26.7	100.0
Tanning	179	120.2	43.5	26.1	57.6	16.3	41.0	60.5	11.6	113.1
Building Materials	125	113.5	73.2	18.2	54.4	27.4	28.6	57.2	19.5	105.3

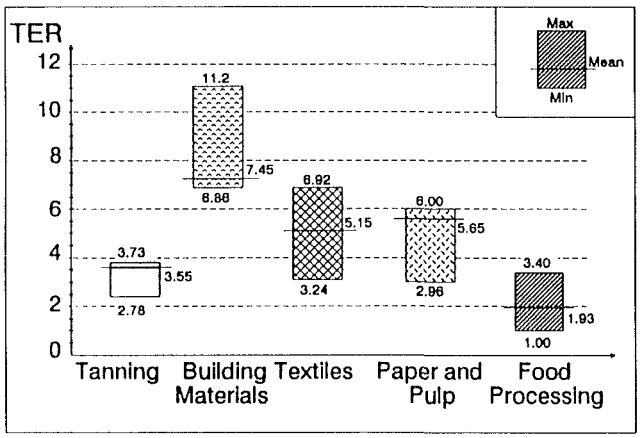

Fig. 3 Thermal-to-electric ratio according to industrial sector

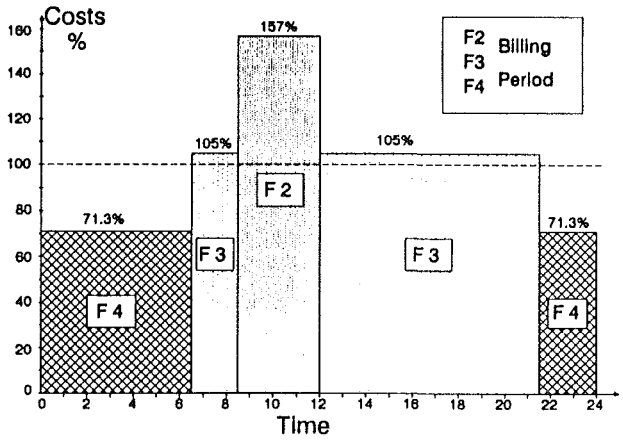

Fig. 4 Cost of electricity versus time of day

Industrial Sectors. The industrial sectors considered (food processing, paper and pulp, building materials, textiles, and tanning) are those in which the installation of a cogeneration plant is viable and/or advantageous. The first three involve three eight-hour shifts, i.e., round-the-clock operation, while the second two involve two eight-hour shifts, i.e., from 6 a.m. to 10 p.m.

All the data regarding energy consumption and costs were normalized so that the results would not be dependent on the size of the facility. The energy consumption data were obtained from a local government planning office. The data based on the cumulative consumptions of thermal and electrical energy were then processed in order to define the characteristic range of variation in each sector's thermal-to-electric ratio (TER) (Fig. 3).

Table 1 shows the energy consumption and costs according to industrial sector. The measured daily consumptions of electrical energy during the warmest—and thus most significant—period of the year were modeled and plotted as characteristic curves. The curves were normalized with respect to average consumptions taking into account the possibility of user-utility energy exchanges within specific billing periods.

Energy Costs. As in most industrialized nations, the cost of electricity in Italy varies according to period of the day. From April to September, there are three periods per day, except in August, when there is a single low-cost period (due to vacation shutdowns).

Figure 4 shows the percent cost variations for each period in relation to the cost computed as a weighted average of the unitary cost over a 24-hour period. The cost of the default electricity is constant and so low as to be negligible in the case of self-production. Table 1 shows the indexes calculated by combining the characteristic curves of measured electricity consumption with those of energy costs. K represents the weighted average of the power output for each period with respect to the total

$$K_i = \frac{P_{mi}}{P_{mT}} \cdot 100 = \frac{\frac{1}{t_i} \cdot \int_0^{t_i} P_e(t)dt}{\frac{1}{t_T} \cdot \int_0^{t_T} P_e(t)dt} \cdot 100 \tag{3}$$

Z represents the percentage of energy consumed for each period with respect to the total:

$$Z_i = K_i \cdot \frac{t_i}{t_T} = \frac{\int_0^{t_i} P_e(t)dt}{\int_0^{t_T} P_e(t)dt} \cdot 100 \tag{4}$$

C determines the weighted cost average for each period with respect to the average cost (Fig. 4):

$$C_{ei} = \frac{UC_i}{C_m} = \frac{UC_i}{\frac{1}{t_T} \cdot \sum_{i=0}^{n} UC_i \cdot t_i}. \tag{5}$$

I, termed "uniformity index," shows the energy cost versus daily consumption:

$$I = \sum_{i=0}^{n} K_i \cdot C_{ei} \cdot \frac{t_i}{t_T} = \sum_{i=0}^{n} \frac{\int_0^{t_i} P_e(t)dt}{\int_0^{t_T} P_e(t)dt} \cdot \frac{UC_i}{C_m} \tag{6}$$

The uniformity index is divided into periods by coefficient R, which is calculated as

$$R_i = K_i \cdot C_{ei} \cdot \frac{t_i}{t_T} \tag{7}$$

In the case of practically constant consumption as in paper and pulp mills, this index results unitary.

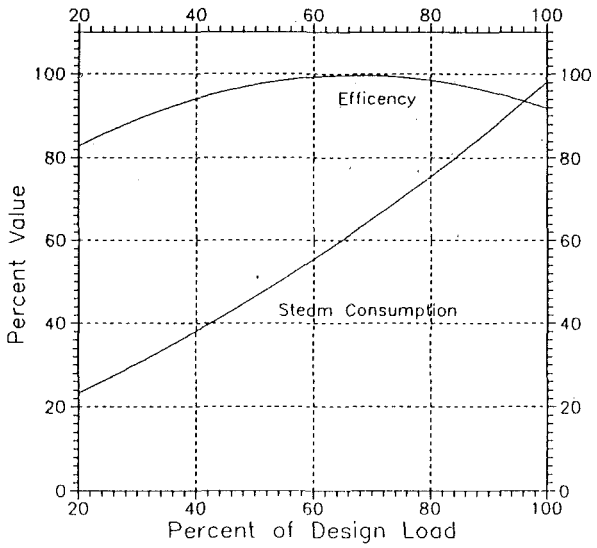

Fig. 5 Absorption cooling unit performance

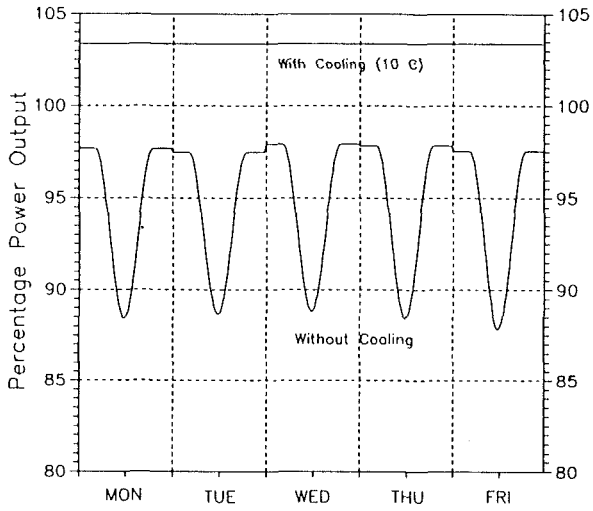

Fig. 7 Simulation of the performance of the 26 MW gas turbine with and without cooling for a July work week

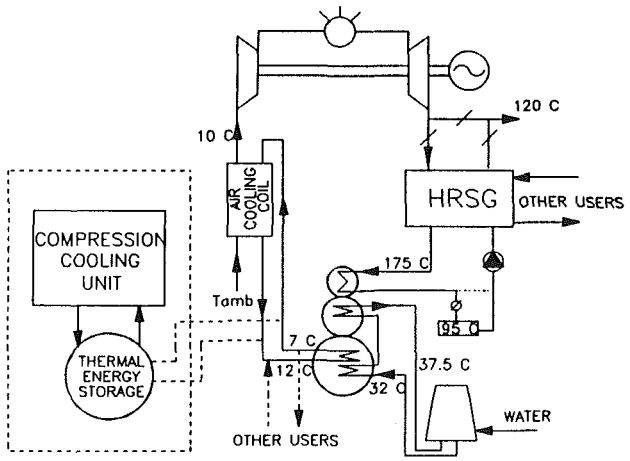

Fig. 6 Proposed plant

Air Cooling Solutions. The major state-of-the-art cooling and thermal energy storage technologies were examined for the air cooling system: These included conventional compression refrigeration and absorption systems.

The performance coefficients of the absorption units, i.e., approximately 0.7 (single-stage) and 1.2 (two-stage) are much lower than that of conventional compressors, i.e., 3.5. However, it should be noted that the compression units are powered by electricity, whereas the absorption units directly utilize primary energy. Actually, a two-stage absorption unit uses about as much thermal energy in the form of steam as the cooling energy produced, whereas the compressors required approximately 0.3 units of electrical energy for each unit of cooling energy produced. This requirement is the equivalent of slightly less than one unit of primary energy at the source—a value that is thus energetically comparable to that of the absorption units. In addition, the absorption units perform better with low loads, since efficiency is virtually unrelated to load up to 20 percent (Fig. 5) and, in several cases, up to 10 percent of nominal, whereas the efficiency of compression systems worsens considerably with decreasing load.

The cost per cooling unit is slightly higher for the absorption units ($125 per $kW_{installed}$, versus $80 per $kW_{installed}$ for compression systems) due to the greater initial investment. (Absorption units are still costly, but they are becoming less so as more are sold.) This higher initial cost is offset, however, by virtually zero maintenance, since the absorption units contain no critical moving parts. The absorption units also provide environmental benefits since (1) they do not require cooling fluids such as CFC and HCFC, which are dangerous for the ozone layer, and (2) being totally vibration-free, they are noiseless.

The absorption units use the heat directly from the turbine exhaust gases via an HRSG—with evident economic and energy gains. Their attainable minimum temperatures do not, however, allow the use of latent heat cooling accumulators, which are smaller than sensible heat accumulators and more efficient. One solution, the use of chilling and ice storage units during low-cost off-peak hours, has been described by Ebeling et al. (1992).

The air cooling plant examined, schematicaly illustrated in Fig. 6, is of simple design and extremely low cost—between 1.3–1.5 percent of gas turbine unit. It cools the compressor inlet air at a temperature of 10°C when the ambient temperature is higher by at least 5°C to prevent the absorption unit from working at loads 20 percent below nominal. The 10°C limitation derives from the minimum cooling temperatures at which an absorption unit retains its efficiency: 5–7°C. However, there is a minimum air cooling temperature (4.4°C) that should be respected to avoid damage to the compressor from condensation or solidification of moisture in the air. At the present state of the art, this limit can be broken only by compression cooling plants.

Only a small percentage of the thermal energy recoverable from the turbine exhaust flows (5 percent) is used to cool the air from 35°C to 10°C, a value that decreases proportionately with temperature. These temperature conditions allow maintaining the gas turbine thermal-to-electric ratio virtually unvaried at optimum cogeneration performance.

An appropriately sized absorption unit might also be used for process cooling, i.e., in food and pharmaceutical processing, with evident benefits in terms of plant costs. These sectors—albeit characterized by lower thermal-to-electric ratios than typical of gas turbines—provide optimum conditions, since the cooling is generally obtained by electric-powered compression plants. The installation of an absorption unit would reduce the amount of electricity used to produce cold air by directly exploiting the thermal energy at the turbine exhaust, thereby increasing the thermal-to-electric ratio.

In Fig. 6, the dashed line indicates the possibility of coupling a conventional cooling unit and a thermal energy storage unit when especially high peak demands must be met. With the coupled solution, the two types of cooling systems are used

Table 2 Month-by-month simulation

a) Two-shift operation

	Results % (6 a.m. - 10 p.m.)					
	Apr	May	Jun	Jul	Aug	Sep
ΔPeak Power Max	+8.5	+13.1	+16.7	+18.5	+19.1	+15.0
ΔOutput Energy	+2.1	+4.8	+8.2	+10.6	+10.2	+6.9
ΔHeat Consumed	+1.4	+2.9	+4.5	+5.1	+5.0	+4.0
$\Delta\eta$ Efficiency	+0.7	+1.8	+3.6	+5.2	+4.9	+2.8
Hours of Operation	36.9	64.3	92.9	100	100	88

b) Round-the-clock operation

	Results % (noon-midnight)					
	Apr	May	Jun	Jul	Aug	Sep
ΔPeak Power Max	+8.5	+13.1	+16.7	+18.5	+19.1	+15.0
ΔOutput Energy	+1.4	+3.2	+6.5	+9.0	+8.6	+5.5
ΔHeat Consumed	+0.9	+2.0	+3.8	+4.7	+4.6	+3.3
$\Delta\eta$ Efficiency	+0.4	+1.2	+2.7	+4.1	+3.9	+2.1
Hours of Operation	24.6	44.0	85.6	100	100	81.0

together, despite increases in the plant's cost, complexity, and management.

The drawbacks of thermal energy storage are higher plant costs and lower efficiency from the unavoidable heat losses. While the ice storage solution described by Ebeling et al. (1992) is able to meet peak demands with power increases of up to 25 percent, nonetheless it entails considerably higher investment costs deriving from the increased plant complexity, which in turn means more complicated maintenance. In addition, if the cogeneration system is sized to meet the electricity demand and allow user-utility energy exchanges within billing periods, the higher plant investment costs would not be offset by economic or energy gains, since the energy storage system is related to plant efficiency that varies considerably (70–90 percent) according to operating conditions.

Figure 7 shows the results of the simulation for the 26 MW gas turbine. The benefits, an increase in the electricity generated and the absence of power output reductions during the costly, peak-demand daytime hours, are evident. Of note is the fact that without cooling, in addition to the decrease in the daytime power output, there is also a decrease in the thermal energy recoverable from the exhaust gases.

Results

Energy Results. Table 2 shows the energy results in summer for the 26 MW turbine with and without a cooling unit. The increase in output (19 percent) is much greater in the hottest months (July and August), thereby providing an incremental increase of approximately 4.35 MW as compared to the 22.8 MW power output without an absorption unit. In the warmer months, the increase in output power exceeds 10 percent, thereby providing a net efficiency increase of 5 percent. The net efficiency was calculated considering an air pressure loss from the heat exchanger of approximately 25 mm of water, although this value is actually reached only at maximum loads and thus only for brief periods.

Table 3 Month-by-month economic results

Industry	ΔCosts %				
	Apr	May	Jun	Jul	Sep
Two Shifts:					
Tanning	-3.4	-7.5	-12.1	-15.2	-10.3
Textiles	-3.4	-7.5	-12.0	-15.0	-10.2
Three Shifts:					
Food Processing	-1.8	-3.9	-7.1	-9.2	-6.0
Paper and Pulp	-1.8	-4.0	-7.1	-9.2	-6.0
Building Materials	-1.8	-3.9	-7.1	-9.2	-6.0

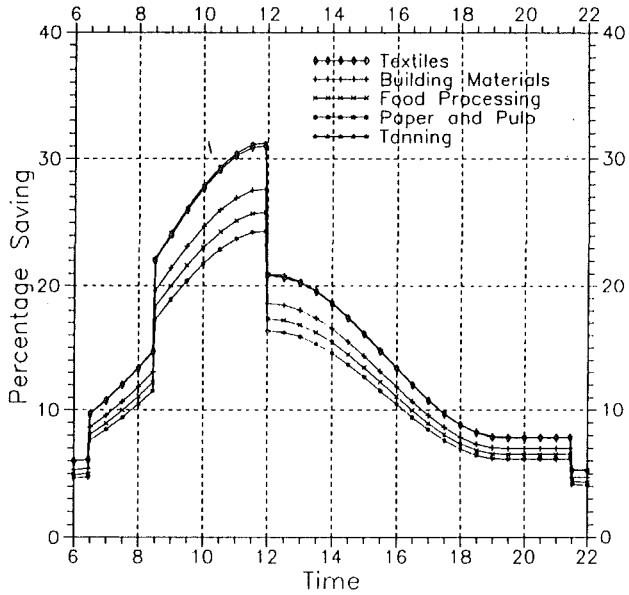

Fig. 8 Economic savings according to industrial sector versus time of day

Note that in July and August, under the conditions illustrated in Table 2, the absorption unit works at 100 percent capacity, 24 hours a day. Thus, from April to September, it works for a total of 2350 out of 2930 operating hours (80 percent) in the case of two-shift operation (*a*) and for a total of 3190 out of 4390 operating hours (73 percent) in the case of round-the-clock operation (*b*). This means that energy may be saved if the absorption unit is operated during the night shift, which will thus afford a significant economic gain.

The operation of an absorption unit as illustrated in Fig. 6, for the 26 MW turbine, at an ambient temperature of 35°C provides a 22 percent increase in the power output and a 5.4 percent increase in the heat recoverable by the HRSG (with a stack temperature 100°C) as compared to the solution without the absorption unit. Considering the necessary heat transfer efficiencies, the absorption unit consumes 5.1 percent of the heat recoverable by the HRSG. The gas-turbine-with-absorption-unit solution requires an increase in fuel of 14.6 percent, which translates to an increase in power output of 22 percent with respect to the no-cooling solution.

Economic Results. The results of the simulation for a typical July day are plotted in Fig. 8, which shows the electricity cost differences between the solutions with and without cooling. The net saving calculation must consider the cost due to the increase in the fuel consumption, which generally has no appreciable effect on the final result.

The savings with respect to the average cost are compared in the *x* axis for plants with and without absorption units. The discontinuities may be attributed to the differences in the electricity rates over the 24-hour period (Fig. 4). At the worst

economic conditions, the maximum savings reach 25–30 percent and are obviously greater for those sectors characterized by higher uniformity indexes (Table 1). A month-by-month balance sheet (Table 3) reveals appreciable average savings even exceeding 15 percent. While the table shows a smaller saving in the three-shift, round-the-clock sectors (food processing, paper and pulp, and building materials) than in the two-shift sectors (textiles and tanning), their consumptions refer to the entire 24-hour period, and are thus comparable in absolute terms.

With the assumption of sizing the turbine on the average load to meet peak demands through user-utility exchange, savings vary only to a slight extent in relation to sector: The sole difference revealed by Table 4 is between the round-the-clock and two-shift sectors. Hence, the extension of these results to other sectors that do not differ to any large extent is, we feel, fully justified.

Conclusions

The following conclusions emerged in a comparison study of cogeneration gas turbines with and without compressor inlet air cooling:

- In a temperature climate such as Italy's, the power output may be increased by 18–19 percent using an absorption unit to cool the compressor inlet air to 10°C. Even greater energy and economic benefits can be envisaged for sites where average temperatures are higher.
- Simulated monthly energy savings increase by 10–11 percent in the warmest periods, with an increase in efficiency of 5 percent, and with a 15 percent decrease in electricity costs.
- The cost of an absorption unit is virtually negligible as compared with that of a cogeneration plant (1.3–1.5 percent) in view of potential energy savings of up to 10–15 percent in the warmest months provided by the absorption unit.
- By installing an absorption unit, the power output can be appreciably increased virtually without altering thermal energy recovery with respect to the no-cooling solution.
- All the cooling plant components are available commercially (but even better results can be obtained with custom designs).
- Since the simulation input data, which were derived from models of the gas turbine and absorption units, can be considered homogeneous, the results for the various industrial sectors can be extended to others where gas turbine cogeneration is a viable solution.
- Although conducted for heavty-duty machines, the evaluations herein are of general validity, thereby enhancing the advantages for machines with greater sensitivity to external temperature, as is often the case for aeroderivative gas turbines.

Acknowledgments

We are grateful to UCEA, IRPET, and NuovoPignone for having furnished the raw data on which this study is based.

References

De Lucia, M., Lanfranchi, C., and Carnevale, E., 1992, "La scelta ottimale del gruppo combinato gas vapore per il repowering di cartiere," *Proceedings 6th Congress on Combined Groups*, Genoa, Italy.

Ebeling, J. E., Halil, R., Bantam, D., Bakenhus, B., Schreiber, H., and Wendland, R., 1992, "Peaking Gas Turbine Capacity Enhancement Using Ice Storage for Compressor Inlet Air Cooling," ASME Paper No. 92-GT-265.

France, J., and Thornley, J. H. M., 1984, *Mathematical Model in Agriculture*, Butterworths, London, United Kingdom.

Hill, J. P., 1992, "Assessing the Economics of Industrial Gas Turbine Cogeneration Applications," ASME Paper No. 92-GT-333.

Kreith, F., and Kreider, J., 1980, *Principles of Solar Energy*, McGraw-Hill, New York, pp. 37–82.

Marsili-Libelli, S., 1989, *Modelli Matematici per l'Ecologia*, Ed. Pitagora, Bologna, Italy, pp. 93–103.

An Assessment of Weighted-Least-Squares-Based Gas Path Analysis

D. L. Doel
Advanced Engineering Technologies Department,
GE Aircraft Engines,
Evendale, OH 45215-6301

Manufacturers of gas turbines have searched for three decades for a reliable way to use gas path measurements to determine the health of jet engine components. They have been hindered in this pursuit by the quality of the measurements used to carry out the analysis. Engine manufacturers have chosen weighted-least-squares techniques to reduce the inaccuracy caused by sensor error. While these algorithms are clearly an improvement over the previous generation of gas path analysis programs, they still fail in many situations. This paper describes some of the failures and explores their relationship to the underlying analysis technique. It also describes difficulties in implementing a gas path analysis program. The paper concludes with an appraisal of weighted-least-squares-based gas path analysis.

Introduction

Gas path analysis is used to decide which gas turbine components are responsible for an observed performance deficit. The deficit may be a loss of performance during revenue service flights, or the failure to achieve performance guarantees in an overhaul acceptance run. In either case, the goal of gas path analysis is to help the user select a work scope to regain performance.

Engine sensors, used as input to gas path analysis, include temperature probes and total and static pressure probes in the gas stream, plus fuel flow and rotor speeds. In the test cell, thrust and total engine airflow are also available (Fig. 1). Pressure and temperature sensors are nearly always single-element probes. They often deviate substantially from plane average temperature or pressure.

Weighted-least-squares has been the predominant technology for gas path analysis for at least a decade. All major jet engine manufacturers offer gas path analysis programs based on this technique (Urban and Volponi, 1992; Barwell, 1987; Doel, 1994). Each manufacturer has needed to augment the basic weighted-least-squares algorithm to achieve effective results. Rolls Royce offers a "concentrator" module to emphasize module problems. GE provides "fault logic" to improve the diagnosis of large component or measurement faults. Hamilton Standard provides a "large measurement error recovery algorithm" (Volponi, 1982).

Users need gas path analysis most when there are large deviations in engine performance or large measurement errors. These large departures from normal behavior usually require special features (concentrator, fault logic) for a successful analysis. Thus, the variations on the weighted-least-squares theme are vital to the perceived success of the gas path analysis algorithm.

Contributed by the International Gas Turbine Institute and presented at the 38th International Gas Turbine and Aeroengine Congress and Exposition, Cincinnati, Ohio, May 24–27, 1993. Manuscript received at ASME Headquarters March 1, 1993. Paper No. 93-GT-119. Associate Technical Editor: H. Lukas.

This paper examines the experience with one gas path analysis algorithm (TEMPER[1]) to identify successes and problems of the weighted-least-squares approach.[2] There is no sure way to determine whether an analysis is correct. The best evaluation of the analysis is derived from the success or failure of the work scope developed from its results (and from other considerations). The evaluation is, therefore, subjective.

A Turbine Problem Correctly Diagnosed, or Was It?

Test Cell TEMPER (Doel, 1994) was introduced during the early 1980s. The initial release relied on the weighted-least-squares algorithm (Bryson and Ho, 1975). Users quickly identified a requirement to improve results for engines with large performance deviations or measurement errors. The TEMPER fault logic was added to address this need.

Almost immediately, the fault logic produced a success story for the TEMPER program. An engine, removed for exceeding its EGT limit, was run in-bound to determine the cause for the low performance. A TEMPER analysis of the data (Fig. 2) showed the high-pressure turbine to have deteriorated by 3 percent in efficiency. It also indicated that the high-pressure turbine flow function was almost 3 percent larger than nominal.[3]

Inspection of the turbine confirmed the damage. The turbine rotor was replaced. No repair was performed on the first-stage nozzle of the turbine. This work scope should restore the turbine efficiency without appreciably changing the turbine flow

[1]TEMPER for "Turbine Engine Module Performance Estimation Routine."

[2]A mathematical description of the weighted-least-squares algorithm, as used in TEMPER, is provided in the appendix.

[3]The TEMPER solution also suggests the possibility of a large error in the Exhaust Gas Temperature (EGT) measurement. This is often observed in combination with significant turbine deterioration. The apparent temperature error often disappears when the turbine is repaired. The cause for this behavior is not known, but it has been observed often enough that experienced users assume the error will be corrected when the faulty hardware is repaired.

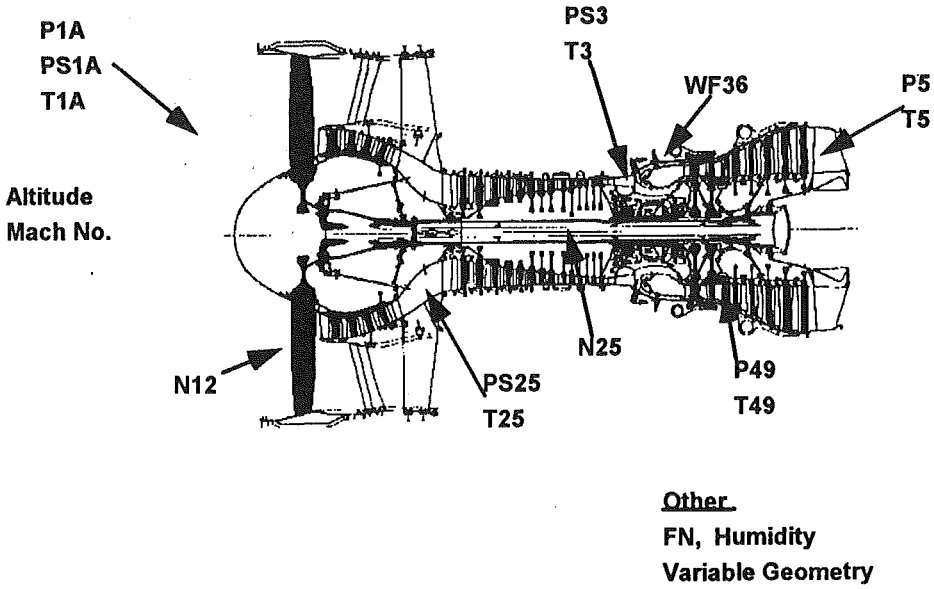

Fig. 1 Typical instrumentation for jet engine gas path analysis

function. When the acceptance data were analyzed (Fig. 3), the turbine efficiency had indeed been restored to a normal level while the turbine flow function was still 3 percent above nominal.

This TEMPER success story was due entirely to the newly added fault logic. Without the fault logic, TEMPER would have assigned roughly half of the problem to the turbine.[4] The remainder would have been attributed to other components and to measurement error. This attenuation of results, typical of the weighted-least-squares algorithm, would have jeopardized the user's ability to seize on the high-pressure turbine as the primary source of the low performance.

Less than a month after this successful result, the TEMPER fault logic was modified as part of the normal development process. The newer version of the fault logic used "solution probability" to choose among candidate faults where the previous version had used "residual error." Solution probability accounts for the "degrees of freedom" used by the fault and the residual error.

[4]Newer versions of TEMPER would do better because of lessons learned over the intervening years. The results would, however, still be fuzzier than the crisp enunciation provided by the fault logic.

Nomenclature

$E(..)$ = expected value operator
$\mathbf{H}$ = matrix of influence coefficients, defining the effect of the engine state variables on the measurements
J = weighted-least-squares objective function (to be minimized)
$\mathbf{M}$ = covariance matrix for state variables
n = number of state variables
$\mathbf{Q}$ = covariance matrix of measurement deviations derived from a large sample of test data
p = number of independent measurements
$\mathbf{R}$ = covariance matrix for measurement errors
$\mathbf{x}$ = state vector composed of the characteristics of the engine expected to vary with time
$\mathbf{x}_0$ = weighted-least-squares solution for $\mathbf{x}$
$\mathbf{z}$ = measurement vector comprised of the independent measurements on which the analysis is based
ν = vector of measurement noise
ν_0 = weighted-least-squares solution for measurement noise

Superscripts

-1 = matrix inverse
T = matrix transpose

TEMPER Parameters

EGT = Exhaust Gas Temperature (also called Control Temperature)
FAN = denotes the engine fan in TEMPER results
FN = net thrust
HPC = denotes the High-Pressure Compressor in TEMPER results
HPT = denotes the High-Pressure Turbine in TEMPER results
HPTR = denotes the High-Pressure Turbine Rotor in TEMPER results
HPTS = denotes the High-Pressure Turbine Stator in TEMPER results
LPC = denotes the Low-Pressure Compressor in TEMPER results
LPT = denotes the Low-Pressure Turbine in TEMPER results
MEAS = denotes EGT Measurement error in TEMPER results
N12 = fan rotation speed
N25 = gas generator rotation speed
P1A = engine inlet total pressure
P49 = high-pressure turbine discharge total pressure
P5 = low-pressure turbine discharge total pressure
PS1A = engine inlet static pressure (used to compute air flow)
PS25 = high-pressure compressor inlet static pressure
PS3 = high-pressure compressor discharge static pressure
SFC = Specific Fuel Consumption
T1A = engine inlet total temperature
T25 = high-pressure compressor inlet total temperature
T3 = high-pressure compressor discharge total temperature
T49 = high-pressure turbine discharge total temperature
T5 = low-pressure turbine discharge total temperature
WF36 = engine fuel flow rate

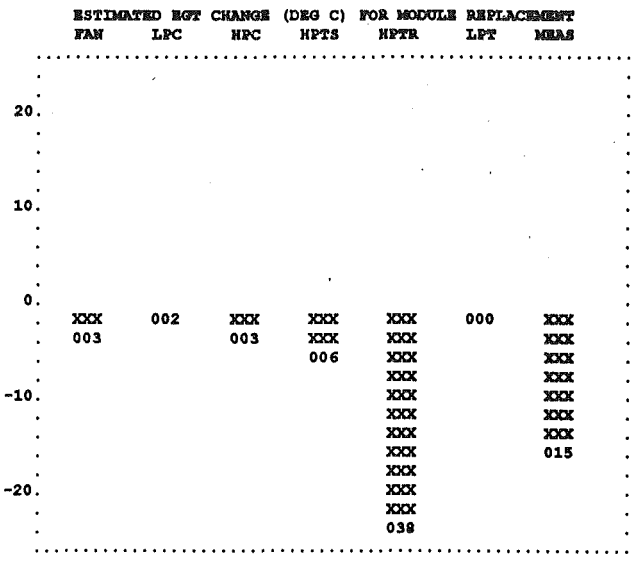

Fig. 2 TEMPER analysis of in-bound run of engine with turbine damage

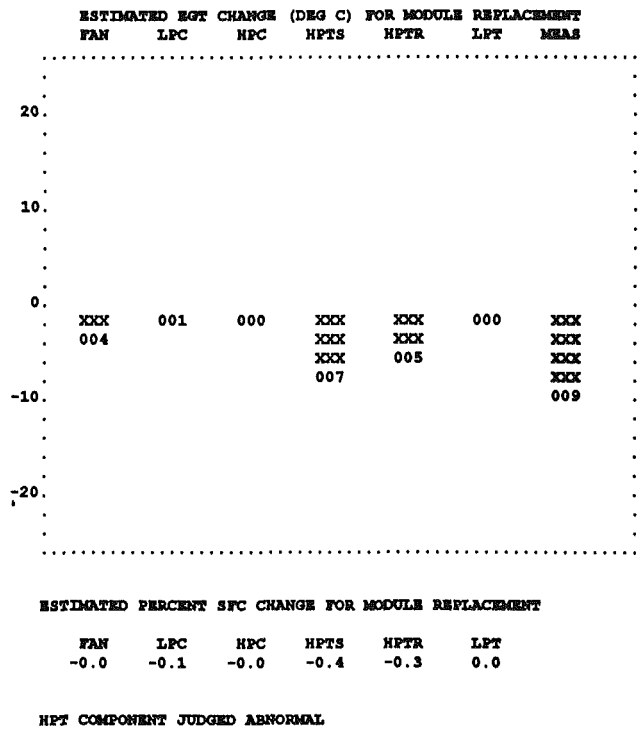

Fig. 3 TEMPER analysis of out-bound run of engine with turbine damage

This change was needed to eliminate an inherent advantage given to faults having more than one element. The turbine fault has both turbine efficiency and turbine flow function to absorb residual error. Conversely, a measurement fault, such as fuel flow measurement error, has only a single element to absorb the residual. When the solutions are compared using residual error, the multiple-fault solutions have an advantage over the single-fault solutions. Using solution probability eliminates the advantage.

After implementing the changes to the fault logic, we ran the data from the engine with the turbine problem through the new program. The out-bound results were unchanged. However, the in-bound solution was completely different. TEMPER now attributed the problem to increased turbine cooling instead of the combination of turbine efficiency and turbine flow function.

This outcome is not surprising. The combination of increased turbine flow function and decreased turbine efficiency, in a one-to-one ratio, cannot be distinguished from a turbine cooling increase, given the available condition monitoring measurements. The turbine performance fault uses two degrees of freedom while the turbine cooling fault uses only one. The turbine performance fault lowered the residual error a little more than the turbine cooling flow fault, but this advantage was overcome by the additional degree of freedom.

To address this new problem, TEMPER now provides the two best fault solutions, whenever their probabilities are within 5 percent of one another. This places a burden on the user to choose the correct result. In the case described, the user can inspect the turbine to see if damage is present. If so, the performance deficit is blamed on the turbine; if not, turbine cooling is suspected.

Base Lines

Ideally, gas path analysis would report absolute performance for engine modules (efficiency and flow capacity). Targets for the components' performance could be developed from production acceptance runs, or from acceptance runs of well-overhauled engines. The analyst could use the differences between the engine's performance and the targets to decide which components need re-work.

This ideal is yet to be reached because of limitations in the measurements. Measurements available in overhaul or in service are usually single element probes. Placement of these probes is dictated more by convenience and ruggedness than by effectiveness. Thus, the probes have unknown biases relative to the plane-average temperatures and pressures needed to calculate component efficiency and flow capacity.

To address the sensor problems, gas path analysis programs provide relative rather than absolute answers. Test cell programs express performance of the modules relative to an average of other engines tested in the same cell. On-wing programs compare performance of the modules to an average of newly installed engines.

The engine's cycle model would seem to be a candidate reference for the gas path analysis. This is not practical, however, because the cycle model represents only plane average temperatures and pressures.[5] Thus, "baselines" are added to the engine cycle model[6] to adjust its predictions to be compatible with actual measurements.

TEMPER works best with a baseline representing expected values of test cell or on-wing measurements. This expected-value baseline gives proper meaning to the solution residual, permitting recognition of abnormal engine behavior. The expected-value baseline may not, however, be an appropriate reference point for citing results. Output from the gas path analysis program is better referred to production or well-overhauled engine performance levels. This gives a more accurate reading of the module's improvement potential to the user.

Development of an expected-value baseline is a tedious, time-consuming effort. The developer assembles data from as many engine runs as possible. The data are carefully reviewed to eliminate outliers. Data that pass the screening are processed

[5]It also may represent a significantly different engine quality than the typical overhauled engine.

[6]Some algorithms eliminate the cycle model altogether through use of an empirical model derived from test cell acceptance or on-wing data.

Table 1 Weighted-least-squares solution for pure turban efficiency fault (+1 percent)

Weighted-Least-Squares Parameter	Result	Ideal Result
Fan Flow Capacity	-.002	0.0
Fan Efficiency	-.046	0.0
Low Pressure Compressor Flow Capacity	.092	0.0
Low Pressure Compressor Efficiency	.206	0.0
High Pressure Compressor Flow Capacity	.049	0.0
High Pressure Compressor Efficiency	.274	0.0
High Pressure Turbine Flow Function	-.088	0.0
High Pressure Turbine Efficiency	.609	1.0
Low Pressure Turbine Flow Function	.081	0.0
Inlet Static Pressure Measurement Error	-.004	0.0
Fan Tip Discharge Pressure Measurement Error	-.013	0.0
Low Pressure Compressor Discharge Static Pressure Measurement Error	-.003	0..0
Low Pressure Compressor Discharge Temperature Measurement Error	.040	0.0
Core Speed Measurement Error	.095	0.0
High Pressure Compressor Discharge Static Pressure Measurement Error	-.009	0.0
High Pressure Compressor Discharge Temperature Measurement Error	.051	0.0
Fuel Flow Measurement Error	-.202	0.0
High Pressure Turbine Discharge Pressure Measurement Error	.096	0.0
High Pressure Turbine Discharge Temperature Measurement Error	-.142	0.0
Thrust Measurement Error	-.027	0.0

to compute the deviations of the measurements from the cycle deck. To complete the expected-value baselines, these deviations are averaged (or curve-fit versus power level).

Each test cell or engine model needs a unique expected-value baseline. Changes to test cell cowling can change the baseline, as can changes to the engine configuration (e.g., control schedules). It is often necessary to develop several baselines for a single test cell. Engine manufacturers frequently have several engine models and as many as a hundred airline customers. Therefore, an engine manufacturer may need to develop hundreds of separate baselines. Changes to the test cells, or other events, dictate regular updates to the baselines.

A new engine model presents an even greater difficulty. There are no data from which to generate baselines. Either the user must await gathering of sufficient data for the generation of baselines, or some other technique must be developed for providing the initial baselines.

An approach that has met with some success is to predict the baseline from production acceptance data and cell correlation results (for the specific engine model and cell). This approach relies on an estimate of the average quality of the overhauled components. It also depends on the use of a single back-to-back cell correlation test. The single test is subject to significant measurement errors that are propagated into the baselines.

The single most important feature of gas path analysis programs is their ability to cope with large deviations (for example, the "fault logic" in TEMPER). This ability depends on having a good prediction for the behavior of the engine—that is, on having good expected-value baselines. For new engine models these do not exist. For mature engine models their existence depends on good communication between the test cell owner and the baseline developer, and upon the diligence of the baseline developer. Thus, baselines represent a major risk to the effectiveness of current gas path analysis algorithms.

Statistics and Weighted-Least-Squares Response

Ordinarily, the TEMPER solution is derived using the pure weighted-least-squares algorithm. The solution from a pure weighted-least-squares algorithm is a linear function of the differences between the measurements and their predicted values (Doel, 1994). The gain matrix, used to compute the solution, is determined by the influence coefficients (also called partial derivatives) and by the assumed variances for the state variables and measurement errors. This gain matrix can be computed without knowledge of the measurements. Thus, it is possible to examine the response of a weighted-least-squares algorithm to specific faults.

Table 1 shows the response of a representative gas path analysis program to a pure turbine efficiency fault. The input to the algorithm of Table 1 represents an engine that agrees with the baseline engine in every respect except that its turbine efficiency is 1 percent better than the baseline engine. Table 1 also provides the ideal result for the algorithm (which mirrors the incoming turbine efficiency problem). The ideal result is unattainable because there are fewer equations (one for each independent measurement) than unknowns (one for each independent measurement plus one for each state variable).

Table 1 records that slightly more than 60 percent of the incoming fault is correctly assigned to turbine efficiency. The remainder of the fault is attributed to other components and to measurement errors. High-pressure compressor efficiency, low-pressure compressor efficiency, fuel flow measurement error, and high-pressure turbine discharge temperature measurement error are all identified as problems by the algorithm.

The influence coefficients, **H**, are determinate for an engine model, but the statistical assumptions for state variables and measurement errors are not. They may be adjusted to tune the response of the algorithm.[7] Increasing the assumed variance of the turbine efficiency while holding all other variances fixed will improve the result for a turbine efficiency problem. However, it will interfere with the ability of the algorithm to diagnose other faults properly. Also, an increase in the assumed variance of the turbine efficiency will increase its response to other faults.

Table 2 gives the response of the Table 1 algorithm to all faults. Entries in Table 2 represent the part of the solution that correctly responds to the input problem. For example, the last entry in the table indicates that the weighted-least-squares analysis of a +1 percent thrust measurement error (with no other deviation) gives an inferred thrust error of +0.559 percent. The remainder of the thrust measurement error is distributed to other measurement errors and to component faults. A table, similar to Table 1, could be produced to show the algorithm's assignment of the thrust measurement error.

Some Table 2 entries are surprisingly small. The high-pressure turbine discharge temperature measurement response is less than 40 percent and other responses are even smaller. These values may be tuned by adjusting the assumptions for measurement error and component standard deviations. If the standard deviation for the high-pressure turbine discharge temperature measurement error were increased, its response also

[7] It should be noted that constraints on the measurement error and state variable variances can be derived from observed variance of the test data. The individual measurement error or state variances is, however, not subject to analytical determination.

Table 2 Weighted-least-squares response for pure component and measurement faults

Weighted-Least-Squares Parameter	Result
Fan Flow Capacity	1.085
Fan Efficiency	0.266
Low Pressure Compressor Flow Capacity	0.091
Low Pressure Compressor Efficiency	0.390
High Pressure Compressor Flow Capacity	0.834
High Pressure Compressor Efficiency	0.419
High Pressure Turbine Flow Function	0.432
High Pressure Turbine Efficiency	0.609
Low Pressure Turbine Flow Function	0.355
Inlet Static Pressure Measurement Error	0.711
Fan Tip Discharge Pressure Measurement Error	0.977
Low Pressure Compressor Discharge Static Pressure Measurement Error	0.146
Low Pressure Compressor Discharge Temperature Measurement Error	0.918
Core Speed Measurement Error	0.870
High Pressure Compressor Discharge Static Pressure Measurement Error	0.232
High Pressure Compressor Discharge Temperature Measurement Error	0.541
Fuel Flow Measurement Error	0.727
High Pressure Turbine Discharge Pressure Measurement Error	0.465
High Pressure Turbine Discharge Temperature Measurement Error	0.373
Thrust Measurement Error	0.559

would increase. However, this would lower the response of the algorithm to other measurement errors and to state variables.

A large sample of data can be used to establish constraints on the standard deviations. The equation defining these constraints is:

$$\mathbf{Q} = \mathbf{R} + \mathbf{HMH}^{\mathbf{T}}$$

where:

- $\mathbf{Q}$ = the covariance matrix of measurement deviations derived from a large sample of test data
- $\mathbf{R}$ = the covariance matrix for the measurement errors
- $\mathbf{H}$ = the matrix of influence coefficients, defining the effect of the state variables on the measurements
- $\mathbf{M}$ = the covariance matrix for state variables

This equation sets limits on R and M, but does not uniquely define them. The developer of the gas path analysis program must make assumptions about the form of R and M (for example, that certain covariances will be zero) and then use the equation to select values consistent with observations. There is some freedom of interpretation, especially regarding the state variables.

Table 2 suggests that the mean response for faults and measurement errors is about 50 percent, given the available sensors. This means that half of the solution, on average, will be erroneous. The only way to improve average response is to increase the number of sensors in proportion to the number of state variables being estimated.[8]

Tables 1 and 2 do not include low-pressure turbine efficiency as one of the state variables. When TEMPER was developed, low-pressure turbine efficiency was omitted because there was not sufficient instrumentation to distinguish it from the fan. Low-pressure turbine efficiency is only the most obvious state variable missing from the analysis. Other faults that could have been included are combustor efficiency and pressure drop, cooling and leakage flows, nozzle performance parameters and setting parameter measurement errors (for instance, inlet temperature and pressure).[9] In every case, there is not adequate instrumentation to determine these parameters, even if there were no sensor error. If they were included as state variables without providing additional sensors, the average response would be lowered further.

[8]It might also be possible to select a better measurement set that does a better job of separating the faults of interest.

[9]While these variables are not included in the basic weighted-least-squares analysis in TEMPER, they are possible choices for the fault logic. However, as pointed out earlier, the fault logic can select the wrong fault because of the unavailability of sensors to distinguish between faults.

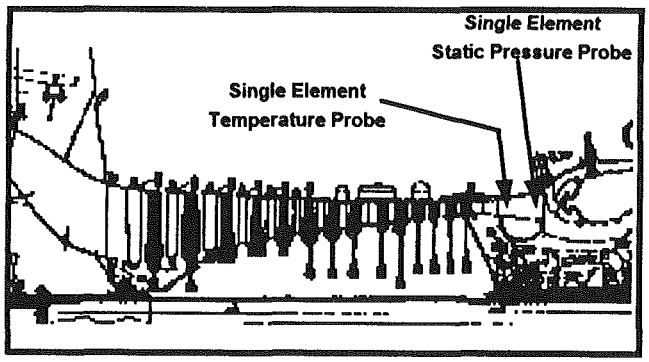

Fig. 4 Monitoring sensors at compressor discharge

When these unmodeled variables change, their changes are interpreted as other state variables or measurement errors. For instance, turbine cooling flow change will be interpreted as a change to the turbine efficiency and flow function. These errors add to the error in the weighted-least-squares analysis. The only way to improve the situation is to add sensors that distinguish the unmodeled faults from those currently included in the gas path analysis.

Single Element Sensors and Deterioration

Most of the gas path temperatures and pressures are single-element probes. The flow fields have large pressure and temperature gradients that vary with power level and operating condition. This is why baselines are required.

One of the underlying assumptions in gas path analysis is that the sensors respond appropriately to component deterioration. Thus, the temperature and pressure probes surrounding the high-pressure compressor are expected to provide an accurate indication of the compressor's efficiency as it changes.

Figure 4 shows a sketch of a jet engine compressor. There is a single exit temperature probe for the compressor and a single static pressure probe. The temperature sensor is immediately behind the last stage, nearly flush with the wall surface to minimize the chance for damage if it should fail. The static pressure probe is located in the transition duct to the combustor.

There are many possible sources for compressor deterioration. Engine transients can result in rubs between the rotor blades and the shrouds or between the stators and the rotor land, increasing clearances. Salt, sand, or other materials can be ingested by the engine causing erosion of the compressor

blades. Pollutants can cause corrosion of the blades that also will alter the surface finish. Rubs can result in splatter on the blades. Foreign or domestic object damage can bend or even break off compressor blades. All of these mechanisms result in reduced compressor efficiency.

Damage can be sustained uniformly throughout the compressor, or can be limited to some stages. It can be uniform around the circumference or can be confined to smaller sectors.

It is difficult to imagine that a single element thermocouple and a single static pressure probe can reflect these damage mechanisms appropriately. This is especially true when there is no testing to establish the optimal placement for these single element probes. Design and placement of gas path sensors must be emphasized in future research if there is to be much improvement in gas path analysis.

Continuous Versus Discrete Analysis

Diagnosis is a classification problem—its goal is to determine the faulted element(s) of a system that fails to meet its expected performance. This is true whether the object of the analysis is a sick child or a deteriorated jet engine. The objective in either case is to identify a course of action that will eliminate the problem.

Weighted-least-squares, in contrast, is a quantification tool. It estimates the efficiency and flow capacity of the components and the measurement errors. The results of the analysis are continuous variables—there is no discrete *classification* of the result. The burden of deciding whether a deviation is significant (warranting maintenance) falls to the user.

This incompatibility of the tool to the problem may seem trivial, even desirable. Shouldn't users decide the threshold for maintenance, rather than the software? Perhaps they should. But the program is evaluated on the success of the chosen maintenance, not the accuracy of the component results and measurement errors. Thus, the user interpretation becomes an essential part of the algorithm.

Different users will reach different conclusions from the same results. Their decisions are often based on a limited understanding of the weighted-least-squares algorithm. For instance, they may not be aware that an indicated EGT measurement error, in concert with an indicated problem in the high-pressure turbine, may be solely the result of the efficiency problem. This may lead them to replace the EGT harness in an attempt to regain the performance associated with the measurement error. This will usually be fruitless, and the failure will be attributed to the algorithm.

The variance of user interpretation may be more significant than the problems in the weighted-least-squares algorithm itself.

A better gas path analysis tool might take advantage of information such as maintenance history and borescope results in addition to the weighted-least-squares results to develop specific maintenance recommendations. The results should be presented in such a way that users can develop their own conclusions. Often, the results of the program would be used as presented. Several developing technologies (expert systems, neural networks, model-based reasoning) might provide the framework for this type of advance. There now appears to be very limited activity in this area.

Summary

There are several difficulties associated with gas path analysis based on the weighted-least-squares algorithm. The algorithm is ineffective without augmentation (for instance, TEMPER's fault logic). The algorithm, by itself, significantly underestimates a true deviation, attributing half or more of the real problem to other faults and measurement errors.

Input needs for the algorithm are a significant problem. Baselines and statistical inputs require extensive data analysis and careful judgment. Accurate baselines are critical to the augmentation strategies. Also, the data needed to generate the baselines and statistics is not available when the engine is introduced to service. Thus, an alternate, less accurate approach must be used initially or gas path analysis capability must await acquisition of sufficient data to generate baselines and statistics.

There are significant engine components that are not "observable" via the current gas path analysis algorithms. For example, combustor performance, high-pressure turbine performance, turbine cooling and overboard leaks are indistinguishable given existing sensor packages.

Single-element sensors cannot be expected to respond consistently to the variety of mechanisms causing component deterioration.

None of these problems is likely to be solved by a different algorithm. The blame should be given to the sensors. No algorithm will consistently interpret poor sensor data. Weighted-least-squares settles for the "most probable" solution.

For gas path analysis to succeed, manufacturers will need to supply enough sensors so that all expected component faults are observable. If sensor problems are also likely, redundant measurements will be needed to be able to diagnose the sensors. The sensors must be designed to give a more reliable indication of the plane average pressures and temperatures. Otherwise, baseline generation will continue to limit the effectiveness of the algorithms, especially during early service. Design rules are needed for placement of sensors so component degradation will be reflected in measured temperatures and pressures. These rules must consider the variety of deterioration mechanisms for each component.

There is a problem to be blamed on the weighted-least-squares algorithm, augmented or not. The engine diagnosis needs to be of a form to help the user to identify the appropriate corrective actions. It should not require the user to be expert on the inner functioning of the algorithm to select the correct maintenance plan. If weighted-least-squares is to be used as the core of the gas path analysis, a shell should be provided to convert the results to discrete action recommendations.

The promise of gas path analysis continues to be viewed from afar. If we are to reach that promise, the next major advance must come from the sensor designers. Without advance in sensor technology, further modification of the algorithm can only produce small gains.

References

Barwell, M. J., 1987, "Compass-Ground Based Engine Monitoring Program for General Application," SAE Technical Paper No. 871734.

Bryson, A. E., Jr., and Ho, Y. C., 1975, *Applied Optimal Control*, Hemisphere Publishing Corporation, New York, pp. 348–352.

Doel, D. L., 1994, "TEMPER—A Gas Path Analysis Tool for Commercial Jet Engines," ASME JOURNAL OF ENGINEERING FOR GAS TURBINES AND POWER, Vol. 116, pp. 82–89.

Gelb, A., ed., 1974, *Applied Optimal Estimation*, The M.I.T. Press, Cambridge, MA, pp. 102–103.

Urban, L. A., and Volponi, A. J., 1992, "Mathematical Methods of Relative Engine Performance Diagnostics," SAE TOPTEC Series, *Turbine Engine Modeling: An Overview of Current Requirements & Capabilities*, Part 2.

Volponi, A. J., 1982, "A Large Measurement Error Recovery Algorithm for Gas Turbine Module Performance Analysis," Hamilton Standard Report No. 3430.

APPENDIX

Mathematical Basis of Statistical Gas Path Analysis

To determine engine component performance from revenue service data, sensor error must be considered. In TEMPER, weighted-least-squares satisfies this need. This appendix gives a brief description of the weighted-least-squares algorithm. For

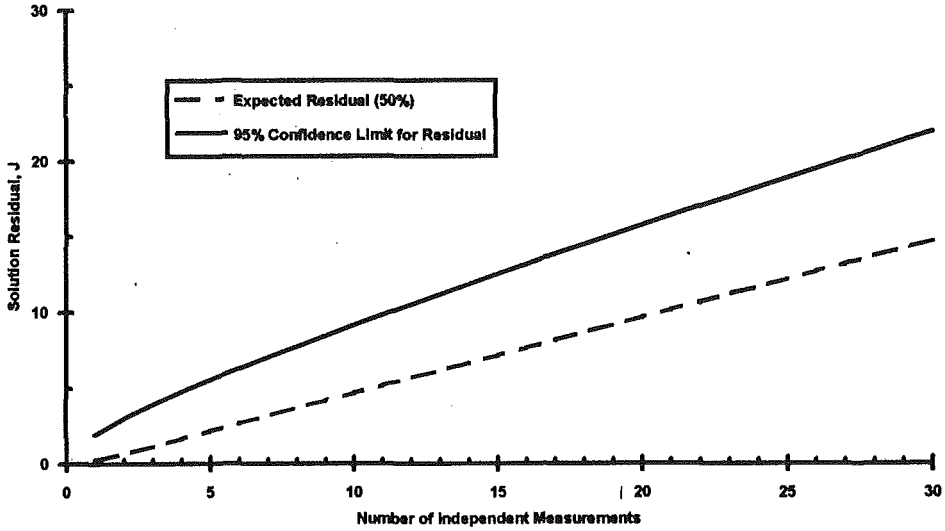

Fig. A-1 Weighted-least-squares solution residual

more detail the reader should consult Doel (1994), Bryson and Ho (1975), or Gelb (1974).

TEMPER uses a model of the measurement process of the form:

$$\mathbf{z} = \mathbf{H}\mathbf{x} + \nu \tag{1}$$

In this equation:

z is the measurement vector comprised of the independent[10] measurements on which the analysis is based (e.g., core speed, fuel flow). **z** has dimension "p."

x is the "state vector," composed of the characteristics of the engine expected to vary with time (e.g., compressor efficiency, turbine flow function). The attributes, not expected to change with time (such as nozzle area), are excluded from **x**. **x** has dimension "*n*."

H is a $p \times n$ matrix describing[11] the effect of the state variables upon the measurements. In the jet engine condition monitoring example, **H** is derived from a cycle model.

ν is the vector of measurement noise. Measurement bias is included in the model.[12]

Several assumptions are made to simplify the mathematics. The measurement error is assumed to be Gaussian, with zero mean. **R** is defined to be the covariance matrix of the measurement error:

$$\mathbf{R} = E(\nu\nu^{\mathrm{T}}) \tag{2}$$

where E is the expected value operator. The diagonal elements of **R** represent the variances of the measurement errors. The off-diagonal elements, representing the covariance of the measurement errors, are assumed to be zero.

The state variables, **x**, are also assumed to be Gaussian. Without loss of generality, their mean can be taken to be zero.[13] **M** is defined to be the covariance matrix for the state vector:

$$\mathbf{M} = E(\mathbf{x}\mathbf{x}^{\mathrm{T}}) \tag{3}$$

Some off-diagonal elements of **M** are expected to be nonzero. For example, any mechanism that changes the flow capacity of the fan will almost certainly affect the fan efficiency. However, most off-diagonal elements of **M** are taken to be zero.

The measurement error, ν, is assumed to be statistically independent of the engine state, **x**:

$$E(\mathbf{x}\nu^{\mathrm{T}}) = 0 \tag{4}$$

With these assumptions, the objective of the weighted-least-squares analysis is to obtain a "best estimate" of the state of the system from a set of measurements, **z**. The assumptions allow definition of a Bayesian probability model for the system. A probability density function is defined for the likelihood that the set of measurements, **z**, originated from an initial state vector, **x**. The designation for this probability density function is $P(\mathbf{x}|\mathbf{z})$. It can be shown (Gelb, 1974) that $P(\mathbf{x}|\mathbf{z})$ is a decreasing monotonic function of the quadratic form, J:

$$J = 1/2\{\mathbf{x}^{\mathrm{T}}\mathbf{M}^{-1}\mathbf{x} + (\mathbf{z}-\mathbf{H}\mathbf{x})^{\mathrm{T}}\mathbf{R}^{-1}(\mathbf{z}-\mathbf{H}\mathbf{x})\} \tag{5}$$

Minimizing J with respect to **x** yields the state vector estimate with highest conditional probability. The minimum J is found by requiring that dJ be zero for arbitrary $d\mathbf{x}^{\mathrm{T}}$. Solving for the state estimate, $\mathbf{x}_0$, gives:

$$\mathbf{x}_0 = (\mathbf{M}^{-1} + \mathbf{H}^{\mathrm{T}}\mathbf{R}^{-1}\mathbf{H})^{-1}\mathbf{H}^{\mathrm{T}}\mathbf{R}^{-1}\mathbf{z} \tag{6}$$

Corresponding to the estimate of the engine state, $\mathbf{x}_0$, is an estimate of the true measurement vector, $\mathbf{z}_0$. This is computed using Eq. (1).

$$\mathbf{z}_0 = \mathbf{H}\mathbf{x}_0$$

This is combined with Eq. (6) to compute the estimated measurement error, ν_0:

$$\nu_0 = [\mathbf{I} - \mathbf{H}(\mathbf{M}^{-1} + \mathbf{H}^{\mathrm{T}}\mathbf{R}^{-1}\mathbf{H})^{-1}\mathbf{H}^{\mathrm{T}}\mathbf{R}^{-1}]\mathbf{z} \tag{7}$$

The corresponding solution residual, J_o, is obtained by substituting $\mathbf{x}_0$ into Eq. (5). It is shown (Bryson and Ho, 1975) that the expected value for J_o is $p/2$ where p is the number of independent measurements. The actual value of J_o will depend on how well the model is able to fit the observed data. As J_o increases, it is less likely that the assumed statistical model (expressed by the engine model, **H**, and the covariance matrices, **M** and **R**) is correct for the particular data sample. When J_o is much greater than $p/2$, it is reasonable to assume that one or more of the statistical assumptions is incorrect.

The solution residual, J_o, provides the means to recognize that a specific case is far from nominal conditions. TEMPER

[10]Some of the measurements are used to specify the operating condition of the engine. These include inlet pressure and temperature, fan speed, humidity, and the variable geometry position variables. These measurements are not available to the analysis. The remaining measurements are the independent measurements.

[11]**Hx** is a linear approximation to the true behavior of the engine represented by the nonlinear function **h(x)**. **H** is computed from **h(x)** at the specific operating condition at which the data were acquired.

[12]In a practical sense, ν will include, in addition to the random measurement errors, the influence of any state variables not included in the state vector, **x**, and any random imperfections in the model.

[13]This can be achieved by defining **x** and **z** as deviations from a nominal condition. Thus **z** is not the raw measurement value, but is instead the deviation of the measurement from a nominal reference condition, and **x** represents the deviation of the state variables from that same nominal point.

assumes that J_o follows the Chi-Squared distribution.[14] The TEMPER fault logic is invoked whenever the residual exceeds the 95 percent confidence limit (Fig. A-1).

When the fault logic is invoked, a weighted-least-squares analysis is performed to evaluate each possible hardware fault or sensor error. To evaluate a specific sensor error fault, its standard deviation is increased by a factor of 100. If the large deviation was due to an abnormally large error in the sensor, the solution residual should be reduced to a reasonable level. A similar technique is used for state variable faults (their standard deviations are also increased by a factor of 100). The technique is even applied to faults not included in the original analysis (such as turbine cooling flow or fan speed measurement error). After testing all possible engine faults and measurement errors, the best solution (based on probability) is accepted if its probability exceeds a minimum value (currently 25 percent).

[14]Actually, $2J_o$ is assumed to obey the Chi-Squared distribution with p degrees of freedom. We are not aware of a proof for this assertion.

Fault Diagnosis in Gas Turbines Using a Model-Based Technique

G. L. Merrington
DSTO,
Aeronautical Research Laboratory,
Victoria, Australia

Reliable methods for diagnosing faults and detecting degraded performance in gas turbine engines are continually being sought. In this paper, a model-based technique is applied to the problem of detecting degraded performance in a military turbofan engine from take-off acceleration-type transients. In the past, difficulty has been experienced in isolating the effects of some of the physical processes involved. One such effect is the influence of the bulk metal temperature on the measured engine parameters during large power excursions. It will be shown that the model-based technique provides a simple and convenient way of separating this effect from the faster dynamic components. The important conclusion from this work is that good fault coverage can be gleaned from the resultant pseudo-steady-state gain estimates derived in this way.

Introduction

The significant cost benefits associated with maintaining gas turbine engines on-condition are now widely recognized. On-condition maintenance is best performed on modular engines and therefore it is desirable to be able to diagnose performance-related problems to module level if possible. It follows then that reliable engine health monitoring and condition assessment techniques are important components of an effective engine maintenance program. Early monitoring techniques mainly involved trending manually recorded data corrected for variations in ambient conditions. Thus important effects, such as measurement noise and sensor biases, were often wrongly interpreted as degraded gas path components. The realization that the problem was basically stochastic in nature rather than deterministic quickly led to the adoption of more advanced signal processing techniques.

Until fairly recently, most of the effort in the engine condition assessment area has been devoted to developing improved techniques for extracting the required information from steady-state data. For example, commercial airline operators have largely based their engine health assessment on cruise data. The major engine companies have proprietary computer-based techniques available for operators to use as part of their engine management programs. For example, General Electric has TEMPER (Doel, 1994) for use with data recorded on the wing and another version for evaluating engines under test-cell conditions. Similarly, Rolls Royce has COMPASS (Provost, 1988), which is capable of providing engine condition information from on-wing engine data (cruise, take-off, ground-run, and start) as well as from test-cell data. These techniques address the stochastic nature of the real problem and use optimal estimation theory to take account of measurement noise. Thus their performance is far superior to many of the earlier methods, which tried to treat the problem as a deterministic one.

Contributed by the International Gas Turbine Institute and presented at the 38th International Gas Turbine and Aeroengine Congress and Exposition, Cincinnati, Ohio, May 24–27, 1993. Manuscript received at ASME Headquarters February 12, 1993. Paper No. 93-GT-13. Associate Technical Editor: H. Lukas.

In many situations, good quality steady-state data are simply not available. However, some current generation aircraft are equipped with Engine Monitoring Systems (EMS), which also have a capability to record transient data. For example, the EMS in the F/A-18 records a range of engine parameters during take-off, in-flight when a parameter excess is detected and at other times when manually selected by the crew. The potential to use the transient takeoff record for engine condition purposes has been recognized by several groups. The techniques that have emerged as likely candidates include correlative methods (Cue and Muir, 1991; Eustace et al., 1994; Henry, 1988; Muir et al., 1988) and model-based methods (Merrington, 1988, 1989; Merrington et al., 1991; Villaneuva et al., 1991). Moreover, it has been shown that the fault coverage capability of these transient techniques is similar to the steady-state methods for a range of operational type faults (Eustace et al., 1994). For some problems, the transient approach gives additional insight that may not be extracted easily from steady-state tests. For example, some fuel control related problems are clearly visible from transient test data. Many engines utilize a $WF/Ps3$ versus corrected compressor speed fuel scheduling loop in order to provide some degree of surge protection during transients. Sensor-type problems, such as a leaky $Ps3$ line, can lead to reduced overfueling, resulting in slow accelerations. Thus by monitoring the $WF/Ps3$ ratio parameter, this type of fault can be readily isolated from other gas path problems.

While the initial impetus for much of this work has stemmed from the military arena, the potential to use transient engine data analysis in other areas is beginning to emerge. There is scope for civil operators to use the technology to estimate take-off power under varying ambient conditions by monitoring previous take-off records. Currently, in most cases, this sort of information is extracted from steady-state cruise data. In addition, there is increasing interest in trying to apply the technology to land-based applications (Meher-Homji and Bhargava, 1992).

In this paper, model-based fault diagnosis in a military turbofan is examined using transient data. A simple technique is

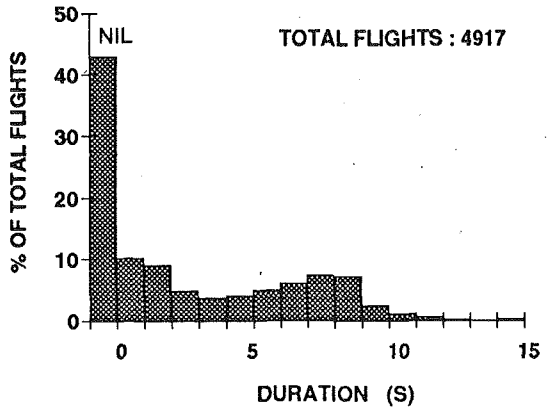

Fig. 1 Distribution of take-off record lengths from operational F/A-18 aircraft (taken from Frith, 1992)

outlined for separating the slower "bulk-temperature" component of an acceleration-type transient from the faster "spooling-up" component. The method is applied to fault implant test data obtained from an F404 engine under Sea-Level-Static (SLS) conditions.

Acceleration Transients

When a gas turbine engine accelerates from one steady-state operating point to another, the process involves two important physical processes. The first is associated with spooling up the engine to the required speed demanded by the power lever movement. The engine controller will limit the degree of overfueling based on prior knowledge of the available surge margin from a specification engine. As the actual spool speed approaches the desired value, the controller enters a governing phase to ensure that the final speed is achieved without excessive overshoot. This process in a current generation military gas turbine takes place in a relatively short time. Typically an acceleration from idle power to maximum dry power takes less than five seconds with a characteristic time constant of the order of 0.5 s. This is accompanied by a much slower thermal process involving heat addition to the metal components surrounding the gas stream. The time taken to achieve thermal equilibrium conditions can be of the order of five minutes for large power excursions. This time is not only strongly dependent on the magnitude of the power lever movement but also on the immediate prior operating history of the engine. This second physical process is often termed the bulk metal temperature effect.

Take-off transient data records from operating aircraft, such as the F/A-18, can vary in duration for a number of reasons. In the F/A-18, the take-off record is terminated when the power lever is moved out of the Intermediate Rated Power (IRP) position or when the weight comes off the wheels. Thus aircraft weight, temperature of the day, and differences in individual crew operating techniques can give rise to considerable scatter in the length of these records. For example, results from RAAF operational aircraft indicate that the length of the take-off record can vary between zero and fifteen seconds, as shown in Fig. 1 (taken from Frith, 1992). These times are certainly well short of the time required to achieve true steady-state conditions. It is therefore important to define a consistent pseudo-steady-state end-point criterion for an acceleration transient if a model-based fault detection technique of the type described in the next section is to be utilized.

In general, as take-off accelerations can be initiated from any part-power position (in the case of the F/A-18, an upper limit of approximately 80 percent power is invoked because of power to weight ratio considerations), an end-point criterion based on a fixed record length from some designated starting point or one based on a fixed time interval after the acceleration peak, is usually not suitable. This is because neither criterion addresses the real problem of how to account for the variability in the bulk metal temperature effect when different size transients are involved. One approach would be to model the bulk metal temperature effect mathematically and incorporate this into the data analysis. An alternative approach is to develop a procedure that is capable of isolating the bulk metal temperature effect from the "fast transient" component. This latter approach is the one that has been adopted here.

Analysis Procedure

A model-based technique based on the method outlined by Merrington (1989) was used. Briefly this technique is given in the form:

$$y_t = \theta^T \varphi_t + \epsilon_t \tag{1}$$

where

$$\varphi_t^T = (-y_{t-1}, \ldots, -y_{t-p}, u_{i-1} \ldots, u_{t-q})$$
$$\theta^T = (a_1, \ldots, a_p, b_1, \ldots, b_q)$$

The least-squares estimate (LSE) is the one that minimizes the cost function,

$$J(\theta) = \sum_{t=1}^{n} (y_t - \varphi_t^T \theta)^2 \tag{2}$$

where n is the number of sample points and the estimate of the model parameters is given by:

Nomenclature

a, b = model parameters
$A8$ = exhaust nozzle area
J = cost function
K = steady-state gain
N = total number of samples
NH = compressor rotor speed
NL = fan rotor speed
P = total pressure
Ps = static pressure
T = total temperature
u = measured inputs
WF = fuel flow
$WFss$ = steady-state fuel flow
y = measured outputs
Δ = difference operator
ϵ = error vector
θ = parameter vector
κ = acceleration starting point
σ = standard deviation
φ = measurement vector

Subscripts

n = number of samples in a record
p, q = number of parameters in Eq. (1)
ss = steady-state
t = sample time

Superscript

T = vector transpose

Acronyms

ARL = aeronautical research laboratory
CBLD = compressor bleed
CVG = compressor variable geometry
EMS = engine monitoring system
EPR = engine pressure ratio
FVG = fan variable geometry
GE = General Electric
IECMS = in-flight engine condition monitoring system
IRP = intermediate rated power
LSE = least-squares estimator
PLA = power lever angle
RAAF = Royal Australian Air Force
SLS = sea level static

$$\hat{\theta} = \left(\sum_{t=1}^{n} \varphi_t^T \varphi_t \right)^{-1} \sum_{t=1}^{n} \varphi_t^T y_t \tag{3}$$

Equation (1) can be re-arranged to enable the steady-state gain, K, corresponding to the slope of the steady-state curve, to be extracted. A steady-state condition exists when $y_t = y_{t-i}$ $(i = 1, \ldots, p)$ and $u_{t-1} = u_{t-i}$ $(i = 1, \ldots, q)$ giving

$$K = \Delta y_{ss} / \Delta u_{ss} = \sum_{i=,1}^{q} \hat{b}_i \Big/ \left(1 + \sum_{i=1}^{p} \hat{a}_i \right) \tag{4}$$

The primary input for a gas turbine is fuel and the effect of the significant nonlinearity in the steady-state relations over the operating speed range is reduced by reformulating the problem (Merrington, 1989) in terms of an overfueling parameter defined by

$$\Delta WF = WF - WFss \tag{5}$$

where $WFss$ is the steady-state fuel at the given speed.

Thus if WF is the only input $(q = 1)$, then u_t becomes

$$u_t = WF_t - WFss_t \tag{6}$$

The start of an acceleration was determined by monitoring the rate of change of the relatively fast response compressor outlet static pressure signal ($Ps3$). The actual sample point κ corresponding to this starting point was obtained from

$$Ps3_{\kappa+1} - Ps3_{\kappa-1} > 4\sigma \tag{7}$$

where σ corresponds to the standard deviation of the measurement noise on the $Ps3$ signal. A forty-point sample of the steady-state segment of the record immediately preceding the acceleration transient was included to identify the initial steady-state condition. The LSE analysis was then performed to determine how the minimum error variance $J(\theta)_{\min}$, varies with record length. Commencing with a record of 80 samples (to ensure a reasonable length of the "fast-response" part of the transient was included) the LSE was then applied to progressively longer records by adding five additional sample points at a time until all the data were included.

Since most of the fault information is contained in the steady-state gain term rather than in the dynamics (Villaneuva et al., 1991), it is important to define a method for isolating that component of the gain attributable to the acceleration from that associated with the bulk metal temperature effect. The bulk metal temperature effect becomes more important as the scale of the transient increases in the absence of re-slam (when a snap acceleration immediately follows a rapid deceleration) effects due to the larger differential between gas and metal temperatures. As re-slam effects are usually absent during pre-takeoff procedures, the distribution of $J(\theta)_{\min}$ with record length can be used to separate these two important effects.

The criterion found most suitable for separating the bulk temperature effect was to locate the minimum of the cost function minima (Eq. (2)) for record lengths in the range $(n_0 < n < N)$ where n_0 is the initial record length (80 sample points) and N is the total record length. Intuition would suggest that for large transients, such as a flight-idle to IRP acceleration, the desired pseudo-steady-state end point should be in close proximity to the peak of the transient and move progressively downstream from the peak as the size of the transient diminishes.

For convenience a first-order model $(p = q = 1)$ was adopted for this investigation. These models are known to give reasonable accuracy in the vicinity of an operating point, that is, for small transients. However, they can also be applied to larger transients to extract useful comparative information. While the errors in the absolute values will tend to increase as the magnitude of the transient increases (when the nonlinear effects become significant), test results indicate that the relative errors between the fault and no-fault cases are still small. Thus the absolute accuracy is less important in the present application than the relatively consistency between the fault and no-fault estimates.

Test Program

The test program has been described in detail by Eustace et al. (1994), and therefore it will suffice, for present purposes, to summarize the important points. The aim of the test program was to implant a range of operating type faults in a military turbofan engine under test-cell conditions and acquire data from a number of simulated take-off transients.

Engine. The engine used in this investigation was a GE-F404 taken from a fleet of engines operated by the RAAF in the F/A-18. The F404 is a low-bypass, twin spool afterburning turbofan. A schematic of the engine showing the major station locations is given in Fig. 2. The engine is designed to be maintained on-condition and has six main modules, comprising the fan, compressor, combustor, high-pressure turbine, low-pressure turbine and afterburner section. Accelerations to maximum dry or Intermediate Rated Power (IRP) are scheduled as a function of corrected compressor speed and then limited near IRP via fan-speed (NL) and low-pressure turbine outlet temperature ($T5$) limiter loops in the controller. The engine has variable geometry in the fan, compressor, and in the final nozzle.

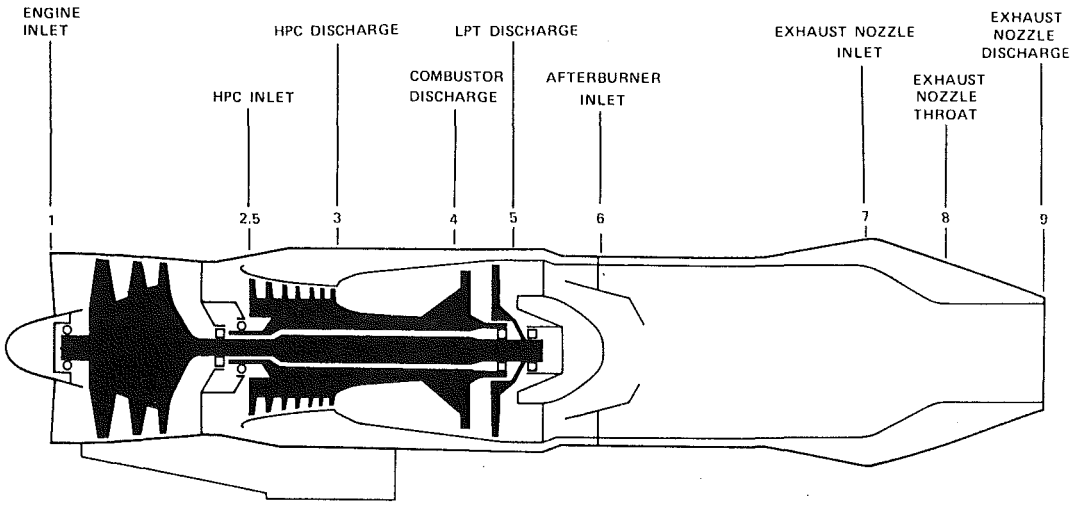

Fig. 2 F404 engine and station locations

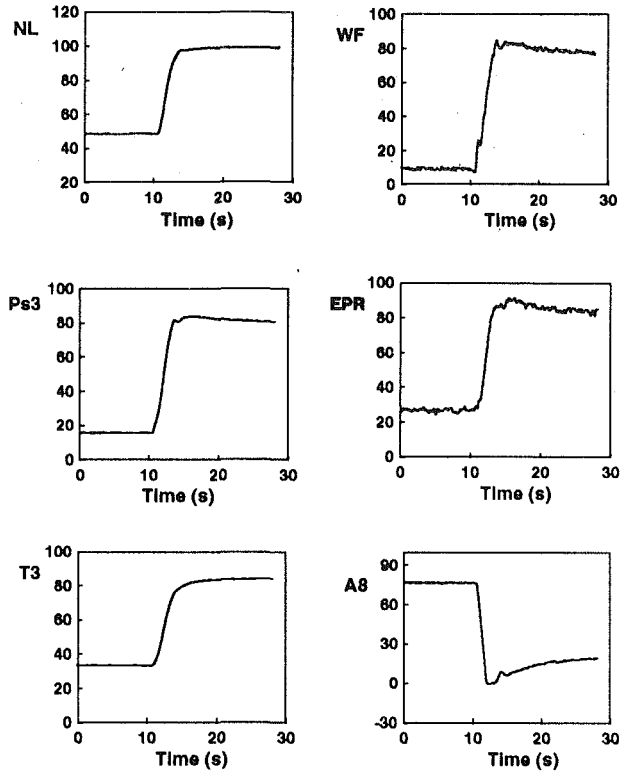

Fig. 3 Parameter variation during a large acceleration from flight idle to IRP

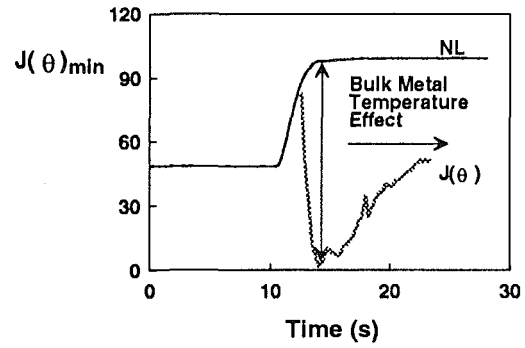

(a) Minimum Variance

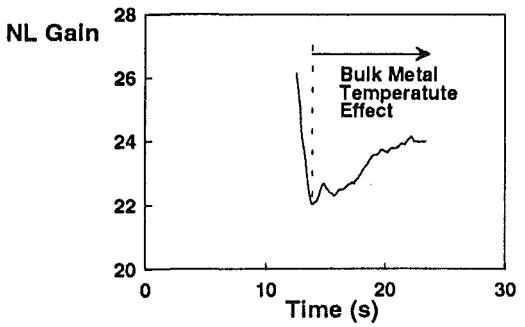

(b) Fan Speed to Fuel Flow Gain

Fig. 4 Minimum variance criterion used to isolate the bulk metal temperature effect from the faster spooling-up component

Test Data. Data from a number of engine-mounted sensors were captured using a transient data acquisition system. These parameters included those normally acquired by the aircraft's EMS, namely, inlet temperature ($T1$), inlet pressure ($P1$), fan speed (NL), compressor speed (NH), compressor outlet static pressure ($Ps3$), fuel flow (WF), turbine outlet pressure ($P56$), low-pressure turbine outlet temperature ($T5$), final nozzle area ($A8$), and power lever angle (PLA). Additional parameters were measured in the test cell including compressor outlet temperature ($T3$) and the variable vane settings in the compression system. Snap accelerations, with and without implanted faults, were performed from several part power positions (PLA = 30, 60, 80, and 90 deg) to IRP (PLA = 102 deg) to simulate typical take-off transients. The data were acquired at a sampling rate of 32 Hz and measured parameters were then corrected to standard day conditions, but no prefiltering was performed. All the data have been normalized to facilitate the presentation of the results.

Implanted Faults. The implanted faults comprised mis-scheduled fan variable geometry (FVG), mis-scheduled compressor variable geometry (CVG), final nozzle biased open 5 percent (A8 + 5 percent), biased $T5$ sensor via a faulty $T5$ harness (Biased $T5$) and a variation in the customer bleed from the outlet of the compressor (CBLD). The FVG was biased 3.5 deg closed. Three levels of the CVG fault were examined consisting of 2 deg further open from the nominal setting (CVG + 2), 2 deg closed from nominal (CVG-2) and 6 deg closed from nominal (CVG-6). The faulty $T5$ harness imposed a positive bias of approximately 60°C.

Results

Data obtained from an F404 engine in a SLS test cell were used to examine the method outlined above as a way of isolating the fast acceleration component from the much slower bulk metal temperature effect. This technique was then applied to the problem of detecting a range of implanted faults.

Separation of the Bulk Metal Temperature Effect. A number of accelerations to IRP from various part power positions was performed on the nonfaulty engine. Corrected data for a snap acceleration from flight idle (PLA = 30 deg) are shown in Fig. 3. The bulk temperature effect is readily apparent from the decay in WF, $Ps3$ and EPR during the latter part of the transient when the engine is under the control of the NL and $T5$ limiters. Moreover, this trend is reflected in the rising $A8$ signal required to maintain the scheduled $T5$ value. The $J(\theta)$ distribution derived from the recursive least-squares method is shown in Fig. 4. The minimum $J(\theta)$ point is located soon after the transient peak, as expected. Furthermore, the minimum variance point closely corresponds to the minimum gain position for this transient (Fig. 4).

By comparison, results for a small transient commencing just below the IRP setting (PLA = 90 deg) are shown in Fig. 5. The bulk temperature effect is less readily discernible in this case because the changes in the metal temperatures will be small. Moreover, the minimum $J(\theta)$ point is located approximately eight seconds after the peak of the transient (Fig. 6).

The trend in the minimum $J(\theta)$ position for snap accelerations commencing at PLAs in the range 30 to 90 deg is shown in Fig. 7. The position of the minimum $J(\theta)$ point for each acceleration is given as a ratio of $\Delta t_n/\Delta t_{Ps3}$, where Δt_n represents the time interval between the minimum $J(\theta)$ point and the initial starting point for the transient (based on the $Ps3$ criterion defined in Eq. (7)) and Δt_{Ps3} is the corresponding $Ps3$ rise time. A suitable definition of $Ps3$ rise time for this purpose is the time taken to reach the peak $Ps3$ value during the transient. This proved to be a convenient and consistent way of scaling the individual transients. The $Ps3$ rise time is shown to vary almost linearly with initial PLA (Fig. 8). The results in Fig. 7

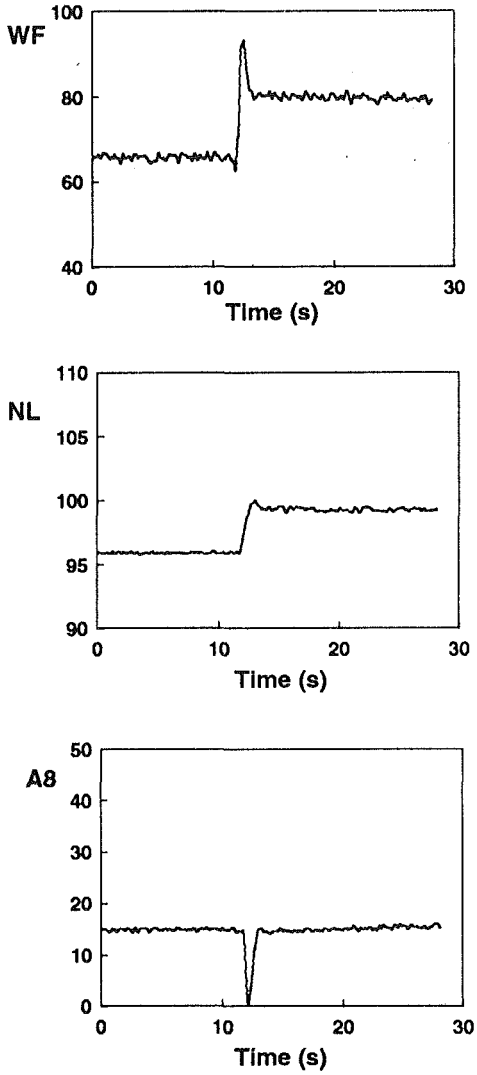

Fig. 5 Parameter variation during a small acceleration; PLA = 90–102 deg

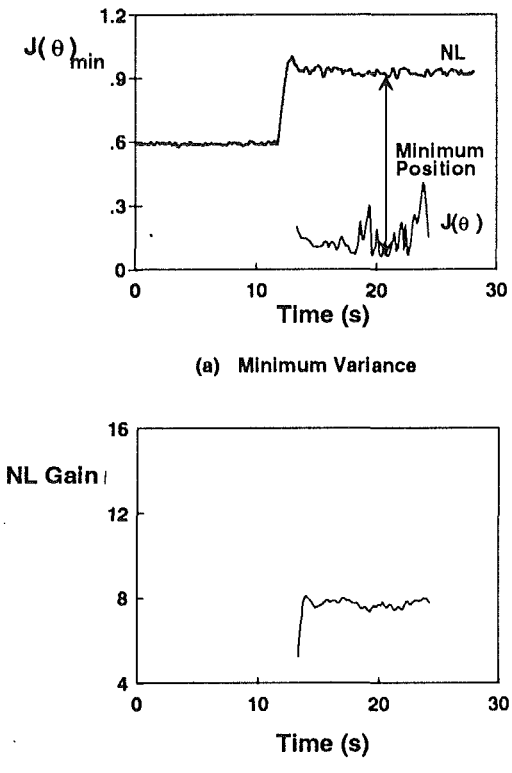

Fig. 6 Minimum variance and gain estimates for a small acceleration

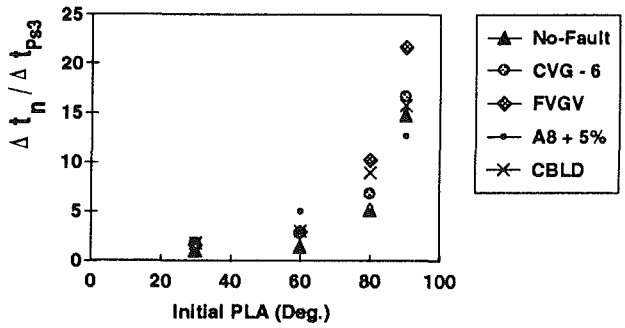

Fig. 7 Record length as a function of *Ps*3 rise time for a range of accelerations

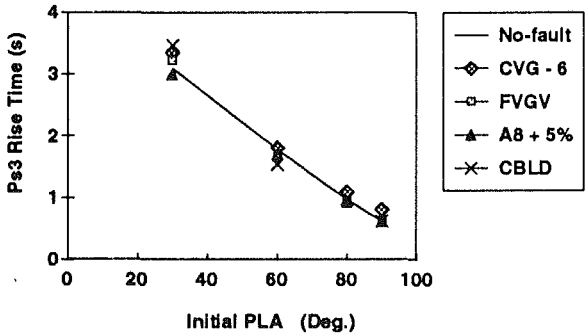

Fig. 8 *Ps*3 rise times for a range of accelerations

indicate that the scatter increases as the scale of the transient decreases, that is, as the influence of the bulk metal temperature effect becomes smaller. The increased level of scatter associated with the small-scale transients is still acceptable because it only has a small effect on the resultant gain estimates (Fig. 6). Conversely, the scatter for the large flight-idle to IRP acceleration is small, indicating that the boundary is clearly delineated under these conditions, as shown by the "peaky" distribution in Fig. 4.

It is immediately apparent from the above results that the boundary between the "fast transient" and the slower "bulk metal temperature" component moves toward the transient peak as the scale of the transient increases. Moreover, the criterion developed here is capable of separating these two effects without reference to any other parameters, such as final nozzle area.

Fault Detection. The next step is to use the criterion above to enhance the detection process for a range of faults using transient data. The fault detection procedure consisted of monitoring the estimated pseudo-steady-state gains from a number of take-off-type acceleration transients, with and without faults. Normalized fault deltas were then formed by taking the difference between the fault and no-fault gain estimates as a percentage of the no-fault value.

Results for the three levels of mis-scheduled CVG fault are given in Fig. 9. It is important to note the difference scales used in Fig. 9 in order to make sensible comparisons between the results for the various accelerations. The 6 deg closed fault condition is clearly evident from all the accelerations. The sensitivity was found to increase as the magnitude of the acceleration decreased, that is, as the initial part-power starting

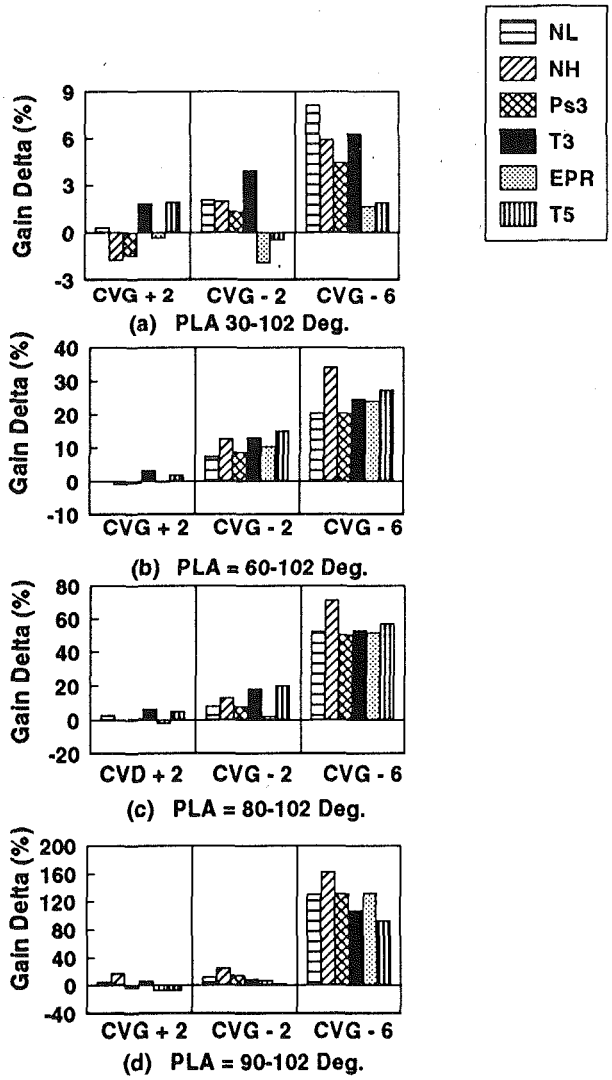

Fig. 9 Gain deltas for three levels of CVG fault

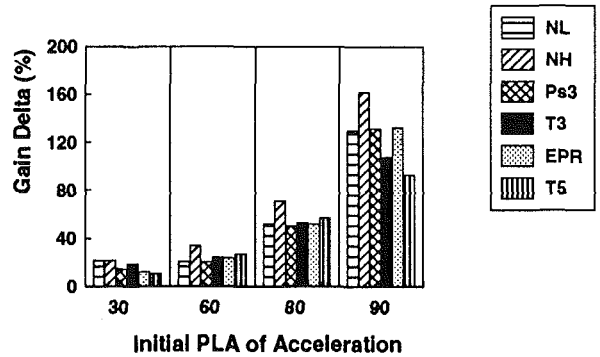

Fig. 10 Gain deltas for 6 deg bias CVG fault

point approached the IRP position. This can be more easily seen if the data for one fault level are plotted for the range of transients as in Fig. 10. Insufficient no-fault data were available to ascertain reliably the variability in the no-fault estimates. Preliminary indications are that for parameter gains based on fuel flow, the no-fault uncertainty appears to fall in the range of 3–5 percent, meaning that parameter deltas that fall below this will be undetectable. The smaller 2 deg closed fault condition is detectable from most of the accelerations except in the flight-idle to IRP case. However, the 2 deg open fault is not easily detected from any of the parameters. One possible

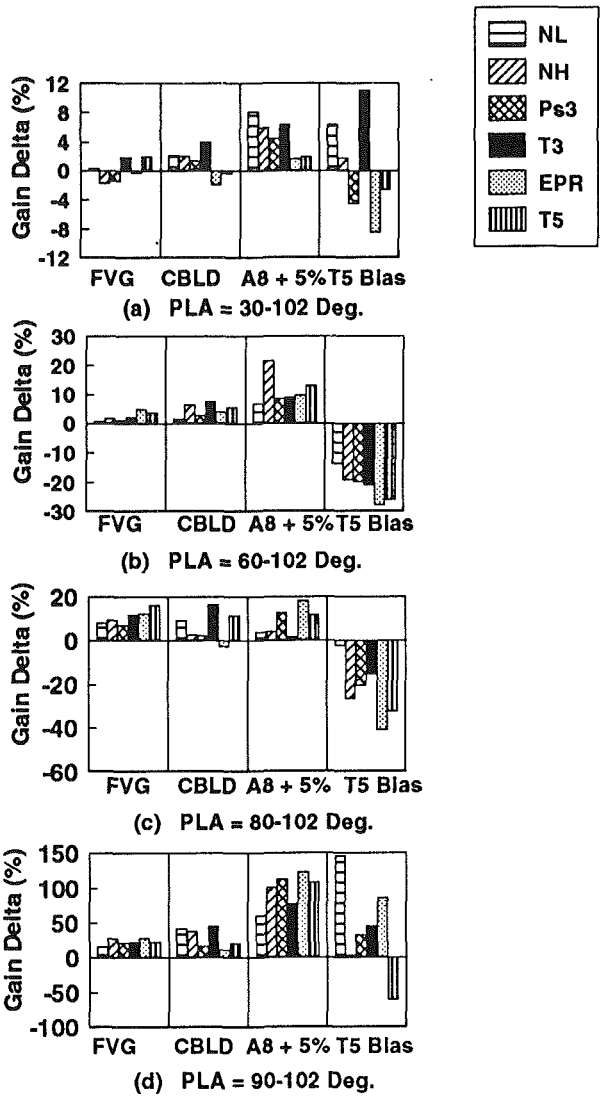

Fig. 11 Gain deltas for four separate faults

explanation for the reduced sensitivity to this latter fault condition is that the adjustable linkage was found to have a residual error.

Results for the other fault conditions are given in Fig. 11. In the case of the FVG fault, in which the blade angles were biased 3.5 deg closed from the nominal no-fault setting, it is detectable from accelerations commencing at or above PLA of 80 deg. However, the parameter set is not adequate for the larger accelerations. The final nozzle fault, comprising a 5 percent bias in the open direction, is readily detectable across the full range of the acceleration transients, but the sensitivity improves as the part-power starting point increases toward the higher power settings.

Again, the biased $T5$ indicator (approximately 60°C) arising from a faulty $T5$ harness is detectable from NH, $Ps3$, $T3$, $T5$, and EPR parameters from the accelerations with initial PLAs in the range 60 to 90 deg. The results from flight idle were mixed, with $T3$ and EPR being the most sensitive parameters. Finally, a small compressor bleed fault was most easily detected from the recorded temperatures, namely $T3$ and $T5$. All other parameters were largely insensitive to this fault. Again the sensitivity to the fault increased as the initial part-power position for the transient increased.

Discussion

The model-based technique examined here is shown to be

capable of detecting a range of operational type faults. The procedure developed to identify the boundary between the faster spooling-up part of the transient and the slower bulk temperature effect proved effective in separating these two quite distinct physical processes. Failure to incorporate this step in the analysis of transient engine data can lead to an increased level of uncertainty in the resultant gain estimates. This aspect is likely to be important when applying the technology to a field based system, such as that for an F/A-18 where the record length can vary significantly.

The model-based method provides additional information to that obtained with a snapshot technique (Eustace et al., 1994) because the gain terms are given by parameter rates of change or slopes rather than absolute values at a particular instant, as is the case with a snapshot method. As a result, the model-based technique will be less sensitive to bias effects in the measured parameters. However, bias effects will still be important in the parameters that are used for some controller functions, such as $T5$, which is used in the F404 for limiting gas temperatures and therefore metal temperatures near IRP.

Some fault conditions were more easily detected than others. For example, the CVG relatively large 6 deg bias fault was easily detected from all part-power accelerations. The remaining faults were best detected from those accelerations commencing at the higher part-power positions. Generally, all fault conditions were less easily detected from the flight-idle to IRP accelerations. The addition of compressor outlet temperature to the instrumentation set increased the resultant fault coverage. This was especially true in the case of the compressor bleed fault.

Further information can be gleaned from the data set by substituting other parameters in place of fuel for the input. In addition, other techniques are being examined to improve the fault coverage capability further. For example, neural networks are being applied to the problem at ARL with encouraging results. However, these methods do require a comprehensive training data-base in order to perform well.

Conclusions

A model-based system for detecting a range of faults in a turbofan engine has been examined. A new procedure has been defined for separating the slower bulk temperature effect from the faster spooling-up effect. This is an important consideration in some field-based engine monitoring systems where the length of the captured record can vary significantly. It was shown that the records derived from the F/A-18 during take-off do not achieve true steady-state conditions and therefore a procedure is required to determine a consistent cut-off point for any transient. The minimum variance condition developed in this paper yielded excellent results when applied to test-cell data. However, the system has yet to be proven on field-based data.

The model-based method provides additional information to that obtained with a snapshot technique. Furthermore, the measurement noise is accounted for in a more meaningful way using the properties of a least-squares estimator.

References

Cue, R. W., and Muir, D. E., 1991, "Engine Performance Monitoring and Troubleshooting Techniques for the CF-18 Aircraft," ASME JOURNAL OF ENGINEERING FOR GAS TURBINES AND POWER, Vol. 113, pp. 11–19.

Doel, D. L., 1994, "TEMPER—A Gas-Path Analysis Tool for Commercial Jet Engines," ASME JOURNAL OF ENGINEERING FOR GAS TURBINES AND POWER, Vol. 116, pp. 000–000.

Eustace, R. W., Woodyatt, B. A., Merrington, G. L., and Runacres, A., 1994, "Fault Signatures Obtained From Fault Implant Tests on an F404 Engine," ASME JOURNAL OF ENGINEERING FOR GAS TURBINES AND POWER, Vol. 116, pp. 000–000.

Frith, P. C. W., 1992, "Trend Analysis of F/A-18 Engine Performance Using IECMS Take-Off Records," ARL-PROP-TM-470.

Henry, J. R., 1988, "CF-18/F404 Transient Performance Trending," AGARD-CP-448, Paper No. 37.

Meher-Homji, C. B., and Bhargava, R., 1992, "Condition Monitoring and Diagnostic Aspects of Gas Turbine Transient Response," ASME Paper No. 92-GT-100.

Merrington, G. L., 1988, "Identification of Dynamic Characteristics for Fault Isolation Purposes in a Gas Turbine Using Closed-Loop Measurements," AGARD-CP-448, Paper No. 36.

Merrington, G. L., 1989, "Fault Diagnosis of Gas Turbines From Transient Data," ASME JOURNAL OF ENGINEERING FOR GAS TURBINES AND POWER, Vol. 111, pp. 237–343.

Merrington, G. L., Kwon, O.-K., Goodwin, G., and Carlsson, B., 1991, "Fault Detection and Diagnosis in Gas Turbines," ASME JOURNAL OF ENGINEERING FOR GAS TURBINES AND POWER, Vol. 113, pp. 276–282.

Muir, D. E., Rudnitski, D. M., and Cue, R. W., 1988, "CF-18 Engine Performance Monitoring," AGARD-CP-448, Paper No. 7.

Provost, M. J., 1988, "COMPASS: A Generalized Ground-Based Monitoring System," AGARD-CP-448, Paper No. 42.

Villaneuva, H., Merrington, G. L., Ninness, B., and Goodwin, G., 1991, "Application of Robust Fault Detection Methods to F404 Gas Turbine Engines," presented at the IFAC/IMACS-Symposium, Baden-Baden, Germany.

Models for Predicting the Performance of Brayton-Cycle Engines

T. Korakianitis
Washington University,
St. Louis, MO 63130

D. G. Wilson
Massachusetts Institute of Technology,
Cambridge, MA 02139

Gas turbine performance is the result of choices of type of cycle, cycle temperature ratio, pressure ratio, cooling flows, and component losses. The output is usually given as efficiency (thermal, propulsive, specific thrust, overall efficiency) versus specific power. This paper presents a set of computer programs for the performance prediction of shaft-power and jet-propulsion cycles: simple, regenerative, intercooled-regenerative, turbojet, and turbofan. Each cycle is constructed using individual component modules. Realistic assumptions are specified for component efficiencies as functions of pressure ratio, cooling mass-flow rate as a function of cooling technology levels, and various other cycle losses. The programs can be used to predict design point and off-design point operation using appropriate component efficiencies. The effects of various cycle choices on overall performance are discussed.

Introduction

Two important parameters in thermodynamic cycles for shaft-power engines are thermal efficiency and specific power. Thermal efficiency is defined as:

$$\eta_{th} \equiv \frac{\dot{W}_S}{\dot{\Omega}_F} \approx \frac{\dot{W}_S}{\dot{m}_F \, \mathrm{LHVF}} \tag{1}$$

In modern gas turbine engines the turbine-inlet temperature is between 1500 K and 1700 K. With ambient temperatures of about 300 K, $5 < T' \equiv T_{\max}/T_{\min} < 5.7$, where $T_{\max}$ and $T_{\min}$ are the maximum and minimum temperatures of the working fluid. The corresponding Carnot coefficients ($\eta_{th,\max}$) are $0.80 < \eta_{\mathrm{Carnot}} = 1 - 1/T' < 0.83$. This is much higher than current simple-cycle thermal efficiencies, the best of which are about 0.4. Regenerative and intercooled-regenerative cycles with low pressure ratios can attain thermal efficiencies between 0.5 and 0.6. Specific power $\dot{W}'$, a nondimensional measure of the power density of the cycle, is defined as:

$$\dot{W}' \equiv \frac{\dot{W}_S}{\dot{H}_{01}} = \frac{\dot{W}_S}{\dot{m}_A h_{01}} \tag{2}$$

A large portion of the expense for the development of gas turbines is devoted to the high-temperature and high-pressure-ratio components. The former are needed for every high-performance heat engine. The latter are essential for aircraft-propulsion applications. High-pressure-ratio compressors are expensive components to design and develop, and they need variable geometry and concentric multishaft arrangements for reasonable starting and part-load performance (Wilson, 1984). Because of the prohibitive cost of developing new gas turbine engines and their components, many shaft-power gas turbine engines are derivatives of existing aero-engines (Harmon, 1990; Slatter, 1982). Gas turbine manufacturers try to develop common components in a gas generator for a series of engines. The exhaust of the gas generator is used in one or more combinations of the following: expanded through a nozzle to produce jet thrust in turbojet applications; expanded through an additional power turbine to drive a shaft in turboshaft and turboprop applications; and partially expanded through a power turbine to drive a fan, partially through a nozzle in turbofan applications. High-pressure-ratio simple cycles are well suited for light high-power-density aircraft engines. The following cycle-performance maps indicate that substantially different thermodynamic-cycle parameter choices should be made for engines intended for different applications.

Shaft-Power Cycles

Simple Cycle (CBE). CBE is a simple-cycle acronym for a shaft-power engine consisting of a compressor (*C*), burner (*B*), and expander (*E*) (Fig. 1). A fraction $x1$ of the compressor flow is used to cool the turbine blades, and another fraction $x2$ is extracted from the compressor-exit flow for auxiliary uses. The remaining flow is directed to the burner where the correct amount of fuel is added to reach $T_{04} = T' \cdot T_{01}$. There is a loss of pressure due to friction from p_{02} to p_{04}. The cooling flow is mixed with the main flow, dropping the temperature to T_{041} and the pressure to p_{041}. (These imply an entropy increase.) Pressure p_{05} will normally be a little above atmospheric. This effect is included in the sum of pressure drops of the cycle, which include: the pressure drops due to friction in the various components; the pressure drop from turbine exit

Contributed by the International Gas Turbine Institute and based on a paper presented at the 37th International Gas Turbine and Aeroengine Congress and Exhibition, Cologne, Germany, June 1-4, 1992. Manuscript received by the International Gas Turbine Institute February 27, 1992; revision received February 23, 1994. Paper No. 92-GT-361. Associate Technical Editor: L. S. Langston.

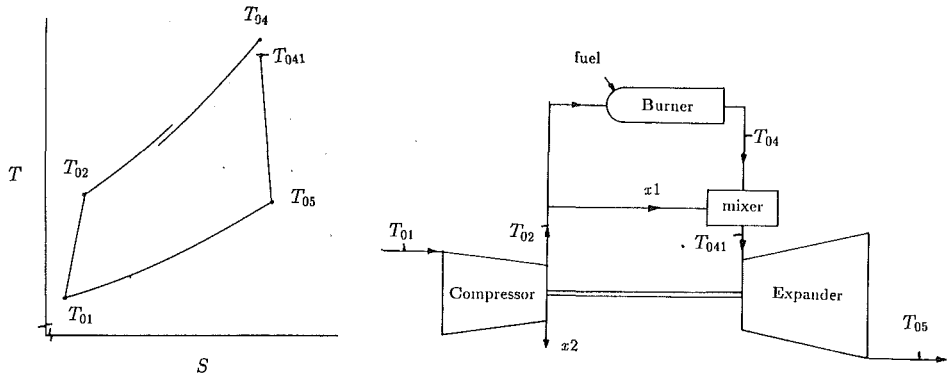

Fig. 1 Temperature-entropy diagram and component arrangements of the simple (CBE) cycle

to atmospheric pressure; and the pressure drop representing the entropy increases due to mixing of the main flow and the cooling flow. In a similar argument, many other penalties to the cycle can be explained in terms of entropy increases that correspond to pressure drops. Thus the total-pressure-drop parameter can be used to model other inefficiencies of all cycles.

Regenerative Cycle (CBEX). CBEX is a regenerative-cycle acronym for a shaft-power engine consisting of a compressor (*C*), burner (*B*), expander (*E*), and heat exchanger (*X*) (Fig. 2). The heat exchanger cold-side and hot-side leakage flows ($x3$ and $x4$) may occur in some heat exchangers such as rotary regenerators.

Intercooled-Regenerative Cycle (CICBEX). CICBEX is an intercooled-regenerative-cycle acronym for a shaft-power engine consisting of a compressor (*C*), intercooler (*I*), compressor (*C*), burner (*B*), expander (*E*), and heat exchanger (*X*) (Fig. 3). The intercooler is an energy-exchange device that uses a different working fluid (such as water from a thermodynamic reservoir) to cool the working fluid from the first compressor delivery before it enters the second compressor. It is assumed that the intercooler splits the cycle pressure ratio equally between the two compressors.

Component and Process Models

In the following c_p and $\bar{c}_p$ of air, fuel-air mixture, and of products of combustion, are evaluated as analytic-polynomial functions of T and f ($c_p = c_p(T, f)$) using the method described by Wilson (1984).

The maximum temperature of hot-section alloys in modern gas turbines is between 1250 K and 1400 K, much lower than current turbine-inlet temperatures. This temperature difference is accommodated by cooling with compressor-outlet air the first, second, and sometimes third turbine stages. The cooling air is ejected around the blades and becomes lower-enthalpy wakes that mix with the main turbine flow while contributing to losses. The frontiers of cooling technology are a trade-off between materials that can withstand hotter temperatures and the development of cooling techniques to minimize the amount of cooling air required by the turbine. Figure 4, derived from Livingood et al. (1971), shows the fraction of compressor-air flow that is used to cool the turbine stages as a function of cooling technology level and nondimensional cooling parameter ω

$$\omega \equiv \frac{(T_{04} - T_{bm})}{(T_{04} - T_{02})} \tag{3}$$

The three lines shown in Fig. 4 change location as cooling technology advances. The cooling-level technology can be assigned any positive value (0.8, 3.2, or 15.0). The corresponding $x1$ is evaluated by linear interpolation between the lines shown in Fig. 4, simulating any level of cooling technology. If the input is such that $x1 \leq 0$, then it is set at $x1 = 0$ (simulating uncooled turbines).

The compressor and turbine performance are computed using

Nomenclature

b = bypass ratio (turbofan cycle)
c_p, $\bar{c}_p$ = specific heat capacity, and mean c_p
C = velocity of nozzle flow, m/s
f = fuel-air ratio
h = specific enthalpy
i = intercooler effectiveness
LHVF = lower heating value of the fuel
$\dot{m}$ = mass flow rate
p = pressure, kPa
r = pressure ratio
R = gas constant = 286.96 J/kg/K for air
s = entropy
T = temperature, K
T' = T_{04}/T_{01} = cycle temperature ratio
t_F = thrust specific fuel consumption
V = aircraft speed, m/s
$\dot{W}$, $\dot{W}'$ = power, specific power (Eq. (2))
$x1$, $x2$, $x3$, $x4$ = leakage and cooling flows
ϵ = heat-exchanger effectiveness
η = efficiency
ω = temperature-difference ratio (Eq. (3))
Ω = thermodynamic availability

Subscripts

0 = total (stagnation) condition
1, 21, 22, 2, 3, 4, 41, 5, 6 = thermodynamic points in the cycles (Figs. 1-3)
A = air
b = burner
bm = surface of blade material
c = compressor
F = fuel
f = fan
j = jet
ov = overall
p = propulsive
r = ram
S = shaft
st = static condition
t = turbine
th = thermal

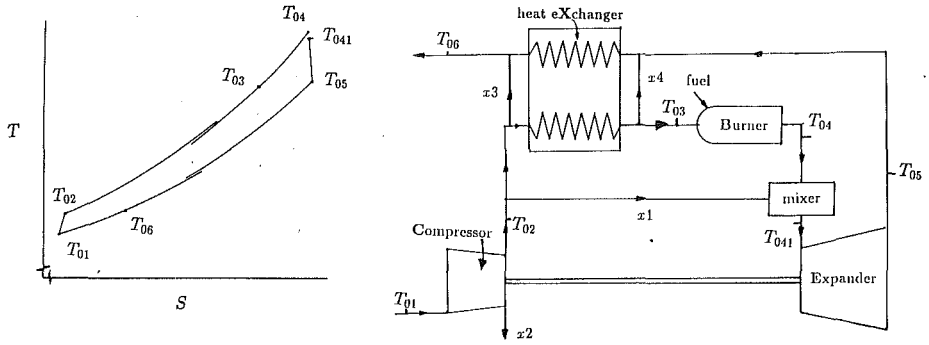

Fig. 2 Temperature-entropy diagram and component arrangements of the regenerative (CBEX) cycle

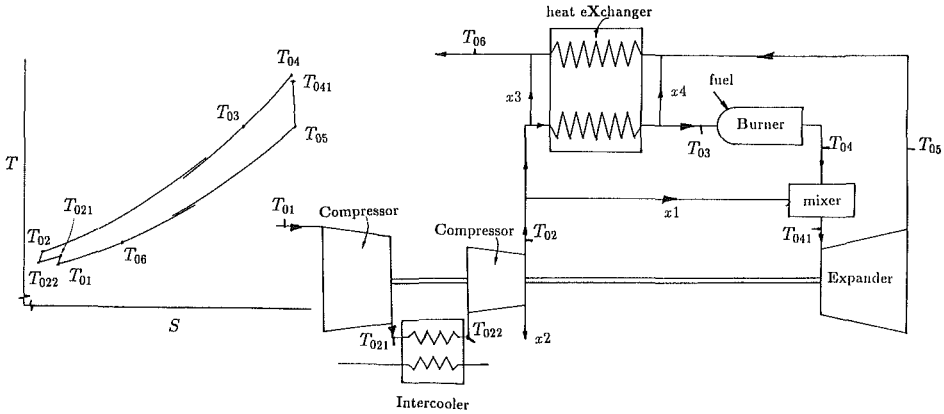

Fig. 3 Temperature-entropy diagram and component arrangements of the intercooled-regenerative (CIC-BEX) cycle

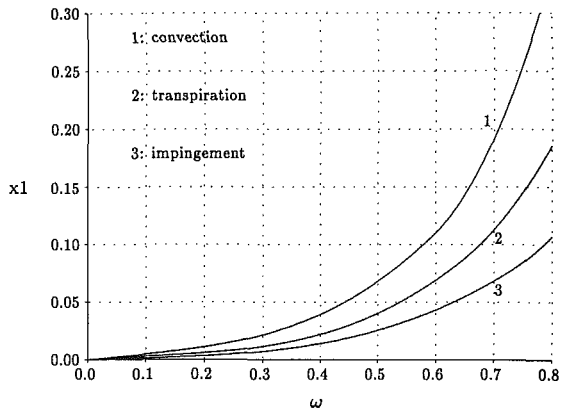

Fig. 4 Compressor-air cooling mass-flow fraction ($x1$) as a function of ω

$$\left(\frac{T_{02}}{T_{01}}\right)=\left(\frac{p_{02}}{p_{01}}\right)^{(R/\bar{c}_p/\eta_c)}$$

$$\dot{W}_c=\dot{m}_c(h_{02}-h_{01})\approx\dot{m}_c\bar{c}_pT_{01}(r_c^{R/\bar{c}_p/\eta_c}-1) \tag{4}$$

$$\left(\frac{T_{05}}{T_{041}}\right)=\left(\frac{p_{05}}{p_{041}}\right)^{(R\eta_t/\bar{c}_p)}$$

$$\dot{W}_t=\dot{m}_c(h_{041}-h_{05})\approx\dot{m}_t\bar{c}_pT_{041}(r_t^{R\eta_t/\bar{c}_p}-1) \tag{5}$$

where $\bar{c}_p$ is the mean c_p for the compression and expansion processes, and η_c and η_t denote the polytropic total-to-total compressor and turbine efficiencies from component inlet to diffuser outlet, excluding bearing losses. Compressor (and turbine) efficiencies decrease with increasing pressure ratio $r_c \equiv p_{02}/p_{01}$ (and $r_t \equiv p_{041}/p_{05}$). Unless otherwise specified, in the following we have used

$$\eta_c=0.91-\frac{r_c-1}{300} \tag{6}$$

$$\eta_t=0.90-\frac{r_t-1}{250} \tag{7}$$

The counterflow heat exchanger or recuperator and intercooler are modeled by the effectiveness of their respective energy-exchange processes. The effects of leakage flows and variation of $\bar{c}_p$ between the two sides of the heat exchanger are neglected. ϵ and i are modeled by:

$$\epsilon\equiv\frac{h_{03}-h_{02}}{h_{05}-h_{02}}\approx\frac{T_{03}-T_{02}}{T_{05}-T_{02}} \tag{8}$$

$$i\equiv\frac{h_{021}-h_{022}}{h_{021}-h_{01c}}\approx\frac{T_{021}-T_{022}}{T_{021}-T_{01c}} \tag{9}$$

All losses modeled as pressure drops reduce r_t from r_c by the sum of the total-pressure-drop fractions in the cycle:

$$r_t=r_c\left(1-\Sigma\frac{\Delta p_0}{p_0}\right) \tag{10}$$

Leakage losses are charged at either side of the wiping seals of the regenerators (see below). In all cycles it was specified $x2 = 0.02$, and mechanical friction was modeled by $\dot{W}_S = 0.98(\dot{W}_t - \dot{W}_c)$.

Theoretical Considerations

For lossless simple (CBE) cycles most thermodynamic texts derive an expression for η_{th} that indicates that it increases

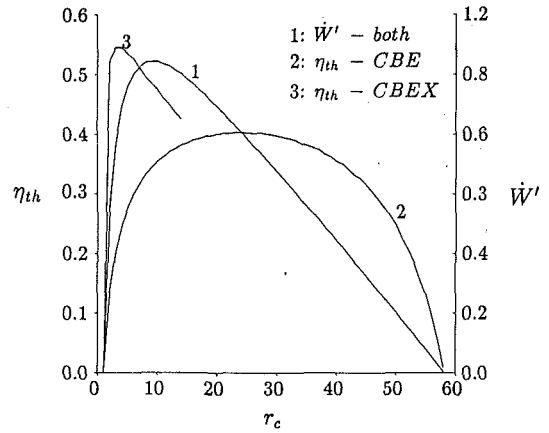

Fig. 5 Thermal efficiency and specific work as functions of pressure ratio for simple and regenerative cycles of $T' = 5$ (other input parameters shown in Table 1)

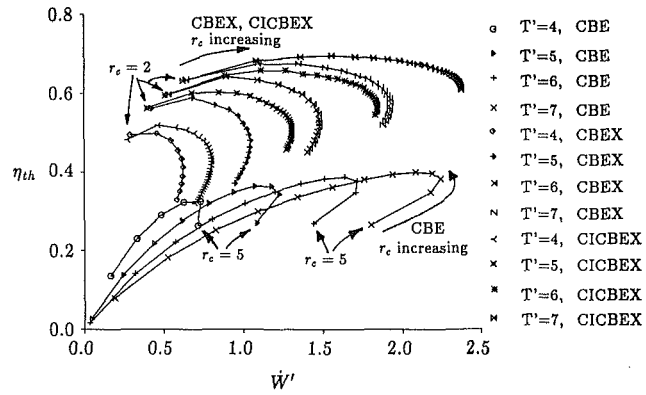

Fig. 6 Thermal efficiency versus specific power for the CBE, CBEX, and CICBEX cycles using the inputs of Table 2

monotonically with increasing pressure ratio. Similarly, for lossless regenerative (CBEX) cycles most thermodynamic texts derive an expression for η_{th} that indicates that it is maximum when the pressure ratio of the cycle is unity. These derivations neglect that in practical gas turbine cycles there is a material limit on the maximum T_{bm}; for practical cooling this imposes a maximum T_{04} or $T_{\max}$. Even though $T_{\max} > T_{bm}$, $T_{\max}$ dictates a maximum allowable pressure ratio $r_{\max}$, corresponding to isentropic compression from ambient conditions to $T_{\max}$ and $p_{\max}$. A simple cycle with isentropic compression from ambient to $T_{\max}$ and $p_{\max}$ needs no burner. Its isentropic turbine will expand from $T_{\max}$ and $p_{\max}$ to ambient, and the cycle will produce zero work with zero energy input. Similarly an ideal regenerative cycle (with infinitesimal isentropic compression and expansion, and unity regenerator effectiveness) when limited to $T_{\max}$ also results in a cycle producing zero work with zero energy input. However, between pressure ratios of unity and $r_{\max}$ there exist cycles with finite positive work and thermal efficiency.

Figure 5 has been computed using the component models described above and other cycle-input parameters shown in Table 1. The values of cooling technology level and T_{bm} are such as to ensure $x1 = 0.0$ (no cooling-flow fraction). Pressure drops and secondary flows are specified equal to zero. The specific work is a function of r_c and is equal for the CBE and CBEX cycles. With $T_{\max} = T_{04} = T' \cdot T_{01} = 1500$ K the maximum pressure ratio for the combination of inputs is about 58:1. Specific power reaches a maximum at $r_c \approx 10$, where η_{th} for the CBE cycle is about 0.36. The corresponding CBEX cycle gives the same amount of work as the CBE cycle, but

Table 1 Inputs used to produce Fig. 5

Cycle	CBE	CBEX
T_{01} (K)	300	300
T'	5.0	5.0
constant η_c	0.900	0.900
constant η_t	0.900	0.900
η_b	1.000	1.000
$\Sigma(\Delta p_0/p_0)$	0.00	0.00
cooling level ($x1 = 0.0$)	9.9	9.9
T_{bm} (K)	1500	1500
$x2$	0.000	0.000
ϵ	-	0.920
$x3$	-	0.000
$x4$	-	0.000

Table 2 Inputs used to produce the cycle performance plots shown in Fig. 6

Cycle	CBE	CBEX	CICBEX
T_{01} (K)	300	300	300
T'	4,5,6,7	4,5,6,7	4,5,6,7
η_b	0.996	0.996	0.996
first r_c	5	2	2
r_c increment	5	1	1
$\Sigma(\Delta p_0/p_0)$	0.07	0.12	0.14
cooling level	2.5	2.5	2.5
T_{bm} (K)	1250	1250	1250
$x2$	0.02	0.02	0.02
ϵ	-	0.975	0.975
$x3$	-	0.025	0.025
$x4$	-	0.025	0.025
i	-	-	0.92
T_e (K)	-	-	300

the heat exchanger reduces the required energy input such that the corresponding η_{th} for the CBEX cycle is about 0.48. The CBE cycle reaches its maximum thermal efficiency $\eta_{th,\max} \approx 0.40$ at $10 < r_c \approx 23$. The CBEX cycle reaches its maximum thermal efficiency $\eta_{th,\max} \approx 0.55$ at $10 > r_c \approx 3$. The heat exchanger becomes infeasible ($T_{05} < T_{02} + 20$ K) for pressure ratios above 14:1. The figure illustrates that there are three "optimum" pressure ratios: for maximum $\dot{W}'$, $r_c \approx 10$; for maximum $\eta_{th,\text{CBE}} \approx 0.40$, $r_c \approx 23$; and for maximum $\eta_{th,\text{CBEX}} \approx 0.55$, $r_c \approx 3$. The designer would choose different pressure ratios depending on cycle and intended application.

Shaft-Power Cycle Performance

The cycle-parameter inputs for the performance of typical CBE, CBEX, and CICBEX cycles shown in Fig. 6 are listed in Table 2 (η_c and η_t have been modeled with Eqs. (6) and (7)). Each cycle is shown for $T' = 4$, 5, 6, and 7, representing, respectively: the last generation of gas turbine technology; current industrial practice; advanced-technology engines; and future engines. Each point plotted in Fig. 6 represents the design-point performance of a different engine. Some additional preliminary choices have been made for the types of components in the cycles. It has been specified that the heat exchanger is a high-effectiveness (0.975) rotary ceramic regenerator, such as the one illustrated in Fig. 2 of Korakianitis and Beier (1994). Such regenerators are better suited to low-pressure-ratio regenerative cycles, which result in relatively higher T_{05}. Conventional metal heat exchangers (such as the one used in the Textron Lycoming AGT 1500 engine) can be used only with relatively lower T_{05} and are better suited to higher-pressure-ratio cycles. The leakage flows past the wiping seals of rotary regenerators ($x3$ and $x4$) increase as r_c increases, and they become excessive for $r_c > 6$ (McDonald, 1978). Values of $x3 = x4 = 0.025$ have been specified, based on the exper-

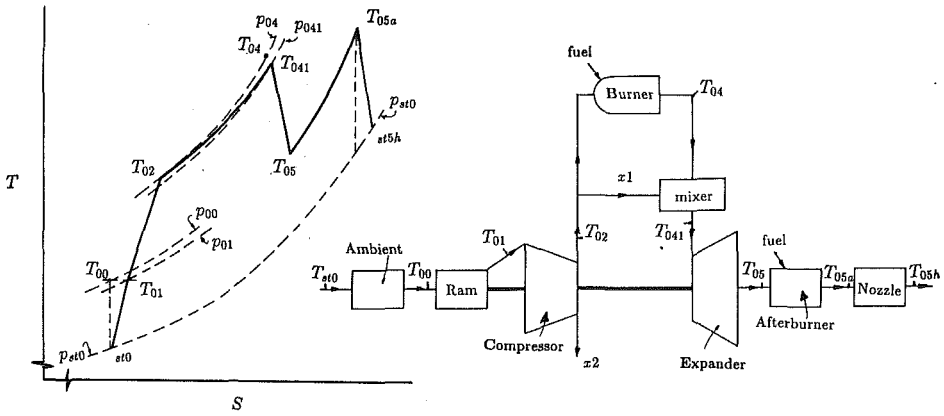

Fig. 7 Temperature-entropy and block diagram of the TBJET cycle

iments reported by Helms et al. (1984). These suggest that the measured effectiveness of rotary ceramic regenerators was between 93.3 and 98.7 percent, the measured pressure drops were between 2.5 and 5.4 percent, and the measured leakages were 3.4 percent with NiO/3O CaF_2 wearface and 4.5 percent with cooled seals. The effects of ϵ on CBEX-cycle performance are illustrated in Fig. 1(*b*) of Korakianitis and Beier (1994).

Equation (4) illustrates one of the advantages of intercooling. The specific work required for a given r_c is proportional to the compressor inlet temperature. Splitting the pressure ratio between two or more compressors and intercooling between them lowers the total amount of compressor work, as well as the final compressor-outlet temperature and specific volume. While the former is beneficial, the latter reduces the blade height of the last compressor stages. As a result, the boundary layers occupy a larger percentage of the passages near compressor outlet, and the component efficiency of smaller compressors will be reduced. These losses can be reduced by the use of a separate high-speed "spool," but at a penalty in increased ducting and shaft-power losses.

Figure 6 illustrates the advantages and disadvantages of the simple, regenerative, and intercooled-regenerative cycle for each application. In all cycles, as r_c increases η_{th} reaches a maximum value and then it declines. In general, the simple cycle has higher $\dot{W}'$ and lower η_{th} than the other cycles. Intercooled-regenerative cycles have higher η_{th} and higher $\dot{W}'$ than regenerative ones. For a given T' the points of increasing r_c move counterclockwise for the simple cycle, and clockwise for the regenerative and intercooled-regenerative cycles.

Jet-Propulsion Cycles

The Turbojet Cycle (TBJET). This cycle (Fig. 7) represents an engine producing thrust by expanding a stream of working fluid in a nozzle. It would normally power an aircraft flying at altitude A with velocity V, corresponding to Mach number M:

$$\mathrm{M} \equiv \frac{V}{\sqrt{c_p \cdot R \cdot T_{st0}/(c_p - R)}} \tag{11}$$

In Fig. 7 the static conditions at inlet correspond to point *st*0. These are evaluated as functions of altitude A, based on Shepherd (1972). For $0 \le A \le 11{,}000$ m, T_{st0} in K and p_{st0} in N/m^2 are given by:

$$T_{st0} = 288.16 - 0.0065 \cdot A$$

$$p_{st0} = 101325 \cdot \left(\frac{T_{st0}}{288.16}\right)^{5.25757} \tag{12}$$

For $A > 11{,}000$ m, T_{st0} in K and p_{st0} in N/m^2 are given by:

$$T_{st0} = 216.66$$

$$p_{st0} = 22622.50 \cdot \exp\left(\frac{11{,}000 - A}{6339.87}\right) \tag{13}$$

The total conditions for M correspond to point 00. The diffuser at the engine inlet recovers part of the dynamic head at the inlet (ram static pressure recovery), with a small loss in total pressure from p_{00} to p_{01}. This process has been modeled using the typical efficiency curve for ram pressure recovery shown in Fig. 3.2 of Kerrebrock (1977, p. 49). Other cycle inputs are similar to those for the CBE cycle. After the turbine the user has the choice of specifying or not specifying an afterburner. If there is an afterburner the flow expands from 05*a* to p_{st0}; otherwise it expands from 05 to p_{st0}. The nozzle pressure ratio is used to evaluate an isentropic temperature ratio, which is combined with a user-specified isentropic efficiency to evaluate a (nonisentropic) enthalpy drop through the nozzle Δh_n, producing a gas stream of velocity C_{5h}:

$$C_{5h} = \sqrt{2(\Delta h_n)} \tag{14}$$

The cycle is deemed infeasible if the pressure drop available for the nozzle is less than 2 percent of the cycle pressure ratio.

The thrust developed by the engine, the power output, and the thrust specific fuel consumption are calculated for unit mass-flow rate through the engine inlet ($\dot{m}_A = 1.0$). Let $\dot{m}_{ht}$ be the mass flow through the (hot) nozzle, $\dot{m}_F$ be the fuel-flow rate to the cycle, and F the jet thrust developed by the engine, given by:

$$F = \dot{m}_{ht} \cdot C_{5h} - \dot{m}_a \cdot V \tag{15}$$

The equivalent useful jet power output $\dot{W}_j$ is given by:

$$\dot{W}_j = F \cdot V \tag{16}$$

The propulsive, thermal, and overall (availability) efficiencies are defined by:

$$\eta_p \equiv \frac{F \cdot V}{(1/2) \cdot (\dot{m}_{ht} \cdot C_{5h}^2 - \dot{m}_a \cdot V^2)}$$

$$\eta_{th} \equiv \frac{F \cdot V + (1/2) \cdot \dot{m}_{ht} (C_{5h} - V)^2}{\dot{m}_F \mathrm{LHVF}}$$

$$\eta_{ov} = \frac{F \cdot V}{\dot{m}_F \mathrm{LHVF}} \tag{17}$$

The specific power $\dot{W}'$ is defined by:

$$\dot{W}' \equiv \frac{F \cdot V}{\dot{m}_A \cdot c_p(T_{01}) \cdot T_{01}} \tag{18}$$

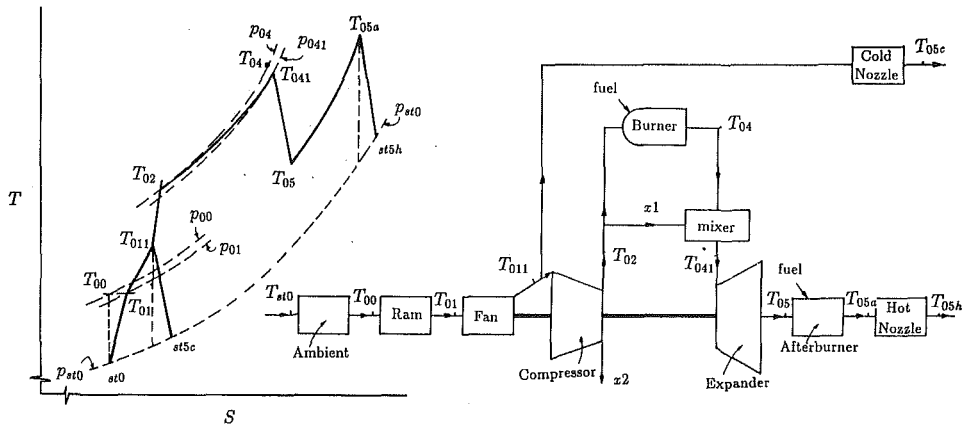

Fig. 8 Temperature-entropy and block diagram of the TBFANS cycle

The thrust specific fuel consumption (for unit mass flow through the engine inlet) is given by

$$t_F = \frac{\dot{m}_F}{F} \tag{19}$$

(This number is multiplied by 1000, so that the units of t_F in the figures are [(kg fuel)/(s • kN)] per unit mass flow rate at the inlet ($\dot{m}_A$).)

The Turbofan Cycle (TBFANS). In this cycle (Fig. 8) the engine core is a turbojet engine whose turbine drives an external fan as well as the compressor. The fan flow expands through a "cold" nozzle, as opposed to the "hot" nozzle of the core. The hot and cold nozzles expand separately to atmospheric conditions. In some turbofan cycles the hot and cold nozzle flows are either fully or partially mixed. The bypass ratio, b, is defined by:

$$b \equiv \frac{\dot{m}_{cd}}{\dot{m}_{ht}} \tag{20}$$

where $\dot{m}_{cd}$ is the mass-flow rate through the cold nozzle and $\dot{m}_{ht} = 1.0$ (the mass-flow rate through the core of the engine in the program is unity).

Much of the cycle is similar to the TBJET cycle. The fan after the ram inlet raises the pressure and the temperature to point 011, which corresponds to the condition at compressor inlet and at cold-nozzle inlet. The total conditions at afterburner exit correspond to point 05a. The hot nozzle expands the flow to p_{st0} producing a gas stream of velocity C_{5h}. The cold nozzle expands the flow to p_{st0} producing a gas stream of velocity C_{5c}. The cycle is deemed infeasible if the pressure drop available for the hot nozzle is less than 2 percent of the cycle pressure ratio. The thrust developed by the engine, the power output, and the thrust specific fuel consumption are calculated for unit mass-flow rate through the core (hot part) of the engine. In the following let $\dot{m}_{cd}$ be the mass flow through the cold nozzle, and $\dot{m}_{ht}$ be the mass flow through the hot nozzle. For unit mass-flow rate through the core of the engine, the mass-flow rate through the inlet of the engine, $\dot{m}_A$, is:

$$\dot{m}_A = 1.0 + \dot{m}_{cd} \tag{21}$$

The thrust F is given by:

$$F = \dot{m}_{ht} \bullet C_{5h} + \dot{m}_{cd} \bullet C_{5c} - \dot{m}_A \bullet V \tag{22}$$

The propulsive, thermal, and overall (availability) efficiencies are defined by:

$$\eta_p \equiv \frac{F \bullet V}{(1/2) \bullet (\dot{m}_{ht} \bullet C_{5h}^2 + \dot{m}_{cd} \bullet C_{5c}^2 - \dot{m}_a \bullet V^2)}$$

$$\eta_{th} \equiv \frac{F \bullet V + (1/2) \bullet [\dot{m}_{ht}(C_{5h} - V)^2 + \dot{m}_{cd}(C_{5c} - V)^2]}{\dot{m}_F \mathrm{LHVF}}$$

$$\eta_{ov} \equiv \frac{F \bullet V}{\dot{m}_F \mathrm{LHVF}} \tag{23}$$

The equivalent $\dot{W}_j$, $\dot{W}'$, and t_F for unit mass flow through the engine inlet are given by Eqs. (15), (17), and (18).

Jet-Power Cycle Performance

The thrust specific fuel consumptions of representative turbojet and turbofan cycles with afterburners are shown in Fig. 9. The tick marks indicate jet-cycle pressure ratio r_j according to the convention of Table 3, where $r_j = r_r \times r_c$ for turbojets and $r_j = r_r \times r_f \times r_c$ for turbofans. The turbojet cycles (shown with the relatively larger tick marks) can be considered as the limiting case of turbofans with zero bypass ratio ($b = 0.0$). The other cases correspond to turbofans with bypass ratios 0.4, 4.0, and 8.0. Four combinations of flight Mach number and altitude are included in Fig. 9: the top left (Fig. 9a) is for M = 0.8 and A = 10 km; the top right (Fig. 9b) is for M = 0.8 and A = 20 km; the bottom left (Fig. 9c) is for M = 2.0 and A = 10 km; and the bottom right (Fig. 9d) is for M = 2.0 and A = 20 km.

Other inputs common to the jet-power cycles shown in Fig. 9 are: overboard leakage $x2 = 0.02$; compressor and turbine polytropic total-to-total efficiencies based on Eqs. (6) and (7); nozzle isentropic efficiencies of 0.96; cooling-technology level 2.5 and T_{bm} = 1250 K; burner and afterburner efficiencies 0.996; afterburner-outlet temperatures $T_{05a} = 1.05 \bullet T_{04}$; fan pressure ratio 2.0:1, fan polytropic total-to-total efficiency 0.89; pressure-loss fraction 0.08 for the turbojet cycle; and pressure-loss fraction 0.10 for the turbofan cycle.

For M = 0.8 the ram pressure ratio $r_r = 1.5$ and for M = 2.0 it is $r_r = 6.7$. The ambient conditions are a function of altitude. Thus for a given engine configuration, r_c, and T_{04}, the values of A and M affect the jet-cycle temperature ratio (corresponding to T' in the shaft-power cycles) and the jet-cycle pressure ratio. Each of these cycles is suitable to distinct ranges of flight Mach number and altitude, and has different performance with an afterburner.

In Figs. 9(a) and 9(b) the turbojet cycle r_j start from r_j = 10 for each T_{04} and they move in increments of 10 counterclockwise tracing letters "U" as r_j increases. For every combination of other inputs there is an optimum cycle (and

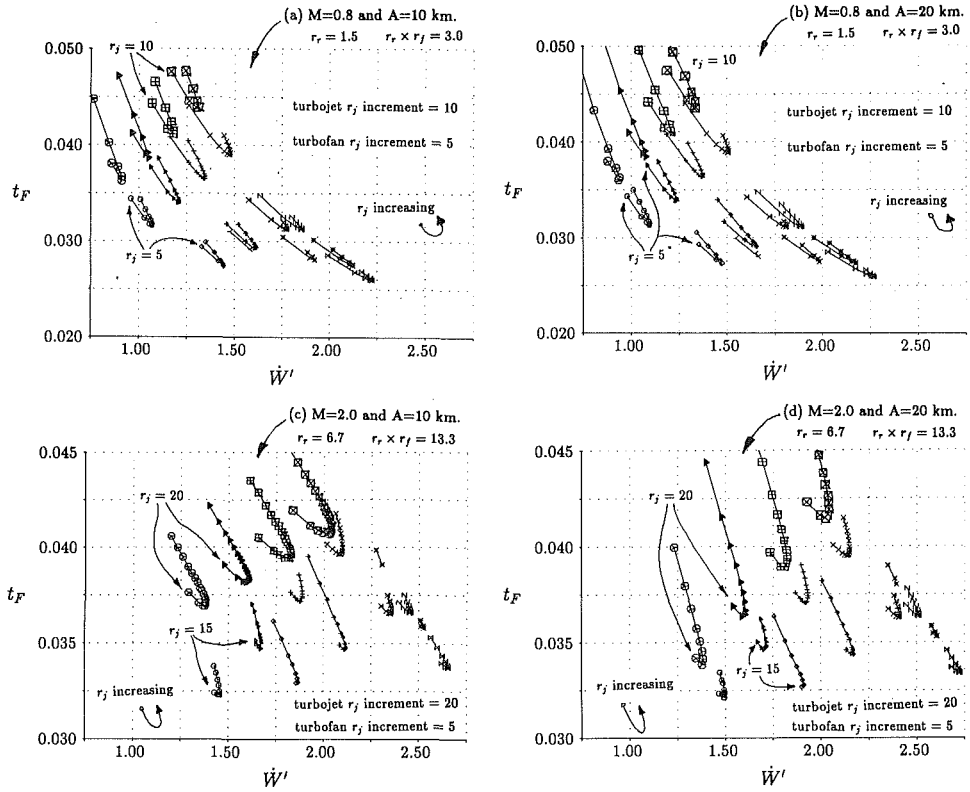

Fig. 9 Thrust specific fuel consumption t_F in units of [(kg fuel)/(s • kN)] versus ($\dot{W}'$) for afterburning turbojet and turbofan cycles at M = 0.8 and 2.0, and A = 10 km and 20 km; the symbols are explained in Table 3 and in the text

Table 3 Symbols used in Fig. 9

	turbojet, b=0.0, T_{04} = 1400 K
	turbojet, b=0.0, T_{04} = 1600 K
	turbojet, b=0.0, T_{04} = 1800 K
	turbojet, b=0.0, T_{04} = 2000 K
	turbofan, b=0.4, T_{04} = 1400 K
	turbofan, b=0.4, T_{04} = 1600 K
+	turbofan, b=0.4, T_{04} = 1800 K
×	turbofan, b=0.4, T_{04} = 2000 K
	turbofan, b=4.0, T_{04} = 1400 K
	turbofan, b=4.0, T_{04} = 1600 K
	turbofan, b=4.0, T_{04} = 1800 K
	turbofan, b=4.0, T_{04} = 2000 K
	turbofan, b=8.0, T_{04} = 1400 K
	turbofan, b=8.0, T_{04} = 1600 K
	turbofan, b=8.0, T_{04} = 1800 K
	turbofan, b=8.0, T_{04} = 2000 K

compressor) pressure ratio for maximum $\dot{W}'$, and a different optimum pressure ratio for minimum t_F. Similar conclusions can be reached for η_{th}, η_p, and η_{ov}. The optimum pressure ratios are finite. The turbofan cycle r_j start from r_j = 5 for each T_{04} and they move in increments of 5 counterclockwise. With other jet-cycle inputs kept constant, as b increases t_F decreases and $\dot{W}'$ increases. (Matching engines with airframes for different applications is complex. These figures do not include the effect of the increased drag on the airframe from the larger inlets and engine diameters as the bypass ratio increases.) Figures 9(a) and 9(b) indicate that the effect of altitude on cycle performance is small, but comparison of cycles should be performed with extreme care. The same r_j in Figs. 9(a) and 9(b) correspond to different ambient conditions, and therefore to different cycle temperature ratios (T').

In Figs. 9(c) and 9(d) the turbojet cycle r_j start from r_j = 20 for each T_{04} and they move in increments of 20 counterclockwise. The turbofan cycle r_j start from r_j = 15 for each T_{04} (ram times fan pressure ratio is 13.3:1 in this case) and they move in increments of 5 counterclockwise. Comparison of Figs. 9(a) and 9(b) with Figs. 9(c) and 9(d) should also be done with care because the different Mach numbers correspond to different ram pressure ratios, and therefore the same r_j correspond to different compressor pressure ratios r_c. Other conclusions are similar to those of the last paragraph.

Higher bypass ratios are more fuel efficient than lower ones, illustrating the reasons for the move to higher-bypass turbofans, unducted fans, and propfans. As flight Mach numbers increase larger engine diameters cause substantial increases in drag from the engine and its inlet. Current fighter planes use turbofan engines with low bypass ratios. The design matrix for jet-power cycles is very complex. Different combinations of cycle variations and cycle parameters are advantageous for different reasons (fuel consumption, propulsive efficiency, etc.) in different regimes. The off-design performance of the cycles in different operating regimes also plays a significant role in the choice of cycle and engine pressure ratios.

Conclusions

Models for turbine-engine components including the effects of cooling-technology levels, cooling flows, leakage and pressure losses, and the effect of varying compressor and turbine efficiencies with pressure ratios have been developed. The models have been used in computer programs that predict the performance of simple, regenerative, intercooled-regenerative, turbojet, and turbofan engines. The performance of various

cycles has been computed. Depending on turbine-inlet temperature and turbine-material temperature limits, and using current-technology components, the "optimum" pressure ratio for regenerative and intercooled-regenerative cycle thermal efficiencies over 55 percent is between 3 and 6. The "optimum" pressure ratio for maximum power output is about 10. The "optimum" pressure ratio for simple-cycle maximum thermal efficiency is over 25. Similarly, the optimum compressor pressure ratio in turbojet and turbofan cycles is finite. The jet-power cycles have been used to illustrate the complexity of choice of aircraft cycles for different aircraft applications.

Acknowledgments

The cycle-performance programs have been developed with partial sponsorship from MIT summer course ME 2.14S and partial sponsorship from the International Gas Turbine Institute. They have been included in an ASME home-study course (Wilson, 1991). The encouragement of Donald Hill and David Lindsay of the IGTI is gratefully acknowledged.

References

Harmon, R. A., 1990, "Marine Gas Turbines: a New Generation," *Mechanical Engineering*, May, pp. 48–51.

Helms, H. E., Heitman, P. W., Lindgren, L. C., and Thrasher, S. R., 1984, "Ceramic Applications in Turbine Engines," NASA CR 174715, Oct.

Kerrebrock, J. L., 1977, *Aircraft Engines and Gas Turbines*, The MIT Press, Cambridge, MA.

Korakianitis, T., and Beier, K. J., 1994, "Investigation of the Part-Load Performance of Two 1.12 MW Regenerative Marine Gas Turbines," ASME JOURNAL OF ENGINEERING FOR GAS TURBINES AND POWER, Vol. 116, this issue, pp. 418–423.

Livingood, J. N. B., Ellerbrock, H. H., and Kaufman, A., 1971, "NASA Turbine-Cooling Research," NASA TM X-2384.

McDonald, C. F., 1978, "The Role of the Recuperator in High-Performance Gas-Turbine Applications," ASME Paper No. 78-GT-46.

Shepherd, D. G., 1972, *Aerospace Propulsion*, American Elsevier Publishing Co.

Slatter, B. H., 1982, "Aero-derived Marine and Industrial Gas Turbines," *Transactions of the Institute of Marine Engineers*, Vol. 95, Paper No. 33.

Wilson, D. G., 1984, *The Design of High-Efficiency Turbomachinery and Gas Turbines*, The MIT Press, Cambridge, MA.

Wilson, D. G., 1991, "The Design of Gas-Turbine Engines," Home-study course (book, video and computer programs) of the International Gas Turbine Institute of the ASME.

I. Fukue

S. Aoki

K. Aoyama

Takasago Machinery Works,
Mitsubishi Heavy Industries, Ltd.,
Takasago, Japan

S. Umemura

Takasago R&D Center,
Mitsubishi Heavy Industries, Ltd.,
Takasago, Japan

A. Merola

M. Noceto

M. Rosso

Fiat Avio S.p.A.,
Turin, Italy

A New High-Efficiency Heavy-Duty Combustion Turbine 701F

The 701F is a high-temperature 50 Hz industrial grade 220 MW size engine based on a scaling of the 501F 150 MW class 60 Hz machine, and incorporates a higher compressor pressure ratio to increase the thermal efficiency. The prototype engine is under a two-year performance and reliability verification testing program at MHI's Yokohama Plant and was initially fired in June of 1992. This paper describes the 701F design features design changes made from 501F. The associated performance and reliability verification test program will also be presented.

Introduction

The 701F is a 3000 rpm heavy-duty combustion turbine designed with a 1.2 scaling factor from the 150 MW, 60 Hz 501F to serve the 50 Hz power generation needs for utility and industrial service. This engine, jointly developed by Mitsubishi Heavy Industries, Ltd., Westinghouse Electric Corporation, and Fiat Avio S.p.A., represents the latest in an evolutionary cycle that continues a long line of large single-shaft heavy-duty combustion turbines. The 701F combines the efficient, reliable design concepts of the 501F with recently developed low-emission combustion technology. The result is an advanced design, high-temperature, efficient, low-NO_x, more powerful combustion turbine based on time-proven reliable design concepts that will satisfy the large combustion turbine power generation needs for the next decade. Currently being targeted for 1992 ~ 1994 performance and durability test, it will have an initial simple cycle ISO rating of 221 MW with a heat rate of 9440 Btu/kWh (9958 KJ/kWh) based on LHV at a turbine inlet temperature of 1260°C (1533 K) on natural gas fuel. In combined cycle applications the heat rate will be better than 6360 Btu/kWh (6709 KJ/kWh) based on LHV with a single-shaft application.

Across the board advances in computer technology have enabled manufacturers to improve analytical procedures in all aspects of design including stress analysis, heat transfer, aerodynamics, fluid mechanics, and structural dynamics. Benefits of these technological advances are shown in Fig. 1, where optimal cooling system design allows metal temperature in the 701F to be kept within MW501D5/MW701D experience, and have been verified in the 501F prototype engine shop test with extensive instrumentation installed in the engine. The first heavy-duty combustion turbine to incorporate advanced cooling technologies was the MF111 with initial commercial operation in August, 1986, at a turbine inlet temperature of 1160°C (1433 K).

For some critical components such as combustor baskets, transition pieces, and turbine row 1 and 2 blades and vanes, the 701F engine utilizes the components of the same size or the same basic dimensions as those of the 501F in order to enhance reliability and performance. This design philosophy enables this engine to benefit from the comprehensive 501F testing program, which consisted of air cascades, turbine model tests, full-scale verification of combustor design, and rotor blade vibratory dynamics. The component testing was followed by an instrumented shop test at load and finally by an instrumented field test, which included tests of several design enhancements. In addition, stringent emission regulations in Japan provided increased incentive to develop the dry low-NO_x Hybrid Combustion system that has operated successfully at Tohoku Electric Power Company Higashi-Niigata Plant since 1984.

Contributed by the International Gas Turbine Institute and presented at the 38th International Gas Turbine and Aeroengine Congress and Exposition, Cincinnati, Ohio, May 24–27, 1993. Manuscript received at ASME Headquarters March 1, 1993. Paper No. 93-GT-146. Associate Technical Editor: H. Lukas.

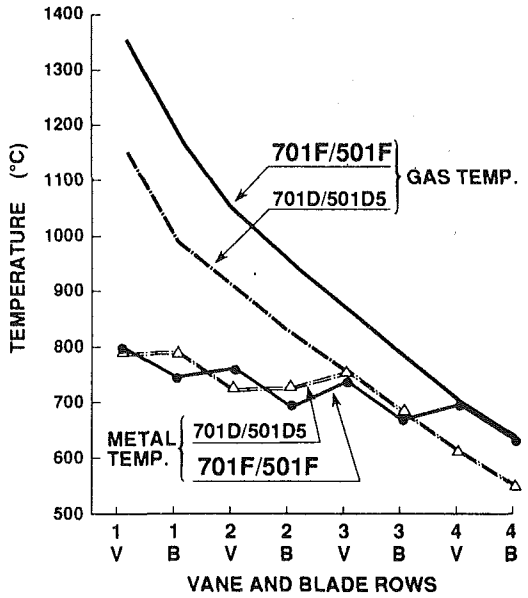

Fig. 1 701F metal and gas temperatures

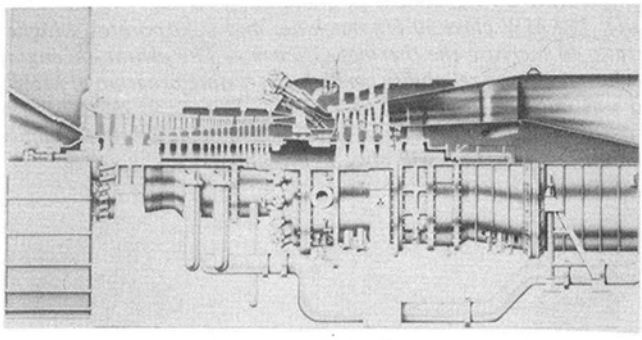

Fig. 2 501F longitudinal section

Engine Design Features

Figure 2 illustrates the general configuration of the 701F heavy-duty combustion turbine. Several basic long-established design concepts and philosophies are evident and are presented below. Those features unique to the 701F are listed separately.

General Description

- Two-bearing single-shaft construction.
- Cold end generator drive to minimize the influence of thermal expansion and to eliminate the need for a flexible coupling.
- Axial flow exhaust system, which has a plant arrangement advantage in combined cycle power plants in meeting the heat recovery requirements.
- Externally cooled and filtered rotor and blade cooling air to eliminate excessive contaminants that could block critically intricate cooling passages of the rotor and blades.
- Tangential exhaust casing struts to maintain bearing housing alignment by rotating as required to accommodate thermal expansion.
- Variable inlet guide vane (IGV) to provide exhaust temperature control for heat recovery applications and to improve starting characteristics.
- Compressor diaphragms and dove-tail rooted blades removable with the rotor in place.
- Three axisymmetric compressor bleeds for turbine cooling with two used to avoid surge during starting.
- Horizontally split casings to facilitate field maintenance with the rotor in place.
- Combustors and transitions removable without lifting cylinder covers.
- Stage 1 vanes removable without lifting cylinder cover.
- Turbine rotor with bolted CURVIC coupled disks providing precise alignment and torque carrying features.
- Fir-tree rooted turbine blades removable on-site with rotor in place.
- Multiple turbine blade ring concept to provide field service of vanes with the rotor in place and a thermal response independent of the outer casing to prevent blade rubs, minimize clearance, and maximize performance.
- Turbine ring segments and isolating ring structure to minimize the thermal distortion of the blade rings that support the turbine vanes.

701F Additional Features

- High-temperature and efficient engine designed based on the proven 501F engine with a scale ratio of 1.2 with the exception of the combustors and turbine row 1 and 2 blade and vane airfoils, which are identical to those of the 501F.
- Advanced hybrid combustion system incorporating low-NO_x features, consisting of 20 cannular combustors with the same diameter and length as the 501F. The hybrid combustor features a two-stage burner assembly and a bypass valve, which directs a portion of the compressor delivery air directly into the transition piece to enhance flame stability during starting and to maintain desired fuel-air ratio during loading. The 701F hybrid system differs from the current one by having the ratio of pilot to main fuel trimmed to reduce pilot burner NO_x generation.
- Twin layer composite structure named "PLATEFIN" and "MTFIN" to provide more efficient cooling on the combustor basket and transition pieces, respectively, thus providing more air for the low-NO_x system.
- Four-stage turbine to maintain low aerodynamic loading even at the increased firing temperature.
- Cooled stage 1 and 2 vane segment and cooled stage 1 and 2 blades with the same basic dimensions as the 501F engine to utilize the 501F component/shop test results and field experiences. The first two stages of vanes and blades are protected by anti-oxidation coating. The first-stage vane shrouds are also protected by thermal barrier coating. The Row 1 vane cooling design utilizes state-of-the-art concepts with three impingement inserts in combination with an array of film cooling exits and a trailing edge pin fin system. The first-stage blade is cooled by a combination of convection techniques via multipass serpentine passages, pin fin cooling in the trailing edge exit slots, and film cooling including a shower head scheme.
- Cooled stage 3 vane segment and turbine blade to improve reliability.
- Integral "Z" tip shrouds in third and fourth-stage rotor blades for increased structural damping to minimize the potential for flow-induced nonsynchronous vibration.
- Damping and sealing pins in the first and second-stage rotor blades to increase structural damping and minimize the leakage of cooling flow.
- Leading Edge Groove (LEG) direct lubricated thrust bearing to reduce the required oil flow and its mechanical loss.
- Two-element tilting pad journal bearings for load carrying and a fixed upper half bearing to eliminate top

pad fluttering concerns and related local babbitt spragging.
- Compressor blade locking feature that is visibly inspectable.
- Improved compressor rotor blade root design that has flat contact faces for ease of manufacturing and inspection.
- Blade rings in compressor section to optimize cylinder to rotor alignment.
- Compressor rotor design with multiple axial tie bolts, which eliminates the shrink-fitted design and main coupling joint to increase rotor dynamic stability margin as well as facilitating fabrication and maintenance of the rotor. Individual disks are positioned radially by bore rabbet joints.
- 17 stage, highly efficient axial flow compressor with pressure ratio of 16:1, incorporating larger diameter rear stages to help balance spindle thrust and two exit guide vanes to straighten the flow leaving the compressor.
- Turbine flow path design utilizing fully three-dimensional flow analysis.

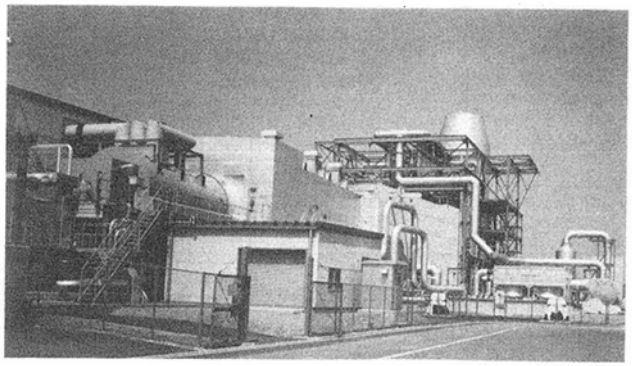

Fig. 3 701F gas turbine plant in Yokohama

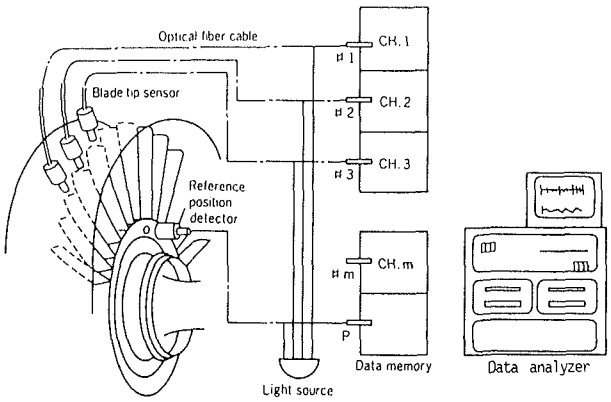

Fig. 4 Blade vibratory stress measuring system

Component Verification

For some critical components, the 701F engine utilizes components of the same size or same basic dimensions as the 501F. This design philosophy enables the engine to benefit from the comprehensive 501F test program and operating experience. As an integral part of the 701F engine development program, performance and durability testing including rotating blade vibration tests, a two-year performance and durability test program for performance measurement in various ambient conditions, and durability and emissions verifications in long-term daily start/stop operation. In the test at MHI's newly constructed power station operating on natural gas in Yokohama, the generator was coupled with the 701F engine in the same manner as in the simple cycle unit with the downstream high-temperature SCR (selective catalytic removal) system as shown in Fig. 3. The generated electrical output is delivered to the 50 Hz utility grid. About 1300 special measurement points were applied to the engine during the integrated testing program.

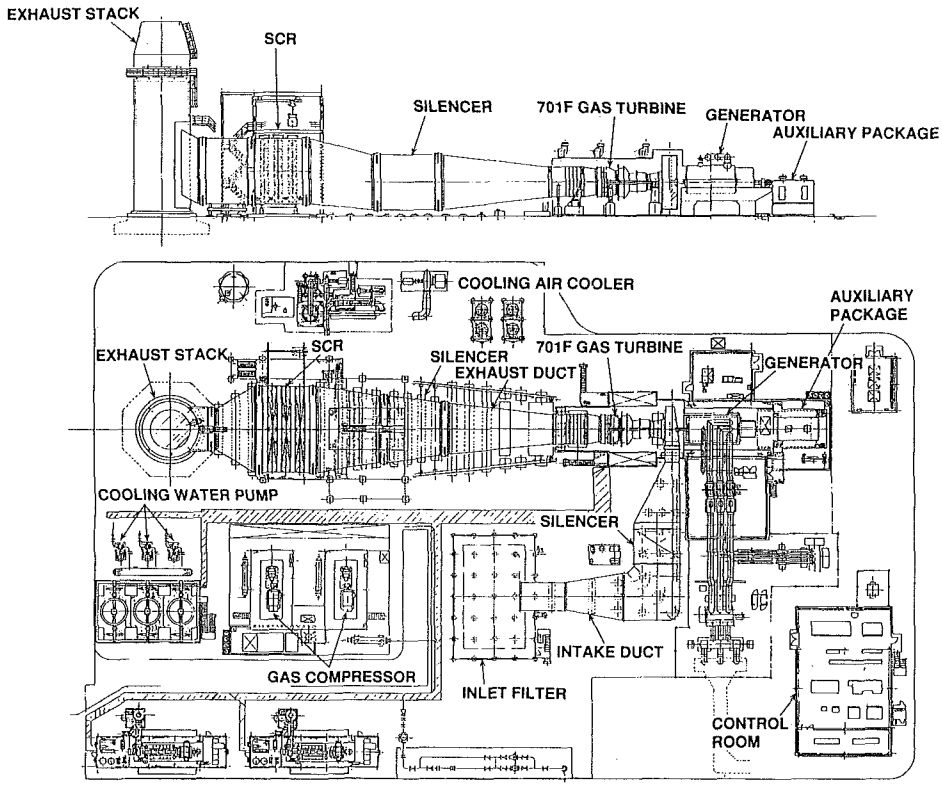

Fig. 5 Plant layout in Yokohama

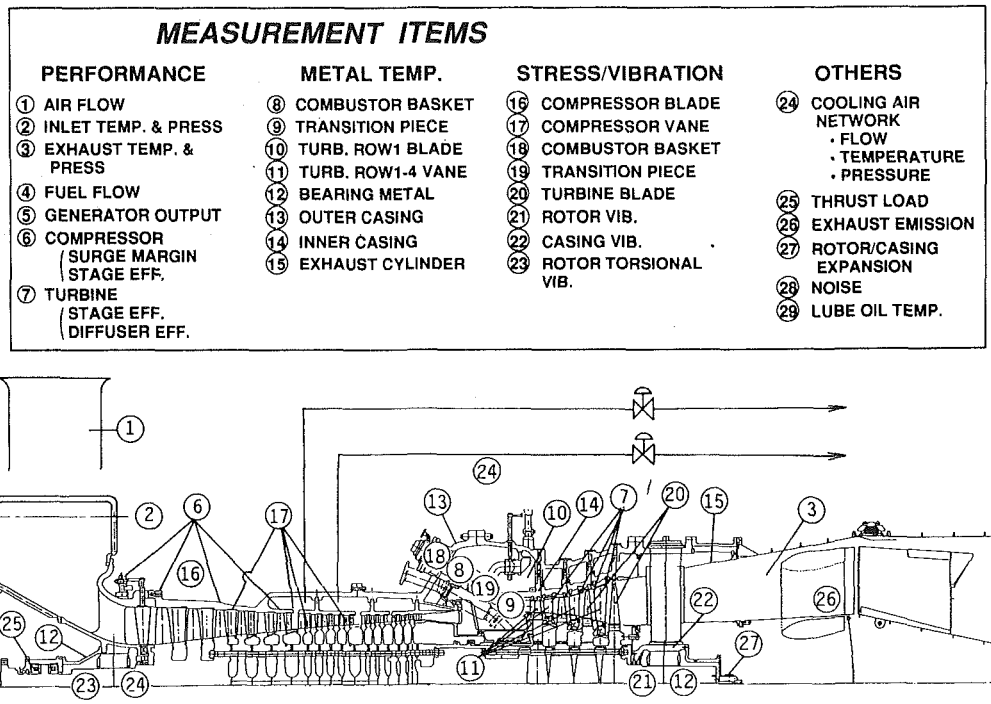

Fig. 6 701F prototype special measurement

Rotating Blade Vibration Test. A rotating blade vibration test was performed to verify the vibration characteristics of selected rotating compressor and turbine blades. The first and second-stage compressor blades and all four turbine stage blades were tested to verify natural frequencies. Damping characteristics were also measured for the turbine first and second-stage blades with seal pins and also the third and fourth-stage shrouded blades of the turbine. These damping characteristics will be used to obtain turbine blade dynamic response via a cyclic symmetry computer routine.

During the test, performed in a vacuum room, the fully bladed rotor was driven by an electric motor up to 110 percent of rated speed. The frequencies and amplitude of compressor blade vibration were measured using a noncontact optical fiber monitoring system. This system measures the movement of each individual blade tip by monitoring the position of each blade tip from several different locations circumferentially and analyzing this information through a synchronizing process. The schematic of this measuring system is shown in Fig. 4. In the turbine, strain gages were applied directly to the blades of each stage and the measured strain signals were transmitted to a data acquisition system through a telemetry system. After analyzing all measured data, it was confirmed that no further tuning was necessary for the blades.

Engine Verification Test. In order to verify the performance and design characteristics of the 701F, a two-year test program for performance, durability, and emissions was started in June, 1992. Figure 5 presents an overall general arrangement of the Mitsubishi Power Station, showing the major components: gas turbine, generator, exciter, control and special instrumentation room, cooling air cooler, gas compressor, SCR, and intake and exhaust stacks.

About 1300 special measurement points were applied to the engine for the confirmation of the following:

- Individual compressor and turbine performance as well as overall gas turbine performance. Parameters included air flow, power output, heat rate, and exhaust temperature.
- Compressor inlet air flow over the entire IGV range. The compressor air supply duct system employed a bell-mouth inlet to measure air flow precisely.
- Engine starting and acceleration characteristics including light-off, rotor vibration, and rotating stall.
- Mechanical operation of the engine from starting to overspeed including rotor vibration characteristics.
- Mechanical and thermal performance of the engine over its entire operating range.
- Reliability of the engine by measurement of gas and metal temperature, pressure, vibratory stresses, etc. The hot parts' metal temperatures will be confirmed to be below allowables at the associated 1260°C (1533 K) rotor inlet temperature. Monitored components include combustor basket, transitions, turbine vanes, blades, and turbine ring segment. Vibratory stresses of the compressor and turbine blades, bearing temperatures, casing temperature, and disk cavity temperatures are monitored continuously during the test. In addition, axial and radial growths are monitored at strategic locations in the engine to verify design calculations.
- Emission characteristics of the engine. Emissions testing includes sampling for nitrogen oxides (NO_x), nitric oxide (NO), volatile organic compounds (VOC), carbon monoxide (CO), unburned hydrocarbons (UHC), carbon dioxide (CO_2), and oxygen (O_2).

Monitoring System During Engine Operation. In addition to the supervisory instrumentation, the engine is extensively instrumented to measure thermodynamic performance parameters, metal temperatures, static and vibratory strains, vibration characteristics, displacements, and other parameters as shown in Fig. 6. Dynamic strain gages will be installed on the turbine blades to verify dynamic responses. The signals from the rotating sensors are transmitted by a telemetry system. Clearance measurement systems using proximity probes allow stator to rotor radial and axial displacement measurements during transients. Through the use of an infrared pyrometer, it will be possible to obtain the temperature distribution on each turbine blade of the first stage under operating conditions. Data acquisition equipment is installed to record the special

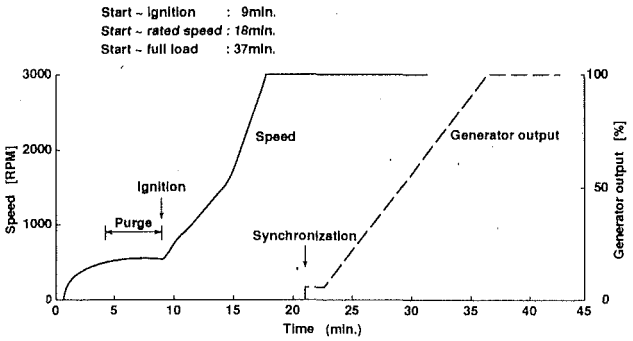

Fig. 7 Starting characteristics

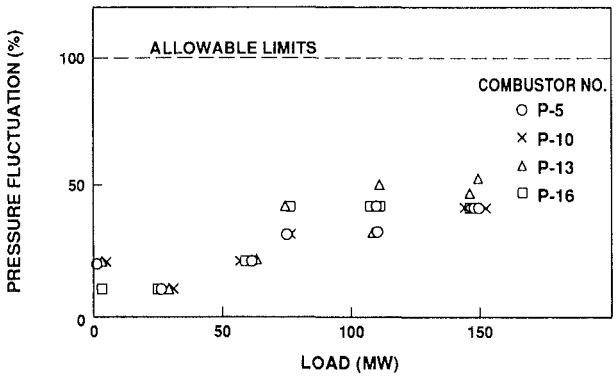

Fig. 8 Combustor pressure fluctuation

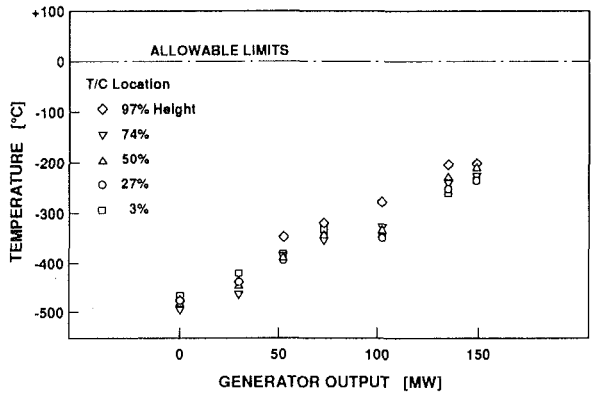

Fig. 9 Turbine row 1 vane metal temperature

engineering test data. This equipment includes tape recorders, spectrum analyzers, plotters, and chart recorders.

Data critical to the continued operation of the engine, such as metal temperatures of hot parts and cavity temperatures, are monitored on computer displays together with associated alarm limits. Turbine inlet temperature of the operating engine can be calculated from measured data using a heat balance calculation program.

Test Results

The 701F performance and durability testing is a two-year program, which started in June, 1992. Summarized below are the test results measured at the initial stage of this program.

Starting and Acceleration. This plant is started by operating the generator as a motor via a static frequency converter. The starting schedule includes a 5-minute exhaust stack purge, ignition at 550–600 rpm, disengagement of the static frequency converter at 2000 rpm, an IGV position change at 2100 rpm, and bleed valve closure at 2755 rpm. The elapsed time from

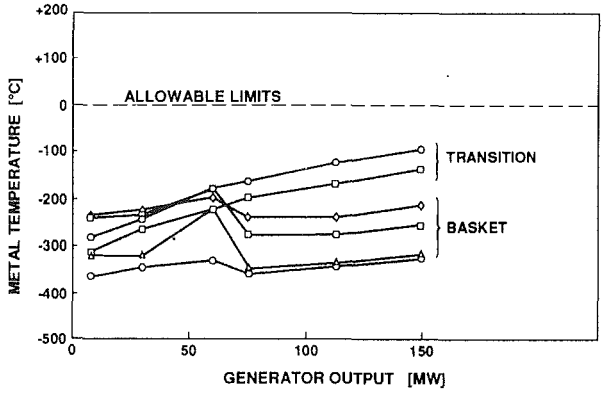

Fig. 10 Combustor metal temperature

pushing starting button to synchronizing speed is under 18 minutes, and time to full load is under 37 minutes, as shown in Fig. 7. At ignition speed, two combustors located at the bottom of the engine are ignited and cross-flame tubes produce complete ignition. Compressor rotating stall was cleared at less than 1700 rpm. Throughout the starting sequence, compressor operating characteristics were stable.

Overall Performance. Measured performance data were analyzed and corrected from shop test conditions to standard ambient conditions. The results show that the measured power output and inlet air flow exceeded the predicted values. In addition, the heat rate is slightly better than the predicted value. Since performance will be measured for the various ambient conditions during the two-year test program, new performance ratings will be established after completion of the test program.

Emission. Nitrogen oxides (NO_x), carbon monoxide (CO), unburned hydrocarbons (UHC), volatile organic compound (VOC), and other emissions were measured. Since premixed type combustors are used, the setting schedules of inlet guide vanes and bypass valves affect the combustion performance. Figure 8 shows the dynamic pressure fluctuation measured inside the combustor. Stable combustion was assured throughout engine start up and load operation. Low-NO_x emission level was measured not only at full-load condition, but also at lower load conditions including idle condition. At rated load (150 MW) of this plant, measured emission levels were by far lower than the target level of 50 ppm at dry conditions.

Hot Part Temperature. Figure 9 presents metal temperatures measured along the span of a row 1 vane leading edge. The temperatures were obtained from thermocouples mounted on the surface of the vane airfoils. Figure 10 presents the combustor system metal temperatures. It was confirmed that the measured hot part temperatures were within the acceptable range and this also verified expected temperature at design conditions. Evaluation of hot part data is continuing and more detailed turbine blade and vane temperatures will be verified in the next stage in the test program.

Vibratory Stresses. Figure 11 presents vibratory stresses as measured during the test along with corresponding design allowables on the Goodman diagram. Frequency and damping factors were also verified during the test. Vibratory stresses of other stationary components, such as a combustor transition, tangential strut shield cover, exhaust diffuser support, etc., were measured. As shown in Fig. 12, all measured stresses were within the design allowables.

Figure 13 summarizes rotor dynamic responses during start up. Vibration levels were low during acceleration to running speed and the associated phase angles during rated speed operation were virtually constant.

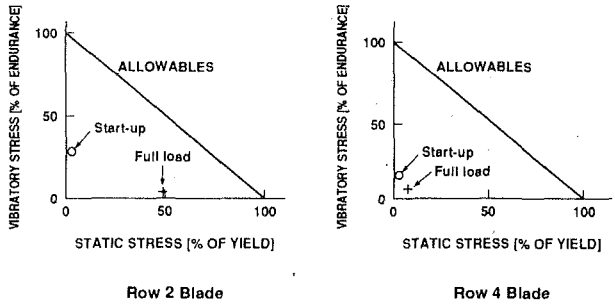

Fig. 11 Compressor blade vibratory stress

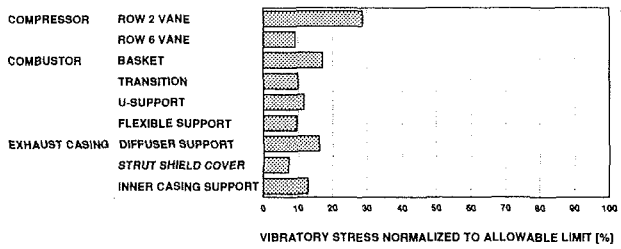

Fig. 12 Summary of vibratory stress

Clearances. Figure 14 presents axial clearance evaluations for both cold and hot start conditions. The hot start measurements were taken shortly after a scheduled turbine shutdown from full load, which analytically is the severest condition for axial clearance verification.

Tip clearances of compressor 14th-stage and turbine second-stage were also measured. Since the second-stage turbine tip clearance was slightly larger than expected, turbine performance will be increased by reducing this clearance.

Cooling Flow Circuit. The measurement results established the correlations between the various engine cavity temperatures and the supervisory instrumentation installed in all engines to assure that specific temperature limits are never exceeded during normal operation. The individual cooling circuit flows were measured via orifice plates installed in the external piping while important engine cavity temperatures were monitored simultaneously with supervisory and special test thermocouples.

Future Test Plan

The two-year test program of the first 701F engine was started at the beginning of June, 1992. Initially, the engine was operated in an introductory rating mode, i.e., the rotor inlet temperature was reduced. This is the only prudent way to introduce a reliable engine to the market that features a step change in firing temperature technology. Mechanical technologies necessary to achieve significant increase in turbine firing temperature should be verified via operating experience prior to operation at the rated rotor inlet temperature of 1260°C (1533 K). This will result in a more reliable product when operated at rated conditions.

Summary

The 701F prototype engine performance and durability testing has been continuing successfully since June, 1992. Overall performance is better than anticipated and NO_x emission levels are far below the target. The operation of the generator as a motor via a static frequency converter was verified to be adequate during the starting and acceleration testing. Mechanical characteristics such as vibratory stresses of blades and diaphragms, thrust force, axial/radial clearances, and bearing and turbine blade and vane metal temperatures were confirmed to be within the design limits. The two-year test program includes more detailed data measurements at various operating conditions. Recently developed low-NO_x combustor and other associated design enhancements will also be verified in this program.

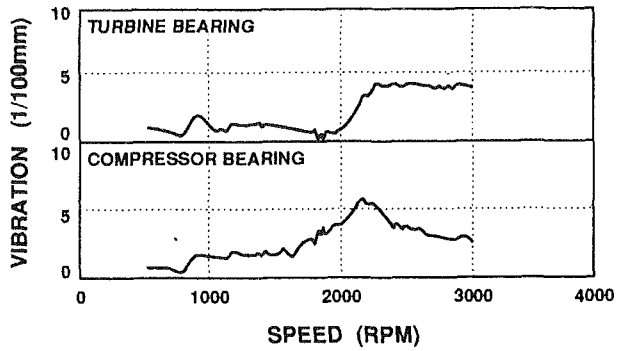

Fig. 13 Rotor vibration

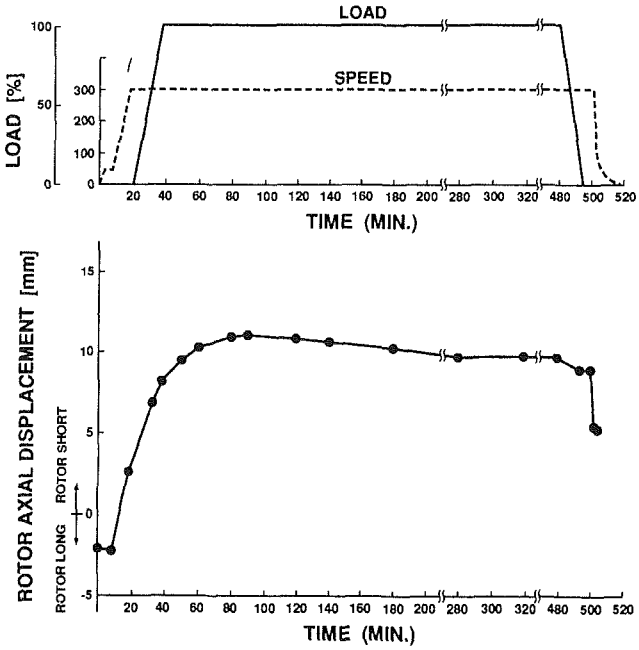

Fig. 14 Rotor/casing relative axial displacement

Table 1 Performance results

	EXPECTED	MEASURED
POWER, NET KW	224,810	+3.8%
HEAT RATE, KJ/KW-HR	9,958	-1.9%
, BTU/KW-HR	9,440	-1.9%
AIR FLOW, KG/SEC	655	+1.0%
, LBS/SEC	1,440	+1.0%
EXHAUST TEMPERATURE, C	554	-3.0C
, K	827	-3.0K

References

1 Entenmann, D. T., North, W. E., Fukue, I., and Muyama, A., "Shop Test of the 501F-A 150 MW Combustion Turbine," ASME JOURNAL OF ENGINEERING FOR GAS TURBINES AND POWER, Vol. 113, 1991, pp. 488-494.

2 Scalzo, A. J., McLaurin, L. D., Howard, G. S., Mori, Y., Hiura, H., and Sato, T., "A New 150-MW High-Efficiency Heavy-Duty Combustion Turbine," ASME JOURNAL OF ENGINEERING FOR GAS TURBINES AND POWER, Vol. 111, 1989, pp. 211-217.

3 Scalzo, A. J., Fukue, I., et al., "Operating Experience Complements New Technology in Design of Advanced Combustion Turbine," ASME Paper No. 88-JPGC/GT-1.

4 Entenmann, D. T., Tsukagoshi, K., et al., "501F Development Update," ASME Paper No. 92-GT-237.

Influence of High Rotational Speeds on Heat Transfer and Oil Film Thickness in Aero-Engine Bearing Chambers

S. Wittig

A. Glahn

J. Himmelsbach

Lehrstuhl und Institut für
Thermische Strömungsmaschinen,
Universität Karlsruhe (T.H.),
Karlsruhe, Federal Republic of Germany

Increasing the thermal loading of bearing chambers in modern aero-engines requires advanced techniques for the determination of heat transfer characteristics. In the present study, film thickness and heat transfer measurements have been carried out for the complex two-phase oil/air flow in bearing chambers. In order to ensure real engine conditions, a new test facility has been built up, designed for rotational speeds up to n = 16,000 rpm and maximum flow temperatures of T_{max} = 473 K. Sealing air and lubrication oil flow can be varied nearly in the whole range of aero-engine applications. Special interest is directed toward the development of an ultrasonic oil film thickness measuring technique, which can be used without any reaction on the flow inside the chamber. The determination of local heat transfer at the bearing chamber housing is based on a well-known temperature gradient method using surface temperature measurements and a finite element code to determine temperature distributions within the bearing chamber housing. The influence of high rotational speed on the local heat transfer and the oil film thickness is discussed.

Introduction

Secondary air/oil systems have a decisive influence on performance characteristics of future as well as of current aero-engines. Therefore, effective heat management and temperature predictions for central engine components of the internal system are necessities within the design process. To meet these requirements, heat transfer and fluid flow in these components are the subject of comprehensive studies and worldwide research activities. A survey of current efforts on heat and mass transfer analysis in secondary air/oil systems of aero engines has been presented by Wittig and Schulz (1992). With respect to bearing chambers, special demands are given. Despite a remarkable advance in the field of gas film bearing technology, characterized, i.e., by the application of tilting pad spring bearings in smaller gas turbines (Domes, 1991), rolling element bearings cannot be substituted in aero-engines within the near future. Therefore, special effort has to be directed to the heat generation due to the bearing friction. For cooling purposes and for the collection of fine particles, which, if left in the bearing housing, can cause rapid failure, these bearings have to be lubricated by oil. To prevent oil fires, bearing chambers have to be built separating the lubricant from the hot zones of the engine.

To prevent oil leakage from these chambers, labyrinths as the most important and widely used sealing elements in turbomachinery, as well as brush seals (Ferguson, 1988), have to be pressurized by air, which is tapped from an appropriate compressor stage. The air enters the chambers, mixes with the lubrication oil, and leaves through the vent lines, carrying a certain amount of oil with it. Finally, the sealing air is discharged overboard or dispelled at a suitable location into the gas stream after separating the oil by use of a breather.

In designing these flow elements contradicting tasks have to be fulfilled. On the one hand, the amount of discharged sealing air has to be kept as small as possible, because it represents an engine power loss and the problem of oil heating becomes greater with increasing amounts of hot air flow into the chamber. On the other hand, small air flows discharged by vents result in small pressure differences across the bearing chamber seals, which can cause oil leakage and in consequence oil fire (Suter and Boyman, 1978). To solve this problem, exact prediction methods for the calculation of appropriate flow rates are required. Unfortunately, the pressure loss inside as well as downstream of the bearing chambers, i.e., in vent pipes, strongly depends on two-phase flow phenomena, such as phase separation, momentum transport to the oil film at the wall, and interaction effects of air/oil mixtures with the wavy film surface, which are difficult to determine in real engine conditions. Up to now, only a little information are available on the described complex flow regimes.

Heat transfer from the hot wall to the air/oil mixture is another problem for the design. In many cases two-phase flow elements are located in hot zones of the engine and, therefore, locally heated up when passing these regions. Matching the

Contributed by the International Gas Turbine Institute and presented at the 38th International Gas Turbine and Aeroengine Congress and Exposition, Cincinnati, Ohio, May 24–27, 1993. Manuscript received at ASME Headquarters March 3, 1993. Paper No. 93-GT-209. Associate Technical Editor: H. Lukas.

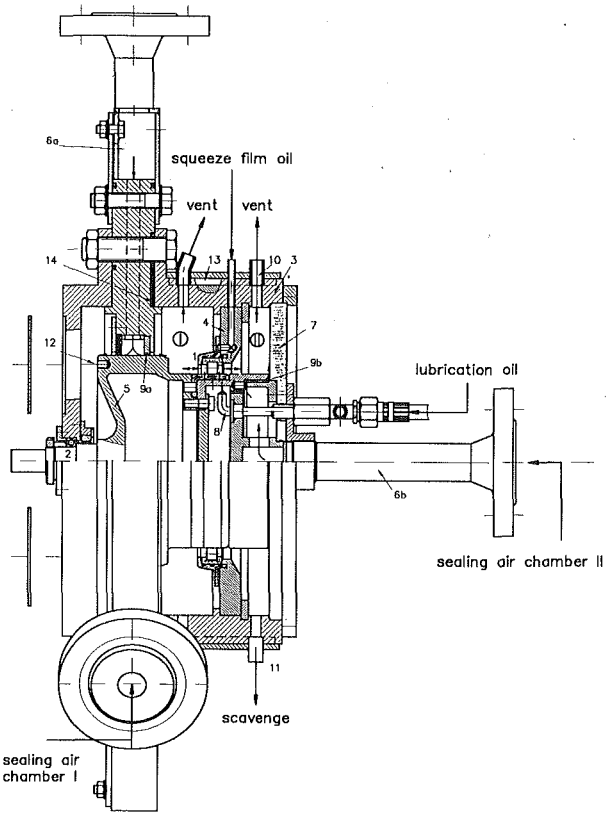

Fig. 1 Compact high-speed bearing chamber: (1) roller bearing, (2) axial fixed ball bearing, (3) housing, (4) roller bearing support unit (flange), (5) rotor, (6*a*) sealing air supply chamber I, (6*b*) sealing air supply chamber II, (7) transparent cover, (8) under race lubrication, (9) labyrinth seal, (10) vent, (11) scavenge, (12) balancing hole, (13) cooling duct, (14) insulation

heat transfer to the mixture is quite problematic, because local temperatures can increase significantly if demixing occurs, caused, i.e., by bends or knee pieces. Even with modern computer codes it is not possible to predict the two-phase flow in aero-engine vent pipes, because at least one of the presuppositions, a reliable model for the computation of free surfaces, is not fulfilled. Besides this, utilization of empirical correlations suffers from a general lack of air/oil data. Investigations made by Zimmermann et al. (1991) have shown that with two-phase flow correlations derived from available air/water test results, only some aspects can be covered. Therefore, the designer is currently forced to overdimension the vent system, with the consequences described above.

Up to now, flow regimes and heat transfer processes at the location of air/oil mixture generation, namely the bearing chamber, have not been studied.

The work described in the present paper is based on a research program that has been incited to improve the design of bearing chambers and air/oil flow elements. In a first step, a test facility has been mounted and measuring techniques for the determination of heat transfer and oil film thickness under real engine conditions have been developed. The quality of the experimental setup has been demonstrated by investigations at rotational speeds up to $n = 12{,}000$ rpm, lubrication oil flows of $\dot{m}_{oil,t} = 50 \times 10^{-3}$ kg/s, and sealing air flows of $\dot{m}_{air,ch} = 12 \times 10^{-3}$ kg/s, both preheated at a temperature of $T_{air} = T_{oil} \geq 373$ K.

Test Facility

The compact high-speed bearing chamber test rig has been built as shown in Fig. 1. At each side of a squeeze-film damped roller bearing (1) separate chambers are formed with an aspect ratio of $(b/h)_1 = 1.0$ and $(b/h)_2 = 0.5$. The chambers are bounded by a thick-walled housing (3), the roller bearing support unit (4), the rotor (5), a radial sealing air supply for chamber I (6*a*) and a transparent disk covering chamber II (7). By use of this cover, made of a special high-temperature thermoplastic material (MAKROLON, $T_{max} = 423$ K), flow regimes inside the bearing chamber are investigated qualitatively.

An under race lubrication (8) supplies the roller bearing with preheated oil. To prevent oil leakage, both chambers are sealed using three fin labyrinth seals (9). Air/oil mixtures are discharged through vents at the top of each chamber (10), while the oil sump at the bottom is dropped out via radial scavenges (11). Components of the rotor line are the seal runner of the radial sealing air supply (9*a*), the inner ring of the roller bearing, the labyrinth rotor of chamber II (9*b*) and a cover, sectioning the inner rotor system. Due to special efforts on the surface finish of the seal runner, which has been nitrided to a hardness of 750 HV, the design of the rotor gives the opportunity of a brush seal application at chamber I. In addition, seal runner supporters are kept flexible to avoid a buckling of the rotor line, which could damage the roller bearing.

The rotor is driven by an electrical motor ($n_{max} = 3000$ rpm) in connection with a flexible coupling and a flat belt (transmission 1:7). The maximum rotor speed of $n_{max} = 16000$ rpm requires special efforts concerning safety and reliability aspects. A precise balancing under operating conditions has led to small rotordynamic vibrations. For the compensation of unbalances two planes are provided with 48 balancing holes (12) at each plane.

The test rig has been optimized for the investigation of the transfer phenomena. Following Jacobsen (1987) the relative error of the local heat transfer coefficient $\Delta\alpha_g/\alpha_g$ is a function of the wall thickness l, the thermal conductivity λ, the heat transfer coefficients at both sides of the wall (α_g, α_c), and the temperature difference $\Delta T = T_g - T_c$. To realize a high temperature difference, cooling ducts (13) are provided with water as a cooling fluid (see also Fig. 3). Wall thickness l and thermal conductivity λ can be adjusted in order to minimize the relative error by use of Eq. (1):

Nomenclature

A = surface, m^2
a = velocity of sound, m/s
b = chamber width, m
d = diameter, m
h = chamber height, m
$\bar{h}_f$ = averaged film thickness, m
l = wall thickness, m
$\dot{m}$ = mass flow, kg/s
n = rotational speed, min^{-1}
Q = heat flux, W
r, ϕ, z = cylindrical coordinates, m
s = gradient of temperature-dependent thermal conductivity, W/(mK^2)
T = temperature, K
t_p = propagation time, s
x = mass flow ratio $= \dot{m}_g/\dot{m}_t$
α = local heat transfer coefficient, W/(m^{2}K)
λ = thermal conductivity, W/(mK)

Subscripts

c = coolant
ch = chamber
f = film
g = gas
max = maximum
min = minimum
opt = optimum
t = total
tc = thermocouple
w = wall
0 = reference
1 = chamber I
2 = chamber II

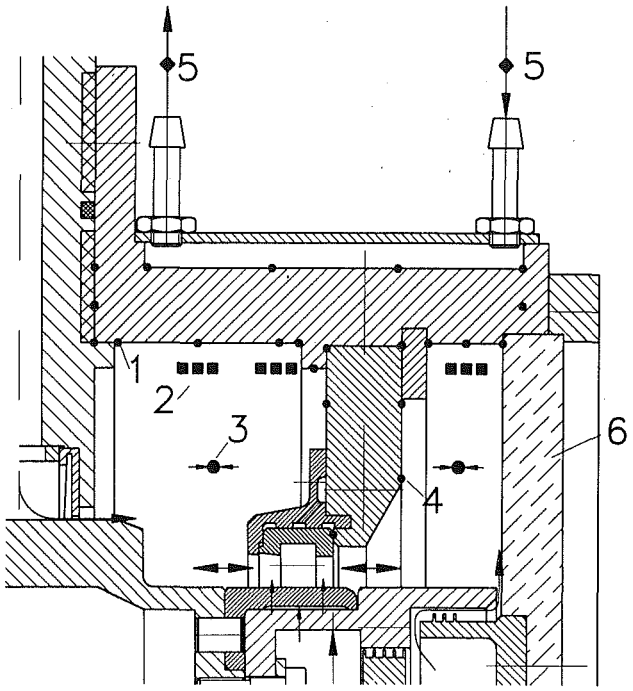

Fig. 2 Instrumentation of the housing: (1) wall temperature, (2) gas temperature, (3) chamber pressure, (4) bearing (flange) temperature, (5) coolant temperature, (6) optical access

$$\left(\frac{\lambda}{l}\right)_{\text{opt}} = \frac{\alpha_g}{\sqrt{1+\frac{\alpha_g}{\alpha_c}}} \tag{1}$$

At a rough guess of heat transfer coefficients, the appropriate wall thickness is fixed by the thermal conductivity of the material used.

The housing is mounted with an insulation layer consisting of ceramic paper (14) in order to reduce boundary effects by heat conduction from the sealing air supply. Surface temperatures of the bearing chamber wall and gas temperatures inside the chambers are measured by NiCr-Ni thermocouples (diameter d_{tc} = 0.5 mm). Figure 2 shows the measuring plane completely instrumented with 18 wall temperature thermocouples. For the determination of gas temperatures 6 thermocouples are located in chamber I, whereas chamber II is provided with 3 thermocouples. Furthermore, the roller bearing support is instrumented to determine heat flux and temperature distribution.

Besides the main plane (A), additional instrumentation is provided as shown in Fig. 3. The finite element code used in the present investigation (see section "Heat Transfer Analysis") presupposes a two-dimensional temperature distribution. To assure that the main instrumentation plane is symmetric with respect to the isothermal lines, two-dimensional reference planes (B) with 8 thermocouples each are instrumented $\Delta\phi$ = 7.5 deg in front and behind the main plane. Another plane (C), completely mounted with 18 thermocouples, is installed to obtain information concerning rotational effects on the heat transfer.

The bearing chamber section described above is part of the test facility shown schematically in Fig. 4. In general, four additional parts can be made out: sealing air supply, lubrication and squeeze film oil supply, separation units, and control devices linked with the data acquisition.

Sealing air is supplied by a compressor (1) with a pressure ratio of π = 4.0 and a maximum air flow of $\dot{m}_{\text{air}}$ = 0.5 kg/s, controlled via bypass. Passing a cooler (2), water traps, filters (3) and orifice meters (4) the air reaches an electrical heater

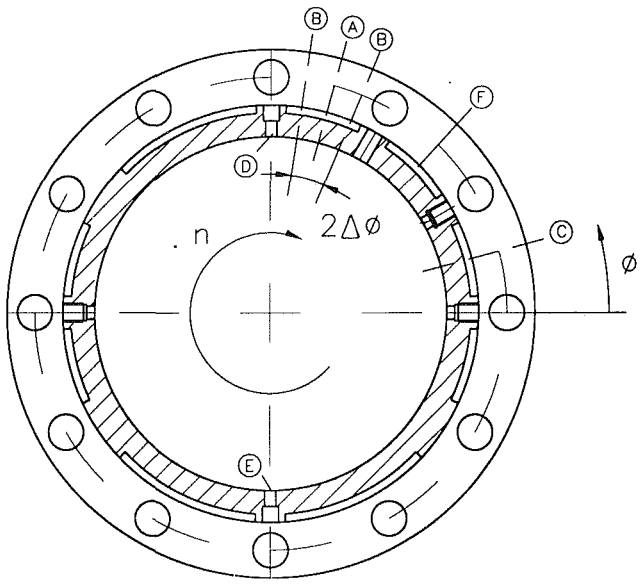

Fig. 3 Measuring planes (axial location $z = 71 \times 10^{-3}$ m): (A) main instrumentation plane, (B) two-dimensional reference instrumentation; (C) circumferential reference instrumentation, (D) vent port, (E) scavenge port, (F) cooling duct

(5), which allows maximum exit temperatures of T_{air} = 623 K. After leaving the heater, the air is split into the two sealing air flows entering the measuring section by an annular gap and 10 radial holes (chamber I) and an axial located pipe (chamber II), respectively. The under race lubrication system consists of an oil delivery pump (7), volumetric flow meters (8), an electrical oil heater (9), designed for an oil inlet temperature of T_{oil} = 473 K at maximum oil flow of $\dot{m}_{\text{oil},l}$ = 0.1 kg/s, and an injection pipe located inside the rotor. The squeeze film oil is supplied analogous with a separate delivery pump and flow meter, but without preheating the oil.

For the analysis of two-phase flow and heat transfer in bearing chambers, exact data of oil flow rates and air mass flow are required. A combination of centrifugal separators (10*a*) and superfine filters (10*b*) consisting of a perforated tube, filled with several layers of woven material, has been found as a very efficient separation system characterized by a residual oil concentration of less than 0.1 mg/m^3. After determining the volumetric flow rates the oil is scavenged back into the reservoir (6). The cleaned air is discharged into the environment by passing orifice meters (11). By operating under high temperatures and high rotational speeds, special demands are given concerning the reliability of the rig and the test facility control. Several gages, i.e., a vibration control system (15), an oil reservoir level control (14), and an axial thrust compensation (16), have been mounted to guarantee secure operation. Regarding the data aquisition, all pressure and temperature signals are recorded via mechanical selector switch (SCV), pressure transducer, multiplexer (MUX), and voltmeter (DVM). The piloting and controlling of measuring devices just as the instrumentation communication and management is done by use of a Personal Computer and a IEC-488-BUS-system.

Measuring Techniques

Heat Transfer Analysis. Various methods of heat transfer analysis have been developed at the Institut für Thermische Strömungsmaschinen during the last years. An illustration of experimental techniques and diagnostics is given by Wittig (1990). Therefore, only a brief introduction of the temperature gradient method used for the determination of heat transfer coefficients in the present investigation is presented here.

Local heat transfer is derived from the heat flux

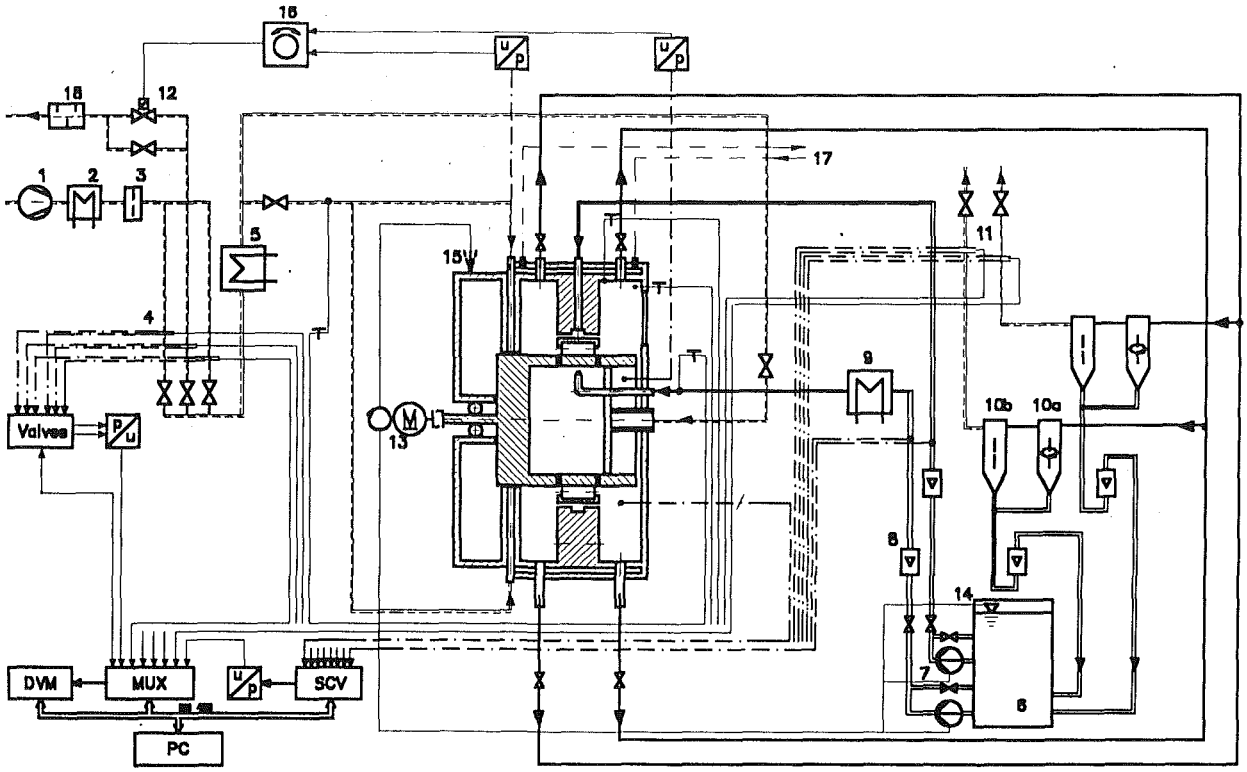

Fig. 4 Test facility: (1) compressor, (2) cooler, (3) water trap and filter, (4) orifice meters, (5) air heater, (6) oil reservoir, (7) oil pumps, (8) volumetric flowmeter, (9) oil heater, (10*a*) centrifugal separator, (10*b*) superfine filter, (11) orifice meters, (12) automatic bypass valve, (13) electromotor, (14) level control, (15) vibration control, (16) axial thrust compensation, (17) domestic water system, (18) silencer

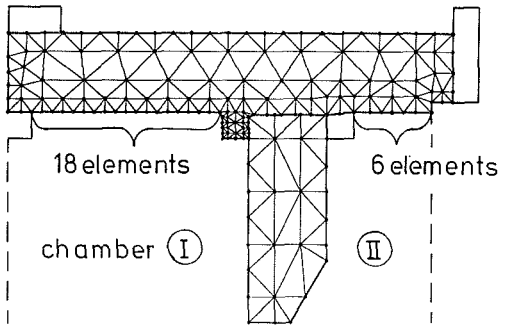

Fig. 5 Discretization

$$d\dot{Q} = -\lambda \cdot dA \cdot \nabla T_{\text{wall}} \tag{2}$$

The local heat flux $d\dot{Q}$ is determined from an assumed two-dimensional temperature distribution in the housing. Temperature distributions are calculated from the wall temperatures using a finite element code developed by Marsal (1976). Wall temperatures T_w at each boundary node of the finite element mesh have to be interpolated from the measured values by spline functions (Späth, 1973). For a high-temperature utilization the dependence of the thermal conductivity λ from the temperature has to be taken into account. Jacobsen (1987) has developed an iterative correction method, considering a linear relation

$$\lambda(T) = \lambda_{0°C} + s \cdot \Delta T \tag{3}$$

where $\lambda_{0°C}$ and s are given by the material.

Marsal's (1976) code has been extended for the calculation of heat transfer coefficients (Schulz, 1986):

$$\alpha = \frac{d\dot{Q}}{dA \cdot (T_g - T_w)} \tag{4}$$

where gas temperatures T_g are determined from local measurements and interpolated analogous to the wall temperatures as described above. In addition, the code has been adapted to applications in cylindrical coordinates (Waschka, 1991).

The discretizations of the bearing chamber housing and the roller bearing support unit are shown in Fig. 5. The finite element mesh of the housing consists of 209 elements and 502 nodes. A cross section of chambers I and II is bounded in the radial direction by 18 and 6 elements, respectively, leading to a corresponding number of local heat transfer coefficients. The finite element mesh of the bearing support unit consists of 32 elements and 85 nodes. Opposite to the heat transfer analysis at the housing of the chambers, a determination of heat transfer coefficients at the bearing support unit has not been performed. Due to the heat generation of the roller bearing, the heat flux within this component is dominated by conduction and not forced by convection from the air/oil mixture. However, an estimation of heat flux in radial direction offers scope for the discussion of heat transfer coefficients at the housing, which are influenced at higher rotational speeds to some extent by heat conduction from the bearing support.

Ultrasonic Film Thickness Analysis. Based on a comprehensive study, analyzing various methods of liquid film thickness measurement on the background of applications inside the bearing chamber, an ultrasonic method has been worked out, characterized by a nonreactive determination of liquid film thicknesses.

The reflection of ultrasonic waves reaching the contact surface of materials with different acoustic resistances (product of density by velocity of sound) is used for measuring tasks. Our measuring device realizes the principle of pulse echo technique. An ultrasonic generator transmits a pulse into the material. At the boundary surface the pulse is reflected and can be recorded in a receiver. Knowing the material velocity of sound, the thickness can be determined by measuring the propagation time.

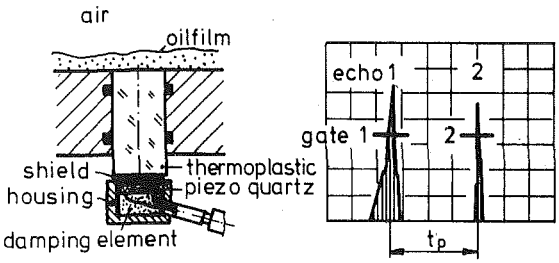

Fig. 6 Ultrasonic film thickness measuring device

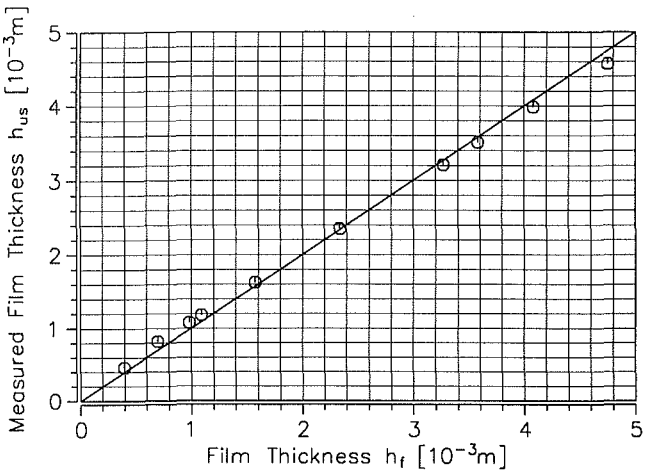

Fig. 7 Performance of the ultrasonic film thickness measuring technique

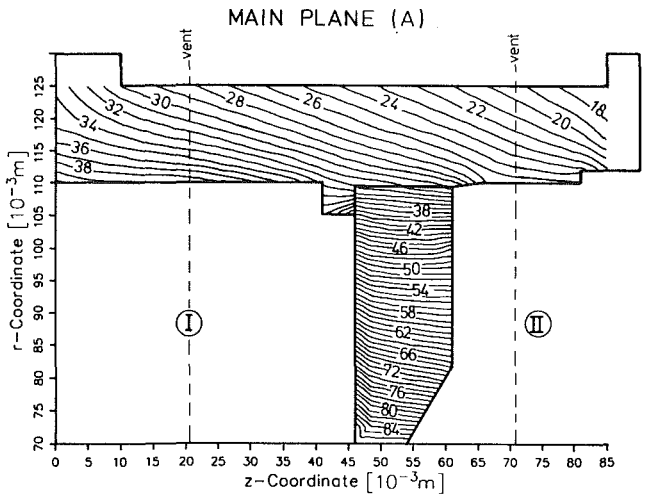

Fig. 8 Isothermal lines: $\dot{m}_{air,ch}$ = 12 × 10^{-3} kg/s; $\dot{m}_{oil,t}$ = 50 × 10^{-3} kg/s; n = 9000 rpm

The success of ultrasonic measurements strongly depends on the boundary conditions given by test rig and the characteristics of the measuring device used. This means that numerous parameters, i.e., measuring frequency, the form of the signal, the focus of the sound field, and the mode of pulsing and receiving of the signal, have to be adapted to the specific tasks. In most of the technical applications, the ultrasonic sensor combines the pulsing and the receiving unit. Since the parameters listed above are fixed by the sensor, its selection has to be made very carefully.

Another important parameter dominating the quality of ultrasonic measurements is the pair of materials. A contact surface of steel and oil would cause a total reflection of the sound energy, thus there would not be enough energy for a detectable wave propagation in the oil film. Therefore, a thermoplastic cylinder with an acoustic density fitted to the oil is used to pulse the ultrasonic wave into the oil film.

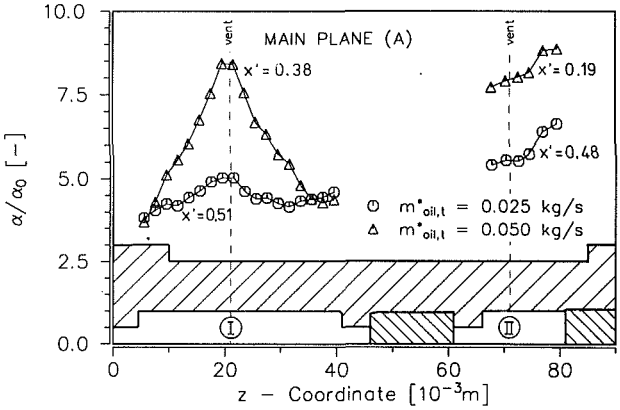

Fig. 9 Local heat transfer coefficients: $\dot{m}_{air,ch}$ = 12 × 10^{-3} kg/s; n = 12000 rpm

Figure 6 shows the measuring device and an oscillogram of a detected signal, which is plotted versus the running time. The first peak, starting the measurement of the propagation time t_p by passing gate 1, represents the echo of the contact surface thermoplastic/oil. The second peak reflects the echo of the contact surface oil/air and stops the propagation time measurement by passing gate 2. With a known velocity of sound for the turbine oil the film thickness can be calculated from the measured time:

$$2\bar{h}_f = a_{oil} \cdot t_p \tag{5}$$

The performance of this technique has been proved under definite boundary conditions simulating bearing chamber applications. The excellent result is demonstrated in Fig. 7. Besides its decisive advantage of nonreactive oil film analysis, the ultrasonic film thickness measuring device is insensitive to vibrations, adaptable to the geometry, and characterized by a wide measuring range in addition to a small lower limit of the measuring range of $\bar{h}_f \simeq 100$ μm.

Experimental Results and Discussion

Heat Transfer Analysis. As described above, the derivation of local heat transfer coefficients is based on a finite element code assuming a two-dimensional temperature distribution. This presupposition has been checked by comparing the temperature values of the two-dimensional reference instrumentation (plane B in Fig. 2). If this temperature difference is found to be negligible ($\Delta T_{B-B} \leq 1$ K) the temperature distribution in the main plane (A) is calculated as described above. As shown in Fig. 8 the result can be visualized by isothermal lines. Some aspects concerning the temperature distribution in the housing are remarkable. The density of isothermal lines is highest in the middle of chamber I (expected location of droplet impingement) and in the fixing fin of the bearing support (due to the heat conduction from the bearing). An increase of wall temperatures due to heat conduction from the sealing air supply of chamber I is minimized by the insulation layer. The wall temperatures are on a lower level in chamber II.

The observations obtained from the isothermal plot are reflected by the heat transfer distribution at the inner surface of the bearing chamber housing. In Fig. 9 local heat transfer coefficients related to pure air conditions are plotted for two operating conditions with different lubrication oil flows versus the contour line of the housing. The local heat transfer distribution is qualitatively nearly the same. Differences can be

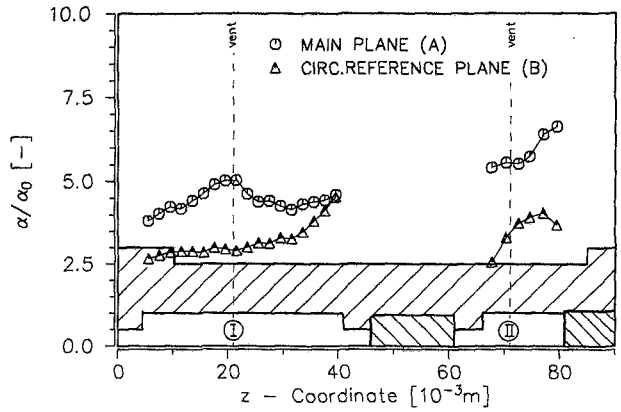

Fig. 10 Three-dimensional effect on the heat transfer: $\dot{m}_{air,ch}$ = 12 × 10^{-3} kg/s; $\dot{m}_{oil,t}$ = 25 × 10^{-3} kg/s; n = 12,000 rpm

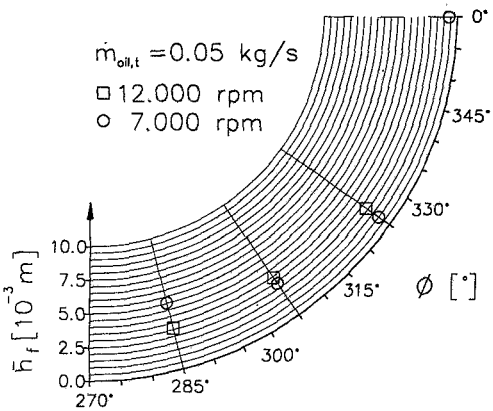

Fig. 12 Oil film thickness: $\dot{m}_{air,ch}$ = 12 × 10^{-3} kg/s; $\dot{m}_{oil,t}$ = 50 × 10^{-3} kg/s

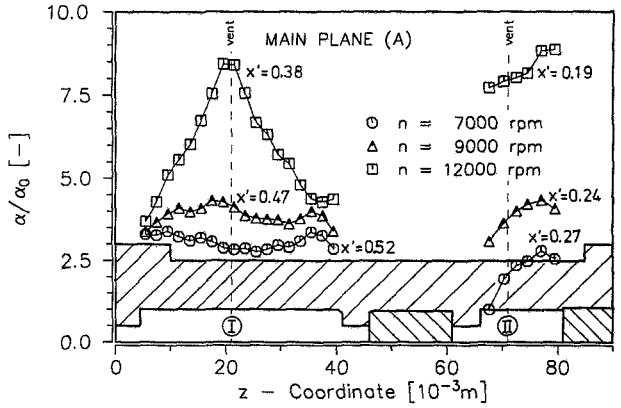

Fig. 11 Variation of rotational speed: $\dot{m}_{air,ch}$ = 12 × 10^{-3} kg/s; $\dot{m}_{oil,t}$ = 50 × 10^{-3} kg/s

seen in the local maximum of α/α_0 values in chamber I and in the level of heat transfer coefficients in chamber II.

Regarding chamber I, the maximum can be related to the location of the vent port (axial position z = 21 mm). An oil droplet impingement forced by the exhausting sealing air flow can be expected in this plane and, in consequence, a higher heat transfer is observed. A higher lubrication oil flow leads to a higher droplet loading in the upper part of the chamber, where these measurements have been carried out (plane A). Thus, opposite the borders of the chamber, where this effect is not relevant, the local heat transfer increases in the middle of the chamber with enhanced oil flow.

The flow regime in chamber II seems to be quite different as expressed in a heat transfer distribution characterized by a maximum next to the cover (axial position z = 80 mm). It can be derived from a qualitative flow investigation, that oil emitted from the bearing impinges at the cover, not directly radial at the housing. Droplets reflected and separated from the vertical wall are carried with the sealing air flow and cause a higher number of α/α_0 values at the housing surface next to the cover. Again enhanced lubrication oil flow leads to a higher local heat transfer because of the increase of oil concentration, especially in the upper part of the chamber. It should be noted that the left limit of the heat transfer distribution in chamber II does not reflect the physical border of this chamber. Because of the mounted circ clip (see Fig. 1: fixing of the bearing support) local heat transfer coefficients cannot be detected up to the vertical wall.

For the question of circumferential symmetry, it must be investigated whether the heat transfer determined in the main instrumentation plane (A) is representative for this bearing chamber. A comparison of α/α_0 values obtained at the circumferential reference plane (plane C, Fig. 3) with those described above is plotted in Fig. 10. Concerning chamber I, the local heat transfer in plane C is nearly constant over the chamber width, but increases next to the bearing support unit (z > 35 mm) due to the heat conduction from the bearing. The higher heat transfer at the main plane (A) can be induced by an acceleration of the fluid in the direction of the vent line as well as by droplets carried over the vent line in circumferential direction. The later effect results in an impinging flow at the wall surface next to the vent port, increasing the heat transfer at this location considerably and leading to the maximum of the heat transfer distribution. In addition to a lower level, the heat transfer distribution in chamber II is characterized by a maximum located inside the chamber. The qualitative flow investigation indicates that this can be related to a missing impingement of oil droplets at this location. Therefore, this distribution represents the heat transfer due to the oil film flow with a lower flow velocity and, in consequence, a lower heat transfer at the borders of the chamber.

For a lubrication oil flow of $\dot{m}_{oil,t}$ = 50 × 10^{-3} kg/s and a sealing air flow in $\dot{m}_{air,ch}$ = 12 × 10^{-3} kg/s, the strong effect of rotational speed on the heat transfer characteristic is shown in Fig. 11. Regarding chamber I, a remarkable increase of local heat transfer coefficients in the middle of the chamber can be observed. The droplet impingement gets stronger with higher circumferential velocity of the rotor. In addition, the oil concentration of the air/oil mixture in chamber I gets higher with increasing rotational speed. This is reflected by a lower mass flow ratio $\dot{x}$, supporting the droplet impingement at the vent/scavenge plane (z = 21 mm). Next to the sealing air supply α/α_0 numbers are nearly the same, implying that the heat transfer at this location is dominated by the heat conduction from the hot oil to the wall and not forced by any increase of local flow velocities or droplet impingement. Due to the induced heat transfer caused by the bearing friction, local heat transfer coefficients next to the fin (z = 40 mm) are getting higher with increasing rotational speed. Concerning chamber II, the percent increase of local heat transfer is nearly the same as detected in the middle of chamber I. The local maximum moves from an inner region of the chamber next to the cover, reflecting the location of droplet impingement described above.

Oil Film Thickness. Some aspects of the development of the bearing chamber oil film thickness are discussed here. Figure 12 shows as an example for a lubrication oil flow of $\dot{m}_{oil,t}$ = 50 × 10^{-3} kg/s and two rotational speeds (n = 7000 rpm and 12,000 rpm) the distribution of the averaged oil film thickness $\bar{h}_f$. The values measured in the middle of chamber II are plotted versus a quadrant of the cross-sectional contour line of the housing.

A strong effect of enhanced rotational speed can be observed. At $n = 7000$ rpm the averaged oil film thickness increases from small values of $\bar{h}_f \simeq 0.7$ mm (azimuthal position: $\phi = 0$ deg, see Fig. 3) up to a maximum value of $\bar{h}_f \simeq 5$ mm in the bottom region of the chamber next to the scavenge port ($\phi = 270$ deg). This nonuniform film thickness distribution is caused by a certain amount of sealing air flow, which leaves the bearing chamber through the scavenge port and, therefore, dammed the oil flow through this port. The shear forces of the gas phase are not high enough to carry the oil over the vent port at this relatively low rotational speed.

Increasing the rotational speed and, in consequence, the circumferential velocity of the gas phase results in a more homogeneous distribution of the oil film thickness. At $n =$ 12,000 rpm a distinct maximum cannot be detected. The averaged film thickness varies in a range of $\bar{h}_f \simeq 2$–3 mm in the bottom region of the chamber (270 deg $\leq \phi \leq$ 330 deg). It can be followed from a viewing through the transparent disc covering chamber II, that at this higher rotational speed a certain amount of oil is driven by the shear forces over the scavenge port. Thus, the shape of the oil film distribution gets more uniform.

Conclusion

With the new test facility presented here, fundamental two-phase flow investigations in bearing chambers have been performed under real engine conditions. Adapting a finite element code for heat transfer analysis to this test rig, local heat transfer coefficients have been determined, showing specific problems in the bearing chamber heat transfer management, which can cause under certain conditions a significant increase of thermal loadings of the bearing chamber walls. A dependency of the heat transfer characteristics on rotational speed and mass flow ratio has been demonstrated.

A new technique for the determination of the oil film thickness has been developed and adapted to the rig. This technique, an ultrasonic measuring device, is characterized by a wide measuring range, the opportunity for adaptable geometry, and the decisive advantage of nonreactive film analysis.

Further investigations will be performed to extend the data base on heat transfer and oil film flow characteristics. It has been shown, that additional effort has to be directed to an extended investigation of three-dimensional effects on the flow pattern and the heat transfer in bearing chambers. The test facility and the measuring techniques developed at the Institut für Thermische Strömungsmaschinen are suitable to perform these investigations.

Acknowledgments

We wish to thank Rolls-Royce plc, Bristol, and Motoren- und Turbinen-Union, München, for funding the research described in this paper. Special thanks are due to H. Zimmermann and R. M. Coleman for the incitement to this study and for helpful discussions.

References

Domes, B., 1991, "Dynamisches Luftlager in Kleigasturbinen," *SIRM—Schwingungen in rotierenden Systemen*, Feb. 26–27.

Ferguson, J. G., 1988, "Brushes as High Performance Gas Turbine Seals," ASME Paper No. 88-GT-182.

Jacobsen, K., 1987, "Experimentelle Untersuchungen zum Durchfluß und Wärmeübergang in Durchblick- und Stufenlabyrinthen," Dissertation Institut für Thermische Strömungsmaschinen, Universität Karlsruhe, Federal Republic of Germany.

Marsal, D., 1976, *Die numerische Lösung partieller Differentialgleichungen*, Bibliographisches Institut.

Schulz, A., 1986, "Zum Einfluß hoher Freistromturbulenz, intensiver Kühlung und einer Nachlaufströmung auf den äußeren Wärmeübergang einer konvektiv gekühlten Gasturbinenschaufel," Dissertation Institut für Thermische Strömungsmaschinen, Universität Karlsruhe, Federal Republic of Germany.

Späth, H., 1973, *Spline-Algorithmen zur Konstruktion glatter Kurven and Flächen*, Verlag Oldenburg.

Suter, P., and Boyman, T., 1978, "Transport Phenomena in Labyrinth-Seals of Turbomachines," AGARD CP-237, pp. 8.1–8.10.

Waschka, W., 1991, "Zum Einfluß der Rotation auf das Durchfluß- und Wärmeübergangsverhalten in Labyrinthdichtungen und Wellendurchführungen," Dissertation Institut für Thermische Strömungsmaschinen, Universität Karlsruhe, Federal Republic of Germany.

Wittig, S., 1990, "Heat Transfer Analysis in Rotating Gas Turbine Components: Experimental Techniques and Non-intrusive Diagnostics," *The 3rd International Symposium on Transport Phenomena and Dynamics of Rotating Machinery*, Vol. 1, Honolulu, HI.

Wittig, S., and Schulz, A., 1992, "A Survey on Efforts in Heat and Mass Transfer Analysis in Aero Engine Secondary Air/Oil Systems," *International Symposium on Heat Transfer in Turbomachinery*, Athens, Greece, Aug.

Zimmermann, H., Kammerer, A., Fischer, R., and Rebhahn, D., 1991, "Two-Phase Flow Correlations in Air/Oil Systems of Aero Engines," ASME Paper No. 91-GT-54.

Induced Draft Fan Innovation for Heat Recovery Steam Generators

O. W. Beasley

E. C. Hutchins

Oklahoma Gas and Electric Company,
Oklahoma City, OK 73101

P. R. Predick

J. M. Vavrek

Sargent & Lundy,
Chicago, IL 60603

A first of its kind, induced draft (ID) heat recovery steam generators (HRSG) have been in service at a cogeneration facility since 1991. A preliminary engineering study considered a forced draft (FD) fan to supply combustion air to the HRSG duct burners (when the combustion turbine (CT) is out of service) as a traditional design; however, the study indicated that the FD fan may require the HRSG duct burner to be shut off following a CT trip and re-ignited after the FD fan was in service. Although the induced draft HRSG design cost more than the FD fan design, the induced draft design has improved the cogeneration facility's steam generation reliability by enabling the HRSG to remain in service following a CT trip. This paper briefly summarizes the preliminary engineering study that supported the decision to select the ID fan design. The paper also discusses the control system that operates the fresh-air louvers, duct burners, HRSG, and ID fan during a CT trip. Startup and operating experiences are presented that demonstrate the effectiveness of the design. Lessons learned are also summarized for input into future induced draft HRSG designs.

Introduction

Oklahoma Gas & Electric Company (OG&E) has installed a cogeneration facility that consists of two refurbished CTs, each exhausting to a dedicated HRSG. Each combustion turbine rating is 26 MW at 105°F ambient temperature.

The cogeneration facility exports steam produced by the HRSGs to an industrial customer. The industrial customer requires a highly reliable source of steam to support the safety and reliability of its operations. Therefore, OG&E selected a first-of-a-kind design to meet their customer's reliability needs.

The cogeneration facility was placed in continuous service in 1991. Since startup, the cogeneration facility has been operated at baseload. The cogeneration facility controls have demonstrated the capability to switch automatically from CT exhaust flow operation to fresh air firing without tripping the HRSG, thereby supporting the steam generating reliability criteria and their continuous process operations for OG&E's customer.

This paper describes the initial studies leading to the selection of an induced draft HRSG, and summarizes operating experiences that have demonstrated the reliability and responsiveness of the design.

Cogeneration Facility Description/HRSG Design Criteria

OG&E's customer steam demand ranges from 250,000 lb/hr (31.5 kg/s) to 600,000 lb/hr (81.9 kg/s) depending on their process needs. OG&E's customer controls the HRSG to meet their steam needs, whereas OG&E controls all other cogeneration facility equipment.

Each HRSG is designed to generate 325,000 lb/hr (41.0 kg/s) of 650 psig (4480 kPa) 725°F (400°C) steam. Up to 25,000 lb/hr is used by each CT for NO_x emission control. When a CT is out of service, approximately 6000 lb/hr (noncoincidental with the CT NO_x emission control steam) is used for duct burner NO_x emission control.

OG&E provides 300,000 lb/hr of steam per HRSG for the customer's use. Each induced draft fan mechanical drive requires 31,000 lb/hr per HRSG. The drives exhaust to the customer's low-pressure steam header. As a result, the net high pressure steam supply is 269,000 lb/hr per HRSG for the customer's use.

The CT exhaust/HRSG design flue gas flow rate is 1,240,000 lb/hr (156.2 kg/s) at 915°F (490°C). Each HRSG is designed to generate approximately 150,000 lb/hr (18.9 kg/s) of steam from the CT exhaust gas heat input (with the duct burners out of service). Duct burners are designed to provide supplemental heat input to each HRSG. The duct burners are designed to increase heat input to the HRSG such that the design steam generation capability can be achieved with and without the combustion turbines in service.

The industrial facility steam header pressure is estimated to drop 10 psi (69 kPa) per second after the loss of an existing boiler or a new HRSG. Since the maximum allowable steam system pressure drop is 50 psi (345 kPa) before the customer's process is affected, the controls are designed to increase duct burner heat input within 5 seconds of a CT trip.

Preliminary Engineering Study

During preliminary engineering, two alternatives for fresh air firing were studied. Alternative 1 was based on a conven-

Contributed by the International Gas Turbine Institute and presented at the 38th International Gas Turbine and Aeroengine Congress and Exposition, Cincinnati, Ohio, May 24–27, 1993. Manuscript received at ASME Headquarters February 18, 1993. Paper No. 93-GT-69. Associate Technical Editor: H. Lukas.

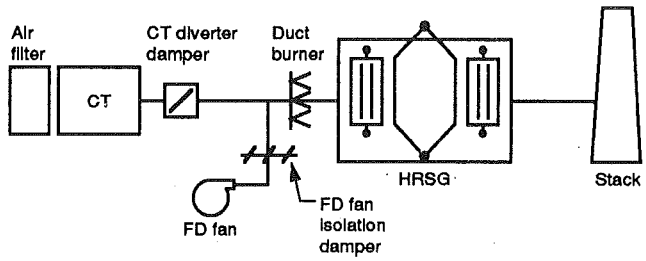

Fig. 1 Forced draft HRSG

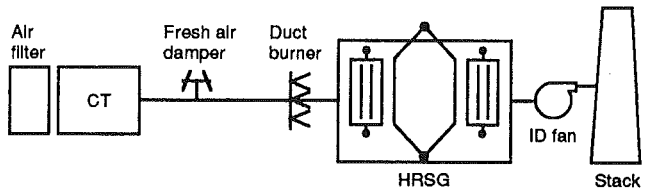

Fig. 2 Induced draft HRSG

tional forced draft (FD) fan and Alternative 2 was based on an induced draft (ID) fan. The innovative use of an ID fan with an HRSG required additional planning and engineering to establish and implement design criteria based on limited experience with this application.

The criteria used to compare the alternatives included estimated costs, site area requirements, operating flexibility, and HRSG reliability. The study is summarized below.

Conceptual Design

Alternative 1. The FD fan conceptual design (Fig. 1) consisted of an FD fan connected to the ductwork upstream of the duct burners to provide backup combustion air. During CT operation, the FD fan would be out of service and isolated by a damper. A diverter damper and bypass stack would be required to isolate the combustion turbine from the HRSG such that the CT may coast down following a trip, exhausting through the bypass stack. As the CT rotating speed decreases, the FD fan would be brought on line to supply combustion air to the HRSG duct burners.

Alternative 2. The ID fan conceptual design consisted of an ID fan (Fig. 2) located downstream of the HRSG. A fresh air damper is located upstream of the HRSG duct burners to provide a backup source of combustion air when the CT is out of service. The ID fan would be in service during CT operation, effectively resulting in a balanced draft HRSG. The ID fan would be controlled to maintain a constant pressure of 0.5 in. water column immediately downstream of the fresh air damper.

Comparison of FD and ID Fan Design Flow. Both FD and ID fans provide the necessary combustion air to the duct burners. The FD fans are sized to provide the duct burner combustion air requirements only when the CT is out of service. The ID fans are sized to accommodate the combustion turbine exhaust flow, which is three times larger than the duct burner combustion air requirements only.

Flow and gas temperature margins are included in the design ID fan flow to account for infiltration and volumetric flow fluctuations that may occur due to variable combustion turbine exhaust gas conditions.

Conceptual Cost. Conceptual cost estimates and equipment manufacturer proposal prices were obtained to compare the cost of both alternatives. The conceptual cost difference between Alternative 1 (FD fan) and Alternative 2 (ID fan) is nominal. The scope estimated includes the fan, isolation damper, ductwork, and ductwork components. The increased cost of the larger ID fan and mechanical steam turbine drives is offset by the savings of the diverter damper and bypass stack, which are not required with the ID fan design.

Site Area Requirements. Alternative 2 (ID fan) requires a longer length site than Alternative 1 based on a horizontal HRSG configuration. This is due to the transition ductwork required at the inlet and outlet of each ID fan. Approximately 40 ft (12 m) of additional length is required for each CT/HRSG train. By comparison, Alternative 1 (FD fan) requires a wider site to accommodate the FD fan, drive, and ductwork.

HRSG Reliability. Alternative 1 (FD fan) required that the duct burners be taken out of service following a CT trip, the HRSG purged, and re-ignited per NFPA recommendations after the FD fan was placed in service and dampers properly positioned. This procedure would result in a brief HRSG forced outage following every CT trip.

NFPA recommendations enable the Alternative 2 (ID fan) HRSG to stay in service following a CT trip through the rapid opening of the fresh air damper. Alterative 2 was, therefore, projected to have a higher HRSG reliability.

Preliminary Engineering Study Conclusion. Since an induced draft HRSG design enables the HRSG to remain on line following a CT trip by providing a continuous supply of combustion air (from CT exhaust gas to fresh air), OG&E, along with their customer, agreed that HRSG reliability should be improved and the risk of forced outages reduced with the induced draft design. An induced draft fan design was, therefore, selected for OG&E's cogeneration facility.

Design Considerations

The following design considerations were implemented during the detailed design of the cogeneration facility:

- Fresh air damper configuration
- ID fan speed control
- Superheater tube metal temperature monitors
- Duct burner gas supply pressure
- Duct burner control system

Fresh Air Damper Configuration and Arrangement. Fresh air damper locations on the side as well as the top of the HRSG inlet duct were studied. The top-mounted location was selected based on the following:

- The site area is better utilized since the area adjacent to side-mounted dampers would have to be restricted for personnel safety.
- The top-mounted damper can open more rapidly since the operator would be assisted by gravity.

A flow model study was performed to confirm acceptable fresh air flow distribution through the open fresh air damper, and across the duct burner as well as to confirm appropriate heat input to the superheater tubes during fresh air firing. The flow model study confirmed that the top-mounted fresh air damper location was acceptable.

The flue gas pressure control set point at the fresh air damper location is set at a slightly negative pressure (see Fig. 3) so that leakage is fresh air infiltration, not flue gas leakage to the atmosphere. Zero leakage damper seals are not required.

ID Fan Speed Control. The ID fan speed is controlled to maintain a constant negative pressure of 0.5 in. water column immediately downstream of the fresh air damper. The fan controls operate independently of whether the combustion turbine is in or out of service. The fresh air flow is not required to be modulated as a function of steam demand during fresh air firing.

Superheater Tube Metal Temperatures. Due to concern

over possible superheater tube metal overheating resulting from heat input when 100 percent of the steam production is generated by the duct burners, OG&E directed the HRSG supplier to install thermocouples to monitor superheater tube metal temperatures. Since superheater tube overheating was a problem during start up (see section on operating experience below), these thermocouples have provided valuable data.

Duct Burner Gas Supply Pressure. The duct burner gas supply system is designed to maintain adequate pressure at the duct burner runners as runners are placed into and taken out of service. Up to half of the 12 duct burner runners are normally in service when the combustion turbine is in service (depending on steam demand). Upon a combustion turbine trip, six additional runners are put in service, and the gas supply flow to the duct burners is designed to increase to maintain the design HRSG steam generating capability.

An engineering study was performed to verify that the gas supply pressure and flow fluctuations would not cause duct burner trips as the gas flow increased/decreased to supply the heat input needed to meet the customer's steam requirements.

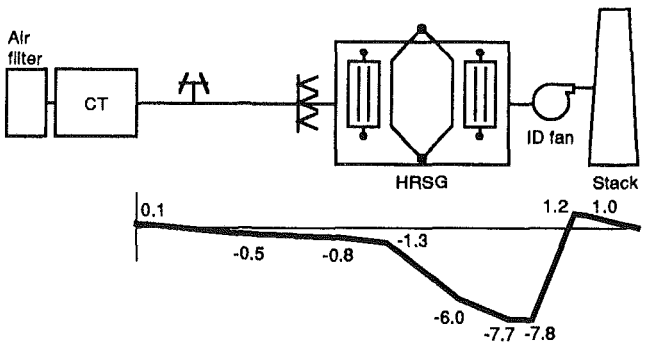

Fig. 3 ID fan design system pressure curve

Duct Burner Control System. One common Integrated Control and Data Acquisition System (IC/DAS) was installed for both CT/HRSG trains (Fig. 4). This system provides combustion control for the combustion turbines as well as boiler control for the HRSGs. A Programmable Logic Controller (PLC) burner management system was furnished with the duct burners and integrated into the IC/DAS. The duct burner runner sequencing design is described below.

In the turbine exhaust mode of operation, steam load demands can be met with the CT at full load and up to six of the twelve duct burner runners in service. These six runners are sequenced on and off as steam load demand and gas pressure vary. Dual redundant gas pressure transmitters sense a rise in gas pressure as the gas control valve is opened in response to increasing steam load demand (steam flow increasing and steam pressure decreasing), and the duct burner runners are sequenced "on" to provide the necessary heat to generate the steam required. The order of runner sequencing is predetermined to provide proper heat distribution in the HRSG. Should a requested runner fail to light when commanded (i.e., both flame scanners for the runner do not detect stable flame), the next runner in the sequence is commanded to light until sufficient runners are in service to support the increase in steam demand and to maintain steam header pressure. On a steam load decrease, duct burner runners are sequenced "off" (determined again by gas pressure) to reduce the heat input to the HRSG.

Should a CT trip, six runners are immediately sequenced "on" (stable flame must be proven for each runner via that runner's two flame scanners) following the predetermined sequence. The logic monitors and controls the successful lighting

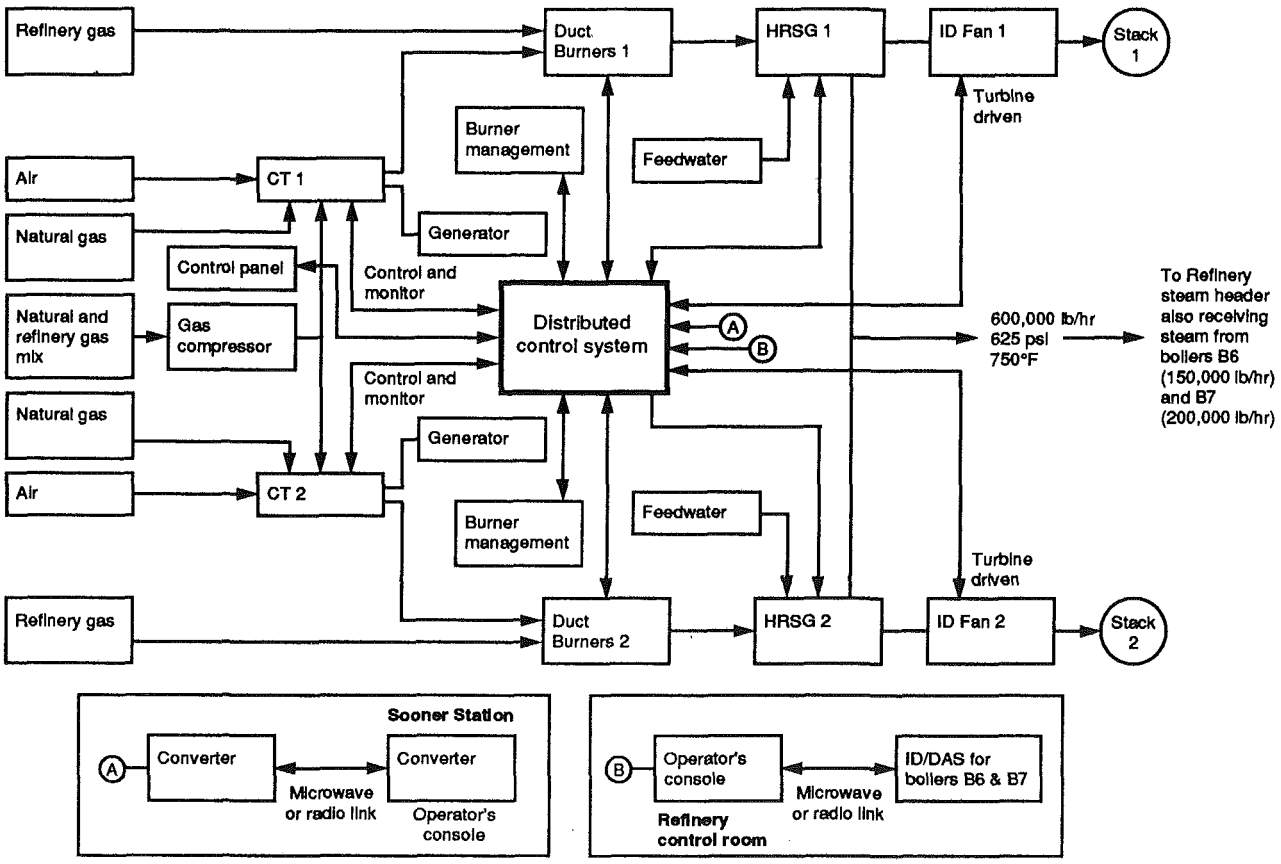

Fig. 4 Integrated control and data acquisition system (IC/DAS)

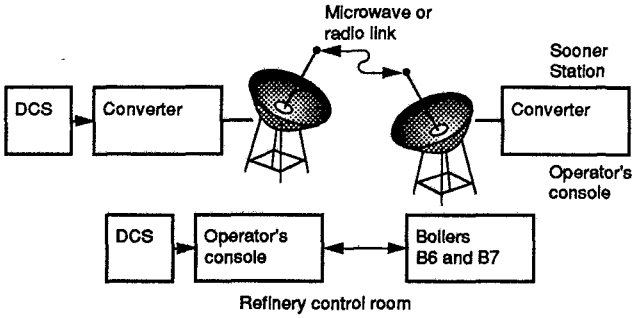

Fig. 5 Integrated control and data acquisition system

of the runners and will continue the lighting sequence, if necessary, until sufficient runners are in service.

Graphic displays that clearly show the status of all duct bruner runners, as well as the appropriate gas and steam system parameters, are provided for the operators via the IC/DAS CRTs. Thus, a common man–machine interface is provided for the operator to monitor and control the cogeneration facility.

Operating Experience

The HRSG was placed into service during 1991 and has since accumulated more than two years' service. The following is a summary of initial operating experience as well as feedback on the design.

Start-up. The individual equipment components (fresh air dampers, ID fans, duct burner control skids, and IC/DAS system controls) were individually checked out. Following HRSG hydrostatic tests and piping steam blows, the HRSGs were successfully placed into service.

Continuous Service. The following sections provide feedback on the design based on more than two years' continuous service. Please note that the cogeneration facility is normally operated remotely from OG&E's Sooner Station (Fig. 5).

Combustion Air System/Duct Burner Controls. Since startup, the fresh air damper controls and induced draft system have operated as designed without any adverse experiences. The ID fan system has not caused any CT trips. Before a planned test of the control system to demonstrate the automatic switch-over from combustion turbine exhaust to fresh air firing could be executed, a severe thunderstorm went through the site late one evening, downing some nearby power lines, which led to tripping the combustion turbine generators. The heat recovery steam generators automatically switched to fresh air firing and remained in service. The successful design of the combustion air and duct burner control system was, therefore, demonstrated in an unplanned test.

Additional planned tests have subsequently been conducted and have confirmed the successful control system design.

Superheater Tube Metal Temperature. Steam temperature is controlled by the duct burner heat input; spray attemperation is not installed. Superheater tube metal temperatures are also controlled by the duct burner heat input. High superheater tube metal temperatures were initially experienced when the CT was in-service. Increased tube metal temperatures occurred at full HRSG load on fresh air firing with duct burners in-service and a CT out-of-service.

The following modifications have been implemented to control superheater tube metal temperatures:

- Superheat surface area was reduced.
- Superheater tube shields were backfit to reduce radiant heat input.

These modifications have achieved compliance with the superheat and main steam temperature design criteria during operation with the CT in and/or out of service.

Combustion Turbine Windmilling. Each of the CTs initially experienced windmilling while the induced draft HRSG was in service following normal coast down after a CT trip. To correct this problem, the compressor bleed isolation valve logic was revised to close and isolate the compressor bleed lines following coast down while the CT remained out-of-service. The bleed line isolation valves are reopened as part of startup. This logic modification has eliminated windmilling.

Duct Burner Gas Supply Pressure. Since startup, the duct burner gas supply control system has performed acceptably. Operating experience has demonstrated that the gas supply pressure to the duct burner does not limit the speed at which the duct burner runners are placed into and taken out of service. The number of runners in service are used to control the HRSG steam production rate to match the customers steam demand.

A duct burner steam injection system has been added to reduce NO_x emissions during fresh air firing. Steam is mixed with the fuel gas upstream of the duct burner runners. The duct burner steam injection system has adversely impacted the gas supply pressure control system. Operating experience indicated that the gas supply pressure was too low for satisfactory mixing with steam. When the pressure was increased, duct burner trips were experience indicated that the gas supply pressure was too low for satisfactory mixing with steam. When the pressure was increased, duct burner trips were experienced due to incorrect high-pressure switch settings on the pilot runner fuel supply. The gas pressure high-pressure trip setting on the pilot runners has, therefore, been increased to reduce duct burner tripping potential successfully during this mode of operation. The duct burner steam injection system has been successfully demonstrated during fresh air firing since the modifications were completed during the fall of 1992.

Conclusion

The induced draft HRSGs have demonstrated successful and reliable operation during continuous service, including automatic switchover from combustion turbine exhaust to fresh air firing with minimal steam header pressure drop transients and less than 10 percent instantaneous reduction in steam generation rates. Demonstrated benefits of this innovation have included:

- Fewer HRSG forced outages
- Improved HRSG reliability
- Automatic switchover from CT exhaust to fresh-air firing
- Uninterrupted steam production to OG&E's customer for both process and safety systems use.

References

Anon., 1990, "I-D Fan Maintains HRSG Output Should Gas Turbine Fail," Industry Notes, *Power*, Jan.

Craig, R., and Biggers, D., 1989, "Induced Draft Heat Recovery Steam Geneator," ASME Paper No. 89-JPGC/Pwr-42.

Predick, P., and Biggers, D., 1990, "Oklahoma Gas and Electric's Cogeneration Facility for a Customer's Refinery," presented at the Frontiers of Power Conference, Stillwater, OK, Oct.

Selection Criteria for Plain and Segmented Finned Tubes for Heat Recovery Systems

D. R. Reid
FINTUBE Corp.,
Tulsa, OK 74157

J. Taborek
Consultant,
Virginia Beach, VA 23451

Heat recovery heat exchangers with gas as one of the streams depend on the use of finned tubes to compensate for the inherently low gas heat transfer coefficient. Standard frequency welded "plain" fins were generally used in the past, until the high-frequency resistance welding technology permitted a cost-effective manufacture of "segmented" fins. The main advantage of this fin design (Fig. 1) is that it permits higher heat flux and hence smaller, lighter weight units for most operating conditions. While the criteria that dictate optimum design, such as compactness, weight, and cost per unit area favor the segmented fin design, a few other considerations such as fouling, ease of cleaning, and availability of dependable design methods have to be considered. This paper analyzes the performance parameters that affect the selection of either fin type.

Historical Background and Overview

Whenever the stream to be used on the outside of tube banks is a gas with inherently low heat transfer coefficient, the use of external high finned tubes is indicated. To obtain the resulting large surfaces, it is more economical to "extend" the plain tube surface with fins than to increase the number of plain tubes. While this was recognized in the 1900's, it was not until the 1920s that manufacturing techniques permitted production of light-duty aluminum helically wound radial fins for air cooled heat exchangers. For high temperatures, welded high longitudinal fins and studs were also introduced at that time. Later, improved resistance welding techniques permitted attachment of helically wound heavy-duty radial fins, with area enlargement factors of about 7 to 15 compared to bare tubes.

Until the 1960s fins with an **L**-shaped foot were used, as the "standard" low-frequency (50 or 60 Hz) electric current required substantial area to form a solid bond with the base tube. The height of a plain fin that can be formed from a metal strip around the bare tube is limited by the drawing process and thus, in the early stages of the technology, the "cut" or "segmented" fins were introduced. The fin material is cut close to the base in intervals of typically 4 to 8 mm (5/32 to 5/16 in.), depending on tube diameter, so that the fin perimeter can expand freely. Typical examples of the two types, plain and segmented fins, are shown in Fig 1.

In the 1970s the modern high-frequency (450 kHz) resistance welding technique was perfected and is now exclusively used (with exception of small tube diameters and some special cases). Because the high-frequency weld forms a strong metallurgical bond, the **L** foot is no longer required and the fins are formed from a simple flat metal strip, sometime referred to as **I** shape. Compared to the low-frequency welding technique, much higher welding speeds are possible and less material is used than for the **L** foot type. Both the plain and segmented fins are manufactured by the high-frequency technique, but the "segmented" fins have several important advantages:

(*a*) easier to manufacture, as no drawing of the material is required;
(*b*) the heat transfer coefficient is higher because of increased turbulence;
(*c*) higher fins are possible because of (*a*), and fin efficiency is also improved;
(*d*) as a consequence of all of the above, the heat exchanger is lighter and cost is reduced.

During the last two decades the modern "segmented" fin design has been rapidly replacing the plain fins, in all suitable applications. For understandable reasons, the power and heat recovery industry is very conservative in the selection of dependable components; however, segmented tubes are fast gaining acceptance even for the most severe duties. This paper clarifies some of the questions commonly asked regarding selection of the fin type for optimum performance application and cost-effective design.

Principles of Finned Tube Application

For finned tube application, it is convenient to write the equation for the overall heat transfer coefficient as U^*, based on a "reference area" A^*:

$$\frac{1}{U^*} = \left[\frac{1}{h_f \Omega_e} + R_{fo}\right]\left(\frac{A^*}{A_o}\right) + \left[\frac{1}{h_i} + R_{fi}\right]\left(\frac{A^*}{A_i}\right) + R_{\text{wall}}\left(\frac{A^*}{A_{w,av}}\right) \quad (1)$$

Here the term $(h_f \Omega_e)$ represents the fin-side heat transfer coef-

Contributed by the International Gas Turbine Institute and presented at the 38th International Gas Turbine and Aeroengine Congress and Exposition, Cincinnati, Ohio, May 24–27, 1993. Manuscript received at ASME Headquarters March 1, 1993. Paper No. 93-GT-131. Associate Technical Editor: H. Lukas.

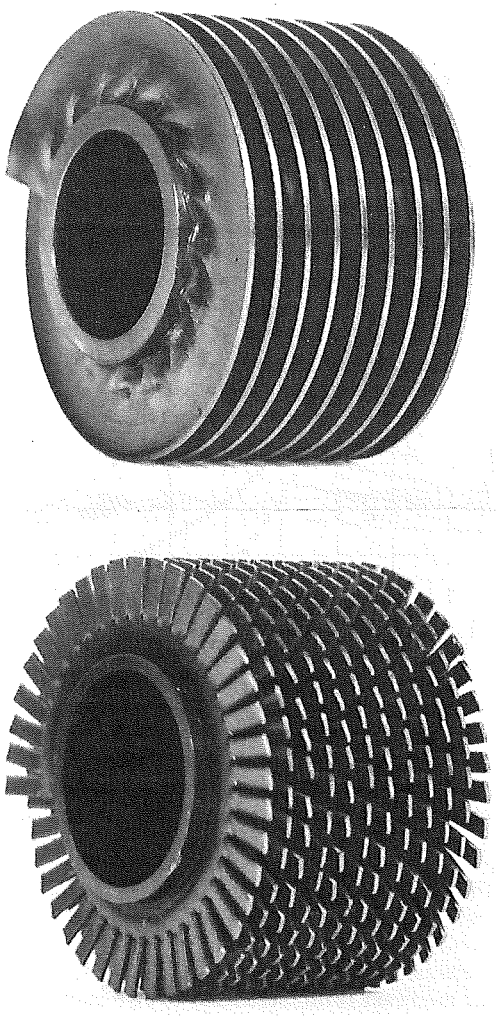

Fig. 1 Plain fin tube (upper) and segmented (lower)

ficient corrected by a weighted "effective" fin efficiency Ω_e; A_o is the total outside tube area (fins and exposed root); R_{fo} and R_{fi} are the outside and inside tube fouling resistances; $A_{w,av}$ is the area at average wall thickness, and R_{wall} is wall resistance.

The advantage of writing the heat transfer equation in this form is that the designer/user can select the most convenient reference area for his application. Three logical selections are possible:

- $A^* = A_o$, that is, the reference area is the total outside area. This is often the usual way of presentation, but the inside tube resistances will appear exaggerated because the area multiplier A_o is between 7 and 15. The U^* value appears low, but the area A^* is large.
- $A^* = A_{pl}$, that is, referring the U coefficient to the outside plain tube surface; the fin tube coefficient will appear high, directly representing the advantage compared to plain tubes.
- $A^* = A_i$, refers the U coefficient to the inside tube surface. The advantage of this presentation is for cases where h_i is important for comparison.

Analysis of Eq. (1) teaches us several important rules of finned tube application:

1 Justification for use of finned tubes occurs when the outside tube resistance is substantially larger than the total inside tube resistance, usually 3:1 or higher, to compensate for the cost of fins.

2 For most effective use of externally finned tubes, the inside tube resistance must be low, i.e., high heat transfer coefficient and low fouling resistance. High inside tube resistance may render the economics of external fins ineffective. Designers should be especially careful in selection of inside tube fouling resistances, which are often exaggerated. For example, the inside tube resistance based on a coefficient of 5700 $W/m^2 \cdot K$ (1000 $Btu/hr \cdot ft^2 \cdot °F$) , will be increased by 100 percent using $R_{fi} = 0.00018\ m^2 \cdot K/W$ [0.001 $(Btu/hr \cdot ft^2 \cdot °F)^{-1}$] by an area enlargement factor of 15.

3 In contrast to item 2 above, the fouling resistance on the finned surface often has only a small effect on U and hence the size of the unit. This is because the low gas coefficient will be only marginally affected by even a large fouling resistance. For example, a typical gas coefficient of 33 $(W/m^2 \cdot K)$ or 6 $(Btu/hr \cdot ft^2 °F)$, combined with a rather large fouling resistance of 0.0035 $(K \cdot m^2/W)$ or 0.02 $(Btu/h \cdot ft^2 °F)^{-1}$, would result in a decrease of U by only 11 percent. While this correctly represents the thermal equations, the selection of high fouling finside resistances often creates a *false sense of safety factor*. Proper design analysis should compare performance under clean and fouled conditions and establish the true safety factor.

Fin Efficiency. The heat transfer from a fin is subject to a penalty called fin efficiency, Ω, which accounts for the temperature gradient between fin root and fin tip due to heat conduction within the fin. Only such principles of fin efficiency are presented here that illustrate the differences between plain and segmented fins. For detailed treatment see Kern and Kraus (1972). Fin efficiency is defined from analysis in terms of a group m the fin height H_f

$$\Omega = \frac{\tanh\,(m_e H_{fe})}{m_e H_{fe}} \quad \psi\ m_e = \sqrt{\frac{2(h_f + 1/R_{fo})}{k_f t_{fe}}} \tag{2}$$

where H_{fe} is "effective" fin height and t_{fe} is "effective" fin thickness. The term "effective" indicates that the actual value is modified from analysis for any specific fin geometry, such as plain radial fins, segmented fins, or stud fins. Thus radial plain fins are penalized because of the much larger fin-tip

Nomenclature

A_f = heat transfer area of fins, m^2, ft^2
A_o = heat transfer area total outside, m^2, ft^2
H = fin height, m, ft
h = heat transfer coefficient, $W/m^2 \cdot K$, $Btu/hr \cdot ft^2 \cdot F$
k = thermal conductivity, $W/m \cdot K$, $Btu/hr \cdot ft \cdot F$
N_f = No. of fins/m or fins/in.
Re = Reynolds number, based on minimum flow area
R_{fo} = fouling resistance outside, $m^2 \cdot K/W$, $hr \cdot ft^2 \cdot °F/Btu$
R_{fi} = fouling resistance inside, $m^2 \cdot K/W$, $hr \cdot ft^2 \cdot °F/Btu$
S_f = fin clearance = $(1/N_f - t_f)$, m, ft
t = fin thickness, m, ft
w = width of fin segment, m, ft
U = overall heat transfer coefficient, $W/m^2 \cdot K$, $Btu/hr \cdot ft^2 \cdot °F$
ψ = gas velocity gradient correction factor
Ω = fin efficiency

Subscripts

av = average
e = effective
f = fin-side
g = referred to gas-side
i = referred to inside tube
o = referred to outside tube
p, pl = referred to plain tube surface
w = referred to tube wall

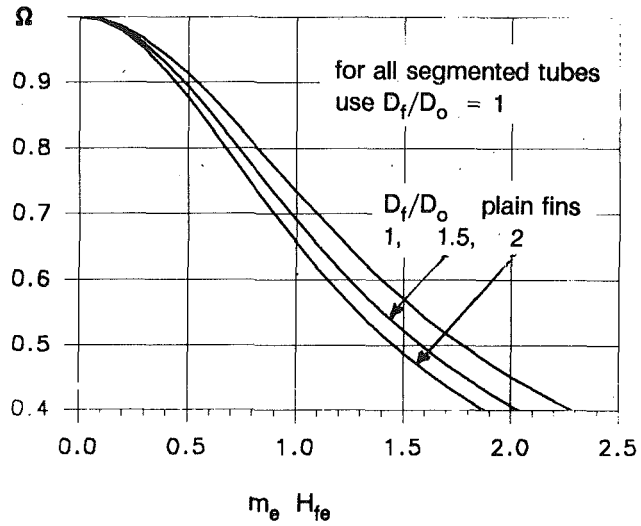

Fig. 2 Fin efficiency as $f(m_e H_{fe})$

circumference compared to the root, as analyzed by Schmidt (1966) and expressed as H_{fe}:

$$H_{fe} = H_f \left[\left(1 + \frac{t}{2\,H_f}\right) \left(1 + 0.35 \ln \frac{D_f}{D_o}\right) \right] \tag{3}$$

where the terms in brackets increases H_f and hence decreases Ω.

The rectangular cross section of the segmented fins is calculated from analysis of round stud fins with a modified expression for fin thickness t_{fe}:

$$t_{fe} = (t \cdot w)/(t + w) \tag{4}$$

The factor ψ is a correction for nonuniform heat transfer coefficient in plain radial fins, accounting for a flow velocity gradient between fin tip and fin root, as analyzed by Lymer and Ridal (1961). Applicable to fin densities of 4.2 mm/fin or 6 fins/in. and higher and fin heights of 20 mm or 0.75 in. and higher, the following correction is suggested:

$$\psi = 0.7 + 0.3\Omega \tag{5}$$

The segmented fin structure permits gas penetration to the fin root, and therefore $\psi = 1$.

Fin efficiency is usually presented in graphic form as Ω versus $(m_e H_{fe})$, as shown in Fig. 2. There the line with $(D_f/D_o) = 1$ applies to segmented fins of all dimensions, while the parameter $(D_f/D_o) > 1$ is used for plain fins. Finally, the finned tube heat transfer coefficient must be multiplied by a "weighted" or "effective" fin efficiency term Ω_e, which penalizes only the finned part of the surface. Thus Ω_e is always larger than Ω, and the following equation applies:

$$\Omega_e = 1 - (1 - \Omega)(A_f/A_o) \tag{6}$$

Heat Transfer Coefficient for High Finned Tubes. Only limited data of uncertain quality were available for high fins until the extensive work at the University of Michigan in the 1950s. Systematic sets of data for welded plain and segmented fins, were obtained in the 1960s at a large-scale wind tunnel at Heat Transfer Research Inc. (HTRI). Selected literature on the subject includes work by Rabas and Eckels (1975), Rosenman et al. (1976), and Weierman et al. (1974). Based on these and other available data, Weierman (1976, 1979) published a comprehensive set of design equations for wide ranges of tube and fin geometry combinations, which is widely quoted in the literature. While it is not the objective of this paper to dwell on thermohydraulics design details, the basic principles of the thermal correlations must be included here as background for the fin selection criteria.

The basis for the heat transfer coefficient of finned tubes

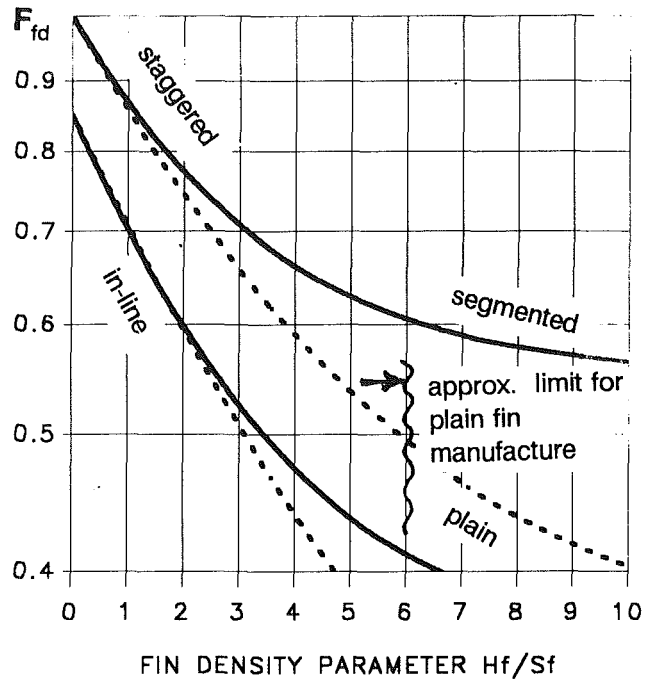

Fig. 3 Correction factor F_{fd} to Eq. (8)

is a correlations for crossflow over *bare tubes*. However, the surface area extension by plain fins is never as effective as the prime tube surface (not considering fin efficiency itself). This is mainly because of incomplete penetration of the gas between the fins. Segmented fins have also a decreased effectiveness, but to a much lesser degree, because they promote gas penetration between the fins and increase turbulence of the gas stream between the fins.

The Weierman heat transfer equation is presented here in a somewhat modified form, restricted to equilateral triangular tube layout and tube rows > 4. The base equation for the Nusselt number for plain tubes

$$\mathrm{Nu}_p = 0.25\ \mathrm{Re}^{0.65}\mathrm{Pr}^{1/3} \left(\frac{T_b}{T_{\mathrm{wall}}}\right)^{0.25}_{\mathrm{abs}} \tag{7}$$

is modified for use with welded fins by two correction factors F_{Df} and F_{fd}, which express the effects of fin height and fin density, as described in principle below:

$$\mathrm{Nu}_f = \frac{h_f D_o}{k_g} = \mathrm{Nu}_p\ [F_{DF} F_{fd}] \tag{8}$$

1 The correction factor F_{fd} penalizes Nu for incomplete gas penetration into the fins. This is shown in Fig. 3 as a function of the fin density parameter H_f/S_f, where $S_f = (1/N_f - t_f)$, the clear space between fins. Logically, it has different values for staggered and in-line tube layout. For low fin heights and low fin densities, i.e., for $(H_f/S_f) < 2$, there is no appreciable difference between segmented and plain fins. However, for higher values of (H_f/S_f), the penalty is much more severe for plain than for segmented fins. This is because the fin segmentation allows better penetration of the gas between the fins. This, in turn, permits the use of greater fin height for segmented fins without excessive penalty. For typical fin densities, the correction factor for segmented fins will be from 10 to 25 percent higher than for plain fins.

2 The correction factor $F_{Df} = (D_f/D_o)^{0.5}$ is always larger than 1.0 and represents the heat transfer enhancing effects of the fins. It is shown in Fig. 4 as $(D_f/D_o)^{0.5}$ plotted against the base tube diameter D_o, with fin height H_f as the main parameter. Restrictive limits are drawn in for plain fins ($F_{Df} = 1.3$) and for segmented fins, with an additional parameter of fin

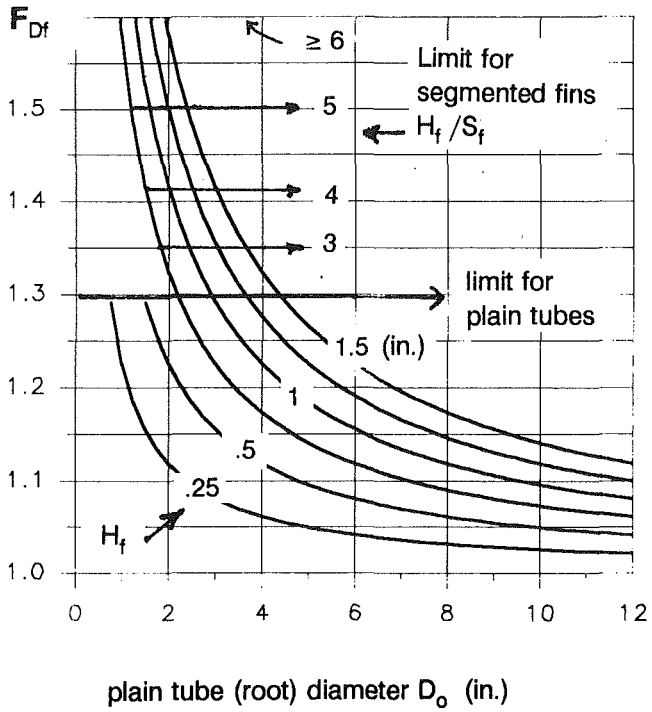

Fig. 4 Correction factor F_{Df} to Eq. (8)

density factor H_f/S_f for segmented fins. The limits roughly coincide with the practical manufacturing restrictions.

Space does not permit analysis and comparison of pressure drop between plain and segmented fins. In general, the same reasons for superior heat transfer performance of segmented finned tubes will also result in increased pressure drop. However, the generally smaller size of segmented fin exchangers (lower number of tube rows) will largerly compensate for the increased friction, as confirmed from numerous designs.

Selection of Fin Design Elements

The design of any finned tube heat exchanger starts with the selection of the fin and tube layout dimensions. Here are some basic guidelines:

Fin Density (Spacing). To produce the maximum outside area per unit of tube length, the highest permissible fin density is used, limited only by:

(*a*) Too high pressure drop, which is a strong function of fin density.
(*b*) The penalty for incomplete gas penetration, especially with high fins, as shown in Fig. 3.
(*c*) The potential for increased fouling. Recommended fin densities are shown in Table 1.

Fin Height. Increasing the fin height increases the outside surface, but this creates complex interactions, requiring a compromise:

(*a*) Fin height dictates the tube pitch and thus the basic parameter of mass flow rate, which affects heat transfer and pressure drop.
(*b*) Manufacturing limitations, more strongly so for plain than for segmented fins.
(*c*) Fin efficiency decreases, again more severely for plain than for segmented fins.
(*d*) For fin height less than 12 mm or 0.5 inch, plain fins are preferred.

For example, if all variables are kept the same and only fin height is increased, the exchanger cost first decreases, then flattens out and finally starts to increase again, as gains in area are offset by effects of large tube pitch, mainly lower gas flow velocity, lower fin efficiency, and lower effectiveness of flow penetration.

Table 1 Recommended fin densities

Fin-side fluid type	Fins/in	mm/fin
Clean air	8 - 11	3.0 - 2.3
Nat. gas combustion	6 - 8	4.2 - 3.0
Light oils combustion	4 - 6	6.3 - 4.2
Heavy oils combustion	3 - 5	8.5 - 5.0
Solid fuel combustion	1 - 2	25 - 12

Fin Thickness. Low fin thickness permits the highest fin density, but also has the lowest fin efficiency and low structural rigidity. The minimum fin thickness is usually 0.036 in. or 0.9 mm. Demand for rugged construction, handling of corrosive/abrasive fluids or high-temperature fluids, dictates the use of thicker fins, which are available up to 0.165 in. or 4.2 mm, subject to some restrictions for smaller diameters. The most popular thickness is 1.2 mm.

Tube Pitch and Layout Type. A staggered, equilateral triangular layout has the highest area density per volume and is regularly used. The tube pitch is usually selected so that about 1/4 of bare tube OD clearance would exist between fin tips, which results is standard dimensions for each tube size. While smaller tube pitch is hardly practical, larger tube pitch will decrease pressure drop, improve "pressure drop to heat transfer conversion," but hurt compactness.

In-line 90 deg layout produces very low pressure drop but also lower heat transfer, as the adjoining tubes are in the "shadow" of the upstream tube rows. Futhermore, stream bypassing in the lane between the tubes distorts the temperature profile and is hard to predict, until for more than about ten tube rows lateral mixing starts being effective, a discussed by Weierman et al. (1974). For these reasons, in-line layouts will be used only when specific advantages, usually connected with cleaning procedures such as soot blowing, become significant.

Comparison of Fin Area. The fin segmentation appears to decrease the heat transfer area (Fig. 1), but if we exclude fin heights of 0.5 in. and lower, and compensate for the sector-cut by adding the area of the fin thickness periphery, the decrease is usually only a few percent, more than compensated for by the higher heat transfer coefficient. Usually segmented fin type is selected simply because the desired fin height cannot be manufactured in plain type.

Gas-Side Fouling. The many types of fouling encountered in heat recovery system are still not quite understood despite considerable progress in this area, as documented in a recent comprehensive review by Marner (1990). The most common fouling forms are fly-ash, chemical reaction products, usually as gluey deposits and hard crust connected with high temperature. Of interest for the fin type selection are the following general observations.

Plain fins with smooth surfaces may have some advantages in particle type fouling as well as for effectiveness and ease of cleaning. On the other hand, segmented fins create turbulence and permit more uniform gas velocity over the fin height. On hard crust fouling deposits, the edges of segmented fins may create faults and promote fouling removal, as was observed on low fin tubes.

A major problem appears to be overly close fin spacing, which may cause "bridging" of fouling deposits and thus substantial deterioration of performance. In the absence of data-supported information, the recommendations by Weier-

man (1974) and Marner and Suitor (1987) will remain the best guidelines.

Design Strategy. The selection of the combination of the fin tube design elements must reconcile often contradictory demands. Practical solutions lean on experiences from similar cases, if such exist, but each case is usually sufficiently different to require detailed attention. The user should rely on a computer-based design analysis, which utilizes the "case-study optimization" technique: Selected design elements are varied within limits compatible with manufacturing and operational practices, until a solution for the least expensive unit is obtained. Help from reliable manufacturers is often available.

Selection Criteria for Plain and Segmented Fins

The most important areas of welded finned tube applications and their specific design aspects are briefly summarized as follows:

1 Heat Recovery Steam Generators (HRSG) use exhaust gas from a turbine to generate steam for a variety of commercial uses, also called cogeneration. This is a rapidly growing application because the overall cycle efficiency is increased. The clean hot gas is ideally suited for segmented fin applications.

2 Fired Heater Convection Sections utilize hot gases in natural draft created by a stack and hence velocity is low and so is permissible pressure drop. Large-diameter tubes at rather low fin densities are used. In general this application is also well suited for segmented fins, but fouling considerations and demands for ruggedness must be observed.

3 Waste Heat Boilers are widely used in power, petrochemical and refinery operations as steam generators, economizers, and superheaters. Demands on the finned tubes are severe, requiring high area extension ratios and often stainless steel fins. In all cases segmented fins have the advantage of producing higher heat transfer coefficients and heat flux than plain fins, and hence more compact design.

Manufacturing Aspects and Cost. Both plain and segmented finned tubes are manufactured by the same high-frequency welding machines. The actual segmenting is done between the fin strip spooling and the welding station without slowing down the welding process. For plain fins, the segmenting station is simply bypassed, but the fin-shaping process is more difficult than for segmented fins. Thus, segmented fins are equally commercially available as plain fins, if the finning machinery is configured accordingly. This is the usual case in USA, where segmented fins have been generally accepted, but not so in all cases in Europe and Asia.

The ease of manufacturing segmented finning is reflected in price comparison with plain fins.This advantage increases for high and dense fins, which are much easier to manufacture in segmented fins. For otherwise identical fin parameters, for a typical boiler tube for turbine exhaust gases, segmented fins would weigh about 80 percent and cost about 84 percent of the values for plain fins (not including cost and weight of the bare tube). For fins thicker than 2.6 mm or 0.105 in. and/or for fin densities below 8 mm/fin or 3 fins/in., there is little price difference between the two fin types.

Usage and Selection Practices. Segmented fin popularity has steadily increased in the last two decades, due to demonstrated reliability and cost advantage. In HRSG applications, segmented fin utilization in the USA is approaching 90 percent, with most of the remaining 10 percent being in superheater coils. The design of convection sections and various heat recovery equipment is also converting to segmented tubes, where properly applicable.

On the other hand, plain fins will remain the exclusive choice for solid fuel fired systems. There is some history and design inertia of using thicker plain fins in such applications, and this is largely responsible for their reputation for durability and life. Plain fins also continue to enjoy a reputation for easier coil fabrication and handling with less damage.

The greater structural strength of plain fins has advantages in bending and tube support bearing, although present designs seldom call for such strength. At least some of the above items are remainders of past practices, and segmented fins were shown to perform satisfactorily in most equipment design and fabrication methods, while providing the advantage of weight and price.

Conclusion

The criteria for selection of the segmented or plain fins can be summarized as follows:

- Segmented fin formation uses faster welding speeds and hence the manufacturing cost is lower.
- Plain fin formation depends on expanding the fin material radially, thus limiting the fin height that can be manufactured. Segmented fin formation requires only "spreading" the segments, thus permitting the manufacture of higher fins.
- The fin segmentation increases turbulence and improves gas penetration to the fin root area, thus equalizing the flow velocity over the fin height. This results in higher heat transfer coefficient than for plain fins by as much as 20 percent.
- Uniform flow velocity over the fin height removes reasons for velocity distribution penalty for fin efficiency, a substantial advantage for higher fins and low-conductivity materials.
- Because of the higher coefficient, the design usually requires fewer tube rows, compensating for the slightly increased pressure drop for segmented fins.
- The segmented fin thickness remains constant over the height of the fin, which results in more rugged construction and resistance to high temperatures.
- In general, plain fins withstand more physical abuse. Fins lower than 12 mm or 0.5 in. and/or fin density less than 8.5 mm/fin or 3 fins/in. are used exclusively in plain fin design, as the advantages of segmentation would not be cost effective.

There are applications and exchanger manufacturing methods for which one or the other fin type is preferred. While in some cases fouling and cleaning considerations will favor plain fins, segmented fins are superior with respect to weight, compactness, and price. Based on the established field performance record for the last two decades, segmented fins should be considered for all future designs.

References

Kern, D. Q., and Kraus, A. D., 1972, *Extended Surface Heat Transfer*, McGraw-Hill, New York.

Lymer, A., and Ridal, B. F., 1961, *Proc. Brit. Nucl. Energy Conf.*, Oct., pp. 307–313.

Marner, W. J., and Suiter, J. W., 1987, "Fouling," in: *Handbook of Single Phase Convective Heat Transfer*, S. Kakaç, R. K. Shah, and W. Aung., eds., New York, Chap. 21.

Marner, W. J., 1990, "Progress in Gas-Side Fouling of Heat-Transfer Surfaces," *Appl. Mech. Rev.*, Vol. 43, No. 1, Mar., p. 35–65.

Rabas, J. T., and Eckels, P. W., 1975, "Heat Transfer and Pressure Drop Performance of Segmented Extended Surface Tube Bundles," presented at the 15th ASME National Heat Transfer Conference, San Francisco.

Rosenman, T., Momoh, S. K., and Pundyk, J., 1976, "Heat Transfer and Pressure Drop Characteristics of Dry Tower Extended Surfaces, Part 1," Battelle Mem. Inst., Report BNWL-PFR 7-100.

Schmidt, T. E., 1966, "Improved Methods for Calculation of Heat Transfer on Finned Surfaces," *Kältetechnik—Klimatisierung* [in Germany], Vol. 18, Part 4.

Weierman, C., Taborek, J., and Marner, W. J., 1974, "Comparison of Performance of Inline and Staggered Banks of Tubes With Segmented Fins," *Heat Transfer—San Francisco 1974*, AIChE Symp. Ser., Vol. 74, No. 174.

Weierman, C., 1976, "Correlations Ease the Selection of Finned Tubes," *Oil and Gas Journal*, Vol. 74, No. 36, Sept. 6.

Weierman, C., 1979, "ESCOA Engineering Manual," ESCOA Corp., Pryor, OK.

Electric Drives on the LV100 Gas Turbine Engine

W. D. Jones

A. R. Fletcher, Jr.

General Electric Aircraft Engines,
Lynn, MA 01910

The LV100 gas turbine engine is being developed for U.S. Army ground vehicle use. A unique approach for controls and accessories is being used whereby the engine has no accessory gearbox. Instead a high-speed starter/generator is mounted directly on the compressor shaft and powers all engine accessories as well as supplies the basic electrical power needs of the vehicle. This paper discusses the evolution of the electrically driven LV100 accessory system starting with the Advanced Integrated Propulsion System (AIPS) demonstrator program, through the current system to future possibilities with electric vehicle propulsion. Issues in electrical vehicle propulsion are discussed including machine type, electrical power type, and operation with a gas turbine.

Introduction

The LV100 gas turbine engine is a 1500 shaft hp recuperated engine being developed for U.S. Army ground vehicle use. The LV100 was conceived as a complete powerpack rather than simply an engine. Hence, the requirements for the engine control and accessories package included not only the control of the engine by means of fuel flow and two variable geometries—compressor variable geometry (CVG) and a variable area turbine nozzle (VATN)—but also engine starting and the production of electrical power for use by the vehicle as a whole. For the Advanced Integrated Propulsion System (AIPS) program, a system was designed and successfully run to demonstrate the relevant technologies in a test cell environment. An updated version of this system is being developed for operation on an Automotive Test Rig (ATR) and is scheduled to run on an engine in 1993 and in the vehicle shortly thereafter.

The All-Electric Concept

A unique approach for controls and accessories called the "all-electric" concept was developed for the LV100. In this concept, the engine has no accessory gearbox, but instead a high-speed starter/generator is mounted directly on the compressor shaft and power from it is used to drive engine accessories as well as to supply the total electrical power needs of the vehicle. This arrangement eliminates the gearbox with the implied weight, cost, and volume savings. This concept was initially explored because of recent technical advances leading to increased power density in electric machines. It promised advantages in terms of flexibility of component location, and lower fuel heating.

Lower volume than earlier powerpacks was one of the primary objectives of the overall LV100 design. With the all-electric system, accessories are not constrained to be mounted on the gearbox. Not having to design for a gearbox and the flexibility to put electrical accessories in whatever space happens to be available have proven to be a significant design advantage on the LV100. Elimination of gearing also reduces required torque during starting at low temperatures, thus allowing more rapid starts at cold ambient temperatures.

Fuel system heat production is diminished by decoupling the fuel pump speed from engine speed. In a conventional engine fuel system, the pump rotates on the gearbox at a speed proportional to engine compressor speed. It must be sized to deliver enough fluid at the one highest fuel-required design point. At all other points it delivers too much fuel, sometimes several times the flow required. A metering valve system passes the proper amount of fuel to the engine and the remainder back to the pump inlet. The bypassed flow represents wasted energy, and increased fuel temperature to the engine since all the fuel is pumped up to pressure, but the pressure of the bypassed flow is dissipated as heat in the fuel. This excess fuel heat potentially leads to a fuel coking problem in the fuel injectors. In contrast, with the LV100 system, the fuel pump is decoupled from the engine speed, and it is possible to modulate the pump speed to minimize or eliminate bypassed flow and the resulting fuel heating.

The LV100 AIPS System. The LV100 AIPS system had several electric drive elements of interest: a three-phase starter/generator (S/G) system, electric motor driven fuel and lube pump systems, and electromechanical CVG and VATN actuators. Overall control and coordination was through a conventional Full Authority Digital Engine Control (FADEC). A schematic of the AIPS system is shown in Fig. 1.

Since the AIPS system was a technology demonstrator, each system was individually designed and no attempt was made to integrate power users with the power generation system.

The AIPS Starter/Generator System. To start the engine, the starter/generator had to rotate the compressor shaft. By the same token, the power to drive the generator was extracted from the engine compressor. For simplicity and to take advantage of the smaller size possible at higher speed, the gen-

Contributed by the International Gas Turbine Institute and presented at the 38th International Gas Turbine and Aeroengine Congress and Exposition, Cincinnati, Ohio, May 24–27, 1993. Manuscript received at ASME Headquarters February 12, 1993. Paper No. 93-GT-7. Associate Technical Editor: H. Lukas.

erator was directly coupled to the compressor shaft and spun at compressor speed. The generator was designed to produce rated power over the speed range from engine idle to rated.

The starter/generator demonstration system consisted of a switched reluctance (SR) machine, an inverter/converter unit (ICU) for electronic commutation, a battery bank for starting energy, and a resistive load bank for dissipating the electric power during generation.

The switched reluctance machine is very simple when compared to other kinds of electrical machines. The actual rotor is constructed of stacked, thin, simple, metal laminations bonded together and shrunk-fit onto the shaft, making the rotor simple and rugged (see Fig. 2). The lack of permanent magnets gives better high-temperature capability for operation in hot environments. Not having rotating magnets or rotating windings allows high-speed operation at compressor speeds without rotor-parts containment problems.

The only windings in the SR machine are stationary, independent stator windings of simple construction, making for a reliable stator winding system. The independent nature of the stator windings on an SR machine provides physical and magnetic isolation of one phase from the other. This greatly minimizes the possibility of internal winding phase-to-phase faults. If a phase fault does occur, the faulted phase can be electronically isolated from the rest of the system without impacting the performance of the remaining two phases. This fault tolerant feature is easily achieved because there is no excitation source on the rotor (neither permanent magnets nor windings) that can feed power into the fault. As expected, with one of the three phases disabled, the maximum output power is reduced to about two thirds of the maximum torque output. A discussion of operation of a switched reluctance machine may be found in MacMinn and Jones (1989).

The AIPS machine was built in a production configuration except for voltage level. It was installed in the front of the engine, and cooled and lubricated with engine oil. The AIPS S/G-ICU system was rated at 105 VDC rather than the objective 270 VDC. 105 VDC was chosen as a convenient voltage level to demonstrate the technology, given the components available at the start of the program.

The required brushless commutation of the SR machine is accomplished through the ICU by properly placing current pulses or exciting the machine winding for motoring or generating action. The ICU is composed of the controller and the power bridge.

The controller accepts rotor position angle information from a brushless resolver mounted on the S/G rotor and fires the appropriate phase of the power bridge which in turns excites the correct phase winding. The prototype S/G controller is a microprocessor based digital control system that includes dedicated hardware for very high bandwidth functions.

The power converter handles the high voltages and currents to and from the machine. There is considerable flexibility in the topology of the power converter used to drive the switched reluctance machine. The topology shown in Fig. 3 was chosen for the starter/generator because it offers maximum possible control flexibility and a high level of fault tolerance.

To produce excitation either for torque or power generation, both switches are turned on and current is allowed to build in the appropriate motor phase winding (see Fig. 4). When commutation occurs, both switches are turned off and the winding current flows through the two diodes back onto the DC link.

The high currents handled by the ICU power bridge generated significant electrical losses (up to 2.5 kW), which had to be removed by active cooling. Because of its effectiveness, liquid cooling was chosen. For laboratory development and demonstration purposes, water was selected as the cooling liquid.

The resulting AIPS ICU power bridge was of a reasonable size for incorporation in a vehicle (about 6.5 in. × 7.5 in. × 20 in.).

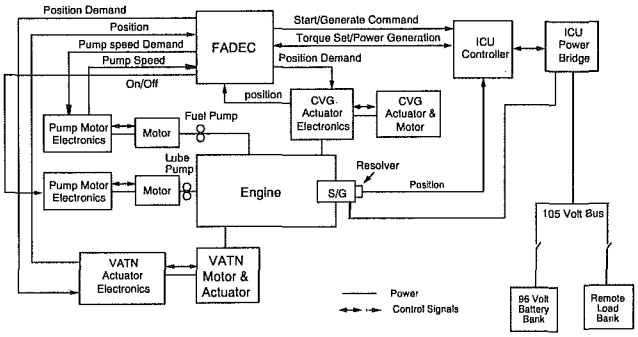

Fig. 1 Control system schematic for AIPS all-electric engine

AIPS Starter/Generator System Testing. Starter/generator and engine integration issues such as increased mechanical vibrations and the impact of load switching on generator output voltage regulation were areas of concern. Bench testing and on-engine testing were conducted and confirmed the system design.

Bench tests verified the ability of the SRM to start, to generate within thermal limits, and to regulate terminal voltage to the rated value of 105 volts DC during steady-state, load switching and speed changing events.

On a LV100 engine in the test cell, the machine was successfully operated as a starter motor for engine starting and once engine idle speed was achieved, it was commanded to begin generating electric power. There was no significant increase in either engine or generator vibration levels due to generation by extracting drive power from the gas turbine engine compressor. Voltage regulation was very good (within 0.1 percent of rated) during electrical load switching. Figure 5 is typical of the excellent power quality obtained through

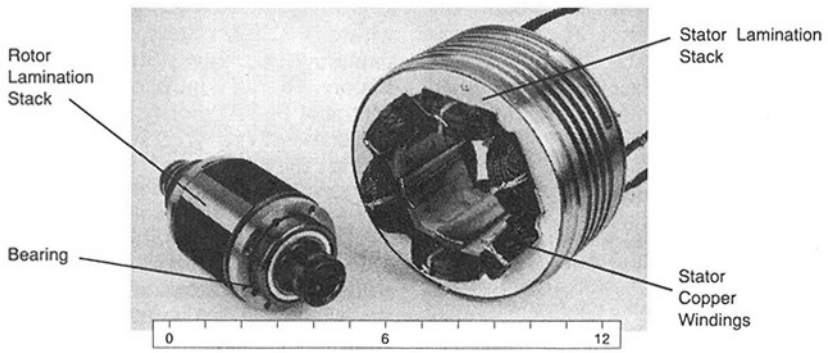

Fig. 2 LV100 starter/generator

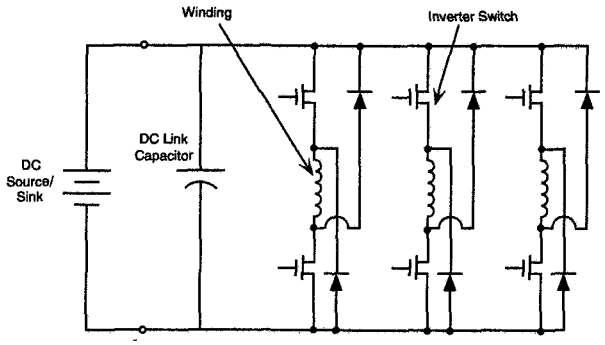

Fig. 3 ICU power bridge connected to S/G machine windings

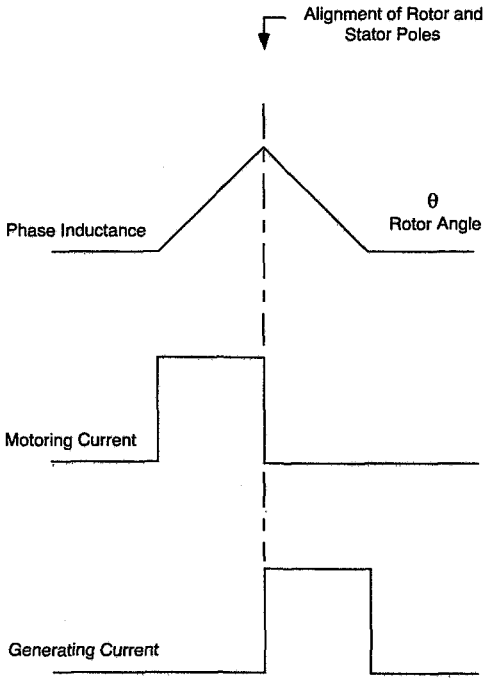

Fig. 4 Placement of excitation current pulses for motoring and generating

close bus voltage regulation during all load switching and speed changing events.

During the course of engine testing, the system showed the benefit of fault-tolerance of a switched reluctance machine. On two occasions a phase of the starter generator system was found to be faulted (once an open circuit; once a short in the phase). In both cases because of testing time constraints, it was inconvenient to repair the machine; so, the system was used to start the engine over a period of several weeks with two of the three phases operating. This continued machine operation under faulted conditions was possible because the windings receive excitation only when commanded by the ICU controller—there are no sources of excitation on the rotor and the three phase windings are virtually uncoupled magnetically. Therefore, the faulted windings could be kept unexcited by simply disabling the winding excitation signal in the ICU. The only operational indication of a fault was, as expected, about a 33 percent reduction in maximum output torque capability.

AIPS Fuel and Lube Systems. AIPS fuel flow was varied by a metering fuel pump. This was a gear pump driven by a variable speed brushless DC motor powered from a 270 VDC lab power supply. By pumping exactly the required fuel flow, fuel bypass was eliminated and heat generation minimized.

The fuel pump was a 3.5 gpm cartridge gear pump coupled

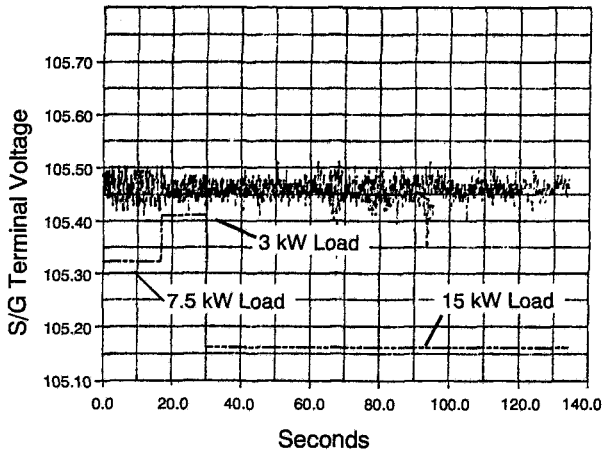

Fig. 5 Voltage regulation of LV100 S/G system during load switching events

directly to the motor and contained within a fuel block, which also housed fuel valve functions. Fuel was metered by varying pump speed. Metering accuracy was totally dependent on the pump displacement and volumetric efficiency.

The fuel pump motor was a 3 phase 2.5 hp brushless DC machine. The motor had samarium cobalt permanent magnets and was driven by a pulse-width modulated servo amplifier. Rotor position for commutation was sensed by a brushless resolver. Motor speed was sensed by a permanent magnet alternator type tachometer.

Extensive bench testing was performed to design the proper dynamics to operate the fuel motor over a very high turndown ratio (approximately 20 to 1). The pump/motor system proved very responsive with a significantly higher bandwidth than conventional metering valves. The fuel pumping system performed well during engine testing.

An off-the-shelf 270 VDC brushless permanent magnet motor was adapted to drive the lube oil pump and air-oil separator. Lube oil cooling was accomplished with a test facility heat exchanger. The lube oil pumping system also performed well during engine testing.

AIPS CVG and VATN Actuators. The AIPS system used rotary electric actuators to drive the compressor and turbine variable geometries. Each actuator system consisted of an electric motor actuator unit and an actuator electronic controller. The CVG and VATN electric motor actuator units were identical. The CVG and VATN electronic controls were slightly different in order to adapt the common actuator for the different angular displacements and directions of the CVG and VATN applications. The electric motor actuator unit consisted of an AC motor, reduction gear train, and position and velocity feedback sensors. Bench and engine testing were very successful.

Summary of AIPS Experience. The electric components described above were extensively tested in the lab and for several hundred hours on engines during the AIPS program. Very few problems were found and what problems were found tended to be typical of problems normally seen in developing a new engine control system and not problems associated with the new technology being tested. In addition to normal temperature range operation, the 17 hp AIPS starter/generator, metering fuel pump, lube oil pump, CVG and VATN actuators were used to successfully start and operate an engine under cold conditions down to −60°F. Total AIPS experience is shown in Table 1.

Some notable achievements with the AIPS electric accessory drives were:

- Provided relatively trouble-free starting and engine control during the course of the AIPS program and for other engine testing, while requiring very little engine test time themselves.
- Demonstrated all-electric engine operation with no gearbox and no hydraulic actuators, with pumping and actuation done electrically.
- Demonstrated engine operation with an electric motor driven metering fuel pump modulating fuel flow with pump speed and with no metering valve.

Some other observations about the system:

- With the fuel system and actuators decoupled from the engine, the whole system could be checked and tested without starting the engine.
- An electrical system almost inherently has more information available to the control, which can be used to refine the control operation and which makes more diagnostic information available.
- With the all-electric system, all features of starting are under the FADEC's control, allowing optimization of the start routine and simplifying the vehicle interface.

Table 1 LV100 AIPS experience

Operating Hours (Approximately)			
Component	Rating	Laboratory	On-Engine
Starter/Generator	17hp/32kW	200	450
Fuel Pump	2 hp	320	350
CVG Actuators	0.13 hp	50	350
VATN Actuators	0.13 hp	50	350
Lube Oil Pump	2 hp	50	350

Designing the ATR System

During the AIPS demonstration period, a number of studies and trade-offs were performed to evaluate the AIPS system and to decide upon a system for the next phase of operation—the Automotive Test Rig (ATR) vehicle demonstration.

An updated tradeoff study of the electrical system compared to a conventional gearbox system suggested that cost and reliability would be similar. The decision was made to continue with the electrical system because of the locational flexibility, the smaller heat rise it offered, the success with the AIPS system, and a belief that rapid gains in power electronics technology promise lower cost and higher reliability in the future.

Significant changes were made in the system to decrease complexity and to make the development challenges more manageable. Also, moving from the test cell to a vehicle meant that the electronics had to be reduced in size and ruggedized and that the power system generator had to be integrated with the power users.

ATR Starter/Generator System. The starter/generator machine for the ATR control system is very similar to the AIPS machine described earlier. However, smaller available space and a smaller estimated power need dictate a 2 in. shorter machine with a 30 kW rating instead of 32 kW. The system voltage rating is the standard 270 VDC instead of 105 VDC for the AIPS system. This increase in voltage gives lower currents and thereby over 50 percent lower resistive electrical losses for the system to handle.

The Inverter/Converter Unit (ICU) power bridge for the ATR S/G is significantly different from the AIPS system. The system is designed for oil instead of water cooling. The oil heat rejection is through vehicle-mounted heat exchangers. The ICU power electronics is packaged to fit into a reduced volume, irregularly shaped space that follows the curvature of the engine bay. This packaging underscores the ability of electric drive technology to make better use of remote, irregular spaces.

The semiconductor switching devices are also different. Because of their higher voltage rating, IGBTs (Insulated Gate Bipolar Transistors) are used as switching devices instead of MOSFETs (Metal Oxide Semiconductor Field Effect Transistors). Smaller, higher temperature ceramic capacitors are used to replace the electrolytic capacitors of the AIPS design. The packaged ATR ICU occupies less than a quarter of the AIPS ICU total volume.

The ATR ICU controller uses the same basic control algorithms as the AIPS controller. However a TMS 320C30 Digital Signal Processor (DSP) is used instead of the Intel 80286 microprocessor. This DSP provides ample computing power for future resolverless operation when that technology becomes available. Good progress is being made toward resolverless operation of switched reluctance machine (Lyons et al., 1992).

The ATR Fuel, Lube, and Actuation Systems. A trade-off study concluded that the system could be simplified by consolidating the fuel and lube pumps onto one shaft running at the same speed and by replacing the electrical actuators with more conventional fuel driven hydraulic actuators and a metering valve. Some of the benefit of reduced heat generation is retained by running the fuel/lube pump at its optimal speed decoupled from engine speed. Some bypass is required, however, as the system has to be sized to slew the actuators on demand.

The resulting ATR fuel module consists of a fuel/lube motor, a fuel pump, a lube pump, and a hydromechanical unit with metering valve and integral CVG and VATN actuators.

The fuel/lube motor is a variable speed three-phase 5.0 hp brushless DC motor of the same design as the AIPS fuel motor but larger in rating and physical size.

The fuel pump is a cartridge style gear pump coupled directly to the motor and located in the hydromechanical unit (HMU). Fuel is metered with a conventional metering valve in the HMU. Hydraulic CVG and VATN actuators are integral to the HMU, eliminating external piping with its associated potential leakage problems.

Future Possibilities for Electric Drives for Tracked Vehicles

The successful operation of a direct-coupled starter/generator and electric accessories without an accessory gearbox suggest a next logical extension of electric drives for the tracked vehicle, eliminating all vehicle gearboxes, including the mechanical transmission.

Electric drives are not constrained to be in-line or closely located to drive train components for bulk power transmission, but can be dispersed and placed in remote locations wherever space exists. This flexibility, along with emerging lower-loss electronic devices, can lead to better overall space utilization, reduced volume or space claim, reduced weight and the associated benefits.

Another attractive feature is the elimination of the clutches, gears, and resulting sharp speed swings associated with shifting gear ranges and steering. In an electric drive system, this is done by changing the speed and direction of the drive motors.

A possible additional attraction is the ability to shift power between propulsion and other vehicle needs.

Sprocket drive power for a 50 ton vehicle can be near 500 hp at each of two sprockets used to drive the tracks. The generator for an electric drive system for such a vehicle must be able to supply about 1000 kW of bulk electric power to drive the two track motors.

Several studies and demonstrations of electric drive technology for a tracked vehicle have recently been initiated in the industry.

Generator Prime Mover. Small size and, to an increasing extent, lower weight are important to a tracked vehicle. The

generator should be integrated with a prime mover in a way that minimizes weight and size. As is well known among electrical machine designers, higher generator speed is a route to smaller size and higher power densities. Gas turbine engines are well suited for driving generators at high speeds. Directly coupling the generator to the output shaft of the engine's power turbine and running at engine speed eliminates the need for a speed-changing gearbox and opens the possibility of developing an optimized integrated power generation module. Proper selection of engine speed for a given load allows operation of engine and generator for optimum overall system efficiency, improving fuel consumption. The prime mover and generator should be treated as a single power-producing unit designed and packaged for optimum performance, size and weight.

System Voltage. System voltage level is key to the basic system architecture and has an impact on weight and volume of system components. For a given electric power rating, higher voltage results in lower current, which results in smaller conductors, lower electrical losses, and lower switching voltage transients. Figure 6 shows the impact of bus voltage level on weight of system copper conductors due to reduced current requirements. A prudent strategy is to use system voltages as high as switching devices will allow without causing significant increases in electrical insulation requirements or decrease in safety.

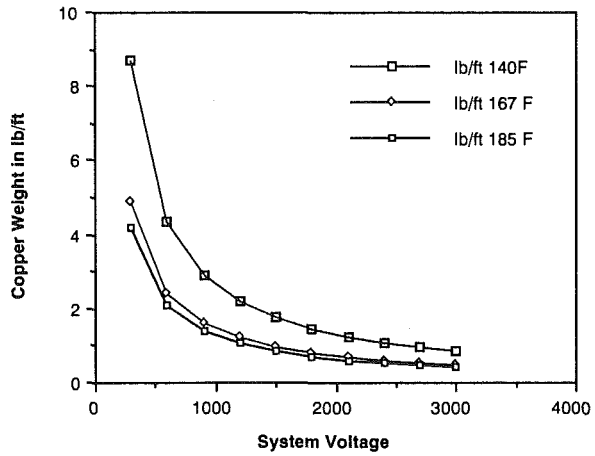

Fig. 6 Electrical conductor weight decreases as system voltage increases

Electric Drive System Architecture. A preliminary architecture for an electric drive system is shown in Fig. 7. An electrical system for such a vehicle might consist of as many as three different power buses. A 28 VDC bus supplies low voltage, low power vehicle loads. A 270 VDC bus supplies low horsepower motor loads, less than 10 hp each. Both of these buses would be built to military standards to provide power to electronics and electrical accessories in the vehicle. Bulk electric power for drive motors is supplied by the high voltage bus with a rated value somewhere between 600 and 2000 volts.

A generator, directly coupled to the power turbine, produces the bulk power for the electric drives system. The generator and the engine are highly interactive and can be thought of as a power pack unit that can be operated with a wide array of electric drive system designs.

Two 500 hp motors are used to drive the vehicle traction sprockets, one on each track. Conceptually, the motors can be either alternating current or direct current. In general, power conditioning electronics is needed to convert the generator power into the form required by the motors. This will usually mean converting power at a DC voltage to an AC voltage required for motor operation. As will be seen later, the motors should be capable of converting from the motoring mode to the generating mode under certain operating conditions to help manage regenerative power.

The electric drive controller interprets steering and traction commands from the vehicle operator and translates them into steering and traction commands to the drive motors. It also communicates with the engine controller to optimize vehicle operation.

Choice of Electrical Machinery. There are many types of electrical machines with comparable performance characteristics from which to choose generators or motors. Using likelihood of trouble-free operation of the rotating members, ruggedness, and compactness as criteria, the long-term choice of machine is expected to be a permanent magnet, an induction, or a switched reluctance machine. At the present time, further

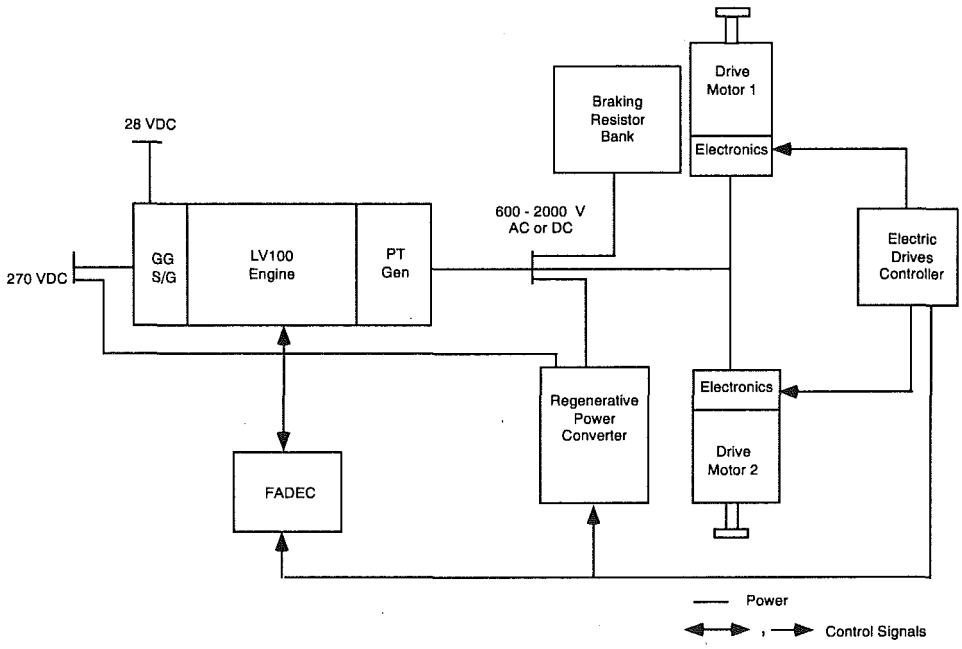

Fig. 7 Preliminary vehicle electrical drive system

development is needed on each of these machine to achieve the desired high power, high speed, capability, and compactness.

Permanent Magnet Machines. A permanent magnet machine's attractive features are its compactness and its ability to start generating without an external energy source by using rotating high energy-product magnets. These magnets also lead to a drawback. The everpresent excitation of permanent magnet machines tends to feed short circuit faults continuously should they occur and thereby make fault management more difficult. The tendency of permanent magnets to demagnetize at elevated temperatures confines PM machines to relatively cool environments. Other issues such as containing the magnets at high rotational speeds, susceptibility to shock and vibration, and rusting, particularly of neodymium, are challenges to be overcome.

Induction Machines. Induction motors are widely used throughout industry and are rugged and relatively simple. They may contain rotating copper conductors, such as a squirrel cage or a solid iron rotor. Solid iron rotor designs have very high-speed capability but produce high rotor iron electrical losses and therefore tend to be impractical for high-speed, high power density operation. On the other hand, the squirrel cage induction motor produces lower losses while maintaining high-speed capability. However, the rotating copper bars are susceptible to breaking under high-speed operation with frequent speed changes.

Switched Reluctance Machines. The switched reluctance machine, similar to the AIPS S/G, has several features that make it attractive. A simple rugged rotor construction with no rotating windings or magnets permits very high-speed, high-temperature operation. SR machines are very fault tolerant and can be made to operate safely with a short circuit in the system by selectively exciting only the good phases. The need of an external excitation source to initiate generation is perhaps the main unattractive feature. Notwithstanding, with bearing replacement being the only maintenance item, a properly designed and built SR machine is very attractive for an electric vehicle drive.

High Power Density Components. Availability of high power density machines and electronics is critical to the practical application of high torque producing electric drives to tracked vehicles.

A survey was conducted to determine the availability of generators that exist or will exist in the near future. A machine envelope target of 15–22 in. in diameter and 10–18 in. in length was sent to twelve potential generator suppliers perceived to have the capability to build a one megawatt generator. Eight of the potential suppliers responded with one or more machine designs, some of which were existing designs and did not fit within the envelope. Figure 8 shows a result of the survey, which indicates the trend of higher power density with higher speeds. The industry survey indicated that electrical machines exist or can be developed to meet the high power density needs of electric drives.

Existence of high power switching capability is key to obtaining high power density in electronic components associated with electric drives. A survey of commercially available semiconductor devices indicated single package devices with adequately high power switching needs: Bipolar transistors rated from 50–1400 volts and 400 amperes; IGBT's rated from 400–1200 volts and 300 amperes; Silicone Controlled Rectifiers rated from 600–5000 volts and 5000 amperes; and Gate Turnoff Thyristors rated from 800–4500 volts and 2500 amperes. High power switching devices are available that make possible compact, high power density electronic converters and inverters for electric drive systems. Furthermore, new switching devices

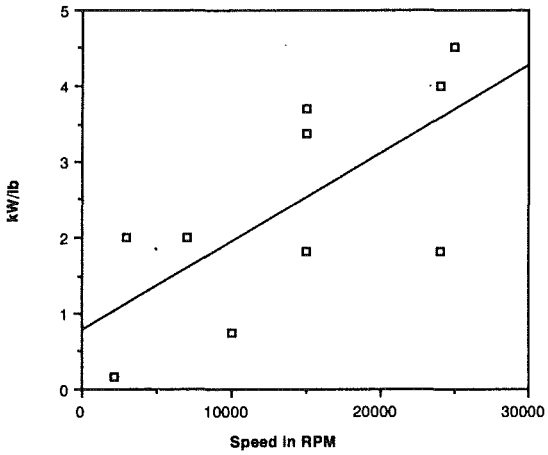

Fig. 8 Results of vendor survey show that generations with higher speeds tend to have higher power densities

being developed such as the MCT (MOS Controlled Thyristor) promise even more compact electronics in the future.

System Operation Issues—Regenerative Power. Under some conditions electric motors can become power producers instead of power users. If not properly managed, this regenerative power can raise the system bus voltage and damage system components. However, under some vehicle maneuvering conditions such as pivot steering, regenerative power can be used in a beneficial manner to reduce the amount of power required from the prime mover and generator. In this case the drive motor on one side operates in the generating mode while the motor on the other side operates in the motoring mode, allowing power to be extracted from the vehicle pivot-point side machine instead of the engine and applied to the higher velocity turning-side motor. This results in improved fuel burn efficiency.

Vehicle braking poses one of the greatest challenges to energy dissipation. The full kinetic energy of the moving vehicle must be dissipated in a short period of time. Mechanical brakes may be used, but there are volume and weight advantages to using the motors in the generating mode to produce maximum braking torque. This puts excess power on the bulk power bus, which must be managed. One way of dealing with this condition is to dissipate the excess electrical power in the form of heat by a bank of resistors. Another solution for the long term is to have the gas turbine engine absorb regenerative power and reduce or eliminate the braking resistors. Conceptually the starter/generator on the compressor and the bulk power generator on the power turbine can be used as motors to feed some or all of the regenerative braking energy back into the engine. Further study and development effort is required before absorption of regenerative power by the engine can be realized.

System Operation Issues—Engine and Generator System Interaction. Since the engine and the generator are closely coupled, load and speed changes on one impact the other. Electrical load rejection of the generator tends to cause the engine to overspeed. Thus the engine control system must be able to detect and protect the engine from dangerously overspeeding whenever electrical load rejection occurs. Close communication between the vehicle driver station, the engine control, and the electrical drive control is required so that load changes required by vehicle speed change, steering, and braking do not cause either engine speed control or bus voltage regulation problems. Feed forward control signals to allow anticipation can make for a smoother, more efficiently operating vehicle.

Summary

Gas turbine engine electrical accessory systems currently of-

fer several advantages, including locational flexibility and reduced fuel heating. Rapid developments in the field of electrical machines and power electronics offer a bright promise for further advantages in the future. The LV100 engine has demonstrated the feasibility of the technology. A significant amount of development work, however, still remains to realize these advantages at a reasonable cost and with good reliability in a production environment.

Electrical drives as the primary drive for a tracked vehicle, powered by a powerpack with a high-speed gas turbine mounted generator, have not yet progressed to the demonstration phase. However, they too show promise of decreased volume and locational flexibility in future systems.

Acknowledgments

Development of Electric Accessory and Drive Technologies requires support, encouragement, and contributions from many organizations and individuals. The authors wish to thank the US Army TACOM for support and encouragement through Contract DAAE07-84-C-R083. The authors also wish to thank Teledyne Continental Motors for support through Subcontract E2-653-001 under US Army Contract DAAE07-91-C-R007. Finally the authors wish to thank GE for supporting the basic development of SR technology and JPO (consisting of GE and Textron Lycoming) for support through fulfilling the aforementioned contracts.

References

Jones, W. D., and Jarvis, M. S., 1990, "Electrically Driven Engine Controls and Accessories for Future Aircraft," presented at the American Helicopter Society Rotary Wing Propulsion Specialists' Meeting, Nov. 13–15.

Lyons, J. P., MacMinn, S. R., and Preston, M. A., 1991, "Flux/Current Methods for SRM Rotor Position Estimation," *IEEE-IAS 1991 Conference Proceedings*, Sept.–Oct., pp. 482–487.

MacMinn, P. M., Szczesny, W. J., Rzesos, W. J., and Jahns, T. M., "Application of Sensor Integration Techniques to Switched Reluctance Motor Drives," Conference Record of the IEEE Industry and Applications Society, Oct. pp. 584–588.

MacMinn, S. R., and Jones, W. D., 1989, "A Very High Speed Switched Reluctance Starter/Generator for Aircraft Engine Applications," *Proceedings of NAECON 89*, Dayton, OH.

Richter, E., 1990, "Switched-Reluctance Machines for High Performance Operation in a Harsh Environment," *Proceedings of the 1990 International Conference on Electrical Machines*, Vol. 1, Aug., pp. 18–24.

Investigation of the Part-Load Performance of Two 1.12 MW Regenerative Marine Gas Turbines

T. Korakianitis

K. J. Beier

Department of Mechanical Engineering,
Washington University,
St. Louis, MO 63130

Regenerative and intercooled-regenerative gas turbine engines with low pressure ratio have significant efficiency advantages over traditional aero-derivative engines of higher pressure ratios, and can compete with modern diesel engines for marine propulsion. Their performance is extremely sensitive to thermodynamic-cycle parameter choices and the type of components. The performances of two 1.12 MW (1500 hp) regenerative gas turbines are predicted with computer simulations. One engine has a single-shaft configuration, and the other has a gas-generator/power-turbine combination. The latter arrangement is essential for wide off-design operating regime. The performance of each engine driving fixed-pitch and controllable-pitch propellers, or an AC electric bus (for electric-motor-driven propellers) is investigated. For commercial applications the controllable-pitch propeller may have efficiency advantages (depending on engine type and shaft arrangements). For military applications the electric drive provides better operational flexibility.

Introduction

Two important parameters in thermodynamic cycles for shaft power engines are thermal efficiency and specific power. Thermal efficiency η_{th} is defined as the ratio of net shaft power delivered, $\dot{W}_S$, divided by the maximum amount of useful power that can be produced by the fuel consumed $\dot{\Omega}_F$; $\dot{\Omega}_F$ is approximately equal to the mass-flow rate of fuel burned $\dot{m}_F$ times the lower heating value of the fuel (LHVF).

$$\eta_{th} \equiv \frac{\dot{W}_S}{\dot{\Omega}_F} \approx \frac{\dot{W}_S}{\dot{m}_F \, \mathrm{LHVF}} \tag{1}$$

Specific power $\dot{W}'$ is a nondimensional measure of the power density of the cycle. It is defined as $\dot{W}_S$ divided by the enthalpy rate of the incoming (ambient) air to the cycle $\dot{H}_{01}$. Defining as thermodynamic point 01 the total (stagnation) condition of the incoming air mass to the cycle $\dot{m}_A$, the specific power is given by:

$$\dot{W}' \equiv \frac{\dot{W}_S}{\dot{H}_{01}} = \frac{\dot{W}_S}{\dot{m}_A h_{01}} \tag{2}$$

For ideal (lossless) gas turbine cycles most thermodynamics texts derive misleading expressions for thermal efficiency indicating that: for the simple (compressor-burner-expander) cycle it increases monotonically with increasing pressure ratio; and for the regenerative cycle it is maximum for a pressure ratio of unity. Cycle-performance plots (produced with realistic assumptions for losses) indicate that for every choice of maximum temperature in the gas turbine cycle there is an optimum pressure ratio for maximum thermal efficiency, which is different from the optimum pressure ratio for maximum specific power. These optima, shown in Figs. 5 and 6 of a related paper (Korakianitis and Wilson, 1994), are drastically different for simple, regenerative, and intercooled-regenerative gas turbines.

Because of the prohibitive cost of developing new gas turbine engines and their components, most shaft-power gas turbine engines (including those for marine propulsion) are existing aero-engine derivatives (Harmon, 1990; Slatter, 1982). The GE LM2500 marine-propulsion gas turbine engine is a derivative of the aircraft CF6 engine. Similarly, the Rolls Royce Avon, Tyne, Spey, Proteus, and Olympus engines, the Pratt & Whitney FT-4 and FT-12 engines, and others, are aero-engine derivatives. A large percentage of the expense for the development of aero-derivative gas turbines is devoted to the development of high-temperature and high-pressure-ratio components. For marine gas turbines thermal efficiencies in excess of 50 percent are possible with less expensive low-pressure-ratio components (at the expense of specific power, which is compensated with engine flow rate and size).

Reviews of technical challenges for automotive regenerative gas turbines have been published, for example, by Walzer (1987). Application on US army tanks with the AGT 1500 Textron Lycoming engine is already in use. In 1953 the Rolls Royce intercooled regenerative gas turbine RM60 was installed in the Royal Navy's HMS *Grey Goose* (Korakianitis and Wilson, 1987; Ferrie, 1990). Harmon (1990) states that "... although the RM60 was efficient, it was too complex for the supporting technology at the time ...". Later it was shown that gas turbines can provide advantages to smaller ships (McCoy, 1981), and operate reliably on heavy fuel (Pavri and

Contributed by the International Gas Turbine Institute and based on a paper presented at the 37th International Gas Turbine and Aeroengine Congress and Exposition, Cologne, Germany, June 1-4, 1992. Manuscript received by the International Gas Turbine Institute February 4, 1992; revision received February 23, 1994. Paper No. 92-GT-86. Associate Technical Editor: L. S. Langston.

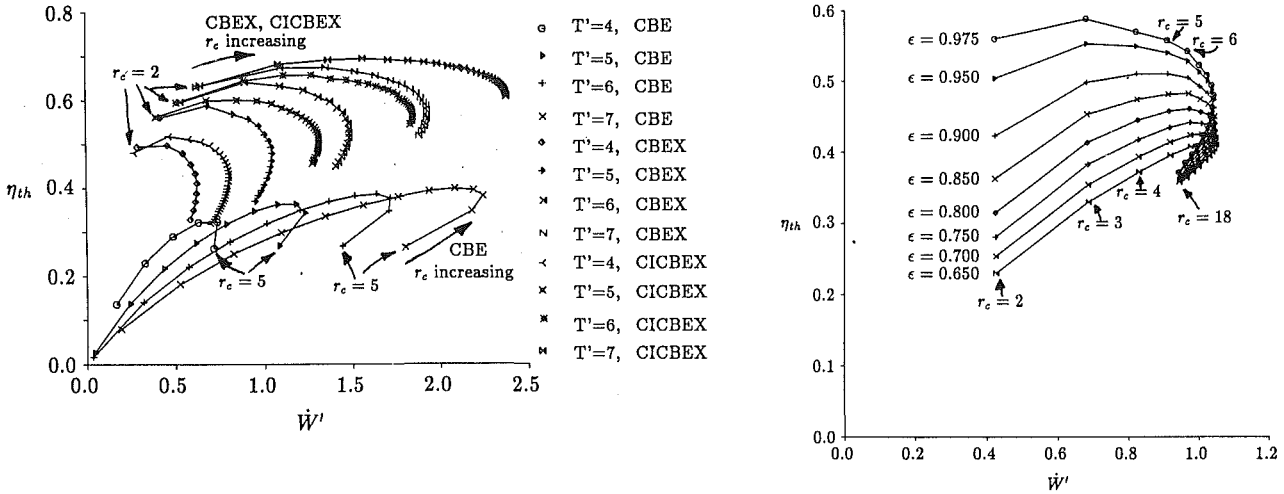

Fig. 1 Left: thermal efficiency versus specific power for simple, regenerative, and intercooled-regenerative cycles using the inputs of Table 1; right: effect of regenerator effectiveness on regenerative cycle performance (for $T' = T_{04}/T_{01} = 5$)

Table 1 Inputs used to produce the cycle performance plots

Cycle	simple	regenerative	intercooled-regenerative
T_{01} (K)	300	300	300
T'	4,5,6,7	4,5,6,7	4,5,6,7
η_b	0.996	0.996	0.996
first r_c	5	2	2
r_c increment	5	1	1
$\Sigma(\Delta p_0/p_0)$	0.07	0.12	0.14
cooling level	2.5	2.5	2.5
T_{bm} (K)	1250	1250	1250
$x2$	0.02	0.02	0.02
ϵ	-	0.975	0.975
$x3$	-	0.025	0.025
$x4$	-	0.025	0.025
i	-	-	0.92
T_c (K)	-	-	300

Hill, 1980; Tomlinson and Alff, 1981). The maintenance requirements are similar to those of other engine types, even during active warfare (Horlick, 1983; Ridley, 1983). Engine start-up time is less than two minutes (Harmon, 1990), much less than that of steam turbines and diesel engines. The US Navy is designing an intercooled regenerative gas turbine (ICR engine) for marine propulsion. Conversion studies to regenerative marine duty by modifying existing aero-derivative engines (Wilson et al., 1985) indicated that trade-off in performance is required, particularly at part-load conditions, in order to use the existing aero-engine-derivative components.

Thermodynamic Cycle Studies

The performance of typical simple (CBE), regenerative (CBEX), and intercooled-regenerative (CICBEX) cycles with realistic component efficiencies has been presented in a related paper (Korakianitis and Wilson, 1994). The shaft-power-cycles portion of that paper forms an integral part of the present article. Using the inputs listed in Table 1, one obtains the cycle performance shown in Figs. 1(*a*) and 1(*b*). Each point plotted in Fig. 1 represents the design-point performance of a different engine. Some additional preliminary choices have been made. The heat exchanger is a high-effectiveness ($\epsilon = 0.975$) rotary ceramic regenerator (Fig. 2). The ceramic matrix is rotating between the hot and cold duct passages at between 1 and 3 rpm. Such regenerators are commonly used in cryogenic applications. Higher-pressure-ratio cycles are better suited to conventional metal heat exchangers (such as the one used in the Textron Lycoming AGT 1500 engine) because they result in relatively lower turbine-outlet/heat-exchanger-inlet temperatures (T_{05}). Low-pressure-ratio regenerative cycles are better suited to rotary ceramic regenerators since they result in relatively higher T_{05}. The leakage flows past the wiping seals of rotary regenerators ($x3$ and $x4$) increase as the cycle pressure ratio increases, and they become excessive for pressure ratios greater than 6 (McDonald, 1978).

The effect of regenerator effectiveness ϵ on regenerative (CBEX) cycle performance is illustrated in Fig. 1(*b*). The other inputs to the cycles are identical to those shown in Table 1, except that for effectiveness less than 0.90 the heat exchanger is assumed to be a metal counterflow type with $x3 = x4 = 0.00$ (no seal leakage). The figure shows that: $\dot{W}'$ is a function of compressor pressure ratio r_c and independent of ϵ; the optimum r_c for maximum η_{th} increases with decreasing ϵ; and the optimum r_c for maximum $\dot{W}'$ is about 9 in all cases. For high η_{th} one must design a high effectiveness regenerator. The figure justifies the philosophy of low-pressure-ratio highly regenerative cycles compromising specific power (compensated with engine size) in order to attain high thermal efficiencies.

Equation (4) of Korakianitis and Wilson (1994) illustrates one of the advantages of intercooling. The specific work re-

Nomenclature

h = specific enthalpy
LHVF = lower heating value of the fuel
m, $\dot{m}$ = mass, mass flow rate
r = pressure ratio
T = temperature, K
$T' = T_{04}/T_{01}$ = cycle temperature ratio
V = ship speed, knots
$\dot{W}$, $\dot{W}'$ = power, specific power (Eq. (2))
ϵ = heat-exchanger effectiveness
η = efficiency
Ω = thermodynamic availability rate

Subscripts

A = air
c = compressor
bm = blading material
F = fuel
S = shaft
th = thermal

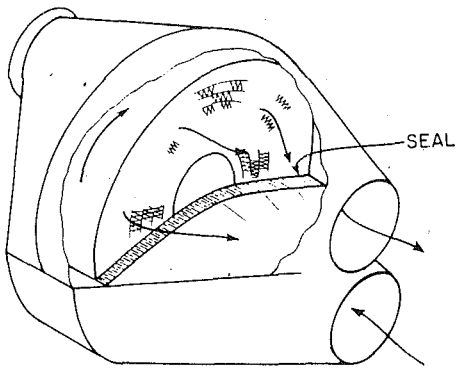

Fig. 2 Sketch of the operation of rotary ceramic regenerators (from Wilson, 1984)

quired for a given compressor pressure ratio is proportional to the compressor inlet temperature. By splitting the pressure ratio between two or more compressors and intercooling between them, one lowers the total amount of compressor work, as well as the final compressor-outlet temperature and specific volume. While the former is beneficial, the latter reduces the blade height of the last compressor stages, reducing compressor efficiency. Therefore there is a minimum limit to the engine size (corresponding to 1.5 MW to 2.0 MW) below which the benefits of intercooling are dwarfed by the penalty of lower compressor efficiency. For marine applications, where engine weight is less important, the intercooled-regenerative cycle is clearly the best choice for engine powers over 2.0 MW. The optimum pressure ratio for maximum η_{th} is between 3 and 4, although for moderate pressure ratios between 4 and 8 η_{th} is still above 55 percent, and $\dot{W}'$ is higher than at a pressure ratio of 3. Engine powers of about 1.12 MW (1500 hp) would be suitable for patrol-boat and numerous smaller commercial-craft main-propulsion applications, and for auxiliary engines in larger ships. For this engine size the regenerative cycle is a better choice than the intercooled-regenerative one.

The following sections compare the part-load performance of two regenerative gas turbines designed for r_c = 3:1, T_{01} = 288 K (59°F), T' = 5.4 (T_{04} = 1555 K, 2340°F), and other inputs as shown in Table 1. The expected thermal efficiency is about 0.55 (depending on pressure losses); the specific power is about 0.7; and for 1.12 MW (1500 hp) the design-point mass flow is about 4.5 kg/s (10 lb/s).

The Two Engine Arrangements

Description of Components. Three different axial-compressor design philosophies have been considered (Korakianitis and Wilson, 1985; Korakianitis, 1987). Compressor *K*1 is a 50 percent reaction design with four axial stages of mean-radius peripheral speed 350 m/s. Compressor *K*2 is a 50 percent reaction design with six axial stages of mean-radius peripheral speed 275 m/s. Compressor *K*3 is a 100 percent reaction design with six axial stages of mean-radius peripheral speed 200 m/s. The design-point and off-design-point performances of these compressors were evaluated by starting from velocity-diagram choices and relating performance and losses using methods described by Horlock (1985) and Lieblein (1959). The peak polytropic efficiency of *K*1 is about 92.5 percent, of *K*2 is about 92 percent, and of *K*3 is about 91 percent. However, *K*3 exhibited wider plateaus of higher off-design efficiencies (Fig. 3). This agrees with the observations of Jeske and Voss (1984) on the comparison of off-design performance of 50 percent reaction and 100 percent reaction stages. High-reaction compressors are also less susceptible to rotating stall and to performance losses from blade fouling (Wilson, 1984). We chose to use compressor *K*3 to enhance the off-design performance of the engine. Similar performance can be expected from centrifugal and mixed-flow compressors, although the off-design range is narrower and the off-design efficiencies are lower (Musgrave and Plehn, 1987).

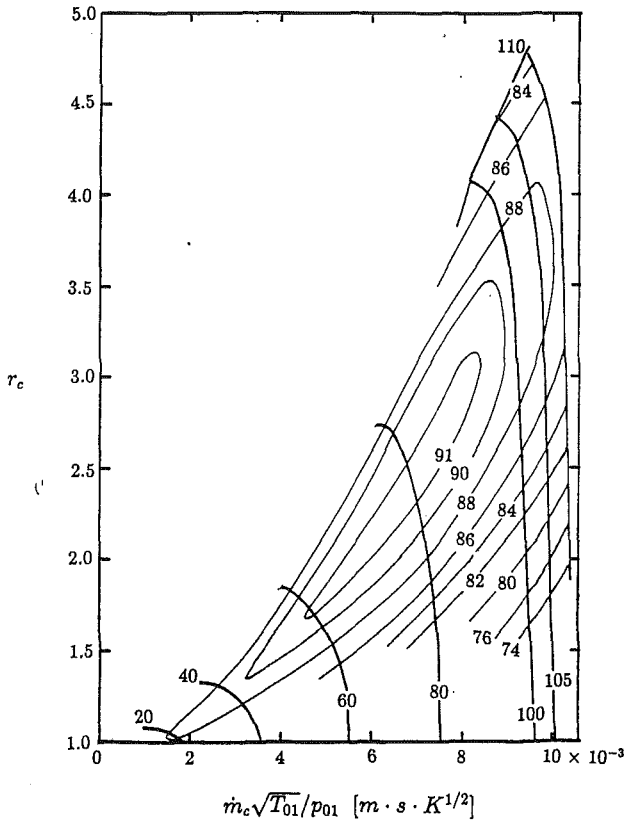

Fig. 3 Performance of compressor *K*3 (total-to-total polytropic efficiency contours)

Two shaft arrangements have been studied. The first, designated LPR-1S, is a single-shaft configuration (Fig. 4). Air enters through the inlet at left, flows through the compressor into the diffuser, and into the high-pressure side of the two rotary ceramic regenerators symmetrically arranged at either side of the engine. Next the air from the two regenerators is collected into a can combustor or combustors located on top of the engine, then into a three-stage axial turbine that drives both the compressor and the output shaft. After the turbine the combustion products pass through the low-pressure side of the regenerator before they are ducted into the engine exhaust. Although the regenerator lowers the temperature of the engine exhaust significantly, there is sufficient availability in the engine exhaust to drive an economizer boiler, an absorption chiller, or other energy-saving device. The second shaft arrangement, designated LPR-2S (Fig. 5), is very similar to LPR-1S, except that the turbine has four axial stages and is split into two parts. The first two higher-pressure stages of the turbine drive the six stages of the compressor, and the next two lower-pressure stages are on a separate power-output shaft.

The same performance map (Fig. 6) was used for the single three-stage turbine of LPR-1S, and for each of the two twin-stage turbines of LPR-2S. This is based on the turbine map shown on page 128 of Glassman (1972). Radial-inflow turbines were not considered because they are susceptible to erosion damage. Preliminary calculations indicate the following. The single-shaft turbine of LPR-1S, and the gas-generator turbine of LPR-2S have outside diameters about 450 mm (17.7 in), and the design speed is 16,700 rpm. The power turbine of LPR-2S can have larger diameter and lower rotational speed. The combustor exit temperature is T_{04} = 1555 K (2340°F), which

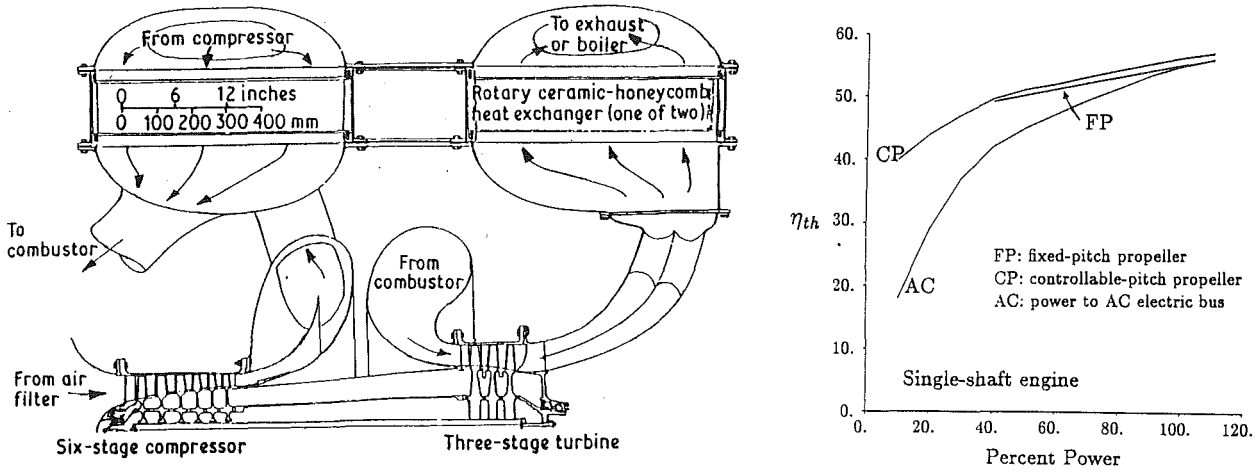

Fig. 4 The single-shaft (LPR-1S) engine configuration and its performance with various propeller types

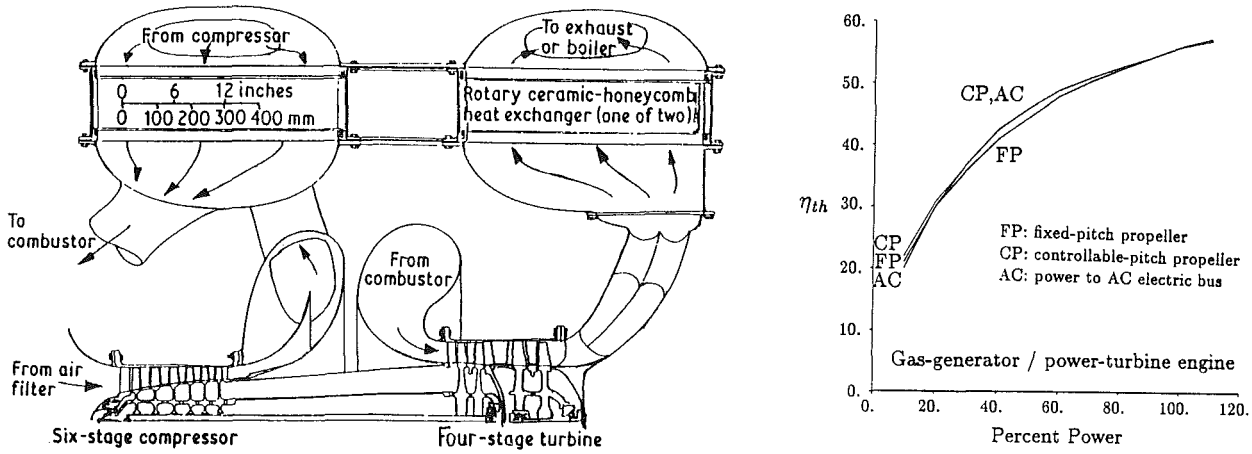

Fig. 5 The gas-generator/power-turbine (LPR-2S) engine configuration and its performance with various propeller types

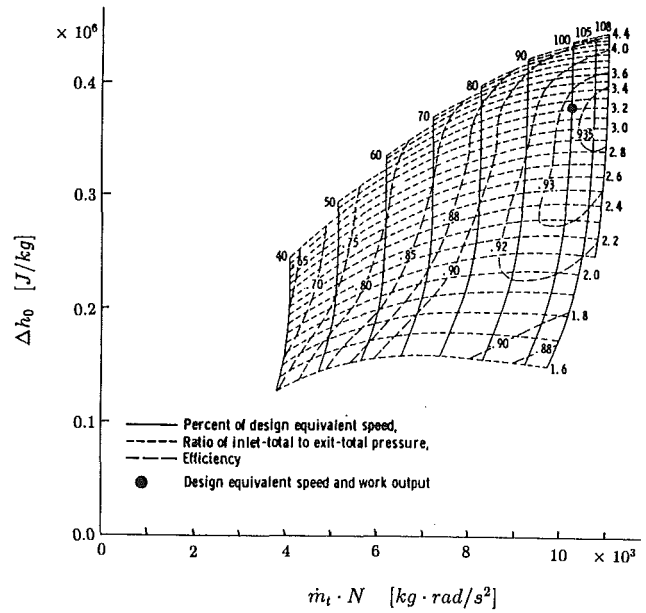

Fig. 6 Performance of turbines (total-to-total isentropic efficiency contours)

allows the turbine to be made either out of conventional alloys with cooled blades, or out of ceramic materials. In the computations we have assumed conventional turbine alloys and appropriate amounts of cooling air. Each ceramic disk would be approximately 1.8 m (70.9 in.) in diameter and 0.15 m (5.9 in.) long. A disk of this size would be made from smaller sections. Each disk is independently driven by a fractional-horsepower electric motor through a standard gear reduction engaging a rim-mounted drive.

Part-Load Performance Comparisons. The design-point and off-design-point performance of the engines has been evaluated using NEPCOMP (Shapiro and Caddy, 1974). This computer program uses the design-point and off-design-point performance of various gas turbine components, which are assembled and controlled in the proper sequence to simulate the operation of turbine engines. The computed thermal efficiency of the two engines is shown in Fig. 7. LPR-2S has 1 percent higher design-point thermal efficiency (because its four-stage turbine has lower loading per stage and slightly higher turbine efficiency than the higher-loading-per-stage three-stage turbine of LPR-1S). While the design-point efficiency of the two engines is similar, configuration LPR-2S can operate at much lower engine speeds and powers than LPR-1S, which cannot operate below about 50 percent engine speed. Both engines operate at lower powers than most published diesel-engine fuel maps. Although diesels will operate at low speed and power combinations for short periods of time, they do so at the expense of forming excessive sludge and increased wear. The only limit on gas turbines is compressor surge and stall, which have been accounted for in producing Fig. 7.

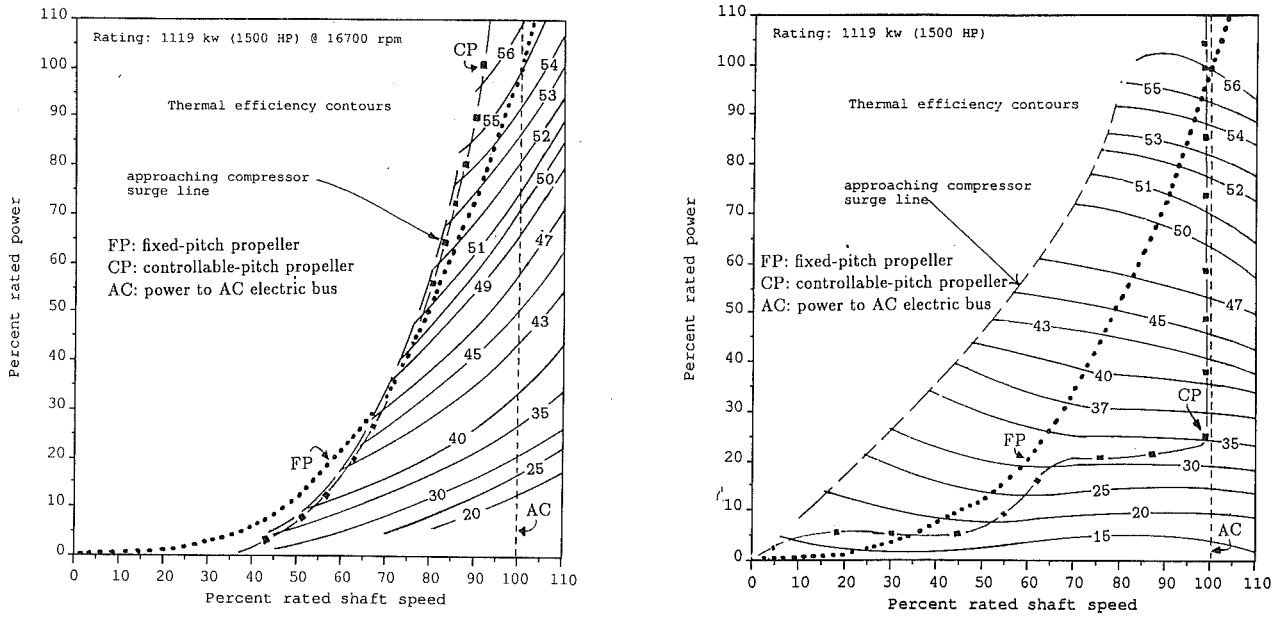

Fig. 7 Thermal efficiency contours and propeller lines for the two engines: left, single-shaft LPR-1S arrangement; right, gas-generator/power-turbine LPR-2S arrangement

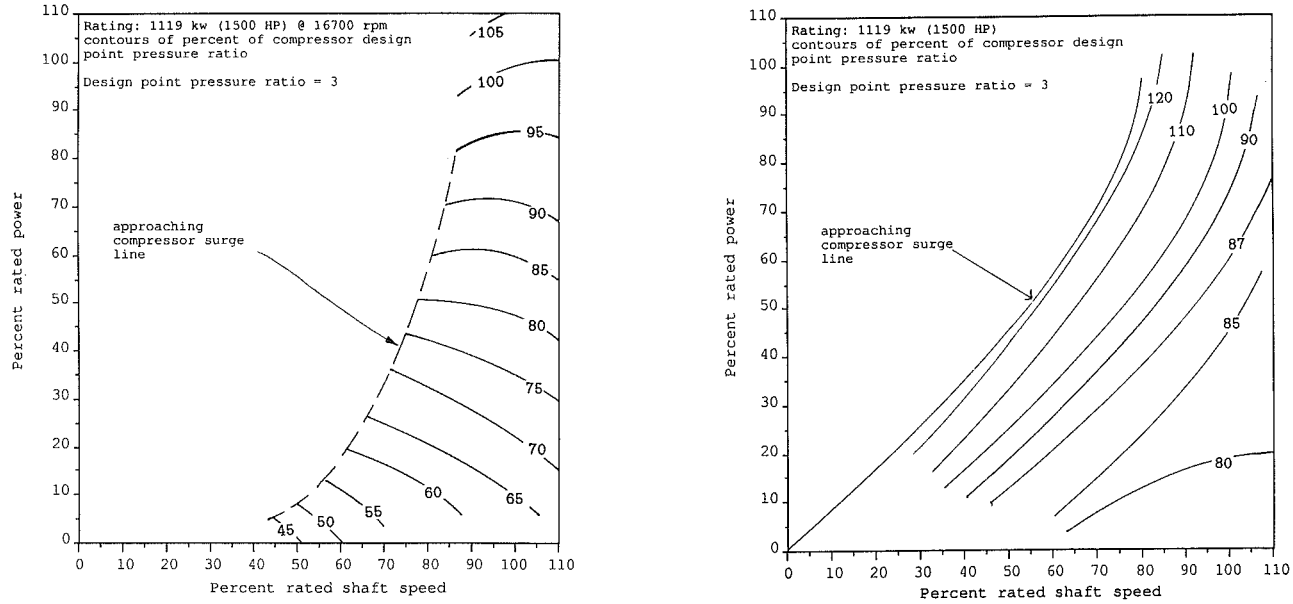

Fig. 8 Percent of design-point pressure ratio contours of the two engines: left, single-shaft LPR-1S arrangement; right, gas-generator/power-turbine LPR-2S arrangement

Advantages of the Power-Turbine Arrangement. Figure 8 shows the corresponding pressure ratio of the compressor in different speed-power levels of the engines. It also explains the reasons for the wider off-design operating regime of configuration LPR-2S. While the computed performance of both engine arrangements is impressive, it is clear that LPR-2S has distinct advantages over LPR-1S. Decoupling the mechanical speed of the gas-generator shaft from the power-turbine shaft permits the compressor to operate at high pressure ratios, in regions where its efficiency is high. This broadens the operating regime of engine LPR-2S into regions where the single-shaft LPR-1S configuration cannot operate. The fact that the power turbine can rotate at a different speed from the gas-generator turbine also means that its size can be increased and its speed decreased proportionately, so that it imposes a less demanding gear ratio between power-turbine and propeller rpm.

Propeller-Type Studies

In Fig. 7 line *FP* is a model of a fixed pitch propeller "law," a cubic line that should pass near the best-efficiency point of the engine at operating (or design) condition. The power $\dot{W}$ is given by

$$\dot{W} = kV^3 \tag{3}$$

where k is a constant and V is the speed of the ship in knots. This model results in a linear relationship between engine rpm and ship speed in knots (Lewis, 1989; Woodward, 1988). Line *AC* is a constant speed drive at 100 percent rpm (with a very small governor droop) modeling the engine providing power to an AC electric bus at synchronous speed (via gearing). Line *CP* models a controllable pitch propeller, and it has been derived assuming that the propeller pitch can be appropriately varied so that the engine delivers the required power to drive

the ship at the most efficient engine rpm. (Line *CP* represents the best efficiency point at each power level.)

Figures 4 and 5 show the η_{th} attained with each engine and propeller type as a function of engine power, derived from the location of the propeller lines in Fig. 7. The flatter efficiency contours of LPR-2S make the efficiencies of the three propeller choices almost identical. A fixed-pitch propeller is a bad choice for LPR-1S, because it cannot operate below (approximately) the combination of 40 percent engine power and 70 percent engine speed. The LPR-1S/CP propeller becomes the preferred combination for reduced fuel consumption (assuming that the *CP* propeller with the LPR-1S arrangement can deliver low powers at over 50 percent of engine speed, as shown in Fig. 7, and that the gear ratio from engine rpm to propeller rpm is acceptable). Controllable-reversible-pitch propellers would also eliminate the need for reverse gearing.

Although the AC electric drives impose additional electrical losses in power transmission and they are not as efficient as controllable-reversible-pitch propellers, they are the preferred propulsor in many modern combatant-vessel applications because they enable one to put two or more similar engines on a common bus arrangement. Since the engines supply electric power to a bus, they can be located anywhere in the ship, and the electric power is distributed by cables. The propellers are driven by AC-to-DC converters followed by DC motors, which are located near the tailshafts. Such arrangements provide a lot of flexibility. For example, if five LPR-2S engines are connected to a common bus, they can input to the bus a minimum mechanical power of 112 kW (one engine operating at 10 percent power, 100 percent speed on line) and a maximum mechanical power of 5.6 MW (all engines at 100 percent power, 100 percent speed on a line). The electric power output of the bus (less than the mechanical input to it due to losses in the conversion) can be distributed between the propulsion, electric, and other auxiliary-power demands of the ship.

Conclusions

The performance of representative cycles with assumptions consistent with marine applications indicates that low-pressure-ratio (about 3:1) highly regenerative (0.975) and intercooled-regenerative cycles can offer thermal efficiencies between 50 and 60 percent. The efficiency gains are quickly diminished for less-regenerative cycles of higher pressure ratios. For less than 1.5 MW, regenerative cycles are a better choice than intercooled-regenerative ones. The conceptual design of two variations of a 1.12 MW regenerative engine are presented and their fuel maps calculated. The single-shaft arrangement cannot operate below 50 percent of engine speed. However, if coupled with a controllable-pitch propeller that can absorb low powers at over 50 percent engine speed, the combination is the most fuel efficient over the engine power range. The gas-generator/power-turbine combination can operate down to 10 percent power and speed. Controllable-reversible-pitch propellers provide the best propulsive efficiency, while the practice of feeding a common AC electric bus with power from many engines on a common electric grid provides flexibility advantages desirable in marine combatant vessels.

Acknowledgments

Part of the investigation was conducted between 1983 and 1985 with partial sponsorship by the MIT Sea Grant College Program under grant number NA-81AA-D-00069, US Department of Commerce. Part of the investigation was completed in 1991 while developing material for a course.

References

Ferrie, J., 1990, "The Rolls-Royce Spey Marine Gas Turbine," *Transactions of the Institute of Marine Engineers*, Vol. 102, pp. 285–298.

Glassman, A. J., ed., 1972, "Turbine Design and Application," NASA SP-200, Vol. 3.

Harmon, R. A., 1990, "Marine Gas Turbines: a New Generation," *Mechanical Engineering*, May, pp. 48–51.

Horlick, E. J., 1983, "Naval Engineering Achievements in the Liberation of the Falklands," *Transactions, The Institute of Marine Engineers*, Vol. 95, Paper No. 41.

Horlock, J. H., 1985, *Axial Flow Compressors*, Krieger (original ed. Butterworth, 1958).

Jeske, H. O., and Voss, H., 1984, "Axial Compressors as Main Air Blowers in FCC Units," *Turbomachinery International*, Apr., pp. 25–30.

Korakianitis, T., and Wilson, D. G., 1985, "Improvements in Part-Load Efficiency by Reducing Pressure Ratio in Regenerative Gas-Turbine Engines," ASME Paper No. 85-GT-147.

Korakianitis, T., 1987, "Introduction of a Low-Pressure-Ratio Regenerative Advanced Brayton-Cycle Engine for Marine Propulsion and Problems of Its Integration in the Fishing Industry," S.M. thesis in Mechanical Engineering and in Ocean Systems Management, MIT, Cambridge, MA.

Korakianitis, T., and Wilson, D. G., 1987, "Low-Pressure-Ratio, Regenerative, Brayton-Cycle Engines: the Next Generation of Marine Prime Movers?" *Transactions, The Institute of Marine Engineers*, Vol. 99, Paper No. 1, pp. 1–19.

Korakianitis, T., and Wilson, D. G., 1994, "Models for Predicting the Performance of Brayton-Cycle Engines," ASME JOURNAL OF ENGINEERING FOR GAS TURBINES AND POWER, Vol. 116, this issue, pp. 381–388.

Lewis, E. V., ed., 1989, *Principles of Naval Architecture*, SNAME.

Lieblein, S., 1959, "Loss and Stall Analysis of Compressor Cascades," ASME JOURNAL OF ENGINEERING FOR POWER, September 1959, pp. 387–400.

McCoy, A. W., 1981, "Regenerative Gas Turbines for Naval Escort Ships," ASME Paper No. 81-GT-115.

McDonald, C. F., 1978, "The Role of the Recuperator in High-Performance Gas-Turbine Applications," ASME Paper No. 78-GT-46.

Musgrave, D. S., and Plehn, N. J., 1987, "Mixed-Flow Compressor Stage Design and Test Results With a Pressure Ratio of 3:1," ASME *Journal of Turbomachinery*, Vol. 109, pp. 513–519.

Pavri, R. E., and Hill, J. M., 1980, "Thermodynamics of Heavy Fuels Operation in Gas Turbine," ASME Paper No. 80-GT-171.

Ridley, P. W. W., 1983, "Royal Navy Marine Gas Turbines in the South Atlantic in 1982," ASME Paper No. 83-GT-19.

Shapiro, S. R., and Caddy, M. J., 1974, "NEPCOMP—the Navy Engine Performance Program," ASME Paper No. 74-GT-83.

Slatter, B. H., 1982, "Aero-derived Marine and Industrial Gas Turbines," *Transactions of the Institute of Marine Engineers*, Vol. 95, Paper No. 33.

Tomlinson, L. O., and Alff, R. K., 1981, "Economics of Heavy Fuels in Gas Turbines and Combined Cycles," ASME Paper No. 81-GT-45.

Walzer, P., 1987, "Automotive Gas Turbines," *Automotive Technology International*, pp. 251–254.

Wilson, D. G., Poole, P. K., Owens, L. D., Jr., and Baglione, J., 1985, "Conversion of Decommissioned Aircraft Gas Turbines to High-Efficiency Marine Units," ASME Paper No. 85-GT-169.

Wilson, D. G., 1984, *The Design of High-Efficiency Turbomachinery and Gas Turbines*, The MIT Press, Cambridge, MA.

Woodward, J. B., 1988, *Low-Speed Marine Diesel Engines*, Krieger (original ed. Wiley, 1981).

V. I. Romanov
SPA Mashproekt,
Nikolayev, Ukraine

"Mashproekt" Scientific and Production Association: A Designer of Gas Turbines for Marine and Industrial Applications

The first gas turbine unit for Navy application was developed in the Soviet Union in the 1950s. It was installed as a boost power unit in a patrol boat and consisted of an aircraft engine rated at about 3000 kW, a free power turbine, and a gear box. Successful experience with the unit application permitted a decision to establish a designing organization and production works for marine gas turbine unit development and manufacturing in Nikolayev. The "Mashproekt" scientific and production association is currently developing technical documentation and prototype engines and units; the "Zarya" production association is manufacturing engines in series production. It was planned to develop a gas turbine engine consisting of a two-spool coaxial compressor, a straight-flow combustion chamber, high-pressure and low-pressure turbines, and a free power turbine. Such a design meets more fully all-mode operation requirements for a marine propulsion unit. At first simple cycle engines were developed consisting of a gas turbine and a gear box, which were used as boost units (CODAG configuration). A significant event was defined with the development of a gas turbine propulsion unit rated at 26,400 kW (13,200 × 2), which consisted of two engines combined through a common gear box (Twin Pac version) (Fig. 1). The gear box provided the propeller shaft reverse with use of special claw-friction and hydraulic couplings.

In 1961 a "Komsomoletz Ukrainy" type surface ship (class "Kashin" according to NATO terminology), powered by two main gas turbine propulsion units, made a long-term cruise from Nikolayev to Yugoslavia (Fig. 2). Seamen valued high gas turbine unit quality. Later on gas turbine unit design has been developed considerably. In order to increase the cruising range, cruise engines with two-speed reduction gears were installed, which provided cruise engine optimum operation during their separate and common operation with main engine (COGAG arrangement).

The next step of the arrangement development was the application of a mechanical cross connection using a gear box. The combined gear box incorporates automatic clutches, which permit operation of one side independently of the other (Fig. 3).

If gearing in the mechanical cross connection is disengaged the cruise engine power is transmitted to its own shaft line. When disengaging clutches of the mechanical cross connection are engaged, power from either of two cruise engines will be transmitted to both shaft lines simultaneously. Much effort was required for gas turbine unit reverse development. As

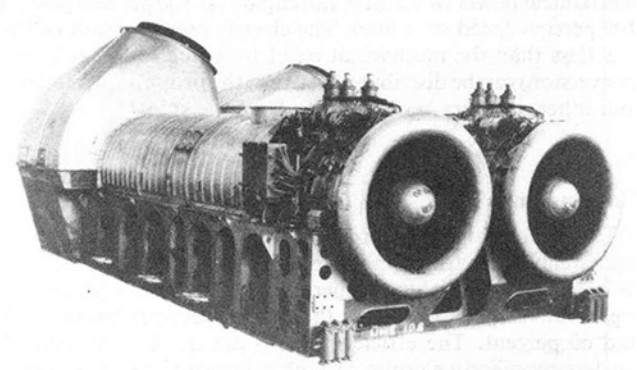

Fig. 1 GT unit rated at 26.4 MW

Fig. 2 "Kashin" class destroyer

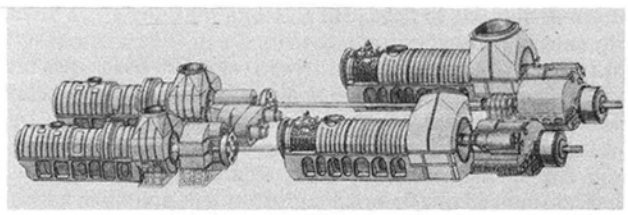

Fig. 3 Marine power unit diagram

Contributed by the International Gas Turbine Institute and presented at the 38th International Gas Turbine and Aeroengine Congress and Exposition, Cincinnati, Ohio, May 24–27, 1993. Manuscript received at ASME Headquarters March 1, 1993. Paper No. 93-GT-143. Associate Technical Editor: H. Lukas.

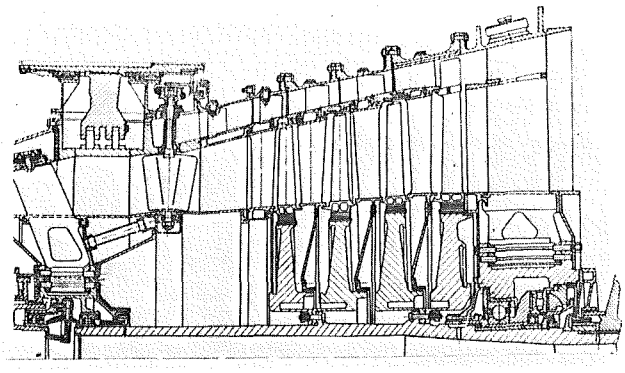

Fig. 4 Reverse power turbine

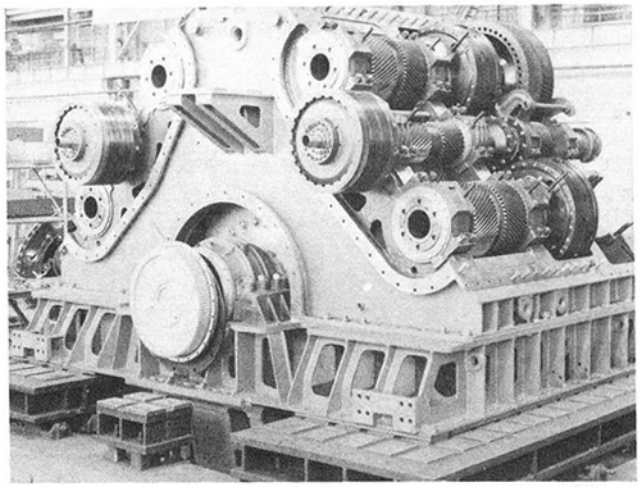

Fig. 5 Reduction gear with spur gear wheels

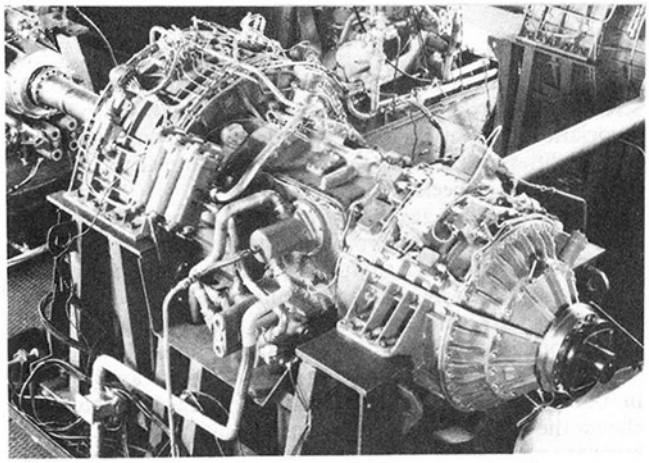

Fig. 6 Reduction gear with bevel gear wheels

Fig. 7 "V. Vaslyaev" Ro-Ro ship

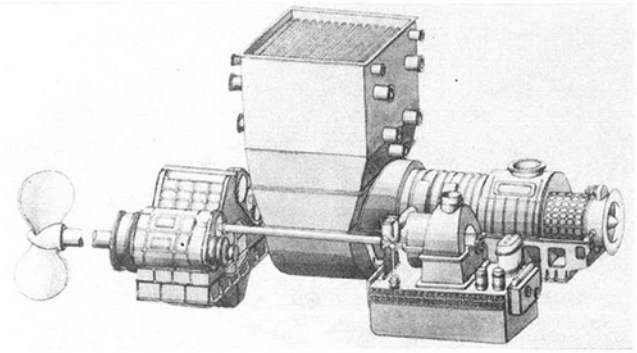

Fig. 8 M25 GT unit diagram

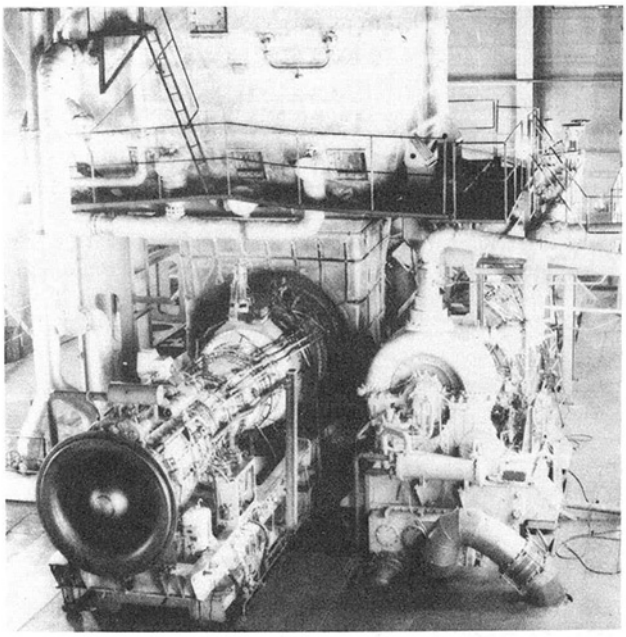

Fig. 9 M25 GT unit on the test rig

noted previously, the reverse of the unit consisting of two engines was accomplished with a reduction gear friction coupling (change-over to ahead from astern) and using hydraulic couplings. The problems were in selection of the material for friction couplings, and in providing acceptable temperature for hydraulic coupling wheels during nonoperative periods when pump and turbine wheels have opposite directions of rotation and different speeds.

In search of the optimum version gas turbine, a reverse mode of operation has been developed. A free power turbine has two-circle blading. Guide vanes and rotor blades of the stage used for asterning are located in the upper circle (Fig. 4).

The power output for asterning is about 20 percent of that for aheading. Power loss during aheading will be about 5 percent. The power output for asterning can be increased to 40 percent as compared with nonreverse power turbine, but power loss will be raised to an unacceptable value. Operational experience has shown that gas turbine reverse provided high ship maneuvering capability. In order to set the reverse gas turbine engine running astern, it is necessary to lower its mode of operation slightly. Gas blow-off from the inner circle into the outer circle (for running astern) takes only five seconds. Thus in a few seconds after the command "reverse" astern torque starts to operate in the ship shaft line providing rapid deceleration of the ship. Devices such as an additional lube oil cooling system, as in the case with the reverse reduction gear, are not required to achieve reverse power. Gear units are

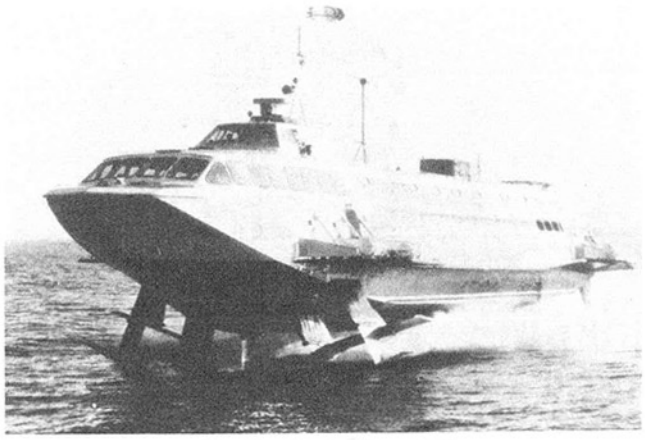

Fig. 10 "Cyclon" hydrofoil

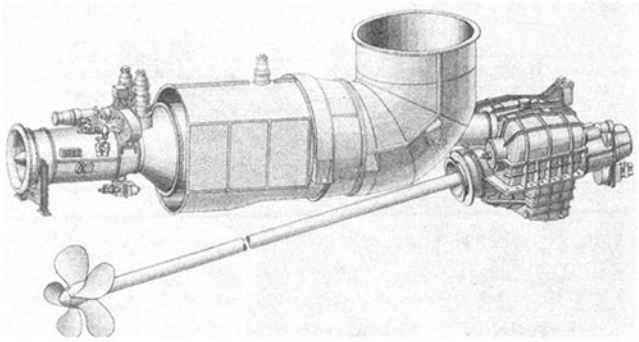

Fig. 11 "Cyclon" GT unit diagram

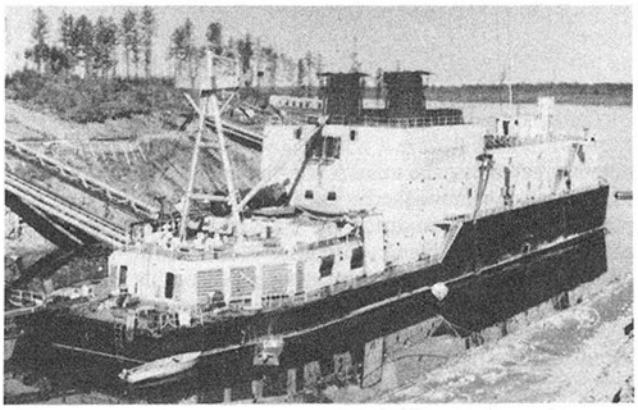

Fig. 12 Northern Lights power station

Fig. 13 Compressor station with GPA10

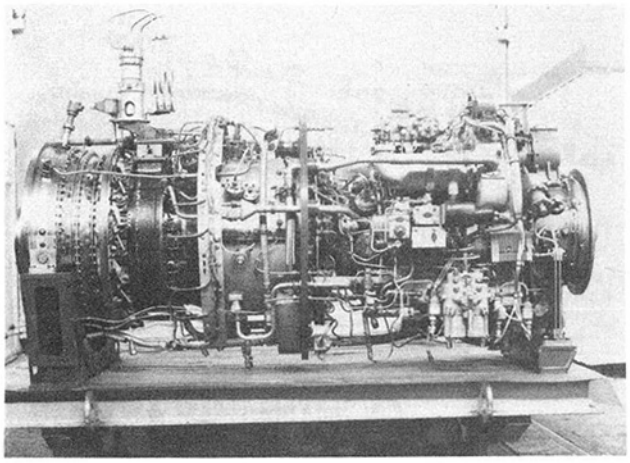

Fig. 14 GTD 3000 GT engine

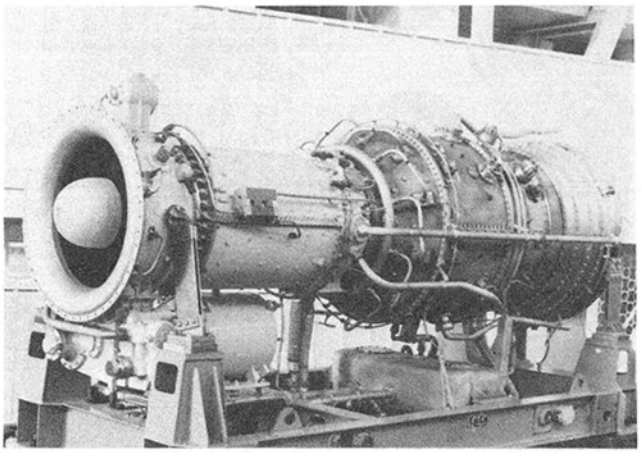

Fig. 15 GTD 8000 GT engine

an integral part of a marine gas turbine unit. "Mashproekt" scientific and production association and "Zarya" production association have at their disposal design and manufacturing potentialities for the development of reduction gears with spur and bevel gear wheels (Figs. 5 and 6).

In the late 1970s a gas turbine unit with a waste heat recovery system was developed for roll-on/roll-off container ships. The gas turbine engine has a shaft output of 14,100 kW; additional power is provided by a steam turbine supplying power to the propeller shaft, which rotates with an operating speed of 130 rpm through a combining reduction gear (Figs. 7–9).

Eight units with waste heat recovery systems are in service in four container ships. Ten years of operating experience have shown the expediency of using power units with a waste heat recovery system, which permitted reduction of fuel consumption to 20–25 percent when compared with a simple cycle unit. The first experience of gas turbine use on board "Cyclon" type hydrofoil craft was gained. Since 1989 "Cyclon" is in successful service at sea (Figs. 10 and 11).

Marine gas turbine engines are successfully being used for electrical generators, for example, in floating electric power stations of the "Northern Lights" type with power outputs of $2 \times 12{,}000$ kW (Fig. 12).

Gas turbine electric power station development with power outputs of 15,000 kW and 6000 kW is being completed. In 1979 marine-derivative gas turbines were applied in the pipeline pumping service. Nearly 500 gas pumping units with power outputs of 10,000 kW have been manufactured and delivered (Fig. 13).

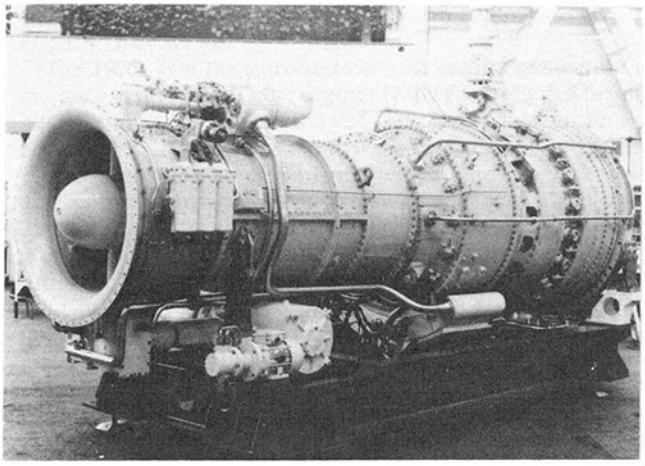

Fig. 16 GTD 15000 GT engine

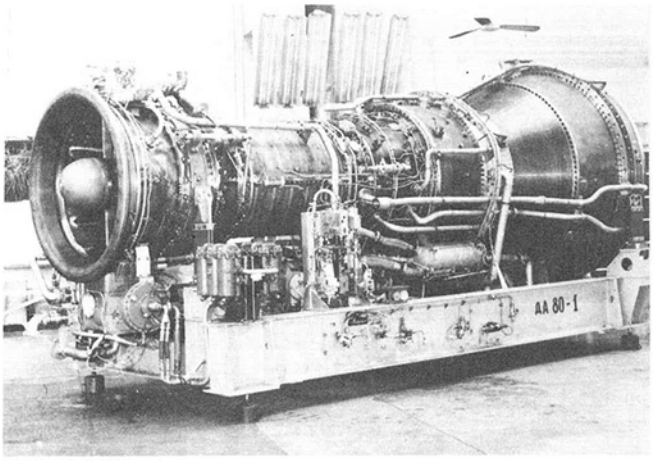

Fig. 17 GTD 25000 GT engine

Leader gas pumping units used in gas transmission have operated nearly 50,000 hours. In 1990 the delivery of gas pumping units with power outputs of 16,000 kW was started. GT-3000, GT-8000, and GT-15000 gas turbine engines having an efficiency of 30–35 percent are currently in series production (Figs. 14–16). A GT-25000 engine having efficiency of 37 percent is now being developed (Fig. 17). "Mashproekt" scientific and production association maintains a design bureau, a research department with a necessary complex of gas dynamic and vibration laboratories, and an experimental plant. In our opinion this structure permits the development of gas turbine engines, gas turbine propulsion units, and reduction gears.

The Increased Use of Gas Turbines as Commercial Marine Engines

C. O. Brady

D. L. Luck

GE Marine and Industrial Engines,
General Electric Company,
Evendale, OH 45215

Over the last three decades, aeroderivative gas turbines have become established naval ship propulsion engines, but use in the commercial marine field has been more limited. Today, aeroderivative gas turbines are being increasingly utilized as commercial marine engines. The primary reason for the increased use of gas turbines is discussed and several recent GE aeroderivative gas turbine commercial marine applications are described with particular aspects of the gas turbine engine installations detailed. Finally, the potential for future commercial marine aeroderivative gas turbine applications is presented.

Introduction

Over the last three decades, aeroderivative gas turbines have become established as naval ship propulsion engines. Initially, gas turbines were considered suitable only for weight-sensitive, high-performance craft and then subsequently for frigates and destroyers as the boost engine in combined engine configurations. Today, the durability, reliability, and thermal efficiency of modern marine aeroderivative gas turbines have thrust them into the forefront of naval propulsion. Naval ship designers now select gas turbine based propulsion systems for ship designs ranging from 300 ton fast patrol boats to 50,000 ton aircraft carriers and support ships.

Gas turbine use in the commercial marine field has been much more limited. Recently, however, aeroderivative gas turbines have increasingly been utilized as commercial marine engines. This paper briefly traces the history of gas turbines in both naval and commercial marine propulsion, discusses the reasons for increased gas turbine use in commercial marine vessels, reviews some recent GE gas turbine commercial marine applications, and then looks at the potential for future commercial applications.

Historical Background

The first vessel to be propelled at sea by a gas turbine was a British motor gun boat in 1947. Following this installation, the British Navy continued with several other patrol boat gas turbine installations during the 1950s. The 1950s also saw two commercial gas turbine installations on the British tanker *Auris* and the U.S. Liberty ship *John Sergeant*. The *Auris* AEI 5500 hp gas turbine plant operated satisfactorily for over 4 years and was withdrawn from service only because 12,000 ton tankers had become uneconomical [1]. The *John Sergeant* was converted to gas turbine power under a U.S. Maritime Administration (MARAD) development program. It was powered by a 6000 hp GE industrial type recuperated gas turbine. The gas turbine powered *John Sergeant* operated satisfactorily at sea for 9270 hours before being removed from service in 1959 due to termination of the MARAD development program [2].

The 1960s saw significant commitments to aeroderivative gas turbines as high-power boost engines in naval ships. The U.S. Navy installed the GE LM1500 engine in 17 PG84 class patrol gunboats. Propulsion systems with large gas turbines for boost power were introduced into several other naval ship classes, including patrol boats, frigates, and destroyers, in the United Kingdom, Canada, and the U.S. Coast Guard. The impact of gas turbines on this first generation of marine gas turbine naval ships was significant. Compared to previous systems, the gas turbines required fewer or simpler support systems and were very amenable to automation, thus affording reductions in manning [3].

Although these first-generation marine gas turbines made a significant positive impact on naval ship propulsion, the extent of the impact was restricted by their performance. Their thermal efficiency was below 30 percent and their accompanying low specific power required large inlet and exhaust ducts. The part power performance of these engines could not satisfy cruise performance requirements, limiting them to boost engine applications. The hot section life to these engines in a marine environment was also rather short, usually less than 3000 hours, again limiting their usefulness as baseload engines.

There were also a few commercial gas turbine vessels built in the 1960s. One of these designs, the British Hovercraft Corporation (BHC) passenger ferry, is still in service today. BHC produced six 200–300 ton SR.N4 hovercraft, plus several smaller craft, in the late 1960s and early 1970s timeframe. The SR.N4s are powered by four 3400 hp first-generation marine gas turbines, each driving an air propeller and lift fan combination. These craft carry 282 passengers and 37 cars at speeds up to 70 knots with average speeds of 40 to 60 knots. As of

Contributed by the International Gas Turbine Institute and presented at the 38th International Gas Turbine and Aeroengine Congress and Exposition, Cincinnati, Ohio, May 24–27, 1993. Manuscript received at ASME Headquarters March 1, 1993. Paper No. 93-GT-142. Associate Technical Editor: H. Lukas.

1990, five SR.N4s were still in service on routes crossing the English Channel [4].

The 1970s saw the introduction of a second generation of marine gas turbines. These engines featured air-cooled turbine blades and vanes, which allowed their firing temperature to be about 500°F higher than that of the first-generation engines. This substantial increase in firing temperature, together with an accompanying increase in pressure ratio, gave them up to 25 percent greater thermal efficiency and almost 100 percent greater specific power than the previously used marine gas turbines. Marine gas turbine technology advances, since this large jump in efficiency and specific power occasioned by the introduction of air cooled turbine airfoils, have been incremental in nature. This is evidenced by the fact that one of the first second-generation engines introduced, the GE LM2500, has a thermal efficiency and specific power that compare very favorably with recently introduced marine gas turbines. An aggressive component improvement program, jointly sponsored by GE and the U.S. Navy, has kept the LM2500 abreast of the incremental technology advances since its introduction.

The hot section life of the LM2500 in a marine environment also showed great improvement over the earlier marine gas turbines. Reid and Hartranft reported that, as of 1991, a large percentage of the LM2500s installed in the first U.S. Navy ship classes to use the engine had achieved hot section lives exceeding 10,000 hours and several had exceeded 15,000 hours [5]. Since then, some engines have achieved hot section lives of over 20,000 hours and the number exceeding 15,000 hours has increased to 34 and is still growing as the later ships of these classes accumulate more operating hours.

The 1970s also saw the introduction of a few additional commercial marine gas turbine installations. Most of these ships were propelled by first-generation gas turbines since second-generation engines were not proven in marine service when these ships were designed. One exception was the GTS *Adm. William M. Callaghan*, a roll on/roll off ship operated by the U.S. Navy Military Sealift Command. The *Callaghan* was delivered with two first-generation marine gas turbines installed, but by 1973 both engines had been replaced by LM2500s. The ship operated as a military cargo carrier primarily between the ports of New York and Bremerhaven, Germany, until 1986 when it was placed in a reserve status. It was reactivated in 1990 to support U.S. forces engaged in Desert Storm and remains in ready reserve service today. The *Callaghan* is successfully operated by a merchant marine crew that receives minimal specialized gas turbine training and is maintained by a typical merchant ship port engineer system.

Other commercial gas turbine ships built in the 1970s, all powered by first-generation marine gas turbines, included four Seatrain Lines high-speed Euroclass container ships and 14 vessels of a variety of ship types including tankers, bulk carriers, roll on/roll off ships, and LNG carriers powered by GE industrial gas turbines. The dramatic increase in the price of fuel during the 1970s when the price of crude oil rose from about $3.50 per barrel to over $20.00 per barrel greatly changed the economic assumptions that were used in the design of these ships. The Euroliner container ships were designed for a service speed of 26 knots with two 30,000 hp first-generation marine gas turbines installed. After the fuel price increases, the optimum speed for their service was only 18 to 20 knots, which required only about one half the installed power. This lower power requirement made it feasible to replace the smaller, lighter gas turbine engines with heavy fuel burning, more thermal efficient diesel engines in 1980 [6].

Some of the vessels powered by the GE industrial gas turbines were also re-engined or removed from service for similar reasons as the Euroliners; however, several continue to be successfully operated today. The most notable of these are the five product tankers owned and operated by the Chevron Oil Company. These ships are a unique electric drive design, each

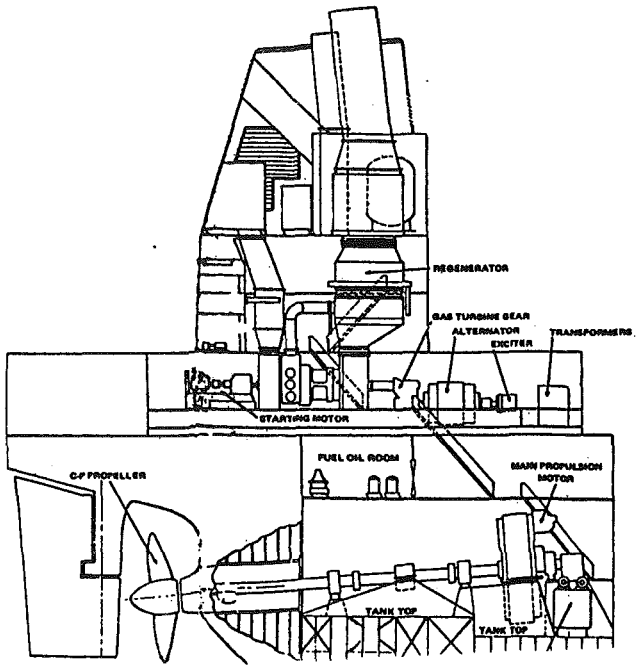

Fig. 1 Chevron tanker

powered by one GE industrial type recuperated gas turbine rated at 12,500 brake hp. As seen in Fig. 1, the arrangement flexibility afforded by gas turbine electric drive was advantageously used in these ships, resulting in a much shorter overall machinery space than would result from other propulsion types. Another advantage of these ships is the small engineering crew size allowed by the few relatively simple gas turbine support systems and the large degree of overall machinery system automation. These ships are routinely operated with four fewer crew members overall than similar diesel powered vessels [7].

Another group of commercial gas turbine vessels built in the 1970s that are still in successful service today are high-speed ferries. The largest, but also the lowest speed, ferry is the 23,000 gross registered ton passenger and car ferry, the *Finnjet*, which provides 30.5 knot service between Finland and Germany. The *Finnjet*, as originally delivered, was powered by two first generation marine gas turbines delivering up to 37,500 hp each [8]. After the large fuel price increases discussed above, it was determined that the winter service speed could be substantially reduced and a 14.5 MW diesel electric drive system was added, but the first-generation gas turbine propulsion system is still used during the peak trade summer months when the higher service speed is considered essential.

Another smaller, but higher speed, gas turbine ferry design from the 1970s still in production today is the Boeing Jetfoil. The Jetfoil is a 250 to 350 passenger vessel with a maximum speed of 50 knots and normal service speed of 42 knots. It is powered by two 3700 hp gas turbines driving waterjets. As of 1990, 31 Jetfoils were in service with another five under construction [4].

Present Gas Turbine Commercial Ship Application Status

The present focus of gas turbine commercial ship application is vessels that provide fast, high-capacity personnel and vehicle transportation. Adding to the objective of greater speed of delivery has been increased vessel size for more passenger carrying capability and the transport of vehicles, both cars and trucks. The volume of passenger traffic can be increased both through improvements in speed and vehicle transportation capacity. The primary reasons for the gas turbine engine's in-

creased use in these high-performance vessels are the engine's low weight, low volume, high availability, low first cost, low exhaust emissions, and acceptable operating costs.

Low Weight. The advantage of low weight per unit power output has long been recognized for gas turbines. Lower weight permits greater payload or additional fuel to be carried. For high-performance hull configurations that derive lift from dynamic forces (planing hulls, hydrofoils) or powered lift (air cushion or surface effect ships), the weight of diesel engines becomes prohibitive at power levels above about 20 MW. The gas turbine then becomes the only practical propulsion choice to provide power for high-speed operation, although a combined plant of gas turbines with smaller diesels for low-speed cruise and maneuvering is an attractive alternative for some applications.

Low Volume. The small volume of a gas turbine package also benefits the design of high-performance craft. Most vessel applications that deliver passengers and time-critical cargo are volume limited. The density of the payload is low, and the requirement to provide volume is the primary design challenge. Compactness of gas turbines is also advantageous for the catamaran hull forms that are currently being used for many high-speed vessel designs. The narrow gas turbine dimensions fit well into the side wall hull sections and have been incorporated into surface effect designs. Other restrictive volume configurations such as the underwater body of a SWATH (Small Waterplane Area Twin Hull) ship can also benefit from a compact propulsion prime mover.

High Availability. Military applications of gas turbines have always placed very high requirements on the reliability and availability of the systems. The accumulated experience of over 5 million operating hours in military marine applications has shown that availability in excess of 99.9 percent can typically be achieved. High availability of propulsion is no less important in commercial applications. Production of revenue depends on continuous operation, and a reputation of reliable and on-time service is mandatory when carrying passengers or time-critical cargo.

Propulsion system availability is dependent upon two parameters, the time between required maintenance actions and the time to effect maintenance when required. Accumulation of experience in gas turbine applications and evolutionary improvements has increased the time between hot section refurbishments from 2000 hours for early gas turbines to typical times of over 14,000 hours for the LM2500 in marine service. The engine parameters that control these intervals are well understood and permit setting of engine rating points at optimum levels.

The other parameter that affects availability is the time required to effect maintenance actions. Major refurbishments are usually accomplished at depot facilities for aeroderivative gas turbines, with the engine being removed and replaced in the ship. The experience in naval applications has resulted in the development of techniques to change out an engine in times ranging from 6 to 24 hours depending upon the exact removal system design. This permits a vessel to be back in service with minimal disruption to required schedules. Alternatively, if the ship's schedule permits, many internal engine components can be replaced on board ship in less than 40 hours. External accessory replacement times are under 3 hours.

The short time periods required to perform on-board maintenance actions for aeroderivative gas turbines has significantly changed the maintenance system for naval vessels and is a major contributor to the high availabilities achieved. A similar impact on the commercial marine maintenance system is anticipated as more gas turbine powered vessels enter the commercial marine field.

Low First Costs. Initial costs for propulsion plants include prime mover and supporting auxiliary systems, plus installation costs including foundations. For equivalent sustained power capability, propulsion system costs are comparable between diesels and gas turbines for moderate total power requirements of 10 to 20 MW. Above about 20 MW, the gas turbine system provides a first cost savings compared to the diesel due to (*a*) the lower $/kW cost for the gas turbines, and (*b*) the considerable installation savings for the smaller, lighter gas turbines with fewer support systems.

Low Exhaust Emissions. Restrictions on exhaust emissions are being imposed in many coastal operating areas and are being considered for broader areas on the high seas. These restrictions are primarily concerned with sulfur oxides (SO_x) and nitrogen oxides (NO_x), and will limit choices of fuel and selection of propulsion prime movers.

The level of SO_x emission is related directly to the amount of sulfur in the fuel. Heavy fuels that can be burned by diesel engines have provided a unit fuel price advantage to those engines. As the level of sulfur in fuel is lowered to meet restrictions on exhaust emissions, the unit price differential between distillate fuel burned by gas turbines and heavy fuels narrows. As emission limits become established, the price advantage of operation on heavy fuels previously enjoyed by diesel engines will no longer be available.

Gas turbine emission of NO_x is lower than diesel engines by a factor of three to four due to the lower temperature and more controlled combustion process of the gas turbine engine. Although application of catalytic convertors to the diesel exhaust can reduce the NO_x output, a penalty in performance is imposed, and considerable weight, volume, operational complexity, and cost penalties are incurred. Gas turbines with an already inherently low NO_x emission level will continue to benefit from ongoing research and development to further reduce the levels for shore-based industrial applications.

Acceptable Operating Costs. The significant recurring cost items are fuel, lube oil, maintenance, and manning. Consideration of these items must be done for specific operating scenarios to determine the relative costs of various propulsion alternatives. However, some general observations can be made for the high-performance vessels being discussed here.

Fast ferries and high priority cargo vessels will spend most of their operating time at or near maximum power. Modern simple-cycle gas turbines have achieved good specific fuel consumption levels at maximum power in relation to that available with other prime movers. Although the gas turbine specific fuel consumption increases at part power, very little time is spent operating at these levels in these applications. When lube oil consumption is included, the cost of consumables is not much greater for gas turbines than for diesels. The difference becomes even less when the additional power required to achieve the same payload and service speed in these high-performance craft with the higher diesel weight is considered.

Maintenance costs for gas turbines are determined primarily by the depot refurbishments for the hot section components and for general overhauls. These costs are well established and competitive because of the multiple sources available to effect the repairs. The result is that the average maintenance cost per horsepower hour of operation for gas turbines is less that that for diesels. In addition, the on-board vessel maintenance actions required for gas turbines are minimal, resulting in a lower manning requirement for the gas turbine.

Recent GE Gas Turbine Commercial Marine Applications

Recent applications of the GE family of aeroderivative gas turbines have included a range of hull forms and a range of

Fig. 2 *Foilcat*

Fig. 3 *Azteca*

power requirements. The flexibility of the gas turbine as the core prime mover for military vessels has been repeatedly demonstrated in combination with diesels in combined propulsion plants, with fixed and controllable pitch propellers, and with waterjets as propulsors. The experience accumulated in this broad range of military applications supports the variety of configurations being developed for commercial requirements. Current commercial marine applications include hydrofoils, planing or semiplaning catamarans and monohulls, and conventional displacement hulls.

The *Foilcat* (Fig. 2) built by Kvaerner Fjellstrand in Norway is a 40 m, 50 knot vessel designed to carry 400 passengers. The propulsion system employs two GE LM500 gas turbines through MAAG reduction gears to KaMeWa waterjets. The LM500 engines are each rated at 6000 hp and provide an extremely light power pack for this dynamic lift, weight critical vessel. The compact LM500 engines can be removed through a deck hatch providing the ease of maintenance and quick turnaround critical in achieving the high availability required for commercial operations [9].

The yacht *Azteca* (Fig. 3) built by Blohm & Voss in Hamburg, Germany, was designed by Martin Francis. It is a displacement hull, 73.5 m in length, powered by a GE LM1600 gas turbine in combination with two Deutz-MWM diesels. Each of the three engines drives an individual waterjet with the diesel-powered outboard jets providing maneuvering and the central gas turbine waterjet providing boost operation. The vessel can achieve approximately 38 knots with this combined plant. Application to this vessel presented challenges with respect to low noise levels. Levels of less than 70 dbA on the sundeck and less than 50 dbA in the interior spaces have been achieved, demonstrating that very quiet operation can be provided for commercial applications.

Fig. 4 *Destriero*

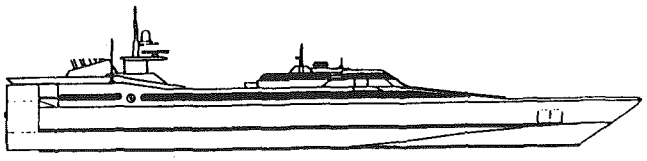

- Displacement 930 tons
- Passengers 400
- Cars 90
- Speed 40+ knots
- Propulsion – CODAG
  - 1 x MTU-GE LM2500
  - 2 x MTU 16V595
  - Water jets

Fig. 5 *Aquastrada*

A recent spectacular application of GE LM1600 gas turbines received wide recognition when the *Destriero* (Fig. 4) completed record-breaking crossings of the Atlantic on Aug. 6, 1992. The *Destriero*, designed by Donald Blount and built by the Fincantieri shipyard in La Spezia, Italy, is a 67.7 m semiplaning hull form powered by three LM1600s driving three KaMeWa waterjets through Renk-Tacke reduction gears [10]. The *Destriero*'s speed on the eastbound record breaking run across the Atlantic averaged over 53 knots, and the vessel crossed the finish line at over 66 knots [11]. The gas turbine propulsion system performed flawlessly during the crossings of the Atlantic, which were accomplished under difficult weather conditions.

The *Aquastrada* class car ferry (Fig. 5), currently under construction in the Rodriquez Canteri Navali shipyard in Genoa, Italy, is a 101.75 m 42 knot monohull vessel designed to carry 450 passengers and up to 154 vehicles [12]. It will be propelled by one LM2500 gas turbine and two MTU 16V 595 TE70 diesel engines. Each engine will drive an individual KaMeWa waterjet through a Renk Tacke reduction gear. The diesel engines will be used for maneuvering and for extended range at a lower cruising speed of about 18 knots. The design provides considerable flexibility for a variety of applications and routes.

Future Gas Turbine Commercial Ship Applications

Future applications of gas turbines for commercial ships fall into two categories. The first category is fast transport at speeds greater than conventional surface ships where transport of people or cargo is time critical. The future looks particularly bright in this area as there are a number of designs of these high-performance vessels, in addition to those discussed above, that have been recently developed, which incorporate gas turbines as main propulsion prime movers; several are expected to move into the building stage in the near future.

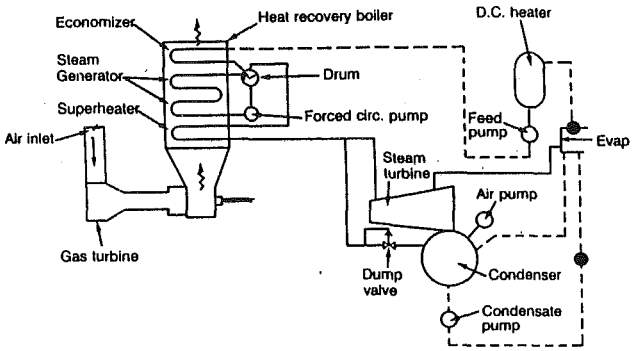

Fig. 6 Combined cycle power system

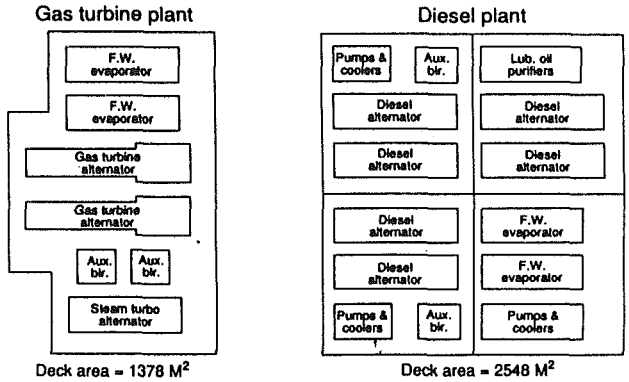

Fig. 7 Machinery plant space comparison

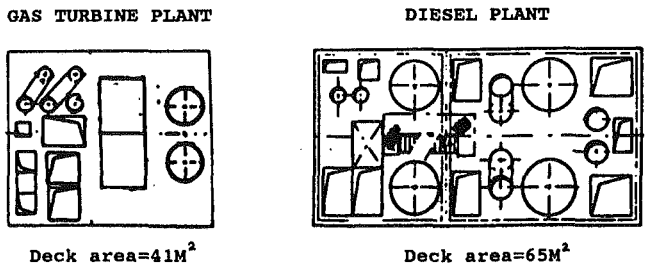

Fig. 8 Engine ventilation trunk space comparison

The second category of expected future applications of gas turbines for commercial ships includes more conventional lower speed vessels where gas turbine propulsion offers other advantages related to their performance capabilities and physical characteristics. Many of the same attributes of the gas turbine, high availability, low first costs, low exhaust emissions, and low volume, that make it attractive for the high-speed vessels also make it attractive for these more traditional marine vessels. Additionally, these ships do not have the severe weight constraints of most high-speed vessels, making it possible to install exhaust energy recovery systems on the gas turbines, such as the steam turbine cycle shown in Fig. 6. With such an exhaust energy recovery system, the fuel consumption rate of a modern aeroderivative gas turbine plant is very competitive with that of a modern diesel plant. At present, higher gas turbine fuel costs do usually result, however, because, as discussed above, large marine diesel engines normally can use a lower unit cost heavy fuel.

However, several studies have shown that in certain volume-limited ship types, such as cruise ships, the high power density of an aeroderivative gas turbine plant makes enough revenue-enhancing space available to more than offset its higher fuel costs. For example, in one independent comparison study of the effect of replacing a medium speed diesel-electric propulsion system in a modern, 2500 passenger cruise ship with a GE LM2500 gas turbine/steam turbine-electric system, it was estimated that increased profitability ranging from 3.9 to 4.2 million U.S. dollars per year could be realized, depending upon the particular operating profile [13].

The space saved by a gas turbine plant in a cruise ship is not limited to machinery rooms, although the space saved in the machinery rooms has been shown to be quite usable by relocating other functions, such as the laundry, from an upper deck to that area [13]. Extensive space can usually also be saved on the upper decks because a gas turbine plant normally requires a smaller engine ventilation casing than is required by a cruise ship medium-speed diesel plant. This is true even though the gas turbine uses more combustion air. The high power density of an aeroderivative gas turbine engine (15 hp/cubic foot) compared to a typical medium-speed diesel engine (3 hp/cubic foot) normally results in a fewer number of engines than for a diesel plant of the same total power level. The greater number of separate exhaust pipes from the diesel engines require as much or more cross-sectional casing area as the fewer higher airflow gas turbine exhausts. Additionally, each diesel engine requires a large exhaust silencer with a cross section typically more than twice the size of the diesel exhaust pipe while the gas turbine normally requires no exhaust silencer.

Figure 7 is an example of a GE LM2500 gas turbine combined cycle electric drive engine room layout showing the space saved compared to a typical medium speed diesel installation [13]. Space in addition to that shown is usually saved due to the need for fewer gas turbine plant support auxiliaries and the greatly reduced fuel treatment plant required for the distillate fuel used by the gas turbine.

Figure 8 shows the reduced cross section of a gas turbine plant engine ventilation trunk above the exhaust boilers compared to that of a typical diesel plant.

As was noted in the discussion of high-speed vessels, it appears the unit fuel cost disparity between the gas turbine and diesel plants is likely to narrow significantly or even disappear completely in the next few years due to the effect of environmental regulations imposing low fuel sulfur limits. The heavy blended fuel currently used by large marine diesel engines can have up to 5 percent sulfur by specification and is reported to average about 3 percent by fuel suppliers. On the other hand, pure distillate fuels used by gas turbines can only have up to 1.5 percent sulfur by specification and average less than 0.5 percent, according to a worldwide survey done by the U.S. Navy [14].

Estimates of the increase in unit cost of heavy blended fuel provided to the International Maritime Organization (IMO) by the Oil Companies International Marine Forum (OCIMF) if the sulfur limit is lowered to 1.5 percent range from 53 to 76 U.S. dollars per ton and from 67 to 95 dollars per ton if it is lowered to 1.0 percent [15]. The IMO and several localized governmental bodies are currently considering such limits. This magnitude of increase in unit cost would essentially erase the cost difference between heavy and distillate fuels in most areas of the world.

If the unit fuel cost advantage of the diesel plant over the gas turbine plant disappears or significantly decreases, the other attributes of the gas turbine that have resulted in it becoming so well established as a naval propulsion engine will also cause it to become a viable choice across the entire spectrum of slower, more traditional monohull displacement-type commercial vessels in addition to cruise ships.

Summary

This paper discusses the recent increased activity in commercial high-speed vessel construction with gas turbine pro-

pulsion. As the designs have become larger and cargo loads have increased, the high power density and low specific weight of the aeroderivative gas turbine engine have made it increasingly attractive to the designers, builders, and operators of these high speed craft. There are a number of new designs of these high-performance vessels that have been recently developed that incorporate gas turbines as main propulsion prime movers. Several of them are already in service or are under construction and more are expected to move into the building stage in the near future.

The advantages of the aeroderivative gas turbine that make it attractive for the high-speed vessels, when combined with an exhaust energy recovery system to give it fuel rates competitive with large diesel engines, are causing it to be seriously considered for certain slower, more traditional monohull commercial ships, such as cruise ships. The high power density of the gas turbine system in these volume-limited high cargo value ships makes enough revenue-enhancing space available to more than offset the current unit fuel price advantage of the diesel.

References

1 Duggan, R. M., and Howell, A. T. O., "The Trials and Operation of the Gas Turbine Ship *Auris*," *Transactions of the Institute of Marine Engineers*, London, Vol. 74(4), 1962.

2 McLean, H. D., Tangerini, C. C., and Van Cott, W. H., "Report on 9000 Hour Operating of Marine Propulsion Gas Turbine in the *John Sergeant*," ASME Paper No. 60-GTP-5, 1960.

3 Palmer, S. J., "The Impact of the Gas Turbine on the Design of Major Surface Warships," 38th Parsons Memorial Lecture, *Transactions RINA*, Vol. 116, 1974.

4 Trillo, R. L., ed., *Jane's High Speed Marine Craft*, published by Jane's Information Group Ltd., Coulsdon, Surrey, United Kingdom, 1990.

5 Reid, R. E., and Hartranft, J. J., "GE LM2500 Marine Gas Turbine Experience Update," ASME Paper No. 91-GT-23.

6 Neut, L. J., "Re-engining Euroliner Class Ships," SNAME Paper presented Dec. 4, 1980.

7 "Profile: Douglas C. Wolcott, President, Chevron Shipping Company," *Surveyor*, Dec. 1991.

8 "Finnjet," *The Motor Ship*, July, 1977.

9 Mullins, P., " 'Low-Flying Cat' Uses Marine Version of GE Gas Turbines," *Diesel & Gas Turbine Worldwide*, Nov. 1991.

10 Blount, D. L., and Codega, L. T., "Designing for the Atlantic Challenge," presented to the Hampton Roads Section SNAME, Oct. 17, 1991.

11 Chellini, R., "Gas Turbine-Powered Yacht Sets New Atlantic Crossing Record," *Diesel & Gas Turbine Worldwide*, Nov. 1992.

12 "Three New Craft Due in Next Six Months," *Fast Ferry International*, Oct. 1992.

13 "Comparative Study of Diesel Electric and Gas Turbine Electric Power Plants for Cruise Ships," Technical Marine Planning Ltd., London, May 1989.

14 "Survey and Characterization of Commercial Marine Fuels," U.S. Navy Report DTNSRDC-PASD-CR-16-84, Dec. 1984.

15 "An Assessment of the Environmental Contribution and Cost Implications of Reducing Emissions of Sulphur Dioxide From Ships in Europe," submitted to IMO by Oil Companies International Marine Forum, July 17, 1992.

G. E. Weber
Commonwealth Edison Co.,
Fossil Technical Services Dept.,
125 South Clark St.,
Chicago, IL 60603

W. M. Worek
Department of Mechanical Engineering
(M/C 251),
University of Illinois at Chicago,
842 West Taylor St.,
Chicago, IL 60607-7022

Development of a Method to Evaluate the Design Performance of a Feedwater Heater With a Short Drain Cooler

A method is developed to determine the shell and tube side heat transfer performance of a feedwater heater with a short drain cooler. The desuperheating, condensing, and drain cooling zones are discussed and analyzed by deriving a modified version of the Delaware Method of Shell-Side Design.

1 Introduction

Electric utilities purchase feedwater heaters for new plants, where they purchase several at a time, and older plants, where the individual heaters are replaced as tube pluggage becomes excessive. A high-pressure feedwater heater costs between one and five hundred thousand dollars depending on its size and design. High-pressure feedwater heaters are essential to the performance of a unit. If a unit is designed to have feedwater heaters in service and they are removed, the furnace heat input must increase. This will increase unit heat rate and may cause furnace tube overheating due to excessive furnace exit gas temperature.

Since feedwater heaters are so important to unit performance, utilities need a method to evaluate the heater manufacturer performance specifications and understand the theory behind a heater's design. Currently there is no method available to the utility that uses the heater manufacturer's design data and accurately calculates the zone heat transfer coefficients and pressure drops when given only the heater design data. There are computer programs that the heater manufacturers use to design the heater, but these programs are proprietary and would be costly for a utility to use for the small number of heaters analyzed on a yearly basis.

This paper uses the Delaware Method for Shell-Side Heat Exchanger Design (Bell, 1986) and modifies the method for feedwater heaters currently in use. The Delaware Method, which was designed in 1960, is an excellent heat exchanger design tool. However, modern feedwater heaters have baffle designs that the method cannot accurately model. Therefore, the Delaware method needs to be modified to predict heat transfer coefficients and pressure drops in modern feedwater heaters accurately.

This paper employs the same concepts as the Delaware Method in calculating an ideal heat transfer coefficient and extends them to be valid for higher Reynolds number flows. The heat transfer coefficient and pressure drop correction factor curves were calibrated using six actual feedwater heater designs courtesy of Marley Heat Transfer Corporation (Biar, 1991).

2 Shell-Side Heat Transfer Analysis

A short drain cooler feedwater heater, shown in Fig. 1, has three zones: a desuperheating, a condensing, and a drain cooling zone. Each zone is treated as a separate heat exchanger in evaluating the heat transfer coefficient and pressure drop. The heater shown in Fig. 1 has a short drain cooler that has all the feedwater tubes passing through it and does not span the entire length of the heater. This is in contrast to a long drain cooler (not shown) that does not have all the feedwater tubes passing through it and spans the entire length of the heater. This paper analyzes a heater with a short drain cooler. Another classification of feedwater heaters is whether they are high or low pressure. A high-pressure heater obtains its extraction steam supply from either the high-pressure or intermediate-pressure turbine and obtains its water supply after the boiler feed pumps. A low-pressure heater obtains its steam supply from the low-pressure turbine and its water supply from a point before the boiler feed pumps. The method developed in this paper may be used for calculating the heat transfer coefficients and shell-side pressure drops for high-pressure heaters but is currently valid only for calculating the heat transfer coefficients for low-pressure heaters. The design parameters needed to perform the shell-side heat transfer analysis are D_{otl}, S, D_i, D_o, $\dot{m}_s$, μ_s, K_s, .

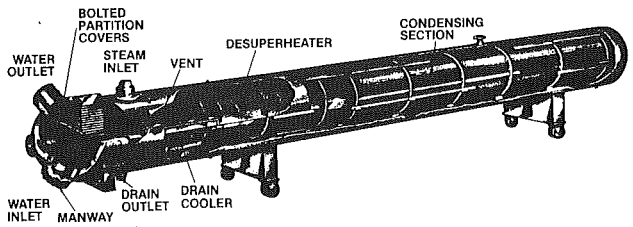

Fig. 1 Three-zone feedwater heater with short drain cooler, with a desuperheating, condensing, and drain cooling zone

Contributed by the Power Division for publication in the JOURNAL OF ENGINEERING FOR GAS TURBINES AND POWER. Manuscript received by the Power Division March 26, 1993. Associate Technical Editor: R. W. Porter.

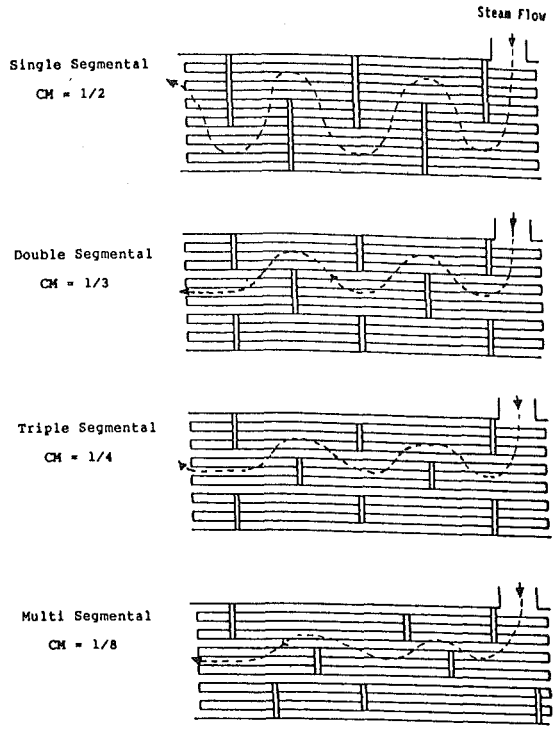

Fig. 2 Baffle types and crossflow multipliers for the desuperheating and drain cooling zones

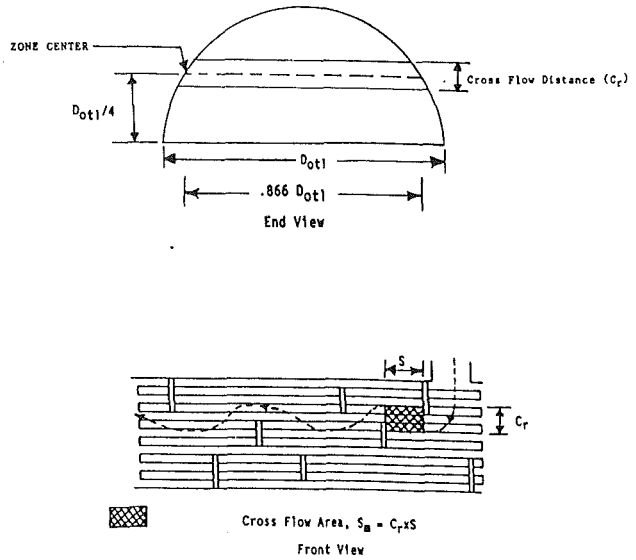

Fig. 3 Crossflow area illustration for the desuperheating and drain cooling zones

C_s, and the baffle type. All of this information is available from the heater manufacturer.

2.1 Desuperheating Zone. The turbine extraction steam enters the heater at the desuperheating zone where it is cooled to within 5–35°C (10–60°F) of its saturation point. Over the last 20 years this has been the area where heater manufacturers have tried to maximize heater efficiency by minimizing the steam-side pressure drop. They have done this by modifying the baffle design to reduce the amount of crossflow. However, in minimizing the crossflow, the heat transfer coefficient is reduced because there is less steam flowing across the tubes. The manufacturers account for this effect by designing a longer zone with more area.

To reflect the actual zone crossflow accurately, a crossflow area multiplier must be assumed. The multipliers, which are shown in Fig. 2, correspond to each baffle type. The single segmental baffles have one half of the tubes available for crossflow. The double segmental baffles have only 1/3 of the tubes available for crossflow. The multiplier keeps decreasing as the amount of crossflow decreases. The multipliers are approximate, but are fine tuned later in this paper when a crossflow correction factor is discussed. The crossflow area can then be calculated using the formula previously developed (Bell, 1986) and modified (Weber, 1992):

$$S_m = (CM)(A)(S)/(0.866\ D_{\text{otl}}) = (Cr)S \tag{1}$$

where S_m represents the crossflow area calculated at the center of the desuperheating zone, and Cr represents the crossflow distance. The term A is the semicircular zone cross-sectional area calculated using:

$$A = \pi(D_{\text{otl}})^2/8 \tag{2}$$

Equation (1) divides by the quantity (0.866 D_{otl}) because the crossflow distance Cr is obtained by dividing the corrected cross-sectional area of the zone by the horizontal distance at its center. The crossflow distance is then multiplied by the baffle spacing to obtain the crossflow area. Figure 3 illustrates the crossflow calculation in the desuperheating zone. The same analysis is valid for the drain cooling zone except that the semicircle is inverted.

Nomenclature

a = baffle window vertical dimension
A = area
A_i = inner area
A_m = mean area
A_o = outer area
b = baffle window horizontal dimension
c = baffle window vertical dimension
CM = crossflow multiplier
C_f = tube-side specific heat
C_s = shell-side specific heat
D_i = inner diameter
D_m = mean diameter
D_o = outer diameter
D_{otl} = outer tube limit
f_i = friction factor
h = corrected shell-side convection heat transfer coefficient
h_{fg} = latent heat of condensation
h_{fwi} = feedwater enthalpy at heater inlet
h_{fwo} = feedwater enthalpy at heater outlet
h_i = tube-side heat transfer coefficient
h_o = shell-side heat transfer coefficient
h_{si} = condensing-zone steam inlet enthalpy
h_{so} = condensing-zone enthalpy at saturation
J_b = bypass correction factor
J_c = crossflow correction factor
J_f = friction correction factor
J_l = leakage correction factor
J_s = baffle spacing correction factor
k = thermal conductivity
k_f = feedwater thermal conductivity
k_s = steam thermal conductivity
k_w = wall material thermal conductivity
L = length
L_s = baffle spacing
L_{si} = baffle spacing at zone inlet
L_{so} = baffle spacing at zone outlet
$\dot{m}_{dr}$ = drain inlet mass flow rate
$\dot{m}_s$ = steam mass flow rate

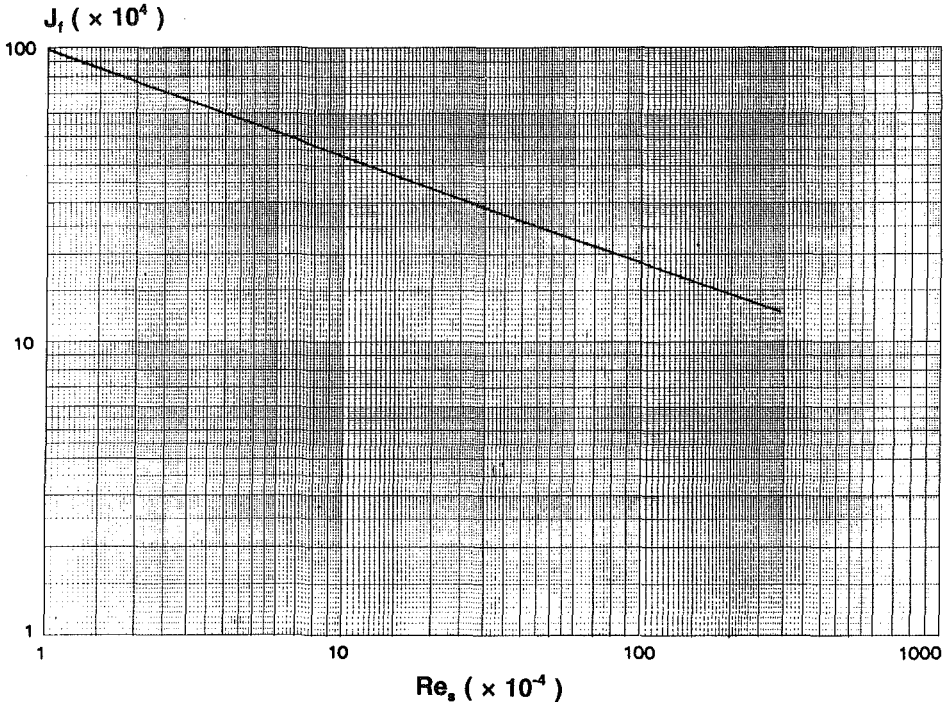

Fig. 4 Correlation of J factor for ideal tube banks

This allows the calculation of a Reynolds number, which is proportional to the crossflow area given by Eq. (1) and the steam mass flow rate (Bell, 1986). The Reynolds number is defined by:

$$\mathrm{Re}_s = D_o \dot{m}_s / (\mu_s S_m) \tag{3}$$

where Re_s is proportional to a friction factor J_f, which is obtained using Fig. 4. The friction factor decreases as Re_s increases because the losses will increase due to higher velocities.

The base heat transfer coefficient is calculated by utilizing the Colburn J factor for heat transfer. The J factor is given by (Bell, 1986; Incropera and Dewitt, 1981):

$$J_f = \mathrm{St}(\mathrm{Pr})^{0.667} = \frac{h}{\rho v C_s}\left[\frac{C_s \mu_s g_c}{k_s}\right]^{0.667}$$

where St and Pr are the Stanton and Prandtl numbers, respectively. Solving for the heat transfer coefficient and incorporating the crossflow area calculated in Eq. (1), we obtain (Bell, 1986):

$$h_{\mathrm{base}} = \frac{J_f C_s \dot{m}_s}{S_m}\left[\frac{k_s}{C_s \mu_s g_c}\right]^{0.667} \tag{4}$$

The base coefficient is calculated assuming that the entire shell-side stream flows across the ideal tube bank formed by the tube array at the centerline of the zone (Bell, 1986). This is the greatest amount of heat transfer attainable. The value obtained is then multiplied by a series of correction factors: J_c, J_l, J_b, and J_s. These correction factors adjust the base heat transfer coefficient (Bell, 1986). They are defined next.

J_c: The Crossflow Correction Factor. This factor is obtained using Figs. 5 and 7 where it is plotted versus S_m (Weber, 1992). The crossflow correction factor decreases with decreasing crossflow area. As the crossflow area decreases, the amount of crossflow decreases, which causes a reduction in the heat transfer.

Nomenclature (cont.)

$\dot{m}_x$ = fraction of drain inlet that flashes
N_c = number of tubes in crossflow
P = pitch
Pr = Prandtl number
St = Stanton number
Q_{cond} = heat transferred in condensing zone
Q_{dc} = heat transferred in drain cooling zone
Q_{ds} = heat transferred in desuperheating zone
Q_{dsc} = desuperheating steam heat release in condensing zone
Q_{fw} = heat transferred to feedwater
Q_s = heat transferred from steam
R_c = condensing heat transfer resistance
Re = Reynolds number
R_{fo} = shell-side fouling resistance
R_h = tube-side heat transfer resistance
R_T = total resistance
R_{ts} = total side fouling resistance
R_w = tube wall resistance
S = spacing
S_m = crossflow area
t = thickness
T_{ci} = feedwater inlet temperature zone
$T_{ci,\mathrm{cond}}$ = feedwater inlet temperature to condensing zone
T_{co} = feedwater outlet temperature from zone
$T_{co,dc}$ = feedwater temperature leaving drain cooler
T_{si} = steam inlet temperature
T_{so} = steam outlet temperature
U = total zone heat transfer coefficient
W = baffle window vertical dimension
X = quality of drains inlet saturated steam
ΔP_b = baffle pressure drop
ΔP_w = window pressure drop
ΔT_{lm} = log mean temperature difference
μ_s = steam viscosity
μ_f = feedwater viscosity

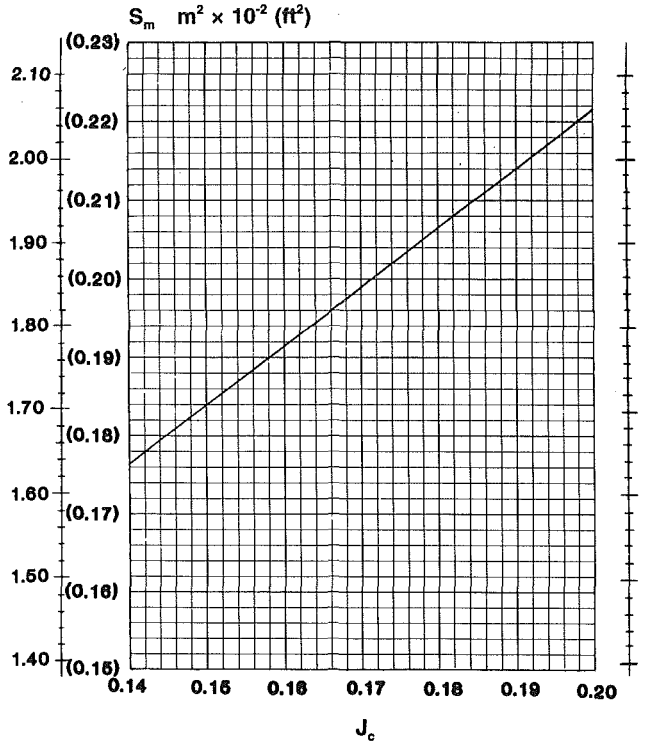

Fig. 5 Crossflow correction factor for the desuperheating zone

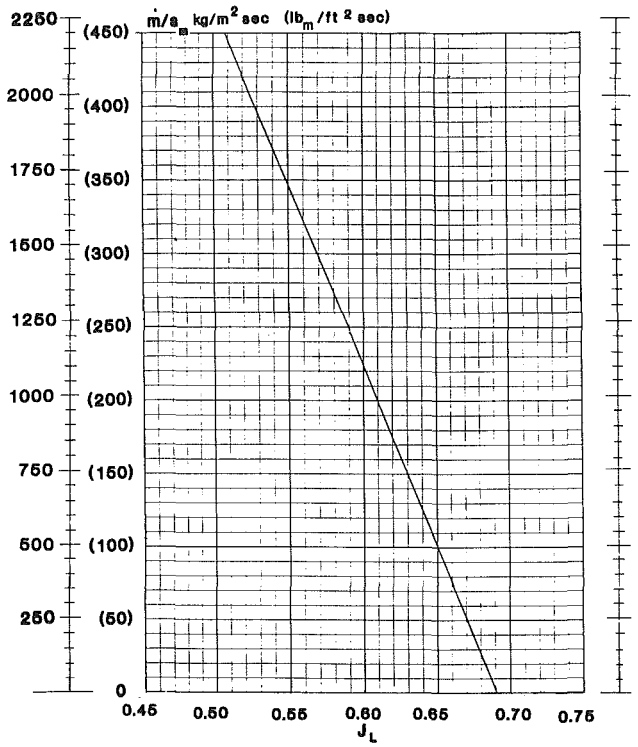

Fig. 6 Leakage correction factor for the desuperheating and drain cooling zones

J_l: The Leakage Correction Factor. This factor includes both shell-to-baffle and tube-to-baffle leakage. It is obtained using Fig. 6 where it is plotted versus the ratio of $\dot{m}_s$ to S_m (Weber, 1992). As $\dot{m}_s/S_m$ increases, more steam or water passes through the zone for a given crossflow area. This causes more leakage to occur.

J_b: The Zone Bypass Correction Factor. This factor is defined as the steam that passes through the zone along the outer circumference and doesn't come in contact with any tubes or baffles. Manufacturers try to minimize leakage by using sealing strips or other methods but still leakage cannot be completely eliminated. Design data to calculate this factor are very difficult or impossible to obtain from the heater manufacturer. Therefore this factor is assumed as 0.9, which is representative of a "well-designed" heater (Mueller, 1986).

J_s: The Inlet and Outlet Baffle Spacing Correction Factor. Depending on the heater design, this factor could be greater than or less than 1 if the inlet and outlet spacing is closer than or greater than the remaining baffles. This factor is obtained using Fig. 8 where it is plotted versus N_B and l_s (Bell, 1986).

The corrected shell-side zone heat transfer coefficient is determined using:

$$h_o = h_{\text{base}} J_c J_L J_b J_s \tag{5}$$

The correction factors J_c, J_L, and J_b are not those calculated using the conventional Delaware Method. New equations were formulated for these factors to reflect the behavior of modern feedwater heaters accurately. The factor J_s is obtained by using the same graph as the Delaware Method for turbulent flow.

2.2 Condensing Zone. The condensing-zone shell-side heat transfer coefficient is the easiest to obtain. The method used is explained in detail by Clemmer and Lemezis (1965). The shell-side heat transfer coefficient is obtained by inverting the sum of the heat transfer resistances. There are four resistances to calculate: condensing heat transfer; shell-side fouling; tube-side convective heat transfer; and tube-wall conduction heat transfer. Condensing heat transfer, R_c, is obtained as (Clemmer and Lemezis, 1965):

$$R_c = 0.0704592 \text{ m}^2\text{°C/kW } (0.0004 \text{ hrft}^2\text{°F/Btu})$$
$$\text{if } T_{\text{sat}} > 160\text{°C } (320\text{°F})$$
$$R_c = 12.03769\ (1.8\ T_{\text{sat}} + 32)^{-0.8912} \text{m}^2\text{°C/kW}$$
$$(0.06834\ (T_{\text{sat}})^{-0.8912} \text{hrft}^2\text{°F/Btu})$$
$$\text{if } T_{\text{sat}} < 160\text{°C } (320\text{°F}) \tag{6}$$

The only heaters tested in the derivation of this paper had steam saturation temperatures above 160°C (320°F).

The tube-side convective resistance R_h is calculated by multiplying h_c by the ratio of the tube inlet and outlet diameters and taking the inverse (Clemmer and Lemezis, 1965). This is expressed as:

$$1/R_h = h_i D_i / D_o \tag{7}$$

The tube-side conduction resistance R_w is calculated by using:

$$R_w = tD_o/(kD_m) \tag{8}$$

The tube-side fouling resistance is calculated using:

$$R_{ts} = 3.522 \times 10^{-5} D_o/D_i \text{ m}^2\text{°C/kW}$$
$$(0.0002\ D_o/D_i \text{ hrft}^2\text{°F/Btu}) \tag{9}$$

The total resistance is the sum of the resistances, given by:

$$R_t = R_c + R_h + R_w + R_{ts}. \tag{10}$$

The condensing zone heat transfer is the inverse of R_t:

$$U = 1/R_t \tag{11}$$

2.3 Drain Cooling Zone. The drain cooling zone heat transfer coefficient is calculated in a manner similar to the way it is calculated in the desuperheating zone with some exceptions noted below.

The same steam mass flow rate used in the desuperheating zone is used in the drain cooling zone if there is no drain inlet to the heater. If a unit is designed with multiple feedwater heaters, the condensate exiting a heater is usually sent to the

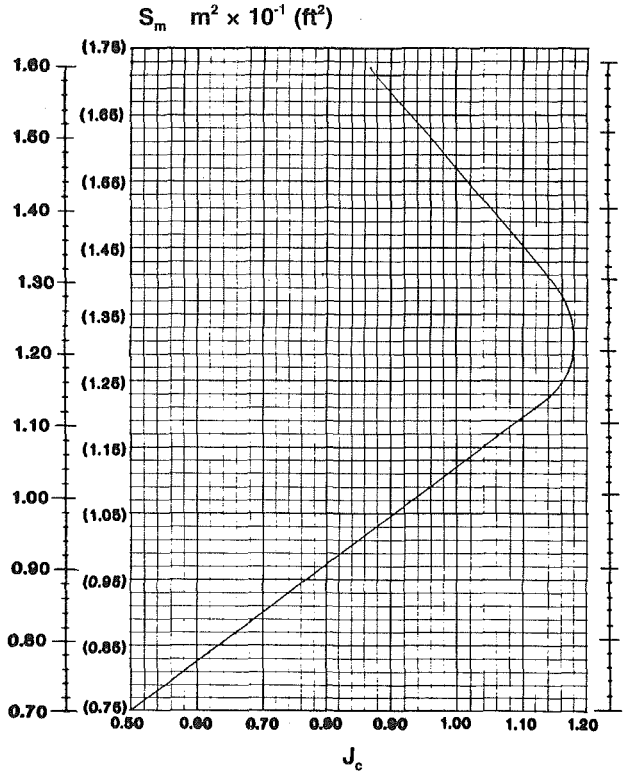

Fig. 7 Crossflow correction factor for the desuperheating and drain cooling zones

heater upstream in the feedwater flow path. On a horizontal heater, the drain inlet from an upper heater flows into the condensing zone as in Fig. 1 and mixes with the condensate already in the heater as it flows to the drain cooling zone.

Because of the increased crossflow in the drain cooling zone, its heat transfer coefficient could be as much as ten times greater than it is in the desuperheating zone. Figure 7 gives the correction factor J_c as a function of S_m. The curve has a parabolic shape because as the amount of crossflow increases there exists a point where further increasing the amount of crossflow will result in channeling and poor flow distribution, which will reduce heat transfer.

The leakage correction factor is calculated the same way as it is in the desuperheating zone using Fig. 6. The leakage will usually be less in this zone because the crossflow area S_m is greater. However, if the drain inlet flow from the upper heater is sufficiently large, it could result in more leakage for the drain cooling zone. Therefore, one should never assume that the drain cooler leakage is the same as the desuperheater leakage.

3 Tube Side Heat Transfer Analysis

The tube-side heat transfer coefficient is calculated using the Dittus–Boelter relation given in Eq. (12) (Clemmer and Lemezis, 1965). The information needed to complete this portion of the analysis is the feedwater properties k_f, μ_f, ρ_f, C_f, and V_f:

$$h_i = (k_f/D_i)(0.023)\mathrm{Re}^{0.8}\mathrm{Pr}^{0.4} \tag{12}$$

where $\mathrm{Pr} = C_f\mu_f/k_f$ and $\mathrm{Re} = \rho_f V_f D_i/\mu_f$.

4 Overall Zone Transfer Coefficient

The overall heat transfer coefficient is calculated by taking the inverse of the sum of the heat transfer resistances given in Eq. (7) (Bell, 1986):

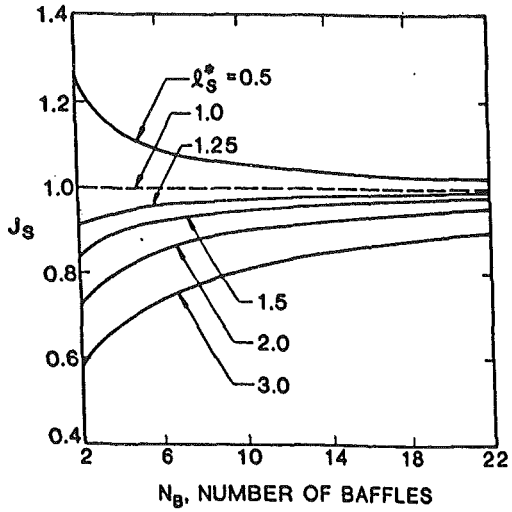

Fig. 8 Baffle spacing correction factor for the drain cooling and desuperheating zone (courtesy of Taylor and Francis, Washington, DC)

$$\frac{1}{h} = \frac{1}{h_o} + R_{fo} + \frac{\Delta x_w A_o}{k_w A_m} + \frac{A_o}{h_i A_i} \tag{13}$$

where R_{fo} is the outside fouling resistance. This is typically taken as 5.283×10^{-5} m²°C/kW (0.0003 hrft²°F/Btu).

5 Pressure Drop Analysis

5.1 Desuperheating Zone. As mentioned previously, the design of the desuperheating zone has been improved significantly over the last several years. Heater manufacturers have minimized the steam-side pressure drop in this zone by using triple and multisegmental baffles. Common multisegmental zone pressure drops range from 3.5 to 7.0 kPa (0.5 to 1.0 psia).

Modifying the original Delaware Method to calculate the pressure drop accurately in this zone is not a straightforward task. This is an area of considerable uncertainty even for the heater manufacturer. Because of the low-zone pressure drop it is very difficult to calculate accurately. The modified Delaware Method given in this paper can be as much as 30 percent higher or lower than the value quoted by the manufacturer. For example, if the method calculates a 4.8 kPa (0.7 psia) pressure drop, the actual pressure drop could be 3.36 to 6.24 kPa (0.47 to 0.93 psia). Therefore, the method is accurate to within 1.4 kPa (0.23 psi) for this case. This is a relatively small amount of error in the overall pressure drop. When analyzed in this manner, the method's accuracy seems acceptable, especially in light of the fact that the manufacturer is not certain of his published pressure drop.

The method calculates two kinds of pressure drops and sums them over the entire zone length. The pressure drop ΔP_b is the pressure drop in one crossflow section if there is no leakage or bypass flow. The pressure drop ΔP_w is the pressure drop in one baffle window section if there is no leakage or bypass flow. The crossflow pressure drop is given by (Bell, 1986):

$$\Delta P_b = \frac{2 f_i \dot{m}_s^2 N_c}{\rho_s g_c S_m^2} \tag{13}$$

where f_i is the friction factor plotted versus Re_s in Fig. 9 and N_c is the number of tubes in crossflow given by:

$$N_c = \frac{(CM)(A)}{D_{\mathrm{otl}}(0.866)P} = \frac{S_m}{S(P)} . \tag{14}$$

The baffle window pressure drop is given by:

$$\Delta P_w = \frac{\dot{m}_s^2}{g_c S_w^2 \rho_s} . \tag{15}$$

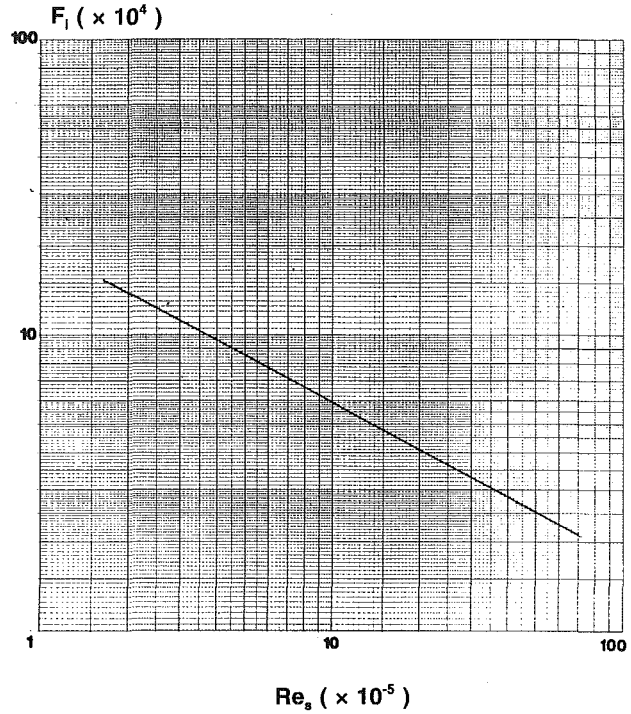

Fig. 9 Pressure drop correction factor for the desuperheating zone

These pressure drops are then corrected for leakage, bypass, and baffle spacing using J_l, J_b, and J_s, respectively. These are the same three factors used in the heat transfer analysis. This is in contrast to the Delaware method, which derives new baffle leakage, bypass, and spacing correction factors in calculating the pressure drop.

The total zone shell-side pressure drop is given by (Bell, 1986):

$$\Delta P_s = ((N_b - 1)\Delta P_b J_b + N_b \Delta P_w) J_l + 2\Delta P_b J_b J_s \quad (16)$$

where N_b is the number of baffles given by:

$$N_b = \frac{L - L_{si} - L_{so}}{L_s} + 1. \quad (17)$$

Equation (12) for ΔP_b is the same equation used in the original Delaware Method except that a different curve is used for f_i and the viscosity ratio is not used. Equation (15) for ΔP_{wo} is different from the original Delaware Method in that it assumes that there is no crossflow in the baffle window and it divides by the quantity S_w^2 instead of $S_m S_w$ (Weber, 1992). These modifications were necessary because of the reduced amount of crossflow and increased amount of baffle window area in modern feedwater heaters. If the baffle window area were used to predict the pressure drop in this zone the calculated values would be as much as ten times greater than what is quoted by the manufacturer.

5.2 Condensing Zone. The pressure drop in the condensing zone is negligible and assumed equal to zero. This is common practice when analyzing feedwater heaters. As the steam exits the desuperheating zone it expands to fill the entire condensing zone and then falls to the bottom of the heater as it condenses. Therefore there is negligible crossflow or window pressure drop.

5.3 Drain Cooling Zone. The drain cooling zone pressure drop is calculated using the same equations as the desuperheating zone except for the baffle window pressure drop, ΔP_w. The window pressure drop is calculated with the same equation used in the Delaware method (Bell, 1986):

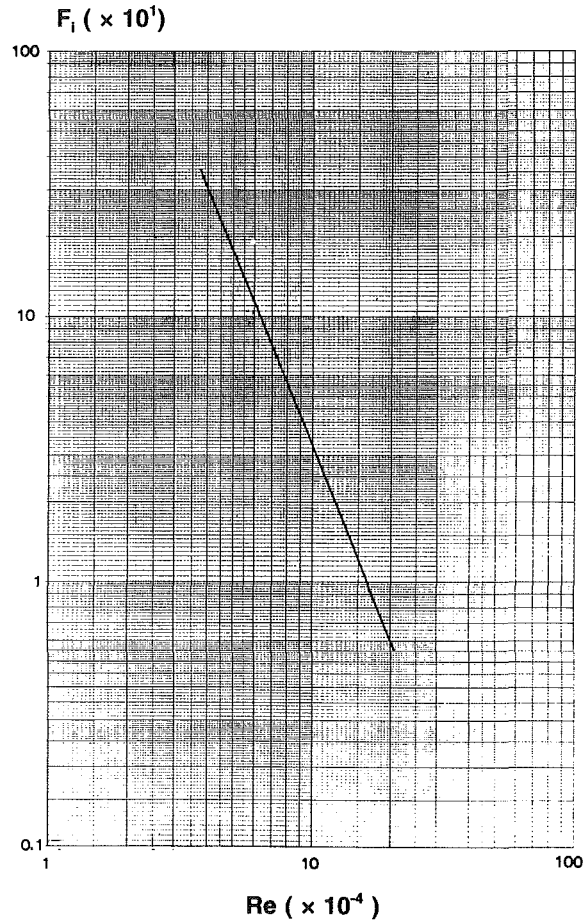

Fig. 10 Pressure drop correction factor for the drain cooling zone

$$\Delta P_w = \frac{\dot{m}_s^2}{g_c S_m S_w \rho_s} \quad (18)$$

Equation (18) may be used in the drain cooling zone because the baffles in this zone are more conventional (i.e., single and double segmental), which is the type of baffles that are better suited for the Delaware method.

6 Calculation of Feedwater Outlet Temperature

After a heat transfer coefficient and pressure drop for each zone has been obtained, the last task in evaluating the feedwater heater design performance is to calculate the feedwater outlet temperature and compare it to what is guaranteed by the heater manufacturer. The heater manufacturer guarantees a terminal temperature difference (TTD) and drain cooler approach (DCA) for the heater.

6.1 Drain Cooling Zone Heat Loss (Q_{dc}). The drain cooling zone heat loss Q_{dc} is calculated first because this is where the feedwater flows initially as it enters the heater. Therefore the feedwater inlet conditions are unknown. The shell-side condensate outlet conditions are also given by the manufacturer in this zone and is used as a first guess in calculating the heat transfer. This guess may need revision after the total zone heat transfer is calculated. The shell-side inlet condensate is assumed to be saturated liquid (quality = 0.0) at heater operating pressure.

The shell-side heat transfer may now be calculated and is given by:

$$Q_{dc} = \dot{m}_s (h_{si} - h_{so}) \quad (19)$$

Using this value and the Law of Conservation of Energy, the

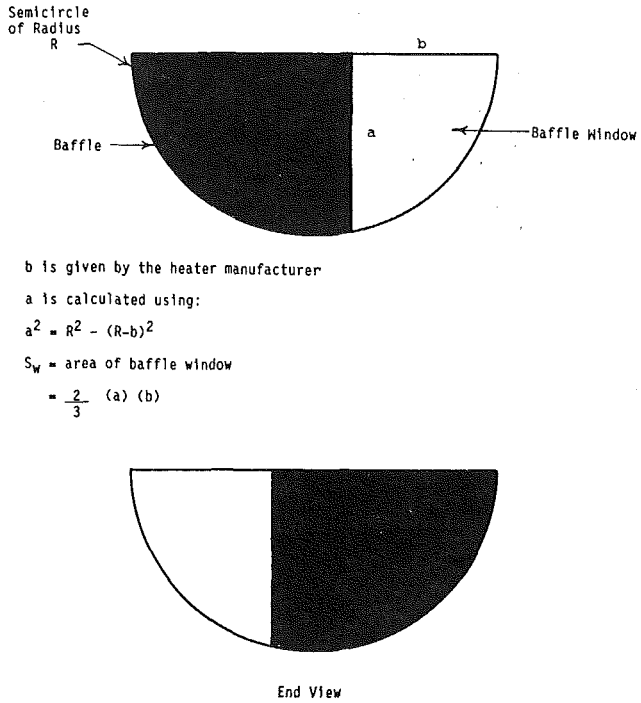

Fig. 11 Baffle window area calculation for single segmental baffles

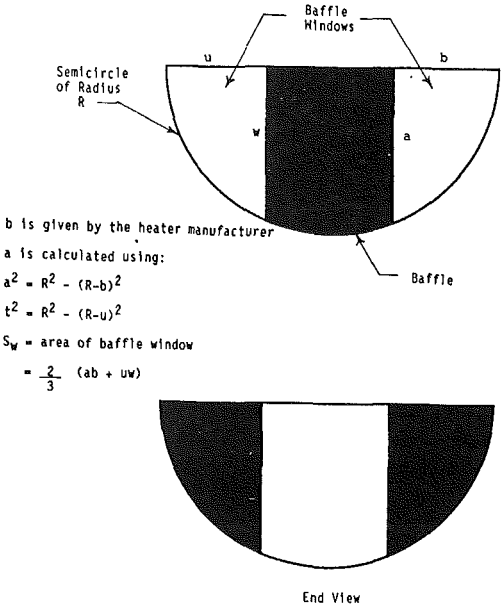

Fig. 12 Baffle window area calculation for double segmental baffles

heat transfer to the feedwater is equal to the heat lost by the condensate, Q_{dc}.

Therefore:

$$Q_{dc} = \dot{m}_s(h_{si} - h_{so}) = \dot{m}_{fw}(h_{fwo} - h_{fwi}) \tag{20}$$

The feedwater side outlet conditions may now be obtained by solving Eq. (20) for h_{fwo}.

The last step in evaluating the drain cooling zone heat transfer is to set Eq. (20) equal to the overall heat transfer for the zone:

$$Q_{dc} = \dot{m}_s(h_{si} - h_{so}) = \dot{m}_{fw}(h_{fwo} - h_{fwi}) = U(A)\Delta T_{lm}(F) \tag{21}$$

where:

U is the calculated overall zone heat transfer coefficient
A is the calculated total zone area
ΔT_{lm} is the log mean temperature difference calculated using:

$$\Delta T_{lm} = \frac{(T_{si} - T_{co}) - (T_{so} - T_{ci})}{\ln \dfrac{T_{si} - T_{co}}{T_{so} - T_{ci}}} \tag{22}$$

F is the log mean temperature difference correction factor F calculated using the method explained by Bowman et al. (1940). The correction factor is obtained by calculating two temperature ratios, R and P:

$$R = (T_{si} - T_{so})/(T_{co} - T_{ci})$$
$$P = (T_{co} - T_{ci})/(T_{si} - T_{ci})$$

These values are utilized to obtain a pure crossflow correction factor, CF:

$$CF = \frac{\dfrac{(R^2+1)^{1/2}}{R-1} \log \dfrac{1-P}{1-PR}}{\log \dfrac{(2/P) - 1 - R + (R^2+1)^{1/2}}{(2/P) - 1 - R - (R^2+1)^{1/2}}} \tag{23}$$

CF assumes that all of the tubes in the zone are in crossflow. However, this is not the case in any of the feedwater heaters that the author has analyzed. Therefore the log mean temperature difference crossflow correction factor CF must be adjusted with the crossflow multiplier discussed previously. The adjusted correction factor F is given by (Weber, 1992):

$$F = 1 - [CM(1 - CF)]$$

The outlet condensate conditions must be adjusted by trial and error until Eq. (21) is satisfied within 0.05 percent error.

The calculated value of the feedwater outlet temperature of the zone, $T_{co,dc}$ is the inlet temperature to the next zone it enters, which is the condensing zone. That is: $T_{co,dc} = T_{ci,\text{cond}}$.

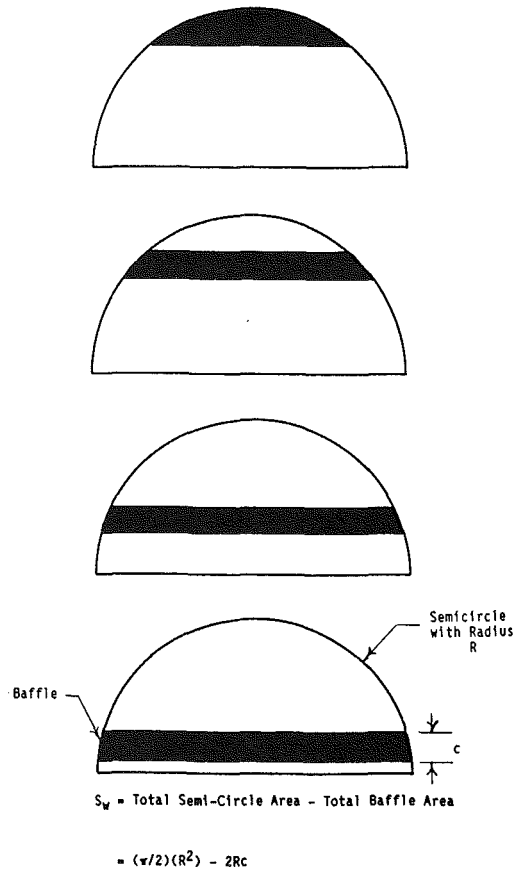

Fig. 13 Baffle window area calculation for multisegmental baffles

The heat loss by the shell-side fluid in the condensing zone is the addition of three sources: Q_{dsc}, Q_{cd}, and Q_{dr}.

6.2 Condensing (Q_{cond}). (1) Q_{dsc} = the heat release by the 6–33°C (10–60°F) superheated steam as it enters the zone from the desuperheating zone. This heat release is given by:

$$Q_{dsc} = \dot{m}_s(h_{si} - h_{so}) \tag{24}$$

where: h_{si} is the inlet enthalpy to the zone; h_{so} is the saturated vapor enthalpy at operating pressure. Using the same logic for the shell-side condensate:

$$T_{si,dc} = T_{so,\text{cond}}$$

(2) Q_{cd} = the latent heat of condensation of the steam is given by:

$$Q_{cd} = \dot{m}_s h_{fg} \tag{25}$$

where h_{fg} is the latent heat of condensation at heater operating pressure.

(3) Q_{dr} = the condensation of drain inlet. If condensate from an upstream heater flows into the heater being analyzed the condensate flashes (vaporizes) due to the pressure differential. The amount that flashes must be recondensed. This heat release is given by:

$$Q_{dr} = \dot{m}_x h_{fg} \tag{26}$$

where h_{fg} is the latent heat of condensation evaluated at the drain inlet temperature and pressure and $\dot{m}_x$ is the fraction of the drain inlet that flashes given by:

$$\dot{m}_x = X\dot{m}_{dr} \tag{27}$$

The value X is the quality of the saturated steam evaluated at the heater operating pressure (ASME, 1967).

The total condensing zone heat release is the addition of the three sources:

$$Q_{\text{cond}} = Q_{dsc} + Q_{cd} + Q_{dr} \tag{28}$$

The zone feedwater outlet temperature is calculated in a manner similar to the drain cooling zone with the use of Eq. (21), except that since there is zero crossflow in this zone, $F = 1.0$.

The zone inlet steam temperature must be adjusted by trial and error until Eq. (21) is satisfied within 0.05 percent error (Weber, 1992).

The calculated value of T_{co} leaving the condensing zone is the inlet temperature to the desuperheating zone. That is:

$$T_{co,\text{cond}} = T_{ci,ds} \tag{29}$$

Similarly, the outlet steam temperature from the desuperheating zone is equal to the inlet steam temperature to the condensing zone:

$$T_{si,\text{cond}} = T_{so,ds} \tag{30}$$

6.3 Desuperheating Zone (Q_{ds}). The heat supplied in the desuperheating zone is given by:

$$Q_{ds} = \dot{m}_s(h_{si,ds} - h_{so,ds}) \tag{31}$$

The zone feedwater outlet temperature is then evaluated as it was in the drain cooling zone using Eqs. (7), (21), (22), and (23), except that the steam conditions in this zone are fixed by the utility's unit that balance at the zone inlet and by the already calculated zone outlet conditions that were used to balance the condensing zone. Therefore if Eq. (21) is not satisfied, the extraction steam flow to the heater must be adjusted and the feedwater and steam conditions recalculated beginning with the drain cooling zone. This trial and error process proceeds until Eq. (21) is satisfied for all three zones.

The feedwater outlet temperature calculated in this zone is the final feedwater outlet temperature from the heater. This value is then compared to what is desired or to what the feedwater heater manufacturer specifies.

Table 1 Heat transfer coefficient and pressure drop comparison

HEAT TRANSFER COEFFICIENT AND PRESSURE DROP COMPARISON				
ZONE	HEAT TRANSFER COEFFICIENT		PRESSURE DROPS	
	AVG. % ERROR	MAX .% ERROR	AVG. % ERROR	MAX. % ERROR
DESUPERHEATING*	4.6%	10.5%	27.8	72.5%
CONDENSING	1.4%	1.8%	NA	NA
DRAIN COOLING	1.1%	2.4%	2.8	4.1

*Four of the six heaters analyzed had desuperheating zones. The other two had only a condensing and drain cooling zone.

6.4 Thermal Temperature Difference and Drain Cooler Approach. The utility normally purchases a feedwater heater by specifying a terminal temperature difference (TTD) and drain cooler approach (DCA). The terminal temperature difference is defined as the saturation temperature at the extraction steam inlet temperature minus the feedwater outlet temperature:

$$\text{TTD} = T_{\text{sat,ext}} - T_{fwo} \tag{32}$$

The drain cooler approach is defined as the drain cooler condensate outlet temperature minus the feedwater inlet temperature to the drain cooling zone:

$$\text{DCA} = T_{co,dc} - T_{fwi} \tag{33}$$

7 Conclusions

This paper has derived a method to evaluate the heat transfer coefficients and pressure drops in a modern feedwater heater. For the six feedwater heaters utilized to design the method, the average and maximum percentage of error of the heat transfer coefficient and pressure drops are listed in Table 1. The heat transfer coefficients exhibit excellent correlation if the calculated Reynolds number is below 10^6. Above 10^6 the percentage of error will be 10 percent or greater. All heat transfer coefficients in the drain cooling and condensing zones correlate very well.

The percentage of error in the desuperheating zone is high because this is an area of considerable uncertainty, even for the heater manufacturer. This is due to the very low shell-side pressure drop (often <1 psia) and high Reynolds number. Note that the method is not valid for drain cooling zones for low-pressure heaters. A new friction factor curve needs to be calibrated for the drain coolers of low-pressure heaters. However, since the condensate enthalpy is relatively unaffected by a pressure change of less than 10 psia, the overall effect of drain cooler pressure drop on heater performance is minimal.

The heat transfer coefficients and pressure drops can then be used to calculate the end results, which are the terminal temperature difference and drain cooler approach. The temperature differences may then be compared to what the heater manufacturer specifies.

References

ASME, 1967, *Steam Tables*, New York.

Bell, K. J., 1986, *Delaware Method for Shell Side Design*, pp. 129–166, cited in Palen, J. W., *Heat Exchanger Sourcebook*, Hemisphere Publishing Corp., New York.

Biar, M., 1991, "Feedwater Heater Design Data," Marley Heat Transfer Corp., Houston, TX.

Bowman, R. A., Mueller, A. C., and Nagle, W. M., 1940, "Mean Difference in Design," ASME *Trans.*, Vol. 62.

Clemmer, A. B., and Lemezis, S., 1965, "Selection and Design of Closed Feedwater Heaters," presented at the ASME 1965 Winter Annual Meeting, Chicago, IL.

Incropera, F. P., and Dewitt, D. P., 1981, *Fundamentals of Heat Transfer*, Wiley, New York, pp. 302–303.

Mueller, A. C., 1986, *Shell and Tube Exchanger Design*, pp. 167–171, cited in Palen, J. W., *Heat Exchanger Sourcebook*, Hemisphere Publishing Corp., New York.

Weber, G. E., 1992, Master's Thesis, University of Illinois at Chicago.

Some Aspects of Erosion Prediction of Steam Turbine Blading

J. A. Krzyzanowski
Prof.Dr.habil.,
Institute of Fluid-Flow Machinery (IFFM),
Polish Academy of Sciences,
Gdańsk, Poland
Mem. ASME

A. E. Kowalski

A. L. Shubenko
kand.t.sc.,
Institute for Problems in Machinery (IPM),
Ukrainian Academy of Sciences,
Kharkov, The Ukraine

This paper deals with an issue of paramount importance for the turbine manufacturer today: the mathematical modeling of erosive wear at the inlet rotor blade edges by streams of coarsely dispersed liquid droplets. In the methodology of blade material wear an important element is the erosion model or material response $Y = Y(\tau)$ to the droplet impact intensity. On the background of this erosion model development the approaches of Szprengiel and Weigle (1983), Szprengiel (1985), and Shubenko and Kovalsky (1987) are presented and applied for erosion calculation of some real turbine blade profiles. There are, however, several factors that affect the erosion prediction quality as well as the field experimental data. Hence a procedure for verifying the methodology of the erosion prediction by experimental data is necessary. Krzyzanowski (1987, 1988, 1991) used for that purpose the calculated and measured erodet area of various turbine blade profiles. Here the comparison of the calculated and measured erosion width $\eta_B \equiv z$ has been used to verify the prediction methodology of erosion. The use of η_B instead of erosion area looked promising since acquiring η_B experimental values seemed easier than any other geometric characteristics of the blade erosion wear. It has been shown, however, that the prediction of η_B underestimates the blade erosion wear for both material response models. To cope with the scatter of experimental data, statistics have been used. Reasons for this scatter and differences between the calculated (η_{Bcalc}) and measured (η_{Bm}) values of the erosion field width have been suggested. The list of factors that affect the erosion prediction quality may be looked upon as a list of promising topics of further research on the subject.

Introduction

Vapor condensation and concentration of liquid droplets in flow passages of turbomachines is a reason for erosive wear of their components. Therefore, the problem of better effectiveness and reliability increase of various power-generating turbomachinery equipment should be solved in close connection with detailed analysis of the erosive damage process of their structural components. This is of particular significance in the case of the last stages of low-pressure sections of high-capacity power-generating turbines, operated with extremely wet vapor and high circumferential velocities of their rotor blades. The above-mentioned circumstances have led in recent years to a significant extension of theoretical and experimental research on the problem.

The important elements of the progress on the subject include:

- Creation of physically justified erosion model $Y = Y(\tau)$, which would form a theoretical basis for development of a practical prediction method of blading wear at prescribed operating conditions [recently the state of the art (Krzyżanowski, 1986) as well as signs of progress on the subject Krzyżanowski, 1987) have been reported].
- Assessment of threats resulting from erosive damages [there exist research results suggesting that even strong erosion influences substantially neither the stress distribution in the blade nor its vibrational characteristics nor the efficiency of the turbine stage (Krzyżanowski, 1991); the fatigue of the eroded blade, however, in particular in an agressive atmosphere of the "prime condensate," is still an open question].
- Development of the blading protection means that would allow one to avoid or diminish the erosive damages (which is still in many cases a subject of engineering intuition rather than rational approach).

In this paper:

- A general outline of the erosion model (or material response) evolution, that is the evolution of the $Y = Y(\tau)$ relationship, over last 20 years will be given. The authors of this paper have also contributed to a certain extent to this evolution.
- The use of this erosion model in the methodology of erosion prediction will be demonstrated. This methodology, however, demands experimental verification due to a series of simplifying assumptions. There are different concepts of such verification: Krzyżanowski (1987, 1991) based this on comparing calculated erosion area $F_{er\ calc}$ with its measured value F_{erm}.
- For the purpose of verification the comparison of the

Contributed by the Power Division for publication in the JOURNAL OF ENGINEERING FOR GAS TURBINES AND POWER. Manuscript received by the Power Division November 18, 1991. Associate Technical Editor: R. W. Porter.

calculated width of the zone of profile erosion ($\eta_{B\text{calc}}$) with its measured value (η_{Bm}) will be used here; acquiring of η_B experimental data seems easier than any other geometric characteristics of the blade erosion wear.

- However, statistics will be used to cope with the number of experimental values of η_{Bm}.
- Finally, critical discussion of the comparison made will be presented.

Phenomenological Model of Droplet Erosion Wear; Estimate of the Incubation Period

When considering development of a mathematical model of turbine blade erosion, the process of erosion modeling for any part of its surface resolves in fact into describing a characteristics curve of material loss due to droplet stream impact at the surface element under consideration.

In the seventies it turned out clear that the accumulated experimental data on the $Y = Y(\tau)$ relationship can be generalized by means of a curve with four characteristic erosion progress stages, Fig. 1.

It was Heymann (1967, 1968) who gave the first relationship determining the maximum slope of this curve as dependent on the collision parameters in the form of

$$U_{eM} = \frac{U_a}{N_e}\left(\frac{w_{*N}}{2500}\right)^5. \tag{1}$$

Based on this result as well as numerous considerations of droplet motion between blade rows, a criterion of erosion threat to steam turbine blading has been development at the Institute of Fluid-Flow Machinery (IF-FM). The assumptions made include:

- Polydisperse structure of the droplet stream described by a distribution function Γ (Hammit et al., 1981) to be determined experimentally.
- A simplified wake description by means of a formula $c = f(c_1)$ and description of the droplet motion based on motion equation of a type (Fadeev, 1974; Krzyżanowski and Weigle, 1976)

$$\frac{d\bar{c}_*}{d\tau} = kc_x \frac{\rho}{\rho_* d_*} |\bar{c} - \bar{c}_*| (\bar{c} - \bar{c}_*). \tag{2}$$

- Assumption of linear superposition principle as applied to erosive effects of individual fractions in the polydisperse droplet stream; relationships

$$Y_i = U_{eM} \cdot \tau \text{ and } Y = \Sigma Y_i = \tau \Sigma U_{eMi} \tag{3}$$

have also been assumed.

More details on the model can be found in the papers by Krzyżanowski and Weigle (1976) and Krzyżanowski and Szprengiel (1978); its applications have been described, for instance, by Krzyżanowski (1986, 1991), and he gave a critical assessment (1983). Justification of the superposition principle (3) was discussed later on in more detail by Szprengiel and Weigle (1983). This concept of calculating the thread of blade erosion has been summarized in Fig. 2. An extensive survey of similar approaches of other authors both of the eastern as well as western hemisphere is presented by Krzyżanowski (1991), just to mention the names of Filippov et al., Fadeev, Valha, Somm, Lord et al., Benvenuto et al., and others.

In the course of developing a description of the experimental curve as shown in Fig. 1, Szprengiel (1985) made a step toward summarization of the existing knowledge. Based on the concepts and results of Heymann (1970, 1979), Poddubenko and Yablonik (1976), and Springer (1976), he approximated the experimental data by means of the formula

$$Y = a\tau U_{eM} (Y/Y_M)^b \exp(cY/Y_M). \tag{4}$$

Using the least-squares approach, he determined for

Nomenclature

$a, \hat{a}, b, \hat{b}, c$ = constants, Eq. (4) and (10), respectively
$\bar{c}, c$ = velocity in an absolute reference frame, m/s
C = constant, Eq. (6)
C_x = drag coefficient of a drop
C_*, C_R, C_M = wave velocity (liquid, Rayleigh, target), m/s
d_* = droplet diameter, m
$F_{\text{er calc}}, F_{\text{erm}}$ = area of eroded fragment of the blade profile, calculated and measured, respectively, Fig. 7, m^2
i_1 = steam enthalpy, kJ/kg
$i_{\max}$ = number of droplet groups in a polydisperse droplet stream
k = constants, Eqs. (2) and (6)
k_e = coefficient concerning the decrease of droplet elasticity at a low collision velocity
$\bar{l}$ = l/l_2 = relative coordinate along the rotor blade
m_{inc} = $U_a \cdot \tau_{\text{inc}} \cdot \rho_*$ = total mass of water impinging on the unit blade surface element for $\langle 0, \tau_{\text{inc}} \rangle$, kg/m^2
n = number of droplets
N_e = normalized erosion resistance
p = impact pressure, N/m^2
p_1 = steam pressure, N/m^2
r_R = Rayleigh wave parameter, m
S = axial gap width, m
t_w = rotor blade spacing, m
u = circumferential velocity, m/s
U_a = total volume of water impinging on the unit blade surface element per unit time, m/s
$U_a \cdot \tau \cdot \rho_*$ = total mass of water impinging on the unit blade surface element, kg/m^2
U_{eM} = maximum instantaneous value of the volume of material loss per unit time and unit blade surface, m/s
w_{*N} = normal component of the droplet impact velocity in the relative reference frame, m/s
Y, Y_M, Y_o = mean erosion depth and its characteristic values, Fig. 1, m
$z \equiv \eta_{\beta\text{calc}}$ = (nonrandom) calculated width of the erosion damage zone, Fig. 7, m
Z, Z_{ij} = (random) measured width of the erosion damage zone, Fig. 7, m
$\hat{Z}$ = predicted width of the erosion damage zone, Eq. (10), m
α_1 = stator blading outlet angle, deg
δ_f = pressure reducing factor, m
ν = Poisson coefficient
ξ, η = blade profile coordinate frame, m
ρ = density, kg/m^3
$\tau, \tau_M, \tau_{\text{inc}}$ = time and its characteristic values, Fig. 1, h
τ_R, σ_R = Rayleigh wave parameters

Subscripts

i = number of droplet fraction
calc = calculated
m = measured
M = refers to the target material
1 = refers to steam
$*$ = refers to droplet

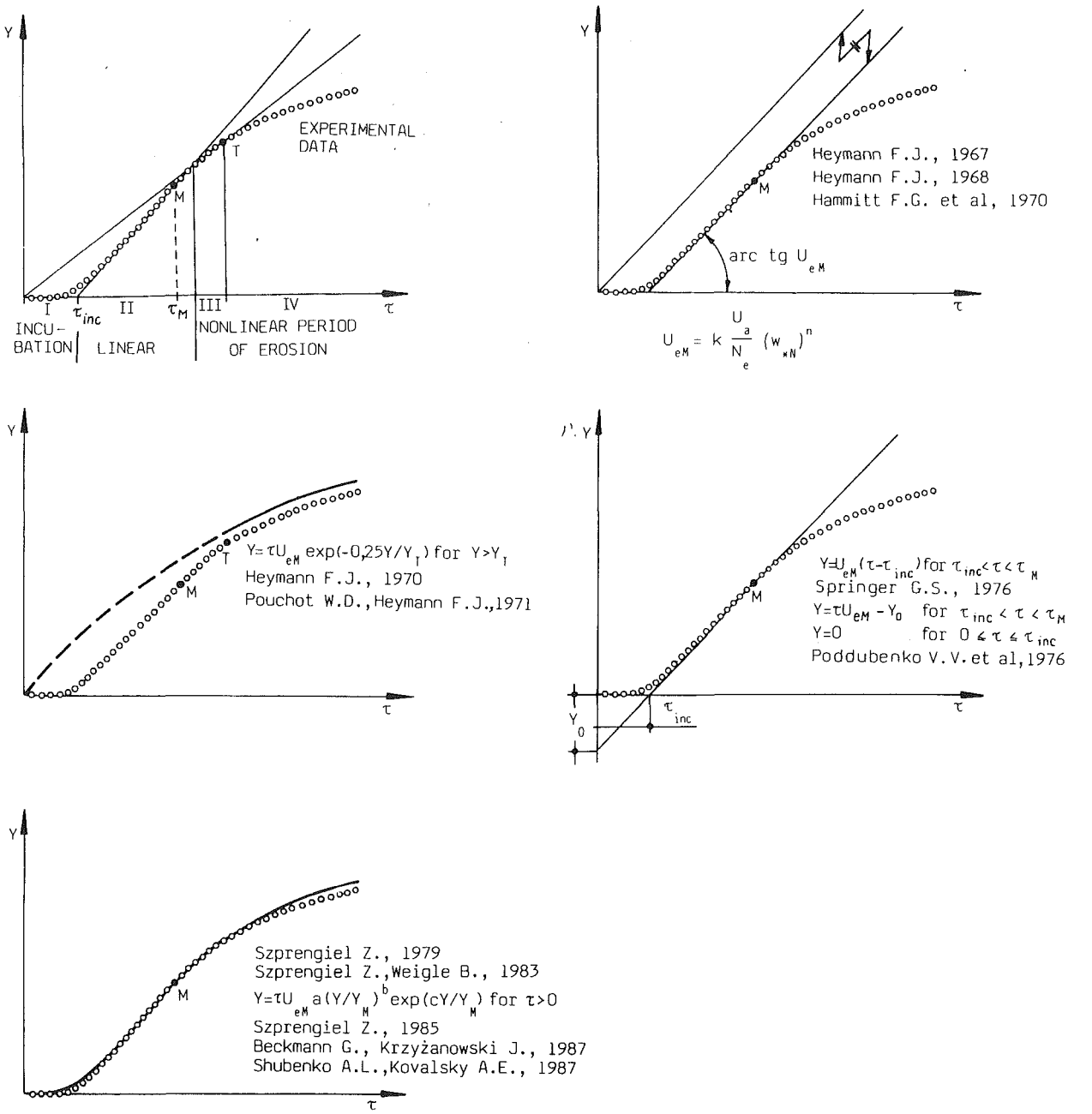

Fig. 1 Characteristic wear versus time erosion pattern and various ways of its approximation over last about 20 years of research

$0<\tau<\tau_M$ and $\tau_M<\tau$ two sets of a, b, and c coefficients; based on the above-mentioned experimental data he assumed also

$$\tau_M = 2.99\tau_{\text{inc}}, \quad Y_M = 1.99 U_{eM}\tau_{\text{inc}} \tag{5}$$

and determined the characteristic quantities U_{eM} and τ_{inc} depending on the target material strength properties and collision parameters U_a, w_{*N}, d_*. This allowed us to predict with a satisfactory precision the time course of shape changes in turbine profiles subjected to erosion. The concept of this calculation is shown in Fig. 2. Examples of such calculations are quoted in his publication (1985), Fig. 3. More comprehensive statistics of comparison between the calculation data and those resulting from measurements of turbine blade sections under field conditions can be found in the papers of Krzyżanowski (1987, 1988).[1]

[1]The data set in Fig. 3 can serve as a basis for experimental verification of various erosion models. More data of that kind can be made available by the IF-FM on request.

Recently, Shubenko and Kovalsky (1987) made a further step toward improving the $Y=Y(\tau)$ curve description. Their main interest concerned determination of the erosion incubation period meant as "a fundamental characteristic of any erosion process." The considerations were based on the "kinetic concept of solid body strength" (Zhurkov, 1967; Betekhin and Zhurkov, 1971; Regel et al., 1974) and its appropriate modifications (Shubenko-Shubin et al., 1984, 1987). It was also assumed that:

1 The droplets interacting with a specific element of the rotor blade inlet edge show a uniform distribution over the surface if the exposure period is long enough.

2 The interaction between the blade material and the droplet having impinged the surface element under consideration can be neglected at the moment the next droplet impinges on the same element. The numerical analysis has proved the above hypotheses to be thoroughly justified when applied to typical

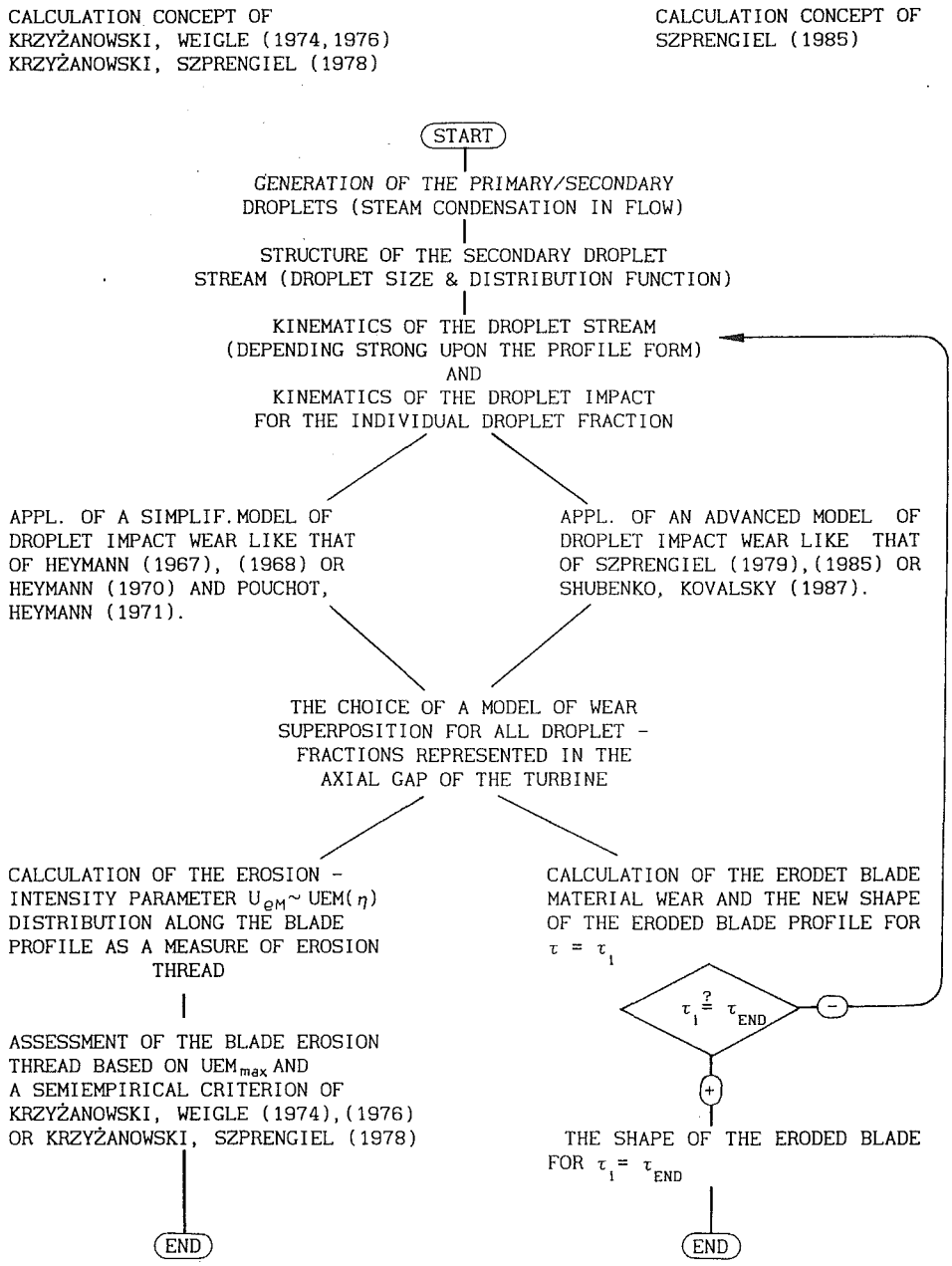

Fig. 2 Two concepts of the calculations: that of the assessment of erosion thread and the prediction of eroded blade shape as a function of time

operating conditions in low-pressure sections of wet steam turbines.

A complex impulse of material loading generated by a droplet impact at a given point of the surface is modeled by two subsequent rectangular pulses. The first pulse determines the tensile stresses in the Rayleigh wave while the second one is responsible for quasi-static stresses assumed to occur immediately after the Rayleigh wave passage (Fig. 4). Such a load idealization allows us to express the incubation period duration in the following general analytical form (Shubenko-Shubin et al., 1987; Shubenko and Kovalsky, 1987):

$$\tau_{\text{inc}} = \frac{1}{2\pi(k+1)C}\left\{\sum_{i=1}^{i_{\max}} n_i \left\{\frac{2\sigma_{Ri}^k \cdot \tau_{Ri} \cdot r_{Ri}^2}{k-4} + d_{*i}^{2k} w_{*Ni}^k [(1-2\nu)/8]^k p_i^k C_*^{-k} \cdot \frac{1}{2}\left[\frac{1}{w_{*Ni} \cdot d_{*i} \cdot r_{Ri}^{2k-4}} \cdot \frac{1}{k^2-3k+2} - \frac{1}{C_R \cdot r_{Ri}^{2k-3}(2k^2-5k+3)}\right]\right\}\right\}^{-1}; \quad (6)$$

where

$$p_i = 1{,}5 k_e \rho_* w_{*Ni} C_* (1 + \rho_* C/\rho_M C_M)^{-1} (1 + 2\delta_f d_{*i}^{-1})^{-2}$$

This represents a modified "water hammer equation";

$$\sigma_{Ri} = 0.75 p_i;$$

$$r_{Ri} = 0.6 d_{*i} w_{*Ni} C_R^{-1};$$

$$\tau_{Ri} = 0.25 C_*^{-2} w_{*Ni} d_{*i}. \quad (7)$$

The authors used this method of determining the incubation period duration τ_{inc} when constructing the $Y = Y(t)$ curve. Also they based their considerations on experimental investigations (Poddubenko and Yablonik, 1976), assuming the linear dependence

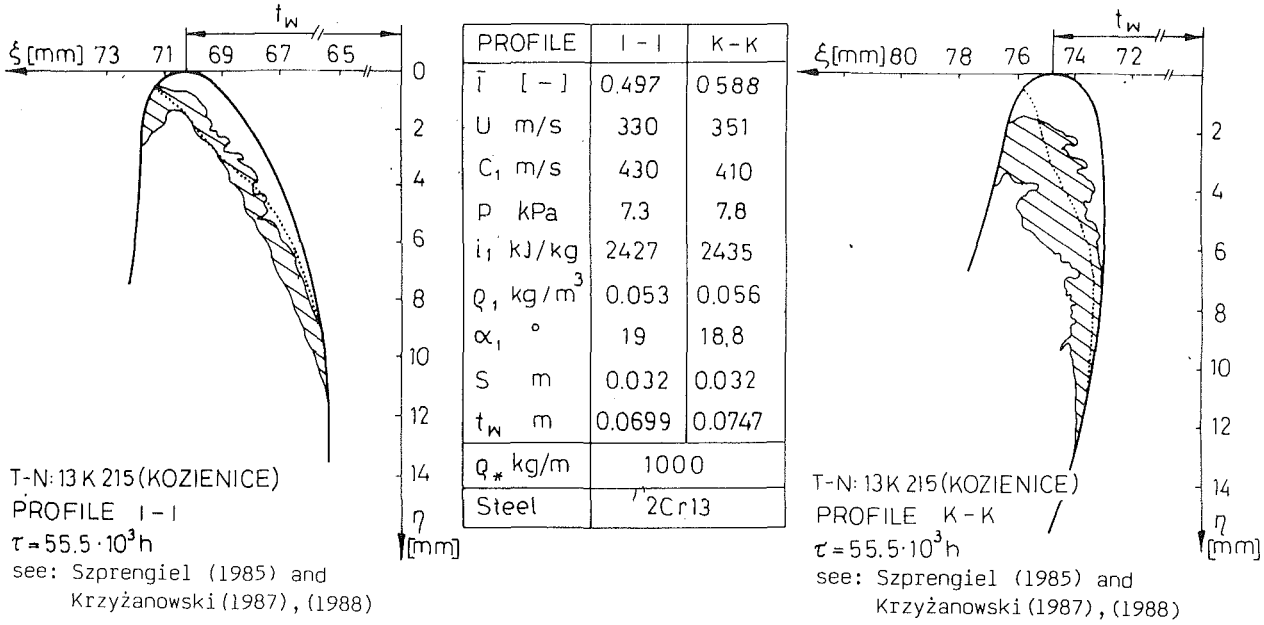

Fig. 3 Examples of the calculated shape of the eroded blade profile and its comparison with experimental data; see Szprengiel (1985), and Krzyżanowski (1987, 1988):
——— **measured shape of two eroded profiles out of the same blade row**
▨ **shaded area represents to some extent the scatter of experimental data**
····· **prediction of erosion**

$$Y = U_{eM} \cdot t - Y_o; \tag{8}$$

for the $\tau_{inc} < \tau < \tau_M$ period (Fig. 1), and the empirical relationship (4) after (Szprengiel and Weigle, 1983; Szprengiel, 1985) for $\tau > \tau_M$. The linear relationship (8) is confirmed satisfactorily by experimental data (Poddubenko and Yablonik, 1976; Povarov et al., 1985; Staniša et al., 1985) quoted in Fig. 5.[2] In many cases the wear depth Y can be conveniently represented in terms of the amount of liquid impinging on the surface unit area, whereas τ_{inc} depends on droplet impact velocity w_{*N} and material properties. Hence, one obtains finally (Shubenko and Kovalsky, 1987)

$$Y = Y_o \left(\frac{m}{m_{inc}} - 1 \right), \quad Y \le Y_M;$$

$$Y = a Y_o \frac{m}{m_{inc}} (Y/Y_M)^b \exp(cY/Y_M), \quad Y > Y_M;$$

$$Y_M = \frac{ae^c}{1 - ae^c} Y_o, \quad m_{inc} \equiv U_a \tau_{inc} \rho_* = \frac{\pi \rho_* \tau_{inc}}{6} \sum_{i=1}^{i_{max}} n_i d_{*i}^3 \tag{9}$$

In order to confirm these dependences a comparison with an experiment is shown by the authors in Fig. 6.

To summarize this section it should be stated that two advanced methods of erosion prediction have been outlined: the method of the IF-FM and that of the IPM. The IF-FM method is based on dependences (4) and (5), the experimental relationships U_{eM}, $\tau_{inc} = f(U_a, w_{*N}, d_*, N_e)$ and the superposition principle (3). The IPM method is based on formulae (9) as derived from relationships (8) and (4), as well as Eqs. (6) and (7). The similarities of both the methods can be resolved to the use of Eq. (4) for $\tau > \tau_M$ while the differences consist in:

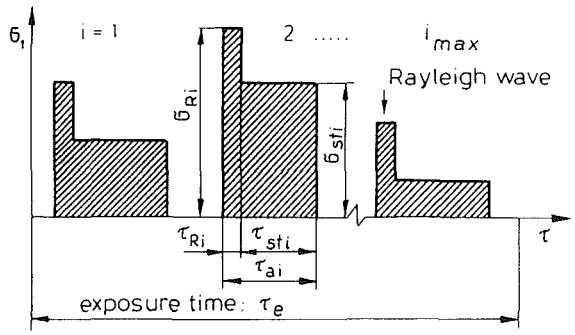

Fig. 4 Idealization of the stress impulses due to the droplet rain impact at the fixed point of the target; (Shubenko-Shubin et al., 1987; also Shubenko and Kovalsky, 1987); first rectangular pulse determines the tensile stresses due to the Rayleigh wave, while the second one represents quasi-static stresses following the Rayleigh wave passage

- Eq. (8) being used by the IPM for $\tau_{inc} < \tau < \tau_M$ instead of Eq. (4) as applied by the IF-FM;
- Different methods of erosion effect superposition in a polydisperse droplet stream: The IF-FM assumes principle (3), summing up the erosive effects for every droplet fraction while the IPM applies Eqs. (6), (7), and (9) to determine an equivalent incubation period corresponding to the polydisperse stream.

Both methods can be used among others to determine a shape change of the profile eroded versus time. The concept of such calculations is explained in Fig. 2; an example of such calculation is shown in Fig. 3, and in the papers of Krzyżanowski (1987, 1988).

In conclusion, in spite of having advanced models of material response, relatively well confirmed by droplet impact experiments, there are still some accuracy limitations of erosion prediction methods. They can be attributed in a considerable extent to the lacks in our knowledge of the physics of steam flow in a turbine. This problem has been discussed in some detail in the publications of Krzyżanowski (1983, 1987, 1988). Here we shall confine ourselves to mentioning only those fac-

[2] It should be noticed that the co-authors' concept as presented above confirms indirectly the approach of Heymann (1968). In fact, based on Eq. (6) one can deduce by means of some simplified considerations that

$$U_{eM} \equiv Y_o / \tau_{inc} \sim w_{*N}^k.$$

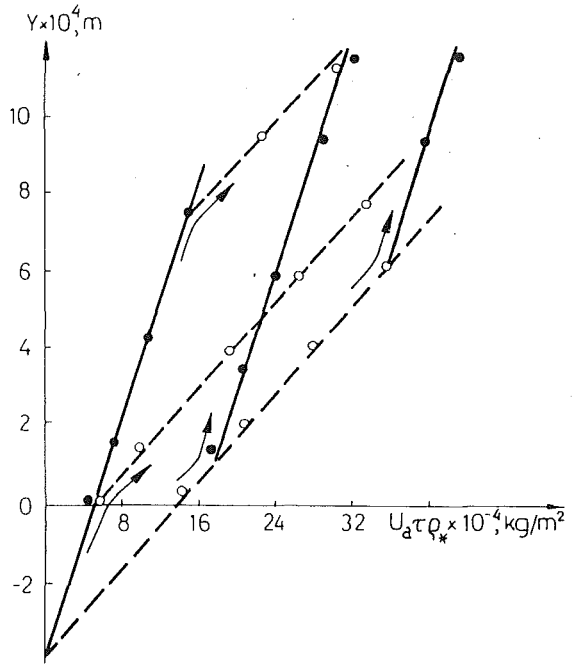

Fig. 5 Experimental evidence for linear relation of $Y(\tau)$ for $\tau_{inc} < \tau < \tau_M$ according to Poddubenko and Yablonik (1976); • for $w_{*N} = 300$ m/s, ○ $w_{*N} = 240$ m/s, 12Cr13 steel; note that the slopes of the lines depend on w_{*N}, also τ_{inc} depends on w_{*N}, Y_0 is a material constant, note also that the slope of $Y(\tau)$ does not depend on the history of the erosion process

tors that affect the erosion prediction quality as well as experimental data used for its verification. They include among others:

- insufficient capability to describe complicated velocity fields of the wet steam gas phase in the area of the rotor blade tips and intense leakage flows;
- lacks in our knowledge of condensation mechanisms in the steam flow in a turbine;
- insufficient capability to determine distribution of the secondary droplet mass flux along a blade in an intercascade axial gap of given stage;
- insufficient capability to determine the structure of the secondary droplet stream in this gap;
- insufficient reliability of the semiempirical $Y = Y(\tau)$ relationships extrapolated for $\tau \gg \tau_M$;
- so far unclarified role of corrosion in the process of blade erosion;
- difficulties in accounting for time-dependent turbine load when predicting the erosion progress;
- significant effect of the blade system assembling quality on its geometric characteristics and the erosion prediction result;
- low class of material loss measurement accuracy at the eroded blade of a full-scale turbine.

The factors mentioned above affect the accuracy of erosion prediction. Thus the intention to verify the prediction method experimentally should be considered natural. This is the subject of the next section.

Verification of the Erosion Prediction Method

By verification we mean here the comparison between the calculated and measured erosion patterns. For this comparison different geometric parameters of the eroded field can be used. In two papers of Krzyżanowski (1987, 1988) verification of the IF-FM method has been based on a comparison between the calculated $F_{er\,calc}$ and measured F_{erm} erosion field area of selected turbine blades (for nomenclature, see Fig. 7). In order to verify the IPM method it has been decided in this paper to search for the relation between the random width $Z \equiv \eta_{Bm}$ of

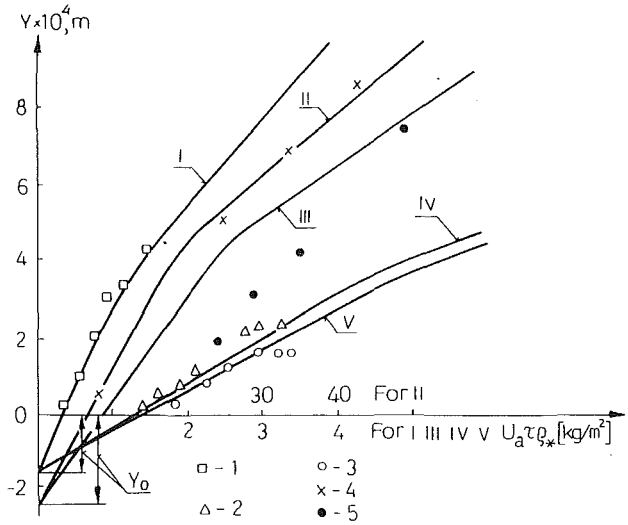

Curve	Experimental data			Teoretical data			Reference
	$d_* \times 10^6$ [m]	w_{*N} [m/s]	HB	k	$C \times 10^{14}$ [$s^{-1}MPa^{-k}$]	$Y_0 \times 10^4$ [m]	
I 1	1100	300	170÷180	6.3	4.6	1.7	Povarov et al, 1985
IV 2	820	250					
V 3	690	250					
II 4	900	240	240÷260	6.3	1.7	2.4	Poddubenko, Yablonik, 1976
III 5	690	360					

Fig. 6 Experimental (Poddubenko and Yablonik, 1976; Povarov et al., 1985) verification of formulae (6), (7), and (8) and alternative formulation (9) for 20Cr13 steel; solid lines—calculations; points—experiments, $a = 0.872$, $b = 0.392$, $c = -0.276$, according to Szprengiel and Weigle (1983)

the erosion zone at the convex surface of a real rotor blade (assumed to be distributed normally) and the nonrandom width $z = \eta_{Bcalc}$ of the erosion zone to be evaluated by calculation. The use of η_B instead of F_{er} looked promising since acquiring its experimental values η_{Bm} seemed easier than any other geometric characteristics of the blade erosion wear of the real turbine blade profiles.

To cope with the large number of the experimental data $Z_{ij} \equiv \eta_{Bmij}$ (i = for the time instant τ_i of the turbine inspection, j = for the number of measured values in an inspected blade row) the statistics was used. Assuming linear regression relationships, one obtains

$$\hat{Z} = \hat{a} + \hat{b}(z - \bar{z}). \tag{10}$$

Regression parameters are estimated by means of the formulae

$$\bar{z}_i = \frac{\sum_{i=1}^{\tilde{m}} \tilde{n}_i \cdot z_i}{\sum_{i=1}^{\tilde{m}} \tilde{n}_i}; \tag{11}$$

$$\hat{a} = \bar{Z} = \frac{\sum_{i=1}^{\tilde{m}} \tilde{n}_i \bar{Z}_i}{\sum_{i=1}^{\tilde{m}} \tilde{n}_i}; \tag{12}$$

$$\hat{b} = \frac{\sum_{i=1}^{\tilde{m}} \tilde{n}_i (z_i - \bar{z}) \bar{Z}_i}{\sum_{i=1}^{\tilde{m}} \tilde{n}_i (z_i - \bar{z})^2}; \tag{13}$$

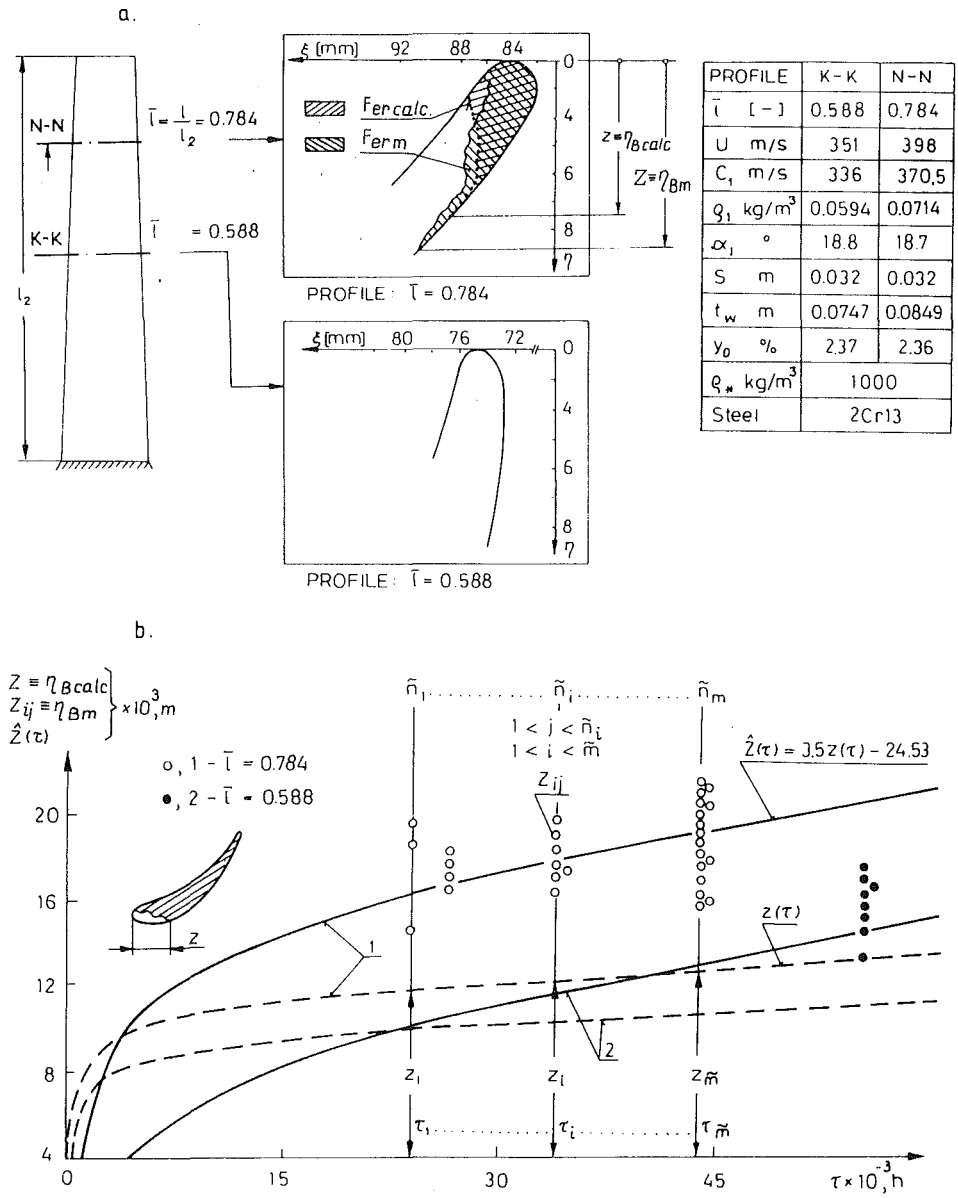

PROFILE	K-K	N-N
$\bar{l}$ [-]	0.588	0.784
U m/s	351	398
C_1 m/s	336	370.5
ϱ_1 kg/m^3	0.0594	0.0714
α_1 °	18.8	18.7
S m	0.032	0.032
t_w m	0.0747	0.0849
y_0 %	2.37	2.36
ϱ_* kg/m^3	1000	
Steel	2Cr13	

Fig. 7 Verification of the model of erosion prediction: (*a*) geometry of the stage and profiles investigated and flow parameters; (*b*) nomenclature of the verification: experimental data (○, •) Z_{ij}, (Szprengiel, 1985), the results of erosion prognosis (– – –) $z(\tau)$ and its regression analysis (——) $\hat{Z}(\tau)$, for two rotor blade profiles of a 200 MW steam turbine

resulting from the least-squares approach with the symbol $\overline{Z}_i$ standing for

$$\overline{Z}_i = \frac{\sum_{i=1}^{\tilde{m}} Z_{ij}}{\tilde{n}_i}. \tag{14}$$

The notation used is explained in Fig. 7.

Verification of the linear regression curve hypothesis is carried out by means of a dispersion coefficient

$$F = S_2^2 / S_1^2; \tag{15}$$

where

S_1^2 = mean selective conditional dispersion

S_2^2 = dispersion around the empirical regression line.

Assuming that dispersion conditions of a random quantity do not depend on the nonrandom quantity value, the S_1^2 and S_2^2 quantities appearing in Eq. (15) are estimated from the relationships

$$S_1^2 = \frac{\sum_{i=1}^{\tilde{m}} \sum_{j=1}^{\tilde{n}_i} (Z_{ij} - \overline{Z}_i)}{\sum_{i=1}^{\tilde{m}} \tilde{n}_i - \tilde{m}}; \tag{16}$$

$$S_2^2 = \frac{\sum_{i=1}^{\tilde{m}} \tilde{n}_i (\overline{Z}_i - \hat{Z}_i)^2}{\tilde{m} - 2}; \tag{17}$$

Assuming further a value of γ we obtain for the numbers of degrees of freedom

$$\tilde{k}_1 = \sum_{i=1}^{\tilde{m}} \tilde{n}_i - \tilde{m} \text{ and } \tilde{k}_2 = \tilde{m} - 2;$$

a corresponding critical value of the dispersion coefficient F_γ (e.g., Stepanov, 1985). If the inequality

Table 1 Regression analysis of full-scale test results of erosion wear characteristics of a rotor blade profile ($\bar{l}=0.784$) of the last stage of a 200 MW turbine

i	$t_{\text{inc},i}$, h	$Z_{i,j}$, mm	$\tilde{n}_i$	z_i, mm	$\tilde{n}_i \cdot z_i$	$\bar{Z}_i$	$\tilde{n}_i \cdot \bar{Z}_i$	$\tilde{n}_i(z_i-\bar{z})^2$	$\tilde{n}_i(z_i-\bar{z})\bar{Z}_i$	$\sum_{j=1}^{\tilde{n}_i}(Z_{i,j}-Z_i)^2$	$\hat{Z}_i$	$\tilde{n}_i(\bar{Z}_i-\hat{Z}_i)^2$
1	2.4×10^4	14.5 18.4 19.4	3	11.6	34.8	17.43	52.3	0.81	−27.2	13.41	16.07	5.55
2	2.65×10^4	16.2 17 17.4 17.8	4	12.0	48	17.1	68.4	0.056	−8.21	1.4	17.47	0.55
3	3.4×10^4	16 16.6 17.2 17.8 19 19.4	6	12.2	73.2	17.67	106.0	0.038	8.48	9.16	18.17	1.5
4	4.4×10^4	15.8 17.8 18.5 19.2 20.4 21.6	6	12.4	74.4	18.88	113.2	0.468	37.71	20.6	18.87	$6\ 10^{-4}$
			19		230.4		339.9	1.37	4.78	44.57		7.6

Table 2 Regression analysis of full-scale test results of erosion wear characteristics of a rotor blade profile ($\bar{l}=0.784$) of the last stage of a 200 MW turbine (calculation of boundaries of the region of 95 percent confidence)

z	$\hat{Z}$	$S_{\hat{b}}^2(z-\bar{z})^2$	$S_{\hat{Z}}^2$	$S_{\hat{Z}}$	$t_{\gamma,\tilde{k}} \cdot S_{\hat{Z}}$	$\hat{Z}-t_{\gamma,\tilde{k}} \cdot S_{\hat{Z}}$	$\hat{Z}+t_{\gamma,\tilde{k}} \cdot S_{\hat{Z}}$
10	10.47	10.1	10.26	3.2	6.75	3.72	17.22
12	17.5	0.032	0.192	0.437	0.925	16.6	18.4
15	28	18.6	18.76	4.33	9.15	18.85	37.15

$$F \le F_\gamma \tag{18}$$

holds then the use of relationship (10) is justified. In such a case the dispersions S_1^2 and S_2^2 can be replaced by an estimate

$$S^2 = \frac{\left(\sum_{i=1}^{\tilde{m}} \tilde{n}_i - \tilde{m}\right) S_1^2 + (\tilde{m}-2) S_2^2}{\left(\sum_{i=1}^{m} \tilde{n}_i - \tilde{m}\right) + (\tilde{m}-2)}, \tag{19}$$

allowing us to assess the dispersions

$$S_{\hat{a}}^2 = \frac{S^2}{\sum_{i=1}^{\tilde{m}} \tilde{n}_i}, \tag{20}$$

$$S_{\hat{b}}^2 = \frac{S^2}{\sum_{i=1}^{\tilde{m}} \tilde{n}_i (z_i-\bar{z})^2}, \tag{21}$$

$$S_{\hat{z}}^2 = S_{\hat{a}}^2 + S_{\hat{b}}^2 (z-\bar{z})^2, \tag{22}$$

of $\hat{a}$ and $\hat{b}$ parameters of the empirical regression line (10) as well as that of the Z value, respectively. The hypothesis on functional correlation between the actual wear Z and the model wear z can be verified by means of the Student criterion, which requires calculating

$$t = \hat{b}/S_{\hat{b}}; \tag{23}$$

to be compared with the γ-limit of the $t_{\gamma,\tilde{k}}$ Student distribution with prescribed number of freedom degrees

$$\tilde{k} = \sum_{i=1}^{\tilde{m}} \tilde{n}_i - 2.$$

If the inequality

$$|t| \ge t_{\gamma,\tilde{k}} \tag{24}$$

holds, then the conclusion on a significant influence of z on the value of the actual wear Z is correct. By taking account of the results obtained from Eqs. (20)–(22) the confidence interval limits of the theoretical regression line parameters and those of the integral mean value can be found from the formulae

$$\left.\begin{aligned} \hat{a}-t_{\gamma,\tilde{k}} \cdot S_{\hat{a}} < \alpha < \hat{a}+t_{\gamma,\tilde{k}} \cdot S_{\hat{a}}, \\ \hat{b}-t_{\gamma,\tilde{k}} \cdot S_{\hat{b}} < \beta < \hat{b}+t_{\gamma,\tilde{k}} \cdot S_{\hat{b}}, \\ \hat{Z}-t_{\gamma,\tilde{k}} \cdot S_{\hat{Z}} < Z < \hat{Z}+t_{\gamma,\tilde{k}} \cdot S_{\hat{Z}}, \end{aligned}\right\} \tag{25}$$

We shall consider as an example identification of the erosion model of inlet rotor blade edges of the last stage of a 200 MW turbine basing on the field observation of wear zone development at the $\bar{l}=0.784$ section. Some stage parameters used in the calculation are summarized in Fig. 7. The regression analysis of results of erosion wear characteristic field investigation is shown in Tables 1 and 2. Evaluation of the regression parameters, carried out according to Eqs. (11)–(13), yields the following results:

$$\bar{z}=12.12, \quad \hat{a}=17.89, \quad \hat{b}=3.5$$

Hence, the empirical regression curve takes the form

$$\hat{Z} = -24.53 + 3.5z \tag{26}$$

In order to verify the hypothesis on the regression curve linearity we shall evaluate the dispersion coefficient (15).

There is $S_1^2=2.97$, $S_2^2=3.8$, and $F=1.28$. The critical value of this coefficient for $\gamma=0.05$ and the number of degrees of freedom equal to $\tilde{k}_1=2$ and $\tilde{k}_2=15$ is $F_\gamma=3.69$, which according to inequality (18) confirms a linear dependence. Further on, we carry out a general evaluation of the conditional dispersion and that of the regression line parameters dispersion

$$S^2=3.07, \quad S_{\hat{a}}^2=0.16, \quad S_{\hat{b}}^2=2.24.$$

The quantity t is calculated from formula (23) and compared with the γ-limit of the $t_{\gamma,\tilde{k}}$ Student distribution for $\gamma=0.05$ and $\tilde{k}=17$. Hence, we obtain $2.34>2.11$, which allows us to conclude one correlation existing between the quantities considered.

Figure 7 shows results of processing the experimental data on erosive damage zone development in the $\bar{l}=0.784$ section of the last stage in a 200 MW turbine by means of Eq. (26). The same regression equation has been applied to prediction of the inlet edge erosion dynamics at the $\bar{l}=0.588$ section of

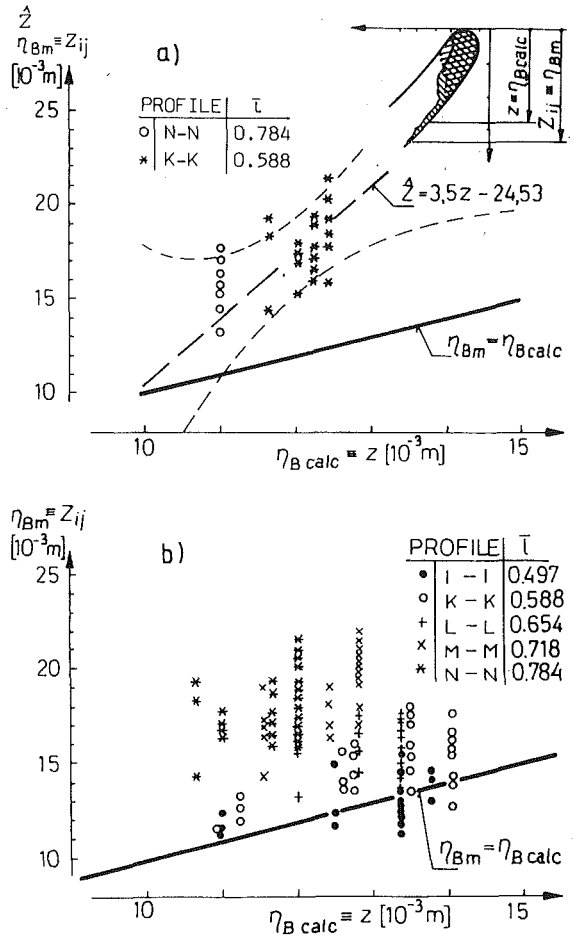

Fig. 8 Empirical regression relation for erosion zone width of the rotor blade profiles of the last stage of a 200 MW turbine: (*a*) IPM prognosis for two profiles; (*b*) IF-FM prognosis for five profiles:
——— line of perfect agreement between $\hat{Z}$ and z
— — — linear regression line
- - - - - - line of 95 percent confidence limits
•, ○, +... etc experimental data $Z_{ij} \equiv \eta_{Bm}$

the rotor blade investigated. Based on the field investigations data shown in the figure it is possible to conclude a satisfactory coincidence between the regression lines and experimental results.

The empirical regression line $\hat{Z} = f(z)$ and the boundary of the 95 percent confidence area are shown in Fig. 8(*a*) together with the Z_{ij} versus z values as calculated for two profiles using the IPM approach and measurement results published by Szprengiel (1985). In Fig. 8(*b*) the IF-FM calculations of the $\eta_{Bcalc} \equiv z$ quantity are put together with the experimental quantities $\eta_{Bm} \equiv Z_{ij}$. Results referring to five profiles applied in a 200 MW turbine of the same type are shown here.

Commenting on the results obtained, the following can be said:

- Apparently the prognosis of IPM underestimates the erosion zone width in particular for high η_{Bcalc} values. For low η_{Bcalc} the agreement between the calculated erosion zone width and measured seems satisfactory. One comes to a similar conclusion analyzing the IF-FM results.
- There is not too big a difference between IF-FM and IPM predictions; it is probably because in both calculations $\tau \gg \tau_M$ and the sophistication of the IPM erosion model for $0 < \tau < \tau_M$ does not influence substantially the results of calculations.
- In view of the satisfactory statistics of agreement between $F_{er\,calc}$ and F_{erm} (Krzyżanowski, 1987, 1988) this underestimating of η_{Bcalc} as compared to η_{Bm} is somehow disappointing because η_{Bm} seemed to be the only easy accessible parameter of the erosion zone that we can see now.
- Two sources of error in measuring η_{Bm} might be indicated: the systematic shift in the position of the measuring device and subjective assessment of the localization erosion zone boundary, Fig. 9. The scatter of experimental data can be explained by the quality of the blade assembly (see Krzyżanowski, 1983).

Conclusions

1 The evolution of the erosion models ($Y = Y(\tau)$) within the last twenty years has been summarized. A new attempt of IPM to formulate a semi-phenomenological erosion model has

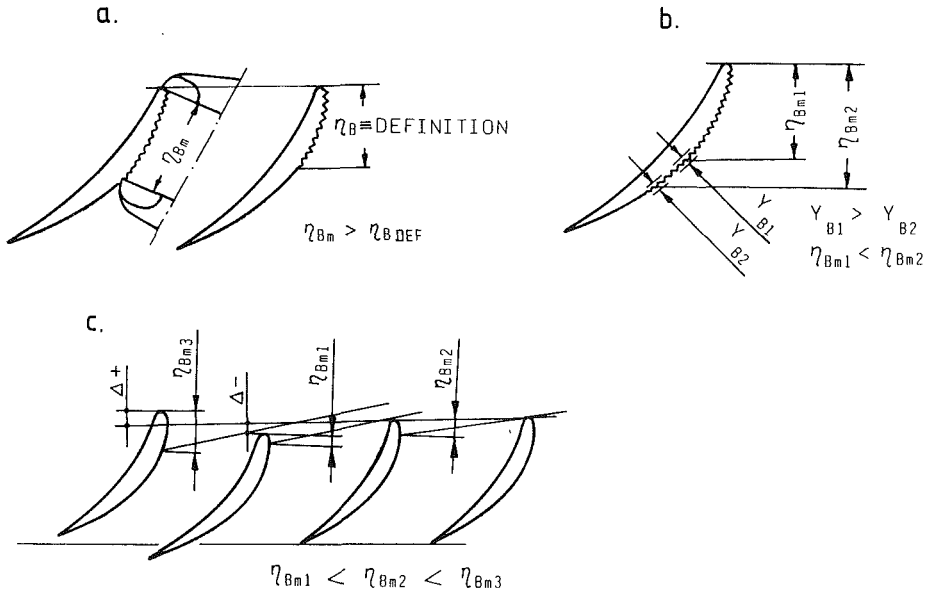

Fig. 9 Comments on accuracy of measuring the width η_{Bm} of the erosion zone: (*a*) the potential influence of the systematic shift in the position of the measuring device, (*b*) subjective assessment of the boundary of the erosion zone, (*c*) influence of the blade on assembly quality

been presented. In this model the new method of τ_{inc} calculation plays an important role.

2 Application of this model of IPM and another, phenomenological model of IF-FM has been demonstrated. Calculated results of the width of erosion zone of the rotor blade profiles of a 200 MW steam turbine have been compared with the experimental data. The originality of the IFFM/IPM approach consist in the merit that the *shape of the eroded blade profile* may be calculated as a function of time.

3 A concept of the statistical identification of the erosion prediction has been presented. The identification has been demonstrated for the width of the erosion damage zone. It can be applied, however, to any reasonable chosen parameter of the erosion pattern. The use of statistics is necessary because of a large number of experimental data and their inevitable scatter.

4 It has been proven, unfortunately, that the easily accessible dimension η_{Bm} of the eroded zone is not very well suited for verification of the predicting methods. Probable reasons for that have been indicated.

5 The verification (identification) of prediction methods of erosion are necessary because of insufficient understanding of the physics of wet steam flows in turbines. The most important factor has been indicated. This list of factors that affect the erosion prediction quality may be looked upon as a list of promising topics of further research on the subject.

6 The software for erosion prediction of steam turbine blading can be used to solve complex problems of synthesis of optimum erosion-resistant design of the low-pressure turbines as well as to diagnose the state of turbine blades from the point of view of erosion progress.

References

Beckmann, G., and Krzyżanowski, J. A., 1987, "New Model of Droplet Impact Wear," *Proc. 7th Int. Conf. on Erosion by Liquid and Solid Impact (ELSI VII)*, Cambridge Univ., Cambridge, United Kingdom.

Betekhin, V. N., and Zhurkov, S. N., 1971, "Vremennaya i temperaturnaya zavisimost prochnosti tverdykh tel," *Probl. prochnosti*, No. 2, Kiev.

Fadeev, I. P., 1974, *Eroziya vlazhnoparowykh turbin*, Mashinostroenie, Moscow.

Hammitt, F. G., Huang, Y. C., Kliang, C. L., Mitchell, T. M., and Solomon, L. P., 1970, "A Statistically Verified Model for Correlating Volume Loss Due to Cavitation or Liquid Impingement," *ASTM Special Technical Publication 474*, ASTM, Philadelphia.

Hammitt, F. G., Krzeczkowski, S., and Krzyżanowski, J. A., 1981, "Liquid Film and Droplet Stability Consideration as Applied to Wet Steam Flow," *Forschung im Ingenieurwesen*, Vol. 81, No. 1, V. D. I. Düsseldorf.

Heymann, F. J., 1967, "On the Time Dependence of the Rate of Erosion Due to Impingement or Cavitation," *ASTM Special Technical Publication 408*, ASTM, Philadelphia.

Heymann, F. J., 1968, "Erosion by Cavitation, Liquid Impingement and Solid Impingement—A Review," *Engineering Report E-1460*, Westinghouse Electric Corporation, Lester, PA.

Heymann, F. J., 1970, "Toward Quantitative Prediction of Liquid Impact Erosion," *ASTM Special Technical Publication 474*, ASTM, Philadelphia.

Heymann, F. J., 1975, "On the Prediction of Erosion in Steam Turbines," *Proc. VIth Conf. on Large Steam Turbines*, Škoda, Plzeň.

Heymann, F. J., 1979, "Conclusions From the ASTM Interlaboratory Test Program With Liquid Impact Erosion Facility," *Proc. 5th Int. Conf. on Erosion by Liquid and Solid Impact (ELSI V)*, Paper No. 20, Cambridge Univ., Cambridge, United Kingdom.

Krzyżanowski, J. A., and Weigle, B., 1974, "Toward the Criterion of Erosion Threat of Steam Turbine Blading Through the Structure of the Droplet Stream," *Proc. 3rd Sci. Conf. Steam Turbines Great Output, Gdańsk, 1974—Trans. Inst. Fluid Flow Machinery*, No. 70–72, 1976, Warszawa-Poznań.

Krzyżanowski, J. A., and Szprengiel, Z., 1978, "The Influence of Droplet Size on the Turbine Blading Erosion Hazard," ASME JOURNAL OF ENGINEERING FOR GAS TURBINES AND POWER, Vol. 100, No. 4.

Krzyżanowski, J. A., 1983, "Comments on Accuracy in Predicting Steam Turbine Blading Erosion," *Proc. 6th Int. Conf. on Erosion by Liquid and Solid Impact (ELSI VI)*, Paper No. 26, Cambridge Univ., Cambridge, United Kingdom.

Krzyżanowski, J. A., 1986, "Tropfenerosion und Erosionsschutzmassnahmen in Dampfturbinen," *Brennstoff-Wärme-Kraft*, Vol. 38, No. 12, Dez., V.D.I., Düsseldorf.

Krzyżanowski, J. A., 1987, "Experience in Predicting Steam Turbine Blading Erosion," *Proc. 7th Int. Conf. on Erosion by Liquid and Solid Impact (ELSI VII)*, Paper No. 11, Cambridge Univ., Cambridge, United Kingdom.

Krzyżanowski, J. A., 1988, "On Predicting Steam Turbine Blading Erosion and Turbine Efficiency Deterioration," ASME Paper No. 88-GT-224.

Krzyżanowski, J. A., Shubenko, L. A., and Kovalsky, A. E., 1990, "Sovershenstvovanye metodov razchota kapleudarnoy erozji rabochikh lopatok parovykh turbin," *Teploenergetika*, No. 7, Moscow.

Krzyżanowski, J. A., 1991, *Erosion of the Turbine Blading* [in Polish], Ossolineum, Wroclaw.

Poddubenko, V. V., and Yablonik, R. M., 1976, "Vliyanie struktury potoka kapel na eroziyu turbinnykh lopatok," *Izv. vuzov. Energetika*, No. 4, Byeloruss. Polyt. Inst., Minsk.

Pouchot, W. D., Heymann, F. J., et al., 1971, "Basic Investigation of Turbine Erosion Phenomena," *NASA Contractor Report*, NASA C 1830, No. 5.

Povarov, O. A., Pryskhin, V. V., Ryzhenkov, V. A., and Bodrov, A. A., 1985, "Erozionny iznos metallov pri soudarenii s kaplyami zhidkosti," *Izv. AN SSSR, Energetika i transport*, No. 4, Moscow.

Regel, V. R., Slutsker, A. I., and Tomashevsky, E. E., 1974, *Kineticheskaya priroda prochnosti tverdykh tel*, Nauka, Moscow.

Shubenko, A. L., and Kovalsky, A. E., 1987, "On Prediction of Erosion Wear of Details on the Basis of Its Kinetic Model by Impact of Liquid Drop of Polydisperse Flows of Moisture," *Proc. 7th Int. Conf. on Erosion by Liquid and Solid Impact (ELSI VII)*, Paper No. 14, Cambridge Univ., Cambridge, United Kingdom.

Shubenko-Shubin, L. A., Shubenko, A. L., and Kovalsky, A. E., 1984, "O kineticheskoi modeli razrusheniya materiala pri erozionnom vozdeistvii vlagi," *Probl. prochnosti*, No. 1, Kiev.

Shubenko-Shubin, L. A., Shubenko, A. L., and Kovalsky, A. E., 1987, "Kineticheskaya model protsessa i otsenka inkubatsionnogo perioda razrusheniya materialov, podvergaemykh vozdeistviyu kapelnykh potokov," *Teploenergetika*, No. 2, Moscow.

Springer, G. S., 1976, *Erosion by Liquid Impact*, Wiley, New York.

Staniŝa, B., Povarov, O. A., and Rizhenkov, V. A., 1985, "Osnovne zakonitosti erozije materijala lopatica parnih turbina pri sudareniju s vodenim kapljicama," *Strojarstvo*, Vol. 27, No. 6, Beogard.

Stepanov, M. N., 1985, *Statisticheskie metody obrabotki resultatov mekhanicheskikh ispytanii—Spravochnik*, Mashinostroenie, Moscow.

Szprengiel, Z., 1979, "Prognosing of the Erosion Wear of the Turbine Blade Material," [in Polish], *Zeszyty Naukowe of IFFM*, No. 55/926/79, Gdańsk.

Szprengiel, Z., and Weigle, B., 1983, "Some Results of Erosion Calculations as Applied to Steam Turbine Blading," *Proc. 6th Int. Conf. on Erosion by Liquid and Solid Impact (ELSI VI)*, Paper No. 27, Cambridge Univ., Cambridge, United Kingdom.

Szprengiel, Z., 1985, "Summary and Critical Survey of Problems and Methods of Erosion Prognosing...," [in Polish], *IFFM Report*, No. Arch. 185/85, Gdańsk.

Zhurkov, S. N., 1967, "Kineticheskaya kontseptsiya prochnosti tverdykh tel (termofluktuatsionny mekhanism razrusheniya)," *Izv. AN SSSR, Neorganicheskie materialy*, Vol. 3, No. 10, Moscow.